



# Konya Mühendislik Bilimleri Dergisi

## Konya Journal of Engineering Sciences



**(KONJES)**  
E-ISSN: 2667-8055



2023 - Cilt : 11 - Sayı : 3  
2023 - Volume : 11 - Issue : 3

**KONYA JOURNAL OF ENGINEERING SCIENCES (KONJES)  
KONYA MÜHENDİSLİK BİLİMLERİ DERGİSİ**

**HAKEMLİ DERGİDİR**

**OWNER/SAHİBİ**

Owner on Behalf of Engineering and Natural Sciences Faculty of Konya Technical University **Prof. Dr. Ali KÖKEN**  
Konya Teknik Üniversitesi Mühendislik ve Doğa Bilimleri Fakültesi Adına Dekan **Prof. Dr. Ali KÖKEN**

**Editor-in-Chief/Şef Editör**

**Prof. Dr. Mustafa TABAKCI**

**Editors/Editörler**

**Prof. Dr. Halife KODAZ**

**Assoc. Prof. Dr. Ömer Kaan BAYKAN**

**Section Editors/Alan Editörleri**

Prof. Dr. Niyazi B L M

Assoc. Prof. Dr. Farabi TEMEL

Assoc. Prof. Dr. smail NCE

Assoc. Prof. Dr. O uzhan ÖZTÜRK

**Assoc. Prof. Dr. Ömer Kaan BAYKAN**

**Assoc. Prof. Dr. Selim DO AN**

**Assoc. Prof. Dr. Sercan BÜLBÜL**

**Assoc. Prof. Dr. Volkan KALEM**

**Assist. Prof. Dr. Alper DÖYEN**

Assist. Prof. Dr. Kemal ERDO AN

Assist. Prof. Dr. Muhammed Arif EN

Assist. Prof. Dr. Muharrem Hilmi AKSOY

**Advisory Board/Danışma Kurulu**

**Prof.Dr. Ferruh YILDIZ, Konya Technical University**

**Prof.Dr. Reşat ULUSAY, Hacettepe University**

**Prof.Dr. Ibaraki SOICHI, Kyoto University**

**Prof.Dr. Matchavariani LIA, Tbilisi State University**

**Prof.Dr. Seref SAGIROGLU, Gazi University**

**Prof.Dr. Vijay P. SINGH, Texas A and M University**

**Prof.Dr.-Ing. Rudolf STAIGER, Bochum University of Applied Sciences**

**Prof.Dr. Chryssy POTSIOU, National Technical University of Athens**

**Prof.Dr. Lena HALOUNOVA, Czech Technical University**

**Prof.Dr. Petros PATIAS, The Aristotle University**

**Prof.Dr. Sitki KULUR, Istanbul Technical University**

**Language Editing/Yabancı Dil Editörü**

**Prof. Dr. Ali BERKTAY**

**Secretary/Sekreter**

Assist. Prof. Dr. Emel Zeray ÖZTÜRK

**Composition and Printing/Baskı ve Dizgi**

Assist. Prof. Dr. smail KOÇ

**Res. Assist. Emir Ali D NSEL**

**Res. Assist. Aybüke BABADA**

**Correspondance Address/ Yazışma Adresi**

Konya Teknik Üniversitesi Mühendislik ve Doğa Bilimleri Fakültesi Dekanlığı

42075-Kampüs, Selçuklu, Konya-TURKEY

Tel : 0 332 223 88 18

Fax : 0 332 241 06 35

E-mail : konjes@ktun.edu.tr

Web : <http://dergipark.org.tr/konjes>

## **Editorial Board/Yayın Kurulu**

Ahmet Afsin Kulaksiz, Konya Technical University, TURKEY

Alla Anohina-Naumeca, Riga Technical University, LATVIA

Ashok K. Mishra, Clemson University, USA

Baris Binici, Middle East Technical University, TURKEY

Coskun Bayrak, University of Arkansas, USA

Demetrio Fuentes Ferrera, University of Castilla-La Mancha, SPAIN

Fahrettin Ozturk, The Petroleum Institute, UAE

Haci Murat Yilmaz, Aksaray University, TURKEY

Heinz Ruther University of Cape Town, SOUTH AFRICA

Homayoun Moghimi, Payame Noor University, IRAN

Ihsan Ozkan, Konya Technical University, TURKEY

John Trinder, The University of New South Wales, AUSTRALIA

Kerim Kocak, Konya Technical University, TURKEY

Loredana Judele, Technical University of Iasi, ROMANIA

Mohamed Bouabaz, Université 20 août 1955-Skikda, ALGERIA

Mohd Arif Wani, California State University, USA

Mortaza Yari, University of Tabriz, IRAN

Ömer Aydan, University of the Ryukyus, JAPAN

Sanchoy K. Das, New Jersey Institute of Technology, USA

Selim Dogan, Konya Technical University, TURKEY

Spase Shumka, Agricultural University of Tirana, ALBANIA

Tahira Geroeva, Baku State University, AZERBAIJAN

Vladimir Androkhonov, Novosibirsk Soil Research Institute, RUSSIA

Ali Kocak, Yildiz Technical University, TURKEY

Alpaslan Yarar, Konya Technical University, TURKEY

Ataur Rahman, University of Western Sydney, AUSTRALIA

Cihan Varol Sam Houston State University, USA

Dan Stumbea, Alexandru Ioan Cuza University of Iasi, ROMANIA

Eva Burgetova, Czech Technical University, CZECH REPUBLIC

Georgieva Lilia, Heriot-Watt University, UNITED KINGDOM

Halil Kursad Ersoy, Konya Technical University, TURKEY

Hi-Ryong Byun, Pukyong National University, SOUTH KOREA

Huseyin Devenci, Konya Technical University, TURKEY

Iraida Samofalova, Perm University, RUSSIA

Juan Maria Menendez Aguado, University of de Oviedo, SPAIN

Laramie Vance Potts, New Jersey Institute of Technology, USA

Mila Koeva, University of Twente, NETHERLANDS

Mohamed Metwaly Abu Anbar, Tanta University, EGYPT

Moonis Ali Khan, King Saud University, KSA

Murat Karakus, University of Adelaide, AUSTRALIA

Saadettin Erhan Kesen, Konya Technical University, TURKEY

Selcuk Kursat Isleyen, Gazi University, TURKEY

Shukri Maxhuni, Prizen University, KOSOVA REPUBLIC

Syed Tufail Hussain Sherazi, University of Sindh, PAKISTAN

Thomas Niedoba, AGH University of Science and Technology, POLAND

Zoran Sapuric, University American College Skopje, MACEDONIA

**KONYA MÜHENDİSLİK BİLİMLERİ DERGİSİ**  
**Konya Journal of Engineering Sciences**  
**(KONJES)**

ISSN 2667 – 8055 (Elektronik/Electronic)

---

Cilt	11	Eylül	2023	Sayı	3
Volume	11	September	2023	Issue	3

---

**İÇİNDEKİLER (CONTENTS)**

**Araştırma Makalesi (Research Article)**

**FEATURES OF THE HAJAR AL-ASWAD, BLACK STONE OF MAKKAH, SAUDI ARABIA**

Kerim KOCAK ..... 601-609

**A DISCRETE PARTICLE SWARM ALGORITHM WITH SYMMETRY METHODS FOR DISCRETE OPTIMIZATION PROBLEMS**

Emine BAŞ, Gülnur YILDIZDAN ..... 610-634

**KİL MİNERALLERİNİN KÖMÜRÜN FLOTASYON PERFORMANSINA VE ORTALAMA KABARCIK BOYUTUNA ETKİSİ**

Effect of Clay Minerals on the Flotation Performance of Coal and Mean Bubble Size

Vildan ÖNEN, Ayşe Zeynep ÇAĞLAR, Hasan Ali TANER ..... 635-644

**NUMERICAL ANALYSES OF THERMAL PERFORMANCES OF THE CONVENTIONAL AND THE IMMERSION COOLING METHODS FOR LITHIUM-ION BATTERY PACKS**

Furkan ERGUL, Kenan TUFEKCI ..... 645-659

**DATA INTEGRITY AND QUALITY ANALYSIS OF LOW COST ZED-F9P U-BLOX GNSS RECEIVER**

Sermet OGUTCU, Salih ALCAY, Huseyin DUMAN, Behlül NUMAN OZDEMİR, Ulkunur KORAY

..... 660-667

**EFFECT OF ORANGE PEEL ESSENTIAL OIL ON THE PROPERTIES OF CHITOSAN: GELATIN CASTED FILMS PREPARED FOR ACTIVE PACKAGING**

Fatma DEMİR, Gülden GÖKŞEN, Didem DEMİR KARAKUŞ ..... 668-677

**PRODUCTION OF OXIDE DISPERSION STRENGTHENED INCONEL 718 ALLOYS USING CONVENTIONAL POWDER METALLURGY AND ADDITIVE MANUFACTURING METHODS**

Eda AYDOĞAN ..... 678-692

**HADİM NAPI ALT-ORTA VİZEYEN İSTİFİNİN MİKROFASİYES VE BİYOFASİYES ÖZELLİKLERİ (ORTA TOROSLAR, GÜNEY TÜRKİYE)**

Microfacies and Biofacies Properties of the Lower-Middle Visean Succession of Hadim Nappe (Central Taurides, Southern TÜRKİYE)

Melikan AKBAŞ ..... 693-705

<b>DETERMINATION OF RESWELLING PROPERTIES AND WATER DIFFUSION MECHANISM OF HYDROGEL COMPOSITES</b> Mehmet YURTTADUR, Gülcihan GÜZEL KAYA, Hüseyin DEVECİ .....	706-714
<b>MODELLING APPROACH FOR ENERGY DEMAND AND CONSUMPTION USING GENERALIZED LINEAR MODELS</b> Fuad ALHAJ OMAR .....	715-729
<b>MODEL REFERANS UYARLAMALI PID DENETLEYİCİ TASARIMI VE DENETLEYİCİ PARAMETRELERİNİN SİSTEM DAVRANIŞINA ETKİ ANALİZİ: DC MOTOR KONUM KONTROLÜ</b> Model Reference Adaptive PID Controller Design and Analysis of the Impact of Controller Parameters on System Behavior: DC Motor Position Control Akif YAVUZSOY, Hüseyin SARGIN, Tuğçe YAREN, Selçuk KIZIR .....	730-747
<b>PHENYLETHYLAMINE DERIVATIVE OF CALIX[4]ARENE SCHIFF BASE FOR FLUOROMETRIC DETECTION OF ZINC ION</b> Egemen OZCELIK, Clever NG'ANDU, Begum TABAKCI, Mustafa TABAKCI .....	748-757
<b>IMPROVEMENT OF HEAT AFFECTED ZONE OF GTAWed 5754 ALUMINUM ALLOY WITH FSP</b> Fatih KAHRAMAN, Gökçe Mehmet GENÇER, Coşkun YOLCU .....	758-769
<b>ENHANCED OSTEOGENIC DIFFERENTIATION OF HUMAN MESENCHYMAL STEM CELLS BY FLEXIBLE <math>\beta</math>-TCP/PLA BONE GRAFTS WITH SILICATE ADDITIVE</b> Günnur ONAK PULAT, Gülşah SUNAL, Ozan KARAMAN .....	770-782
<b>DETERMINING THE MOST POWERFUL FEATURES IN THE DESIGN OF AN AUTOMATIC SLEEP STAGING SYSTEM</b> Seral ÖZŞEN, Yasin KOCA, Gülay TEZEL, Sena ÇEPER, Serkan KÜÇÜKTÜRK, Hülya VATANSEV .....	783-800
<b>OPTIMAL LOCATION OF ACTION POTENTIAL GENERATION BASED ON ACTIVATION FUNCTION USING COMPUTATIONAL MODELLING</b> Enver SALKIM .....	801-811
<b>BELEDİYE OTOBÜSLERİNİN YHT İSTASYONU İÇİN İLÇE GÜZERGÂHLARININ ÇKKV İLE BELİRLENMESİ: KIRIKKALE İLİ ÖRNEĞİ</b> Determination of District Routes of Municipal Buses for YHT Station with MCDM: The Case of Kirikkale Province Buse BAYRAM, Mert KARA, Rabia YUMUŞAK, Ahmet CÜREBAL, Tamer EREN .....	812-830
<b>NEW METRIC FOR THE CALCULATION OF SENSITIVITY ANALYSIS INDEX OF FLEXIBLE PAVEMENT USING MECHANISTIC-EMPIRICAL APPROACH, TURKEY-CASE STUDY</b> Saadoon Obaid EYADA, Osman Nuri ÇELİK, Nibras Y. ABDULLA .....	831-870
<b>THE EMPIRICAL STABILITY EVALUATION OF THE KÖRÜKINI CAVE, DEREBUCAK, KONYA</b> Ali Ferat BAYRAM, Naji Saleh AL-QUBALI .....	871-879
<b>COMPARISON OF INNOVATIVE TREND ANALYSIS METHODS FOR HYDROMETEOROLOGICAL PARAMETERS IN THE KARASU SUB-BASIN</b> Cihangir KÖYCEÇİZ, Meral BÜYÜKYILDIZ .....	880-893



## FEATURES OF THE HAJAR AL-ASWAD, BLACK STONE OF MAKKAH, SAUDI ARABIA

Kerim KOÇAK 

*Konya Technical University, Engineering and Natural Science Faculty, Geological Engineering Department,  
Konya, TÜRKİYE*  
[kkocak@ktun.edu.tr](mailto:kkocak@ktun.edu.tr)

### *Highlights*

- The Black Stone is possibly the most respected rock in the whole world, but its features and origin has not been constrained very well.
- The size of gravel and its constituents in the Black stone of Kaaba were determined by an image process software. Modal mineralogical composition of the Kaaba stone in Edirne was also determined, with the size of its minerals.
- It is suggested that the Stone in Edirne could be from the Yemeni Corner of Kaaba originated from Makkah batholith, and different from those of İstanbul and Kaaba based on its colour and texture the origin of the black stone remains the subject of speculation due to a lack of analyses of modern scientific techniques



## FEATURES OF THE HAJAR AL-ASWAD, BLACK STONE OF MAKKAH, SAUDI ARABIA

Kerim KOÇAK

*Konya Technical University, Engineering and Natural Science Faculty, Geological Engineering Department,  
Konya, TÜRKİYE  
kkocak@ktun.edu.tr*

(Geliş/Received: 29.01.2023; Kabul/Accepted in Revised Form: 24.04.2023)

**ABSTRACT:** The Black Stone is composed of several dark-coloured gravels (9.7-27 mm) held together by a silver frame in the eastern wall of the Kaaba (Makkah). It contains long prismatic white crystal (0.64-1.11 mm) and short prismatic black (0.33-0.85 mm in length) crystal in an equigranular texture. Six and one additional pieces of the Black Stone are claimed to be in Istanbul and Edirne, Turkey. The stone of Edirne is composed of quartz (0.45-6.57 mm, 47.02 %), white plagioclase (0.81-2.97 mm, 38.49 %) and black amphibole (0.9-2.43 mm, 14.49 %) crystals in a coarse-grained texture, with the composition of tonalite. It is suggested that the stone could be from the Yemeni Corner of Kaaba originated from Makkah batholith, and different from those of İstanbul and Kaaba based on its colour and texture. In the whole world, the Black Stone is possibly the most respected rock believed to be as old as Adam and Eve, and an "Object from Heaven". It is suggested to be glass, granite, agate, pseudometeorite or most popularly stony meteorite. But the origin of the black stone remains the subject of speculation due to a lack of analyses of modern scientific techniques.

*Keywords: Hajar Al-Aswad, Meteorite, Kaaba, Makkah*

### 1. INTRODUCTION

The Hajar al-Aswad is located on the eastern wall of the Ka'ba in the centre of the Grand Mosque, Islam's most important mosque, in Makkah, Saudi Arabia. It is named as "Object from Heaven, Star of the Paradise and The Black Stone". It contains seven or eight small black pieces of distinct rock cemented together and encased in a silver frame, which leaves an area of [1] ~30 cm in diameter, 1.5 meters above the ground (Figure 1-2).

Besides, six and one additional pieces are believed to be in Istanbul and Edirne, Turkey; four are exhibited in the Sokollu Mehmet Pasha Mosque (Figure 3), one in the mihrab of the Blue Mosque (Figure 4), and one above the entrance of the tomb of Sulaiman the Magnificent (Figure 5). During the preservation of Hacer-ül Esved stone was being renovated, pieces with a total length of 10 cm were torn off from its edges and used in the Sokullu Mehmet Pasha Mosque in Istanbul, which completed its construction in 1571. A sample exists in the Grand Mosque in Edirne (Figure 6), Northwestern Turkey. The Black Stone is considered to be as old as Adam and Eve, and "Object from Heaven", to serve as the world's first temple, Ka'ba. Muslims traditionally kiss or touch the stone during their pilgrimage to Makkah, known as the Hajj and Umrah. It is considered to be a representation of the unity of all Muslims and one of the most important symbols of Islam. The stone is also possibly the most revered rock in the world. Though various origins have been suggested for the stone; from granite through agate and most likely a stony meteorite, its features and origin is still subject to speculation. Thus, it is aimed to characterize the Black stone, both in Makkah and in Turkey in the light of previous studies with its macroscopic features.



**Figure 1.** Black stone in Kaaba.

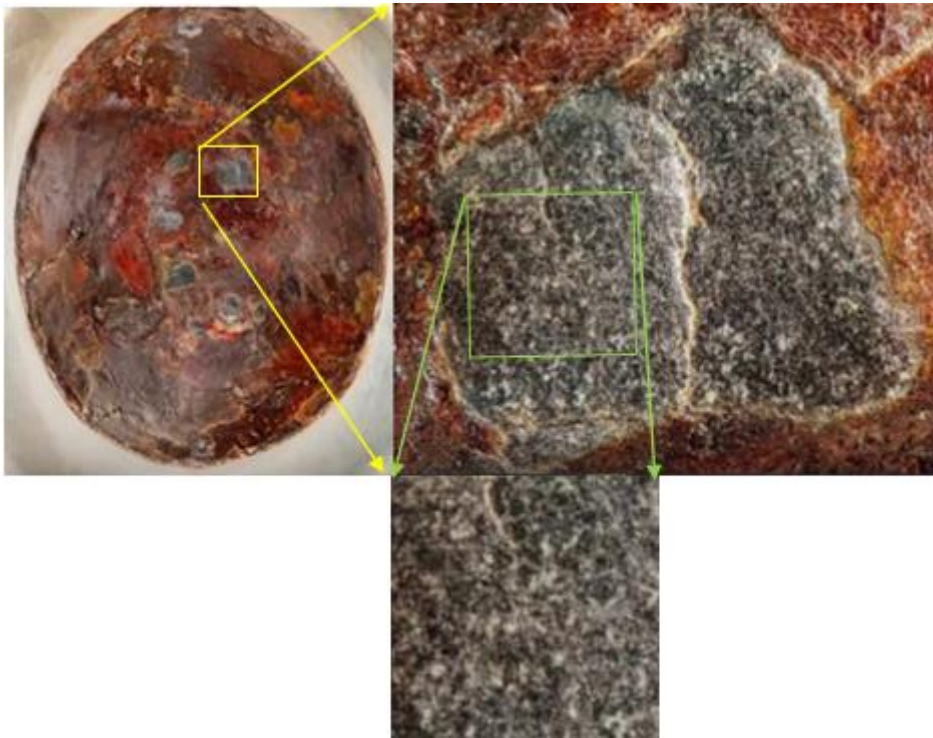


**Figure 2.** Photograph of the Black stone

## 2. MATERIAL AND METHOD

The Black stone in Kaaba is the most sacred object in Islam, hence no sample is available to study on. But the detailed pictures of the Black Stone taken by Saudi Government, and that of the stones in Istanbul and Edirne evaluated on the light of the previous studies. An image processing software (Kameram



1.6.1.3) is applied to the Black stone in Kaaba to determine the size of gravels and their crystals. The software was also applied to the Edirne sample to measure the sizes of its constituents and to constrain its modal mineralogical composition.



**Figure 3.** The Sokollu Mehmet Pasa Mosque

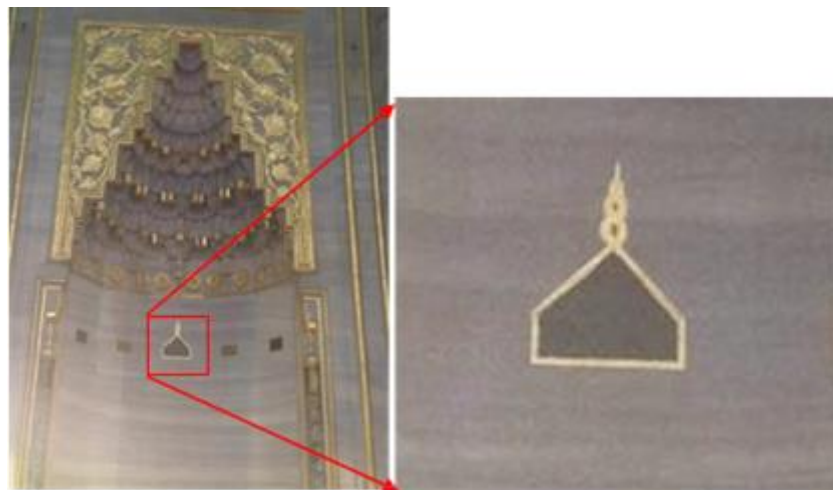


**Figure 4.** Blue Mosque.

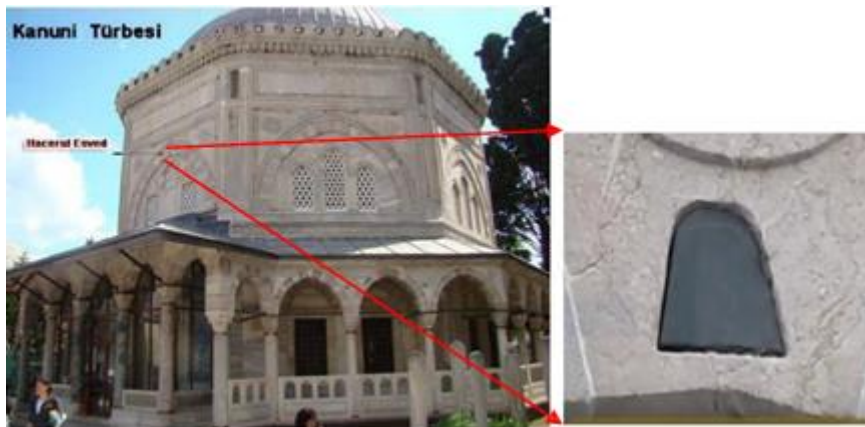


Figure 5. The tomb of Sulaiman the Magnificent

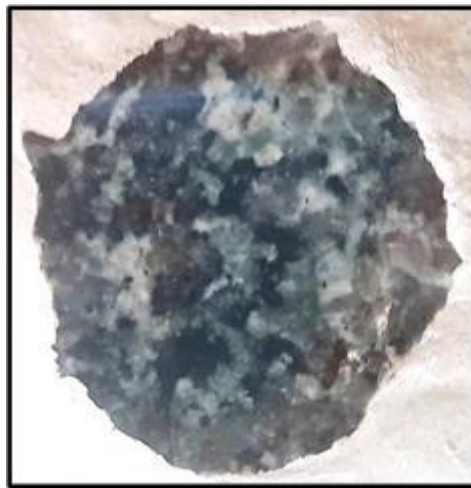
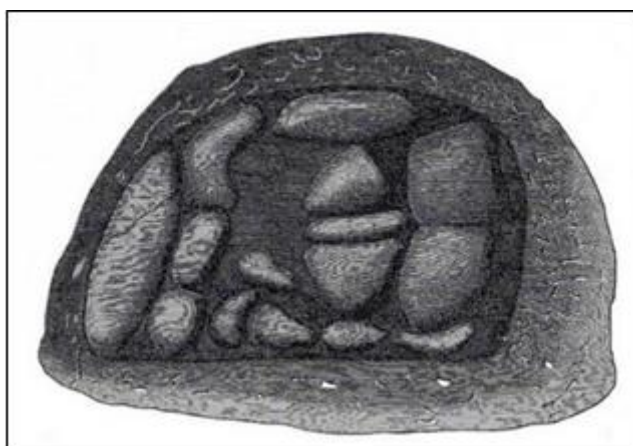


Figure 6. Kaaba stone from the old mosque in Edirne. The figure has a diameter of ~4.5 cm.

### 3.HISTORY

The Hajar al-Aswad was originally a complete stone. The Islamic prophet Muhammad even placed the stone as one piece into the Kaaba's wall in 605. However, the stone suffered from considerable damage over with time; cracked, repaired, stolen and even burnt: The stone was broken into three pieces by a fire during the Umayyad Caliphate's siege of Makkah in 683 [3]. From Bahrain, Qarmatian warriors led by Abu Tahir al-Qarmati stole the Hajar al-Aswad in 930, kept it in all-Hasa, (Medieval Bahrein) and restored to its original location after twenty-three years, which induce breaking the stone into seven pieces [4]. The Kaaba was burned at an early date, and the stone may have broken into three pieces. The stone included 15 pieces in 1825 [al-Kurdi, 1875; in [5]] (Figure 7). Therefore, the missing pieces can be covered with cement from previous restorations, or they might be lost. Because of this, it is challenging to describe the Stone's original shape and dimensions, but it may be assumed that they were at least 25 X 20 X 20 cm [1]. The Kaaba was burned during Mohammed's rule, between A.D. 570 and A.D. 632, which may have caused the stone to break in A.D. 1050. A man of Al-Mustansir Billah, Egyptian caliph broke to numerous minor pieces in A.D. 1050. In 1626, Mecca was seriously flooded, leading to the fall of three of the walls of the Kaaba [6].



**Figure 7.** Views of the Black stone's front and side with ~ 16 cm by 10 cm in size [7].

The Black Stone was first pointed out in Western literature by European travellers to Arabia, who visited the Kaaba in the 19th and early 20th centuries. Johann Ludwig Burckhardt visited Makkah and described the stone in 1814 [6] as irregularly shaped oval Hajar Aswad, and about eighteen cm diameter with irregular surfaces. In 1817, Ritter von Laurin had a chance to inspect a fragment of the Stone, which was removed by Muḥammad 'Alī Bāshā, viceroy of Egypt [8]. He described that it had a pitch-black exterior and a silver-grey, fine-grained interior in which tiny cubes of a bottle-green material were embedded. Thomas E. Lawrence, known as Lawrence of Arabia (1888-1935), had a chance to visit Kaaba [9].

#### 4. FEATURES AND ORIGIN OF THE BLACK STONE

The stone is reported to have blackish and brownish colours. Its matrix is coloured like coal, according to "Ali Bey" [1816 in [7]]. Furthermore, the matrix contains scattered white and yellow spots, tiny, pointed crystals, and maybe feldspar phenocrysts (e.g. [5-7, 10]). However, it is problematic to define its colour as it is composed of various broken pieces. Dietz and McHone [5] point out that the stone is hummocky and "muscled," which demonstrates to considerable hardness, possibly Mohs 7, since the touches of millions of hands have not worn away the stone. The stone has mirror-like luster produced by rubbing, suggesting an aphanitic texture. Detailed picture of the stone (Figure 2) has been revealed first time in 2021 by the Saudi government. It was obtained by the focus stacking method [2] after taking more than 50 hours and producing images that were up to 49.000 megapixels in size. Using an image processing software (Kameram 1.6.1.3), the size of the gravels and its constituents were measured in the Kaaba stone. Figure 2 clearly shows various gravels (9.7-27 mm) and short prismatic black crystals (0.33-0.85 mm in length) in a brownish to reddish cement. It also shows that the stone appears to have an equigranular texture, excluding a volcanic origin.

In general, dark color is observed in all black stones from both Kaaba, and Istanbul. The Black stones in both Kaaba and Sokollu Mehmet Pasa Mosque have discernible long prismatic white crystals (0.64-1.11 mm in Kaaba), similar to plagioclase (Figure 2, Figure 3). The stone is reported to float on water [11].

Paul Partsch [12], the curator of the Austro-Hungarian imperial collection of minerals, was the first to declare the Black Stone as a meteorite stone in 1857 by extensive study. Khan [7] also considers the stone as likely a stony meteorite, and the Catalogue of Meteorites by Prior-Hey [13] lists it as a possible example. However, [5] indicate that the black stone is unlikely to be a stony meteorite as the stone floats. The stone is suggested to have high hardness, possibly Mohs 7 [5], which is also against an origin of stony meteorite. The fractured nature of the stone has also ruled out an origin of a nickel-iron meteorite [5] as nickel-iron meteorites are characterized by hard and a bit ductile structure.

Thomas E. Lawrence (1888-1935) examine the surface of the holy stone by magnifying glass hidden in his dress during pilgrimage/umra, and confirmed that the stone was granite rock, which is dark grey,

composed of mainly quartz, feldspars and mica [9]. However, the predominant dark colour of the stone is not in favour of this suggestion. [5] also point out that an anonymous, Arab geologist who had a chance to examine the stone carefully during the Hajj, explains the existence of clearly discernible diffusion banding in the stone, which points rather clearly to its being an agate [5]. However, Thomsen [1] suggests the Black Stone to be a glass fragment or impactite from the impact of a fragmented meteorite. The crystalline texture of the stone (Figure 2) however, disagrees with this suggestion.

The stone of Edirne is distinct from those of İstanbul and Kaaba, regarding its colour and texture. The composition of the sample is also constrained by modal analysis using Kameran 1.6.1.3 software based on macroscopic features. The Edirne stone contains glassy quartz (0.45-6.57 mm, 47.02 %), white plagioclase (0.81-2.97 mm, 38.49 %) and black amphibole (0.9-2.43 mm, 14.49 %) crystals in a coarse-grained texture (Figure 8), with a composition similar tonalite.

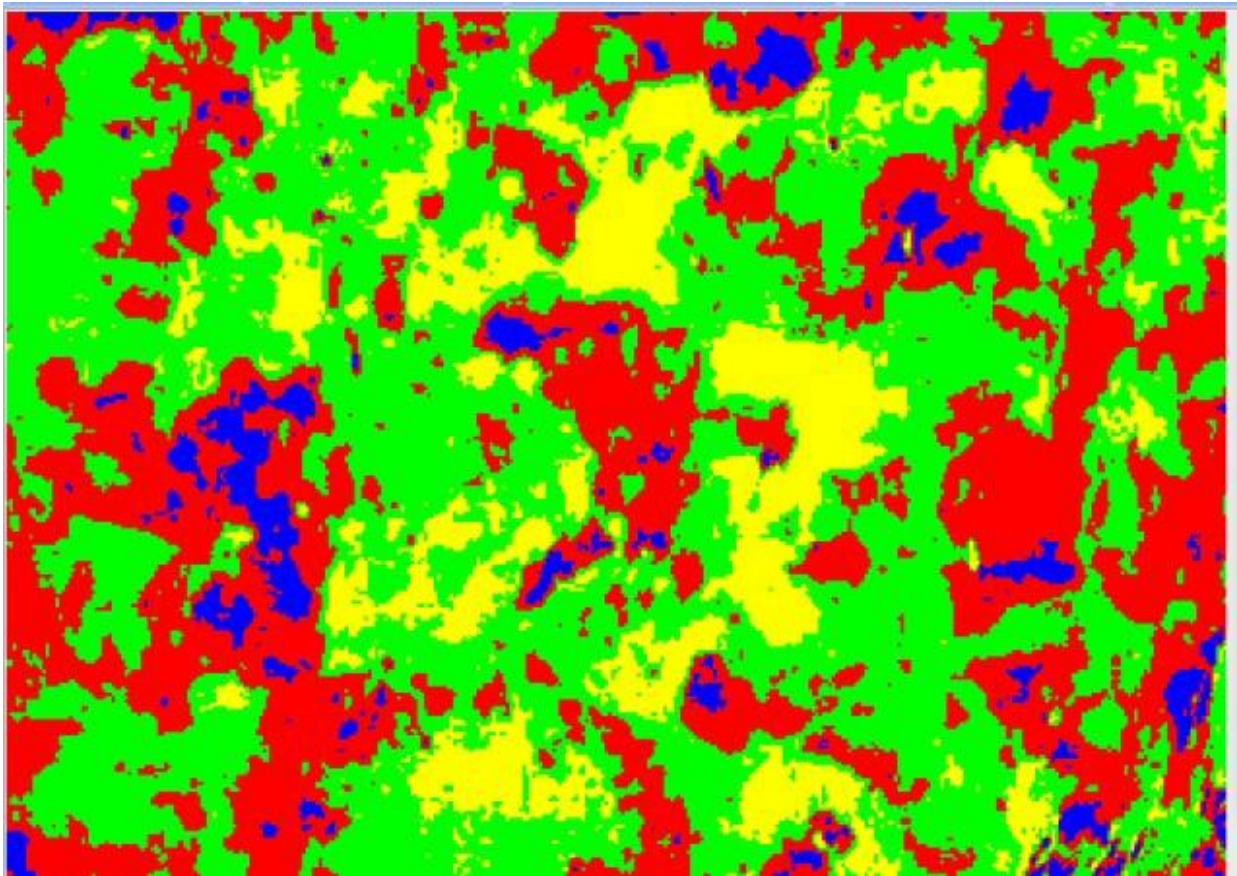


**Figure 8.** Modal analysis of the Edirne sample.; amphibole (yellow), quartz (green), plagioclase (red, blue)

## 5.DISCUSSIONS&CONCLUSIONS

Muslims consider the Black Stone as a metaphysical rather than a natural thing, therefore the meteorite suggestion is not likely to be accepted by Muslims. However, no scientific investigation exists on the basis of mineral/rock chemistry and isotopic studies on the Black Stone, its origins remain the subject of speculation.

The texture of the stone of Edirne is different from the those of Kaaba and Istanbul and show similarities to tonalite. Similarly, Bünyamin Kerçin, Imam of the Grand Mosque in Edirne, suggests that it is not from the black stone, but pieces of the Alemanni pillar, the southern corner of the Kaaba (Rük-nü Yemani, The Yemeni Corner) [14]. Figure 9 shows that the Yemeni corner may contain several types of

stones, but light coloured one (“a” in Figure 9), is similar to the stone of Edirne.



Figure 9. The Yemeni Corner. A refers the stone similar to the one in Edirne.

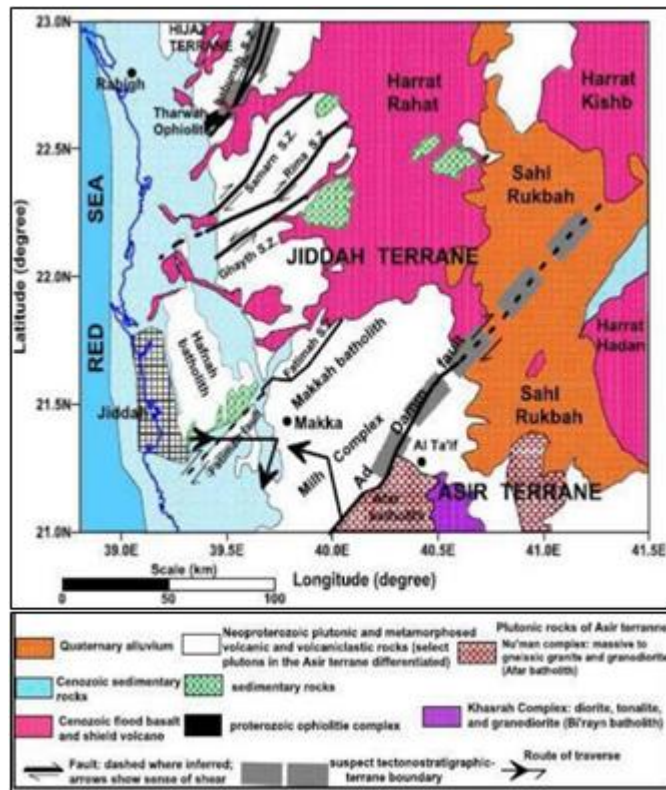


Figure 10. A Geologic map of the Makkah region [17].

Makkah city is located in the Precambrian Arabian shield, which is suggested to have ~50% plutonic and ~50% volcanic and sedimentary rocks, and that granitic rocks make up ~70% of all plutons at the surface [15].

Ju'ranah complex is exposed in the northwest of Makkah batholith (Figure 10), and composed hornblende tonalite and tonalite to granodiorite; minor biotite and biotite-hornblende tonalite [16]. Therefore, it is likely that the Edirne stone may come from the complex.

### Declaration of Ethical Standards

As the author of this study, I declare that all ethical standards have been complied with.

### Credit Authorship Contribution Statement

In this study, the author contribution rate was determined as 100%.

### Declaration of Competing Interest

As the author of this study, I declare that there are no declarations of conflict.

### Acknowledement

Thanks to A. Ayar for getting the picture from Sokollu Mehmet Pasha Mosque.

### Data Availability

This study does not contain usable data.

### REFERENCES

- [1] E. Thomsen, "New Light on the Origin of the Holy Black Stone of the Ka'ba," *Meteoritics*, vol. 15, p. 87, March 01, 1980. [Online]. Available: <https://ui.adsabs.harvard.edu/abs/1980Metic..15...87T>.
- [2] E. McSweeney and M. Salem. "The Black Stone of Mecca like you've never seen before." CNN. <https://edition.cnn.com/travel/article/saudi-arabia-black-stone-scli-intl/index.html> (accessed 4th May,2021).
- [3] H. J. Axon, "The black stone of the Ka'ba: suggestions as to its constitution," *J Mater Sci Lett*, vol. 1, no. 1, pp. 10-12, 1982/01/01 1982, doi: 10.1007/BF00724705.
- [4] S. Chopra, "Black Stone of Mecca," in *Encyclopaedia Britannica*, T. e. o. E. Britannica, Ed., ed, 2012.
- [5] R. S. Dietz and J. McHone, "Kaaba Stone: Not a meteorite, probably an agate," *Meteoritics*, vol. 9, no. 2, pp. 173-179, 1974, doi: 10.1111/j.1945-5100.1974.tb00072.x.
- [6] J. L. Burckhardt, *Travels in Arabia; comprehending an account of those territories in Hedjaz which the Mohammedans regard as sacred* 1829.
- [7] M. A. R. Khan, "On the meteoritic origin of the Black Stone of the Ka'bah.," *Popular Astronomy*, vol. 46, pp. 403-407, 1938.
- [8] J. G. Burke, *Cosmic debris : meteorites in history*. Berkeley (Calif.) [etc.: University of California Press (in English), 1986.
- [9] T. E. Lawrence, *Seven pillars of wisdom : a triumph*. (in English), 2013.
- [10] A. Sprenger, *Die alte Geographie Arabiens als Grundlage der Entwicklungsgeschichte des Semitismus*. Bern,: Commissionsverlag von Huber, 1875, p. 343 p.
- [11] H. von Maltzan, *Meine Wallfahrt nach Mekka. Reise in der Kiistengegend und im Innern von Hedschas I-II*. Leipzig: Dyk'sche Buchliand- lung, , 1865.
- [12] P. M. Partsch, *Über den schwarzen Stein in der Kaaba zu Mekka*. [Wien]: [K.K. Hof-und Staatsdruckerei] (in German), 1857.
- [13] G. T. Prior, *Catalogue of Meteorites*. London: British Museum (Nat. Hist.), 1953.
- [14] C. Demirci, "Hacer-ül Esved'in bir parçası da Edirne'de." [Online]. Available: <https://www.aa.com.tr/tr/kultur-sanat/hacer-ul-esvedin-bir-parcasi-da-edirne/842769>
- [15] M. E. Gettings, H. R. Blank Jr., W. D. Mooney, and J. H. Healey, "Crustal structure of southwestern Saudi Arabia," *Journal of Geophysical Research: Solid Earth*, vol. 91, no. B6, pp. 6491-6512, 1986, doi: <https://doi.org/10.1029/JB091iB06p06491>.

- [16] K. Abdelrahman, A. M. Alamri, N. Al-Otaibi, and M. Fnais, "Geotechnical assessment for the ground conditions in Makah Al-Mukarramah city, Saudi Arabia," *Journal of King Saud University - Science*, vol. 32, no. 3, pp. 2112-2121, 2020/04/01/ 2020, doi: <https://doi.org/10.1016/j.jksus.2020.02.011>.
- [17] P. Johnson, "Tectonic map of Saudi Arabia and adjacent areas," Ministry for Mineral Resources, 1997.



## A DISCRETE PARTICLE SWARM ALGORITHM WITH SYMMETRY METHODS FOR DISCRETE OPTIMIZATION PROBLEMS

<sup>1,\*</sup>Emine BAŞ , <sup>2</sup>Gülnur YILDIZDAN 

<sup>1</sup>Konya Technical University, Engineering and Natural Sciences Faculty, Software Engineering Department,  
Konya, TÜRKİYE

<sup>2</sup>Selcuk University Kulu Vocational School, Konya, TÜRKİYE  
[ebas@ktun.edu.tr](mailto:ebas@ktun.edu.tr), [gavsar@selcuk.edu.tr](mailto:gavsar@selcuk.edu.tr)

### Highlights

- DPSO is a discrete optimization method for discrete optimization problems.
- The DPSO has been applied to solve sixteen different TSPs taken from TSPLIB.
- The variations of the DPSO have occurred according to the selected method (DPSO1 (swap method), DPSO2 (shift method), DPSO3 (swap and shift methods), DPSO4 (symmetry method), DPSO5 (swap, shift, and symmetry methods), DPSO6 (swap, shift, symmetry, and 2-opt methods)).
- In this study, the shift and symmetry method is applied for the first time for DPSO.





## A DISCRETE PARTICLE SWARM ALGORITHM WITH SYMMETRY METHODS FOR DISCRETE OPTIMIZATION PROBLEMS

<sup>1,\*</sup>Emine BAŞ , <sup>2</sup>Gülnur YILDIZDAN 

<sup>1</sup>Konya Technical University, Engineering and Natural Sciences Faculty, Software Engineering Department, Konya, TÜRKİYE

<sup>2</sup>Selcuk University Kulu Vocational School, Konya, TÜRKİYE

<sup>1</sup>[ebas@ktun.edu.tr](mailto:ebas@ktun.edu.tr), <sup>2</sup>[gavsar@selcuk.edu.tr](mailto:gavsar@selcuk.edu.tr)

(Received: 04.11.2022; Accepted in Revised Form: 28.04.2023)

**ABSTRACT:** Particle Swarm Optimization (PSO) is a commonly used optimization to solve many problems. The PSO, which is developed for continuous optimization, is updated to solve discrete problems and Discrete PSO (DPSO) is obtained in this study. With DPSO, the Traveling Salesman Problem (TSP), which is well-known in the literature as a discrete problem, is solved. In order to improve the results, the swap method, the shift method, and the symmetry method are added to DPSO. The symmetry method is a new and successful method. The variations of the DPSO occurred according to the selected method type (DPSO1 (swap method), DPSO2 (shift method), DPSO3 (swap and shift methods), DPSO4 (symmetry method), DPSO5 (swap, shift, and symmetry methods), DPSO6 (swap, shift, symmetry, and 2-opt methods)). The effect of each method on the performance of the DPSO has been studied in detail. To demonstrate the success of the variations of the DPSO, the results are additionally compared with many well-known and new discrete algorithms in the literature. The results showed that the performance of DPSO has improved with the symmetry method and it has achieved better results than the discrete heuristic algorithms recently proposed in the literature.

**Keywords:** Swap, Shift, Symmetry, 2-OPT, Discrete Optimization, TSP

### 1. INTRODUCTION

In the literature, many researchers have either developed old methods or proposed new methods to solve problems that are difficult to solve. In recent years, metaheuristic algorithms for such problems have gained great importance due to their success. Metaheuristic algorithms are created by imitating events that exist in nature. Most metaheuristic algorithms are created by imitating the feeding, hunting, cohabitation, and similar behaviors of living creatures. Many metaheuristic algorithms have been proposed in the literature. The oldest and most frequently used of these are Particle Swarm Optimization (PSO) [1], Ant Colony Optimization (ACO) [2], and Artificial Bee Colony (ABC) [3]. These algorithms have produced solutions for many different problems in the literature. Apart from these, there are different heuristic algorithms that have been newly proposed in the literature in recent years. Some of these are as follows: Snake Optimizer (SO) has created by snakes imitating their special mating behaviors [4], War Strategy Optimization (WSO) has based on the strategic movements of army weapons during the war [5], Red Fox Optimization (RFO) has created by imitating the hunting and feeding behavior of red foxes living in nature on the snowy ground [6], etc. PSO is chosen for discrete optimization problems in this paper. PSO is a heuristic algorithm based on mimicking bird and fish foraging behavior. PSO is simple to code, has few parameters, and has a fast convergence rate [7]. That's why it has been used by many researchers to solve engineering problems. It is used in a wide range of applications, including function optimization, neural network training, fuzzy system control, classification, pattern recognition, signal processing, and robot technology [7], [8], [9], [10], [11]. Gaing has proposed the discrete Binary PSO (BPSO) method in the literature. Gaing has combined BPSO and Lambda iteration methods in the study [12]. For the feature subset selection problem, Unler and Murat have created a modified discrete PSO algorithm [13]. Strasser et al. present a PSO version that can optimize over discrete variables [14]. To solve the no-wait flow shop

\*Corresponding Author: Emine BAŞ, [ebas@ktun.edu.tr](mailto:ebas@ktun.edu.tr)

scheduling problem with both makespan and total flowtime criteria, a Discrete PSO (DPSO) algorithm is presented [15]. Izakian et al. propose a discrete PSO (DPSO) method for grid job scheduling [16].

The optimization process is the process of obtaining the best value of a problem. In the optimization process, if the search space variables take continuous values, it is called continuous optimization, and if they take discrete values, it is called discrete optimization. Due to the nature of some problems, they take discrete values. The Traveling Salesman Problem (TSP) is one such problem. The TSP is a well-known multidisciplinary problem in operations research and computer science in which the goal is to find the shortest Hamiltonian cycle (circuit) in a network of cities (cost). The problem can be described as follows, given a set of cities (nodes) and the distances between them: A salesman should visit each of the remaining cities exactly once, starting and ending in a single depot city, to minimize the salesman's total journey distance (cost). Various scholars have investigated the TSP thoroughly, and as a result, several viable solutions (shift, swap, use the 2-opt algorithm, use the 3-opt algorithm, etc.) have been proposed [17], [18], [19], [20], [21]. Osaba et al. have proposed an improved discrete version of the WCA (dubbed the DWCA) to solve the Symmetric and Asymmetric TSPs [22]. The inclination feature in DWCA improves exploration and exploitation. Choong et al. have proposed a modified choice function for the TSP as a hyper-heuristic method [23]. Dahan et al. present a TSP adaptation of the Flying Ant Colony Optimization (FACO) algorithm [24]. For the TSP, Zhong et al. have proposed a hybrid discrete artificial bee colony algorithm with a threshold acceptance criterion [25]. Gao has suggested a new ACO algorithm [26]. A strategy of combining pairs of searching ants is used in this algorithm to diversify the solution space. Dong and Cai have introduced a new genetic algorithm for large-scale colored balanced TSPs [27]. Rokbani et al. have used FPA, PSO, and ant colony optimization heuristic algorithms as a hierarchical whole within the local search mechanism for TSP in 2021 [28]. Wu et al. have proposed a novel greedy genetic sparrow search algorithm based on a sine and cosine search strategy (GGSC-SSA) for TSP in 2021 [29]. Zhang and Han have proposed a discrete sparrow search algorithm (DSSA) with a global perturbation strategy to solve the TSP [30]. Huang et al. have proposed a discrete shuffled frog-leaping algorithm for TSPs. They have designed a new individual generation operator and four improved searching strategies to improve the algorithm performance [31]. Panwar and Deep have proposed a novel discrete GWO algorithm (D-GWO) to solve complex discrete TSPs [19]. Zhang and Yang have proposed a discrete cuckoo search algorithm based on the random walk and cluster analysis to solve the TSPs [32]. Zhang et al. have proposed a Discrete Mayfly Algorithm (DMA) for solving spherical asymmetric TSP. The DMA has had inver-over operator, a crossover operator, and a 3-opt operator [33].

In this study, the PSO, which is developed for continuous optimization, is updated to solve discrete problems and Discrete PSO (DPSO) is obtained. With DPSO, TSP, which is well known in the literature as a discrete problem, is solved. In order to improve the results, the swap method, the shift method, the symmetry method, and 2-opt method are added to DPSO. The symmetry method is a newly developed and successful method [21]. The variations of the DPSO have occurred according to the selected method type (DPSO1 (swap method), DPSO2 (shift method), DPSO3 (swap and shift methods), DPSO4 (symmetry method), DPSO5 (swap, shift, and symmetry methods), DPSO6 (swap, shift, symmetry, and the 2-opt methods)). Sixteen low, medium, and large-sized TSP datasets are solved with the variations of the DPSO and the results are compared with each other. In order to demonstrate the success of the variations of the DPSO, the results are compared with many well-known and new discrete algorithms in the literature.

### 1.1. The Primary Significant Contribution of the Research

The significant distinctions between our study and previous research, as well as the major additions to the literature, are noted below.

- ✓ DPSO is a discrete optimization method for discrete optimization problems.
- ✓ DPSO produces adequate and similar TSP solutions, according to the findings of the experiments.
- ✓ The DPSO has been applied to solve sixteen different TSPs taken from TSPLIB.

- ✓ The variations of the DPSO have occurred according to the selected method (DPSO1 (swap method), DPSO2 (shift method), DPSO3 (swap and shift methods), DPSO4 (symmetry method), DPSO5 (swap, shift, and symmetry methods), DPSO6 (swap, shift, symmetry, and 2-opt methods)).
- ✓ In this study, the shift and symmetry method is applied for the first time for DPSO in the literature.
- ✓ In this study, a population size (N) and the number of candidate solutions (CS) are examined in detail. Their effects on performance are shown.
- ✓ According to the best (Min), the worst (Max), mean (Avg), standard deviation (Std), relative error, and CPU time, the TSP results show that the proposed algorithm is a viable and competitive optimizer.

In this study, the materials and methods used in the paper (PSO, DPSO, TSP, the swap method, the shift method, the symmetry method, and the 2-opt method) are explained in Section 2, and the experimental results of the variations of the DPSO are given and discussed in Section 3. In Section 4 and Section 5, the results are explained and discussed.

## 2. MATERIAL AND METHODS

### 2.1. Particle Swarm Optimization (PSO)

Particle Swarm Optimization (PSO) was modeled in 1995 and is widely used today [1]. PSO is modeled with inspiration from flocks of birds and fish. In the first stage, birds do not know where the food is and look for food in different places. Every bird is considered a particle. All particles work to find the optimum result or solutions that are close to the optimum result. Particles are placed randomly or regularly. There is information sharing between all particles. According to the information sharing, the best position is found and that movement moves in other particles. The optimum result can be reached easily and quickly by sharing information about the particles.

In the PSO, each particle represents the solution-seeking agents of the swarm. It tries to get the best position by changing the positions of search agents in the search space depending on their local and global search capabilities. Each search agent updates its *position* ( $a$ ) and *velocity* ( $vel$ ) according to Equation 1 and Equation 2. Here,  $Best$  denotes the best search agent value and  $GBest$  denotes the global best search agent value.

$$vel_{ij}(t + 1) = w * vel_{ij}(t) + k_1 rand_1 (Best_{ij}(t) - a_{ij}(t)) + k_2 rand_2 (GBest_{ij}(t) - a_{ij}(t)) \quad (1)$$

$$a_{ij}(t + 1) = a_{ij}(t) + vel_{ij}(t + 1) \quad (2)$$

where,  $vel_{ij}(t + 1)$  denotes velocities of agent in range  $[-Vel_{max}, Vel_{max}]$  ( $i$ =agent name,  $j$ =dimension name,  $t$ = iteration number).  $a_{ij}(t + 1)$  denotes positions of agent.  $w$  is the inertia weight. It is used to check the effect of previous speed history.  $k_1$  and  $k_2$  are the cognition learning factor and social learning factor.  $rand_1$  and  $rand_2$  are random numbers in range  $[0, 1]$  [1], [7]. The PSO's pseudo-code has been explained in Algorithm 1.

---

**Algorithm 1:** Pseudo-code of the PSO

---

```

1: Assign parameter values ( $c_1, c_2, w, etc.$ ) of PSO and initialize.
2: Initialize the positions of the particles randomly. (Particle:  $i=1, \dots, N$ ) (Dimension:  $j=1, \dots, D$ )
3: while ( $iter < max\_iter$ ) do
4:   Calculate the objective function for the given particles
5:   Find the value of the best particle ( $Best$ ) and find the value of the global best particle ( $GBest$ )
6:   for ( $i=1$  to  $N$ ) do
7:     for ( $j=1$  to  $D$ ) do
8:       Generate a random values between  $[0, 1]$  ( $rand_1$  and  $rand_2$ )
9:       Calculate velocities of particles with Eq. (1)
10:      Calculate positions of particles with Eq. (2)
11:     end for
12:   end for
13:    $iter=iter+1$ 
14: end while
15: The value of the global best particle

```

---

## 2.2. Discrete Particle Swarm Optimization (DPSO)

PSO is modified to solve discrete optimization problems as follows: The particles are generated as random permutations during the initialization phase. In the PSO, each dimension of the particles holds the destination city information for the TSP. These values are obtained from the continuous search space obtained in PSO. Figure 1 shows the generation of the discrete search space from the continuous search space in PSO. For example, for a TSP with 10 cities, random variable values are generated with PSO in the range of  $[1] - [10]$ . These values are rounded to integer values to make them discrete. Since each city is visited once in TSP, the variable value should not repeat. Recurring variable values are detected with DPSO and the city name that is not included in the particle is added.

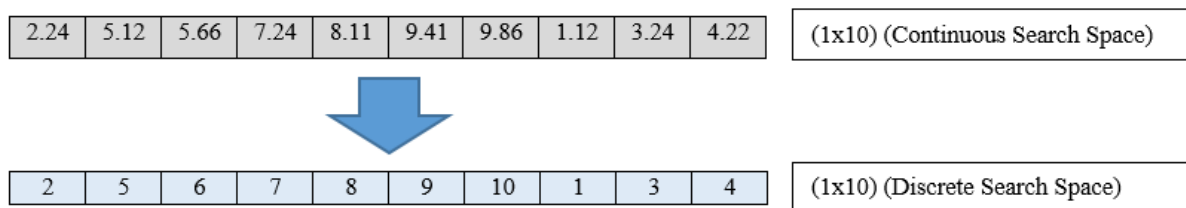


**Figure 1.** Generation of discrete search space (for DPSO) from continuous search space in PSO

The fitness value of each particle in the swarm is calculated. The individuals in the DPSO population randomly generate the city route to be visited. The resulting random route does not always perform well. Therefore, updates should be made on this route. DPSO generates candidate solutions for each particle by various methods (the swap method, the shift method, the symmetry method, and the 2-opt method). If the fitness value of the produced candidate solution is better, the current individual is replaced with the candidate solution. The swap method, the shift method, the symmetry method, and the 2-opt method are used for new candidate particles in the DPSO. The variations of the DPSO have occurred according to the selected method type (DPSO1 (swap method), DPSO2 (shift method), DPSO3 (swap and shift methods), DPSO4 (symmetry method), DPSO5 (swap, shift, and symmetry methods), DPSO6 (swap, shift, symmetry, and 2-opt methods)). The swap, shift, symmetry, and 2-opt methods are described in Section 2.3. The best solution is obtained after the termination criterion is met. The DPSO's pseudo-code is explained in Algorithm 2. Figure 2 shows the DPSO model.

**Algorithm 2:** Pseudo-code of the DPSO

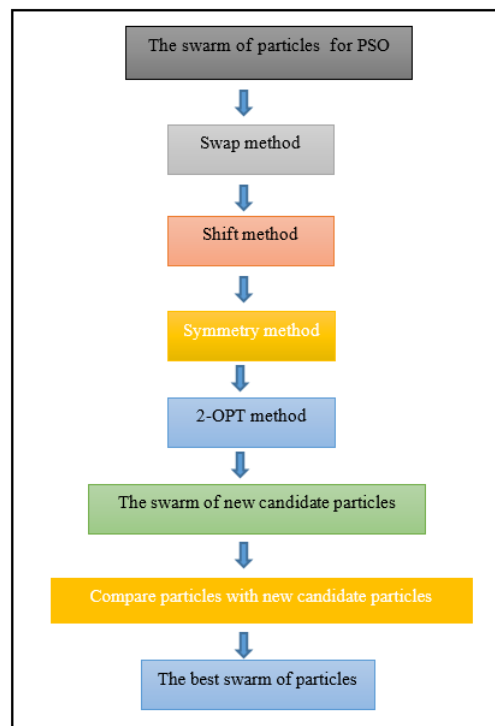
---

```

1: Assign parameter values ( $N, D, CS, c_1, c_2, w, etc.$ ) of DPSO and initialize.
2: Initialize the positions of the particles randomly. (Particle:  $i=1, \dots, N$ ) (Dimension:  $j=1, \dots, D$ ) ( $D$ =
total number of cities) (Particle: 1, 2, ..., N)
3: while (iter < max_iter) do
4: Calculate the objective function for the given particles for TSP (Total route length)
5: Find the value of the best particle ( $Best$ ) and find the value of the global best particle ( $GBest$ )
6: for ( $i=1$  to  $N$ ) do
7:   for ( $j=1$  to  $D$ ) do
8:     Generate a random values between  $[0, 1]$  ( $rand_1$  and  $rand_2$ )
9:     Calculate velocities of particles with Eq. (1)
10:    Calculate positions of particles with Eq. (2)
11:   end for
12: end for
13: for ( $i=1$  to  $N$ ) do
14:   for ( $j=1$  to  $CS$ ) do
15:     Apply swap method on new candidate particle
16:     Apply shift method on new candidate particle
17:     Apply symmetry method on new candidate particle
18:     Apply 2-opt method on new candidate particle
19:   end for
20: Calculate the objective function for the new candidate particles for TSP (Total route length)
21: for ( $i=1$  to  $N$ ) do
22:   if the fitness of new candidate particle ( $i$ ) > the fitness of particle ( $i$ )
23:     Update particle ( $i$ ) as new candidate particle ( $i$ )
24:   end if
25: end for
26: iter=iter+1
27: end while
28: The value of the global best particle

```

---

**Figure 2.** The DPSO model

### 2.3. Swap, Shift, Symmetry, and 2-opt Methods

#### 2.3.1. Swap method

The swap transformation is based on swapping two randomly selected cities in each particle [21]. Thus, a new candidate particle is created. Although the swap transform is a simple method, it has been used by many researchers in the literature to create new candidate particles. It enables DPSO to approach the optimum result. The swap method is shown in Figure 3.

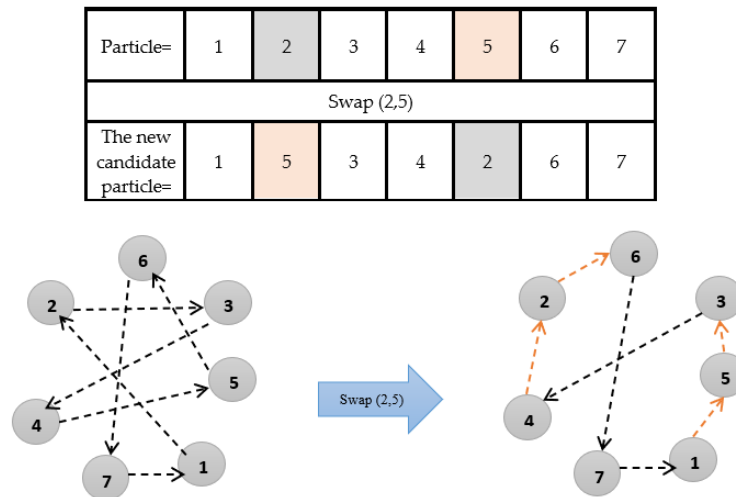


Figure 3. The swap method

#### 2.3.2. Shift method

Each particle holds the city route information that will be visited by the vendor to calculate the fitness function of the problem. In order to generate candidate solutions in the Shift method, two different random cities are selected for each particle [21]. These two cities in the particle are swapped to create a new candidate particle, as in the swap method. During this change, the city location adjacent to the second randomly selected city is also included in the change. Shift transform causes position changes on the particle. In the swap method, two-city locations are changed, while in the shift method, three-city locations are changed. This creates a more efficient solution for finding the optimum route length. The shift method is shown in Figure 4 in detail.

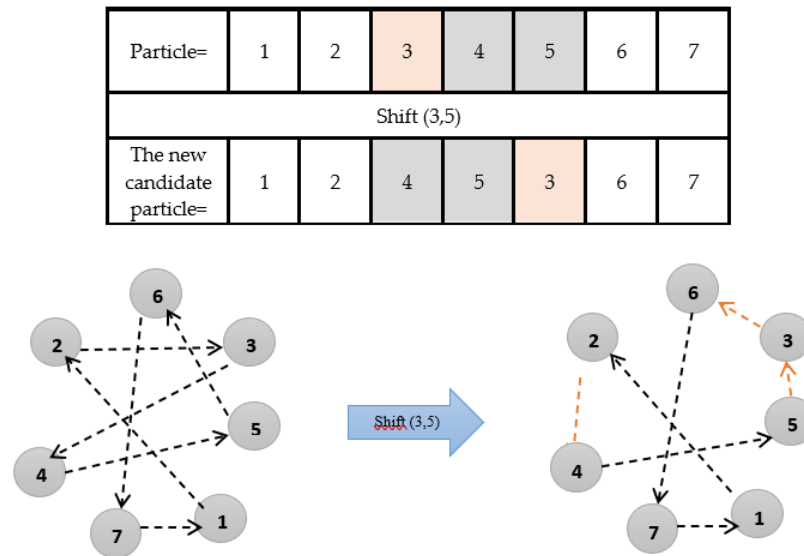


Figure 4. The shift method

### 2.3.3. Symmetry method

The symmetry method is a method based on randomly changing city locations, as in the swap and shift methods [21]. In the symmetry method, there is more city location change than in the swap and shift methods. In the symmetry method, first of all, the city location is chosen randomly from 1-D in the form of two different groups. First of all, these two groups are subjected to a change of place among themselves, then the members of each group change their ranks among themselves. Thus, four different city locations are randomly changed. It also enhances the global search capability of the DPSO by placing groups of pairs at random locations in the search space. Relocation within the group also improves the local search capability of the DPSO in the search space. Thanks to this method, both the local and global search capability of DPSO is improved at the same time. While the swap method improves DPSO's global search capability, the shift method improves DPSO's local search capability. The success of a discrete heuristic algorithm depends on its ability to search both locally and globally. The symmetry method is shown in Figure 5 in detail.

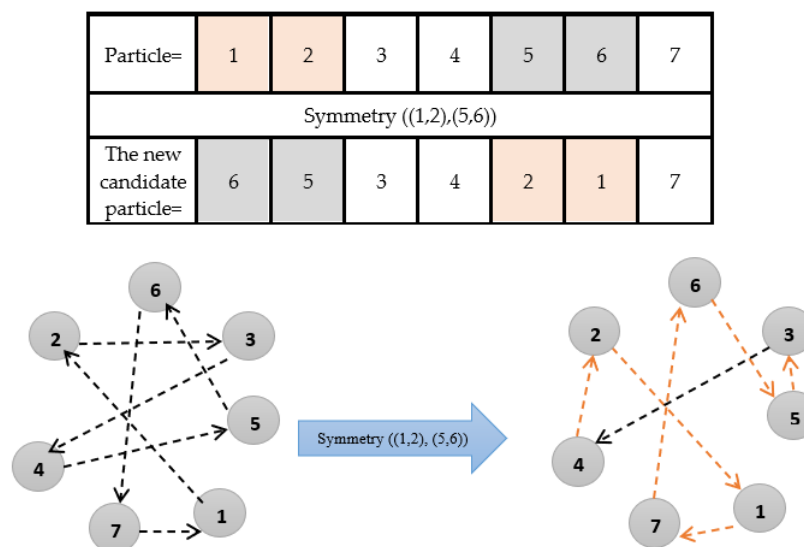


Figure 5. The symmetry method

### 2.3.4. 2-OPT method

A local search algorithm begins with a candidate solution and progresses iteratively to a neighboring solution. It is often referred to as k-opt. In the literature, 2-opt and 3-opt forms are mostly used in discrete optimization problems. The 2-opt algorithm is most likely the simplest and most widely used algorithm for solving TSP problems. It was first developed by Croes in 1958. The 2-opt local search algorithm seeks two distinct neighbor solutions. To improve the quality of the solution, a 2-opt local search method is implemented on the best individual [38]. Working with local search logic, the algorithm makes improvements by removing two edges from the round and connecting the remaining parts differently. The solution is obtained after all possible changes have been made is called 2-optimal. It can be defined as deleting the two edges in the tour and connecting the tour divided into two parts differently, reducing costs. The 2-opt method is shown in Figure 6 and Figure 7 in detail. In this study, the 2-OPT algorithm is applied on the last route obtained after the methods applied in DPSO.

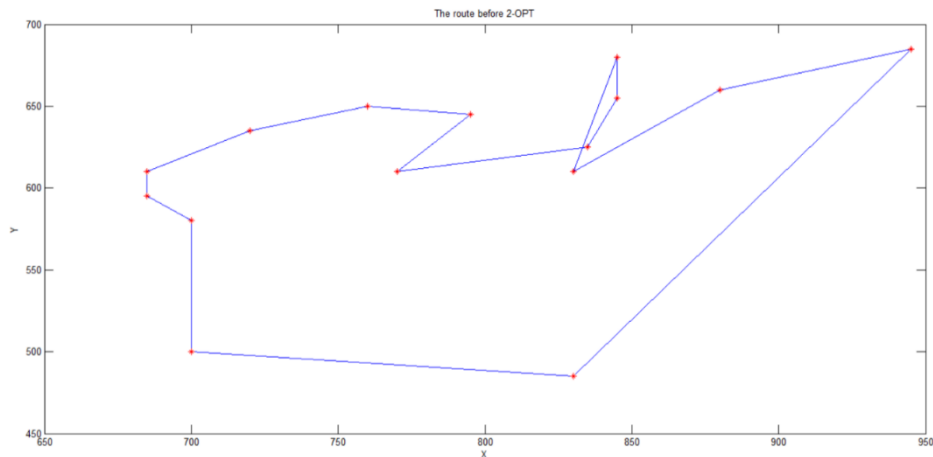


Figure 6. The route before 2-Opt method

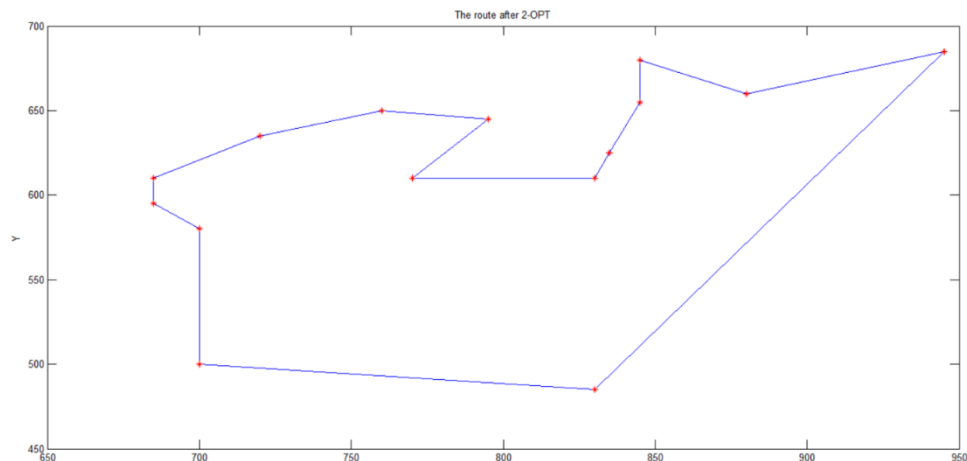


Figure 7. The route after 2-Opt method

## 2.4. Travelling Salesman Problem (TSP)

TSP has a route consisting of different cities. A random city is selected from the cities and a tour is created by visiting each city once. TSP aims to create the shortest route and the shortest distance. Let there be  $D$  cities that a salesperson has to visit. The maximum number of routes to follow in all cities  $(D-1)!/2$  for  $D$  cities [21]. For example, there are 25 cities to visit, and the number of routes the algorithm will



review is considered to be  $((25-1)!/2=24!/2)$ . In this paper, we calculate the distance between cities  $m$  and  $n$  using Euclidean distance as follows:

$$distance_{m,n} = \sqrt{(a_m - a_n)^2 + (b_m - b_n)^2} \quad (3)$$

where  $distance_{m,n}$  is the distance between city  $m$  and city  $n$ .  $a_m$  and  $a_n$  are a coordinates for city  $m$  and city  $n$ .  $b_m$  and  $b_n$  are  $b$  coordinates for city  $m$  and city  $n$ . We use the  $func$  function to calculate the entire tour length as follows [21]:

$$func = distance_{D,i} + \sum_{c=1}^{n-1} distance_{c,c+1} \quad (4)$$

$D$  denotes the total number of cities. The fundamental goal is to find the Hamiltonian path with the lowest cost on a weighted graph.

## 2.5. TSP datasets used in the paper

TSPLIB contains the problems that are utilized to generate experimental findings [39]. The majority of the problems in TSPLIB have been solved, and the best values have been reported. The city numbers are indicated by the numbers in the problem names. These optimum values are used to make comparisons. Euclidean problems are the coordinated kinds of these problems (EUC). Some studies in the literature calculate other types of problems (for example, geographical-GEO) as EUC, which leads to errors in comparisons. OLIVER30, EIL51, Eil76, EIL101, BERLIN52, ST70, PR76, KROA100, KROB100, KROC100, KROD100, KROE100, KROB150, TSP225, CH150, and A280 datasets selected from the TSPLIB library are used to solve the TSP problem with the DPSO algorithm. There are sixteen low, medium, and high dimensional data sets commonly used in TSP. The optimum values of these TSP datasets are given in Table 1.

**Table 1.** The optimum values of these TSP datasets [20; 21].

ID	TSP Name	Dimension size (D=city size)	Optimum value
1	OLIVER30	30	423.74
2	EIL51	51	428.87
3	BERLIN52	52	7542 (7544.37)
4	ST70	70	677.11
5	EIL76	76	545.38
6	PR76	76	108159.44
7	KROA100	100	21282 (21285.44)
8	KROB100	100	22141
9	KROC100	100	20749
10	KROD100	100	21294
11	KROE100	100	22068
12	EIL101	101	642.31
13	KROB150	150	26130
14	CH150	150	6532.10
15	TSP225	225	3859
16	A280	280	2586.77

### 3. RESULTS AND DISCUSSION

The variations of the DPSO (DPSO1, DPSO2, DPSO3, DPSO4, DPSO5, and DPSO6) have occurred according to the selected method type (DPSO1 (swap method), DPSO2 (shift method), DPSO3 (swap and shift methods), DPSO4 (symmetry method), DPSO5 (swap, shift, and symmetry methods), and DPSO6 (swap, shift, symmetry, 2 opt methods)). The success of each method on DPSO is tested separately. In the variations of the DPSO results, the best fitness values (Min), the average of the fitness values (Avg), maximum (Max) fitness values, the standard deviation of the fitness values (Std), and the mean CPU time are stored. Error (%) values are presented to measure the performances of the algorithms. The relative error (Error) is determined as follows using Eq. 5. The resulting answer (mean of 20 different runs) is referred to as Result, while the optimum value of the problem is referred to as Optimum. To make the comparisons easier, Error (%) values are used, and the best results are noted in boldface font type. During performance measurements, the experiment set is run 20 times. All experiments are run on a Windows 7 using Intel(R) Core(TM) i5-2410M, 4 GB of RAM, and the codes are implemented in Matlab R2014a.

$$Error = \frac{Result - Optimum}{Optimum} \times 100 \quad (5)$$

The application of the developed methods (swap, shift, and symmetry methods) in DPSO has been investigated by experimental studies.

#### 3.1. The Parameters of the DPSO

For determining the optimum parameters for DPSO, the number of the particle (N) and the number of candidate solutions (CS) are analyzed. Ten different population size values (10, 20, 30, 40, 50, 60, 70, 80, 90, 100, 200, and 300) are tested on the BERLIN52, EIL76, and KROA100 TSPs to see the effect of population size (N) on performance (for DPSO1). The function evaluations (MaxFEs) and the number of candidate solutions (CS) are used as 800000 and 5, respectively. Obtained results are shown in Table 2. According to the results, the population size does not have a significant effect on the results. In many studies in the literature, population size is taken as equal to the total number of cities [17], [21]. In this study, the population size amount is chosen as 100.

Five different numbers of candidate solutions (CS) values (1, 5, 10, 15, and 20) are tested on the BERLIN52, EIL76, and KROA100 TSPs to see the effect of the number of candidate solutions (CS) on performance (for DPSO1). The MaxFEs and population size (N) parameters are used as 800000, and 100, respectively. Obtained results are shown in Table 3. According to the results, as the number of candidate solutions (CS) increases, the performance increases. The number of candidate solutions is determined as the most appropriate value in this study. Experiments are carried out with the given parameter values. All parameters values use in the study are shown in Table 4.

**Table 2.** Population size (N) analyses of DPSO1.

<b>BERLIN52</b>						
<i>N</i>	<i>Min</i>	<i>Max</i>	<i>Avg</i>	<i>Std</i>	<i>Mean Error(%)</i>	<i>Mean CPU time</i>
10	8040.00	8133.00	8100.00	38.12	7.84	26.92
20	8035.00	8133.00	8066.50	39.88	7.08	18.83
30	8032.00	8133.00	8075.50	46.40	6.54	18.08
40	8035.00	8133.00	8052.55	31.27	6.54	19.09
50	8032.00	8133.00	8065.90	39.62	6.60	16.96
60	8032.00	8133.00	8049.60	28.67	6.60	19.53
70	8032.00	8059.00	8037.80	5.49	6.85	20.64
80	8032.00	8066.00	8038.65	6.81	6.95	12.88
90	8035.00	8040.00	8037.25	2.49	6.54	14.04
100	8032.00	8040.00	8036.40	2.46	<b>6.50</b>	14.31
200	8035.00	8076.00	8039.55	8.71	6.60	16.08
300	7542.00	8063.00	8014.85	108.64	6.60	15.63
<b>EIL76</b>						
<i>N</i>	<i>Min</i>	<i>Max</i>	<i>Avg</i>	<i>Std</i>	<i>Mean Error(%)</i>	<i>Mean CPU time</i>
10	606.79	608.39	607.75	0.78	11.44	24.55
20	606.79	606.79	606.79	0.00	11.26	15.47
30	592.21	608.39	602.69	6.63	10.51	12.13
40	606.79	608.39	607.27	0.73	11.35	10.74
50	586.45	606.79	604.75	6.10	10.89	10.41
60	592.21	606.79	602.57	6.45	10.49	10.52
70	592.21	606.79	605.33	4.37	10.99	10.31
80	592.21	606.79	605.33	4.37	10.99	10.28
90	586.27	606.79	603.70	6.58	10.69	9.69
100	592.21	606.790	603.19	5.66	10.60	10.43
200	594.47	608.39	602.34	4.50	<b>10.44</b>	10.72
300	598.01	608.39	605.39	3.63	11	11.25
<b>KROA100</b>						
<i>N</i>	<i>Min</i>	<i>Max</i>	<i>Avg</i>	<i>Std</i>	<i>Mean Error(%)</i>	<i>Mean CPU time</i>
10	22261.64	22643.48	22560.04	100.89	6.01	26.1
20	22586.91	22864.92	22619.22	82.18	6.28	17.05
30	22586.91	22601.93	22589.66	5.52	6.14	13.72
40	22479.11	22652.94	22588.39	43.77	6.14	12.54
50	22453.36	22634.11	22587.11	47.18	6.13	12.2
60	22500.58	22861.06	22640.55	115.69	6.38	11.81
70	22274.08	22746.07	22505.67	127.51	<b>5.75</b>	11.37
80	22586.91	22712.84	22622.9	44.78	6.30	11.52
90	22586.91	22923.99	22658.08	93.69	6.47	11.00
100	22586.91	22984.92	22653.87	116.17	6.45	10.09
200	22586.91	23114.58	22839.32	142.92	7.32	10.71
300	22991.37	23349.15	23180.61	141.05	8.92	10.77

**Table 3.** The number of candidate solutions (CS) analyses of DPSO1.

BERLIN52							
CS	Min	Max	Avg	Std	Mean Error(%)	Mean time	CPU
1	8035.00	8063.00	8038.70	6.11	6.54	16.82	
5	8035.00	8130.00	8050.60	26.08	6.54	20.57	
10	8032.00	8076.00	8038.40	8.97	7.08	21.09	
15	8032.00	8040.00	8036.55	2.99	6.54	16.21	
20	8035.00	8076.00	8040.60	12.01	6.54	15.25	
EIL76							
CS	Min	Max	Avg	Std	Mean Error(%)	Mean time	CPU
1	593.48	608.39	605.62	4.07	11.04	14.77	
5	592.21	606.79	604.27	5.12	10.80	10.65	
10	588.07	606.81	602.42	6.93	10.46	9.90	
15	593.74	607.60	603.29	5.56	10.62	10.18	
20	592.87	607.60	603.41	5.55	10.64	9.81	
KROA100							
CS	Min	Max	Avg	Std	Mean Error(%)	Mean time	CPU
1	22465.06	22992.03	22619.06	139.62	6.28	16.42	
5	22575.24	22918.82	22702.58	124.21	6.68	11.57	
10	22465.06	22794.71	22649.42	96.35	6.43	10.89	
15	22500.58	23391.24	22720.08	239.07	6.76	10.83	
20	22601.33	22850.81	22663.12	70.40	6.49	10.52	

**Table 4.** The sets of parameters of the variations of the DPSO.

Parameters	Values
Number of particles	100
MaxFEs	800000
$k_1$ (social constant)	0.2
$k_2$ (cognitive constant)	0.2
w (inertia weight)	0.4
$Vel_{max}$ (maximum velocity)	0.8
The number of candidate solutions	20

### 3.2. The Comparison of the Variations of the DPSO

The variations of the DPSO (DPSO1, DPSO2, DPSO3, DPSO4, DPSO5, and DPSO6) have occurred according to the selected method type (DPSO1 (swap method), DPSO2 (shift method), DPSO3 (swap and shift methods), DPSO4 (symmetry methods), DPSO5 (swap, shift, and symmetry methods), and DPSO6 (swap, shift, symmetry, 2 opt methods)). The success of each method on DPSO has been tested separately. The performance improvement of each method over the result of DPSO is shown in detail. Parameter settings in Table 4 are used in the tests. Minimum result (Min), maximum result (Max), mean result (Avg), the standard deviation of results (Std), mean CPU time, and error rate results have been calculated for all DPSO variations. The results of the DPSO1, DPSO2, DPSO3, DPSO4, DPSO5, and DPSO6 are shown in Tables 5, 6, 7, 8, 9, and 10, respectively. Table 11 shows the comparison results for all DPSO variations (for

error rate (%)). Table 12 shows the comparison results for all DPSO variations (for mean CPU time). Figure 8 shows the convergence graph of mean error (%) for all methods.

According to Table 11, the most successful DPSO variations are DPSO5 and DPSO6. While DPSO5 achieves success in 9 of 16 TSP benchmarks, DPSO6 achieves successful results in 8 of 16 TSP benchmarks. The symmetry method provides a noticeable performance increase in the result. Swap, shift, and symmetry methods have improved DPSO to achieve optimum results. The 2-opt algorithm is a local search algorithm. DPSO6 is obtained as a result of running the 2-opt algorithm on the optimum route. It is noteworthy that the results of some TSP benchmarks have improved with the 2-opt algorithm (OLIVER30, KROB150, CH150, TSP225, A280, etc.). The results show that the application of many different methods to the result increases the result performance.

**Table 5.** The performance analysis of DPSO1 on TSPs (swap method).

ID	TSP Name	Min	Max	Avg	Std	Mean CPU time
1	OLIVER30	425.27	435.07	433.04	3.89	15.08
2	EIL51	470.58	485.64	482.80	4.47	24.30
3	BERLIN52	8032.00	8077.00	8039.75	12.41	25.20
4	ST70	721.68	728.39	724.04	1.82	21.85
5	EIL76	592.21	606.81	604.46	4.73	18.08
6	PR76	125407.46	127838.70	126536.58	683.54	15.59
7	KROA100	22530.16	22716.90	22615.91	39.16	16.25
8	KROB100	24071.69	25046.60	24554.27	280.58	16.90
9	KROC100	23096.50	23190.43	23152.98	21.41	20.69
10	KROD100	24410.01	24774.30	24659.44	90.02	23.65
11	KROE100	23633.66	24084.27	23841.04	106.15	20.44
12	EIL101	719.19	722.66	720.91	1.11	31.36
13	KROB150	29808.01	30198.10	29952.17	96.08	18.69
14	CH150	6923.70	6969.94	6943.05	11.84	17.43
15	TSP225	4549.02	4598.76	4576.86	13.13	20.71
16	A280	3028.03	3081.84	3063.75	14.21	23.02

**Table 6.** The performance analysis of DPSO2 on TSPs (shift method).

ID	TSP Name	Min	Max	Avg	Std	Mean CPU time
1	OLIVER30	425.27	465.25	451.21	14.57	11.32
2	EIL51	451.09	470.43	458.86	6.56	9.62
3	BERLIN52	7542.00	7954.00	7857.35	123.74	9.68
4	ST70	715.95	725.83	721.42	2.71	8.31
5	EIL76	575.78	583.07	578.04	2.56	8.45
6	PR76	119750.16	122922.17	120272.00	925.37	8.40
7	KROA100	22664.62	23606.64	22969.30	289.26	8.95
8	KROB100	24003.06	24577.97	24273.99	166.30	8.92
9	KROC100	21866.45	22272.47	22030.39	112.44	9.07
10	KROD100	23619.72	24578.48	24299.20	337.92	9.47
11	KROE100	23493.46	23787.04	23626.89	83.83	9.13
12	EIL101	706.88	711.55	707.98	1.21	9.11
13	KROB150	29680.74	30082.38	29919.49	103.96	10.14
14	CH150	6847.14	6921.75	6875.98	17.79	9.72
15	TSP225	4386.69	4495.04	4452.49	24.30	11.39
16	A280	3027.92	3054.05	3041.06	6.85	12.26

**Table 7.** The performance analysis of DPSO3 on TSPs (swap and shift methods).

ID	TSP Name	Min	Max	Avg	Std	Mean CPU time
1	OLIVER30	425.27	435.07	432.37	4.10	15.74
2	EIL51	444.13	463.04	453.57	4.44	16.47
3	BERLIN52	7542.00	7938.00	7879.60	81.35	16.63
4	ST70	715.95	721.63	718.39	2.05	17.91
5	EIL76	575.78	582.49	577.95	2.40	19.34
6	PR76	117564.11	119986.96	119070.04	900.90	19.91
7	KROA100	22332.50	22911.56	22542.78	170.54	20.52
8	KROB100	23841.97	24370.47	24016.02	132.10	19.90
9	KROC100	21840.52	22191.96	22012.09	108.50	27.38
10	KROD100	23450.54	24577.59	24067.38	388.39	26.29
11	KROE100	22970.94	23558.86	23181.96	156.66	33.16
12	EIL101	702.77	707.29	705.71	1.30	23.87
13	KROB150	29243.13	29480.60	29406.41	67.71	34.72
14	CH150	6817.49	6873.62	6841.92	17.50	42.44
15	TSP225	4383.50	4461.97	4423.66	20.90	49.68
16	A280	2952.77	3030.44	2997.28	20.00	48.70

**Table 8.** The performance analysis of DPSO4 on TSPs (symmetry methods).

ID	TSP Name	Min	Max	Avg	Std	Mean CPU time
1	OLIVER30	448.74	449.17	449.11	0.16	9.69
2	EIL51	451.19	467.79	455.11	4.88	10.95
3	BERLIN52	7679.00	7713.00	7694.20	13.83	8.74
4	ST70	733.01	742.31	740.88	3.14	12.18
5	EIL76	573.37	584.62	578.54	3.67	14.02
6	PR76	114508.51	122436.35	116638.10	1959.10	10.50
7	KROA100	23309.00	23629.08	23445.80	69.49	9.27
8	KROB100	23713.21	24608.14	24113.70	202.28	10.51
9	KROC100	22272.29	22736.49	22601.11	138.05	9.26
10	KROD100	22632.36	23514.86	23031.71	258.70	9.06
11	KROE100	23162.77	23366.24	23236.92	42.65	9.04
12	EIL101	684.04	703.93	687.23	4.68	9.11
13	KROB150	28250.12	29012.15	28437.25	215.15	12.88
14	CH150	6865.71	6897.39	6871.80	10.42	16.39
15	TSP225	4169.75	4312.46	4238.54	38.59	15.81
16	A280	2850.60	2946.29	2899.01	26.92	15.59

**Table 9.** The performance analysis of DPSO5 on TSPs (swap, shift, and symmetry methods).

ID	TSP Name	Min	Max	Avg	Std	Mean CPU time
1	OLIVER30	423.74	434.61	425.71	2.80	26.96
2	EIL51	431.17	440.60	434.68	3.31	22.72
3	BERLIN52	7542.00	7542.00	7542.00	0.00	22.67
4	ST70	677.19	708.38	688.14	7.14	23.69
5	EIL76	562.14	581.02	568.06	4.78	23.30
6	PR76	109686.79	116262.26	112127.67	1734.91	26.84
7	KROA100	21294.40	21910.66	21440.43	173.54	24.22
8	KROB100	22323.35	23331.36	22696.48	213.23	30.72
9	KROC100	21185.42	21904.06	21498.03	178.89	38.58
10	KROD100	21712.39	23286.89	22183.73	325.28	33.13
11	KROE100	22208.15	22614.14	22388.35	112.23	25.43
12	EIL101	660.91	677.49	669.04	4.18	28.18
13	KROB150	26628.34	27513.26	27021.26	223.87	33.99
14	CH150	6565.05	6710.59	6635.86	44.40	41.96
15	TSP225	4100.57	4218.32	4158.55	32.94	43.42
16	A280	2763.18	2895.39	2836.20	34.08	42.83

**Table 10.** The performance analysis of DPSO6 on TSPs (swap, shift, symmetry, and 2opt methods).

ID	TSP Name	Min	Max	Avg	Std	Mean CPU time
1	OLIVER30	423.74	425.27	424.66	0.75	24.04
2	EIL51	431.17	443.47	436.76	4.13	26.92
3	BERLIN52	7542.00	7542.00	7542.00	0.00	22.82
4	ST70	686.62	699.77	688.62	2.66	25.27
5	EIL76	559.33	573.39	565.85	4.07	26.25
6	PR76	109352.49	116314.51	112372.04	1835.62	25.45
7	KROA100	21294.40	21907.55	21476.41	216.52	31.30
8	KROB100	22581.92	23061.09	22749.21	122.01	31.99
9	KROC100	21234.64	21967.34	21449.68	179.66	31.03
10	KROD100	21801.09	23474.44	22293.46	393.48	35.23
11	KROE100	22161.11	22706.73	22438.09	120.84	32.82
12	EIL101	657.28	679.33	669.39	4.38	34.09
13	KROB150	26527.84	27536.51	26919.52	251.46	33.75
14	CH150	6557.63	6697.65	6622.86	44.58	28.86
15	TSP225	4001.42	4132.14	4057.05	38.00	35.31
16	A280	2653.03	2833.05	2758.15	39.80	39.10

**Table 11.** The performance analysis of variations of the DPSO on TSPs (according to mean error (%)).

ID	TSP Name	DPSO1	DPSO2	DPSO3	DPSO4	DPSO5	DPSO6
1	OLIVER30	2.19	6.48	2.04	5.99	0.46	<b>0.22</b>
2	EIL51	12.57	6.99	5.76	6.12	<b>1.35</b>	1.84
3	BERLIN52	6.60	4.18	4.48	2.02	<b>0.00</b>	<b>0.00</b>
4	ST70	6.93	6.54	6.10	9.42	<b>1.63</b>	1.70
5	EIL76	10.83	5.99	5.97	6.08	4.16	<b>3.75</b>
6	PR76	16.99	11.20	10.09	7.84	<b>3.67</b>	3.89
7	KROA100	6.27	7.93	5.92	10.17	<b>0.74</b>	0.91
8	KROB100	10.90	9.63	8.47	8.91	<b>2.51</b>	2.75
9	KROC100	11.59	6.18	6.09	8.93	3.61	<b>3.38</b>
10	KROD100	15.80	14.11	13.02	8.16	<b>4.18</b>	4.69
11	KROE100	8.03	7.06	5.05	5.30	<b>1.45</b>	1.68
12	EIL101	12.24	10.22	9.87	6.99	<b>4.16</b>	4.22
13	KROB150	14.63	14.50	12.54	8.83	3.41	<b>3.02</b>
14	CH150	6.29	5.26	4.74	5.20	1.59	<b>1.39</b>
15	TSP225	18.60	15.38	14.63	9.84	7.76	<b>5.13</b>
16	A280	18.44	17.56	15.87	12.07	9.64	<b>6.63</b>

**Table 12.** The performance analysis of variations of the DPSO on TSPs (according to mean CPU time).

ID	TSP Name	DPSO1	DPSO2	DPSO3	DPSO4	DPSO5	DPSO6
1	OLIVER30	15.08	11.32	15.74	9.69	26.96	24.04
2	EIL51	24.30	9.62	16.47	10.95	22.72	26.92
3	BERLIN52	25.20	9.68	16.63	8.74	22.67	22.82
4	ST70	21.85	8.31	17.91	12.18	23.69	25.27
5	EIL76	18.08	8.45	19.34	14.02	23.30	26.25
6	PR76	15.59	8.40	19.91	10.50	26.84	25.45
7	KROA100	16.25	8.95	20.52	9.27	24.22	31.30
8	KROB100	16.90	8.92	19.90	10.51	30.72	31.99
9	KROC100	20.69	9.07	27.38	9.26	38.58	31.03
10	KROD100	23.65	9.47	26.29	9.06	33.13	35.23
11	KROE100	20.44	9.13	33.16	9.04	25.43	32.82
12	EIL101	31.36	9.11	23.87	9.11	28.18	34.09
13	KROB150	18.69	10.14	34.72	12.88	33.99	33.75
14	CH150	17.43	9.72	42.44	16.39	41.96	28.86
15	TSP225	20.71	11.39	49.68	15.81	43.42	35.31
16	A280	23.02	12.26	48.70	15.59	42.83	39.10



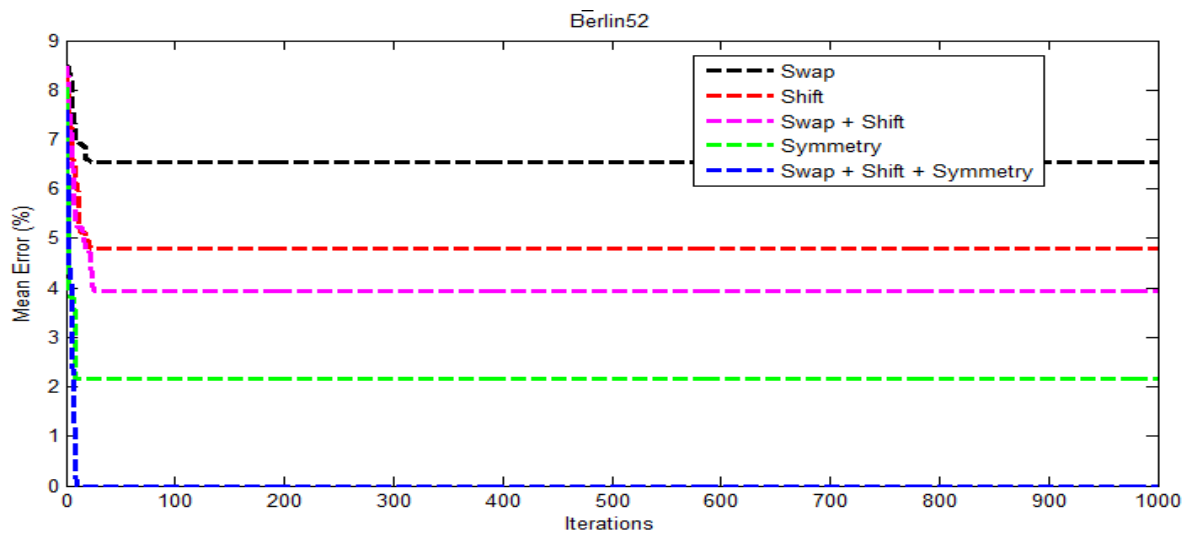


Figure 8. Convergence graph of mean error (%) for all methods.

### 3.3. The comparison of the variations of the DPSO with DJAYA, SA, ACO, STA, and DTSA

The first comparison is performed with Chunhua et al., Cinar et al., and Gunduz and Aslan [20], [21], [34]. In this study, the DPSO is compared with DJAYA, STA, SA, ACO, and DTSA on the BERLIN52 problem. Comparison results of STA, SA, and ACO are directly taken from Chunhua et al., DTSA is directly taken from Cinar et al., and DJAYA is directly taken from Gunduz and Aslan. For a fair comparison, MaxFES is set to 4000 for all methods. The parameter settings are shown in Table 13. Comparison results are shown in Table 14. According to the minimum results (Min), DPSO, DJAYA, and DTSA have reached the optimum results. According to the average results (Avg), DPSO has performed better than DTSA, DJAYA, STA, SA, and ACO algorithms. The reason for this success is due to the methods developed by DPSO on a randomly generated route.

Table 13. The sets of parameters of DPSO, STA, SA, DTSA, DJAYA, and ACO.

Parameters	Population size	MaxFES	Other parameters
STA	20	4000	Temperature=50000; cooling rate=0.97
SA	20	4000	
ACO	20	4000	$\alpha=1, \beta=5, \rho=0.9$
DJAYA	20	4000	
DTSA	20	4000	NS=6; ST=0.5
DPSO	20	4000	CS=20

Table 14. The Comparison of DPSO, SA, ACO, STA, DTSA, and DJAYA on BERLIN52 TSP.

TSP name	Algorithm	Min	Max	Avg	Std
BERLIN52	SA	8186.40	9585.80	8983.80	380.10
	ACO	8240.40	9151.30	8777.60	267.11
	STA	7544.40	8630.50	8247.20	273.45
	DTSA	<b>7542.00</b>	7929.00	7689.17	108.40
	DJAYA	<b>7542.00</b>	7831.00	7668.35	112.50
	DPSO5	7725.00	7905.00	7823.40	50.70
	DPSO6	<b>7542.00</b>	7804.00	<b>7637.55</b>	95.89

### 3.4. The comparison of the variations of the DPSO with DJAYA, SA, DSTA0, DSTAI, DSTAII, and DTSA

The second comparison is performed with Zhou et al., Cinar et al., and Gunduz and Aslan [20], [21], [35]. In this study, the DPSO is compared with DJAYA, SA, DSTA0, DSTAI, DSTAII, and DTSA on KROA100, KROB100, KROC100, KROD100, and KROE100 problems. Comparison results of SA, DSTA0, DSTAI, and DSTAII are directly taken from Zhou et al., DTSA is directly taken from Cinar et al., and DJAYA is directly taken from Gunduz and Aslan. MaxFEs is set to 90000 for all methods to ensure a fair comparison. Initial temperature and cooling rate are the algorithmic parameters of SA, and they are set to 2000 and 0.97, respectively. The maximum iteration number for DSTA variations is set to 900 and the search enforcement is set to 100. Comparison results are shown in Table 15. According to the results, DSTAII and DPSO have performed better than other algorithms.

### 3.5. The comparison of the variations of the DPSO with DJAYA, ACO, ABC, HA, and DTSA

The other comparison is performed with Gündüz et al., Cinar et al., and Gunduz and Aslan [20], [21], [36]. In this study, the DPSO is compared with DJAYA, ACO, ABC, HA, and DTSA on EIL51, EIL76, EIL101, KROA100, OLIVER30, BERLIN52, ST70, PR76, CH150, and TSP225 problems. Comparison results of ACO, ABC, and HA are directly taken from Gündüz et al., DTSA is directly taken from Cinar et al., and DJAYA is directly taken from Gunduz and Aslan. MaxFEs is set to  $D \times 500$  for all methods to ensure a fair comparison ( $D$ =the number of cities of the TSP). But, the population size and limit parameters of ABC are set to  $D$  and  $D \times D \times 500$ , respectively. ACO's specific parameters are  $\alpha = 1$ ,  $\beta = 5$ , and  $\rho = 0.65$ . For ACO, the number of ants is set to  $D$ , and the maximum number of iterations is set to 500. HA stands for 50% ABC and 50% ACO, which implies the parameter values are the same, but the population sizes are half of  $D$ . Comparison results are shown in Table 16.

According to the results, DPSO has achieved more successful results than other algorithms except HA. Out of 10 TSP benchmark datasets, DPSO has performed well in 4 (EIL51, PR76, KROA100, EIL101) of them. DJAYA has outperformed 2 (CH150 and TSP225) out of 10 TSP benchmark datasets. HA has been shown superior success in the 4 TSP benchmark dataset. ACO has been shown superior success in 1 TSP benchmark dataset. This has proven that DPSO has been developed and is an alternative discrete optimization algorithm in the literature.

**Table 15.** Comparison of DPSO with DJAYA, SA, DSTA0, DSTAI, DSTAII, and DTSA.

TSP name	Algorithm	Avg	Std	Error(%)	Rank
KROA100	SA	22635.00	778.72	6.36	5
	DSTA0	23213.00	906.11	9.07	7
	DSTAI	22835.00	715.85	7.30	6
	DSTAI	21767.00	221.64	2.28	4
	DTSA	21506.78	260.55	1.06	2
	DJAYA	21705.98	290.22	1.99	3
	DPSO6	<b>21434.36</b>	<b>178.50</b>	<b>0.72</b>	<b>1</b>
KROB100	SA	23657.00	445.78	6.85	5
	DSTA0	23794.00	517.05	7.47	7
	DSTAI	23734.00	507.38	7.19	6
	DSTAI	<b>22880.00</b>	302.14	<b>3.34</b>	<b>1</b>
	DTSA	23139.26	181.74	4.51	4
	DJAYA	22973.73	234.79	3.76	3
	DPSO6	23334.86	<b>158.64</b>	5.39	2
KROC100	SA	22223.00	522.20	7.10	6
	DSTA0	22877.00	709.87	10.26	7
	DSTAI	21891.00	536.88	5.50	5
	DSTAI	<b>21378.00</b>	246.34	<b>3.03</b>	<b>1</b>
	DTSA	21817.08	217.77	5.15	4
	DJAYA	21702.02	186.32	4.59	2
	DPSO6	21703.96	<b>40.20</b>	4.60	3
KROD100	SA	22911.00	483.01	7.59	5
	DSTA0	23043.00	565.80	8.21	7
	DSTAI	22665.00	592.53	6.44	3
	DSTAI	<b>21991.00</b>	<b>315.32</b>	<b>3.27</b>	<b>1</b>
	DTSA	22972.26	390.50	7.88	6
	DJAYA	22631.25	487.62	6.28	2
	DPSO6	22834.33	375.98	7.23	4
KROE100	SA	23125.00	389.42	4.79	5
	DSTA0	23738.00	450.82	7.57	7
	DSTAI	23371.00	678.69	5.90	6
	DSTAI	22637.00	166.82	2.58	4
	DTSA	22547.00	121.96	2.17	2
	DJAYA	22582.47	252.07	2.33	3
	DPSO6	<b>22545.57</b>	<b>87.98</b>	<b>2.16</b>	<b>1</b>

**Table 16.** The comparison of DPSO with DJAYA, ACO, ABC, HA, and DTSA.

TSP name	Algorithm	Avg	Std	Error(%)	Rank
OLIVER30	ACO	424.68	1.41	0.22	2
	ABC	462.55	12.47	9.16	6
	HA	<b>423.74</b>	<b>0.00</b>	<b>0.00</b>	<b>1</b>
	DTSA	428.50	4.21	1.12	5
	DJAYA	426.88	2.74	0.74	4
	DPSO6	425.28	0.05	0.36	3
EIL51	ACO	457.86	4.07	6.76	5
	ABC	457.86	4.07	6.76	5
	HA	443.39	5.25	3.39	3
	DTSA	443.93	4.04	3.51	4
	DJAYA	440.18	4.95	2.64	2
	DPSO6	<b>436.11</b>	<b>3.18</b>	<b>1.69</b>	<b>1</b>
BERLIN52	ACO	7659.31	38.70	1.52	5
	ABC	10390.26	439.69	37.72	6
	HA	7544.37	<b>0.00</b>	<b>0.00</b>	<b>1</b>
	DTSA	7545.83	21.00	0.02	3
	DJAYA	7580.30	80.60	0.48	4
	DPSO6	7542.50	1.50	0.01	2
ST70	ACO	709.16	8.27	4.73	5
	ABC	1230.49	41.79	81.73	6
	HA	<b>7544.37</b>	<b>0.00</b>	<b>0.00</b>	<b>1</b>
	DTSA	7545.83	21.00	0.02	2
	DJAYA	702.30	9.56	3.72	4
	DPSO6	700.53	9.14	3.46	3
EIL76	ACO	561.98	3.50	3.04	2
	ABC	931.44	24.86	70.78	6
	HA	<b>557.98</b>	4.10	<b>2.31</b>	<b>1</b>
	DTSA	578.58	3.93	6.09	5
	DJAYA	573.17	6.33	5.10	4
	DPSO6	572.98	<b>2.60</b>	5.06	3
PR76	ACO	116321.22	885.79	7.55	5
	ABC	205119.61	7379.16	89.65	6
	HA	115072.29	742.90	6.39	4
	DTSA	114930.03	1545.64	6.26	3
	DJAYA	113258.29	1711.93	4.71	2
	DPSO6	<b>112937.44</b>	<b>681.34</b>	<b>4.42</b>	<b>1</b>
KROA100	ACO	22880.12	235.18	7.49	5
	ABC	53840.03	2198.36	152.94	6
	HA	22435.31	231.34	5.40	4
	DTSA	21728.40	358.13	2.08	2
	DJAYA	21735.31	331.33	2.13	3
	DPSO6	<b>21599.07</b>	<b>190.63</b>	<b>1.49</b>	<b>1</b>
EIL101	ACO	693.42	6.80	7.96	5
	ABC	1315.95	35.28	104.88	6
	HA	683.39	6.56	6.40	3
	DTSA	689.91	4.47	7.41	4
	DJAYA	677.37	4.87	5.46	2
	DPSO6	<b>677.34</b>	<b>0.58</b>	<b>5.45</b>	<b>1</b>
CH150	ACO	6702.87	20.73	2.61	3
	ABC	21617.48	453.71	230.93	6
	HA	6677.12	<b>19.30</b>	2.22	2
	DTSA	6748.99	32.63	3.32	5
	DJAYA	<b>6638.63</b>	52.79	<b>1.63</b>	<b>1</b>
	DPSO6	6723.35	33.01	2.93	4
TSP225	ACO	4176.08	<b>28.34</b>	8.22	4
	ABC	17955.12	387.35	365.28	6
	HA	4157.85	26.27	7.74	3
	DTSA	4230.45	58.76	9.93	5
	DJAYA	<b>4095.02</b>	42.54	<b>6.12</b>	<b>1</b>
	DPSO6	4152.81	43.42	7.61	2

### 3.6. The comparison of the variations of the DPSO with DJAYA, ACO, GA, BH, and DTSA

The last comparison is performed with Hatamlou, Cinar et al., and Gunduz and Aslan [20], [21], [37]. In this study, the DPSO is compared with DJAYA, ACO, GA, BH, and DTSA on EIL51, EIL76, EIL101, BERLIN52, and ST70 problems. Comparison results of, ACO, GA, and BH are directly taken from Hatamlou, DTSA is directly taken from Cinar et al., and DJAYA is directly taken from Gunduz and Aslan. MaxFEs and population size (N) are set to 20000 and 100 for all methods to ensure a fair comparison. ST is set to 0.5 for DTSA. The ACO parameters are  $\alpha = 1.5$ ,  $\beta = 2$ , and  $\rho = 0.7$ . For ACO, the number of ants is set to 100, while the maximum number of iterations is set to 200. Comparison results are shown in Table 17. According to the results, DPSO has been achieved more successful results than other heuristic algorithms in 4 of 5 different TSP datasets. DJAYA, on the other hand, has been showed superior success in 2 of 5 different TSP datasets. According to the results, DJAYA and DPSO outperform other heuristic algorithms. DPSO owes this outstanding success to symmetry and 2-opt methods developed for local search.

**Table 17.** The comparison of DPSO with DJAYA, ACO, GA, BH, and DTSA.

TSP name	Algorithm	Avg	Std	Rank
EIL51	ACO	461.0175	6.2974	6
	GA	453.4773	9.4157	3
	BH	458.9252	38.6365	5
	DTSA	456.5184	8.9247	4
	DJAYA	440.4394	<b>3.1055</b>	2
	DPSO6	<b>439.11</b>	3.23	<b>1</b>
EIL76	ACO	594.1442	40.2152	4
	GA	652.0593	122.0972	5
	BH	659.1021	152.1754	6
	DTSA	588.0623	5.7296	3
	DJAYA	<b>574.4803</b>	5.6710	<b>1</b>
	DPSO6	575.07	<b>3.89</b>	2
EIL101	ACO	763.9207	59.9684	4
	GA	838.8307	9.9642	5
	BH	897.3813	210.1446	6
	DTSA	689.8384	7.2994	3
	DJAYA	686.8843	<b>6.0664</b>	2
	DPSO6	<b>685.92</b>	6.23	<b>1</b>
BERLIN52	ACO	8522.9017	1152.2000	4
	GA	9288.4483	1301.2108	5
	BH	8455.8304	508.9871	3
	DTSA	7761.6000	<b>62.8594</b>	2
	DJAYA	<b>7627.0000</b>	120.3869	<b>1</b>
	DPSO6	<b>7627.0000</b>	103.89	<b>1</b>
ST70	ACO	757.7540	59.6079	4
	GA	1158.8458	52.1734	6
	BH	797.5745	125.2272	5
	DTSA	710.4037	2.7956	3
	DJAYA	707.2151	15.3049	2
	DPSO6	<b>707.08</b>	<b>1.84</b>	<b>1</b>

### 3.7. Discussion

The PSO has been updated for discrete optimization problems, and the results of DPSO have been examined in this study on TSPs of 16 different sizes. Four different methods have been proposed to improve the performance of DPSO (swap, shift, symmetry, and 2-opt methods). Various DPSO variations are obtained according to the addition of each method to DPSO. Thus, the success of each method on DPSO is examined in detail. The symmetry method provides a noticeable performance increase in the result. Swap, shift, and symmetry methods have improved DPSO to achieve optimum results. DPSO6 is obtained as a result of running the 2-opt algorithm on the optimum route. When DPSO is compared with the literature, it is a remarkable success. Thus, the success of the proposed methods for DPSO has been proven.

## 4. CONCLUSIONS

PSO is a heuristic algorithm based on swarm intelligence developed to solve continuous optimization problems. Due to its success in solving continuous optimization problems, it has often been preferred by many researchers in the literature for solving real-world problems. But real-world problems do not always consist of continuous problems. Sometimes real-world problems are problems involving independent variables. Such problems are called discrete optimization problems. TSP is a discrete optimization problem that is frequently used in the literature to measure the success of discrete optimization algorithms. In this study, a Discrete PSO (DPSO) is proposed. In order to increase the success of DPSO, new methods have been added in the new candidate particle generation stage. These methods are swap, shift, symmetry, and 2-OPT methods. Although the swap, shift, and symmetry methods are frequently used in the literature, they are used for the first time in DPSO. The symmetry method is a new and successful method. The variations of the DPSO have occurred according to the selected method type (DPSO1 (swap method), DPSO2 (shift method), DPSO3 (swap and shift methods), DPSO4 (symmetry method), DPSO5 (swap, shift, and symmetry methods), DPSO6 (swap, shift, symmetry, and 2-opt methods)). The performance increase of each method on DPSO is examined in detail. Thus, the contribution of each method to the performance of the DPSO is shown. The performance of DPSO is studied on sixteen different TSP datasets with low and high scales. The performance of DPSO is compared with the performances of DJAYA, DTSA, SA, DSTA0, DSTAI, DSTAIL, ACO, ABC, HA, ACO, GA, and BH which are recently proposed new discrete optimization algorithms in the literature. Since DPSO is a well-established heuristic algorithm in the literature, it has competed with the newly proposed discrete algorithms. DPSO has excelled in many TSPs. DPSO's success is thanks to the swap, shift, and symmetry methods that it has developed the ability to search locally and globally. In future studies, the success of DPSO is thought to be demonstrated in different discrete optimization problems such as the knapsack problem and discrete real-world problems.

### Declaration of Ethical Standards

Not applicable.

### Credit Authorship Contribution Statement

Emine BAŞ: Conceptualization, Investigation, Methodology, Software, Writing – review, Original draft & editing.

Gülnur YILDIZDAN: Conceptualization, Investigation, Methodology, Writing - review, Software, Original draft & editing.

### Declaration of Competing Interest

The authors declare that they have no known competing financial interests or personal relationships that could have appeared to influence the work reported in this paper.

### Funding / Acknowledgements

This study was not funded by any institution.

### Data Availability

The dataset used during the current study was obtained from the TSPLIB library (<http://comopt.ifl.uni-heidelberg.de/software/TSPLIB95/>).

### 5. REFERENCES

- [1] R. Eberhard, J. Kennedy, "A New Optimizer Using Particle Swarm Theory," Proceedings of 1995 IEEE 6th International Symposium, pp. 39 – 43.
- [2] M. Mahi, Ö.K. Baykan, H. Kodaz, "A new hybrid method based on Particle Swarm Optimization, Ant Colony Optimization and 3-Opt algorithms for Traveling Salesman Problem," *Applied Soft Computing*, vol. 30, pp. 484-490, 2015.
- [3] Ş. Öztürk, R. Ahmad, N. Akhtar, "Variants of Artificial Bee Colony algorithm and its applications in medical image processing," *Applied Soft Computing*, vol. 97, Part A, pp. 106799, 2020.
- [4] F. A. Hashim, A. G. Hussien, "Snake Optimizer: A novel meta-heuristic optimization algorithm," *Knowledge-Based Systems*, vol. 242, pp. 108320, 2022.
- [5] T. S. L. V. Ayyarao, N. S. S. Ramakrishna, R. M. Elavarasan, N. Polumahanthi, M. Rambabu, G. Saini, B.Khan, B.Alatas, "War Strategy Optimization Algorithm: A New Effective Metaheuristic Algorithm for Global Optimization," in *IEEE Access*, vol. 10, pp. 25073-25105, 2022.
- [6] D. Połap, M. Woźniak, "Red fox optimization algorithm," *Expert Systems with Applications*, vol. 166, pp. 114107, 2021.
- [7] L. Yi, "Study on an Improved PSO Algorithm and its Application for Solving Function Problem," *International Journal of Smart Home*, vol. 10, no. 3, pp. 51 – 62, 2016.
- [8] W. Deng, R. Chen, B. He, Y.Q. Liu, L. F. Yin, J. H. Guo, "A novel two-stage hybrid swarm intelligence optimization algorithm and application," *Soft Computing*, vol. 16, no. 10, pp. 1707-1722, 2012.
- [9] W. Deng, H. M. Zhao, J. J. Liu, X. L. Yan, Y. Y. Li, L. F. Yin, C. H. Ding, "An improved CACO algorithm based on adaptive method and multi-variant strategies," *Soft Computing*, vol. 19 no. 3, pp. 701- 713, 2015.
- [10] X. H. Shi, Y. Zhou, L. M. Wang, Q. X. Wang, Y. C. Liang, "A Discrete Particle Swarm Optimization Algorithm for Travelling Salesman Problem," *Computational Methods*, 2006, pp. 1063–1068.
- [11] O. E. Turgut, M. S. Turgut, M. T. Coban, "Chaotic quantum behaved particle swarm optimization algorithm for solving nonlinear system of equations," *Computers and Mathematics with Applications*, vol. 68, no. 4, pp. 508-530, 2014.
- [12] Z. L. Gaing, "Discrete particle swarm optimization algorithm for unit commitment," 2003 IEEE Power Engineering Society General Meeting (IEEE Cat. No.03CH37491), 2003, pp. 418-424.
- [13] A. Unler, A. Murat, "A discrete particle swarm optimization method for feature selection in binary classification problems," vol. 206, no. 3, pp. 528-539, 2010.
- [14] S. Strasser, R. Goodman, J. Sheppard, S. Butcher, "A New Discrete Particle Swarm Optimization Algorithm," GECCO '16: Proceedings of the Genetic and Evolutionary Computation Conference 2016, 2016, pp. 53–60.
- [15] Q. K. Pan, M. F. Tasgetiren, Y. C. Liang, "A discrete particle swarm optimization algorithm for the

- no-wait flowshop scheduling problem," vol. 35, no. 9, pp. 2807-2839, 2008.
- [16] H. Izakian, B. T. Ladani, A. Abraham, V. Snasel, "A Discrete Particle Swarm Optimization Approach For Grid Job Scheduling," *International Journal of Innovative Computing, Information and Control*, vol. 6, no. 9, pp. 1-09, 2010.
- [17] E. Baş, E. Ülker, "Discrete social spider algorithm for the traveling salesman Problem," *Artificial Intelligence Review*, vol. 54, pp. 1063–1085, 2021.
- [18] M. A. Al-Furhud, Z. H. Ahmed, "Genetic Algorithms for the Multiple Travelling Salesman Problem," (*IJACSA*) *International Journal of Advanced Computer Science and Applications*, vol. 11, no. 7, 2020.
- [19] K. Panwar, K. Deep, "Discrete Grey Wolf Optimizer for symmetric travelling salesman problem," *Applied Soft Computing*, vol. 105, pp. 107298, 2021.
- [20] M. Gunduz, M. Aslan, "DJAYA: A discrete Jaya algorithm for solving traveling salesman problem," *Applied Soft Computing*, vol. 105 pp. 107275, 2021.
- [21] A. C. Cinar, S. Korkmaz, M. S. Kiran, "A discrete tree-seed algorithm for solving symmetric traveling salesman Problem," *Engineering Science and Technology*, vol. 23, pp. 879–890, 2020.
- [22] E. Osaba, J. D. Ser, A. Sadollah, M. N. Bilbao, D. Camacho, "A discrete water cycle algorithm for solving the symmetric and asymmetric traveling salesman problem," vol. 71, pp. 277-290, 2018.
- [23] S. S. Choong, L. P. Wong, C. P. Lim, "An artificial bee colony algorithm with a Modified Choice Function for the traveling salesman problem," vol. 44, pp. 622-635, 2019.
- [24] F. Dahan, K. El Hindi, H. Mathkour, H. AlSalman, "Dynamic Flying Ant Colony Optimization (DFACO) for Solving the Traveling Salesman Problem," *Sensors*, vol. 19, no. 8, pp. 1837, 2019.
- [25] Y. Zhong, J. Lin, L. Wang, H. Zhang, "Hybrid discrete artificial bee colony algorithm with threshold acceptance criterion for traveling salesman problem," *Information Sciences*, vol. 421, pp. 70-84, 2017.
- [26] W. Gao, "New Ant Colony Optimization Algorithm for the Traveling Salesman Problem," vol. 13, no. 1, pp. 44 – 55, 2020.
- [27] X. Dong, Y. Cai, "A novel genetic algorithm for large scale colored balanced traveling salesman problem," vol. 95, pp. 727-742, 2019.
- [28] N. Rokbani, R. Kumar, A. Abraham, A. M. Alimi, H. V. Long, S. Priyadarshini, L. H. Son, "Bi-heuristic ant colony optimization-based approaches for traveling salesman problem," *Soft Computing*, vol. 25, pp. 3775–3794, 2021.
- [29] C. Wu, X. Fu, J. Pei, Z. Dong, "A Novel Sparrow Search Algorithm for the Traveling Salesman Problem," in *IEEE Access*, vol. 9, pp. 153456-153471, 2021.
- [30] Z. Zhang, Y. Han, "Discrete sparrow search algorithm for symmetric traveling salesman problem," *Applied Soft Computing*, vol. 118, pp. 108469, 2022.
- [31] Y. Huang, X. N. Shen, X. You, "A discrete shuffled frog-leaping algorithm based on heuristic information for traveling salesman problem," *Applied Soft Computing*, vol. 102, pp. 107085, 2021.
- [32] Z. Zhang, J. Yang, "A discrete cuckoo search algorithm for traveling salesman problem and its application in cutting path optimization," *Computers & Industrial Engineering*, vol. 169, pp. 108157, 2022.
- [33] T. Zhang, Y. Zhou, G. Zhou, W. Deng, Q. Luo, "Discrete Mayfly Algorithm for spherical asymmetric traveling salesman problem," *Expert Systems with Applications*, vol. 221, pp. 119765, 2023.
- [34] Y. Chunhua, T. Xiaolin, Z. Xiaojun, G. Weihua, "State transition algorithm for traveling salesman problem," in: *Proceedings of the 31st Chinese Control Conference IEEE*, 2012, pp. 2481–2485.
- [35] X. Zhou, D. Y. Gao, C. Yang, W. Gui, "Discrete state transition algorithm for unconstrained integer optimization problems," *Neurocomputing*, vol. 173, pp. 864–874, 2016.
- [36] M. Gündüz, M. S. Kiran, E. Özceylan, "A hierarchic approach based on swarm intelligence to solve the traveling salesman problem," *Turkish Journal of Electrical Engineering and Computer Sciences*, vol. 23, no. 1, pp. 103- 117, 2015.



- [37] A. Hatamlou, "Solving travelling salesman problem using black hole algorithm," *Soft Computing*, vol. 22, pp. 8167–8175, 2018.
- [38] G. A. Croes, "A method for solving traveling-salesman problems", *Operations research*, vol. 6, no. 6, pp. 791–812, 1958.
- [39] G. Reinelt, "TSPLIB—A traveling salesman problem library", *ORSA Journal on Computing*, vol. 3, no. 4, pp. 267–384, 1991.



## KİL MİNERALLERİNİN KÖMÜRÜN FLOTASYON PERFORMANSINA VE ORTALAMA KABARCİK BOYUTUNA ETKİSİ

<sup>1\*</sup>Vildan ÖNEN , <sup>2</sup>Ayşe Zeynep ÇAĞLAR , <sup>3</sup>Hasan Ali TANER 

*Konya Teknik Üniversitesi, Mühendislik ve Doğa Bilimleri Fakültesi, Maden Mühendisliği Bölümü, Konya, TÜRKİYE*

<sup>1</sup>[vonen@ktun.edu.tr](mailto:vonen@ktun.edu.tr), <sup>2</sup>[aysezeynepcaglar@gmail.com](mailto:aysezeynepcaglar@gmail.com), <sup>3</sup>[hataner@ktun.edu.tr](mailto:hataner@ktun.edu.tr)

### Önemli Katkılar (Highlights)

- Kil minerallerinin (kaolin ve montmorillonit) linyit kömürünün flotasyon performansına ve ortalama kabarcık boyutuna etkisi araştırılmıştır.
- Kaolin içerikli numunelerde %40-55, montmorillonit içerikli numunelerde ise %30-47 aralığında yanabilir verim değerleri elde edilmiştir.
- Montmorillonit içerikli flotasyon deneylerinde Dowfroth 250 ile; kaolin içerikli flotasyon deneylerinde ise MIBC ile nisbeten daha büyük boyutlu kabarcıklar elde edilmiştir.



## KİL MİNERALLERİNİN KÖMÜRÜN FLOTASYON PERFORMANSINA VE ORTALAMA KABARCIK BOYUTUNA ETKİSİ

<sup>1</sup>\*Vildan ÖNEN , <sup>2</sup>Ayşe Zeynep ÇAĞLAR , <sup>3</sup>Hasan Ali TANER 

Konya Teknik Üniversitesi, Mühendislik ve Doğa Bilimleri Fakültesi, Maden Mühendisliği Bölümü, Konya,  
TÜRKİYE

<sup>1</sup>vonen@ktun.edu.tr, <sup>2</sup>aysezeynepcaglar@gmail.com, <sup>3</sup>hataner@ktun.edu.tr

(Geliş/Received: 28.12.2022; Kabul/Accepted in Revised Form: 03.05.2023)

**ÖZ:** Flotasyon, ince boyutlu kömürlerin zenginleştirilmesinde kullanılan en etkili yöntemlerdendir. Bununla birlikte, kömürün yan kayaç olarak kil minerallerini bulundurması flotasyon işlemini olumsuz etkilemektedir. Bu çalışmada kil minerallerinin (kaolin ve montmorillonit) ve flotasyon reaktiflerinin Tunçbilek linyit kömürünün flotasyon performansına ve ortalama kabarcık boyutuna etkisi araştırılmıştır. Deneysel çalışmalarda; bastırıcı olarak sodyum silikat, toplayıcı olarak gaz yağı kullanılırken, köpürtücü olarak ise metil izobütil karbinol (MIBC) ve Dowfroth 250 kullanılmıştır. Kil türü ve miktarı, bastırıcı miktarı ve köpürtücü türü ve miktarı çalışılan deneysel parametrelerdir. Bastırıcı miktarı ve kil içeriğinin etkisinin belirlendiği deneysel çalışmalarda, kaolin içerikli numunelerde %40-55, montmorillonit içerikli numunelerde ise %30-47 aralığında yanabilir verim değerleri elde edilmiştir. Köpürtücü olarak Dowfroth 250 ile daha iyi sonuçlar elde edilmiş ve montmorillonit içeren kömür numunesi, kaolin içeren kömür numunesine göre daha büyük kabarcıklar oluşmasına neden olmuştur. Bu çalışmadan elde edilen sonuçlar yan kayaç olarak kil bulunduran kömürlerin flotasyon davranışlarının anlaşılabilmesi ve çözüm önerileri sunulabilmesi için temel bir altyapı oluşturacaktır.

**Anahtar Kelimeler:** Kömür Flotasyonu, Kil Mineralleri, Ortalama Kabarcık Boyutu, Kaolin, Montmorillonit

### Effect of Clay Minerals on the Flotation Performance of Coal and Mean Bubble Size

**ABSTRACT:** Flotation is one of the most effective methods used in the enrichment of fine sized coals. However, the presence of clay minerals as gangue minerals in coal affects the flotation process negatively. In this study, the effects of clay minerals (kaolinite and montmorillonite) and flotation reagents on the flotation performance and mean bubble size of Tunçbilek lignite coal were investigated. In the experimental studies; sodium silicate was used as depressant, kerosene was used as collector, methyl isobutyl carbinol (MIBC) and Dowfroth 250 were used as frother. Clay type and amount, depressant amount and frother type and amount were the experimental parameters studied. In experimental studies in which the effect of depressant amount and clay content was determined, combustible recovery values were obtained in the range of 40-55% for samples containing kaolinite and 30-47% for samples containing montmorillonite. Better results were obtained with Dowfroth 250 as the frother, and the coal sample containing montmorillonite caused larger bubbles to form than the coal sample containing kaolinite. The results obtained from this study will form a basic infrastructure to understand the flotation behavior of coals containing clay minerals as gangue and to offer solutions.

**Keywords:** Coal Flotation, Clay Minerals, Mean Bubble Size, Kaolinite, Montmorillonite

### 1. GİRİŞ (INTRODUCTION)

Kömür yataklarının değerlendirilmesi; petrol ve doğal gaz yataklarının hızla tükenmesi, sık sık yaşanan petrol krizi ve değişken doğal gaz fiyatları nedeniyle günümüzde daha da önemli hale gelmektedir. Kömürün kullanılmasıyla asit yağmuru ve çevreye zararlı emisyon oluşmaktadır. Bu

\*Corresponding Author: Vildan ÖNEN, [vonen@ktun.edu.tr](mailto:vonen@ktun.edu.tr)

çevresel etkileri en aza indirmek için temiz kömür üretim teknolojilerinin geliştirilmesine yönelik kapsamlı araştırma çalışmaları yapılmaktadır. Kömür üretimini ve kullanımını en üst düzeye çıkarmak amacıyla kömür madenciliği son yıllarda mekanize yöntemlerle gerçekleştirilmektedir. Endüstriyel gelişimle artan üretim, mekanize yöntemler ve madencilik faaliyetlerinin derinleşmesi ile birlikte özellikle kil mineralleri olmak üzere daha fazla gang minerali içeren ham kömür ortaya çıkmaktadır. Üretilen kömür sıklıkla %40 kadar mineral madde içermektedir. Bu yüksek mineral madde içeriği, kömür damarlarında iç içe geçmiş şeyl bantlarının varlığı ve/veya kil açısından zengin mineral maddelerin yan kayaçlardan istenmeden kömüre dahil olmasından kaynaklanmaktadır. Kaolin, illit ve montmorillonit gibi çeşitli killer, kül oluşturan mineral maddelerin ana bileşenleri olarak kabul edilmekte ve killer kömürdeki toplam mineral maddelerin ortalama %60-80'ini oluşturmaktadır [1-3].

Kömürün fosil yakıt olarak kullanılmasına yönelik çevresel düzenlemeler nedeniyle, mineral madde ve kükürt içeriğini azaltmak amacıyla kömür flotasyonu artık bir gereklilik halini almıştır. Ancak kil varlığı tüm cevher hazırlama proseslerinde olduğu gibi kömür flotasyonunda da şlam kaplama, mekanik taşıma, fazla reaktif tüketimi ve yüksek köpük kararlılığı gibi bazı problemlerin ana kaynağıdır [4]. Çok küçük boyutlu parçacıklarının pülp içerisinde köpük bölgesine transferi olarak tanımlanan mekanik taşıma, gang minerallerinin taşındığı en etkili mekanizma olarak kabul edilmektedir. Karıştırma hızı, hava akış hızı, pülp katı oranı, köpük özellikleri ve elektrolitlerin mekanik taşımada önemli etkilere sahip olduğu belirlenmiştir [5-6]. Elektriksel çift tabaka teorisiyle açıklanan şlam kaplama, değerli tane yüzeylerinin kil mineralleri tarafından kaplanmasına ve böylece değerli mineral yüzeyinde toplayıcı adsorpsiyonunun engellenmesine neden olmaktadır [3,6]. Köpük kararlılığının flotasyon performansı için önemli bir faktör olduğu bilinmektedir. İyi köpük kararlılığının oluşturularak korunması kolay değildir. Kömür-su arayüzeyinde kil mineralleri tarafından sert bir film tabakası meydana gelmekte ve bu durum artan köpük kararlılığı ile sonuçlanmaktadır. Yüksek köpük kararlılığı nedeniyle pülp içerisinde asılı olan mineraller köpükle birlikte yukarı doğru hareket ederek selülü terk etmekte ve mekanik taşımaya neden olmaktadır [7]. Sonuç olarak, kil minerallerinin varlığından dolayı yüksek yanabilir verime ulaşılması genellikle zordur.

Yapılan çalışmalarda kaolin ve illit gibi killerin kömür flotasyonu üzerinde çok az etkisi olduğu, ancak az miktarda montmorillonitin bile kömür flotasyonunu son derece olumsuz etkilediği belirlenmiştir [3, 5,6,8]. Bu araştırmalar kil tipinin etkileme mekanizmasında temel faktör olduğunu göstermiştir. Kil mineralleri arasındaki yapısal farklılıklar flotasyondaki davranışlarında etkili olmaktadır. Bu noktadan hareketle bu çalışmada, farklı kil minerallerinin (kaolin ve montmorillonit) ve flotasyon reaktiflerinin kömür flotasyon performansına ve ortalama kabarcık boyutuna etkisi araştırılmıştır. Günümüzde kil içeren minerallerin zenginleştirilmesini iyileştirmek için kullanılan stratejiler, optimum operasyonel sonuçların elde edilmesinde yetersiz kalmakta ve kaliteli kömür yataklarının azalmasıyla birlikte kil minerallerinin etkilerinin araştırılması ve etki mekanizmalarının anlaşılması daha da önemli hale gelmektedir. Bu çalışmadan elde edilen sonuçların, kil sorunu yaşayan kömür tesisleri için performansı artırmaya yönelik yeni çalışma koşullarının ortaya konmasına ve çözüm önerileri geliştirilmesine katkı sağlayabileceği düşünülmektedir.

## 2. MALZEME VE YÖNTEM (MATERIAL AND METHOD)

### 2.1. Malzeme (Material)

Çizelge 1'de özellikleri verilen linyit kömürü, Kütahya-Tunçbilek'te bulunan bir özel işletmeden parça kömür halinde getirilerek laboratuvar tipi çeneli kırıcıda kırıldıktan sonra laboratuvar tipi bir çubuklu değirmen ile boyut küçültme işlemine tabii tutulmuştur. Numunenin  $d_{80}$  tane boyutu 300  $\mu\text{m}$ 'dur. Deneysel çalışmalar hazırlanan bu kömür numunesinin farklı oranlarda kil mineralleri (kaolin ve montmorillonit) ile karıştırılması ile gerçekleştirilmiştir.

**Çizelge 1.** Kömür numunesi analiz sonuçları

*Figure 1. Analysis results of coal sample*

Analiz	Değerler
Kül içeriği (%)	14,8
Uçucu madde (%)	30,5
Toplam kükürt (%)	1,83
Sabit karbon (%)	33,22
Üst ısıl kalori değeri (kcal/kg)	4790
Alt ısıl kalori değeri (kcal/kg)	4495

Yapay karışım hazırlamak için kullanılan kaolin numunesi Esan Eczacıbaşı AŞ'den, montmorillonit (sodyum içerikli) ise Karakaya Bentonit AŞ'den temin edilmiştir. XRD analizi (Bruker D8) ile kaolin numunesinin kaolin mineralinden başka halloysit de içerdiği, montmorillonit numunesinin ise iki farklı kimyasal bileşime sahip montmorillonit içerdiği tespit edilmiştir [9]. D<sub>80</sub> tane boyutu; kaolin numunesi için 28 µm ve montmorillonit numunesi için 60 µm olarak belirlenmiştir. Tane boyut analizleri yaş olarak gerçekleştirilmiş (Malvern Mastersizer 2000) ve ölçümlerde kaolin için distile su, montmorillonit için ise suda dağılmadığı için distile su yerine aseton kullanılmıştır. Deneysel çalışmalarda, bastırıcı olarak sodyum silikat (Na<sub>2</sub>O.nSiO<sub>2</sub>), toplayıcı olarak gaz yağı, köpürtücü olarak ise MIBC (metil izobütil karbinol, C<sub>6</sub>H<sub>14</sub>O) ve Dowfroth 250 (polipropilen glikol metil eter, C<sub>7</sub>H<sub>16</sub>O<sub>3</sub>) kullanılmıştır. Deneyler iletkenlik değeri 293 µS/cm ve doğal pH değeri 7.5 olan musluk suyu ile gerçekleştirilmiştir. Musluk suyu, ICP analizine göre 57.2 mg/L Ca; 8.92 mg/L Mg ve 2.9 mg/L Na içermektedir.

## 2.2. Yöntem (Method)

### 2.2.1. Zeta Potansiyeli Ölçümleri (Zeta Potential Measurements)

Zeta potansiyeli ölçümleri için ilk olarak kömür içeren pH değeri ayarlanmış çözeltiler, 10 dk manyetik karıştırıcıda karıştırılmıştır. Daha sonra hazırlanan bu stok çözeltilerden alınan numuneler pleksiglas hücrelere aktarılarak ZetaPlus (Brookhaven) cihazında ölçümler gerçekleştirilmiştir. Cihaz her bir numune için 10 ölçüm yaparak ortalama değer ve standart sapma vermektedir. Her numune için üç okuma yapılarak ortalaması alınmıştır. Cihaz ölçüm için elektroforez yöntemini kullanmakta ve "Smoluchowski" eşitliği ile zeta potansiyeli değerlerini hesaplamaktadır.

### 2.2.2. Flotasyon Deneylemleri (Flotation Experiments)

Flotasyon deneylemleri, Denver tipi flotasyon makinasında, 1 cm köpük yüksekliğinde, 1350 dev/dk karıştırma hızında, %10 katı oranında ve doğal pülp pH'ında (7,8) gerçekleştirilmiştir. Tüm flotasyon deneylemlerinde ilk olarak, kömür ve belirli oranda kil içeren pülp homojen bir karışım elde etmek için 5 dk karıştırılmıştır. Daha sonra sırasıyla bastırıcı, toplayıcı ve köpürtücü eklenmiş ve her reaktif için 3 dk karıştırma süresi uygulanmıştır. Sisteme hava verilerek, 4 dk süreyle köpük alımı gerçekleştirilmiştir. Elde edilen ürünler filtre edilerek etüvde kurutulmuş (105 °C) ve konsantrenin kül içerikleri belirlenerek yanabilir verim değerleri hesaplanmıştır (Eşitlik 1).

$$\text{Yanabilir verim (\%)} = \frac{M_t \times (100 - K_t)}{M_b \times (100 - K_b)} \times 100 \quad (1)$$

Burada; M<sub>t</sub> temiz kömür miktarını (%), K<sub>t</sub> temiz kömür kül değerini (%), M<sub>b</sub> besleme kömür miktarını (%) ve K<sub>b</sub> besleme kömür kül değerini (%) ifade etmektedir.

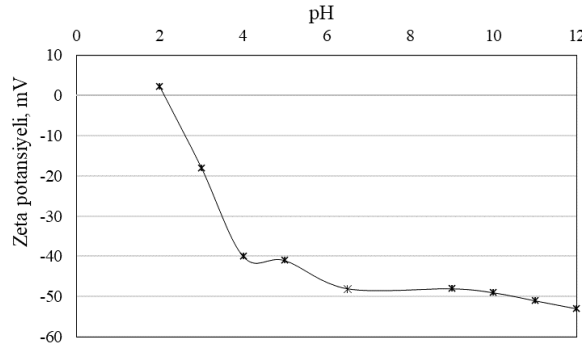
Deneysel değişkenler kil türü (kaolin ve montmorillonit) ve miktarı (%5-10-15), bastırıcı miktarı ve köpürtücü türü ve miktarı olarak belirlenmiştir. Farklı köpürtücülerle gerçekleştirilen deneylemlerde, köpük

fazındaki ortalama kabarcık boyutlarının belirlenebilmesi amacıyla deney düzeneğine video kamera ve ışık düzeneğinden oluşan bir görüntüleme sistemi eklenmiştir. Bu amaçla deneysel çalışmalarda camdan imal edilmiş 1,5 L hacimli cam selül kullanılmıştır. Deney sırasında fotoğraf makinesi ile 250 kare/saniye olacak şekilde çekilen yavaşlatılmış video görüntüleri içerisinde, belirlenen sürelerdeki görüntüler Image-Pro Premier Software bilgisayar programına yüklenmiştir. Program kalibre edildikten sonra, kabarcıkların netleme ayarı yapılarak ortalama kabarcık boyutu ölçülmüştür.

### 3. BULGULAR VE TARTIŞMA (RESULTS AND DISCUSSION)

#### 3.1. Zeta Potansiyeli Sonuçları (Zeta Potential Results)

Zeta potansiyeli ölçümlerinde kömür numunesi için sıfır yük noktası pH 2,1 olarak tespit edilmiştir (Şekil 1). Sıfır yük noktası katı yüzeyinin toplam elektriksel yükünün sıfır olduğu potansiyel tayin edici iyonların kritik konsantrasyonudur. Mineral yüzeyinin yük kazanması bu iyonlar sayesinde olmaktadır. Kömür için potansiyel belirleyici iyonlar  $H^+$  ve  $OH^-$  iyonlarıdır. Çözelti pH değeri sıfır yük noktasındaki pH değerinden büyükse katı yüzeyi negatif, küçük ise pozitif yüklü olmaktadır. Kömürün sıfır yük noktası, kömürleşme derecesine ve dolayısıyla karbon içeriğine göre değişmektedir. Molatlhegi ve Alagha [10], temiz kömürün sıfır yük noktasını yaklaşık pH 3,5 olarak belirleyerek, kömür yüzeyinin düşük pH değerlerinde  $H^+$  iyonu adsorpsiyonuyla pozitif, pH 3,5 üzerinde ise  $OH^-$  iyonlarının adsorpsiyonuyla negatif olduğunu ifade etmişlerdir. Çalışılan kil minerallerinden montmorillonit için sıfır yük noktası tespit edilemezken, kaolin için tespit edilen sıfır yük noktası pH 2,5'tir. Flotasyon pülpünün doğal pH'ında kömür, montmorillonit ve kaolinin zeta potansiyeli değerleri sırasıyla -47 mV, -44 mV ve -40 mV olarak belirlenmiştir [9].



Şekil 1. Linyit kömürünün farklı pH değerlerine bağlı zeta potansiyeli değerleri

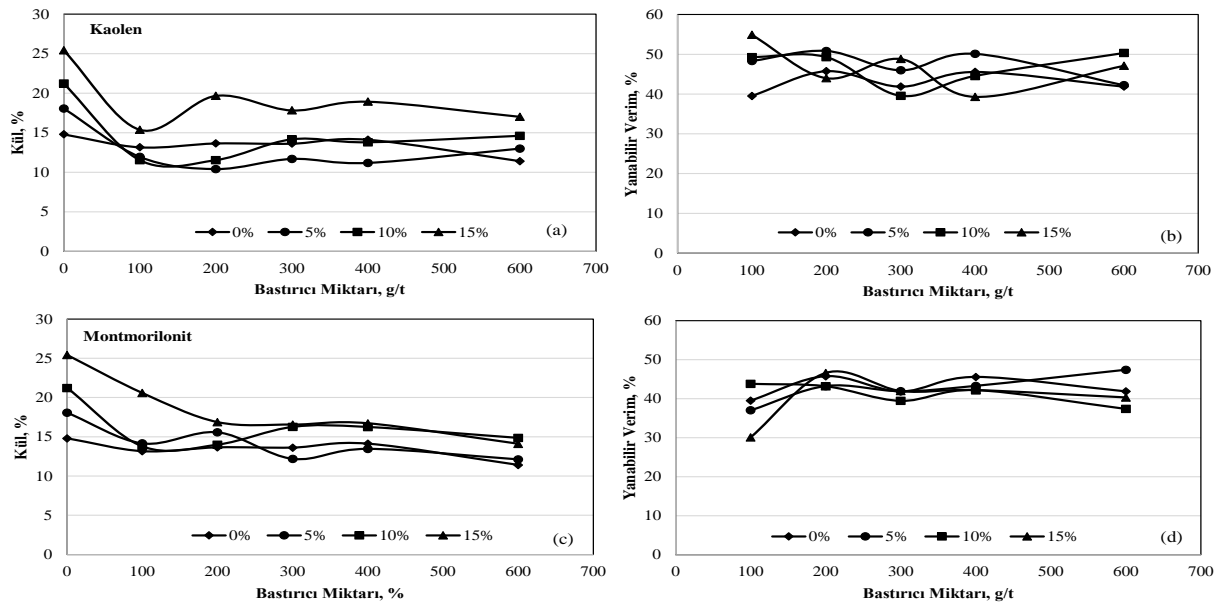
Figure 1. Zeta potential values of lignite coal depending on different pH values

Kömürde gang minerali olarak kil minerallerinin bulunması flotasyonda yüzey kimyasını önemli ölçüde etkilemektedir. Kil mineralleri pH'a bağlı olarak negatif yüzey yüküne sahiptir. Nötr ve asidik pH değerlerinde ise kil minerallerinin kenar kısımları pozitif yüklüdür. Literatürde kil minerallerinin köşelerinde ve yüzeylerindeki anizotropik yüklerin, mineral yüzeyinde şlam kaplamaya neden olduğu ifade edilmektedir. Bu durum, flotasyon veriminin azalmasına yol açmaktadır [7]. Xu ve diğ. [3], montmorillonit ve kaolinin kömür flotasyonuna etkilerini pH'a bağlı zeta potansiyeli ölçümleri yaparak araştırmışlar ve kömür-montmorillonit karışımlarında, montmorillonitin tek başına ölçülen zeta potansiyeli değerine yakın değerler tespit ederek, kömür yüzeylerinin neredeyse tamamının montmorillonit tarafından kaplanmış olduğunu belirlemişlerdir. Ancak söz konusu olan bu çalışmada, kaolin ve kömürün zeta potansiyeli değerleri birbirine çok yakın olduğundan süspansiyonun zeta potansiyeli değerine bakarak kaolinin kömürün yüzeyini kapladığını söylemenin zor olduğu ifade edilmektedir. Sunulan bu çalışmada da benzer şekilde çalışılan pH aralığında kömür ve kil mineralleri yakın zeta potansiyeli değerlerine sahip olduğu için ayrıca mineral karışımları için zeta potansiyeli ölçümleri gerçekleştirilmemiştir.

### 3.2. Kil Mineralleri ve Bastırıcı Miktarının Kömür Flotasyonuna Etkisi (Effect of Clay Minerals and Amount of Depressant on Coal Flotation)

Bastırıcılar, elektrostatik ve/veya sterik itme yaratarak parçacıklar arasındaki kolloidal etkileşimleri değiştirmek için yaygın olarak kullanılır. Genellikle anyonik polimerlerdir ve mineral yüzeyine adsorbe olarak mineral yüzeyini daha negatif yaparlar [11,12]. Uygun bastırıcı ve miktarının seçilmesi, flotasyon performansı ve seçicilik için önemlidir. Köpük flotasyonunda sodyum silikatın ( $\text{Na}_2\text{SiO}_3$ ) gang minerallerini daha hidrofilik hale getirerek silikat ve karbonat minerallerini bastırıldığı bilinmektedir. Aynı zamanda sodyum silikat, gang minerali yüzeyine adsorbe olan ve negatif yüklü mineraller ile gang mineralleri arasındaki elektrostatik itme kuvvetini  $\text{SiO}_3^{2-}$  ve  $\text{HSiO}_3^-$  iyonlarıyla artıran etkili bir dağıtıcıdır[13].

DeneySEL çalışmalar kil içermeyen ve her iki kili değişen oranlarda (%5-10-15) içeren kömür numuneleri ile gerçekleştirilmiştir. Kil içermeyen besleme ile 600 g/t bastırıcı miktarında %11,4 kül içerikli konsantre %42 yanabilir verimle elde edilirken, 200 g/t bastırıcı miktarında ise %13,6 kül içerikli konsantre %46 yanabilir verimle elde edilmiştir. %5 ve %10 kaolin ilaveli deneylerde 200 g/ton bastırıcı ilavesinden sonra kül içeriği artarken yanabilir verim değerlerinde düşüş gözlenmiştir (Şekil 2a-b). Genel olarak kaolin içerikli numunelerle yanabilir verim %40-55 aralığında değişmektedir (Şekil 2b). Kaolin ile gerçekleştirilen deneylerde, optimum bastırıcı miktarı 200 g/t olarak tespit edilmiştir. Montmorillonit içerikli deneylerde bastırıcı miktarındaki değişimin konsantre külü ve yanabilir verim üzerinde önemli bir etkisi gözlenmemiştir ve yanabilir verim %30-47 aralığında değişmektedir (Şekil 2c-d).



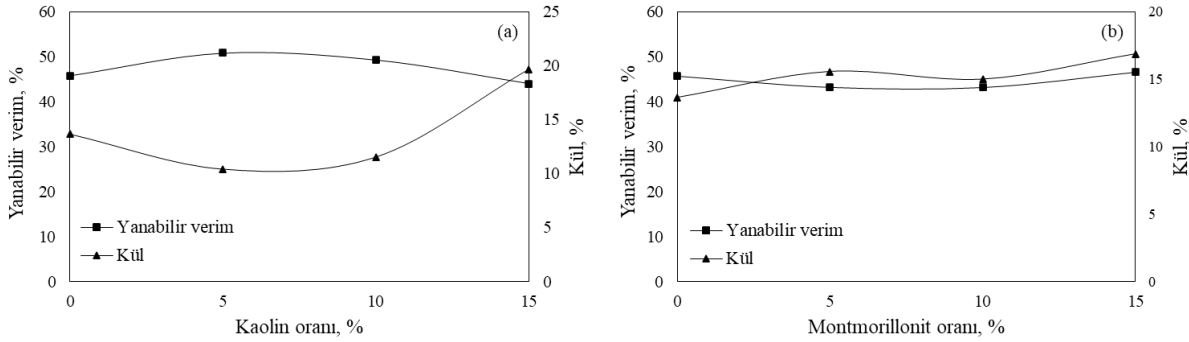
**Şekil 2.** Kil içermeyen ve farklı oranlarda (%5-10-15) kil içeren kömür numunelerinin flotasyonunda bastırıcı miktarının kül içeriğine (kaolin-a ve montmorillonit-c) ve yanabilir verime (kaolin-b ve montmorillonit-d) etkisi

*Figure 2.* The effect of the amount of depressant on the ash content (kaolin-a and montmorillonite-c) and combustible recovery (kaolin-b and montmorillonite-d) in the flotation of coal samples that do not contain clay and contain clay at different rates (5-10-15%)

Literatürde, yanıcı madde kazanımının, kömür-montmorillonit numunesi için kömür-kaoline göre daha düşük olduğu belirtilmekte ve bu bulgular genellikle montmorillonitin düşük konsantrasyonda bile yüksek viskozite artışına sebep olmasıyla açıklanmaktadır [5]. Kaolin ise montmorillonitin aksine pülp viskozitesini üzerinde çok az etkiye sahiptir. Ancak kaolinin de önemli ölçüde gang sürüklenmesine neden olduğu bilinmektedir. Zhang ve diğ. [14], kaoline kıyasla bentonitin daha düşük sürüklenme derecesi gösterdiğini belirterek, bu durumu kaolin parçacıklarının düşük yoğunluklu gevşek ağ yapılarının oluşumu ile ilişkilendirmiştir. Kaolin taneleri flotasyon sırasında suda ve kabarcıkları çevreleyen sıvı

filimde kolayca süspanse edilerek pülp fazından köpük fazına ve mekanik sürüklenme mekanizmasıyla konsantreye taşınabilmektedir.

200 g/ton bastırıcı miktarı için her iki kilin etkileri karşılaştırıldığında; kaolin miktarı arttıkça yanabilir verim azalmış ve konsantredeki kül içeriği %15 kaolin eklenmesiyle önemli miktarda artmıştır. Buna karşılık montmorillonitin eklenmesiyle, kil miktarının artmasıyla konsantrenin kül içeriği artarken, yanabilir verimde belirgin bir değişiklik gözlenmemiştir (Şekil 3). Literatürde montmorillonitin hacimce %4 katı oranında, kaolin süspanسیونlarının ise hacimce %10 katı oranından daha yüksek konsantrasyonlarda sorunlu hale geldiği ifade edilmektedir [15]. Farklı bastırıcı konsantrasyonlarında yapılan flotasyon deneyleri ile yanabilir verimin önemli ölçüde artmadığı görülmüştür. Arnold ve Aplan [8], kaolinin dağıtıcı ile tamamen bastırılmadığını ve mekanik taşınmayla flotasyon verimini düşürdüğünü; bentonitin ise dağıtıcı ile bastırılmasına rağmen şlam kaplama ile flotasyon verimini düşürdüğünü ifade etmiştir. Flotasyon verimini artırmak amacıyla kil minerallerini zenginleştirme öncesi hidrosiklonlar gibi mekanik yollarla uzaklaştırmanın belirli ölçüde katkı sağlayabileceği düşünülebilir. Ancak bu uygulamanın da önemli ölçüde cevher kaybına yol açabileceği unutulmamalıdır. Ayrıca, linyit yüzeyinde oksijen içeren çok sayıda fonksiyonel grup bulundurmakta ve oldukça hidrofilik özellik göstermektedir. Yüksek dereceli kömürlere göre linyit flotasyonu daha zordur ve yüzeyi genellikle gözenekli yapıdadır. Su, kömür yüzeyindeki gözenekleri doldurabilir, bu da su filminin stabilitesini artırdığından kömür ve kabarcık tutunmasını engellemektedir. Diğer bir deyişle, kalın bir su filmi kabarcık ve kömürün tutunmasını engellediği gibi toplayıcıların linyit yüzeyinde adsorpsiyonunu da önlemektedir [16]. Bu nedenle bu çalışmada linyitin genellikle düşük yanabilir verimle yüzdürüldüğü söylenebilir.



Şekil 3. Kil miktarının (kaolin-a ve montmorillonit-b) kül içeriğine ve yanabilir verime etkileri (200 g/t bastırıcı miktarda)

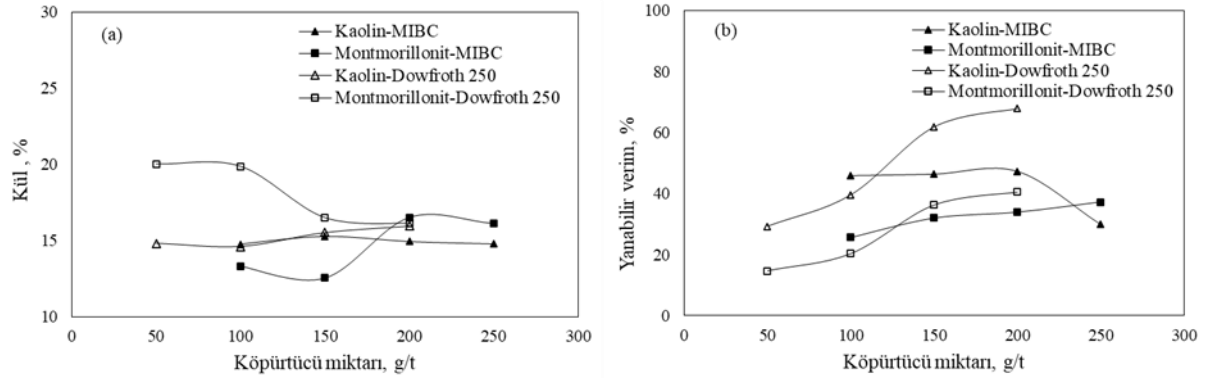
Figure 3. Effects of clay amount (kaolin-a and montmorillonite-b) on ash content and combustible recovery (200 g/t depressant amount)

### 3.3. Kil Mineralleri Varlığında Köpürtücü Türü/Miktarının Kömür Flotasyonuna ve Ortalama Kabarcık Boyutuna Etkileri (Effects of Frother Type/Amount on Coal Flotation and Mean Bubble Size in the Presence of Clay Minerals)

Köpürtücüler pülp içerisine kabarcık özelliklerini ve mineral-kabarcık çarpışmasını iyileştirmek için ilave edilir. Su-hava arayüzünde köpürtücünün adsorpsiyonu ile kabarcığın su tabakası kalınlaşır, boyutu küçülür, yükselme hızı düşer ve deformasyonu azalır. Bunlar, kömürün yüzdürülmesini önemli ölçüde etkileyen temel faktörler olarak kabul edilmektedir [17]. Flotasyonda temel süreçler olarak kabul edilen mineral-kabarcık çarpışması, bağlanma ve ayrılma mekanizmaları büyük ölçüde kabarcık boyutuna ve köpük kararlılığına bağlıdır. Bu nedenle, flotasyonda köpüğün oluşumu ve kararlılığı önemlidir ve konsantre tenör-verimini belirleyen önemli bir faktördür. Köpürtücü, flotasyonda önemli bir rol oynar ve seçimi köpük üzerinde büyük bir etkiye sahiptir. Yapılan çalışmalar alkil zincir uzunluğunun, hidroksil pozisyonunun ve köpürtücü tiplerinin kabarcık yükselme hızı üzerinde farklı etkilere neden olduğunu göstermiştir. Köpüğün oluşumu ve kararlılığı flotasyon için gerekli bir koşul olduğundan, farklı tipte



yüzey aktif maddelerin ve hidrokarbonların köpük kararlılığı üzerindeki etkileri de önemlidir [18]. Bu amaçla kil varlığında köpürtücü türü ve miktarının etkisinin belirlendiği deneysel çalışmalar gerçekleştirilmiştir (Şekil 4). Bu deneylerde toplayıcı miktarı 6700 g/ton ve bastırıcı miktarı kaolin için 200 g/t, montmorillonit için ise 300 g/t olarak seçilmiştir [19].



**Şekil 4.** %10 kil (kaolin ve montmorillonit) içeren kömür numunelerinin köpürtücü türü (Dowfroth 250 ve MIBC) ve miktarına bağlı kül içeriği (a) ve yanabilir verim değerleri (b)

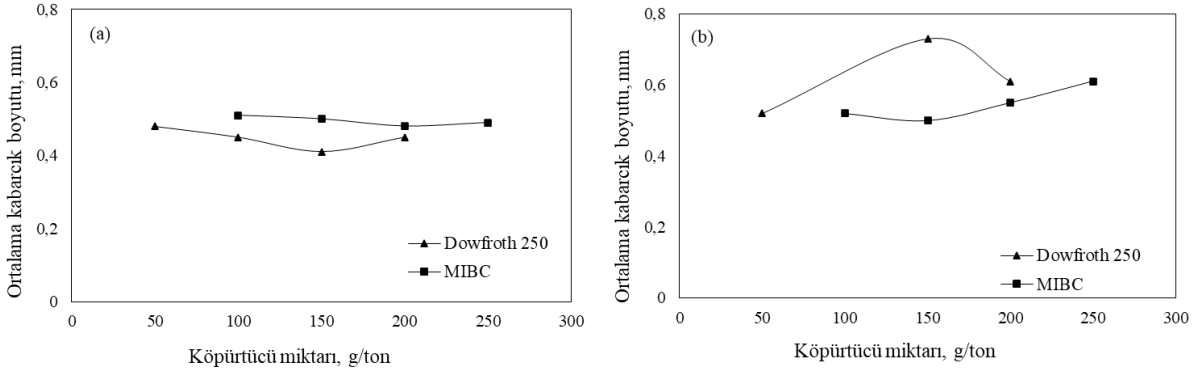
*Figure 4.* Ash content (a) and combustible recovery values (b) of coal samples containing 10% clay (kaolin and montmorillonite) depending on the type (Dowfroth 250 and MIBC) and amount of frothers

Kömür-kaolin karışımlarında her iki köpürtücü için yaklaşık %15 kül içeriğine sahip kömür konsantreleri elde edilmiştir. Dowfroth 250 miktarının artması ile birlikte yanabilir verim önemli ölçüde artarken, 200 g/ton köpürtücü konsantrasyonunda yaklaşık %68 yanabilir verim değeri elde edilmiştir. Kömür ve yanıcı maddenin geri kazanımının, köpürtücü konsantrasyonuyla önemli ölçüde arttığı bilinmektedir [17]. Buna kabarcık boyutu ve hızındaki dikkate değer bir azalma neden olmaktadır [20]. Düşük köpürtücü miktarlarında ise köpük tabakası kolayca bozulmaktadır ve köpükteki mineraller pülpe geri dönmektedir [21]. MIBC kullanıldığında ise 200 g/t üzerinde yanabilir verim değerinin önemli ölçüde azaldığı gözlenmiştir. Kömür-montmorillonit karışımlarında ise kaolin içerikli numunelere göre daha yüksek kül içeriğine sahip konsantreler daha düşük yanabilir verim değerlerinde elde edilmiştir. Bu karışımlarda MIBC için yanabilir verim değerleri %25-37; Dowfroth 250 için ise %15-41 aralığında değişmektedir. Yapılan çalışmalar genel olarak köpürtücü türünün verimden ziyade flotasyon hızını etkilediğini göstermektedir. Flotasyon hızındaki artış tane etrafındaki sıvı filminin kalınlığının azalması sonucunda tanelerin kabarcıklara tutunma olasılığının artması ile ilişkilendirilmiştir. Sıvı filmin kalınlığının azalması adsorbe olan toplayıcı miktarının artmasına neden olmaktadır [21]. Sonuç olarak her iki kil mineralini içeren kömür karışımları için, Dowfroth 250 ile daha iyi sonuçlar elde edildiği söylenebilir. Literatürde Dowfroth 250 ile oluşan köpüğün daha akışkan ve hareketli bir yapıya sahip olduğu ifade edilmektedir [22].

Flotasyon performansı, oluşan kabarcığın boyutu ile yakından ilişkilidir. Mineral ve kabarcığın çarpışma ve tutunma olasılığı küçük kabarcıklar varlığında artmaktadır. Yapılan çalışmalarda köpük yükselme hızının artan köpük boyutu ile; mineral-kabarcık çarpışma olasılığının ise daha küçük kabarcıkların oluşması ile arttığı belirlenmiştir [21]. Bu nedenle ortalama kabarcık boyutunun belirlenmesi ve kontrol edilmesi flotasyon performansı açısından çok önemlidir. Aynı zamanda, görüntü analiz teknikleri ile flotasyon köpüğünün incelenmesi sonucu flotasyon konsantrasyonunun kalitesi de belirlenebilmektedir [23]. Köpürtücü miktarının kabarcığın boyutu üzerinde belirgin bir etkisi olduğu bilinmektedir. Ayrıca daha önce ifade edildiği gibi kil mineralleri de köpük kararlılığını değiştirerek ortalama kabarcık boyutu üzerinde etkili olmaktadır.

Kil türü ve köpürtücü miktarına bağlı olarak belirlenen ortalama kabarcık boyutları Şekil 5'te sunulmuştur. Montmorillonit ilaveli kömür numunesiyle gerçekleştirilen flotasyon deneylerinde Dowfroth 250 ile, kaolin ilaveli kömür numunesiyle gerçekleştirilen flotasyon deneylerinde ise MIBC ile daha büyük kabarcıklar elde edilmiştir. Kaolin ilaveli kömür numunesiyle oluşan kabarcıkların

boyutlarında artan köpürtücü konsantrasyonlarına bağlı etkili bir değişim gözlenmemektedir. Montmorillonit ilavesinde 150 g/ton köpürtücü konsantrasyonunun üzerinde Dowfroth 250 ile ortalama kabarcık boyutları küçülürken, MIBC ile büyümektedir. Genel olarak montmorillonit ilavesiyle daha büyük kabarcıklar elde edildiği gözlenmektedir. Köpürtücüden beklenen daha küçük boyutlu kabarcıklar meydana getirmesidir. Böylece, flotasyon selülü içindeki havanın daha iyi dağılması sağlanabilir [24]. Ayrıca, küçük boyutlu kabarcıklar ile artan yüzey alanı toplanabilen hidrofobik tane miktarının artması anlamını taşımaktadır [25]. Şekil 4'te de montmorillonit ilavesiyle daha düşük yanabilir verim değerleri elde edilmesi bu sonucu destekler niteliktedir.



Şekil 5. Kil türü (kaolin-a ve montmorillonit-b) ve köpürtücü miktarına bağlı olarak ortalama kabarcık boyutlarının değişimi (%10 kil oranı için)

Figure 5. Variation of the mean bubble size depending on the clay type (kaolin-a and montmorillonite-b) and amount of frother (for 10% clay ratio)

#### 4. SONUÇLAR ve ÖNERİLER (RESULTS and SUGGESTIONS)

Bu çalışmada, kil minerallerinin (kaolin ve montmorillonit) ve flotasyon reaktiflerinin Tunçbilek bölgesi linyit kömürünün flotasyon performansına ve ortalama kabarcık boyutuna etkisi araştırılmıştır.

Kömür numunesi için zeta potansiyelinin sıfır olduğu nokta pH 2,1 olarak belirlenmiştir. Optimum bastırıcı miktarı kaolin içerikli numuneler için 200 g/t olarak tespit edilmiştir. Montmorillonit içerikli deneylerde ise bastırıcı miktarındaki değişimin konsantre külü ve yanabilir verim üzerinde önemli bir etkisi gözlenmemiştir. Genel olarak kaolin içerikli numunelerde yanabilir verim %40-55, montmorillonit içerikli numunelerde ise %30-47 aralığında değişmektedir.

Montmorillonit ilavesiyle gerçekleştirilen flotasyon deneylerinde Dowfroth 250 ile; kaolin ilavesiyle gerçekleştirilen flotasyon deneylerinde ise MIBC ile daha büyük kabarcıklar elde edilirken; montmorillonitin flotasyonda daha büyük kabarcıklar oluşmasına neden olduğu belirlenmiştir. Dowfroth 250 ile kömür flotasyonunda daha iyi sonuçlar elde edilmiştir.

#### Etik Standartlar Bildirimi (Declaration of Ethical Standards)

Çalışma etik standartlara uygun olarak gerçekleştirilmiştir.

#### Yazar Katkı Beyannamesi (Credit Authorship Contribution Statement)

**Vildan Önen:** Deneylerin tasarlanması, orjinal taslak yazma-düzenleme-revizyon, **Ayşe Zeynep Çağlar:** Araştırma, deneysel çalışmaların yürütülmesi **Hasan Ali Taner;** Analizler, orjinal taslak düzenleme, görselleştirme.

**Çıkar Çatışması Beyannamesi (Declaration of Competing Interest)**

Yazarlar herhangi bir çıkar çatışması olmadığını beyan etmektedir.

**Destek / Teşekkür (Funding / Acknowledgements)**

Bu çalışmanın yürütülmesi esnasında herhangi bir kurum veya kuruluştan maddi bir destek alınmamıştır.

**Veri Kullanılabilirliği (Data Availability)**

Uygulanamaz.

**KAYNAKLAR (REFERENCES)**

- [1] J. W. Leonard III, *Coal preparation*, Society of Mining, Metallurgy and Exploration Inc., Littleton, CO (USA), 1991.
- [2] F. F. Aplan, "The historical development of coal flotation in the United States", *Advances in flotation technology*, pp. 269-287, 1999.
- [3] Z. Xu, J. Liu, J. W. Choung, and Z. Zhou, "Electrokinetic study of clay interactions with coal in flotation", *International Journal of Mineral Processing*, vol. 68, pp. 183-196, 2003.
- [4] H. A. Taner ve V. Önen, "Killerin pülp ortamındaki davranışı ve flotasyona etkisi", *Madencilik Dergisi*, Cilt 55, ss 45-51, 2016.
- [5] Y. Xing, X. Xu, X. Gui, Y. Cao, and M. Xu, "Effect of kaolinite and montmorillonite on fine coal flotation", *Fuel*, vol. 195, pp. 284-289, 2017.
- [6] Y. Xing, M. Xu, F. Guo, J. Luo, Y. Zhang, Y. Cao and X. Gui, "Role of different types of clay in the floatability of coal: Induction time and bubble-particle attachment kinetics analysis", *Powder Technology*, vol. 344, pp. 814-818, 2019.
- [7] B. Wang and Y. Peng, "The interaction of clay minerals and saline water in coarse coal flotation", *Fuel*, vol. 134, pp. 326-332, 2014.
- [8] B. J. Arnold and F. F. Aplan, "The effect of clay slimes on coal flotation, part I: The nature of the clay", *International Journal of Mineral Processing*, vol. 17, No. 3-4, pp. 225-242, 1986.
- [9] H. A. Taner, "Kil minerallerinin yapısal özelliklerinin metal sülfürlerin flotasyon performansına etkisi", Doktora Tezi, Konya Teknik Üniversitesi, Lisansüstü Eğitim Enstitüsü, Konya, 2019.
- [10] O. Molatlıhegi and L. Alagha, "Ash depression in fine coal flotation using a novel polymer aid", *International Journal of Clean Coal and Energy*, vol. 5, No. 4, pp. 65-85, 2016.
- [11] L. Huynh, A. Feiler, A. Michelmores, J. Ralston and P. Jenkins, "Control of slime coatings by the use of anionic phosphates: A fundamental study", *Minerals Engineering*, vol. 13, No. 10-11, pp. 1059-1069, 2000.
- [12] W. J. Oats, O. Özdemir and A. V. Nguyen, "Effect of mechanical and chemical clay removals by hydrocyclone and dispersants on coal flotation", *Minerals Engineering*, vol. 23, No. 5, pp. 413-419, 2010.
- [13] Y. Yu, L. Ma, M. Cao and Q. Liu, "Slime coatings in froth flotation: A review", *Minerals Engineering*, vol. 114, pp. 26-36, 2017.
- [14] M. Zhang, N. Xu and Y. Peng, "The entrainment of kaolinite particles in copper and gold flotation using fresh water and sea water", *Powder Technology*, vol. 286, pp. 431-437, 2015.
- [15] X. Chen and Y. Peng, "Managing clay minerals in froth flotation—A critical review", *Mineral Processing and Extractive Metallurgy Review*, vol. 39, No. 5, pp. 289-307, 2018.
- [16] Y. Peng, Y. Mao, W. Xia and Y. Li, "Ultrasonic flotation cleaning of high-ash lignite and its mechanism", *Fuel*, vol. 220, pp. 558-566, 2018.

- [17] H. Zhu, J. Zhu, F. Min, A. L. Valdivieso, M. A. C. Arroyo and H. Wang, "Effect of frother addition mode on coal flotation in downflow flotation column", *Journal of Cleaner Production*, vol. 278, No. 123844, 2021.
- [18] Y. Cheng, F. Min, H. Li, J. Chen and X. Fu, "Effect of reagent interaction on froth stability of coal flotation", *Fuel*, vol. 318, No. 123417, 2022.
- [19] A. Z. Çağlar, "Kil minerallerinin kömürün flotasyon performansına ve köpük boyutuna etkisi", Yüksek Lisans Tezi, Konya Teknik Üniversitesi, Lisansüstü Eğitim Enstitüsü, Konya, 2019.
- [20] M. Maldonado, J. J. Quinn, C. O. Gomez and J. A. Finch, "An experimental study examining the relationship between bubble shape and rise velocity", *Chemical Engineering Science*, vol. 98, pp. 7-11, 2013.
- [21] S. Saklara, S. Ersayın ve İ. Bayraktar, "Flotasyon modelleri", *Bilimsel Madencilik Dergisi*, Cilt 37, No 2, ss. 3-20, 1998.
- [22] H. Hacıfazlıoğlu, "Kolon flotasyonu ile bitümlü kömür atıklarından temiz kömür kazanımı", *AKÜ Fen Bil. Der.*, Cilt 2, ss. 11-19, 2008.
- [23] Z. Ekmekçi, M. Can, D. Sutterland, A. Aslan, E. Bağcı ve Ç. Ökten, "Flotasyonda palp kimyasındaki değişimlerin köpük fazına etkilerinin görüntü analiz sistemi ile belirlenmesi", *TÜBİTAK Projesi*, Ankara, 2005.
- [24] S. M. Bulatovic, "*Handbook of flotation reagents: chemistry, theory and practice: Volume 1: flotation of sulfide ores*", Elsevier, Boston, U.S.A., 2007.
- [25] C. Chen, Development of measurement of froth characteristics, Master of Science Thesis in the Master Degree Program, Chalmers University of Technology, Advanced Engineering Materials, Gothenburg, 2012.



## NUMERICAL ANALYSES OF THERMAL PERFORMANCES OF THE CONVENTIONAL AND THE IMMERSION COOLING METHODS FOR LITHIUM-ION BATTERY PACKS

<sup>1,3</sup>\*Furkan ERGÜL , <sup>2</sup>Kenan TUFEKCI 

<sup>1</sup>Bursa Uludag University, Graduate School of Natural and Applied Science, Bursa, TÜRKİYE

<sup>2</sup>Bursa Uludag University, Engineering Faculty, Mechanical Engineering Dept., Bursa, TÜRKİYE

<sup>3</sup>Ulutek Technology Development Zone, Pracen Technology, Bursa, TÜRKİYE

<sup>1,3</sup>[furkanergul78@gmail.com](mailto:furkanergul78@gmail.com), <sup>2</sup>[kenantufekci@uludag.edu.tr](mailto:kenantufekci@uludag.edu.tr)

### Highlights

- Transition to electric vehicles has surged to reduce carbon emissions and utilize accessible energy.
- Key challenges for electric vehicle adoption include limited battery capacity, lengthy charging times, thermal management during rapid charging/discharging, and thermal runaway risks.
- Inhomogeneous temperature distribution's negative impact on electric vehicles underscores the need for a thermal management system.
- Widely employed thermal management systems include air-cooled, cooling plate (pipe) systems and the increasingly prevalent direct dielectric cooling systems.
- This study focused on thermal analyses of various cooling methods using Ansys Fluent software.
- The newest method, direct dielectric cooling, exhibited a 12% performance improvement over other systems under normal operating conditions (1C).



## NUMERICAL ANALYSES OF THERMAL PERFORMANCES OF THE CONVENTIONAL AND THE IMMERSION COOLING METHODS FOR LITHIUM-ION BATTERY PACKS

<sup>1,3</sup>\*Furkan ERGÜL , <sup>2</sup>Kenan TUFEKCI 

<sup>1</sup>Bursa Uludağ University, Graduate School of Natural and Applied Science, Bursa, TÜRKİYE

<sup>2</sup>Bursa Uludağ University, Engineering Faculty, Mechanical Engineering Dept., Bursa, TÜRKİYE

<sup>3</sup>Ulutek Technology Development Zone, Pracen Technology, Bursa, TÜRKİYE

<sup>1,3</sup>[furkanergul78@gmail.com](mailto:furkanergul78@gmail.com), <sup>2</sup>[kenantufekci@uludag.edu.tr](mailto:kenantufekci@uludag.edu.tr)

(Received: 26.01.2023; Accepted in Revised Form: 06.05.2023)

**ABSTRACT:** The transition from fossil fuel vehicles to electric has increased rapidly in recent years to reduce carbon emissions and use accessible energy. The main obstacles to the widespread use of electric vehicles are limited battery capacities, long charging times, thermal management in sudden charge and discharge situations and thermal runaway risks. The adverse effects of non-homogeneous temperature distribution on electrically driven vehicles have demonstrated the necessity of a thermal management system. The most used thermal management systems in practice are air-cooled, cooling plate (pipe) systems and direct dielectric cooling systems, which have recently become widespread. This study focused on the thermal analyses of the different thermal cooling methods. All analyses have been conducted using Ansys Fluent software. It has been observed that the dielectric direct cooling method, which is the newest method, has a performance value of 12% better than other systems at 1C normal operating conditions.

**Keywords:** Battery Pack Thermal Management, Dielectric Coolant, Efficiency and Performance, Electrical Vehicles, Energy, Finite Volumes Analysis

### 1. INTRODUCTION

Transportation in the world is mainly provided by internal combustion engine vehicles. The limited and gradually decreasing oil reserves in the world, being open to global manipulations and more importantly, posing a threat to the sustainable future, such as air pollution and climate change, have directed the transportation sector to alternative energy sources. It seems that the most convenient alternative energy source for vehicles is electric energy. On the other hand, It cannot be said that using electricity in vehicles is completely clean. Nevertheless, the total greenhouse gas emissions associated with the production, charging and use of an electric car is lower than the total greenhouse gas emissions associated with a gasoline car [1], [2], [3].

Thermal management of EV battery systems is the key to solving current problems surrounding the EV industry [4], [5], [6]. In research on battery pack thermal management, the best operating conditions for Li-ion batteries are between 25 °C and 40 °C. Studies have shown that at temperatures above 50 °C, the charging efficiency and the battery's working life will decrease considerably. Li-ion batteries lose 60% of their initial capacity after 600 cycles at 50 °C and 70% after 500 cycles at 55 °C [7].

The temperature distribution of the battery cells within the battery pack is of paramount importance for the performance of electric vehicles. Various cooling methods are available to ensure a homogeneous temperature distribution, among which the most prevalent are air-cooling and indirect liquid-cooling methods. The next generation immersion cooling method represents a promising alternative for achieving more effective thermal management in battery packs.

Air-cooled systems have a simple design and low operating and maintenance costs. However, these systems require more volumetric flow, more space and more power for sufficient heat transfer. Liquid-cooled systems are used in applications where high energy is required, so more heat transfer is needed.

\*Corresponding Author: Furkan ERGÜL, [furkanergul78@gmail.com](mailto:furkanergul78@gmail.com)

However, the reasons such as the complex designs of the indirect liquid cooling systems, the presence of more equipment, the increase in weight and the lack of thermal homogeneity in aggressive working conditions have led to the emergence of cooling systems with the direct immersion method [4], [6], [8].

In the direct immersion method, the battery cells are in direct contact by immersed in a dielectric liquid with specific thermal properties. Since the battery cells are in direct contact with the coolant, it is called a direct contact cooling method. The advantage of this method is that extremely high heat transfer rates can be achieved through direct contact of the cells with the immersion fluid. In addition, immersion fluids specially developed for electric vehicles can act as fire extinguishers and reduce the risk of thermal runaways [2], [9], [10].

Recent studies in battery pack thermal management have demonstrated that the direct immersion cooling method is a more effective solution compared to other cooling strategies for electric vehicle batteries. One notable study conducted by Zhang et al. found that the direct immersion method offers the fastest cooling rates, leading to improved battery performance and a longer lifespan under 1C working conditions [11]. In a similar comparative study conducted by Chen et al., the performance of different cooling methods on a lithium-ion battery pack was evaluated under a 1C working condition, where it was found that the direct immersion method resulted in the lowest temperature rise and the highest heat dissipation efficiency, making it the most effective thermal management strategy [12]. Furthermore, immersion fluids used in direct immersion cooling have been found to have fire extinguishing capabilities, as highlighted by a study conducted by Zhang et al. which significantly reduces the risk of thermal runaways in the event of battery failure [11]. Overall, the direct immersion method is a promising solution for efficient and safe thermal management of electric vehicle batteries, especially in aggressive working conditions.

Several academic studies [10, 13, 14] have compared the performance of different cooling methods for electric vehicle battery packs, including air-cooling, cold-plate liquid-cooling and immersion cooling. These studies have utilized both numerical simulations and experimental tests to evaluate the cooling efficiency, temperature uniformity and overall performance of each method. In the study conducted by Roe et al., the performance of three cooling methods was compared using indicators such as maximum temperature difference between battery cells and temperature standard deviation. The results showed that immersion cooling was the most effective method and had the least temperature difference between the cells. The air-cooling method performed the worst in terms of maximum temperature difference compared to the other two methods, while the cold-plate liquid-cooling method was in between.

The use of electric vehicles (EVs) has been on the rise in recent years due to growing environmental concerns and the need to reduce greenhouse gas emissions. However, effective and safe management of their batteries remains a significant challenge. Thermal management is critical to the performance and durability of electric vehicle batteries, especially during extreme weather conditions or high-demand driving scenarios. Various thermal management strategies have been proposed and tested to address this issue, such as liquid cooling, air cooling, phase-change materials and direct immersion cooling. Direct immersion cooling has gained increasing attention due to its promising performance in terms of cooling efficiency, safety and simplicity. In this context, this study aims to design and analyze a battery pack for a passenger electric car using the direct immersion cooling method and to evaluate its thermal performance through numerical simulations using the finite volume method. The performance of the immersion cooling method will be compared to other cooling methods, such as air-cooling and cold-plate liquid cooling, by analyzing factors like temperature uniformity, cooling efficiency and maximum temperature difference between battery cells.

## 2. MATERIAL AND METHODS

To conduct a thermal analysis of the indirect liquid cooling system, the dimensions of battery packs in a commercial vehicle were used as a reference. The thermal performance of the currently used cooling system for this vehicle [15] was compared with the direct cooling system designed in this study. The module is made of Al6061 T1 material and has dimensions of 1854 x 292 x 66 mm, which are approximately the same size as the original commercial vehicle's module.

The analysis model shown in Figure 1a was used in the indirect liquid cooling analysis, while the model in Figure 1b was used for analyzing direct cooling methods and the model in Figure 1c was used for analyzing direct cooling with air method.

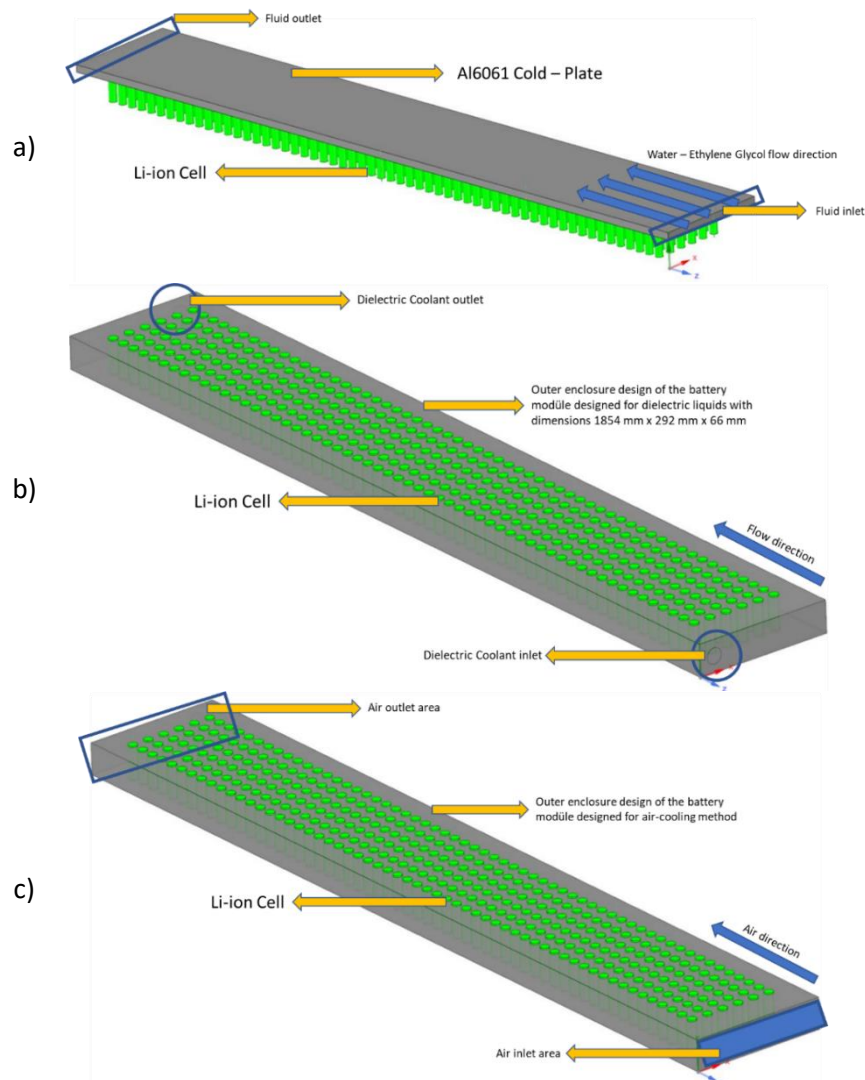


Figure 1. CAD Design of 1 Module a) Indirect Liquid Cooling b) Direct c) Air-cooling CAD Model



## 2.1. Battery Selection

Lithium-ion battery cells are commonly used in electric vehicles due to their reliability and high energy density per unit mass [16], [17]. For this reason, the Panasonic NNP Series NCR-18650A Li-ion batteries were selected for this study. The technical specifications of these batteries are presented in Table 1 [18].

**Table 1.** Technical Specifications and Calculations of Panasonic NNP Series NCR-18650A Battery Cell [18].

Battery Cell Voltage (Nominal)	3.75 V
Group (1 Module) Voltage	22.5 V (6S – 6 x 3.75 V)
Battery Cell Current Rating (Nominal)	3750 mAh
Group (1 Module) Current Capacity	217.5 Ah (58P – 58 x 3750 mAh)
1 Module Power Capacity	22.5 V x 217.5 Ah = 4.89 kWh
1 Battery Pack (16 Modules)	16 x 4.89 kWh = 78.24 kWh
Dimensions of Battery Cell	Diameter: 18.6 mm Length: 65.2 mm

## 2.2. Fluid Selection

Various methods exist for the thermal management of battery packs, with the air and liquid cooling method being the most used. To determine the best cooling method for the battery pack, the required thermal load must be calculated. Generally, the air-cooling method is used in vehicles that require less power density [16]. However, with increasing demand for more powerful vehicles and longer ranges, the need for advanced liquid cooling methods is growing. Different liquids are used based on the design and power density of the battery model. In the indirect liquid cooling method, the most used cooling liquid is a 50/50 Water Ethylene Glucose solution, while dielectric liquids are used in the direct liquid cooling method [18].

Due to the widespread use of the immersion cooling method, special chemicals have been developed to produce dielectric liquids. The most used dielectric liquids are Novec and Engineered Fluids. Table 2 presents the necessary equations to calculate the thermo-physical properties of the dielectric liquid at 20°C in the given operating range, as well as the thermo-physical properties of the dielectric liquid calculated using these equations.

**Table 2.** Thermo-physical property equations of dielectric fluid [18].

Thermo-Physical Properties	Equations	Working Range	Calculated Values
$\rho$ [kg/m <sup>3</sup> ]	$-2.0845 \times T [^{\circ}\text{C}] + 1665.8$	20 °C ≤ T ≤ 70 °C	1624.11
$\mu$ [Pa sec]	$1 \times 10^{-7} \times T^2 [^{\circ}\text{C}] - 3 \times 10^{-5} \times T [^{\circ}\text{C}] + 0.0018$	20 °C ≤ T ≤ 70 °C	1.24 x 10 <sup>-3</sup>
$C_p$ [J/ (kg K)]	$1.4982 \times T [^{\circ}\text{C}] + 1091$	20 °C ≤ T ≤ 70 °C	1120.96
$k$ [W/ (m K)]	$4 \times 10^{-7} \times T^2 [^{\circ}\text{C}] - 0.0002 \times T [^{\circ}\text{C}] + 0.069$	20 °C ≤ T ≤ 70 °C	0.06516

For the analysis of the indirect liquid cooling method, 50/50 Water-Ethylene Glycol solution will be utilized. Table 3 provides the necessary equations to calculate the thermo-physical properties of the 50/50 Water-Ethylene Glycol solution at 293.15 K, as well as the thermo-physical properties calculated using these equations.

**Table 3.** Thermo-physical property equations of 50-50 Water Ethylene Glycol Solution liquid [18].

Thermo-Physical Properties	Equations	Working Range	Calculated Values
$\rho$ [kg/m <sup>3</sup> ]	$-0.615 \times T[\text{K}] + 1259.5$	293.15 K $\leq$ T $\leq$ 353.15 K	1079.2
$\mu$ [Pa sec]	$2.48 \times 10^{-8} \times T^3[\text{K}] + 2.47 \times 10^{-5} \times T^2[\text{K}] - 8.2$ $2 \times 10^{-3} \times T[\text{K}] + 0.92$	293.15 K $\leq$ T $\leq$ 353.15 K	1.259
Cp [J/ (kg K)]	$3.06 \times T[\text{K}] + 2574.8$	293.15 K $\leq$ T $\leq$ 353.15 K	3471.84
k [W/ (m K)]	$-2 \times 10^{-7} \times T^3[\text{K}] + 0.0002 \times T^2[\text{K}] - 0.048 \times T$ $[\text{K}] + 5.38$	293.15 K $\leq$ T $\leq$ 353.15 K	3.457

The thermo-physical properties of the fluid air to be used in the air-cooling method are readily available in the Fluent library [20] and are given in Table 4.

**Table 4.** Thermo-physical property values for air [20].

Thermo-Physical Properties	Values from Fluent Library
$\rho$ [kg/m <sup>3</sup> ]	1.125
$\mu$ [Pa sec]	$1.7894 \times 10^{-5}$
Cp [J/ (kg K)]	1006.43
k [W/ (m K)]	0.0242

### 2.3. Thermal Analysis of Battery Pack Modules with Liquid Cooling System Using Finite Volume Method

To start the analysis of direct liquid cooling, the meshing process was applied to the simplified CAD model with dimensions of 1854 x 292 x 66 mm. The creation of a smooth and high-quality mesh is critical for obtaining accurate results. However, as the complexity of the geometry increases, it becomes challenging to achieve this mesh quality. One method for verifying numerical studies is the mesh independence test, where a specific value is determined for the number of mesh structures required to obtain accurate results [20]. In this study, a summary of the mesh independence tests conducted is shown in Table 5. To create the desired number of mesh structures at various skewness ratios, both triangular and quadrilateral meshes were modified by changing their minimum and maximum dimensions. The analysis was carried out using the same turbulence models and mesh independence studies were conducted with seven different mesh numbers. As Table 5 shows, the temperature values of the battery cell obtained in the number of 2,112,173 elements were like each other. Therefore, this number of elements was determined as the appropriate value for achieving minimum error levels.

**Table 5.** Mesh Independent Study with Dielectric Liquid at 20 °C

	Number of Elements	Battery Cell Minimum Temperature [°C]	Battery Cell Maximum Temperature [°C]
1	546066	19.665	25.078
2	555354	19.8	24.5
3	822385	20.01	22.079
4	1322101	20	20.134
5	2112173	20	20.179
6	3294243	19.99	20.180
7	6207887	20	20.183

The skewness value was assessed to evaluate the mesh quality level, revealing an average value of approximately 0.21. Considering that skewness values below 0.4 are typically deemed acceptable in the literature [1], the analysis was conducted using this mesh generation. Additionally, the orthogonal quality value of the model was scrutinized, exhibiting an average value of 0.83. Given these findings, it was concluded that the mesh quality was adequate for obtaining precise outcomes.

Once the mesh preparations are finished and the mesh sizes are determined, the meshing process is completed. The geometric model, as displayed in Figure 2a, was designed for the dielectric direct liquid cooling and air-cooling methods and is composed of 975,648 nodes and 2,112,173 elements. On the other hand, the geometric model created for the cold plate indirect liquid cooling method, as seen in Figure 2b, contains 2,224,287 nodes and 7,262,536 elements. A detailed representation of the mesh structure on the battery cell is shown in Figure 2c.

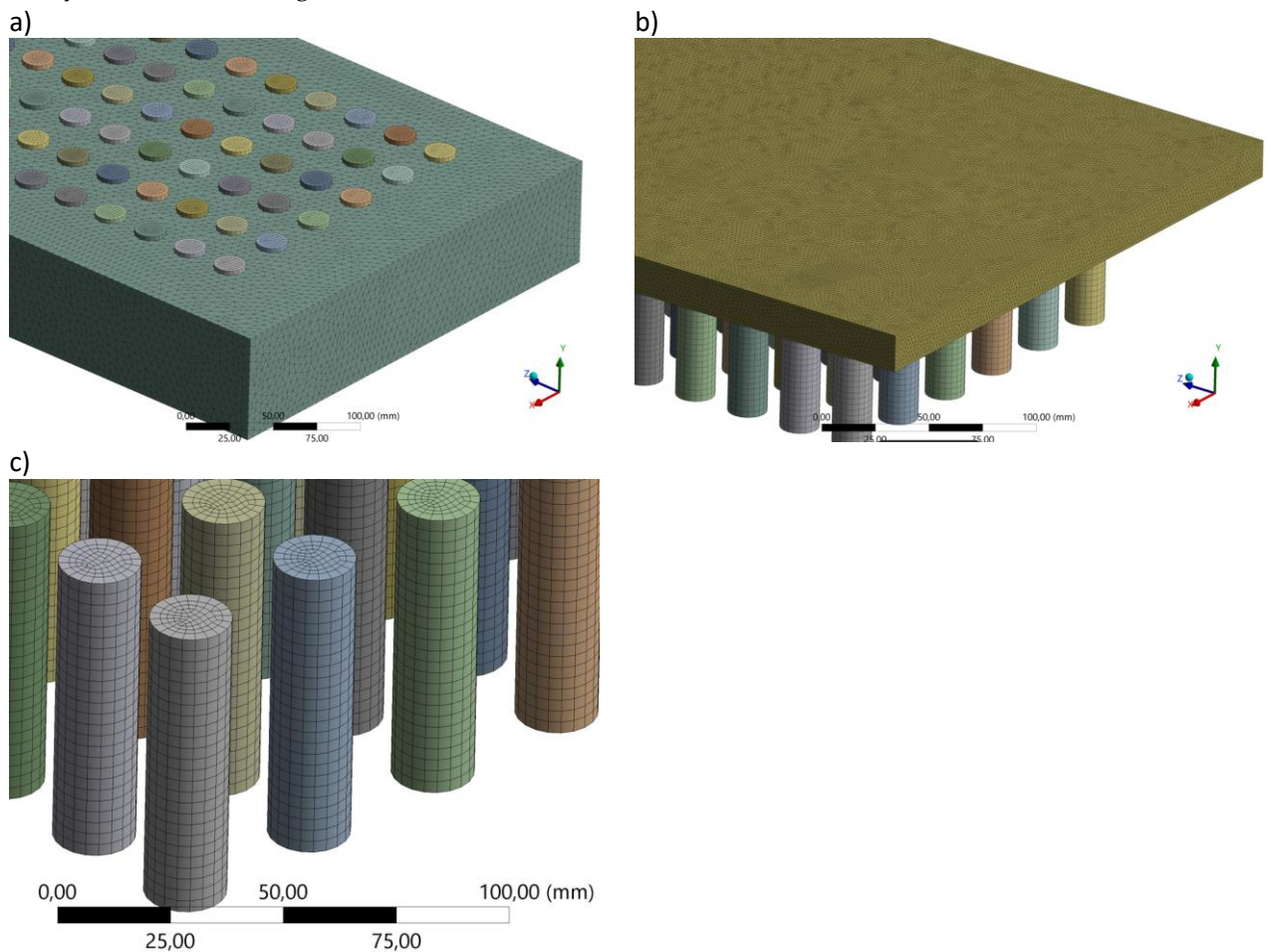


**Figure 2.** Mesh Structure a) for dielectric direct cooling and air cooling method b) for cold plate indirect cooling method c) detailed view of cells.

The energy equation shown in Equation 1, the continuity equation shown in Equation 2 and the momentum equation shown in Equation 3 were solved by the program for thermal analysis the battery pack by the finite volumes.

$$\frac{\partial(\rho e_t)}{\partial t} + \nabla x [Vx(\rho e_t + p)] = \nabla x [k\nabla T + (\tau x V)] + S_g \quad (1)$$

$$\rho_1 x v_1 x A_1 = \rho_2 x v_2 x A_2 \quad (2)$$

$$F = \frac{d(mV)}{dt} = m \frac{dV}{dt} = m x a \quad (3)$$

In the analysis study to be conducted, the definition of boundary conditions has been explained in detail:

Firstly, a significant portion of total heat production in battery cells is generated due to the ohmic resistance [11]. The heat produced through ohmic resistance heats up the surface of the battery cell through conduction. This heat generated on the surfaces of the battery cell is removed by convective heat transfer with the help of the coolant fluid. The amount of heat generation occurring in a battery cell due to ohmic resistance is calculated by  $I^2 \times R$ , where I represent the standard capacity under working conditions and R is defined as the internal resistance of the battery cell. The heat amount produced by the battery cell with this formula is also the minimum amount of heat transfer that needs to be exceeded by convection. Table 1 shows that 6S58P (348 pieces of 18650 Li-ion battery cells) are used in the analysis model. In this case, the total heat energy that will occur in a module can be calculated. Under 1C operating conditions, the heat production occurring in one battery cell is calculated as  $3.1^2 \times 0.1 = 0.96 \text{ W}$ . The total heat production due to ohmic resistance in a module is found to be 335.04 W by multiplying 0.96 with 349. Therefore, a heating boundary condition of 0.96 W for each battery cell through conduction is defined.

This heat needs to be removed through convection. The heat transfer coefficients for the forced air, dielectric liquid and water ethylene glycol solution that will be used in the analysis model are determined as shown in Table 6. For forced air, 70 W/m<sup>2</sup>K, for forced water ethylene glycol solution, 600 W/m<sup>2</sup>K and for dielectric liquid, 1750 W/m<sup>2</sup>K, are defined under the convective boundary condition [21]. As a result of the research conducted, it was found that the coolant fluids in vehicles are usually circulated within the range of 1-9 LPM [22]. In the analysis study, this value was accepted as 6 LPM and the flow rate was defined as the flow rate in the analysis program.

**Table 6.** Convective Heat Transfer Coefficient [22].

Convection Type	Convective Heat Transfer Coefficient	
	Btu / (h <sup>2</sup> ft <sup>2</sup> R)	W / (m <sup>2</sup> K)
Air, Free Convection	1 – 5	2.5 – 25
Air, Forced Convection	2 – 100	10 – 500
Liquid, Forced Convection	20 – 3000	100 – 15000
Boiling Water	1000 – 20000	2500 – 25000
Condensing Water Vapor	1000 – 20000	5000 – 100000

Convective heat transfer will help to balance this generated heat. Numerically, if we calculate this example:

The internal resistance of a classical 18650 Lithium-ion battery cell can be selected as an average of 0.1 Ohm [11]. The heat generated in one Lithium-ion battery cell is found to be  $I^2 \times R$ , which is 0.96 W under 1C operating conditions. The minimum amount of heat energy that needs to be removed is determined by multiplying this value by the number of battery cells. It is found to be 335.04 W by multiplying 0.96 W with 349, which is the number of cells used in the analysis model. This heat generation must be removed from the surface of the battery cells to the fluid through convective heat transfer. The expression for this is shown in Equation 4.

$$Q = h A (T_{surface} - T_{fluid}) \tag{4}$$

- Q : Heat Transfer Rate
- h : Heat transfer coefficient
- A : Surface Area
- T<sub>s</sub> : Surface Temperature
- T<sub>w</sub> : Fluid Temperature

The surface temperatures expected in different fluids are approximately as follows:

The surface temperature of the battery cell in the module cooled using dielectric liquid:

$$335.04 \text{ W} = 1750 \frac{\text{W}}{\text{m}^2\text{x}} 1.36 \text{ m}^2 x(T_s - 20) \quad \rightarrow \quad T_s = 20.14 \text{ }^\circ\text{C}$$

The surface temperature of the battery cell in the module cooled using water ethylene glycol:

$$335.04 \text{ W} = 600 \frac{\text{W}}{\text{m}^2\text{x}} 0.56 \text{ m}^2 x(T_s - 20) \quad \rightarrow \quad T_s = 21 \text{ }^\circ\text{C}$$

The surface temperature of the battery cell in the module cooled using air cooling:

$$335.04 \text{ W} = 70 \frac{\text{W}}{\text{m}^2\text{x}} 1.3 \text{ m}^2 x(T_s - 20) \quad \rightarrow \quad T_s = 23.7 \text{ }^\circ\text{C}$$

The numerical calculations reveal that the best thermal performance is achieved with the dielectric liquid cooling method. The verification of these values and results against the boundary condition defined in the analysis will be examined in Section 3.

### 3. RESULTS AND DISCUSSION

Battery packs in electric vehicles directly influence the battery's service life and, thus, the car's performance, depending on the cooling method [23]. Sudden rises in temperature in the battery cells are one of the cases that adversely affect the battery's life and safety [23]. A sudden rise in temperature in the battery pack or a decrease in thermal homogeneity between battery cells causes the risk of thermal runaway and explosion [7].

The temperature distribution results performed under normal operating conditions using forced air as the refrigerant in the direct cooling method are shown in Figures 3a and 3b. The difference between the inlet and outlet temperature values of the battery cells has reached approximately 20%.

In Figure 3, the difference in temperature between the battery cells is relatively high (approximately 21%), so it doesn't seem good enough. For this reason, it is thought that the air-cooling method wouldn't supply sufficient thermal homogeneity in fully electric vehicles. Similar results have been demonstrated by Kaba et al. [16]. One of the reasons for the temperature differential among battery cells in an air-cooled battery thermal management system is a lack of sufficient heat transfer coefficient. Heat transfer coefficient is a measure of how effectively heat is transferred between the surface of the battery cells and the cooling air. If the heat transfer coefficient is not sufficient, some cells may not receive enough cooling air, leading to higher temperatures and a temperature differential among the cells. To ensure uniform cooling and minimize temperature differentials among the cells, it is important to optimize the heat transfer coefficient in the battery thermal management system. This can be achieved through careful design of the cooling channels and flow rates, as well as regular maintenance and cleaning of the cooling system.

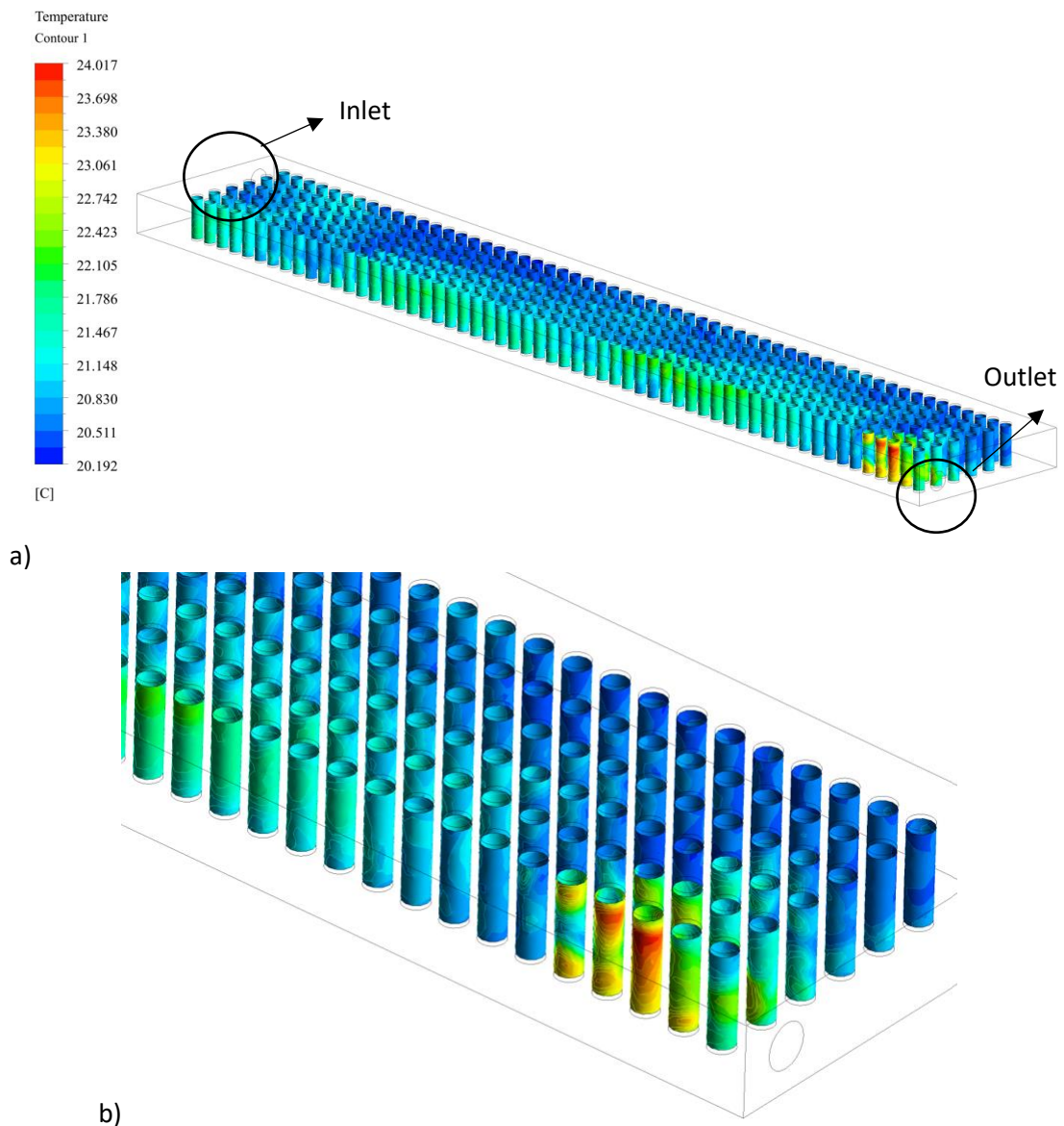


**Figure 3.** Air Cooling Method Temperature Distribution a) General View b) Detail View

In indirect cooling thermal management systems, the heat is carried by a heat sink plate or pipes. Unlike the direct liquid cooling system, the coolant doesn't contact the battery cells in this method. The post-analysis temperature distribution of the indirect cooling system modeled in this situation is shown in Figures 4a and 4b. The analysis made by passing a water-glycol solution through the cooling plate, it is seen that the maximum temperature difference between battery cells is approximately 10%. Also, the difference between inlet and outlet coolant temperatures was about 13%. Although this is a better performance value compared to the air-cooled system, the indirect liquid cooling method may not provide sufficient performance values in systems that require high power density [23], [24].

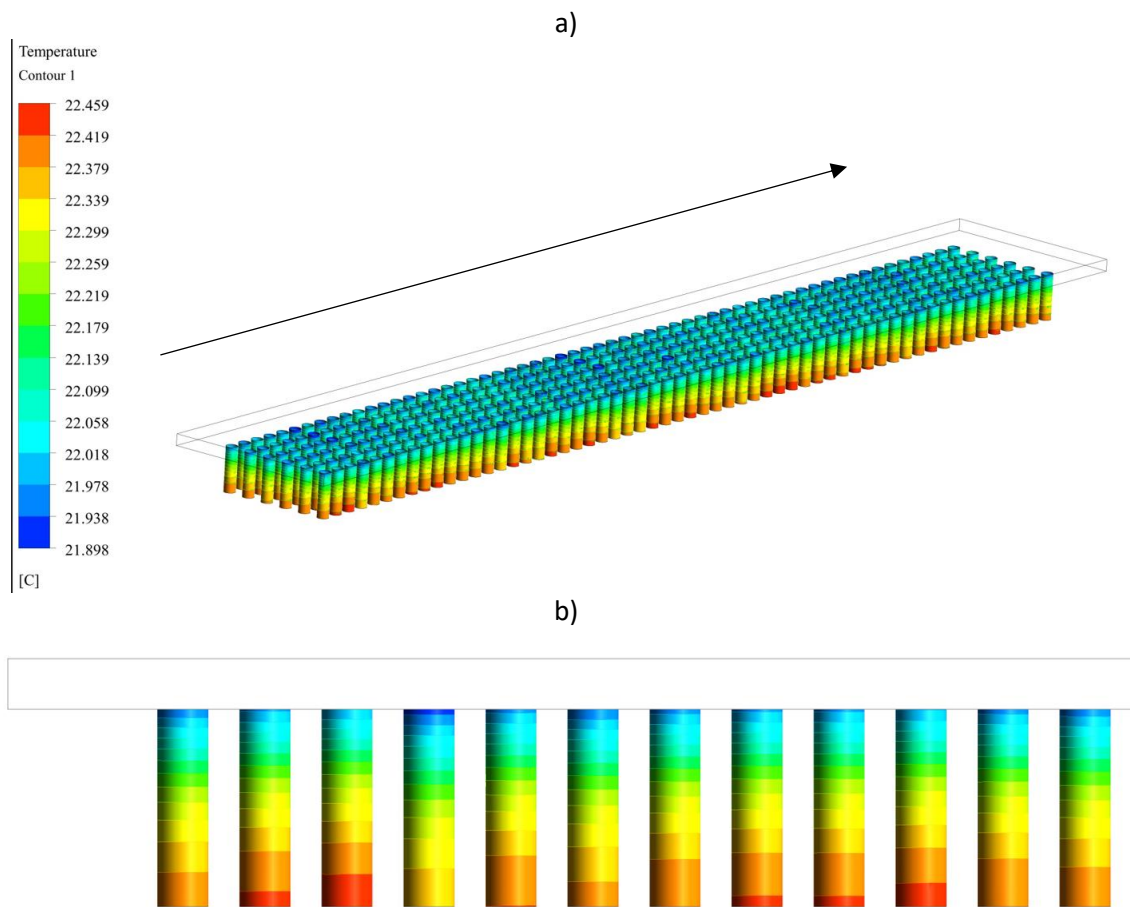


**Figure 4.** Cold Plate Cooling Method Temperature Distribution a) General View b) Detail View

In the Cold plate liquid-cooled battery thermal management system, a cooling fluid is circulated through Cold-plate in contact with the battery cells to remove heat. However, due to the geometry and placement of the cells, not all cells receive the same amount of cooling fluid, leading to temperature variations among the cells. This variation in cooling leads to a temperature differential between the cells with some cells being cooler than others. The heat generated is not uniform among the cells and cells that are generating more heat will become hotter than those generating less heat. This uneven heat generation can exacerbate the temperature differential between cells, especially if the heat transfer coefficient is not optimized.

The results of direct cooling analysis have been demonstrated in Fig 5a and Fig 5b. The maximum temperature difference between the battery cells was found to be approximately 0.89%. Since the temperature difference between the battery cells is so low compared to the other methods and the thermal homogeneity is good, it can be expected that the battery pack has superior thermal performance, decrease the risk of thermal and leakage and directly increase vehicle performance. The summary of the results of the finite volume analyses performed for the dielectric liquid direct cooling method, the air direct cooling method and the cold plate cooling method was shown in Table 7. Looking at the difference between the inlet and outlet temperatures, it is seen that the most homogeneous thermal distribution is the direct immersion method with the dielectric liquid, the indirect cooling system with the help of the plate and the air-cooling method, respectively.

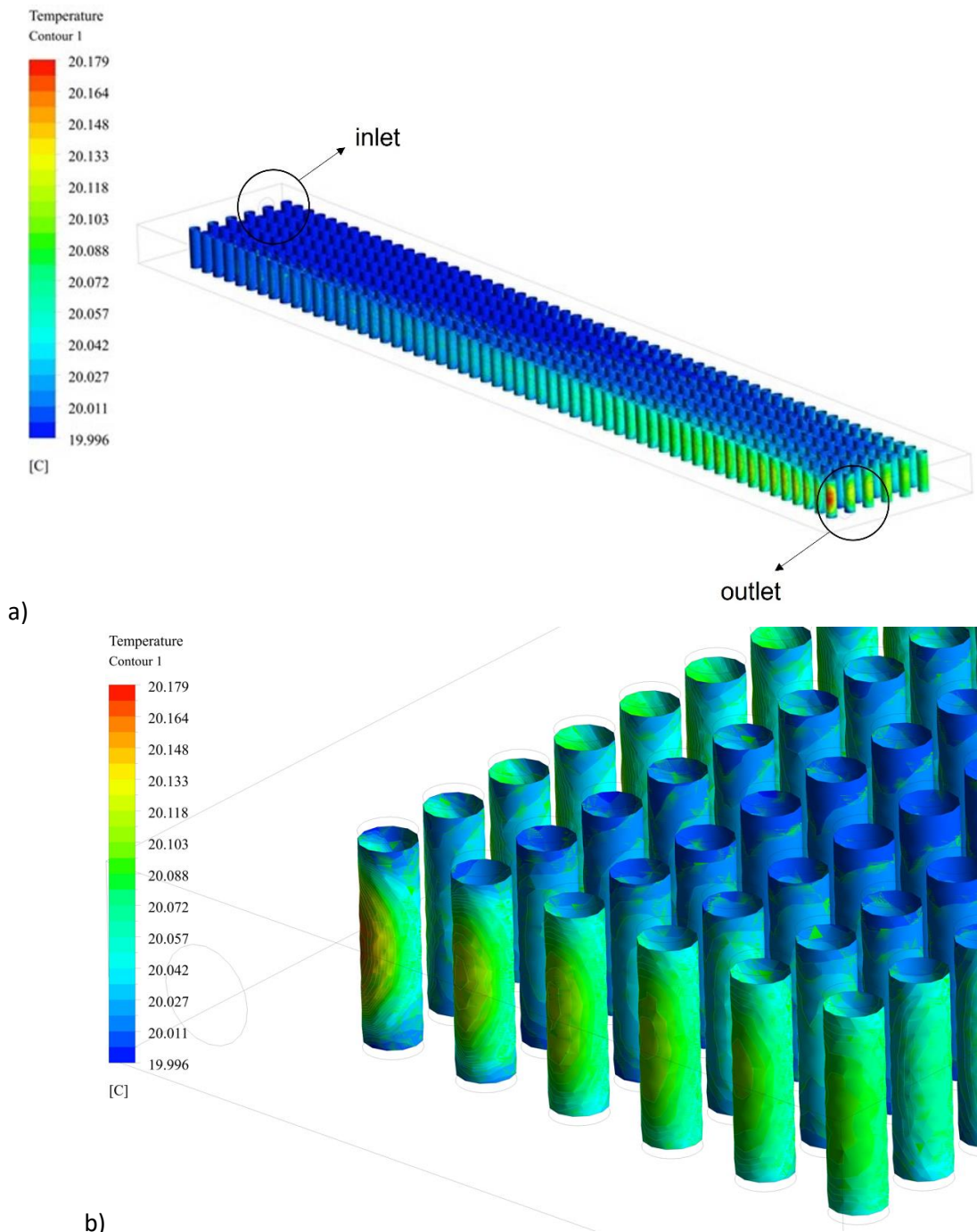


**Figure 5.** Dielectric Liquid Cooling Method Temperature Distribution a) General View b) Detail View

In a dielectric liquid-cooled battery thermal management system, a dielectric fluid is circulated through channels in contact with the battery cells to remove heat. Dielectric fluids have higher heat transfer coefficients compared to air and can more effectively transfer heat from the battery cells to the cooling system. This results in more uniform cooling across the battery pack and reduces temperature variations among the cells. In a dielectric liquid-cooled system, the heat transfer coefficient is higher than in an air-cooled system and cold-plate based system due to the higher thermal conductivity of the dielectric fluid. This allows for more efficient heat transfer between the battery cells and the cooling system, resulting in a more uniform temperature distribution across the battery pack.

In summary, the higher heat transfer coefficient of dielectric liquid cooling methods can provide more uniform cooling and reduce temperature variations among battery cells, leading to improved battery pack



performance and longevity. It is desirable that the temperature difference between the battery cells be as low as possible. Thermal runaway is a very serious problem that will cause the surrounding battery cell ignites and explode if even a single cell in the battery pack gets too hot. Having better thermal homogeneity of Lithium-Ion batteries, which are the most widely used in electric vehicles, leads directly affects vehicle performance and minimizes the risk of thermal runaway and explosion.

**Table 7.** Comparison of the minimum and maximum temperature values of battery cells according to the analysis results.

	Inlet Temperature	Minimum Temperature	Maximum Temperature	Temperature Difference Between Battery Cells
Air Cooling	20°C	20.192 °C	24.017 °C	3.825 °C
Indirect Cooling with Cold Plate	20°C	21.898 °C	22.459 °C	0.561 °C
Direct Cooling with Immersion Cooling	20°C	20.011 °C	20.179 °C	0.168 °C

#### 4. CONCLUSIONS

During charging or discharging of a battery cell, ohmic heat is generated due to the resistance of the cells. This heat can cause an increase in the temperature of the battery, which can be detrimental to the cells. Convective heat transfer helps to balance this heat by transferring it away from the battery cells. Direct liquid cooling uses a dielectric cooling fluid to directly cool the heat-generating battery cells, while indirect liquid cooling uses a coolant to first cool a cold plate, which in turn indirectly cools the battery cells. In this study, the thermal performance of different cooling methods in a battery module under 1C operating conditions was compared based on the total heat generation and convective heat absorption. When the direct cooling method was examined in detail, it was found to have a lower surface temperature output value for the battery cells in a battery module than all other methods under the determined conditions and dimensions. This provides the desired homogeneity output and demonstrates the suitability of this study for further academic research.

- ✓ The research findings indicate that the immersion liquid cooling technique offered superior thermal uniformity in comparison to the other methods investigated. This method has been shown to be particularly effective in high-power-density vehicles, as it can efficiently dissipate heat and prevent localized temperature hotspots that may lead to thermal runaway or other safety hazards. In contrast, the air-cooling method, while being an eco-friendly and cost-effective alternative, demonstrated inadequate thermal management performance in high-power-density applications. This method is less efficient in dissipating heat due to the low thermal conductivity of air and thus may lead to localized hotspots that can negatively impact battery performance and longevity. Additionally, the indirect liquid cooling method, which involves cooling the battery through a coolant flow in a separate circuit, requires additional design and auxiliary equipment, thereby making it more challenging to maintain and potentially more expensive. Overall, the results highlight the importance of selecting an appropriate cooling method based on the specific application and design requirements to ensure optimal thermal management performance and battery safety.
- ✓ The maximum temperature difference between the immersion cooling method and the liquid plate cooling method was determined to be 12%. This temperature difference, however, may vary depending on the type of cooling method used, as XING Mobility, a new venture company in the field of dielectric cooling, claims that their method can achieve temperature differences of up to 20% to 30%. It is worth noting that the use of air cooling and indirect liquid cooling methods may result in localized temperature increases in the battery cell, which can potentially lead to thermal runaways and even explosions, as reported in various studies [1], [7], [25], [26], [27].

In the next research, by taking this study as a reference, the thermal performance of the battery cells and battery module can be examined in sudden charge and discharge situations (4C and 5C standards), which require the change of the thermal parameters of the finite volume model.

### **Declaration of Ethical Standards**

The authors of this article declare that the materials and methods used in this study do not require ethical committee permission and/or legal-special permission.

### **Credit Authorship Contribution Statement**

Conceptualization, F.E. and K.T.; methodology, F.E. and K.T.; FEM analysis, F.E; validation, K.T.; investigation, F.E. and K.T.; data curation, F.E. and K.T.; writing—original draft preparation, F.E. and K.T.; writing—review and editing, M.R. and K.T.; visualization, M.R. and K.T.; supervision, M.R. and K.T.; funding acquisition, F.E. and K.T. All authors have read and agreed to the published version of the manuscript.

### **Declaration of Competing Interest**

The authors declared that they have no conflict of interest.

### **Funding / Acknowledgements**

The author(s) received no financial support for the research

### **Data Availability**

The data that support the findings of this study are available from the corresponding author upon reasonable request.

### **REFERENCES**

- [1] Amalesh, T., Narasimhan, L. N., "Cooling of a lithium-ion battery using phase change material with air/dielectric fluid media: A numerical study", *Journal of Power and Energy*, vol. 234(5), pp. 722-738, 2020.
- [2] E. Langer, "Liquid cooling for EV charging – what we know to keep electric vehicles on the go," 2019. [Online]. Available: <https://www.cpcworldwide.com/Portals/0/Library/Resources/Literature/WhitePapers/Documents/CPC-Liquid%20Cooling%20in%20Electric%20Vehicles.pdf> [Accessed Feb. 2023].
- [3] EPA, "US Environmental Protection Agency," 2022. [Online]. Available: <https://www.epa.gov/> [Accessed Jan. 2023].
- [4] Castrol, "Castrol Coolant Fluent," 2022. [Online]. Available: [https://www.castrol.com/tr\\_tr/turkey/home/technology-and-innovation/castrol-e-sivilari/sogutucu-e-sivilari.html](https://www.castrol.com/tr_tr/turkey/home/technology-and-innovation/castrol-e-sivilari/sogutucu-e-sivilari.html) [Accessed Feb. 2023].
- [5] Mivolt, "Liquid Immersion Cooling," 2022. [Online]. Available: <https://mivoltcooling.com/> [Accessed Feb. 2023].
- [6] Zhao, G., Wang, X., Negnevitsky, M., Li, C., "An up-to-date review on the design improvement and optimization of the liquid-cooling battery thermal management system for electric vehicles", *Applied Thermal Energy*, vol 219, part B, 25 Jan 2023, 119626, Nov. 2022.
- [7] Xing, "Xing Mobility Technology," 2022. [Online]. Available: <https://www.xingmobility.com/> [Accessed Feb. 2023].

- [8] Z. Rao, S. Wang, "A review of power battery thermal energy management", *Renewable and Sustainable Energy Reviews*, vol 15, issue 9, pp 4551-4571, Dec 2011.
- [9] J. Han, S. K. Garud, S. Hwang, Y. Lee, "Experimental Study on Dielectric Fluid Immersion Cooling for Thermal Management of Lithium-Ion Battery", *Symmetry/Asymmetry in Advanced Research for Efficient Electric Vehicles*, vol 14(10), 2126, 2022.
- [10] C. Roe, X. Feng, G. White, R. Li, H. Wang, R. Xinyu, X. Li, F. Zhang, V. Null, M. Perkes, Y. Patel, Y. Wang, H. Wang, M. Ouyang, G. Offer, B. Wu, "Immersion cooling for lithium-ion batteries – A review", *Journal of Power Sources*, vol 525, 231094, March 2022.
- [11] X. Zhang, L. Zhao, L. Luo, Y. Fan, Z. Du, "A review on thermal management of lithium-ion batteries for electric vehicles", *Energy*, Volume 238, Part A, 121652, January 2022.
- [12] D. Chen, J. Jiang, G. Kim, C. Yang, "Comparison of different cooling methods for lithium-ion battery cells", *Applied Thermal Engineering*, 94(2), September 2015.
- [13] M. Liu, Y. Ouyang, Y. Cheng L. Lu, "A comparative study of air cooling, liquid cooling and phase change cooling in lithium-ion batteries thermal management for electric vehicles," *Applied Energy*, vol. 211, pp. 51-60, Feb. 2018.
- [14] M. Zhao, Z. Lu, W. Wang, J. Liu, K. Cheng, "Experimental Study on Thermal Performance of Three Kinds of Cooling Methods for Lithium-Ion Power Battery," *Applied Thermal Engineering*, vol. 145, pp. 87-94, Oct. 2018.
- [15] A. Herman, "Liquid cooling manifold with multi-function thermal interface," U.S. Patent US8263250B2, 2010.
- [16] M. S. Çetin, B. Karakaya, T. M. Gençoğlu, "Modelling of Lithium-Ion Batteries for Electric Vehicles", *Firat University Journal of Engineering Sciences*, vol. 33(2), 755-763, 2021.
- [17] P. Ramadass, B. Haran, R. White, N. B. Popov, "Capacity fade of Sony 18650 cells cycled at elevated temperatures: Part I. Cycling performance", *Journal of Power Sources*, vol. 112, issue 2, pp. 606-613, Nov. 2002.
- [18] E. Çetkin, "The rise of electric vehicles and battery thermal management system", *Engineer and Machine*, pp. 29-33, Nov. 2020.
- [19] Alldatasheet, Cell Properties, 2022. [Online]. Available: <https://www.alldatasheet.com/> [Accessed Jan. 2023].
- [20] ANSYS, Fluent. ANSYS, Inc. [Online]. Available: <https://www.ansys.com/products/fluids/ansys-fluent> [Accessed Jan. 2023].
- [21] C. Bayındırlı, M. Çelik, M. Demiraylı, "The Investigation of Flow Characteristic Around a Bus Model by CFD Method and Improvement of Drag Force by Passive Flow Control Method", *Journal of Polytechnic*, vol. 21(4), pp. 785-795, 2018.
- [22] G. A. Stefanopoulou, Y. Kim, "System-level management of rechargeable lithium-ion batteries", *Rechargeable Lithium Batteries from Fundamentals to Applications*, Woodhead Publishing Series in Energy, pp. 281-302, 2015.
- [23] P. Kosky, G. Wise, "Convection Heat Transfer Coefficient – An overview", *Exploding Engineering*, 2013.
- [24] Y. M. Kaba, O. Kalkan, A. Celen, "The Investigation of Batteries and Thermal Management Systems Used in Electric Vehicles", *Konya Journal of Engineering Sciences*, vol.9, no. 4, 1119-1136, 2021.
- [25] V. Mali, R. Saxena, K. Kumar, A. Kalam, B. Tripathi, "Review on battery thermal management systems for energy-efficient electric vehicles", *Renewable and Sustainable Energy Reviews*, vol 151, 111611, Nov. 2021.
- [26] P. Dubey, G. Pulugundla, K. A. Srouji, Direct Comparison of Immersion and Cold-Plate Based Cooling for Automotive Li-Ion Battery Modules, *Energies*, vol. 14(5), 1259, 2021.
- [27] K. V. Jithin, P. K. Rajesh, "Numerical analysis of single-phase liquid immersion cooling for lithium-ion battery thermal management using different dielectric fluids", *International Journal of Heat and Mass Transfer*, vol. pp. 188, 2022.

- [28] S. M. Patil, J. Seo, M. Lee, "A novel dielectric fluid immersion cooling technology for Li-ion battery thermal management", *Energy Conversion and Management*, vol. 229, 113715, Feb. 2021.



## DATA INTEGRITY AND QUALITY ANALYSIS OF LOW COST ZED-F9P U-BLOX GNSS RECEIVER

<sup>1,\*</sup>Sermet OGUTCU , <sup>2</sup>Salih ALCAY , <sup>3</sup>Huseyin DUMAN ,  
<sup>4</sup>Behlul NUMAN OZDEMIR , <sup>5</sup>Ulkunur KORAY 

<sup>1,2,5</sup>Necmettin Erbakan University, Geomatics Engineering, Konya, TÜRKİYE

<sup>3</sup>Sivas Cumhuriyet University, Geomatics Engineering, Sivas, TÜRKİYE

<sup>4</sup>Konya Technical University, Geomatics Engineering, Konya, TÜRKİYE

<sup>1</sup>[sermetogutcu@erbakan.edu.tr](mailto:sermetogutcu@erbakan.edu.tr), <sup>2</sup>[salcay@erbakan.edu.tr](mailto:salcay@erbakan.edu.tr), <sup>3</sup>[hduman@cumhuriyet.edu.tr](mailto:hduman@cumhuriyet.edu.tr),

<sup>4</sup>[behlulnuman@gmail.com](mailto:behlulnuman@gmail.com), <sup>5</sup>[nurkoray98@gmail.com](mailto:nurkoray98@gmail.com)

### Highlights

- Data integrity and quality of low-cost GNSS receiver were investigated.
- Data integrity and SNR of low-cost GNSS receiver are comparable to the geodetic-one.
- The number of cycle slips of low-cost GNSS receiver is higher than the geodetic-one.



## DATA INTEGRITY AND QUALITY ANALYSIS OF LOW COST ZED-F9P U-BLOX GNSS RECEIVER

<sup>1,\*</sup>Sermet OGUTCU , <sup>2</sup>Salih ALCAY , <sup>3</sup>Huseyin DUMAN ,  
<sup>4</sup>Behlul NUMAN OZDEMIR , <sup>5</sup>Ulkunur KORAY 

<sup>1,2,5</sup>Necmettin Erbakan University, Geomatics Engineering, Konya, TÜRKİYE

<sup>3</sup>Sivas Cumhuriyet University, Geomatics Engineering, Sivas, TÜRKİYE

<sup>4</sup>Konya Technical University, Geomatics Engineering, Konya, TÜRKİYE

<sup>1</sup>sermetogutcu@erbakan.edu.tr, <sup>2</sup>salcay@erbakan.edu.tr, <sup>3</sup>hduman@cumhuriyet.edu.tr,

<sup>4</sup>behlulnuman@gmail.com, <sup>5</sup>nurkoray98@gmail.com

(Received: 22.03.2023; Accepted in Revised Form: 29.06.2023)

**ABSTRACT:** Thanks to the rapidly emerging low-cost dual-frequency GNSS receivers, a feasible alternative for geodetic-grade GNSS receivers became available for some GNSS applications. In this study, the performance of data integrity and quality of a low-cost ZED-F9P u-blox GNSS receiver was investigated by comparing it with a geodetic-grade GNSS receiver. Availability of the epoch and phase/code signal channels, signal-to-noise ratio (SNR), code multipath, and cycle slips were analyzed for the geodetic-grade and low-cost ZED-F9P u-blox GNSS receivers. One month's data of GPS, GLONASS, and Galileo constellations were analysed using the RINEX files of the receivers. The results showed that the epoch availability of the geodetic-grade and u-blox GNSS receiver is comparable to each other, while the availability of phase/code signal channels of the geodetic-grade receiver is higher than the u-blox receiver. In terms of data quality, SNR values from both receivers are comparable, while the multipath level of the u-blox GNSS receiver is significantly higher than the geodetic-grade one. The results also showed that the number of cycle slips of the u-blox receiver is significantly higher than the geodetic-one.

**Keywords:** Cycle Slip, GNSS, Low-cost, Multipath, U-blox

### 1. INTRODUCTION

Since low-cost Global Navigation Satellite System (GNSS) receivers have been available for a relatively short time compared with the geodetic ones, the GNSS market share of low-cost GNSS receivers, especially for dual-frequency ones, is gradually increasing [1]. Precise Point Positioning (PPP) and relative positioning using low-cost dual frequency receivers became available due to the mitigation of the first-order ionospheric effect as one of the biggest error sources [2,3,4].

The major drawback of the geodetic-grade GNSS receivers is their high costs, such as several thousand to tens of thousands of dollars, whereas low-cost dual-frequency GNSS receivers usually cost several hundred dollars. One of the most commonly used low-cost GNSS receivers is u-blox ZED-F9P module (<https://www.u-blox.com/en/product/zed-f9p-module>). Due to the dual-frequency and multi-constellation (GPS+GLONASS+Galileo+BeiDou-2) availability, u-blox ZED-F9P GNSS receivers support a variety of GNSS applications. Since only the civil signals L1 and L2C are available for the u-blox GNSS receiver, the second frequency of some GPS satellites belonging to older than BLOCK IIR-M cannot be tracked by the u-blox GNSS receiver [5]. As of January 2023, seven GPS satellites (G02, G13, G16, G19, G20, G21, G22) are not broadcasting the L2C civil signal (<https://www.navcen.uscg.gov/gps-constellation>). This causes the loss of the number of the tracked dual-frequency GPS satellites by u-blox GNSS receiver compared with the geodetic ones. This may affect the positioning accuracy of the u-blox GNSS receiver, especially for constrained satellite visibility. This GPS BLOCK dependent for second civil signal frequency is not existing for GLONASS, Galileo, and BeiDou constellations. Besides the GPS

second civil frequency restriction, the total GNSS channel number of low-cost GNSS receivers is significantly lower than the geodetic ones.

Generally, studies mainly focused on the positioning performance of the u-blox GNSS receiver [6,7,8]. To the best of the authors' knowledge, no comprehensive assessment on the data integrity and quality of the u-blox GNSS receiver was conducted. Here, we present one-month observations of a u-blox and a geodetic-grade GNSS receiver that were placed in close proximity to each other. The paper is organized as follows: first, we elaborate on a detailed methodology for assessing data integrity, multipath levels, signal-to-noise ratios (SNR), and cycle slips. Next, we discuss the main findings and their possible causes. Finally, we provide general remarks in the concluding section.

## 2. MATERIAL AND METHODS

To thoroughly evaluate the u-blox and geodetic-grade GNSS receivers' data, two receivers were placed on the roof of the Necmettin Erbakan University Engineering Faculty. The antennas are approximately 3 meters away from each other. Figure 1 shows the antennas of the receivers mounted on the pillars. For this ultra-short baseline, tropospheric, ionospheric effects, multipath, and satellite geometry are safely assumed identical for each receiver.



**Figure 1.** The u-blox and geodetic-grade antennas, which were placed on the Faculty of Engineering, Necmettin Erbakan University

CHC P5-U receiver and C220GR2 choke ring antenna were used for the geodetic-grade receiver and antenna configuration. For the u-blox receiver, low-cost Survey GNSS Multiband antenna (<https://www.ardusimple.com/product/survey-gnss-multiband-antenna/>) was used. This antenna is usually preferred over the u-blox ANN-MB L1/L2 multi-band GNSS patch antenna (<https://www.u-blox.com/en/product/ann-mb-series?legacy=Current>) due to the higher signal-to-noise ratio (SNR) and low multipath.

The u-blox receiver was configured to work as a Continuously Operating Reference Station (CORS) using Raspberry Pi. One month of RINEX 3.0,4 data (from DOY 347, 2022 to DOY 11, 2023) was collected from both receivers. GPS, GLONASS and Galileo data with 30-s sampling rate was collected for each receiver. 30-s interval was intentionally chosen because most of the CORS stations data interval is 30-s and it is suitable for data capacity. Since the u-blox receiver cannot support BDS-3 data and BDS-2 satellite visibility is significantly low in Turkey the data of BDS satellites were ignored.

The u-blox receiver only supports L1 C/A and L2C, G1 and G2 C/A, and E1 (B+C) and E5b (I+Q) for

GPS, GLONASS, and Galileo constellations, respectively. Unlike the u-blox receiver, the geodetic-grade receivers can support multi-frequency and multi-modulation channels. Most of the geodetic-grade receivers support L1 C/A and L2 (Z-tracking), G1 (C/A) and G2 (P), and E1 and E5a frequency bands. These frequency bands are also used in International GNSS Service (IGS) and most of the Analysis Centers (ACs) conventions [9,10,11] and also mainly used for PPP [12,13]. To follow the IGS conventions and better represent the geodetic-grade receivers, these frequency bands were chosen for the CHC P5-U receiver.

RINEX data of the receivers was investigated in terms of the data integrity and quality. The data integrity consists of the epoch and phase/code frequency availability. Epoch availability is computed as the ratio between the theoretically expected number of epochs (i.e., 2880 epochs for 30-sec sampled observations for a daily RINEX file) and the actual number of epochs recorded by the receivers. Phase/code frequency availability is computed by counting the missing observations on the first and second phase/code frequencies.

Data quality analysis consists of code multipath level from the continuous cycle-slip free arcs, the number of observed cycle slips, and SNR values.

SNR value indicates the signal strength of the direct signal from GNSS antenna. In other words, SNR refers to the ratio of the direct signal power and noise power in a corresponding signal channel for the receivers.

For each chosen frequency bands, epoch/frequency signals availability, code multipath, cycle slips, and SNR analysis were conducted for the u-blox and CHC P5-U receivers. In-house software was used for the data integrity and quality analyses. In addition to these analyses, the average number of tracked satellites during a one-month period for each GNSS constellation was also analyzed. The cutoff angle and sampling rate of each receiver were set  $7^\circ$  (to collect enough satellite data) and 30-sec, respectively. The findings were discussed in detail in the Results section.

### 3. RESULTS AND DISCUSSION

Table 1 provides the analysis of the phase and code frequency availability for each receiver and GNSS constellation during the one-month period. Table 2 shows the mean, maximum, and minimum number of observed satellites in each epoch for the receivers.

**Table 1.** The results of the phase and code frequency availability (Unit: %)

Receivers	GPS				GLONASS				Galileo			
	$G_{p1}$	$G_{p2}$	$G_{\phi1}$	$G_{\phi2}$	$R_{p1}$	$R_{p2}$	$R_{\phi1}$	$R_{\phi2}$	$E_{p1}$	$E_{p2}$	$E_{\phi1}$	$E_{\phi2}$
CHC P5-U	100	96.7	99.9	96.5	100	87.5	100	87.5	100	99.8	99.9	99.1
U-blox	99.6	77.3	99.6	77.3	97.2	87.0	97.2	87.0	99.1	95.6	99.1	95.6

**Table 2.** The results of the satellite visibility

Receivers	GPS			GLONASS			Galileo		
	mean	max	min	mean	max	min	mean	max	min
CHC P5-U	9.3	12	8	7.3	10	4	8.1	12	5
U-blox	9.0	12	6	7.4	10	4	8.0	12	5

For simplicity, sub-indexes of  $P$  and  $\phi$  in Table 1 denote the code and phase observations in the corresponding signals. 1C/2W, 1C/2P, 1C/5Q (for the CHC P5-U receiver) and 1C/2X, 1C/2C, 1X/7X (for the u-blox receiver) code/phase observations were processed for GPS, GLONASS, and Galileo, respectively. The first and second observations of the receivers were denoted as 1 and 2 for brevity.

As shown in Table 1, CHC P5-U data availability of code and phase observations is much more compared with the u-blox receiver. This can be more evident for GPS because u-blox only tracks L2C observation that is broadcasting only BLOCK IIR-M and later block types as described in the



introduction section. For the older block types, GPS L2C observation is not available, and this causes the data loss of the second frequency code/phase observations of the u-blox receiver, while the first frequencies of the u-blox receiver are not affected by this phenomenon. Except for this restriction, the performance of the u-blox and CHC P5-U receivers are close to each other for GLONASS and Galileo receivers.

When the second frequency availability of GLONASS is investigated, it is seen that approximately 13% of second frequency code/phase data are lost for each receiver. When some IGS stations' data are investigated, it is seen that the second frequency code/phase data of R06 and R23 GLONASS satellites are not available during the test period. The frequency and epoch availability are more critical for kinematic applications than those of static applications.

The satellite visibility results show that the performances of each satellite visibility are nearly identical for each GNSS constellation. But it should be kept in mind that some recorded GPS satellites from the u-blox receiver are not broadcasting the second L2C civil frequency.

When the epoch availability of the CHC P5-U receiver is investigated, it is observed that epoch availability of the CHC P5-U receiver is 100% for each day. For the u-blox receiver, the mean epoch availability is nearly 100% (99.7%) which proves the nearly same tracking performance as the geodetic-grade receivers. The minimum epoch availability was observed as 98.7% in a daily RINEX file for the u-blox receiver.

The mean code multipath and SNR values of the receivers during one-month period were given in Figures 2 and 3. Code multipath value was computed using the generalized formula for all frequencies similar to G-Nut/Anubis [14].

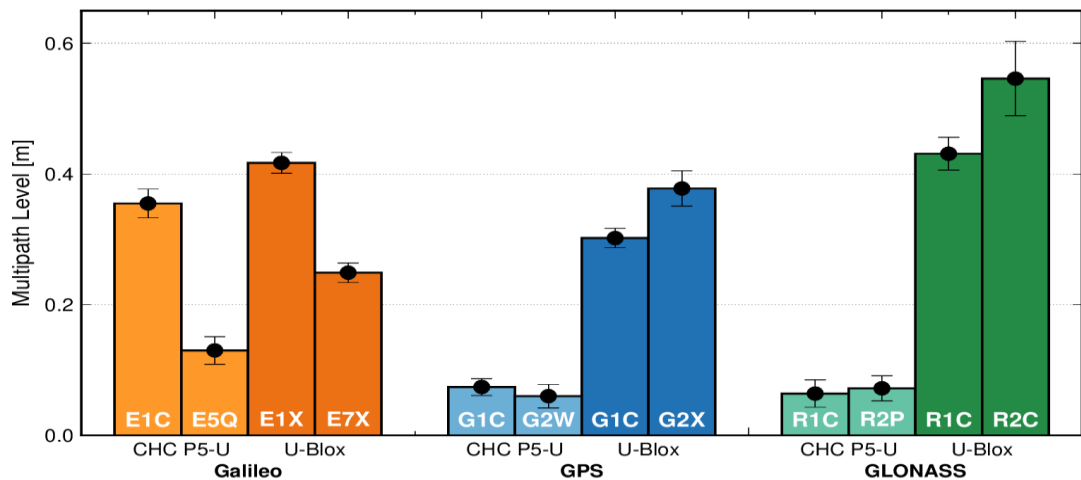


**Figure 2.** Code multipath levels of the CHC P5-U and u-blox receivers for GPS, GLONASS and Galileo

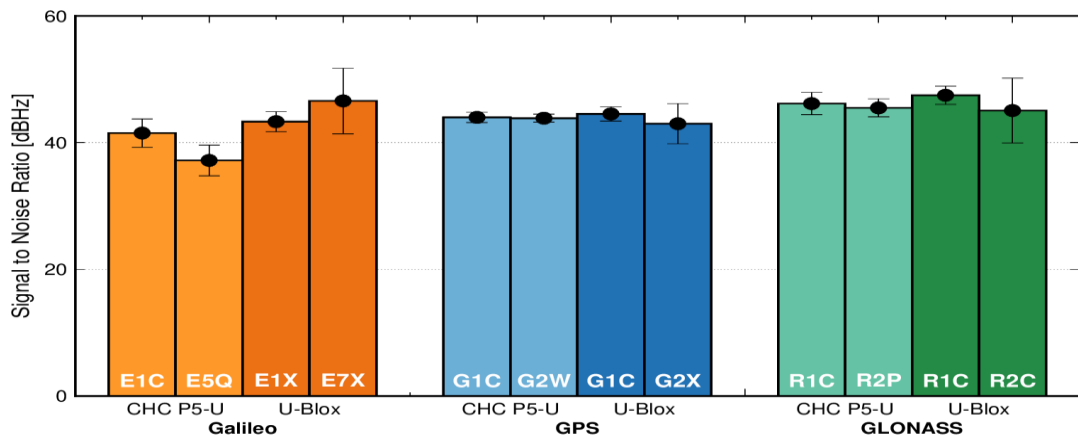


**Figure 3.** SNR values of the CHC P5-U and u-blox receivers for GPS, GLONASS and Galileo

Code multipath values were computed for each arc with no data gap and cycle slip. In this way, constant ambiguity was kept for each arc during the multipath computation. As shown in Figure 2, the code multipath level of the CHC P5-U receiver is significantly lower than the u-blox receiver which is using the low-cost external Survey GNSS multiband antenna. It is thought that if the u-blox patch antenna was used, the code multipath level would be much higher for the u-blox receiver because the patch antenna is more vulnerable to multipath. Multipath is dependent on the antenna environment, receiver, antenna, signal channel, type of modulation, and the multipath suppression algorithm. Most of the geodetic receivers, including the CHC P5-U receiver support the multipath mitigation algorithm (<https://www.surveying-company.net/c220gr2-details>). The u-blox ZED-F9P receiver also employs a similar multipath mitigation technique [15]. However, due to the low-cost antenna effect, the multipath level of the u-blox receiver is still higher than the geodetic one. When the signal channels are investigated, the multipath level of the second frequencies of Galileo (E5Q for CHC P5-U and E7X for u-blox) from the receivers is smaller than the first frequencies of Galileo. For GPS and GLONASS, the multipath level of each frequency within each receiver is comparable. Due to the quality difference between low-cost and geodetic receivers, as expected, the multipath level of geodetic-grade receiver is significantly low compared to the low-cost receiver.

When SNR values are investigated, it is seen that mean SNR values from CHC P5-U and u-blox receivers are comparable, and no significant differences of SNR values between the GNSS constellations are observed for each receiver.

The number of cycle slips was computed for each receiver using the Geometry-Free phase and Melbourne-Wubenna combination [16,17]. When detecting the cycle slips, data gaps within the continuous arcs were also accepted as cycle slip. The total number of cycle slips over one month was converted to the mean cycle slip number of each satellite and each day. The results are given in Figure 4.

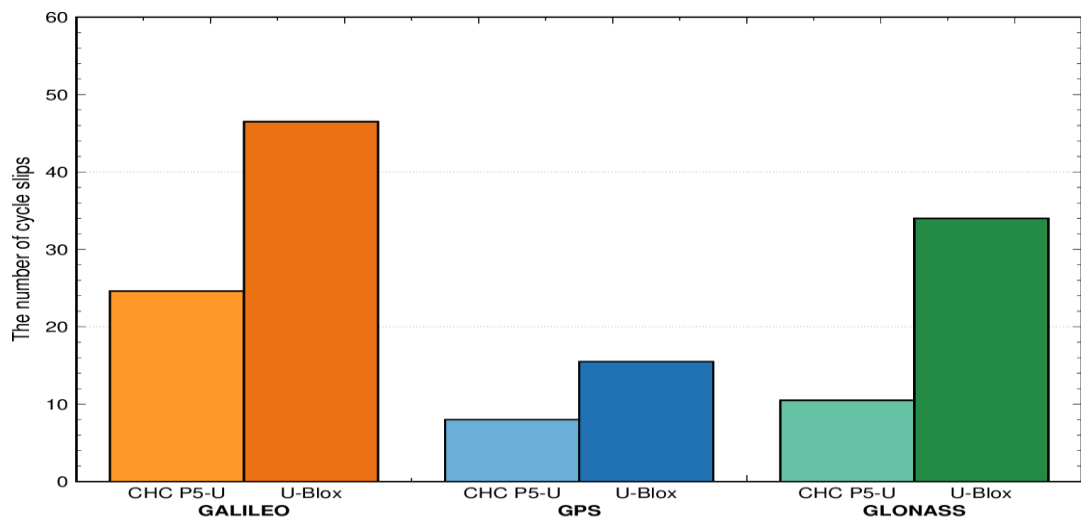


**Figure 4.** Average cycle slips per day for GPS, GLONASS and Galileo

As seen in Figure 4, the number of detected cycle slips from the u-blox receiver is significantly higher than the CHC P5-U receiver. When each GNSS constellation is considered, the lowest number of cycle slips was observed for GPS, while the highest number of cycle slips was observed for Galileo. Cycle slips can happen due to various factors, such as loss of line-of-sight, high ionospheric activity, and some receiver problems. A cycle slip causes a jump in carrier-phase measurements. Frequent cycle slips can be problematic for precise positioning due to re-initializing ambiguity parameters [18]. This effect can be more pronounced, especially in an environment where satellite visibility is constrained. Ambiguity re-convergence during cycle slips can be mitigated by the exact estimation of the size of the cycle slips (repairing process), but this requires a robust and computationally intensive process, and exact estimation of the size is not possible all the time. If triple-frequency GNSS observations are available, reliable estimation of the size of cycle slips can be utilized using extra-wide lane (EWL), wide lane (WL), and narrow lane (NL) combinations as a cascading step [19]. However, this approach cannot be feasible for low-cost receivers due to the lack of the third frequencies.

#### 4. CONCLUSIONS

This experiment presented the performance of the RINEX data integrity and quality of the low-cost u-blox receiver while comparing it with the geodetic-grade CHC P5-U receiver. Low-cost Survey GNSS Multiband antenna was used for the u-blox receiver instead of the patch antenna. RINEX data was collected over a one-month period under the same conditions for each receiver. Data integrity analysis consisted of the epoch and dual frequencies phase/code availabilities of each GNSS constellation. Data quality analysis consisted of the code multipath, SNR, and cycle slips analysis. The main findings can be summarized as follows:

- ) The epoch availability of the u-blox and CHC P5-U receivers was computed as 99.7% and 100%. This can prove that nearly all required epochs in the test period were recorded by the u-blox receiver.
- ) The frequency availability analysis showed that the u-blox receiver recorded less dual frequency phase/code observations compared to the CHC P5-U receiver. The loss of the observations is more evident for GPS because u-blox receiver only tracks L2C observation as a second GPS frequency. For GLONASS and Galileo, the results are more comparable, a maximum 4% difference was observed for the second frequency of Galileo between the u-blox and CHC P5-U receivers.
- ) Multipath results show that the u-blox receiver significantly exhibited higher code multipath values with respect to the CHC P5-U receiver for GPS, GLONASS, and Galileo. Nevertheless, code multipath values from the u-blox receiver are within the acceptable range for most of the receivers.
- ) SNR values of each receiver were found to be comparable, and no significant differences were

observed. It is shown that SNR values of each GNSS constellation are close to each other for each receiver.

-) Cycle slip analysis showed that the u-blox receiver exhibited significantly low performance compared to the CHC P5-U receiver. Approximately two times higher cycle slip numbers from the u-blox receiver were computed compared to the CHC P5-U receiver. The differences were found to be much higher for GLONASS. Despite all observations were collected under clear sky visibility, cycle slips can be occurred regardless of the interruptions of line-of-sight between satellite and receiver.

This should be emphasized that the low-cost external antenna was used for the u-blox receiver in this study. The data quality metrics found from the u-blox receiver in this study may be much worse if the patch antenna was used.

### Declaration of Ethical Standards

As the authors of this study, we declare that all ethical standards have been complied with.

### Credit Authorship Contribution Statement

Author contribution rates in this study as follows: Sermet Ogutcu 30%, Salih Alcay 20%, Huseyin Duman 20%, Behlül Numan Ozdemir 15%, and Ulkunur Koray 15%.

### Declaration of Competing Interest

The authors declare no conflict of interest.

### Funding / Acknowledgements

No funding is available for this research.

### Data Availability

All data used for this study are available from the corresponding author upon reasonable request.

### REFERENCES

- [1] D. Janos, and P. Kuras, "Evaluation of low-cost GNSS receiver under demanding conditions in RTK network mode," *Sensors*, 21(16), 5552, 2021.
- [2] R. Hohensinn, R. Stauffer, M.F. Glaner, I.D. Herrera Pinzón, E. Vuadens, Y. Rossi and M. Rothacher, "Low-Cost GNSS and Real-Time PPP: Assessing the Precision of the u-blox ZED-F9P for Kinematic Monitoring Applications," *Remote Sensing*, 14(20), 5100, 2022.
- [3] N. Wielgocka, T. Hadas, A. Kaczmarek, and G. Marut, "Feasibility of using low-cost dual-frequency gnss receivers for land surveying," *Sensors*, 21(6), 1956, 2021.
- [4] S. Mahato, M. Goswami, S. Kundu, and A. Bose, "On usability of dual-frequency, compact GNSS modules for long baseline RTK," In 2022 3rd URSI Atlantic and Asia Pacific Radio Science Meeting (AT-AP-RASC) (pp. 1-4). IEEE, 2022.
- [5] A. Elmezayen, and A. El-Rabbany, "Performance assessment of real-time multiconstellation GNSS PPP using a low-cost dual-frequency GNSS module," *Artificial Satellites: Journal of Planetary Geodesy*, 56, 3, 2021
- [6] A. Cina, and M. Piras, "Performance of low-cost GNSS receiver for landslides monitoring: test and results," *Geomatics, Natural Hazards and Risk*, 6(5-7), 497-514, 2015.
- [7] Z. Nie, F. Liu and Y. Gao, "Real-time precise point positioning with a low-cost dual-frequency GNSS device," *Gps Solutions*, 24, 9, 2020.
- [8] D. Janos and P. Kuras, "Evaluation of low-cost GNSS receiver under demanding conditions in

- RTK network mode," *Sensors*, 21(16), 5552, 2021.
- [9] N. Wang, Z. Li, B. Duan, U. Hugentobler, and L. Wang, "GPS and GLONASS observable-specific code bias estimation: comparison of solutions from the IGS and MGEX networks," *Journal of Geodesy*, 94, 74, 2020.
- [10] M.S. Circiu, M. Felux, B. Belabbas, M. Meurer, J. Lee, M. Kim, and S. Pullen, "Evaluation of GPS L5, Galileo E1 and Galileo E5a performance in flight trials for multi frequency multi constellation GBAS". In Proceedings of the 28th International Technical Meeting of The Satellite Division of the Institute of Navigation (ION GNSS+ 2015) (pp. 897-906), 2015.
- [11] F. Guo, X. Li, X. Zhang, and J. Wang, "Assessment of precise orbit and clock products for Galileo, BeiDou, and QZSS from IGS Multi-GNSS Experiment (MGEX)," *GPS solutions*, 21(1), 279-290, 2017.
- [12] M. Glaner, and R. Weber, "PPP with integer ambiguity resolution for GPS and Galileo using satellite products from different analysis centers," *GPS Solutions*, 25, 102, 2021.
- [13] S. Ogutcu, "Assessing the contribution of Galileo to GPS+ GLONASS PPP: Towards full operational capability," *Measurement*, 151, 107143, 2020.
- [14] J. Douša and P. Václavovic, "G-Nut/Anubis User Manual".
- [15] R. Hohensinn, R. Stauffer, M.F. Glaner, I.D. Herrera Pinzón, E. Vuadens, Y. Rossi and M. Rothacher "Low-Cost GNSS and Real-Time PPP: Assessing the Precision of the u-blox ZED-F9P for Kinematic Monitoring Applications," *Remote Sensing*, 14(20), 5100, 2022.
- [16] S.B. Bisnath, "Efficient, automated cycle-slip correction of dual-frequency kinematic GPS data". In Proceedings of the 13th International Technical Meeting of the Satellite Division of The Institute of Navigation (ION GPS 2000) (pp. 145-154), 2000.
- [17] I.V. Bezmenov, I.Y. Blinov, A.V. Naumov and S.L. Pasynok, "An algorithm for cycle-slip detection in a Melbourne–Wübbena combination formed of code and carrier phase GNSS measurements," *Measurement Techniques*, 62, 415-421, 2019.
- [18] D. Chai, W. Sang, G. Chen, Y. Ning, J. Xing, M. Yu and S. Wang, "A novel method of ambiguity resolution and cycle slip processing for single-frequency GNSS/INS tightly coupled integration system," *Advances in Space Research*, 69(1), 359-375, 2022.
- [19] Q. Zhao, B. Sun, Z. Dai, Z. Hu, C. Shi and J. Liu, "Real-time detection and repair of cycle slips in triple-frequency GNSS measurements," *GPS solutions*, 19, 381-391, 2015.



## EFFECT OF ORANGE PEEL ESSENTIAL OIL ON THE PROPERTIES OF CHITOSAN: GELATIN CASTED FILMS PREPARED FOR ACTIVE PACKAGING

<sup>1</sup>Fatma DEMİR , <sup>2</sup>Gülden GÖKŞEN , <sup>3,\*</sup>Didem DEMİR KARAKUŞ 

<sup>1,3</sup>Tarsus University, Vocational School of Technical Sciences at Mersin Tarsus Organized Industrial Zone,  
Department of Chemistry and Chemical Process Technologies, Mersin, TÜRKİYE

<sup>2</sup>Tarsus University, Vocational School of Technical Sciences at Mersin Tarsus Organized Industrial Zone,  
Department of Food Technology, Mersin, TÜRKİYE

<sup>1</sup>[fatma\\_demir@tarsus.edu.tr](mailto:fatma_demir@tarsus.edu.tr), <sup>2</sup>[guldengoksen@tarsus.edu.tr](mailto:guldengoksen@tarsus.edu.tr), <sup>3</sup>[didemdemir@tarsus.edu.tr](mailto:didemdemir@tarsus.edu.tr)

### Highlights

- Biologically active films were prepared for food packaging
- OEO improved physicochemical properties positively
- Composite films showed inhibitory activity on *E. coli* and *S. aureus*



## EFFECT OF ORANGE PEEL ESSENTIAL OIL ON THE PROPERTIES OF CHITOSAN: GELATIN CASTED FILMS PREPARED FOR ACTIVE PACKAGING

<sup>1</sup>Fatma DEMİR , <sup>2</sup>Gülden GÖKŞEN , <sup>3\*</sup>Didem DEMİR KARAKUŞ

<sup>1,3</sup>Tarsus University, Vocational School of Technical Sciences at Mersin Tarsus Organized Industrial Zone,  
Department of Chemistry and Chemical Process Technologies, Mersin, TÜRKİYE

<sup>2</sup>Tarsus University, Vocational School of Technical Sciences at Mersin Tarsus Organized Industrial Zone,  
Department of Food Technology, Mersin, TÜRKİYE

<sup>1</sup>fatma\_demir@tarsus.edu.tr, <sup>2</sup>guldengoksen@tarsus.edu.tr, <sup>3</sup>didemdemir@tarsus.edu.tr

(Geliş/Received: 29.12.2022; Kabul/Accepted in Revised Form: 10.05.2023)

**ABSTRACT:** Food packaging is a passive barrier that protects food against environmental factors such as ultraviolet light, oxygen, water vapor, pressure, heat, chemical, and microbiological contaminants. In a changing and developing world, consumers now want to reach healthier, fresher, and more diverse foods. In response to consumer demands and expectations, the food sector has focused on developing active and intelligent packaging. The purpose of active packaging is to protect the properties of the food by interacting with the coating material and prolonging the shelf life. In this context, it is aimed to prepare active package films by integrating bioactive agents into films prepared based on biodegradable polymers. It is an important point that is determined how the characteristics of the films such as morphology, molecular structure, surface property, and antimicrobial activity, will shift depending on the type and quantity of bioactive agent addition. Based on this, packaging films loaded with different concentrations of orange peel essential oil (OEO) (25, 50 and 100% of total polymer weight) were produced on the basis of chitosan and gelatin natural polymers. The changes that occur in the active films as a result of the increasing amounts of oil were revealed by determining the molecular structure, surface property, morphological characteristics, solubility quality, and antibacterial activity. The solubility of the films, which is an effective parameter in the evaluation of the environmental impact of the films that will be released as waste after use, varied between 20% and 25% at the end of 48 hours. The 100OEO@CH:GEL film showed the highest antibacterial properties against *Escherichia coli* and *Staphylococcus aureus*.

**Keywords:** Chitosan, Gelatin, Orange Peel Essential Oil, Solvent Casting, Food Packaging

### 1. INTRODUCTION

Food packaging plays a primary role in protecting the food product from external environmental effects (germs, insects, light, heat, oxygen, water vapor, odours, dirt, dust, etc.). The main purpose of packaging is to ensure food safety and extend the shelf life of food by minimizing environmental impacts to meet both industrial and consumer needs [1]. Plastic packaging has been widely used in the food industry for many years due to its advantageous properties. They are economical, functional, lightweight and versatile as they can be prepared in rigid (bottles, jars, cans), thermoformed (trays) or flexible (woven mesh, multilayer films) forms. Therefore, they have until recently replaced other traditional food packaging materials such as glass, metals (aluminium, laminated, tin and steel), paper and cardboard [2]. On the other hand, this extensive use of plastics has caused serious environmental problems, as most of these materials are petroleum derivatives, cannot be degraded and pollute the environment during their production and disposal [3]. In order to keep up with current trends and meet the demands of consumers, the food industry market has recently demonstrated new technological breakthroughs in the form of

\*Corresponding Author: Didem DEMİR KARAKUŞ, didemdemir@tarsus.edu.tr

environmentally friendly packaging with novel packaging solutions. As a result of these advances, work on developing active and smart packaging has been initiated.

Active packaging is a new method used to extend the shelf life of perishable foods, to protect or improve the quality and safety of prepared foods due to their interaction with the product. Furthermore, active packaging can replace active compounds in foods, reduce particle movement from packaging materials to food, and eliminate industrial processes that can introduce pathogenic microorganisms into the product. This packaging system also has an advantage in reducing foodborne illness outbreaks, and food recalls [4]. Active packaging systems can be divided into active cleaning systems (absorbers) and active release systems (emitters). The first is the removal of unwanted compounds such as moisture, carbon dioxide, oxygen, ethylene or odor from the food or its environment, while the second one is the release of compounds such as antimicrobials and antioxidants into the packaged food or the air space inside the packaging [5]. When the studies conducted in recent years are examined, it shows that there is more interest in the production of packages that can release antioxidants. In this context, there is increasing relevance in incorporating natural antioxidant agents such as plant extracts and essential oils into polymer-based active packaging materials.

Essential oils are the volatile liquids collected from diverse plant parts such as flowers, leaves, seeds, peels, fruits and barks. These oils, which are the most characteristic features of plants and are directly related to many vital functions of the plant, are valuable compounds that are generally known for their distinctive odor and colorless structure. It is considered as one of the important herbal products because it contains a meager amount of the total mass. They are known for their potential benefits to human health due to their biological properties such as anticancer, anti-inflammatory, antidiabetic, antiulcerogenic, antidepressant, anti-anxiety and high antioxidant and antimicrobial activities. These include basil (*Ocimum basilicum* L.) [6], chamomile (*Matricaria chamomilla* L.) [7], peppermint (*Mentha piperita* L.) [8] and rosemary (*Rosmarinus officinalis* L.) [9] essential oils which have been approved by the Food and Drug Administration (FDA) as food additives. In addition, they have been recognized as safe (GRAS) for use in the food packaging industry [10]. It is possible to produce packaging material by dispersing these oils in a polymeric film. The films in active packaging technology are preformed thin sheets and can be applied directly on the product as a wrap or cover [11]. With this packaging, it is aimed to extend the shelf life of the food while preserving the nutritive and sensory quality of the food. Active packaging combined with essential oils has so far been applied to a variety of foods such as beef, butter, ham, chicken, dairy products and seafoods [10].

Chitosan is produced from seafood waste and is biocompatible, biodegradable, has a high adsorption capacity, and antibacterial properties, making it suitable for food packaging materials [12]. In recent years, many scientists have been interested in gelatin, a water-soluble protein product formed from the partial hydrolysis of collagen, because of its remarkable properties. These include its biodegradability, edibility, non-toxic and good film-forming capability. So, it is a feasible alternative for producing films or coatings included in food packaging.

Within the scope of the study, essential oil incorporated polymeric films were prepared. Chitosan and gelatin were selected to obtain the main polymeric structure of films. Since both polymers have been proven to be biocompatible and biodegradable in other studies carried out so far, they are suitable for safe use in packaging material production [13]–[15]. Orange peel essential oil (OEO) was chosen as the essential oil because of its potent antibacterial properties. Polymer film based on chitosan and gelatin and with and without OEO-integrated active films were produced using the solvent-casting technique. The films were characterized with employed chemical, morphological and biological analyses, the effect of OEO enrichment on the films was discussed, and the usability of films as food packaging material was assessed in the light of the findings.



## 2. MATERIAL and METHOD

### 2.1. Material

Chitosan with medium molecular weight, gelatin for microbiology, glacial acetic acid, glycerol for molecular biology and tween 20 were purchased from Sigma Aldrich (USA). OEO was obtained from a herb market in Mersin Province, Turkey. Distilled water was used in all solution preparation and washing steps. The strain of *Staphylococcus aureus* CECT 435 (ATCC 25923) and *Escherichia coli* O157:H7 (ATCC 35150) were obtained from from KWIK STIK™. Tryptone Soy Broth (TSB), Tryptone Soy Agar (TSA) and Mueller Hinton agar (MHA) were purchased from Conda (Spain).

### 2.2. Preparation of films

The chitosan:gelatin (CHI:GEL) film and different amounts of OEO added films (OEO@CHI:GEL) were prepared using a traditional solvent-casting method. First, to obtain the polymer solution, CHI and GEL solutions were prepared separately. For CHI solution, the calculated amount of CHI (2%, w/v) was weighed and dissolved in 4% (v/v) acetic acid solution. For GEL solution, the certain amount of GEL (6%, w/v) was dissolved in distilled water at 65°C. Afterwards, a final solution was obtained by mixing both solutions, tween 20 and glycerol by using a magnetic stirrer at room temperature for 30 min. The 2 mL of solution was poured into glass Petri dishes coated with Teflon tape with a diameter of 5 cm and spread over carefully to result in a film. The polymeric film was solidified by evaporating the solvent at 60°C during overnight using a temperature-set oven. After 24 h incubation, the films were peeled from the Petri dishes. Each film was cut into small pieces of 1x1 cm appropriate for further tests and kept in a desiccator (with approximately 20-30% relative humidity provided by the use of silica gel as a conventional desiccant) until use.

To prepare the OEO@CHI:GEL films, different amounts of OEO were added to the 2 mL of the final solution based on the total polymer weight (25, 50 and 100% of polymer weight). The essential oil-added solutions were stirred continuously until a homogeneous mixture was obtained. After preparing the composite solution, the OEO loaded films were carried out by following all the other steps described above for CH:GEL film. The experimental steps of film preparation are summarized in Figure 1. Film samples prepared from only polymer solutions named as CH:GEL, and film samples integrating 25, 50 and 100% OEO were coded as 25OEO@CH:GEL, 50OEO@CH:GEL and 100OEO@CH:GEL, respectively.

### 2.3. Morphology

For determination of surface morphology of the CH:GEL film as control and films incorporated with different amounts of OEO, microscopic analysis was performed using an optical microscopy (Zeiss, Eco 40, Germany) at 4x magnification.

### 2.4. Fourier Transform Infrared spectroscopy (FTIR)

The chemical structure of CH:GEL film and OEO@CHI:GEL films was characterized by Fourier Transform Infrared (FTIR) spectrum obtained by using a spectrometer (Perkin-Elmer Spectrum 1000, USA), equipped with an attenuated total reflection (ATR) accessory. The FTIR spectra were performed from wavenumber 400-4000  $\text{cm}^{-1}$  with a resolution of 4  $\text{cm}^{-1}$  and 128 scans.

### 2.5. Solubility

The solubility was tested in water based on the weight loss of films. First, each film was cut into pieces, and the initial dry weights were measured. In order to test the solubility of the films in water, the cut samples were placed in Eppendorf tubes, and 10 mL of water was added to them. After the tubes were

kept at room temperature for 48 hours, the samples were removed and dried in an oven at 60°C. The completely dried samples were weight again. The solubility in water was calculated by using the following equation:

$$\text{Solubility (\%)} = [\text{final weight}/\text{initial weight}] \times 100$$

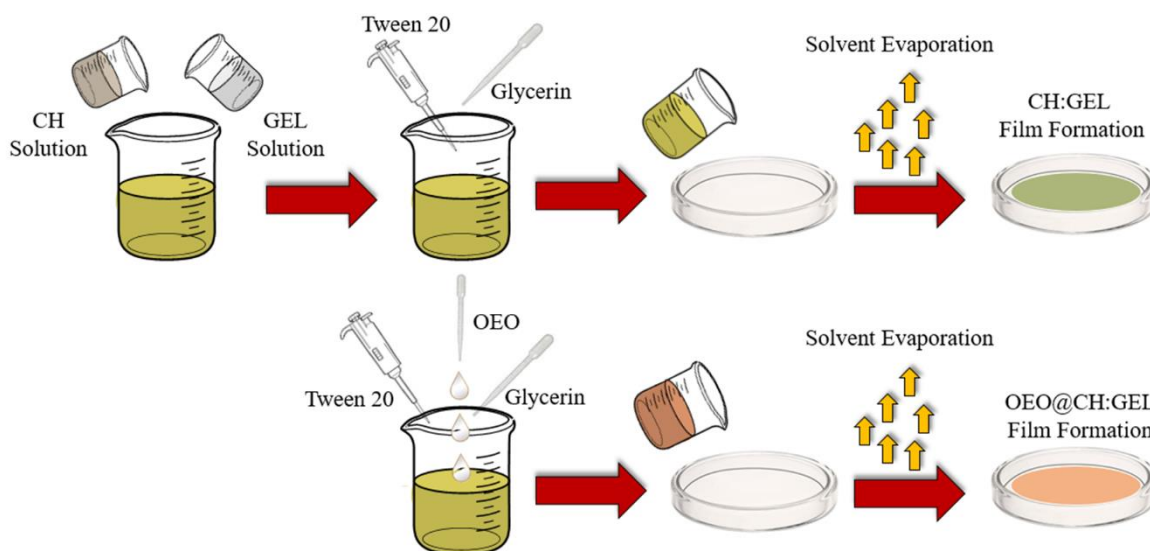


**Figure 1.** Experimental steps of the formation of CH:GEL and OEO@CHI:GEL film using solvent-casting method

## 2.6. Antibacterial Activity

The antibacterial activity was first determined by the agar disc diffusion method, according to Clinical and Laboratory Standards Institute. Briefly, 100  $\mu\text{L}$  of bacterial cell suspensions ( $10^8$  CFU  $\text{mL}^{-1}$ ) were spread on the surfaces of MHA using sterile cotton swabs. Films were cut as disc shapes, and they were sterilized under UV light for 30 mins. Then sterile film disk samples (8 mm) were placed on MHA's surface and incubated overnight at 37 °C. After 24 h incubation, the diameter of the resulting inhibition zone was measured using a micrometer and expressed in mm. Experiments were done in triplicate.

## 2.7. Statistical Analysis

All experiments were performed in triplicate and all data were statistically analyzed. Data are expressed as mean  $\pm$  standard deviation (SD). Analysis of variance (ANOVA) was performed using SPSS 16.0 (SPSS, Chicago, IL, USA) to compare means by Duncan test with a significance level of 0.05.

## 3. RESULTS and DISCUSSIONS

The films for active food packaging were successfully produced using chitosan and gelatin polymers and the addition of different amounts of OEO to these polymers. The photographs of the produced films are given in Figure 2. As can be seen, the films were easily peeled off from Teflon-coated petri dishes ( $\text{O}=5$  cm) in one piece without any tearing. In particular, it can be said that the film prepared with the highest oil content (100OEO@CHI:GEL) has a more uniform and homogeneous structure visually. In addition, all films generally exhibited a transparent structure. Transparency is a crucial intrinsic parameter for the shelf-life evaluation of food packaging materials [16]. Therefore, photographs of films were taken to show optical properties (Figure 2). The addition of increasing concentration OEO into the polymer structure

decreased the transparency. is decrease in the transparency rate of OEO@CH:GEL films can possibly be due to the presence of pigments of the OEO.

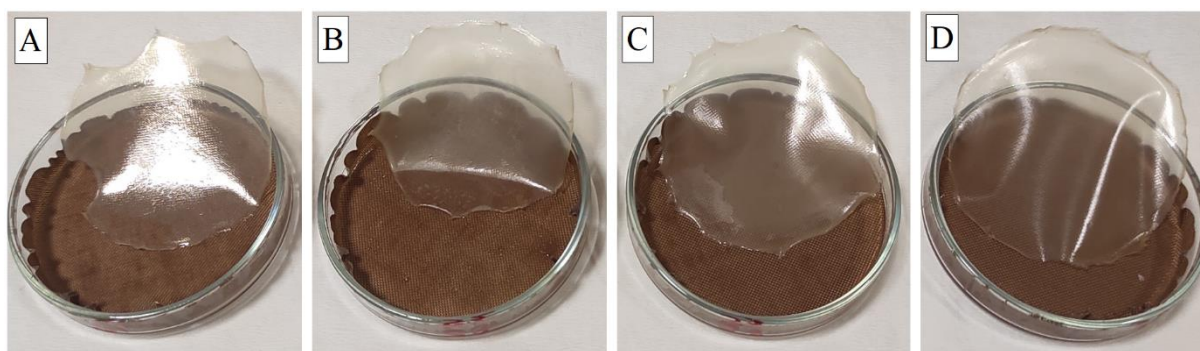


**Figure 2.** Images of films. A) CH:GEL, B) 25OEO@CHI:GEL, C) 50OEO@CHI:GEL and D) 100OEO@CHI:GEL

The films were examined with an optical microscope to confirm the changes in morphology with the addition of increased OEO amounts. Figure 3 shows the images of the films obtained at the same magnification. As is seen from the figure, morphology of 100OEO@CHI:GEL film was observed as smooth, compact and without any crack or pores. Nevertheless, CH:GEL film exhibited irregular forms with many bulges, tiny particles and droplets on the surface. 50OEO@CHI:GEL film also exhibited a heterogeneous structure, but it had lower bulges. An increase in the viscosity of the final solution was observed with the addition of essential oil to the polymer solution. With increasing viscosity, the resulting surface may have been smoother as the evaporation of solvent from the mixture was delayed [17]. This result created a more stable structure especially in the film sample with the highest oil content (100OE@CHI:GEL). In the daylight photographs in Figure 2 above, it can be easily seen with its circular peeling without any deformation from the petri dish due this flexibility and stability. According to other similar studies, essential oil incorporation could improve the elasticity of biofilms' matrix by their possible plasticizing effect [12], [18], [19] and adding essential oil to the polysaccharide structure improved the functional properties of edible films and coatings [20].

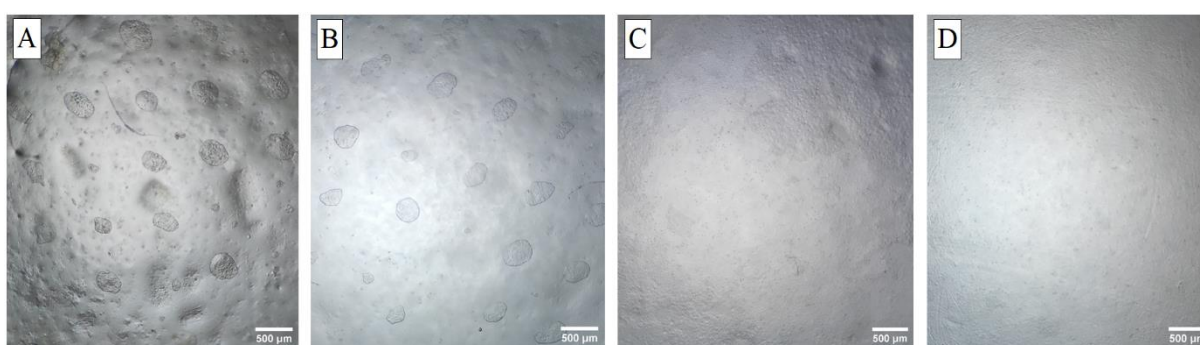


**Figure 3.** Optical microscopy images of films. A) CH:GEL, B) 25OEO@CHI:GEL, C) 50OEO@CHI:GEL and D) 100OEO@CHI:GEL

In order to study the interaction between chitosan, gelatin and essential oil and identify any changes in the molecular structure that could have occurred with varying OEO amount, FTIR spectrum of films were measured. Figure 4 displays FTIR spectra of the CH:GEL film (considered as control) and films loaded with different amounts of OEO. The broad absorption band between  $3000\text{ cm}^{-1}$  to  $3650\text{ cm}^{-1}$  corresponds to O-H and N-H stretching vibrations of hydrogen-bonded O-H and N-H functionalities (Amide A). The band duo seen at wavenumbers of  $2929/2873\text{ cm}^{-1}$  are related to the asymmetric and symmetric stretching vibrations of the  $\text{CH}_3$  and  $\text{CH}_2$  functionalities (Amide B) [12]. In the spectrum of the

films, C=O stretching at  $1647\text{cm}^{-1}$  (Amide I), N-H stretching at  $1552\text{cm}^{-1}$  (Amide II), and C-N and N-H stretching at  $1240\text{cm}^{-1}$  (Amide III) peaks are associated with the functional structure of both chitosan and gelatin polymers [15], [21]. In addition, the bands in the range of  $1033\text{cm}^{-1}$  is attributed to the saccharide structure of the polymers. With the addition of OEO, no change was observed in the FTIR spectrum of films, showing absorption bands similar to the CH:GEL film spectrum. However, some difference in the positions of the absorption peaks was observed depending on the added OEO levels. In detail, at the highest amount of OEO, the peaks of Amide A was moved to  $3290\text{cm}^{-1}$  and the Amide B absorption peak was moved to  $2925\text{cm}^{-1}$ . In addition, a new small peak (at  $1742\text{cm}^{-1}$ ) was observed in relation to the carbonyl C=O stretching vibration from the ester linkage of triacylglycerol [22].

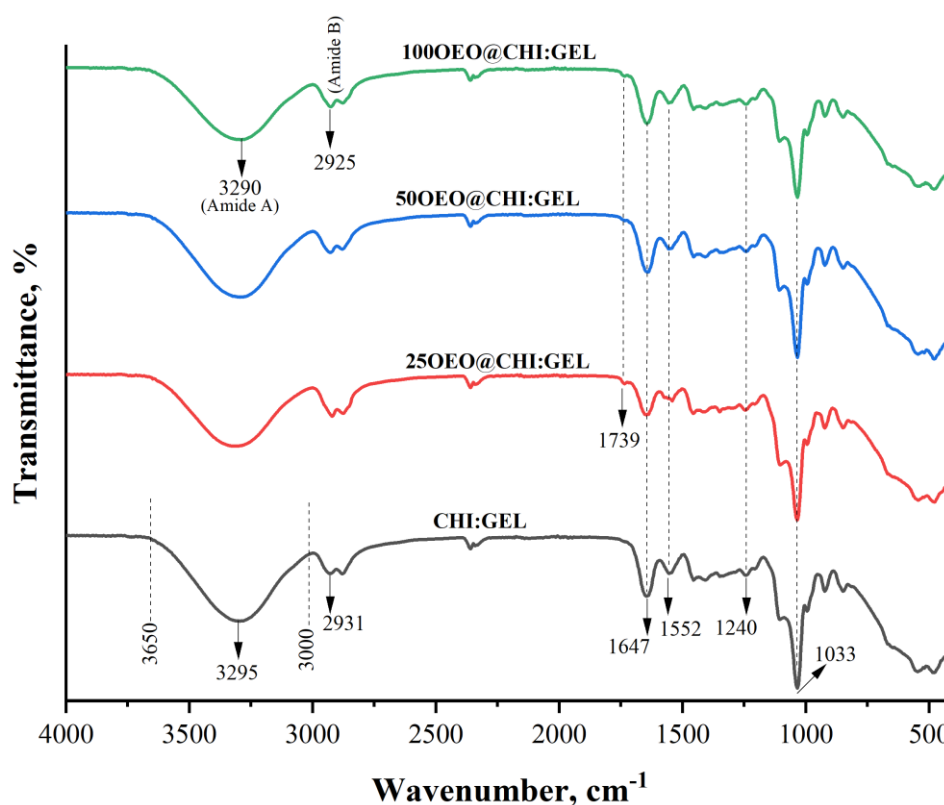


**Figure 4.** FTIR spectrums of CH:GEL and different concentrations of OEO incorporated into OEO@CH:GEL films.

A key parameter for food packaging, film solubility is a measure of the film's resistance to liquids. In our study, the solubility of films was carried out with distilled water for 48 h, and the results are displayed in Figure 5. The solubility (% wt.) values are seen to vary between 20% and 25%. The increasing amount of OEO into the polymer solution resulted in decreased water solubility from 25.06% to 20.14%. The decline in water solubility of OEO@CH:GEL films should be attributed to the hydrophobic effect of oil molecules. The interaction between the polymers and phenols (in the structure of the oil) reduced the availability of hydroxyl and amino groups in the structure of chitosan and gelatin. With OEO present, the hydrogen bond interactions among chitosan, gelatin, and water were disrupted, emerged leading to a decrease in solubility. A similar result was observed in the water solubility of fennel and peppermint essential oils loaded active chitosan films as previously reported by Liu et al. [23].

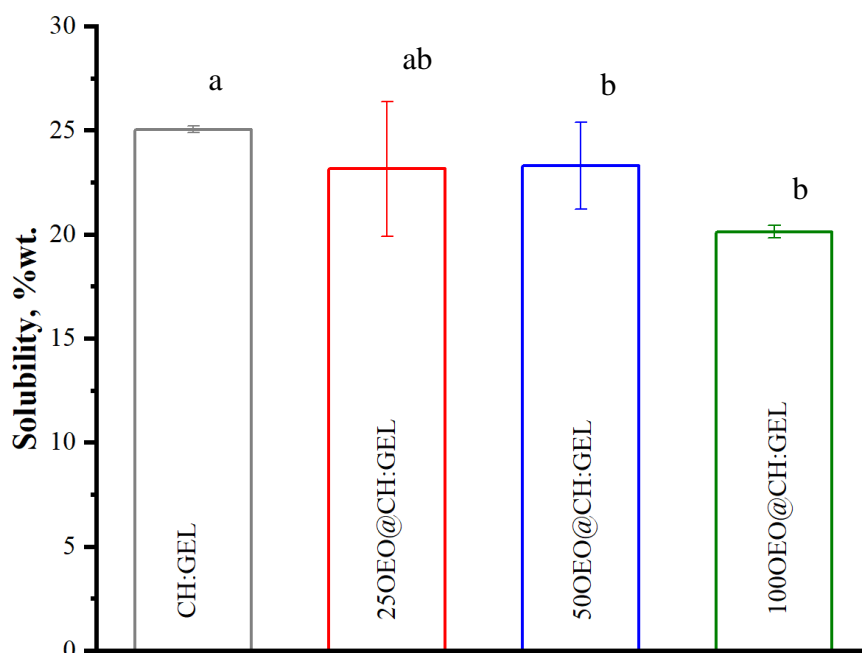


**Figure 5.** The solubility of films against water for 48 h. Different letters in the bar indicate a significant difference ( $p < 0.05$ ).

The antibacterial activity of the films against Gram-positive (*Staphylococcus aureus*) and Gram-negative bacteria (*Escherichia coli* O157:H7) was also carried out via the disk-diffusion method (shown in Table 1). The results for the inhibition zones (mm) of microorganisms shown that Gram-positive bacteria were more sensitive than the Gram-negative ones. For instance, CH:GEL, 25OEO@CH:GEL, 50OEO@CH:GEL, 100OEO@CH:GEL indicated inhibition zones between 19.74 and 24.14 mm for *E.coli*, while inhibition zones of these films were not measured due to partial growth of bacteria in the petri dish for *S. aureus*. These films exhibited more sensitive properties against *S. aureus* than *E.coli*. Chitosan has bactericidal properties, making it particularly appropriate for food packaging materials [24]. So results of all films showed that these films had inhibitory activity on *E. coli* and *S. aureus*, obviously. Increasing the concentration of EO in the films were emerged rising of the inhibitory activity. The anti *Escherichia coli* O157:H7 activity of CH:GEL film showed significance differences from 50 and 100% OEO loaded CH:GEL samples. Li et al. reported similarly that orange peel essential oil inhibited *S. aureus* and *E.coli* [18]. The results of the current study suggest that the addition of OEO (50 and 100%) significantly increased the antibacterial activity of the CH:GEL film.

**Table 1.** Results antibacterial activity of films against *Escherichia coli* O157:H7 ve *Staphylococcus aureus* via disc diffusion method.

Sample	Inhibition zone (mm)	
	<i>Escherichia coli</i> O157:H7	<i>Staphylococcus aureus</i>
CH:GEL	17.74±2.40 <sup>a</sup>	ZN
25OEO@CH:GEL	20.29±1.00 <sup>ab</sup>	ZN
50OEO@CH:GEL	23.35±1.99 <sup>b</sup>	ZN
100OEO@CH:GEL	24.14±2.81 <sup>b</sup>	ZN

<sup>1</sup>ZN: Zone measurement was not performed; growth of bacteria was partial in the petri dish. Mean±standard deviation. Different letters in the same column indicate a significant difference ( $p < 0.05$ ).

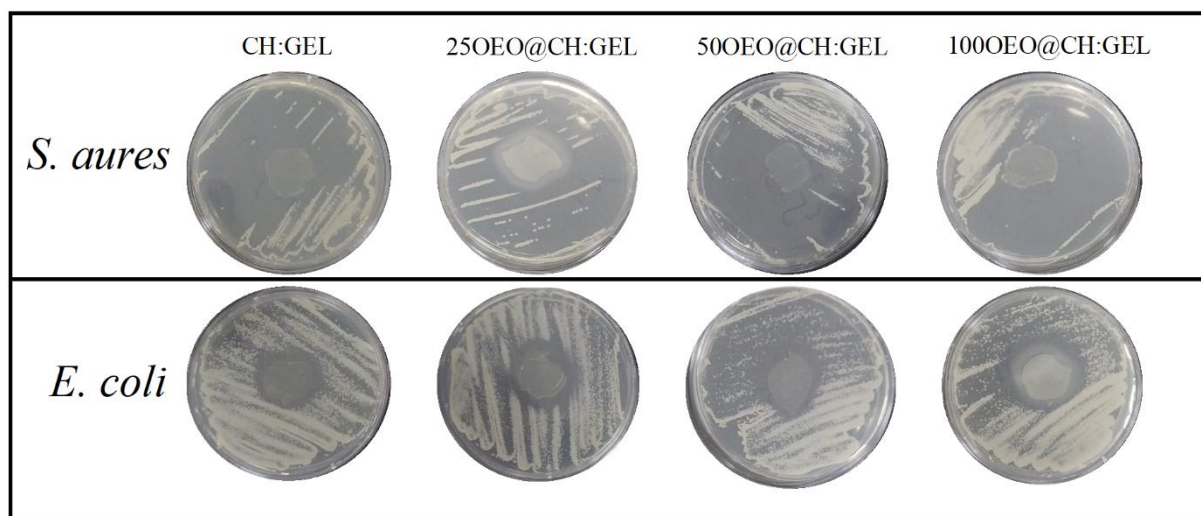


**Figure 6.** Antibacterial activity of the packaging films against to *S. aureus* and *E. coli* via disc diffusion method.

#### 4. CONCLUSION

In this research, a novel biocomposite film was developed using polymers from sustainable and low-cost sources (chitosan and gelatin) and incorporated with OEO. The incorporation of OEO could positively improve morphological, molecular structure, physical and antibacterial properties of the films, linked on the determined concentrations. Addition of OEO (25, 50 and 100%, w/w) into the CH:GEL films greatly assisted solubility, and light barrier properties while boosting their antibacterial activity, compared with the control film without OEO. Analyses of FTIR spectra indicated the presence of multiple CH-GEL-OEO interactions. Solubility properties decreased, while antibacterial activities increased with increasing concentration of OEO addition to CH:GEL. In conclusion, CH:GEL films enriched with OEO could be provided for an efficient coating that extends the shelf life and preserves the quality attributes of perishable foods.

#### Declaration of Ethical Standards

The authors declare that the materials and methods used in this study do not require ethical committee permission.

#### Credit Authorship Contribution Statement

FD carried out the experiments related to film production and characterization studies of the produced films. GG performed antimicrobial analysis and contributed to the writing of the manuscript. DD conceived the original idea, processed the experimental data, supervised the project and performed writing of the manuscript. All authors have read and agreed to the published version of the manuscript.

#### Declaration of Competing Interest

The authors declare that they have no known competing financial interests or personal relationships.

## Acknowledgement

The authors acknowledge the financial support of The Scientific and Technological Research Council of Türkiye under (TUBITAK) 2209-A Research Project Support Programme for Undergraduate Students (Project No: 1919B012114370).

## Data Availability

The data used to support the findings of this study are included within the article.

## REFERENCES

- [1] G. Fuertes, I. Soto, M. Vargas, A. Valencia, J. Sabattin, and R. Carrasco, "Nanosensors for a monitoring system in intelligent and active packaging," *J. Sensors*, vol. 2016, 2016, doi: 10.1155/2016/7980476.
- [2] P. R. Salgado, L. Di Giorgio, Y. S. Musso, and A. N. Mauri, "Recent Developments in Smart Food Packaging Focused on Biobased and Biodegradable Polymers," *Front. Sustain. Food Syst.*, vol. 5, p. 125, Apr. 2021, doi: 10.3389/FSUFS.2021.630393/BIBTEX.
- [3] P. Cazón, G. Velazquez, J. A. Ramírez, and M. Vázquez, "Polysaccharide-based films and coatings for food packaging: A review," *Food Hydrocoll.*, vol. 68, pp. 136–148, Jul. 2017, doi: 10.1016/J.FOODHYD.2016.09.009.
- [4] H. Piri, S. Moradi, and R. Amiri, "The fabrication of a novel film based on polycaprolactone incorporated with chitosan and rutin: potential as an antibacterial carrier for rainbow trout packaging," *Food Sci. Biotechnol.*, vol. 30, no. 5, pp. 683–690, May 2021, doi: 10.1007/S10068-021-00898-9/TABLES/2.
- [5] S. Yildirim *et al.*, "Active Packaging Applications for Food," *Compr. Rev. Food Sci. Food Saf.*, vol. 17, no. 1, pp. 165–199, Jan. 2018, doi: 10.1111/1541-4337.12322.
- [6] H. C. Bravo, N. V. Céspedes, L. Zura-Bravo, and L. A. Muñoz, "Basil Seeds as a Novel Food, Source of Nutrients and Functional Ingredients with Beneficial Properties: A Review," *Foods 2021, Vol. 10, Page 1467*, vol. 10, no. 7, p. 1467, Jun. 2021, doi: 10.3390/FOODS10071467.
- [7] Y. Tang *et al.*, "Electrospun Gelatin Nanofibers Encapsulated with Peppermint and Chamomile Essential Oils as Potential Edible Packaging," *J. Agric. Food Chem.*, vol. 67, no. 8, pp. 2227–2234, Feb. 2019, doi: 10.1021/ACS.JAFC.8B06226/SUPPL\_FILE/JF8B06226\_SI\_001.PDF.
- [8] A. Amiri, M. M. Sourestani, S. M. H. Mortazavi, A. R. Kiasat, and Z. Ramezani, "Fabrication of the antimicrobial sachet by encapsulation of peppermint essential oil in active packaging of strawberry fruit," *J. Food Process. Preserv.*, p. e17181, 2022, doi: 10.1111/JFPP.17181.
- [9] M. Abdollahi, M. Rezaei, and G. Farzi, "Improvement of active chitosan film properties with rosemary essential oil for food packaging," *Int. J. Food Sci. Technol.*, vol. 47, no. 4, pp. 847–853, Apr. 2012, doi: 10.1111/J.1365-2621.2011.02917.X.
- [10] R. Ribeiro-Santos, M. Andrade, N. R. de Melo, and A. Sanches-Silva, "Use of essential oils in active food packaging: Recent advances and future trends," *Trends Food Sci. Technol.*, vol. 61, pp. 132–140, Mar. 2017, doi: 10.1016/J.TIFS.2016.11.021.
- [11] M. Jouki, F. T. Yazdi, S. A. Mortazavi, and A. Koocheki, "Quince seed mucilage films incorporated with oregano essential oil: Physical, thermal, barrier, antioxidant and antibacterial properties," *Food Hydrocoll.*, vol. 36, pp. 9–19, May 2014, doi: 10.1016/J.FOODHYD.2013.08.030.
- [12] H. Haghighi *et al.*, "Comprehensive characterization of active chitosan-gelatin blend films enriched with different essential oils," *Food Hydrocoll.*, vol. 95, pp. 33–42, Oct. 2019, doi: 10.1016/J.FOODHYD.2019.04.019.
- [13] F. Ayaz, D. Demir, and N. Bölgen, "Differential anti-inflammatory properties of chitosan-based cryogel scaffolds depending on chitosan/gelatin ratio," *Artif. Cells, Nanomedicine, Biotechnol.*, vol. 49, no. 1, pp. 682–690, 2021, doi: 10.1080/21691401.2021.2012184.

- [14] P. Kumar, B. S. Dehiya, and A. Sindhu, "Comparative study of chitosan and chitosan-gelatin scaffold for tissue engineering," *Int. Nano Lett.*, vol. 7, no. 4, pp. 285–290, Dec. 2017, doi: 10.1007/s40089-017-0222-2.
- [15] Y. Yao, D. Ding, H. Shao, Q. Peng, and Y. Huang, "Antibacterial Activity and Physical Properties of Fish Gelatin-Chitosan Edible Films Supplemented with D-Limonene," *Int. J. Polym. Sci.*, vol. 2017, 2017, doi: 10.1155/2017/1837171.
- [16] S. Guzman-Puyol, J. J. Benítez, and J. A. Heredia-Guerrero, "Transparency of polymeric food packaging materials," *Food Res. Int.*, vol. 161, p. 111792, Nov. 2022, doi: 10.1016/J.FOODRES.2022.111792.
- [17] M. B. M. Y. Ang *et al.*, "Correlating PSf Support Physicochemical Properties with the Formation of Piperazine-Based Polyamide and Evaluating the Resultant Nanofiltration Membrane Performance," *Polym. 2017, Vol. 9, Page 505*, vol. 9, no. 10, p. 505, Oct. 2017, doi: 10.3390/POLYM9100505.
- [18] Y. Li, C. Tang, and Q. He, "Effect of orange (*Citrus sinensis* L.) peel essential oil on characteristics of blend films based on chitosan and fish skin gelatin," *Food Biosci.*, vol. 41, p. 100927, Jun. 2021, doi: 10.1016/J.FBIO.2021.100927.
- [19] P. Tongnuanchan, S. Benjakul, and T. Prodpran, "Properties and antioxidant activity of fish skin gelatin film incorporated with citrus essential oils," *Food Chem.*, vol. 134, no. 3, pp. 1571–1579, Oct. 2012, doi: 10.1016/J.FOODCHEM.2012.03.094.
- [20] A. Anis, K. Pal, and S. M. Al-Zahrani, "Essential Oil-Containing Polysaccharide-Based Edible Films and Coatings for Food Security Applications," *Polym. 2021, Vol. 13, Page 575*, vol. 13, no. 4, p. 575, Feb. 2021, doi: 10.3390/POLYM13040575.
- [21] M. Pereda, A. G. Ponce, N. E. Marcovich, R. A. Ruseckaite, and J. F. Martucci, "Chitosan-gelatin composites and bi-layer films with potential antimicrobial activity," *Food Hydrocoll.*, vol. 25, no. 5, pp. 1372–1381, Jul. 2011, doi: 10.1016/J.FOODHYD.2011.01.001.
- [22] A. Rohman and R. Ariani, "Authentication of nigella sativa seed oil in binary and ternary mixtures with corn oil and soybean oil using FTIR spectroscopy coupled with partial least square," *Sci. World J.*, vol. 2013, 2013, doi: 10.1155/2013/740142.
- [23] T. Liu, J. Wang, F. Chi, Z. Tan, and L. Liu, "Development and Characterization of Novel Active Chitosan Films Containing Fennel and Peppermint Essential Oils," *Coatings 2020, Vol. 10, Page 936*, vol. 10, no. 10, p. 936, Sep. 2020, doi: 10.3390/COATINGS10100936.
- [24] Y. Alparslan and T. Baygar, "Effect of Chitosan Film Coating Combined with Orange Peel Essential Oil on the Shelf Life of Deepwater Pink Shrimp," *Food Bioprocess Technol.*, vol. 10, no. 5, pp. 842–853, May 2017, doi: 10.1007/S11947-017-1862-Y/METRICS.





## PRODUCTION OF OXIDE DISPERSION STRENGTHENED INCONEL 718 ALLOYS USING CONVENTIONAL POWDER METALLURGY AND ADDITIVE MANUFACTURING METHODS

\*Eda AYDOĞAN 

Middle East Technical University, Metallurgical and Materials Engineering Department, Ankara,  
TÜRKİYE  
[aydogane@metu.edu.tr](mailto:aydogane@metu.edu.tr)

### *Highlights*

- ODS IN718 alloys were produced by powder metallurgy and SLM additive manufacturing
- PM samples have nanograins with high-density homogenously distributed nano-oxides
- SLM samples have cellular structure and high-density grouped nano-oxides
- Nano-oxides are determined to be mostly  $Y_2Ti_2O_7$ ,  $Y_2TiO_5$  or  $YTiO_3$  and Y-Al-O
- There are bi-phase particles in SLM-produced alloys due to rapid cooling



## PRODUCTION OF OXIDE DISPERSION STRENGTHENED INCONEL 718 ALLOYS USING CONVENTIONAL POWDER METALLURGY AND ADDITIVE MANUFACTURING METHODS

\*Eda AYDOĞAN

Middle East Technical University, Metallurgical and Materials Engineering Department, Ankara, TÜRKİYE  
[aydogane@metu.edu.tr](mailto:aydogane@metu.edu.tr)

(Received: 22.02.2023; Accepted in Revised Form: 11.05.2023)

**ABSTRACT:** Oxide dispersion strengthened (ODS) Ni-based alloys having a high density of nano-oxides (NOs) (<10 nm) are considered to be good candidates for extreme environments, such as high temperature, radiation, and corrosion. In this study, ODS IN718 alloys have been produced using conventional powder metallurgy (PM) and novel selective laser melting (SLM) additive manufacturing. The effect of processing routes on the microstructure, in particular on the nano-oxide formation and structure has been investigated. It has been found that the powder metallurgy method that consists of compressing followed by sintering at 1250 and 1500 °C results in a nano-granular structure with homogenously distributed fine nano-oxides having a high number density. Similarly, SLM results in a high number density of fine nano-oxides; however, the particles exist in groups with the grains/cells. The nano-oxides are determined to be  $Y_2Ti_2O_7$ ,  $Y_2TiO_5$  or  $YTiO_3$  and Y-Al-O. The deviation in the lattice parameters of  $Y_2Ti_2O_7$  infers the existence of some Al in the structure. This study sheds light on producing ODS IN718 alloys with high-density nano-oxides using powder metallurgy and additive manufacturing methods.

**Keywords:** Additive Manufacturing, Inconel 718, Nano-Particle, Oxide Dispersion Strengthened Alloy, Powder Metallurgy, Transmission Electron Microscopy

### 1. INTRODUCTION

Ni-based superalloys have been widely used for extreme applications such as gas turbines, turbo motors and nuclear reactors due to their high strength and creep resistance at high temperatures, thermal stability and high corrosion resistance [1, 2]. Even though they have exceptional properties up to ~700 °C, the properties degrade suddenly above this temperature as a result of coarsening and dissolution of strengthening phases, namely  $\gamma'$  and  $\gamma''$ . On the other hand, oxide dispersion strengthened (ODS) alloys have shown exceptional thermal stability above 1000 °C and almost zero radiation-induced swelling due to the existence of high-density nano-oxides having sizes less than 5 nm [3, 4]. These nano-oxides are reported to pin the dislocations and grain boundaries impeding grain growth and recrystallization, thus improving the high temperature stability and creep resistance. Moreover, the high number density of fine nano-particles provides a large interfacial area acting as the sinks for point defects [5-7].

The nano-oxides are mostly in  $Y_2Ti_2O_7$  and  $Y_2TiO_5$  form in Al-free ferritic systems [4, 8]. On the other hand, Y-Al-O particles with YAP ( $YAlO_3$ , perovskite), YAG ( $Y_3Al_5O_{12}$ , garnet), YAM ( $Y_4Al_2O_9$ , monoclinic), YAP ( $YAlO_3$ , pseudo-perovskite), YAH ( $YAlO_3$ , hexagonal), and YAT ( $Y_3Al_5O_{12}$ , tetragonal) structures have been reported in the ferritic alloys such as MA956 having up to ~6 wt.% Al [9]. Moreover, Park et al. have studied spark plasma sintered ODS Ni-based alloys and found the formation of  $Y_2Ti_2O_7$  and complex Y-Al oxides such as  $Y_4Al_2O_9$  and  $Y_3Al_5O_{12}$  [10].

The composition and production method of the ODS alloys determine the final properties of the alloys. The Oxygen content of the material has a profound effect on the size and number density of nano-oxides [11]. Moreover, the nano-oxide size has been reported to be coarser in the existence of Al in the system [10]. ODS alloys are conventionally produced by powder metallurgy methods such as ball milling followed by hot pressing, hot rolling, hydrostatic extrusion, spark plasma sintering etc. [10, 12, 13] which result in fine microstructures with superior high temperature mechanical properties. For instance, Hoelzer

\*Corresponding Author: Eda AYDOĞAN, [aydogane@metu.edu.tr](mailto:aydogane@metu.edu.tr)

et al. and Miller et al. have produced 14YWT ferritic alloys using consolidation, hot extrusion and annealing steps, and these alloys have microstructural stability up to  $\sim 1300$  °C and tensile and creep strength up to 800 °C [12, 14]. Furthermore, Nickel-based ODS alloys have been reported to show improved tensile strength as a result of the refinement in grain size due to the existence of Al [15]. However, conventional powder metallurgy methods consist of many steps, thus they are both time intensive and expensive.

Additive manufacturing (AM) methods such as selective laser melting (SLM), laser directed energy deposition (LDED), and electron beam melting (EBM) have been developed to produce complex-shaped alloys with high densification in a near net-shaped state [16, 17]. However, due to the high thermal gradients during the AM processes, columnar-shaped grains are formed along the building direction of the materials which causes anisotropic properties [18]. There is an immense literature to solve this problem. For instance, Oliveira et al. [19] studied the process parameters to control the microstructure. Ni et al. [20] Popovich et al. [21] and Tillmann et al. [22] investigated post-processing methods such as heat treatments and hot isostatic pressing to modify the as-built microstructure after additive manufacturing. On the other hand, nano-particle reinforcement has been reported to hinder columnar structure formation, reducing the texture in the AM samples [23, 24]. Besides controlling the microstructure, nano-particle dispersion improves high temperature strength and creep resistance of the materials [25, 26]. Studies on the development of nano-particle reinforced metal alloys using additive manufacturing have been increasing. For example, 17-4 PH steels with high number density TiN particles have been produced using SLM [27]. Moreover, ferritic ODS Fe14Cr as well as Nickel-based ODS IN738LC, NiCrFeY and Hastelloy X have been produced by SLM [28-31]. Recently, we have produced ODS IN718 alloys having different compositions using SLM and reported their behavior under heavy ion irradiation at 200 and 450 °C [32, 33]. However, the particle size of the AM produced ODS alloys is coarser and the number density of the particles is smaller compared to the conventional PM produced alloys, with the nano-oxide density in the order of  $\sim 10^{23} \text{ m}^{-3}$ .

In this study, ODS-IN718 alloys which were designed in our previous studies have been produced using both conventional powder metallurgy method of compression followed by sintering and novel SLM additive manufacturing methods. Detailed microstructural analyses have been conducted to determine the type of nano-particles as well as their size and number density in PM and SLM produced alloys. It has been found that both PM and SLM methods result in a high number density of  $\text{Y}_2\text{Ti}_2\text{O}_7$ ,  $\text{Y}_2\text{TiO}_5$  or  $\text{YTiO}_3$  and  $\text{Y-Al-O}$ , except for the difference in their distribution. This is the first study comparing the microstructure, especially the nano-particles forming as a result of PM and AM production methods to the best of the author's knowledge.

## 2. MATERIAL AND METHODS

In this study, spherical IN718 powders having 20-55  $\mu\text{m}$  size were used for conventional powder metallurgy and additive manufacturing methods. The powders were provided by EOS GmbH. Moreover,  $\text{Y}_2\text{O}_3$  nano-powders having the size of 18-38 nm were provided by Nanografi Nanotechnology Co. The composition of the IN718 powders is measured as 53Ni-17.7Fe-19.4Cr-5.1Nb-3.1Mo-0.94Ti-0.46Al-0.1Co-0.1Mn (in wt.%) [33].

First of all, IN718 powders were mixed with 0.3 wt% of  $\text{Y}_2\text{O}_3$  nano-powders using a Fritsch Pulverisette P6 classic line ball mill without balls operating under Ar atmosphere at 300 rpm for 10 mins. The powders were compressed up to 200 psi in 10 mm diameter cylinders using a uniaxial press followed by sintering at 1000, 1250 and 1500 °C for 10 h. These samples are nominated as PM1000, PM1250 and PM1500. The pre-mixed powders were deposited by SLM layer by layer with a laser power of 220 W and a scan speed of 960 mm/sec using an EOS M 290 machine [33]. Table 1 summarizes the SLM production parameters. After the deposition, the AM parts were removed from the substrate using electro-discharge machining (EDM).

**Table 1.** SLM production parameters

Parameter	Value
Power (W)	220
Scan speed (mm/sec)	960
Laser spot size ( $\mu\text{m}$ )	100
Layer thickness ( $\mu\text{m}$ )	40
Hatch spacing ( $\mu\text{m}$ )	110
Rotation degree ( $^{\circ}$ )	67

The density of the samples was measured by Archimedes method in ethanol. The microstructural investigations have been carried out using optical microscopy (OM), scanning electron microscopy (SEM) and transmission electron microscopy (TEM). For the metallographic investigations, the samples were coarse grinded to determine the efficiency of the sintering parameters. Detailed OM and SEM analyses were conducted on the samples grinded and polished down to  $0.04 \mu\text{m}$  colloidal silica followed by etching with 2 ml  $\text{HNO}_3$  – 4 ml  $\text{HCl}$  – 4 ml  $\text{HF}$  solution. OM analyses were carried out using a Huvitz HDS-5800 digital microscope while a FEI Nova Nano SEM 430 was used for SEM investigations. The composition of second phase particles was determined using energy dispersive X-ray spectroscopy (EDX) with EDAX SSDD Apollo10 EDX system under SEM. Data collection times during point analyses for each precipitate were at least 60 s to be able to get high peak-to-background ratios. After the polishing step, TEM samples were punched into 3 mm disks which were electropolished using 95% methanol – 5% perchloric acid solution at  $-40 \text{ }^{\circ}\text{C}$  with a 15-18 V. TEM analyses were conducted using a JEOL JEM-ARM200CFEG UHR-TEM.

Microhardness tests were performed using a Shimadzu HMV-2 E microhardness tester with 1 kg load and 10 s holding time. At least 10 indents were taken from different locations on the surface of the samples.

### 3. RESULTS AND DISCUSSION

IN718 powders and the oxide former ( $\text{Y}_2\text{O}_3$ ) were mixed before production. In the case of powder bed fusion processes, the shape of the powder is critical for the flowability which determines the quality of the production. Thus, the sphericity of the powders should be kept during mixing which was also reported by Karakilinc et al. [34]. Figure 1 shows the morphology of the powders after mixing in a ball mill for 10 mins as described in the previous section. The  $\text{Y}_2\text{O}_3$  nano-powders pointed by the red arrows in a zoomed micrograph are attached to the spherical IN718 micro-powders forming satellites.

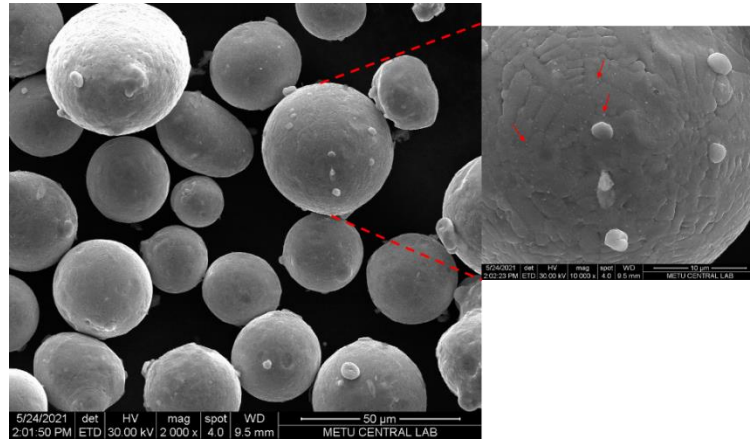


**Figure 1.** SEM micrographs showing the morphology of the powders after mixing in a ball mill for 10 mins.

Figure 2(a-c) shows the microstructure of PM samples after sintering at 1000, 1250 and 1500 °C for 10h. Clearly, 1000 °C is not enough for obtaining a dense material, while dense materials (>99.6%) can be produced after sintering at 1250 and 1500 °C for 10 h. Moreover, the hardness of the samples presented in Figure 2d indicates that porosity in the case of PM1000 sample deteriorates the mechanical properties. Besides, PM1500 sample exhibits the highest hardness which is ~30HV higher than the hardness of PM1250. This will be further investigated in the following sections. It should be noted that high-porosity PM1000 samples have not been considered for future studies.

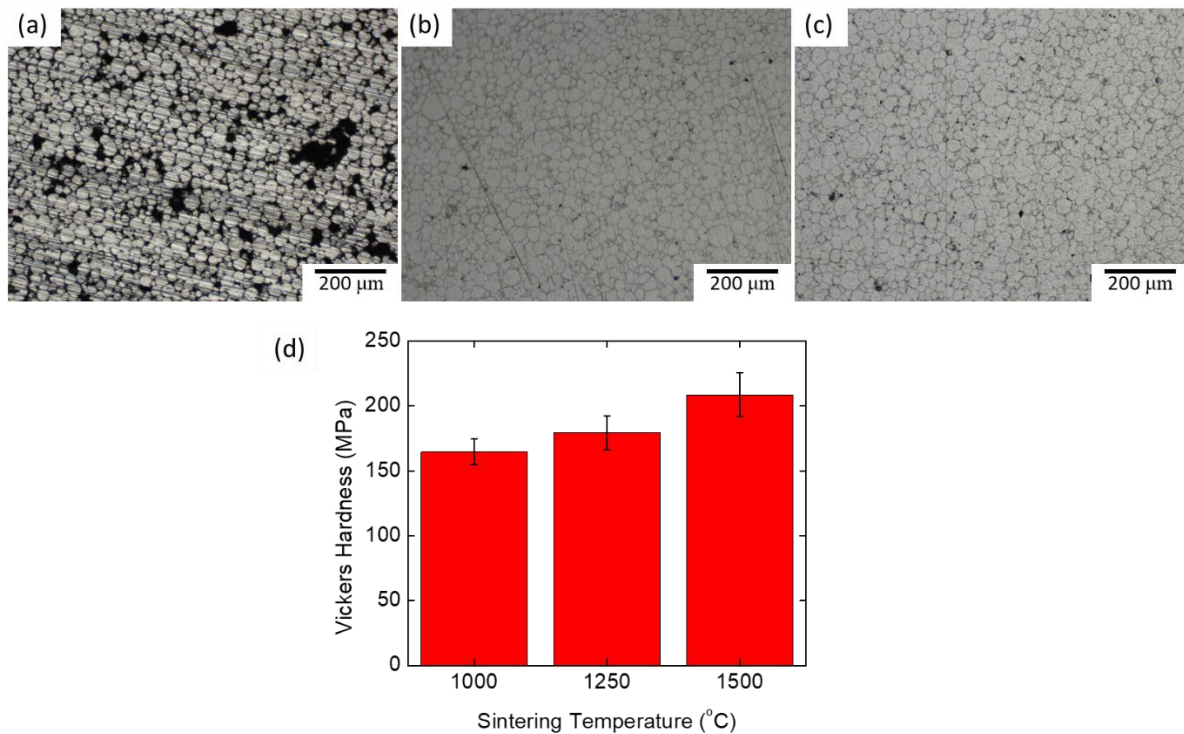


**Figure 2.** OM images of PM samples sintered at (a) 1000 °C (b) 1250 °C (c) 1500 °C for 10 h; and (d) microhardness plot with respect to the sintering temperature.

Figure 3 shows the SEM (Figure 3(a-c)) and OM micrographs (Figures 3(d-g)) of PM1250, PM1500 and SLM samples. Figure 3 (a-c) shows the SEM micrograph of the PM1250 sample. Even though there are a few empty triple junctions, the space between the powders is well covered. At high magnifications, the existence of nano-particles especially around the grain boundaries, is seen. Similarly, besides a small

amount of porosity, PM1500 sample is dense and there are spherical-shaped particles that are coarser compared to the ones in PM1250 sample (Figures 3d and e). Figures 3f and g show the microstructure of the additively manufactured alloy. The microstructures of PM and SLM produced alloys are quite different. While the PM alloys show the powders sintered each other with spherical shapes, SLM produced sample shows melt pools having a thickness of  $\sim 100 \mu\text{m}$  indicating the deposition layers. Besides, there are Laves phase as well as the carbides and coarse oxide particles. During the SLM process, the cooling rate reaches  $\sim 10^6 \text{ K/sec}$ . Thus, cellular structure is observed, as seen in Figure 3g.

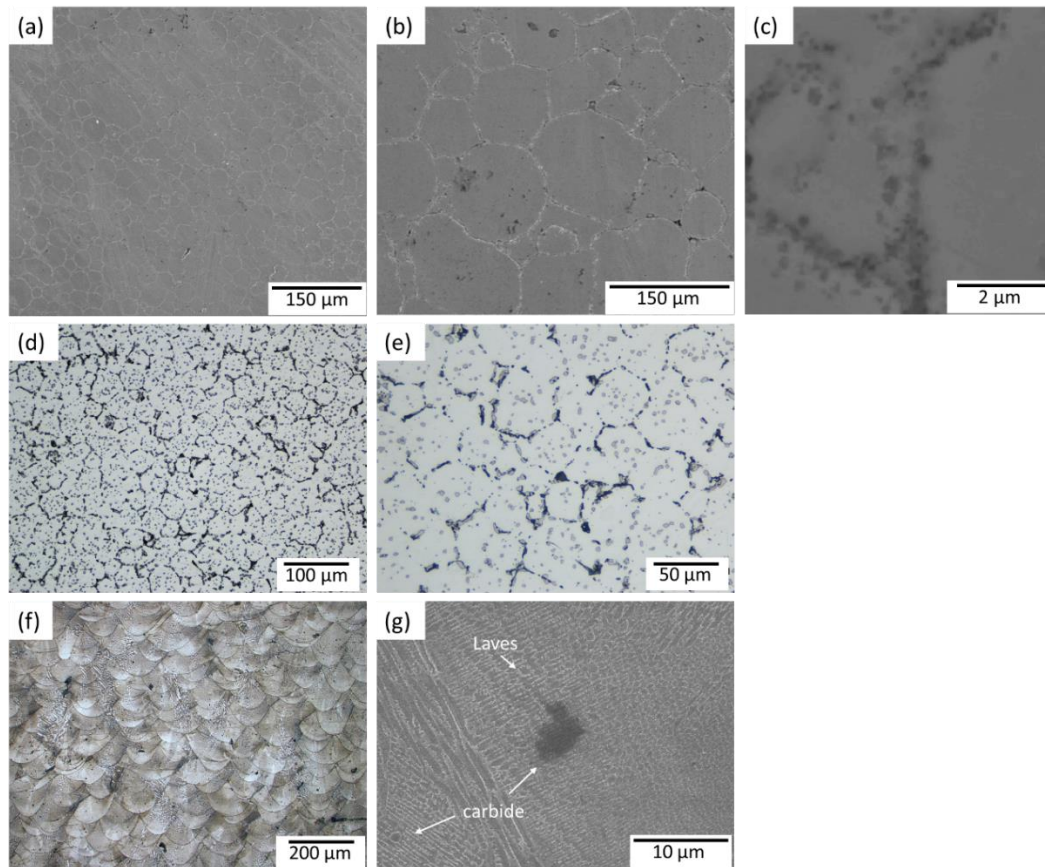


**Figure 3.** Microstructures of (a-c) PM1250 (d,e) PM1500 and (f,g) SLM alloys.

It has been reported that oxide nano-particles in ODS alloys can stabilize the microstructure by pinning the grain boundaries and dislocations, restricting the recrystallization, grain growth and thus creep. Besides, the interface between the nano-oxides and matrix act as sinks for point defects which results in a reduced amount of radiation damage [5-7]. On the other hand, the size and number density of the particles become critical. The smaller the particle size and the higher the number density of the particles, the better the resistance of the alloy in the extreme conditions. Aydogan et al. have reported that the strength of the ODS ferritic alloys is closely related to the size and number density of the nano-oxides [3]. Furthermore, while the 14YWT alloy having  $\sim 7 \text{ nm}$  particle size with a number density in the order of  $\sim 10^{21} \text{ m}^{-3}$  shows  $\sim 7\%$  of swelling, the same alloy with  $\sim 3 \text{ nm}$  particle size and a number density in the order of  $\sim 10^{23} \text{ m}^{-3}$  shows almost no swelling [3]. Thus, it is critical to determine the size and number density of the nano-particles after production, and in this study, the nano-particles produced as a result of powder metallurgy and additive manufacturing have been investigated.

Figure 4 presents the TEM micrographs of the PM1250 alloy having a high density of nano-particles mostly with  $< 10 \text{ nm}$  size (Figures 4a and b). Figures 4c and d show the high resolution TEM (HRTEM) image of a nano-particle having a diameter  $\sim 5 \text{ nm}$  and the corresponding fast fourier transform (FFT) spectrum. Moreover, Figures 4e and f show the HRTEM image of a smaller nano-particle having a

diameter  $\sim 2$  nm and corresponding FFT spectrum. HRTEM images exhibit that while  $\sim 2$  nm size nano-particle has a coherent interface inferred from the continuity of the atomic order, larger size particle has a disruption in coherency. It has been reported that fine dispersoids are most likely to be coherent while the larger particles tend to be incoherent [7, 35, 36]. Moreover, the coherency of the particles has been shown to affect the properties of the materials due to the different interaction mechanisms of these particles with dislocations and grain boundaries. The coherent particles are observed to be efficient in pinning the grain boundaries while the incoherent particles are more capable of restricting the dislocation motion [35, 37-39].

The interplanar distances and angles have been tabulated in Table 2. It has been found that while the larger size particle has the crystal structure of either  $Y_2Ti_2O_7$  or  $YTiO_3$ , the smaller size particle is  $Y_2Ti_2O_7$ . Similarly, Yu et al. have found that large particles have crystal structures different than pyrochlore  $Y_2Ti_2O_7$  and have Y/Ti ratio between 1 to 2 [8]. Furthermore, the size and number density of the nano-oxides in PM1250 sample have been found to be  $3.9 \pm 0.5$  nm and  $1.6 \times 10^{22} \text{ m}^{-3}$ , respectively.

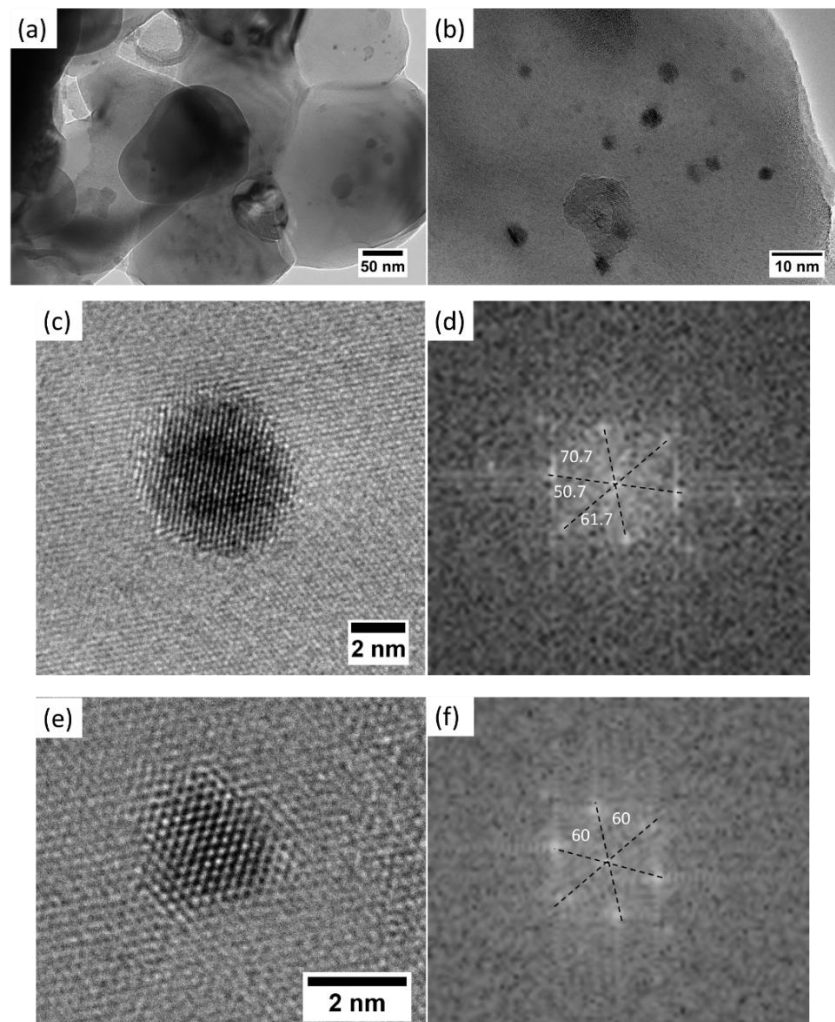


Figure 4. TEM micrographs of PM1250 sample, showing (a) the nano-grains and (b) nano-particles; HRTEM micrographs of (c) a particle with  $\sim 5$  nm size and (d) corresponding FFT spectrum; (e) a particle with  $\sim 2$  nm size and (d) corresponding FFT spectrum.

**Table 2.** Measured and theoretical interplanar distances and angles for the particles in Figure 4.

		$d_1$ (Å)	$d_2$ (Å)	$d_3$ (Å)	$\alpha_{12}$ (°)	$\alpha_{23}$ (°)	$\alpha_{13}$ (°)
	Measured	2.63	2.06	2.14	61.7	70.7	50.7
Figure 4c	Y <sub>2</sub> TiO <sub>5</sub>	2.52 (401)	2.09 (313)	2.18 ( $\bar{1}\bar{1}\bar{4}$ )	62.5	67.6	50.2
	YTiO <sub>3</sub>	2.50 ( $\bar{1}20$ )	2.09 (202)	2.18 (122)	62.3	67.3	50.4
Figure 4e	Measured	1.92	2.02	2.04	60	60	60
	Y <sub>2</sub> Ti <sub>2</sub> O <sub>7</sub>	1.79 (0 $\bar{4}$ 4)	1.79 (404)	1.79 (440)	60	60	60

Sintering at 1250 °C occurs mostly in the solid state while sintering at 1500 °C occurs above the liquidus temperature of IN718, inferring at least a partial melting [33]. To determine if the sintering temperature affects the characteristics of the nano-particles, detailed TEM analyses have been conducted on PM1500 sample. Figures 5a and b exhibit the nano-structure of the alloy. Clearly, the microstructure is composed of nano-grains having a size 100-200 nm and nano-particles having a particle size <30 nm. One of the largest particles has been investigated using HRTEM as seen in Figure 5c. FFT diffraction spectrum indicates that this particle has an FCC crystal structure with a lattice parameter of 14.4 Å, which is identified as Ni<sub>2</sub>Y intermetallic. Ni-Y intermetallic phases have been observed in IN625 alloy coated with NiCrAlY using a laser-engineered net shaping (LENS) system. The formation of such intermetallic having different stoichiometry is reported to occur instantaneously directly from the liquid [40-42]. Table 2 shows the measured and theoretical lattice spacing and angles. Figures 5e and f show an HRTEM micrograph of ~7 nm size nano-particle and corresponding FFT diffractogram, respectively. It has been found that the measured interplanar distances and angles in Table 3 are close to the parameters of hexagonal Y-Al-O (PDF# 00-054-0621) whose lattice parameters are,  $a = b = 0.368$  nm,  $c = 1.052$  nm, and  $\gamma = 120^\circ$  [43]. However, the stoichiometry of the observed particle seems to be slightly different which is inferred from the values which are slightly off. It should be noted that Al content of these particles varies considerably and can reach up to ~45 at.% while there is some Titanium (2-5 at.%). Moreover, Figures 5g and h show an HRTEM image and corresponding FFT of another particle having a size of ~7-8 nm. The measured parameters are slightly different than the theoretical values (Table 2). This has been attributed to the existence of Al in the Y-Ti-O particles. Since this particle has a presumably small amount of Al, it may still hold the pyrochlore structure and can be identified as Y<sub>2</sub>Ti<sub>2</sub>O<sub>7</sub>. Clearly, at higher sintering temperatures, Al seems to participate more in the nano-particles, forming Y-Al-O particles as well as Y-Ti(Al)-O particles. It has been reported that when a local melting occurs, Y-Al-O or Y-Ti-O rich in Al particles form [10]. However, this composition in solid-state does not yield the formation of Y-Al-O; rather Y-Ti-O particles rich in Al can exist [33]. This might explain the reason for observing more Y-Ti-O particles in the solid-state sintering case of PM1250.



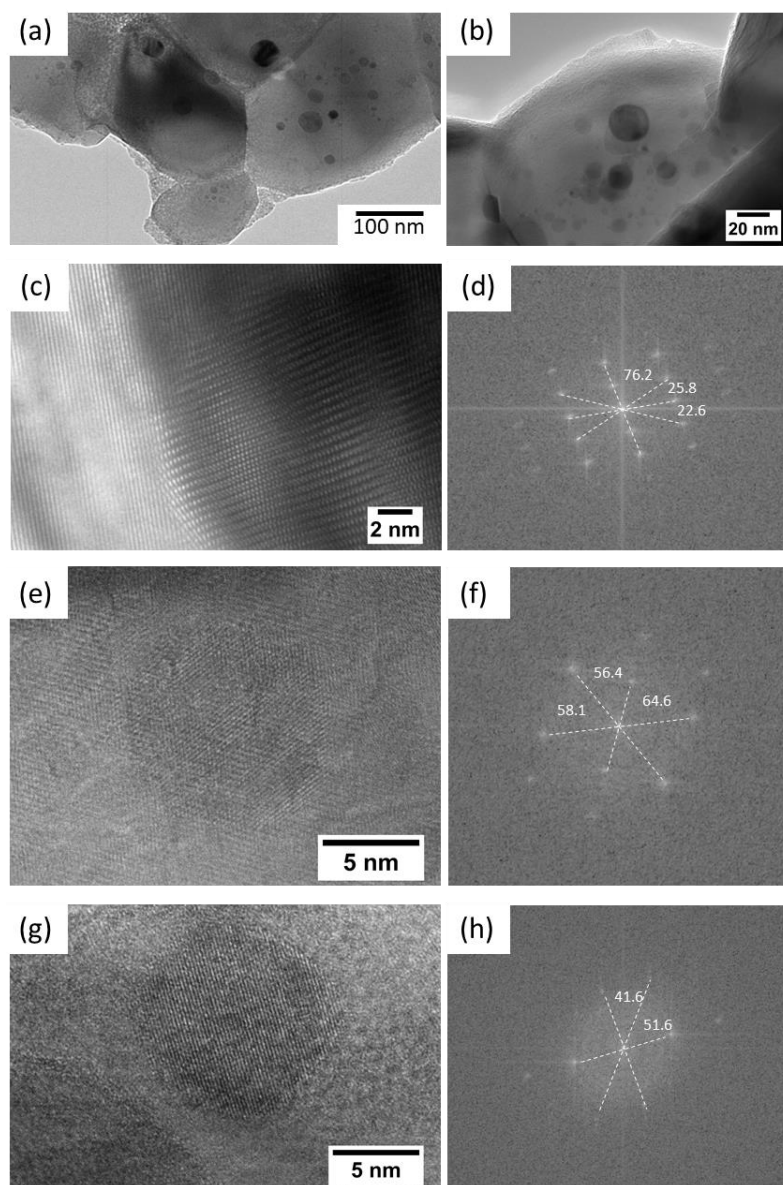


**Figure 5.** TEM micrographs of PM1500 sample, showing (a) the nano-grains and (b) nano-particles; HRTEM micrographs of (c) a large particle and (d) corresponding FFT spectrum; (e,g) particles with ~7 nm size and (f,h) corresponding FFT spectra.

**Table 3.** Measured and theoretical interplanar distances and angles for the particles in Figure 5.

		$d_1$ (Å)	$d_2$ (Å)	$d_3$ (Å)	$\alpha_{12}$ (°)	$\alpha_{23}$ (°)	$\alpha_{13}$ (°)
Figure 5c	Measured	2.4	2.4	5.2	25.8	76.2	102
	Ni <sub>2</sub> Y	2.4 ( $\bar{2}4\bar{4}$ )	2.4 ( $\bar{4}2\bar{4}$ )	5.1( $\bar{2}\bar{2}0$ )	27.3	76.4	103.7
Figure 5e	Measured	2.02	1.97	3.42	64.6	56.4	58.1
	Y-Al-O	1.86 ( $2\bar{2}01$ )	1.86 ( $0\bar{2}21$ )	3.18 ( $10\bar{1}0$ )	57.7	61.2	61.2
Figure 5g	Measured	2.13	1.56	1.99	41.6	51.6	93.2
	Y <sub>2</sub> Ti <sub>2</sub> O <sub>7</sub>	1.87 ( $\bar{4}40$ )	1.68 (060)	1.87 (440)	45	45	90

During the SLM process, the local temperature increases above 2000 °C, which can melt the powders including  $Y_2O_3$ . Moreover, the composition would be homogenized due to the Marangoni mixing effect in the melt pool. Thus, ideally, precipitation of Y-Ti-O particles occurs homogeneously within the melt pool. TEM analyses have been conducted on the SLM produced alloys to investigate the nano-particle characteristics. Figures 6a and b present the TEM micrographs of the SLM produced alloy. Similar to the compressed and sintered PM samples, there are nano-particles as well as larger irregular-shaped particles. However, as opposed to the PM samples, SLM results in micron-level grain size with micron/submicron level cellular structure (Figure 3g), rather than nano-grains. Figure 6c shows the HRTEM micrograph of a particle having a size of ~6-7 nm. Interplanar distances and angles have been determined from the HRTEM image in Figure 6d and FFT diffractogram in Figure 6e. The measured values match well with the interplanar spacing and angle of  $Y_2Ti_2O_7$  particles, as seen in Table 4. Figures 6f and g show the HRTEM micrograph of a particle having a size of ~4 nm and the corresponding FFT diffractogram. Even though the lattice parameters are different than the parameters of  $Y_2Ti_2O_7$  (PDF# 01-072-0302), the angles and ratio between the interplanar spacings are similar to pyrochlore structure; therefore, this particle is determined to be  $Y_2Ti_2O_7$ , as shown in Table 4. The reason for the smaller lattice parameter might be related to stoichiometry or composition. Similarly, Figure 6h shows the HRTEM micrograph of another small particle having a size of ~4 nm and the corresponding FFT diffractogram is presented in Figure 6i. This particle is also determined to be  $Y_2Ti_2O_7$  even though the lattice parameter is smaller. Besides these fine oxides having sizes <5nm, there are coarser oxides that contain Al, as reported in Ref [33].

It has been observed that some particles are composed of multiple compositions or stoichiometry which results in crystallography change within the same particle in SLM produced alloy. For instance, in Figure 7a, the left and right parts of the particle have different crystallography. While the particle in Figure 7a has an incoherent interface around its periphery, the particle in Figure 7b exhibits a crystalline structure with semi-coherency with the matrix on the left side and a certain level of amorphization on the right side. A similar phenomenon which is called 'bi-phase' formation has been reported by Sinha et al in ODS IN617 alloys [43]. This has been attributed to the formation mechanisms of the Y-Al-O particles due to the reaction between  $Y_2O_3$  and  $Al_2O_3$  [44]. In other words, the existence of such particles infers incomplete transformation due to rapid cooling during SLM production.

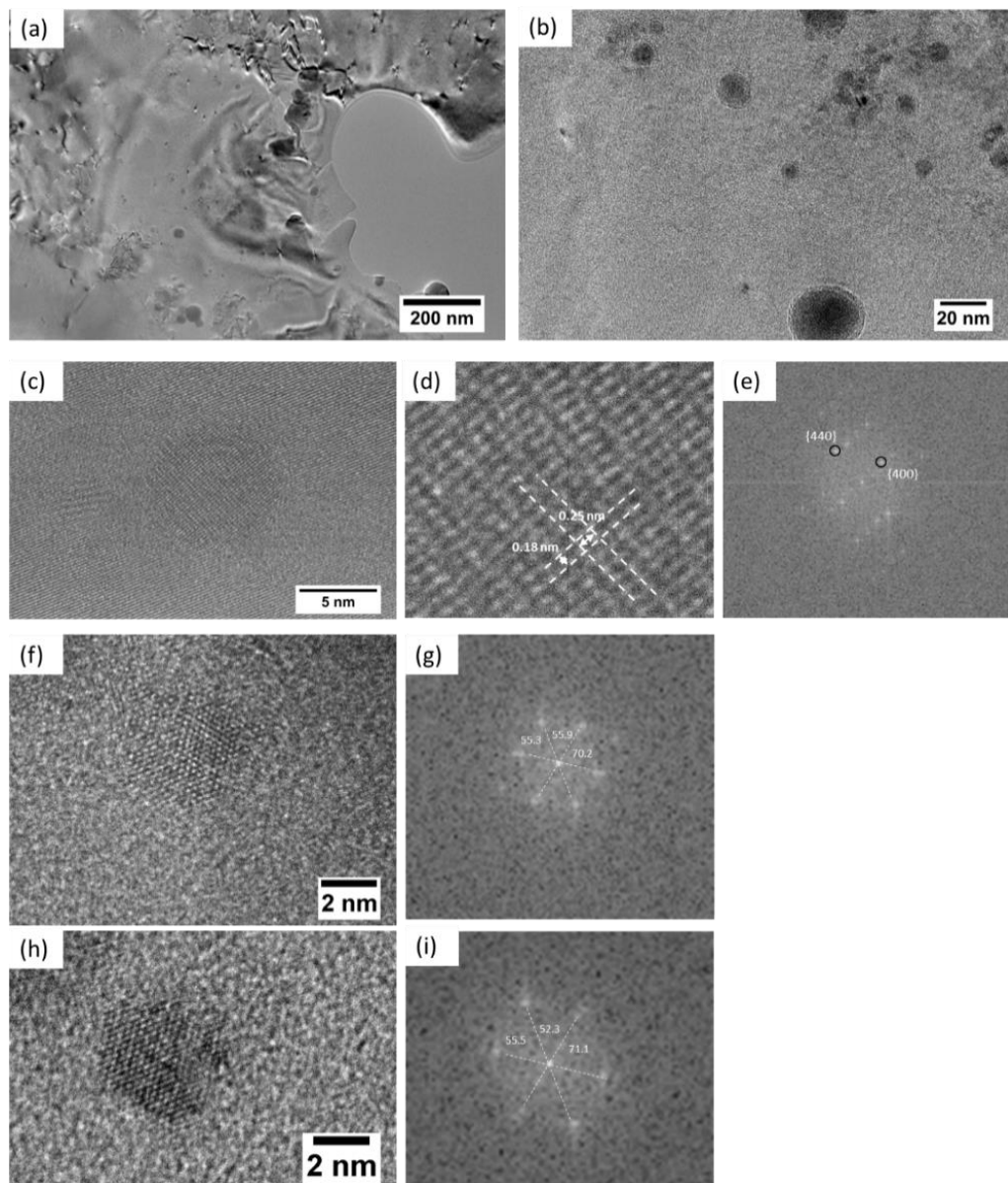


**Figure 6.** TEM micrographs of as-built SLM sample showing (a,b) the overall structure with nano-particles; HRTEM micrographs of (c,d) a particle with ~6-7 nm size and (e) corresponding FFT spectrum; (f,h) particles with ~4 nm size and (g,i) corresponding FFT spectra.

**Table 4.** Measured and theoretical interplanar distances and angles for the particles in Figure 6.

		$d_1$ (Å)	$d_2$ (Å)	$d_3$ (Å)	$\alpha_{12}$ (°)	$\alpha_{23}$ (°)	$\alpha_{13}$ (°)
Figure 6c	Measured	2.49	1.60	1.76	57.7	35.3	89.2
	$Y_2Ti_2O_7$	2.52 (400)	1.46 ( $44\bar{4}$ )	1.78 ( $04\bar{4}$ )	54.7	35.3	90
Figure 6f	Measured	2.53	2.2	2.55	55.3	55.9	70.2
	$Y_2Ti_2O_7$	2.9 ( $\bar{2}\bar{2}2$ )	2.5 ( $\bar{4}00$ )	2.9 ( $\bar{2}\bar{2}\bar{2}$ )	54.7	54.7	70.5
Figure 6h	Measured	2.4	2.2	2.5	55.5	52.3	71.1
	$Y_2Ti_2O_7$	2.9 ( $\bar{2}\bar{2}2$ )	2.5 ( $\bar{4}00$ )	2.9 ( $\bar{2}\bar{2}\bar{2}$ )	54.7	54.7	70.5

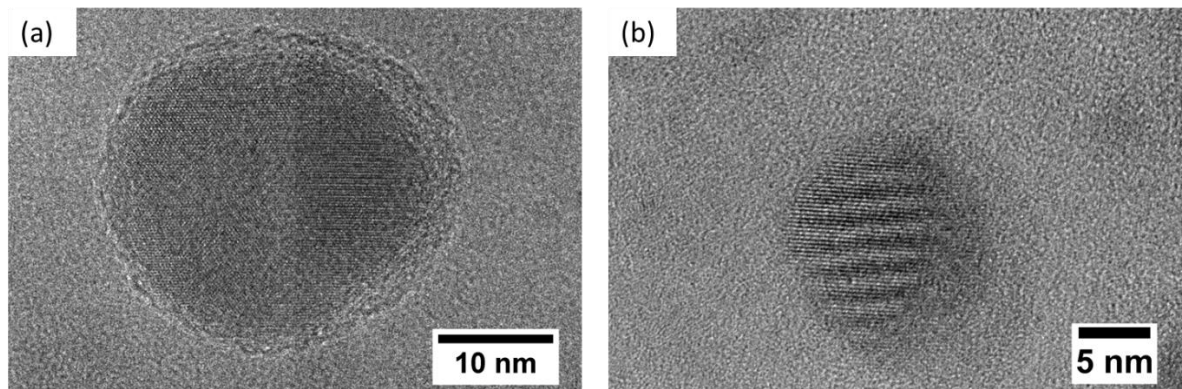


**Figure 7.** Two different particles having (a) crystallography district regions (b) coherency change within the same particle in SLM produced alloy.

The sizes of nano-particles (up to  $\sim 30$  nm) were measured manually from the TEM images using the ImageJ v1.49 digital processing software including 75 to 150 counts for each foil. Number density which is defined as the number of particles per unit volume is calculated by assuming the foil thickness as 100 nm. When the nano-particles up to  $\sim 30$  nm are considered, the particle size and number density graphs can be seen in Figure 8. The particle size of PM1250 sample is the smallest ( $\sim 4$  nm) while PM1500 and SLM samples have  $\sim 6$  nm and  $\sim 5.2$  nm, respectively. On the other hand, PM1500 has almost two times higher amount of nano-oxides with  $\sim 3.5 \times 10^{22} \text{ m}^{-3}$ , compared to PM1250. Moreover, the SLM sample has nano-particles having a number density of  $\sim 2.5 \times 10^{22} \text{ m}^{-3}$ . It should be noted that nano-particle distribution is relatively homogenous within the nano-grains in AM samples. On the other hand, the distribution of nano-particles is inhomogeneous in such a way that the particles precipitate in agglomerated clusters within the grain (or cell). Therefore, as the regions where the particles are populated are investigated, the number density is quite high compared to our previous study which considers the overall nano-particle distribution [33]. Moreover, high density-nanoparticles in the case of PM1500 sample result in higher hardness which is presented in Figure 2.

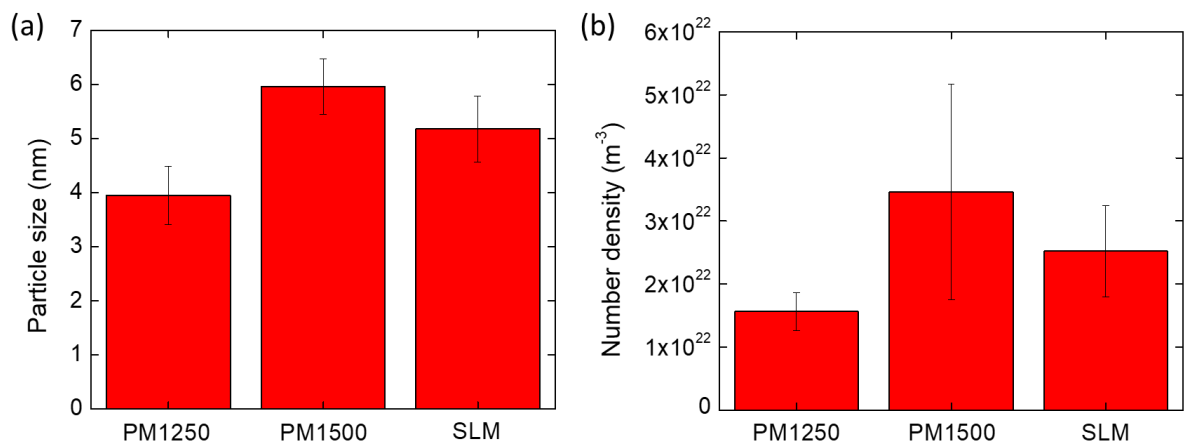


**Figure 8.** (a) Particle size and (b) number density of the nano-particles in PM and SLM samples.

#### 4. CONCLUSIONS

In this study, oxide dispersion strengthened IN718 alloys have been produced using powder metallurgy and selective laser melting additive manufacturing. The effect of processing routes on the microstructure, in particular the nano-particle formation and structure has been investigated. It has been

found that compressing followed by sintering at 1250 and 1500 °C yields high density ODS alloys. The hardness of PM1500 sample is ~30 HV higher than that of PM1250 which is attributed to the lower nano-oxide number density in PM1250 alloy. It has been found that PM results in a nano-grained structure with nano-particles while SLM produced alloy has a larger cellular structure with Laves phase, carbides and oxides. The nano-particles have been determined to be  $Y_2Ti_2O_7$ ,  $Y_2TiO_5$  and/or  $YTiO_3$  in PM1250 alloys while there are some  $Ni_2Y$  intermetallic particles as well as Y-Al-O and  $Y_2TiO_5$  oxides. In the case of SLM produced alloy, fine  $Y_2Ti_2O_7$  particles with smaller lattice parameter and larger size Y-Ti-Al-O particles have been observed. The PM1250, PM1500 and SLM samples have 4, 6 and 5.2 nm sized nano-oxides with  $\sim 1.6 \times 10^{22} m^{-3}$ ,  $\sim 3.5 \times 10^{22} m^{-3}$  and  $\sim 2.5 \times 10^{22} m^{-3}$  number densities, respectively. It is noted that while the nano-oxides are distributed homogenously within nano-grains in PM samples, they exist in groups within the grain in the case of SLM sample. Besides, there are bi-phase particles in SLM produced alloys due to rapid cooling and incomplete transformation. This study shows that ODS IN718 alloys with high-density fine nano-oxides (<10 nm) can be produced using both powder metallurgy and additive manufacturing methods.

### Declaration of Competing Interest

The authors declare that they have no known competing financial interests or personal relationships that could have appeared to influence the work reported in this paper.

### Funding / Acknowledgements

This study is funded by LOREAL UNESCO For Women in Science 2021 Grant and the Scientific and Technological Research Council of Turkey (TUBITAK) under the grant No: 219M500.

### REFERENCES

- [1] H. Zhang, C. Li, Q. Guo, Z. Ma, H. Li, and Y. Liu, "Improving creep resistance of nickel-based superalloy Inconel 718 by tailoring gamma double prime variants," *Scripta Materialia*, vol. 164, pp. 66-70, 2019/04/15/ 2019, doi: <https://doi.org/10.1016/j.scriptamat.2019.01.041>.
- [2] S. Pratheesh Kumar, S. Elangovan, R. Mohanraj, and J. R. Ramakrishna, "A review on properties of Inconel 625 and Inconel 718 fabricated using direct energy deposition," *Materials Today: Proceedings*, vol. 46, pp. 7892-7906, 2021/01/01/ 2021, doi: <https://doi.org/10.1016/j.matpr.2021.02.566>.
- [3] E. Aydogan *et al.*, "Effect of tube processing methods on microstructure, mechanical properties and irradiation response of 14YWT nanostructured ferritic alloys," *Acta Materialia*, vol. 134, pp. 116-127, 2017/08/01/ 2017, doi: <https://doi.org/10.1016/j.actamat.2017.05.053>.
- [4] E. Aydogan, O. El-Atwani, S. Takajo, S. C. Vogel, and S. A. Maloy, "High temperature microstructural stability and recrystallization mechanisms in 14YWT alloys," *Acta Materialia*, vol. 148, pp. 467-481, 2018/04/15/ 2018, doi: <https://doi.org/10.1016/j.actamat.2018.02.006>.
- [5] G. R. Odette, "Recent Progress in Developing and Qualifying Nanostructured Ferritic Alloys for Advanced Fission and Fusion Applications," *JOM*, Article in Press 2014, doi: 10.1007/s11837-014-1207-5.
- [6] G. R. Odette, M. J. Alinger, and B. D. Wirth, "Recent Developments in Irradiation-Resistant Steels," *Annual Review of Materials Research*, vol. 38, no. 1, pp. 471-503, 2008, doi:10.1146/annurev.matsci.38.060407.130315.
- [7] T. Chen *et al.*, "Microstructural changes and void swelling of a 12Cr ODS ferritic-martensitic alloy after high-dpa self-ion irradiation," *Journal of Nuclear Materials*, Article vol. 467, pp. 42-49, 2015, Art no. 49325, doi: 10.1016/j.jnucmat.2015.09.016.


- [8] Y. Wu, E. M. Haney, N. J. Cunningham, and G. R. Odette, "Transmission electron microscopy characterization of the nanostructures in nanostructured ferritic alloy MA957," *Acta Materialia*, vol. 60, no. 8, pp. 3456-3468, 5// 2012, doi: <http://dx.doi.org/10.1016/j.actamat.2012.03.012>.
- [9] Z. Zhang, T. A. Saleh, S. A. Maloy, and O. Anderoglu, "Microstructure evolution in MA956 neutron irradiated in ATR at 328 °C to 4.36 dpa," *Journal of Nuclear Materials*, vol. 533, p. 152094, 2020/05/01/ 2020, doi: <https://doi.org/10.1016/j.jnucmat.2020.152094>.
- [10] C. W. Park, J. M. Byun, W. J. Choi, S. Y. Lee, and Y. D. Kim, "Improvement of high temperature mechanical properties of Ni-based oxide dispersion strengthened alloys by preferential formation of Y-Ti-O complex oxide," *Materials Science and Engineering: A*, vol. 740-741, pp. 363-367, 2019/01/07/ 2019, doi: <https://doi.org/10.1016/j.msea.2018.10.004>.
- [11] N. J. Cunningham *et al.*, "Effect of bulk oxygen on 14YWT nanostructured ferritic alloys," *Journal of Nuclear Materials*, vol. 444, no. 1, pp. 35-38, 2014/01/01/ 2014, doi: <https://doi.org/10.1016/j.jnucmat.2013.09.013>.
- [12] D. T. Hoelzer, J. Bentley, M. A. Sokolov, M. K. Miller, G. R. Odette, and M. J. Alinger, "Influence of particle dispersions on the high-temperature strength of ferritic alloys," *Journal of Nuclear Materials*, vol. 367-370, pp. 166-172, 2007/08/01/ 2007, doi: <https://doi.org/10.1016/j.jnucmat.2007.03.151>.
- [13] S. Ukai and M. Fujiwara, "Perspective of ODS alloys application in nuclear environments," *Journal of Nuclear Materials*, vol. 307-311, pp. 749-757, 2002/12/01/ 2002, doi: [https://doi.org/10.1016/S0022-3115\(02\)01043-7](https://doi.org/10.1016/S0022-3115(02)01043-7).
- [14] M. K. Miller, D. T. Hoelzer, E. A. Kenik, and K. F. Russell, "Stability of ferritic MA/ODS alloys at high temperatures," *Intermetallics*, vol. 13, no. 3, pp. 387-392, 2005/03/01/ 2005, doi: <https://doi.org/10.1016/j.intermet.2004.07.036>.
- [15] L. Yu *et al.*, "Effects of Al content on microstructure and tensile properties of Ni-based ODS superalloys," *Journal of Alloys and Compounds*, vol. 941, p. 168965, 2023/04/25/ 2023, doi: <https://doi.org/10.1016/j.jallcom.2023.168965>.
- [16] E. Hosseini and V. A. Popovich, "A review of mechanical properties of additively manufactured Inconel 718," *Additive Manufacturing*, vol. 30, p. 100877, 2019/12/01/ 2019, doi: <https://doi.org/10.1016/j.addma.2019.100877>.
- [17] M. M. Attallah, R. Jennings, X. Wang, and L. N. Carter, "Additive manufacturing of Ni-based superalloys: The outstanding issues," *MRS Bulletin*, vol. 41, no. 10, pp. 758-764, 2016/10/01 2016, doi: 10.1557/mrs.2016.211.
- [18] M. Ni *et al.*, "Microstructure and mechanical properties of additive manufactured Inconel 718 alloy strengthened by oxide dispersion with 0.3 wt% Sc addition," *Journal of Alloys and Compounds*, vol. 918, p. 165763, 2022/10/15/ 2022, doi: <https://doi.org/10.1016/j.jallcom.2022.165763>.
- [19] J. P. Oliveira, A. D. LaLonde, and J. Ma, "Processing parameters in laser powder bed fusion metal additive manufacturing," *Materials & Design*, vol. 193, p. 108762, 2020/08/01/ 2020, doi: <https://doi.org/10.1016/j.matdes.2020.108762>.
- [20] M. Ni, S. Liu, C. Chen, R. Li, X. Zhang, and K. Zhou, "Effect of heat treatment on the microstructural evolution of a precipitation-hardened superalloy produced by selective laser melting," *Materials Science and Engineering: A*, vol. 748, pp. 275-285, 2019/03/04/ 2019, doi: <https://doi.org/10.1016/j.msea.2019.01.109>.
- [21] V. A. Popovich, E. V. Borisov, A. A. Popovich, V. S. Sufiiarov, D. V. Masaylo, and L. Alzina, "Impact of heat treatment on mechanical behaviour of Inconel 718 processed with tailored microstructure by selective laser melting," *Materials & Design*, vol. 131, pp. 12-22, 2017/10/05/ 2017, doi: <https://doi.org/10.1016/j.matdes.2017.05.065>.
- [22] W. Tillmann, C. Schaak, J. Nellesen, M. Schaper, M. E. Aydinöz, and K. P. Hoyer, "Hot isostatic pressing of IN718 components manufactured by selective laser melting," *Additive Manufacturing*, vol. 13, pp. 93-102, 2017/01/01/ 2017, doi: <https://doi.org/10.1016/j.addma.2016.11.006>.

- [23] J. Deng, C. Chen, X. Liu, Y. Li, K. Zhou, and S. Guo, "A high-strength heat-resistant Al-5.7Ni eutectic alloy with spherical Al<sub>3</sub>Ni nano-particles by selective laser melting," *Scripta Materialia*, vol. 203, p. 114034, 2021/10/01/ 2021, doi: <https://doi.org/10.1016/j.scriptamat.2021.114034>.
- [24] D.-R. Liu, S. Wang, and W. Yan, "Grain structure evolution in transition-mode melting in direct energy deposition," *Materials & Design*, vol. 194, p. 108919, 2020/09/01/ 2020, doi: <https://doi.org/10.1016/j.matdes.2020.108919>.
- [25] S. Xu *et al.*, "Combination of back stress strengthening and Orowan strengthening in bimodal structured Fe-9Cr-Al ODS steel with high Al addition," *Materials Science and Engineering: A*, vol. 739, pp. 45-52, 2019/01/02/ 2019, doi: <https://doi.org/10.1016/j.msea.2018.09.111>.
- [26] S. Ukai *et al.*, "Directional recrystallization by zone annealing in a Ni-based ODS superalloy," *Journal of Alloys and Compounds*, vol. 744, pp. 204-210, 2018/05/05/ 2018, doi: <https://doi.org/10.1016/j.jallcom.2018.01.406>.
- [27] A. Ozsoy, E. Aydogan, and A. F. Dericioglu, "Selective laser melting of Nano-TiN reinforced 17-4 PH stainless steel: Densification, microstructure and mechanical properties," *Materials Science and Engineering: A*, vol. 836, p. 142574, 2022/03/02/ 2022, doi: <https://doi.org/10.1016/j.msea.2021.142574>.
- [28] E. Vasquez *et al.*, "Elaboration of oxide dispersion strengthened Fe-14Cr stainless steel by selective laser melting," *Journal of Materials Processing Technology*, vol. 267, pp. 403-413, 2019/05/01/ 2019, doi: <https://doi.org/10.1016/j.jmatprotec.2018.12.034>.
- [29] C. Guo, Z. Yu, C. Liu, X. Li, Q. Zhu, and R. Mark Ward, "Effects of Y<sub>2</sub>O<sub>3</sub> nanoparticles on the high-temperature oxidation behavior of IN738LC manufactured by laser powder bed fusion," *Corrosion Science*, vol. 171, p. 108715, 2020/07/15/ 2020, doi: <https://doi.org/10.1016/j.corsci.2020.108715>.
- [30] R. Xu *et al.*, "Microstructure and mechanical properties of in-situ oxide-dispersion-strengthened NiCrFeY alloy produced by laser powder bed fusion," *Advanced Powder Materials*, vol. 1, no. 4, p. 100056, 2022/10/01/ 2022, doi: <https://doi.org/10.1016/j.apmate.2022.100056>.
- [31] J. U. Rakhmonov, C. Kenel, A. De Luca, C. Leinenbach, and D. C. Dunand, "Effect of Y<sub>2</sub>O<sub>3</sub> dispersoids on microstructure and creep properties of Hastelloy X processed by laser powder-bed fusion," *Additive Manufacturing Letters*, vol. 3, p. 100069, 2022/12/01/ 2022, doi: <https://doi.org/10.1016/j.addlet.2022.100069>.
- [32] E. Aydogan *et al.*, "In-situ radiation response of additively manufactured modified Inconel 718 alloys," *Additive Manufacturing*, vol. 51, p. 102601, 2022/03/01/ 2022, doi: <https://doi.org/10.1016/j.addma.2022.102601>.
- [33] M. Yesim Yalcin, D. Bora, and E. Aydogan, "Development and additive manufacturing of oxide dispersion strengthened inconel 718: Thermochemical and experimental studies," *Journal of Alloys and Compounds*, vol. 914, p. 165193, 2022/09/05/ 2022, doi: <https://doi.org/10.1016/j.jallcom.2022.165193>.
- [34] B. Y. v. B. E. U. Karakılınç "Toz Yataklı/Beslemeli Eklemeli İmalatta Kullanılan Partiküllerin Uygunluk Araştırması ve Partikül İmalat Yöntemleri," *Politeknik Dergisi*, vol. 22, no. 4, pp. 801-810, 2019, doi: 10.2339/politeknik.423707.
- [35] T. Chen *et al.*, "Temperature dependent dispersoid stability in ion-irradiated ferritic-martensitic dual-phase oxide-dispersion-strengthened alloy: Coherent interfaces vs. incoherent interfaces," *Acta Materialia*, vol. 116, pp. 29-42, 2016/09/01/ 2016, doi: <https://doi.org/10.1016/j.actamat.2016.05.042>.
- [36] Y. Miao *et al.*, "The interfacial orientation relationship of oxide nanoparticles in a hafnium-containing oxide dispersion-strengthened austenitic stainless steel," *Materials Characterization*, vol. 101, pp. 136-143, 2015/03/01/ 2015, doi: <https://doi.org/10.1016/j.matchar.2015.01.015>.
- [37] M. Mujahid and J. W. Martin, "The effect of oxide particle coherency on Zener pinning in ODS superalloys," *Journal of Materials Science Letters*, vol. 13, no. 3, pp. 153-155, 1994/01/01 1994, doi: 10.1007/BF00278146.

- [38] L. F. He *et al.*, "Mechanical properties of Y<sub>2</sub>Ti<sub>2</sub>O<sub>7</sub>," *Scripta Materialia*, vol. 64, no. 6, pp. 548-551, 2011/03/01/ 2011, doi: <https://doi.org/10.1016/j.scriptamat.2010.11.042>.
- [39] K. Mo *et al.*, "Synchrotron study on load partitioning between ferrite/martensite and nanoparticles of a 9Cr ODS steel," *Journal of Nuclear Materials*, vol. 455, no. 1, pp. 376-381, 2014/12/01/ 2014, doi: <https://doi.org/10.1016/j.jnucmat.2014.06.060>.
- [40] G. Moskal *et al.*, "Microstructural characterization of laser-cladded NiCrAlY coatings on Inconel 625 Ni-based superalloy and 316L stainless steel," *Surface and Coatings Technology*, vol. 387, p. 125317, 2020/04/15/ 2020, doi: <https://doi.org/10.1016/j.surfcoat.2019.125317>.
- [41] N. Mattern, M. Zinkevich, W. Löser, G. Behr, and J. Acker, "Experimental and thermodynamic assessment of the Nb-Ni-Y system," *Journal of Phase Equilibria and Diffusion*, Article vol. 29, no. 2, pp. 141-155, 2008, doi: 10.1007/s11669-007-9243-2.
- [42] Y. Zhou, M. Hu, P. Yan, X. Shi, X. Chong, and J. Feng, "A first-principles calculation of structural, mechanical, thermodynamic and electronic properties of binary Ni-Y compounds," *RSC Advances*, Article vol. 8, no. 72, pp. 41575-41586, 2018, doi: 10.1039/c8ra09383k.
- [43] S. K. Sinha, A. Dasgupta, M. Sivakumar, C. Ghosh, and S. Raju, "Unraveling the Complexity of Nano-Dispersoids in the Oxide Dispersion Strengthened Alloy 617," *Microscopy and Microanalysis*, vol. 28, no. 5, pp. 1463-1471, 2022, doi: 10.1017/S143192762200071X.
- [44] M. Sivakumar, S. K. Sinha, A. Dasgupta, and S. M. Shaikh, "Structure and Texture of Oxide Dispersion Strengthened Alloy 617 for Very High Temperature Applications," *Metallurgical and Materials Transactions A*, vol. 52, no. 11, pp. 4974-4986, 2021/11/01 2021, doi: 10.1007/s11661-021-06442.



## HADİM NAPI ALT-ORTA VİZEYEN İSTİFİNİN MİKROFASİYES VE BİYOFASİYES ÖZELLİKLERİ (ORTA TOROSLAR, GÜNEY TÜRKİYE)

\*Melikan AKBAŞ 

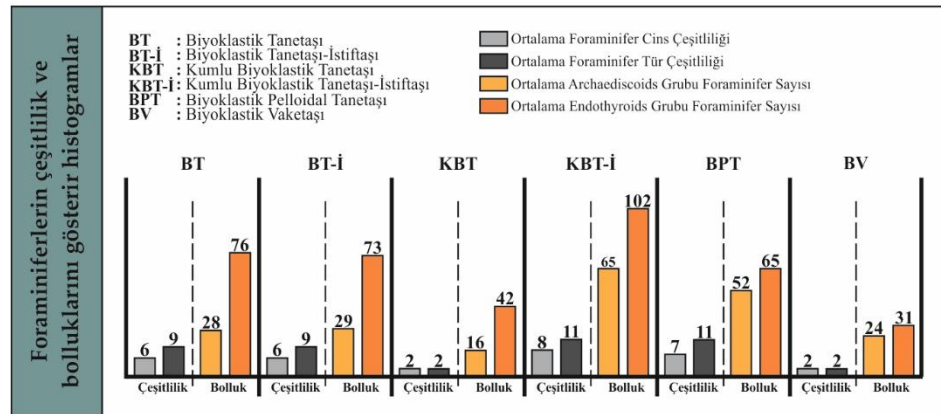
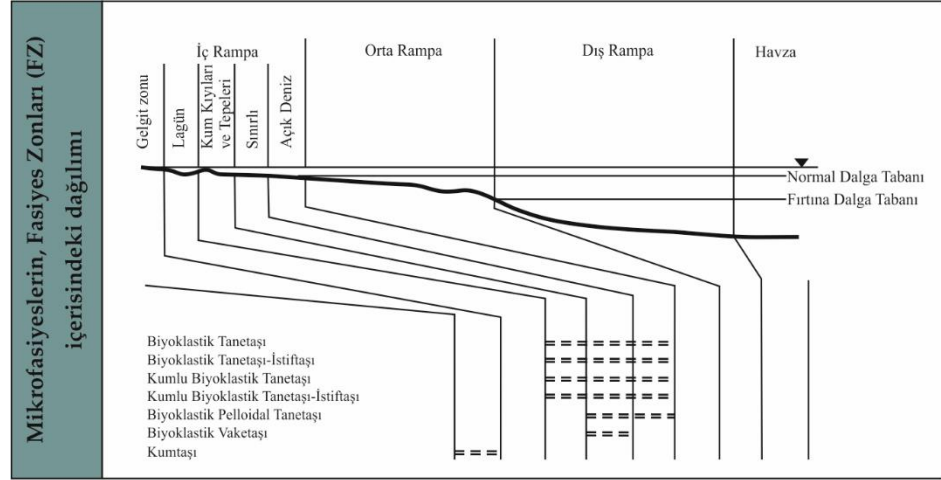
Konya Teknik Üniversitesi, Mühendislik ve Doğa Bilimleri Fakültesi, Jeoloji Mühendisliği Bölümü, Konya,  
TÜRKİYE

[makbas@ktun.edu.tr](mailto:makbas@ktun.edu.tr)

### Öne Çıkanlar (Highlights)

- Çalışılan istif yedi farklı mikrofasiyes tipiyle temsil olmaktadır.
- Çalışılan istif stabil bir İç Platform ürünü sığ denizel çökellerden oluşmaktadır.
- Mikrit çamuru ve/veya kuvars varlığının faunayı etkilediği görülmektedir.

### Grafiksel Özet (Graphical Abstract)





## HADİM NAPI ALT-ORTA VİZEYEN İSTİFİNİN MİKROFASİYES VE BİYOFASİYES ÖZELLİKLERİ (ORTA TOROSLAR, GÜNEY TÜRKİYE)

\*Melikan AKBAŞ

*Konya Teknik Üniversitesi, Mühendislik ve Doğa Bilimleri Fakültesi, Jeoloji Mühendisliği Bölümü, Konya,  
TÜRKİYE*

[1makbas@ktun.edu.tr](mailto:makbas@ktun.edu.tr)

(Geliş/Received: 30.11.2022; Kabul/Accepted in Revised Form: 12.05.2023)

**ÖZ:** Toroslar'daki allohton tektono-stratigrafik birimlerden biri olan Hadim Napı Orta(?)–Üst Devoniyen–Üst Kretase sığ platform karbonatları ve kırıntılı kayaçlardan oluşan kesintisiz bir istifte sahiptir. Hadim Napı'nın iyi yüzeylendiği Bademli stratigrafik kesiti alt-orta Vizeyen istifinin mikrofasiyes incelemeleri sonucunda İç Platform Kıyı, Sınırlı ve/veya Açık Deniz depolanma ortamlarını yansıtan yedi mikrofasiyes tanımlanmıştır. Bunlar; Biyoklastik Tanetaşı, Biyoklastik Tanetaşı-İstiftaşı, Kumlu Biyoklastik Tanetaşı, Kumlu Biyoklastik Tanetaşı-İstiftaşı, Biyoklastik Pelloidal Tanetaşı, Biyoklastik Vaketaşı ve Kumtaşı mikrofasiyesleridir. Tanımlanan mikrofasiyeslerin yapılan biyofasiyes incelemelerine göre genel olarak zengin bir çeşitlilik ve bolluk sunan foraminifer faunasına sahip olduğu görülmektedir. Genel olarak stabil bir depolanma ortamını işaret eden alt-orta Vizeyen karbonatlarındaki foraminifer faunasının depolanma ortamındaki ufak değişimlerden olumsuz olarak etkilendiği görülmektedir.

**Anahtar Kelimeler:** *Toroslar, Hadim Napı, Vizeyen, Mikrofasiyes, Biyofasiyes*

### Microfacies and Biofacies Properties of the Lower-Middle Visean Succession of Hadim Nappe (Central Taurides, Southern TÜRKİYE)

**ABSTRACT:** The Hadim Nappe, which is one of the allochthonous tectono-stratigraphic unit of the Taurides, has a complete succession includes Middle(?)–Upper Devonian–Upper Cretaceous shallow marine carbonates and terrigenous rocks. According to the microfacies analyses of the lower-middle Viséan succession of the Bademli stratigraphic section, where the Hadim Nappe was well exposed, seven microfacies, which are inditing Inner Platform Shoal, Restrict and/or Open Marine depositional environments, were indentified. These are; Bioclastic Grainstone, Bioclastic Grainstone-Packstone, Sandy Bioclastic Grainstone, Sandy Bioclastic Grainstone-Packstone, Bioclastic Pelloidal Grainstone, Bioclastic Wackestone and Sandstone microfacies. The identified microfacies have diverse and rich foraminiferal fauna based on the biofacies analyses. The foraminiferal fauna of the lower-middle Viséan carbonates, which generally indicates stable depositional environments, are adversely affected by minor changes in the depositional environments.

**Keywords:** *Taurides, Hadim Nappe, Viséan, Microfacies, Biofacies*

#### 1. GİRİŞ (INTRODUCTION)

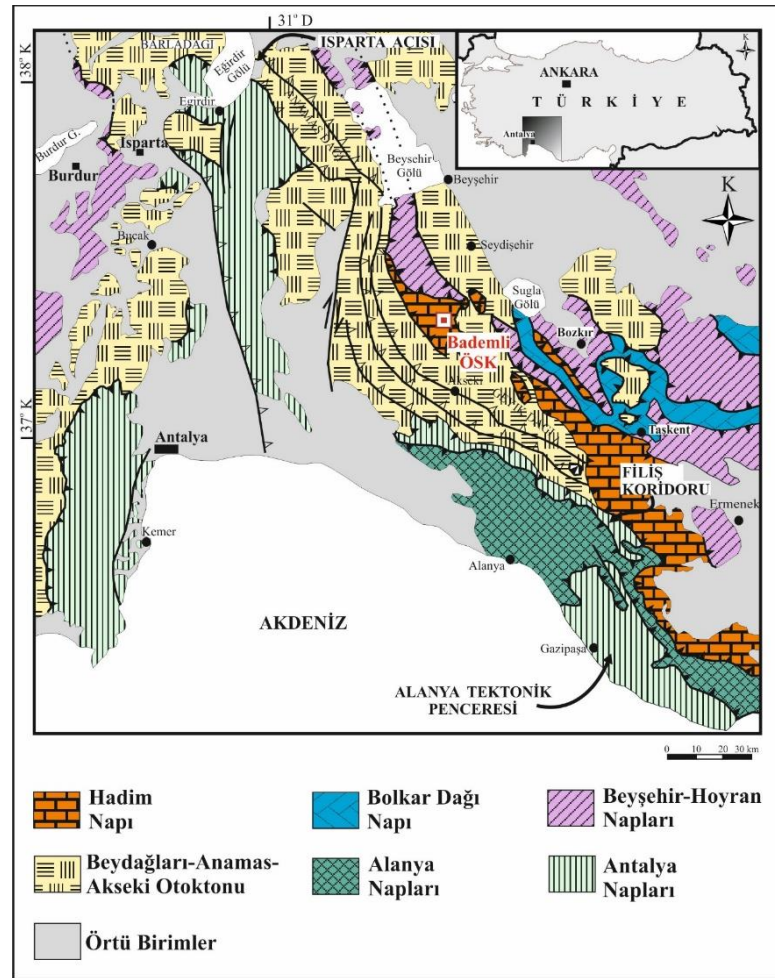
Geç Devoniyen'de başlayıp Erken Permiyen'de sona eren Geç Paleozoyik Buzul Dönemi, Fanerozoik'teki en uzun süreli buzullaşma olarak bilinmektedir [1-3]. Geç Paleozoyik Buzullaşması veya Gondwana Buzullaşması olarak da bilinen bu buzul dönemi özellikle Gondwana ve Avustralya gibi bölgeleri direk etkilerken Euramerica, Rusya ve Gondwana'nın kuzey ucunda yer alan Türkiye, İran ve Güney Çin bölgelerini ise dolaylı şekilde etkilemiştir [3-20]. Geç Paleozoyik buzullaşmasının uzak etkilerinin gözlemlendiği alanlarda, Erken Karboniferdeki (Orta-Geç Misisipiyen) buzul arası dönem

\*Corresponding Author: Melikan AKBAŞ, [makbas@ktun.edu.tr](mailto:makbas@ktun.edu.tr)

süresince deniz seviyesi değişimine de bağlı olarak denizel karbonat doygunluk/çökelim artışı ve denizel organizmalarda bolluk/çeşitlenme görülmektedir [1,11, 21-23]. Bu çalışmanın konusunu oluşturan Hadim Napı'na ait Alt Karbonifer (Orta-Üst Misisipiyen) çökelleri de benzer şekilde sığ denizel şelf platformu karbonatlarından oluşmakta ve zengin bir denizel fauna/flora içermektedir [24-27]. Bu kapsamda gerçekleştirilen çalışmayla, ideal bir karbonat çökelinin görüldüğü Hadim Napı alt-orta Vizeyen sığ-denizel platform karbonatlarının mikrofasiyes özellikleri ve foraminifer faunasının mikrofasiyeslerdeki dağılımının incelenmesi amaçlanmıştır.

## 2. BÖLGESEL JEOLJİ (GEOLOGICAL SETTINGS)

Toroslar birbirlerinden stratigrafik, yapısal ve metamorfik özellikleri bakımından ayrılan [28-30] biri otokton/paraotokton diğerleri allokton toplam altı tektono-stratigrafik birimden oluşmaktadır. Bunlar; Beydağları-Anamas-Akseki Otoktonu, Hadim Napı, Bolkar Dağı Napı, Beyşehir-Hoyran Napı, Antalya Napları ve Alanya Napları'dır [25-26,31-36] (Şekil 1).

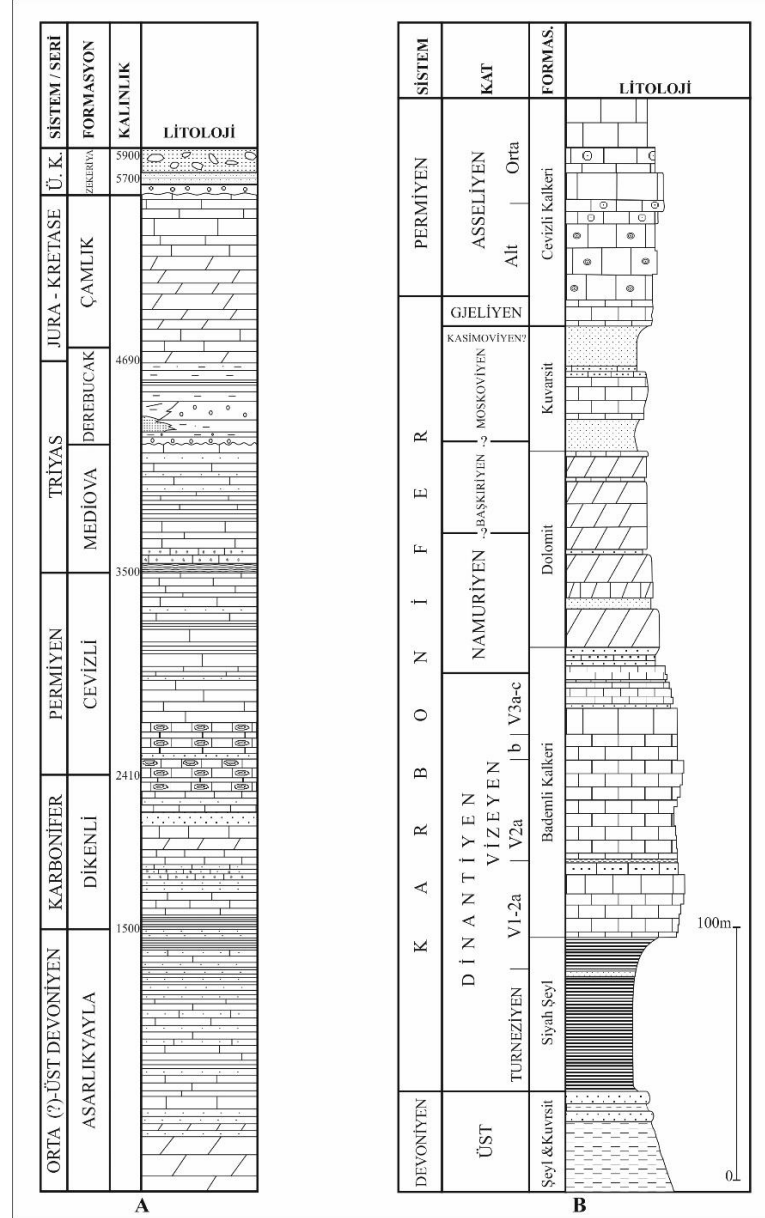


Şekil 1. Orta Toroslar'ın batı kesiminin tektono-stratigrafik birliklerini ve çalışma alanını gösterir harita ([29]'den değiştirilerek alınmıştır).

Figure 1. Schematic map showing the tectono-stratigraphic units in the western part of the Central Taurides and location of the study area (revised after [29]).

Bunlardan Hadim Napı Orta(?) - Geç Devonyen - Geç Kretase zaman aralığında çökelmiş sığ-denizel platform karbonatları ve silisiklastik kayalardan oluşmaktadır [24, 26, 28, 30, 37-38] (Şekil 2A). Hadim Napı kronostratigrafik olarak alttan üste doğru sırasıyla Orta-Üst Devonyen Asarlıkyayla formasyonu

(dolomit, kumtaşı, şeyl, kumlu kireçtaşı, resifal kireçtaşı, şeyl silttaşı ardalanması), Karbonifer Dikenli formasyonu (şeyl silttaşı ardalanması, kireçtaşı, kumtaşı, dolomit, *Girvanella*'lı kireçtaşı), Permiyen Cevizli formasyonu (*Girvanella*'lı kireçtaşı, kireçtaşı, şeyl, kumtaşı), Alt Triyas Mediova formasyonu (stromatolitik ve oolitik kireçtaşı, kumtaşı, kumlu kireçtaşı, kireçtaşı, şeyl), Üst Triyas-Alt (?) Jura Derebucak formasyonu (killi kireçtaşı, kumtaşı, konglomera, gösel kireçtaşı), Alt Jura-Kretase Çamlık formasyonu (kireçtaşı, dolomit) ve Üst Kretase Zekeriya formasyonuna (konglomera, kumtaşı, olistosrom) ait kayaç topluluklarından oluşmaktadır [26, 30, 38] (Şekil 2A).



Şekil 2. A) Hadim Napı genelleştirilmiş kolon kesiti ([26, 30, 37-40]'den derlenerek hazırlanmıştır), B) Hadim Napı Bademli Bölgesi genelleştirilmiş kolon kesiti ([26]'den Türkçeleştirilerek alınmıştır).

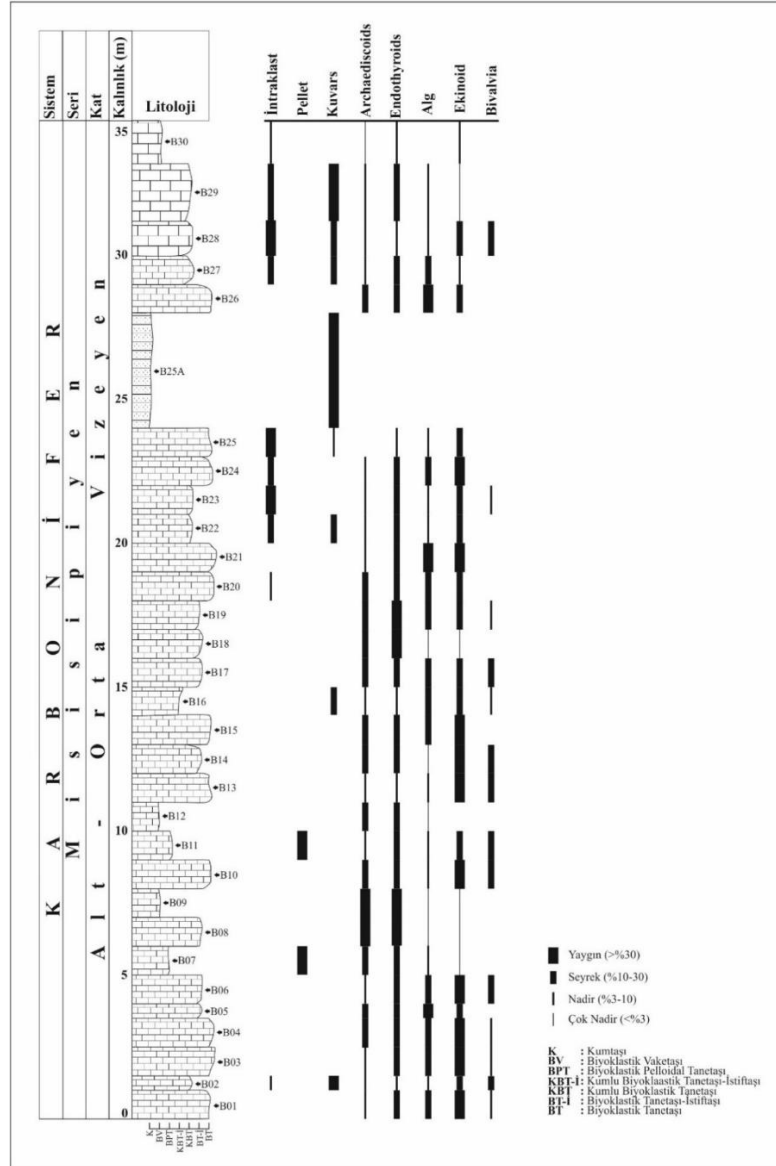
Figure 2. A) Generalized columnar section of the Hadim Nappe (modified after [26, 30, 37-40]), B) Generalized columnar section of the Hadim Nappe in the Bademli Region (modified in Turkish from [26])

Monod [26] tarafından Antalya'nın Akseki İlçesi'nin Bademli Kasabası'nda çalışılan Hadim Napı'na ait istif yazar tarafından Bademli-Çamlık Birimi olarak tanımlanmıştır. Monod [26] bu çalışmasında Karbonifer ve Permiyen istifini kronostratigrafik olarak Siyah Şeyl birimi (Turneziyen-alt Vizeyen), Bademli Kalkeri birimi (orta Vizeyen-alt Serpukhoviye), Dolomit birimi (Namuriyen-Başkriyen),

Kuvarsit birimi (Moskoviyen-Kasimoviyen) ve Cevizli Kalkeri birimlerine (Gijeliyen-Permien) ayırmıştır (Şekil 2B).

### 2.1. Bademli Ölçülü Stratigrafik Kesiti (Bademli Measured Stratigraphic Section)

Bu çalışma kapsamında Hadim Napı'na ait Bademli ölçülü stratigrafik kesiti Antalya'nın Akseki İlçesi'nin Bademli Kasabası'nda ölçülmüş olup 1/25.000 ölçekli Konya N27-a3 paftasında yer almaktadır (Kesit başlangıç ve bitiş UTM koordinatları: 36S 388776E/4130367N - 36S 388897E/4130590N) (Şekil 1). Ölçülen alt-orta Vizeyen karbonat istifi yaklaşık 35 metre kalınlığa sahip olup, istifin alt ve orta kısımları orta-kalın tabakalı gri renkli kireçtaşlarından, üzerleyen bölümü kalın tabakalı sarı renkli kireçtaşlarından ve en üst bölümü ise kalın tabakalı gri renkli kireçtaşlarından oluşmaktadır (Şekil 3).



Şekil 3. Bademli ölçülü stratigrafik kesiti ve mikrofasiyeler içerisindeki allokem ve ekstraklastların oransal dağılımı.

Figure 3. Bademli measured stratigraphic section and the proportional distribution of allochems and extraclasts in microfacies.

### 3. MATERYAL VE METOT (MATERIAL AND METHOD)

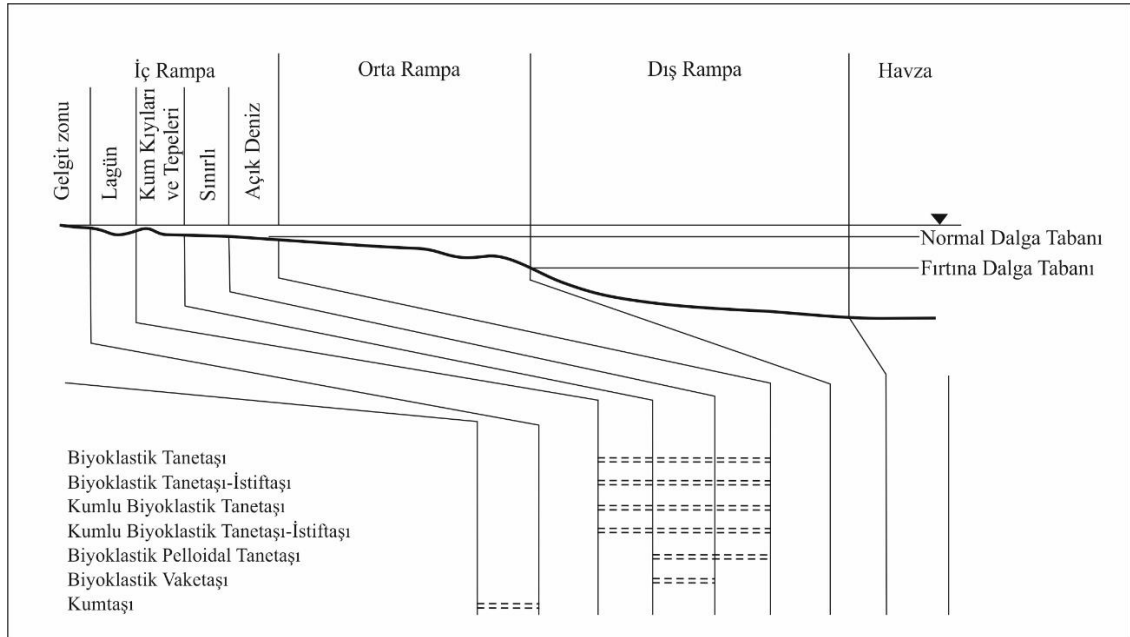
Bu çalışmada ölçülen 35 metre kalınlığındaki karbonat baskın alt-orta Vizeyen istifinden yaklaşık birer metre aralıklarla 30 adet kayaç örneği derlenmiştir. Derlenen örneklerin foraminiferlere dayalı detaylı biyostratigrafik bölümlenmesi Akbaş [27] tarafından gerçekleştirilmiştir. Örnek alınan her seviyeden 4,5x6,5 cm boyutlarında ikişer adet ince kesit hazırlanmıştır. Hazırlanan ince kesitler "Zeiss Primo Star" marka binoküler biyolojik mikroskopta incelenerek detaylı allokem ve bağlayıcı yüzdelemeleri yapılmış ve "Mshot MD50-B" marka mikroskop görüntüleme sistemiyle 4x objektif altında fotoğrafları çekilmiştir. Detaylı allokem ve bağlayıcı yüzdelemelerinin yanı sıra mikrofasiyesler içerisindeki bolluk, çeşitlilik ve dağılımlarının tespiti için kesitlerdeki foraminiferlerin sayımları da yapılmıştır. Allokem yüzdelemeleri Baccelle ve Bosellini [41] tarafından hazırlanan yüzdeleme abakları kullanılarak yapılmış olup mikrofasiyes analizi için ise Flügel [42] tarafından hazırlanan standartlar takip edilmiştir.

### 4. MİKROFASİYES ANALİZİ (MICROFACIES ANALYSES)

Bademli kesiti karbonat baskın alt-orta Vizeyen istifinden derlenen örnekler ait ince-kesit incelemeleri sonucu İç Platform Kıyı, Sınırlanmış ve/veya Açık Deniz depolanma koşullarını yansıtan yedi mikrofasiyes tanımlanmıştır; Biyoklastik Tanetaşı, Biyoklastik Tanetaşı-İstiftaşı, Kumlu Biyoklastik Tanetaşı, Kumlu Biyoklastik Tanetaşı-İstiftaşı, Biyoklastik Pelloidal Tanetaşı, Biyoklastik Vaketaşı ve Kumtaşı (Şekil 4).

#### 4.1. Biyoklastik Tanetaşı (Bioclastic Grainstone)

Bademli kesiti karbonat istifinin alt, orta ve üst bölümlerinin çeşitli seviyelerinde tanımlanan bu mikrofasiyesteki baskın allokemleri değişen oranlarla foraminifer, alg, ekinoid ve bazı seviyelerde bivalvia fosilleri oluşturmaktadır (Şekil 3, 5A). Bağlayıcı olarak ise allokemler arasında baskın bir şekilde sparit çimento olup ince-kesitlerin bazılarında oldukça az miktarda (%1-2) mikrit çamuru da gözlenmektedir.

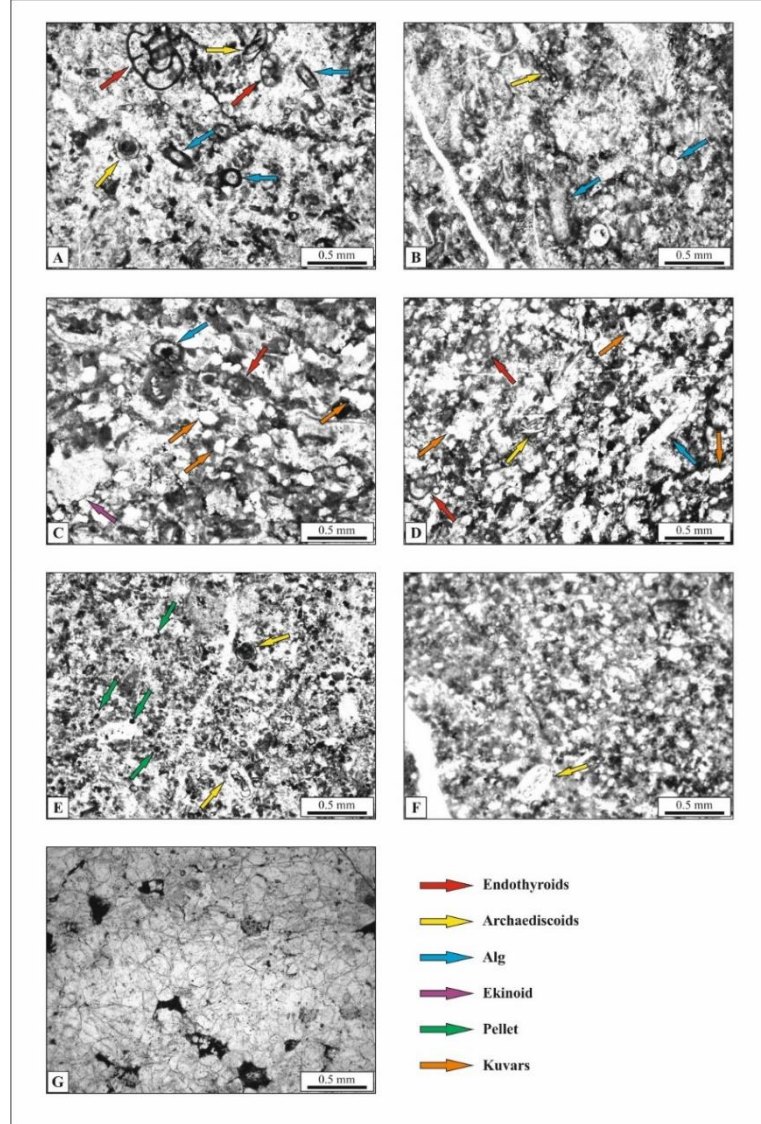


**Şekil 4.** Bademli ölçülü stratigrafik kesiti mikrofasiyeslerinin, Rampa Tipi Platform modelinde yer alan Fasiyes Zonları (FZ) içerisindeki dağılımı ([42]'den Türkçeleştirilerek alınmıştır).

*Figure 4. The distribution of the microfacies of the Bademli measured stratigraphic section in the Facies Zones (FZ) of the Ramp Type Platform model (modified in Turkish from [42]).*

Belirgin alg ve foraminifer topluğunun varlığı ve baskın sparit çimento bağlayıcısıyla bu mikrofasiyes FZ 7-8 (İç platform Kıyı, Sınırlı ve/veya Açık Deniz depolanma ortamı) Fasiyes Zonu'na ve Standart Mikrofasiyes tiplerinden SMF-18'e Rampa Türü Mikrofasiyes tiplerinden ise RMF-27'ye karşılık gelmektedir (Şekil 4).

Foraminiferlerce (endothyroids ve archaediscoids) zengin olan bu mikrofasiyese ait seviyelerde gerçekleştirilen ince-kesit analizlerine göre kesitlerin 1-11 arasında değişen (çoğunlukla 7-9) farklı cins ve bu cinslere ait 1-19 arasında değişen (çoğunlukla 9-19) farklı tür foraminifer içerdiği gözlemlenmiş olup ortalama 6 cins ve 9 tür foraminiferle temsil olduğu belirlenmiştir (Çizelge 1, 2; Şekil 6). Biyoklastik Tanetaşı mikrofasiyesi içerisindeki zengin foraminifer faunasında yer alan ve Vizeyen biyostratigrafisinde oldukça önemli olan endothyroids ve archaediscoids fosil gruplarının ince-kesitlerdeki sayısal değerlerine bakıldığında çeşitlilikle paralel bir şekilde belirgin bir bolluğun varlığı da gözlenmektedir.



**Şekil 5.** Bademli ölçülü stratigrafik kesitinde tanımlanan mikrofasiyelere ait ince-kesit mikrofotografaları. A) Biyoklastik Tanetaşı, B) Biyoklastik Tanetaşı-İstiftaşı, C) Kumlu Biyoklastik Tanetaşı, D) Kumlu Biyoklastik Tanetaşı-İstiftaşı, E) Biyoklastik Pelloidal Tanetaşı, F) Biyoklastik Vaketaşı, G) Kumtaşı.

**Figure 5.** Thin-section microphotographs of the microfacies identified in the Bademli measured stratigraphic section. A) Bioclastic Grainstone, B) Bioclastic Grainstone-Packstone, C) Sandy Bioclastic Grainstone, D) Sandy Bioclastic Grainstone-Packstone, E) Bioclastic Pelloidal Grainstone, F) Bioclastic Wackestone, G) Sandstone

İnce-kesitlerde 3-71 arasında değişen sayılarda bireye sahip archaediscoids grubu fosillerin kesitlerdeki ortalama birey sayısı 28 bireyken, endothyroids gurubu fosiller 39-145 arasında değişen sayılarda bireye sahip olup ortalama 76 bireyle temsil olmaktadır (Çizelge 3, 4; Şekil 6).

#### 4.2. Biyoklastik Tanetaşı-İstiftaşı (Bioclastic Grainstone-Packstone)

Çalışılan ölçülü stratigrafik kesitin genel olarak alt ve orta bölümlerindeki seviyelerde tanımlanan Biyoklastik Tanetaşı-İstiftaşı mikrofasiyesinin baskın bileşenlerini biyoklastlar oluşturmakta olup bazı örneklerinde az miktarda intraklastlar da gözlenmektedir (Şekil 3, 5B). Baskın allokem içeriğini oluşturan biyoklastlar azalan oranda sırasıyla foraminifer, ekinoid, alg ve bivalvia fosillerinden oluşmaktadır. Bağlayıcı olarak ise spartit çimento ve değişen oranlarda (%5-25) mikrit çamuru bulunmaktadır. Bu mikrofasiyes Biyoklastik Tanetaşı mikrofasiyesine benzer şekilde Standart Mikrofasiyes tiplerinden SMF-18'e Rampa Türü Mikrofasiyes tiplerinden ise RMF-27'ye ve orta-yüksek enerjili, İç Platform Kıyı, Sınırlı ve/veya Açık Deniz depolanma ortamını işaret eden FZ 7-8 Fasiyes Zonu'na karşılık gelmektedir (Şekil 4).

Biyoklastik Tanetaşı-İstiftaşı mikrofasiyesinin tanımlandığı seviyelere ait ince-kesitlerdeki foraminifer (endothyroids ve archaediscoids) topluluğuna bakıldığında 3-9 arasında değişen (çoğunlukla 6-7) farklı cins ve bu cinslere ait 4-18 arasında değişen (çoğunlukla 8-9) farklı tür foraminifer içeriğine sahip olup ortalama 6 cins ve 9 tür foraminiferle temsil olduğu gözlenmiştir (Çizelge 1, 2; Şekil 6). Biyoklastik Tanetaşı mikrofasiyesindeki gibi zengin bir foraminifer faunasına sahip bu mikrofasiyesteki endothyroids ve archaediscoids foraminiferlerin bolluklarının da benzer şekilde olduğu belirlenmiştir.

Archaediscoids grubu foraminiferler bu mikrofasiyes içerisinde 15-62 arasında değişen sayıda bireylere sahip olup ortalama birey sayısı 29 bireyle, endothyroids gurubu foraminiferler ise 3-162 arasında değişen sayılarda bireye sahip olup ortalama 73 bireyle temsil olmaktadır (Çizelge 3, 4; Şekil 6).

**Çizelge 1.** Bademli ölçülü stratigrafik kesitinde tanımlanan mikrofasiyeslere ait foraminifer cins çeşitliliği

*Table 1. Diversity of the foraminiferal genera in the microfacies identified in the Bademli measured stratigraphic section*

Fasiyes Tipi	Ortalama Cins Sayısı	En Düşük Cins Sayısı	En Yüksek Cins Sayısı
Biyoklastik Tanetaşı	6	1	11
Biyoklastik Tanetaşı-İstiftaşı	6	3	9
Kumlu Biyoklastik Tanetaşı	2	1	3
Kumlu Biyoklastik Tanetaşı-İstiftaşı	8	8	8
Biyoklastik Pelloidal Tanetaşı	7	2	12
Biyoklastik Vaketaşı	2	2	2

**Çizelge 2.** Bademli ölçülü stratigrafik kesitinde tanımlanan mikrofasiyeslere ait foraminifer tür çeşitliliği

*Table 2. Diversity of the foraminiferal species in the microfacies identified in the Bademli measured stratigraphic section*

Fasiyes Tipi	Ortalama Tür Sayısı	En Düşük Tür Sayısı	En Yüksek Tür Sayısı
Biyoklastik Tanetaşı	9	1	19
Biyoklastik Tanetaşı-İstiftaşı	9	4	18
Kumlu Biyoklastik Tanetaşı	2	1	3
Kumlu Biyoklastik Tanetaşı-İstiftaşı	11	11	11
Biyoklastik Pelloidal Tanetaşı	11	2	19
Biyoklastik Vaketaşı	2	2	2



**Çizelge 3.** Bademli ölçülü stratigrafik kesitinde tanımlanan mikrofasiyeslere ait archaediscoids grubu foraminiferlerin birey sayıları

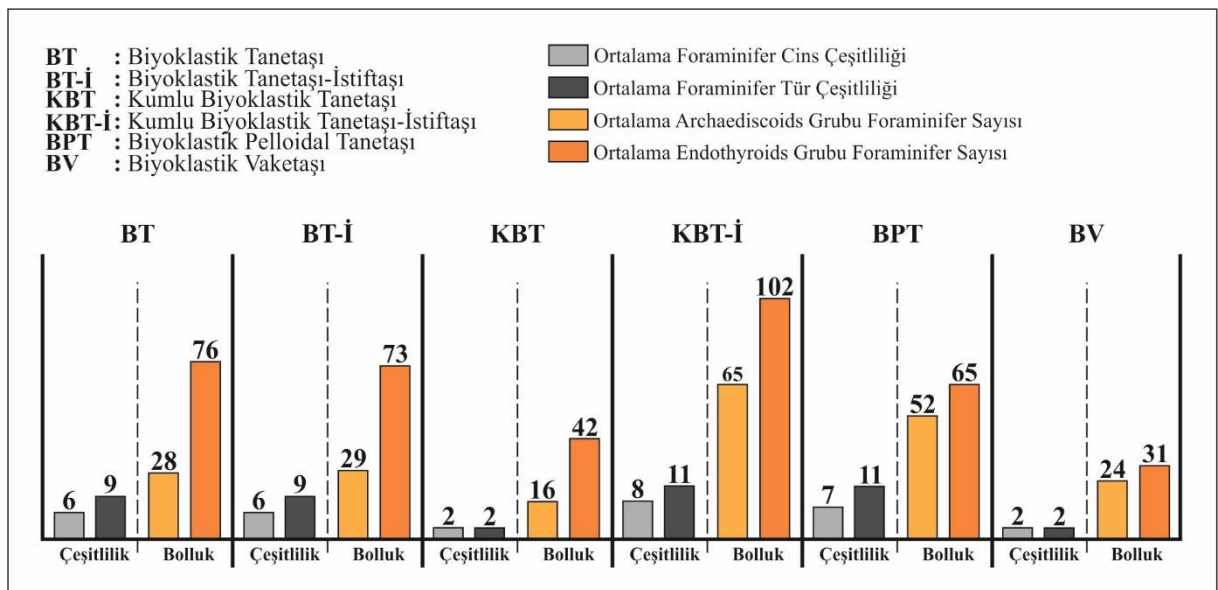
*Table 3. Individual numbers of archaediscoids group foraminifers in the microfacies identified in the Bademli measured stratigraphic section*

Fasiyes Tipi	Ortalama Birey Sayısı	En Düşük Birey Sayısı	En Yüksek Birey Sayısı
Biyoklastik Tanetaşı	28	3	71
Biyoklastik Tanetaşı-İstiftaşı	29	15	62
Kumlu Biyoklastik Tanetaşı	16	1	30
Kumlu Biyoklastik Tanetaşı-İstiftaşı	65	65	65
Biyoklastik Pelloidal Tanetaşı	52	51	52
Biyoklastik Vaketaşı	24	12	36

**Çizelge 4.** Bademli ölçülü stratigrafik kesitinde tanımlanan mikrofasiyeslere ait endothyroids grubu foraminiferlerin birey sayıları.

*Table 4. Individual numbers of endothyroids group foraminifers in the microfacies identified in the Bademli measured stratigraphic section*

Fasiyes Tipi	Ortalama Birey Sayısı	En Düşük Birey Sayısı	En Yüksek Birey Sayısı
Biyoklastik Tanetaşı	76	39	145
Biyoklastik Tanetaşı-İstiftaşı	73	3	162
Kumlu Biyoklastik Tanetaşı	42	9	60
Kumlu Biyoklastik Tanetaşı-İstiftaşı	102	102	102
Biyoklastik Pelloidal Tanetaşı	65	63	66
Biyoklastik Vaketaşı	31	21	40



**Şekil 6.** Bademli ölçülü stratigrafik kesitinde tanımlanan mikrofasiyeslerdeki foraminiferlerin çeşitlilik ve bolluklarını gösterir histogramlar.

*Figure 6. Histograms showing the diversity and abundance of foraminifera in the microfacies identified in the Bademli measured stratigraphic section*

#### 4.3. Kumlu Biyoklastik Tanetaşı (Sandy Bioclastic Grainstone)

Kumlu Biyoklastik Tanetaşı mikrofasiyesi ekinoid, foraminifer ve alg fosillerinin baskın faunayı oluşturduğu biyoklastlar, değişen oranlarda intraklast ve kuvars tanelerinden oluşan bileşenleri içermektedir (Şekil 3, 5C). Bu mikrofasiyes Bademli kesitinin üst kısımlarında gözlenmektedir (Şekil 3). Allokem ve ekstraklastlar (kuvars taneleri) bağlayıcı olarak baskın şekilde sparit çimento ile bağlanmıştır.

Tane içeriği ve bağlayıcı tipiyle bu mikrofasiyes SMF-18 Standart Mikrofasiyes tipi ve FZ 7-8 Fasiyes Zonu'na karşılık gelmekte olup İç Platform Kıyı, Sınırlı ve/veya Açık Deniz depolanma ortamını işaret etmektedir (Şekil 4).

Belirli bir foraminifer faunasına sahip olsa da Kumlu Biyoklastik Tanetaşı mikrofasiyesinde çeşitlilik ve bolluğun düşük olduğu gözlemlenmektedir. Bu mikrofasiyesteki foraminifer topluluğu 1-3 arasında değişen farklı cins ve bu cinslere ait 1-3 arasında değişen farklı tür içeriğine sahip olup ortalama 2 cins ve 2 türle temsil olmaktadır (Çizelge 1,2; Şekil 6). Ortalama-düşük bir foraminifer çeşitliliğe sahip Kumlu Biyoklastik Tanetaşı mikrofasiyesinde çeşitliliğin düşük olmasına paralel bir şekilde archaedisoids ve endothyroids grubu foraminiferlerin sırasıyla ortalama 16 ve 42 bireyle nispeten düşük bir bolluğa sahip oldukları gözlenmektedir. İncelenen ince-kesitlerin tamamına bakıldığında, archaedisoids grubu foraminiferlerin en az 1 en fazla 30 bireyle, endothyroids grubu foraminiferlerin ise 9-60 arasında değişen sayılarda bir bollukla temsil oldukları gözlenmektedir (Çizelge 3, 4; Şekil 6).

#### 4.4. Kumlu Biyoklastik Tanetaşı-İstiftaşı (Sandy Bioclastic Grainstone-Packstone)

Bademli kesitin orta bölümlerindeki tek bir seviyede tanımlanan Kumlu Biyoklastik Tanetaşı-İstiftaşı mikrofasiyesi kuvars tanelerinden oluşan ekstraklastlar ile baskın ekinoid ve alg fosilleriyle birlikte foraminiferlerden oluşan allokem topluluğu ile karakterizedir (Şekil 3, 5D). Bağlayıcı olarak ise baskın bir şekilde mikrit çamuru gözlenmektedir. Kumlu Biyoklastik Tanetaşı-İstiftaşı mikrofasiyesi İç Platform Kıyı, Sınırlı ve/veya Açık Deniz depolanma ortamını işaret eden SMF-18 Standart Mikrofasiyes tipi ve FZ 7-8 Fasiyes Zonu'na karşılık gelmektedir (Şekil 4).

Bademli kesiti boyunca tek bir seviyede bulunan Kumlu Biyoklastik Tanetaşı-İstiftaşı mikrofasiyesinde 8 foraminifer cinsi ve bu cinslere ait 11 farklı tür belirlenmiştir (Çizelge 1, 2; Şekil 6). Tanımlanan foraminifer topluluğunda archaedisoids grubu foraminiferlerin 65, endothyroids grubu foraminiferlerin ise 102 bireyle zengin bir bolluğa sahip olduğu gözlenmektedir (Çizelge 3, 4; Şekil 6).

#### 4.5. Biyoklastik Pelloidal Tanetaşı (Bioclastic Pelloidal Grainstone)

Biyoklastik Pelloidal Tanetaşı mikrofasiyesinin başlıca allokemlerini foraminifer, alg, ekinoid ve bivalvia fosillerinden oluşan zengin biyoklastlar oluşturmakta olup belirli bir oranda pellet içeriği de gözlenmektedir (Şekil 3, 5E). Bağlayıcı olarak ise sparit çimento bulunmaktadır. İncelenen ölçülü stratigrafik kesitin orta bölümlerindeki iki seviyede tanımlanan bu mikrofasiyes SMF-16 Standart Mikrofasiyes tipine ve FZ-8 Fasiyes Zonu'na karşılık gelmekte olup İç Platform Kıyı veya Sınırlı-Denizel depolanma ortamını işaret etmektedir (Şekil 4).

Biyoklastik Pelloidal Tanetaşı mikrofasiyesi olarak tanımlanan iki seviyedeki örnekler ait ince-kesitler üzerinde gerçekleştirilen foraminifer çeşitlilik incelemelerinde örneklerden birinin 2 cins ve bu cinslere ait 2 farklı türe, diğer örneğin ise 12 cins ve bu cinslere ait 19 farklı türe sahip oldukları belirlenmiş olup ortalama 7 cins ve 11 tür foraminiferle temsil olduğu gözlenmektedir (Çizelge 1, 2; Şekil 6). İnce-kesitlerde belirlenen foraminifer topluluğuna ait bolluğun ise archaedisoids grubu foraminiferlerde ortalama 52 birey, endothyroids grubu foraminiferlerde ise ortalama 65 bireyle temsil olduğu gözlemlenmiştir (Çizelge 3, 4; Şekil 6).

#### 4.6. Biyoklastik Vaketaşı (Bioclastic Wackestone)

İncelenen Bademli ölçülü stratigrafik kesitin orta bölümündeki iki seviyede tanımlanan Biyoklastik Vaketaşı mikrofasiyesi fakir bir foraminifer faunası ve yer yer bivalvialardan oluşan allokemler ile karakterizedir (Şekil 3, 5F). Bağlayıcı olarak ise değişen oranlarda mikrit çamuru ve sparit çimento bulunmaktadır. Nispeten az da olsa belirli bir foraminifer topluluğunun varlığına bağlı olarak bu mikrofasiyes İç Platform Sınırlı-Açık Deniz depolanma ortamını temsil eden FZ-8 Fasiyes Zonu, SMF-23 Standart Mikrofasiyes tipi ve RMF-20 Rampa Türü Mikrofasiyes tipine karşılık gelmektedir (Şekil 4).

Biyoklastik Vaketaşı mikrofasiyesinin tanımlandığı her iki örnekte de foraminifer çeşitliliği 2 farklı cins ve bu cinslere ait 2 farklı tür ile temsil olmaktadır (Çizelge 1, 2; Şekil 6). Tanımlanan foraminiferlerin bolluk açısından incelenmesinde ise çeşitliliğin az olmasıyla paralel bir şekilde archaediscoids grubu foraminiferlerin ortalama 24 birey, endothyroids grubu foraminiferlerin ise ortalama 31 bireyle temsil olduğu gözlemlenmiştir (Çizelge 3, 4; Şekil 6).

#### 4.7. Kumtaşı (Sandstone)

Bademli kesitinin orta-üst bölümünde tanımlanan Kumtaşı mikrofasiyesi genel olarak iyi boylanmış ve karbonat çimento ile bağlanmış kuvars içeriğiyle karakteristiktir (Şekil 3, 5G). Bu mikrofasiyesi İç Platform gelgit zonu depolanma ortamını işaret eden FZ10 Fasiyes Zonu'na karşılık gelmektedir (Şekil 4).

### 5. TARTIŞMALAR (DISCUSSIONS)

Geç Paleozoyik Buzullaşma dönemi içerisinde Geç Devoniyen (Fransiyen-Fameniyen)-Erken Karbonifer (Turneziyen) zaman aralığında gerçekleşen 1. buzul dönemi [1,2,3] sonrası Vizeyen zaman aralığında buzul etkilerinin olmayışıyla bu dönemde ideal bir sığ denizel platforma ait etkin bir karbonat çökelişi görülmektedir [1, 11, 21-23]. Hadim Napı erken-orta Vizeyen yaşlı Bademli ölçülü stratigrafik kesitinde tanımlanan mikrofasiyesler benzer şekilde İç Platform sığ denizel çökeltme ortamında çökelmiş karbonat baskın bir istifi işaret etmektedir. İdeal karbonat platformunda uygun şartların oluşması ve bu zaman aralığı boyunca stabilizasyonun korunması organizmaların gelişimini de olumlu olarak etkilemiş olup genel olarak sedimanter kayıtlarda zengin bir foraminifer faunası sunmaktadır. Tanımlanan mikrofasiyeslerde foraminifer faunası genel olarak zengin bir çeşitlilik ve bolluk sunmaktadır ancak her ne kadar tüm mikrofasiyesler platform içi sınırlı ve/veya açık deniz çökeltme ortamını işaret etse de en fazla çeşitlilik ve bolluk Biyoklastik Tanetaşı, Biyoklastik Tanetaşı-İstiftaşı, Biyoklastik Pelloidal Tanetaşı mikrofasiyeslerinde gözlenmektedir. Çökeltme ortamdaki kuvars ve/veya mikrit çamuru varlığının sedimanter kayıtlara yansıdığı Kumlu Biyoklastik Tanetaşı ve Biyoklastik Vaketaşı mikrofasiyeslerinde ise foraminifer faunasının olumsuz olarak etkilendiği dolayısıyla da çeşitlilik ve bolluğun az olduğu gözlenmektedir. Stabil bir İç Platform sığ denizel ortam koşullarını işaret eden Hadim Napı alt-orta Vizeyen karbonat istifinde kuvars taneleri ve mikrit çamurunun varlığıyla sedimanter kayıtlara geçen çökeltme ortamındaki ufak değişikliklerin faunayı doğrudan etkilediği söylenebilmektedir.

### 6. SONUÇLAR (CONCLUSIONS)

Hadim Napı alt-orta Vizeyen istifi Bademli ölçülü stratigrafik kesitinde gerçekleştirilen mikrofasiyesi ve foraminifer dağılım incelemelerinde aşağıdaki sonuçlar elde edilmiştir;

- 1) İncelenen karbonat baskın alt-orta Vizeyen istifinde 7 adet mikrofasiyesi tanımlanmıştır; Biyoklastik Tanetaşı, Biyoklastik Tanetaşı-İstiftaşı, Kumlu Biyoklastik Tanetaşı, Kumlu Biyoklastik Tanetaşı-İstiftaşı, Biyoklastik Pelloidal Tanetaşı, Biyoklastik Vaketaşı ve Kumtaşı mikrofasiyesi.
- 2) Tanımlanan mikrofasiyesler Hadim Napı alt-orta Vizeyen istifinin stabil bir İç Platform sığ denizel çökeltme ortamında çökeldiğini göstermektedir.
- 3) Hadim Napı alt-orta Vizeyen istifi zengin çeşitlilik ve bolluğa sahip bir foraminifer topluluğu sunmaktadır.
- 4) Foraminifer topluluğundaki çeşitlilik ve bolluğun tanımlanan mikrofasiyesi tiplerindeki mikrit çamuru ve/veya kuvars varlığına bağlı olarak bazı farklılıklar gösterdiği belirlenmiştir.

#### Etik Standartlar Bildirimi (Declaration of Ethical Standards)

Yazar yapılan analiz çalışmalarının yürütülmesinde, ilgili literatürün taranmasında ve verilerin toplanmasında etik ilkelere ve standartlara bağlı kaldığını ve makalenin özgün olduğunu beyan eder.

**Yazar Katkı Beyannamesi (Credit Authorship Contribution Statement)**

Bu çalışmanın tüm aşamaları Arş. Gör. Dr. Melikan Akbaş tarafından yürütülmüştür.

**Çıkar Çatışması Beyannamesi (Declaration of Competing Interest)**

Yazarlar herhangi bir çıkar çatışması olmadığını beyan etmektedir.

**Destek / Teşekkür (Funding / Acknowledgements)**

Bu çalışmanın yürütülmesi esnasında herhangi bir kurum veya kuruluştan maddi bir destek alınmamıştır.

**Veri Kullanılabilirliği (Data Availability)**

Yazar bu çalışmadan elde edilen verilerin diğer araştırmacılar tarafından kullanılmayacağını ifade etmektedir.

**KAYNAKLAR (REFERENCES)**

- [1] J.L. Isbell, M.F. Miller, K.L. Wolfe, P.A. Lenaker, "Timing of Late Paleozoic glaciation in Gondwana: was glaciation responsible for the development of Northern Hemisphere cyclothems?: *Extreme depositional environments: mega end members in geologic time*," Eds.: M.A. Chan, A.W. Archer, *Geological Society of America, Boulder, Colorado, special paper*, vol. 370, pp 5–24, 2003.
- [2] I.P. Montañez, C.J. Poulsen, "The Late Paleozoic ice age: an evolving paradigm," *Annual Review of Earth and Planetary Sciences*, vol. 41, pp. 629–656, 2013.
- [3] E.L.M. Rosa, J.L. Isbell, "Late Paleozoic glaciation," *Encyclopedia of Geology, 2nd edition*, Eds: D. Alderton, S.A. Elias, Elsevier, Amsterdam, pp 534–345, 2020.
- [4] E.L. Grossman, P. Bruckschen, H.S. Mii, B.I. Chuvashov, T.E. Yancey, J. Veizer, "Carboniferous paleoclimate and global change: isotopic evidence from the Russian Platform: Carboniferous stratigraphy and paleogeography in Eurasia," *Institute of Geology and Geochemistry, Russian Academy of Sciences, Urals Branch, Ekaterinburg*, pp 61–71, 2002.
- [5] E.L. Grossman, T.E. Yancey, T.E. Jones, P. Bruckschen, B.I. Chuvashov, S.J. Mazzullo, H.S. Mii, "Glaciation, aridification, carbon sequestration in the Permo-Carboniferous: the isotopic record from low latitudes," *Palaeogeography, Palaeoclimatology, Palaeoecology*, Vol. 268, pp. 222–233, 2008.
- [6] C.R. Fielding, T.D. Frank, L.P. Birgenheier, M.C. Rygel, A.T. Jones, J. Roberts, "Stratigraphic imprint of the Late Palaeozoic ice age in eastern Australia: a record of alternating glacial and non-glacial climate regime," *Journal of the Geological Society of London*, vol. 165, no. 1, pp. 129–140, 2008a.
- [7] C.R. Fielding, T.D. Frank, L.P. Birgenheier, M.C. Rygel, A.T. Jones, J. Roberts, "Stratigraphic record and facies associations of the Late Paleozoic ice age in eastern Australia (New South Wales and Queensland): *Resolving the Late Paleozoic Ice Age in time and space*," Eds.: C.R. Fielding, T.D. Frank, J.L. Isbell, *Geological Society of America Special Paper*, vol. 441, pp. 41–57, 2008b.
- [8] C.R. Fielding, T.D. Frank, J.L. Isbell, "The Late Paleozoic ice age—a review of current understanding and synthesis of global climate patterns: *Resolving the Late Paleozoic Ice Age in time and space*," Eds.: C.R. Fielding, T.D. Frank, J.L. Isbell, *Geological Society of America Special Paper*, vol. 441, pp. 343–354, 2008c.
- [9] W. Buggisch, X. Wang, A.S. Alekseev, M.M. Joachimski, "Carboniferous-Permian carbon isotope stratigraphy of successions from China (Yangtze platform), USA (Kansas) and Russia (Moscow Basin and Urals)," *Palaeogeography, Palaeoclimatology, Palaeoecology*, vol. 301, pp. 18–38, 2011.

- [10] V.N. Kuleshov, K.M. Sedaev, V.M. Gorozhanin, E.N. Gorozhanina, "Hypostratotype of the Bashkirian stage of the carboniferous system (Askyn River, Bashkortostan): lithology, isotopes ( $\delta^{13}\text{C}$ ,  $\delta^{18}\text{O}$ ), and carbonate depositional settings," *Stratigraphy and Geological Correlation*, vol. 26, no. 6, pp. 698–719, 2018.
- [11] C. Okuyucu, U.K. Tekin, P.J. Noble, Y. Bedi, D.G. Saydam-Demiray, K. Sayit, "Foraminifera, radiolaria and conodont assemblages from the early Mississippian (late Tournaisian)/early Pennsylvanian (early Bashkirian) blocks within the Mersin Melange, southern Turkey: biochronological and paleogeographical implications," *Palaeoworld*, vol. 27, no. 4, pp. 438–457, 2018.
- [12] M.S. Abadi, G.S. Soreghan, N.G. Heavens, D.F.A.E. Voeten, R.M. Ivanova, "Warm-water carbonates in proximity to Gondwanan ice-sheets: a record from the Upper Paleozoic of Iran," *Palaeogeography, Palaeoclimatology, Palaeoecology*, vol. 531, pp. 1-17, 2019.
- [13] J. Chen, Q. Sheng, K. Huc, L. Yao, W. Lin, I.P. Montañez, X. Tian, Y. Qi, X. Wang, "Late Mississippian glacio-eustasy recorded in the eastern Paleo-Tethys Ocean (South China)," *Palaeogeography, Palaeoclimatology, Palaeoecology*, vol. 531, pp. 1-12, 2019.
- [14] X. Tian, J. Chen, L. Yao, K. Hu, Y. Qi, X. Wang, "Glacio-eustasy and  $\delta^{13}\text{C}$  across the Mississippian-Pennsylvanian boundary in the eastern Paleo-Tethys Ocean (South China): implications for midcarboniferous major glaciation," *Geological Journal*, vol. 55, pp. 2704–2716, 2019.
- [15] X.D. Wang, K.Y. Hu, W.K. Qie, Q.Y. Sheng, B. Chen, W. Lin, L. Yao, Q.L. Wang, Y.P. Qi, J.T. Chen, Z.T. Liao, J.J. Song, "Carboniferous integrative stratigraphy and timescale of China. *Sci China, Earth Science*, vol. 62, no. 1, pp. 135–153, 2019.
- [16] J. Chen, S. Shen, Y. Zhang, L. Angiolini, M.N. Gorgij, G. Crippa, W. Wang, H. Zhang, D. Yuan, X. Lif, Y. Xua, "Abrupt warming in the latest Permian detected using high-resolution in situ oxygen isotopes of conodont apatite from Abadeh, central Iran," *Palaeogeography, Palaeoclimatology, Palaeoecology*, vol. 560, pp. 1-11, 2020.
- [17] S.A. Dub, G.A. Mizens, V.N. Kuleshov, T.I. Stepanova, N.A. Kucheva, S.V. Nikolaeva, O.Yu. Melnichuk, E.I. Kulagina, O.L. Petrov, "The mid-carboniferous boundary in the eastern slope of the southern and middle Urals: carbon and oxygen isotopic composition in limestones," *Litosfera*, vol. 20, no. 3, pp. 305–327, 2020. (in Russian)
- [18] B. Yang, X. Zhang, W. Qie, Y. Wei, X. Huang, H. Xia, "Variabilities of carbonate  $\delta^{13}\text{C}$  signal in response to the Late Paleozoic glaciations, Long'an, South China," *Frontiers in Earth Science*, vol. 14, no. 2, pp. 344–359, 2020.
- [19] H.C. Yu, K.F. Qiu, M. Li, M. Santosh, Z.G. Zhao, Y.Q. Huang, "Record of the Late Paleozoic ice age from Tarim, China," *Geochemistry, Geophysics, Geosystems*, Vol. 21, pp. 1–20, 2020.
- [20] M. Akbaş, C. Okuyucu, İ.Ö. Yılmaz, "Microfacies and stable isotope analyses ( $\delta^{13}\text{C}$  and  $\delta^{18}\text{O}$ ) of the upper Serpukhovian-Moscovian carbonates in the Hadim Nappe, southern Turkey: an approach to document the Late Paleozoic Ice Age (LPIA)," *Facies*, Vol. 68, No. 12, pp. 1-19, 2022.
- [21] L.B. Smith, J.F. Read, "Rapid onset of late Paleozoic glaciation on Gondwana: evidence from Upper Mississippian strata of the Midcontinent, United States," *Geology*, vol. 28, pp. 279–282, 2000.
- [22] V.P. Wright, S.D. Vanstone, "Onset of Late Paleozoic glacio-eustasy and the evolving climates of low latitude areas: a synthesis of current understanding," *Journal of the Geological Society*, vol. 158, pp. 579–582, 2001.
- [23] V.I. Davydov, B.R. Wardlaw, F.M. Gradstein, "The Carboniferous Period" *A geologic time scale 2004*, Eds.; F.M. Gradstein, J.G. Ogg, A.G. Smith, Cambridge, United Kingdom: Cambridge University Press, pp. 222-248, 2004.
- [24] T. Güvenç, *Etude stratigraphique et micropaléontologique du Carbonifère et du Permien des Taurus occidentaux dans l'arrière-pays d'Alanya (Turquie)*, PhD Thèse, Université de Paris, 1965.
- [25] N. Özgül, "Toroslar'ın bazı temel jeoloji özellikleri," *Türkiye Jeoloji Kurumu Bülteni*, cilt 19, ss. 65-78, 1976.

- [26] O. Monod, *Recherches Geologiques Dans le Taurus Occidental au Sud de Beyşehir (Turquie)*, PhD Thèse, l'Univ. de Paris Sud, Paris, 1977.
- [27] M. Akbaş, "New data on the Lower-Middle Viséan (MFZ10-MFZ13) foraminifers from the Hadim Nappe, southern Turkey: Biostratigraphic implications", *Micropaleontology*, 2023 (in press).
- [28] N. Özgül, "Orta Torosların kuzey kesiminin yapısal gelişiminde blok hareketlerinin önemi," *Türkiye Jeoloji Kurumu Bülteni*, cilt 14, sayı 1, ss. 85-101, 1971.
- [29] N. Özgül, "Stratigraphy and tectonic evolution of the Central Taurides: Eds: O. Tekeli, M.C. Göncüoğlu," *International Symposium on Geology of the Taurus Belt, Ankara*, ss. 77-90, 1984.
- [30] N. Özgül, "Bozkır-Hadim-Taşkent (Orta Toroslar'ın kuzey kesimi) dolayında yer alan tektono-stratigrafik birliklerin stratigrafisi," *Maden Tetkik ve Arama Dergisi*, cilt 119, ss. 113-174, 1997.
- [31] M.M. Blumenthal, "Bozkır güneyinde Toros sıradağlarının serisi ve yapısı," *İstanbul Üniversitesi Fen Fakültesi Mecmuası*, seri B, cilt 9, sayı 2, ss. 95-125, 1944.
- [32] M.M. Blumenthal, "Karaman Konya Havzası Güneybatısında Toros Kenar Silsileleri ve şist radyolarit formasyonu stratigrafi meselesi," *Maden Tetkik ve Arama Dergisi*, cilt 48, ss. 1-36, 1956.
- [33] M. Gutnic, D. Kelter, O. Monod, "Découverte de nappes de charriage dans le Nord de Taurus occidental (Turquie)," *Comp Rend Acad Sci, sér D*, vol. 266, pp. 988-991, 1968.
- [34] M. Gutnic, O. Monod, A. Poisson, F. Dumont, "Géologie des Taurides Occidentales (Turquie)," *Mémoir Soc Geol France*, vol. 137, pp. 1-112, 1979.
- [35] J.H. Brunn, P.C. De Graciansky, M. Gutnic, T. Juteau, R. Lefevre, J. Marcoux, O. Monod, A. Poisson, "Structures majeures et corrélations stratigraphiques dans les Taurides occidentales," *Bulletin de la Societe geologique de France*, Vol. 7, No. 3, pp. 515-556, 1970.
- [36] J.H. Brunn, J. Dumont, P.C. De Graciansky, M. Gutnic, T. Juteau, J. Marcoux, O. Monod, A. Poisson, "Outline of the geology of the western Taurids," *Geology and history of Turkey*, Eds: Campbell, A.S., Petroleum Exploration Society of Libya, Tripoli, pp. 225-255, 1971.
- [37] T. Güvenç, "Stratigraphie du Carbonifère et du Permien de la Nappe de Hadim," *6th Colloquium of the Geology of Aegean Regions, Aegean University, İzmir*, pp. 251-261, 1977b.
- [38] A. Turan, *Toroslar'da Hadim (Konya) ve güneybatısının jeolojisi, stratigrafisi ve tektonik gelişimi*, Doktora Tezi, Selçuk Üniversitesi, Fen Bilimleri Enstitüsü, Konya, 1990.
- [39] T. Güvenç, "Permian of Turkey," *6th Colloquium of the Geology of Aegean Regions, Aegean University, İzmir*, pp. 263-282, 1977a.
- [40] C. Okuyucu, T. Güvenç, "Hadim Napı'nda Karbonifer-Permien geçişi, *Girvanella* kireçtaşı oluşum paleontolojisi," *Yerbilimleri*, cilt 30, ss. 463-473, 1997.
- [41] L. Baccelle, and A. Bosellini, *Diagrammi per la stima visiva: della composizione percentuale nelle rocce sedimentarie*, Università degli studi di Ferrara, 1965.
- [42] E. Flügel, *Microfacies of carbonate rocks: analysis, interpretation and application*, 2nd edition, Springer, Heidelberg Dordrecht, London, 2010.



## DETERMINATION OF RESWELLING PROPERTIES AND WATER DIFFUSION MECHANISM OF HYDROGEL COMPOSITES

<sup>1</sup>Mehmet YURTTADUR , <sup>2</sup>Gülcihan GÜZEL KAYA , <sup>3\*</sup>Hüseyin DEVECİ 

*Konya Technical University, Engineering and Natural Sciences Faculty, Chemical Engineering Department,  
Konya, TÜRKİYE*


<sup>1</sup>yurttadurmehmet@gmail.com, <sup>2</sup>ggkaya@ktun.edu.tr, <sup>3</sup>hdeveci@ktun.edu.tr

### *Highlights*

- Hydrogel composites were prepared by free radical polymerization technique
- The composites had higher equilibrium water content in water and at different pHs
- Water diffusion of the composites was governed by less Fickian diffusion mechanism



## DETERMINATION OF RESWELLING PROPERTIES AND WATER DIFFUSION MECHANISM OF HYDROGEL COMPOSITES

<sup>1</sup>Mehmet YURTTADUR , <sup>2</sup>Gülcihan GÜZEL KAYA , <sup>3,\*</sup>Hüseyin DEVECİ 

*Konya Technical University, Engineering and Natural Sciences Faculty, Chemical Engineering Department,  
Konya, TÜRKİYE*

<sup>1</sup>yurttadurmehmet@gmail.com, <sup>2</sup>ggkaya@ktun.edu.tr, <sup>3</sup>hdeveci@ktun.edu.tr

(Received: 06.03.2023; Accepted in Revised Form: 22.05.2023)

**ABSTRACT:** This study focused on acrylamide/*N*-vinyl-2-pyrrolidone chemically cross-linked hydrogel composites. As fillers, sepiolite and alkyl ammonium salt modified sepiolite were used in the preparation of the hydrogel composites. Characterization of the hydrogel composites was carried out with X-ray diffraction (XRD), Fourier transform infrared spectroscopy (FTIR) and scanning electron microscopy (SEM) analyses. Swelling of the hydrogel composites as a function of time was investigated with tea-bag method. Reswelling ability of the hydrogel composites was revealed after the three cycles. In the third swelling test, the swelling percentage of the NVP hydrogel was about 1690%. The swelling percentage of the NVP+MSP hydrogel composite increased from approximately 1610% to 1760% after the three repeated swelling tests. The hydrogel composite including modified sepiolite showed higher equilibrium water content (EWC) in the distilled water and at different pHs compared to other samples. The highest EWC value was obtained for the hydrogel composite including modified sepiolite (0.9637) in alkali conditions. Water diffusion mechanism of the hydrogel composites was examined based on the Fickian diffusion index (*n*). *n* values of the hydrogel composites were lower than 0.5 which is indication of water diffusion governed by less Fickian diffusion mechanism. The results showed that hydrogel composites can be used in various applications required the reswelling ability and high EWC value.

**Keywords:** *Alkyl Ammonium Salt, Hydrogel, Reswelling Ability, Sepiolite, Water Diffusion Mechanism*

### 1. INTRODUCTION

Hydrogels are defined as 3D polymer networks which uptake a large quantity of water or various biological fluids [1]. The main advantages of hydrogels such as high water uptake, responsiveness to external factors (light, pH, temperature, electrical and magnetic field *etc.*), biocompatibility and biodegradability make hydrogels smart materials [2, 3]. Due to their desired properties, hydrogels are utilized in drug delivery, tissue engineering, contact lenses, hygiene materials, electrochemical applications, separation processes, food industry and agriculture [4, 5].

In general, hydrogels are synthesized with chain growth polymerization or step growth polymerization. Owing to hydrophilic segments of hydrogels, cross-linking step is required to prevent the hydrophilic segment dissolution in an aqueous medium. Hydrophilic polymers exhibit Newtonian behavior in the absence of cross-linker. When cross-linkers are used, hydrogels exhibit visco-elastic or non-Newtonian behavior [6]. Based on cross-linking methods, hydrogels are separated into: chemically and physically cross-linked hydrogels. Chemically cross-linking is conducted through chemical reactions of complementary groups, high energy radiation, free radical polymerization and cross-linking with enzymes. On the other hand, hydrogen bonding, chain entanglements,  $\pi$ - $\pi$  stacking, metal-ligand coordination, ionic interactions, hydrophobic interactions, crystallization, Van der Waals forces and protein interactions are effective for physically cross-linking [7, 8].

Swelling is one of the most important properties for hydrogel applications. The swelling process takes place in three stages: water diffusion into hydrogel structure, polymer chain loosening and hydrogel expansion, respectively [9]. Swelling ratio of hydrogels generally changes depending on monomer type and concentration, cross-linking degree, external stimuli, solvent type and concentration,

\*Corresponding Author: Hüseyin DEVECİ, [hdeveci@ktun.edu.tr](mailto:hdeveci@ktun.edu.tr)



initiator content as well as surface functionalization of hydrogels [10, 11]. For example, low amount of cross-linker can hinder formation of hydrogel network effectively which adversely affects water uptake. Using high amount of cross-linker can result in high cross-linking degree, so leading limited water diffusion into hydrogel structure [12]. Moreover, type of monomer including hydrophilic or hydrophobic groups alters swelling properties of hydrogels. Hydrophilic groups have synergistic effects on the swelling ratio of hydrogels. However, hydrophobic groups prevent interactions between water and hydrogel network that decreases swelling capacity [13].

To enhance swelling properties, incorporation of fillers such as metals, metal oxides, polymers, clays and carbonaceous materials is a promising strategy [14]. Clays (kaolin, vermiculite, montmorillonite, bentonite, sepiolite, and so on) are widely used as filler owing to their abundance, low-cost, hydrophilic structure and easiness of preparation [15]. In case of preparation of hydrogel composites, hydrophobic structure of polymers can limit homogeneous dispersion of clays. So, clay modification is generally applied using alkyl ammonium salts such as tetramethyl ammonium bromide, hexadecyl ammonium chloride and octadecyl trimethyl ammonium bromide to provide uniform dispersion of clays in polymer network [16, 17].

This study focused on acrylamide/*N*-vinyl-2-pyrrolidone chemically cross-linked hydrogel composites. Reswelling in water and equilibrium water content of the hydrogel composites were determined based on data collected by tea-bag method. Water diffusion mechanism of the hydrogel composites was investigated with Fick's law of diffusion. Effects of presence of sepiolite in the hydrogel network and sepiolite modification with an alkyl ammonium salt on the swelling/reswelling properties, equilibrium water content and water diffusion were studied in detail. Characterization of the hydrogel composites was carried out X-ray diffraction (XRD), Fourier transform infrared spectroscopy (FTIR) and scanning electron microscopy (SEM) analyses. When compared to literature studies related to hydrogel composites including clays, significant advantages of the hydrogel composites prepared in this study were discussed.

## 2. MATERIAL AND METHODS

### 2.1. Materials

Acrylamide (Merck) and *N*-vinyl-2-pyrrolidone (Sigma-Aldrich) as a monomer were used. Ammonium persulfate (Sigma-Aldrich) was utilized as reaction initiator. Ethylene glycol dimethacrylate (Sigma-Aldrich) and *N,N,N',N'*-tetramethylethylenediamine (Sigma-Aldrich) were used as cross-linker and accelerator, respectively. Sepiolite with the molecular formula of  $Mg_8Si_{12}O_{30}(OH)_4(H_2O)_{4.8}H_2O$  was evaluated as a filler. Tetramethyl ammonium chloride (Merck) was used to modify sepiolite. Distilled water was used for synthesis and swelling studies.

### 2.2. Hydrogel Synthesis

Free radical polymerization technique was used for hydrogel synthesis [18]. Acrylamide solution and *N*-vinyl-2-pyrrolidone were mixed with the mole ratio of 1:1. Cross-linker (0.05 mL) was added to monomer solution under the reflux. After the addition of 0.01 g initiator and 100  $\mu$ L accelerator into the solution, gel was obtained at 50 °C. Removal of impurities from the gel was provided with water washing at room temperature and the gel was dried at 50 °C until reaching to constant mass. The hydrogel was called as *N*-vinyl-2-pyrrolidone (NVP) hydrogel.

### 2.3. Preparation of Hydrogel Composites

Following to the cross-linker mixing with monomer solution, sepiolite with 1 wt% was added to the solution. After the homogeneous dispersion of sepiolite, initiator and accelerator was added to suspension. Gel formation was observed at 50 °C, and then similar washing and drying were applied to

prepare hydrogel composite as in the hydrogel synthesis. The hydrogel composite was called as *N*-vinyl-2-pyrrolidone + sepiolite (NVP+SP) hydrogel composite.

Hydrogel composite was also prepared by using modified sepiolite as mentioned above. For sepiolite modification, sepiolite was dispersed in distilled water (1:5, w:v) and tetramethyl ammonium chloride solution was added to suspension. The suspension was stirred for 24 h at room temperature. Modified sepiolite was washed with distilled water until removal of Cl<sup>-</sup> ions which was controlled with 0.1 N AgNO<sub>3</sub> solution. The modified sepiolite was dried at 60 °C. The hydrogel composite was called as *N*-vinyl-2-pyrrolidone + modified sepiolite (NVP+MSP) hydrogel composite.

#### 2.4. Characterization of Samples

XRD analyses were performed by Bruker D8 Advance equipment (Cu-K $\alpha$  radiation,  $\lambda$ : 1.54 Å). FTIR analyses were conducted on Bruker Vertex 70 spectrometer in the range of 4000-1000 cm<sup>-1</sup>. SEM analyses were carried out by SM Zeiss LS-10 device.

#### 2.5. Swelling and Diffusion Studies of Samples

To examine water uptake of the samples through tea-bag method, the samples were put in distilled water at room temperature. The samples were taken out from the water and wiped excess water with a tissue paper. The mass of the samples were recorded and swelling percentage (*S*, %) was determined by the following equation [19]:

$$S = \frac{m_1 - m_0}{m_0} \times 100 \quad (1)$$

where *m*<sub>1</sub> and *m*<sub>0</sub> indicate mass of the samples at time *t* and initial, respectively.

Reswelling behaviour of the samples was investigated in distilled water with repeating swelling experiment three times at room temperature. After each swelling test, the swollen samples were dried at 50 °C. The dried samples were used again for the next swelling test.

Equilibrium water content (EWC) of the samples in distilled water and at different pHs was determined by the following equation [20]:

$$EWC = \frac{m_1 - m_0}{m_1} \quad (2)$$

Water diffusion mechanism of the samples in distilled water and at different pHs was explained based on the following equation [21]:

$$F = \frac{m_1}{m_\infty} = kt^n \quad (3)$$

where *m*<sub>∞</sub> shows mass of the sample at equilibrium point. *k* is swelling rate constant and *n* is diffusion index which is used to determine type of the water diffusion. This equation can be applied in case of *F* < 0.6 [22].

### 3. RESULTS AND DISCUSSION

Figure 1 shows XRD pattern of the samples. With the incorporation of 1 wt% sepiolite or 1 wt% modified sepiolite, no significant change was specified XRD pattern of the samples. A common broad diffraction peaks at about 2 $\theta$  = 13° and 22° in the XRD pattern of the samples indicated that the samples were in the amorphous state [23].

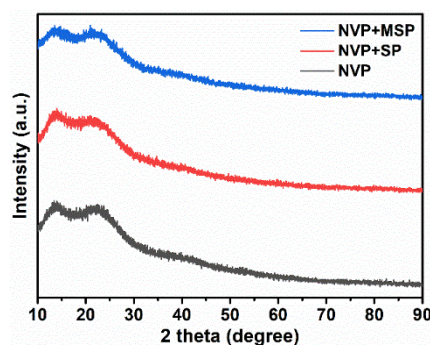


Figure 1. XRD pattern of the samples

Figure 2 shows FTIR spectrum of the samples. The band related to stretching of  $\text{-OH}$  was determined at the centered of  $3400\text{ cm}^{-1}$ . The peak at  $3166\text{ cm}^{-1}$  was attributed to N-H stretching vibrations. The peaks at  $2927\text{ cm}^{-1}$  and  $2880\text{ cm}^{-1}$  were contributed to asymmetric and symmetric stretching vibrations of C-H, respectively. Formation of C=O groups between acrylamide and *N*-vinyl-2-pyrrolidone resulted in appearance of the peak at  $1670\text{ cm}^{-1}$ . The peaks at  $1460\text{ cm}^{-1}$  and  $1280\text{ cm}^{-1}$  were assigned to C-H deformation of  $\text{CH}_2$  groups and C-N stretching, respectively [24]. The peak at  $1172\text{ cm}^{-1}$  was originated from C-C stretching of *N*-vinyl-2-pyrrolidone ring [25].

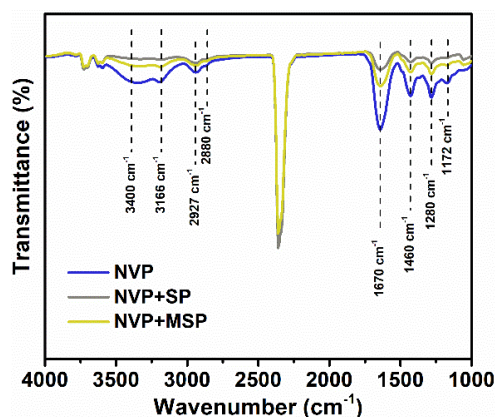
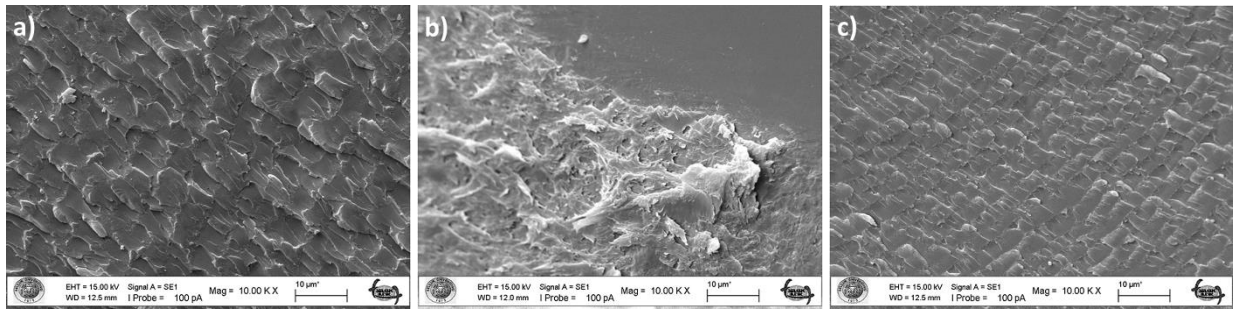


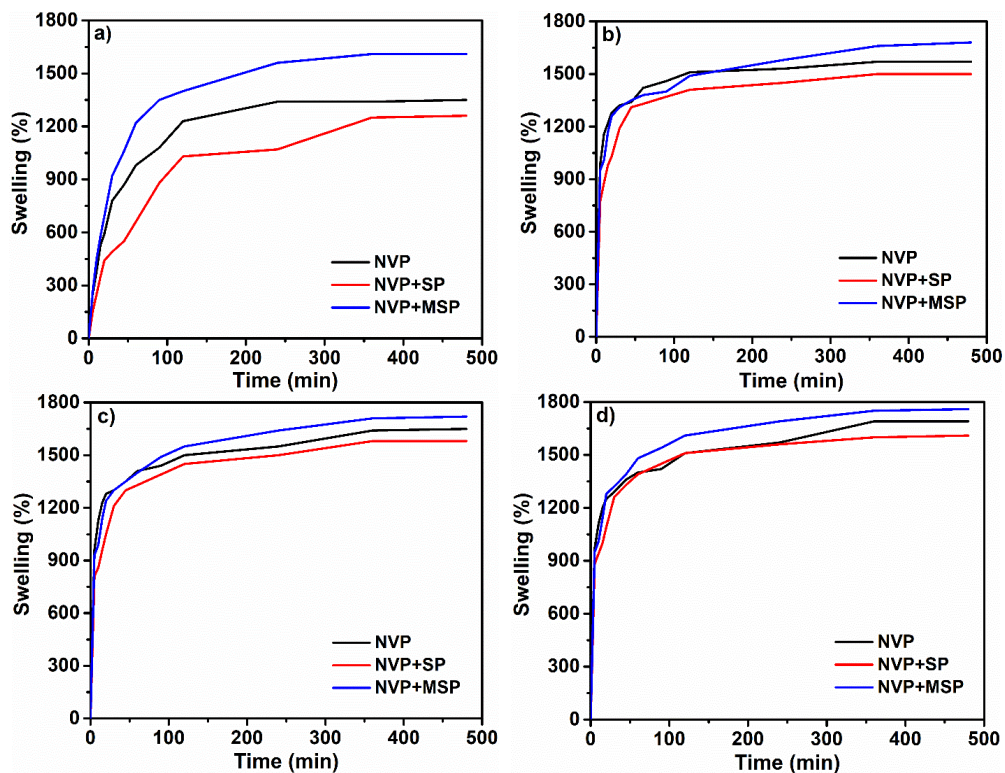
Figure 2. FTIR spectrum of the samples

Figure 3 shows morphological structure of the samples. In the SEM image of the NVP hydrogel (Figure 3a), regular layers which are effective in water diffusion were observed. While using unmodified sepiolite, uneven surface belonged to the NVP+SP hydrogel composite was obtained (Figure 3b). And also, formation of the agglomerated structure was determined that has generally adverse effects on the water uptake of the materials [26, 27]. Whereas, homogeneous dispersed NVP+MSP hydrogel composite including regular layers was prepared with the incorporation of modified sepiolite into the hydrogel network as shown in Figure 3c. It is known that interlayer distance between the clay plates increase in case of mixing with monomer molecules providing the formation of layered structure that makes diffusion of water molecules easy into the hydrogel network [28].



**Figure 3.** SEM image of the a) NVP hydrogel, b) NVP+SP hydrogel composite and c) NVP+MSP composite hydrogel

Figure 4a shows swelling percent of the samples in time. In the beginning, swelling percentage of the samples rapidly increased, and then swelling rate slowed down. In case of using neat sepiolite, a slight decrease in the swelling percentage of the NVP hydrogel was observed which was attributed to nonhomogeneous dispersion of the sepiolite in the hydrogel structure. However, the swelling percentage of the NVP hydrogel increased with the incorporation of modified sepiolite. By the help of modification, separation of layers of the sepiolite as well as uniform dispersion of the sepiolite had synergistic effects on the water uptake of the NVP+MSP hydrogel composite.



**Figure 4.** a) Original swelling, b) first reswelling, c) second reswelling and d) third reswelling of the samples

Figure 4b-d show ability of the samples to swell in the water over several cycles. It was clear that all the samples exhibited similar reswelling behaviour in the water. Original swelling percentage of the NVP hydrogel was determined as about 1350%. In the third swelling test, the swelling percentage of the NVP hydrogel was about 1690%. The swelling percentage of the NVP+MSP hydrogel composite increased from approximately 1610% to 1760% after the three repeated swelling tests. The results revealed that the swelling percentage of the samples was higher than that of their original swelling percentage based on the repeated swelling tests. No defect in the hydrogel network such as crack and

degradation was observed. So, it was obvious that the samples can be used for many times in various applications including reswelling ability.

EWC of the samples is given in Table 1. The samples had considerably high EWC which is associated with good biocompatibility of the materials in general [29]. EWC of the NVP hydrogel and NVP+SP hydrogel composite was about 0.95 in distilled water and at different pHs. Due to the utilization of modified sepiolite, NVP+MSP hydrogel composite exhibited higher EWC compared to other samples. At low pH, EWC of the NVP+MSP hydrogel composite was lower than that assigned to packed form of polymer chains due to hydrogen bonds between  $-\text{COOH}$  groups [30]. Ionization of  $-\text{COOH}$  groups into  $-\text{COO}^-$  ions with increasing pH leads to repulsion forces between polymer chains that contribute higher swelling capacity [31]. The lowest EWC of the NVP+MSP hydrogel composite was 0.9561 at pH 2, while the highest EWC was specified as 0.9637 at pH 9 in this study.

**Table 1.** EWC of the samples

Samples	Distilled water	pH 2	pH 7	pH 9
NVP	0.9547	0.9545	0.9559	0.9539
NVP+SP	0.9523	0.9519	0.9555	0.9523
NVP+MSP	0.9609	0.9561	0.9593	0.9637

Figure 5 shows  $\ln F$  vs.  $\ln t$  curves of the samples. Water diffusion mechanism is generally specified based on the slope of the curves ( $n$  value). Depending on  $n$  value, diffusion mechanism is classified as less Fickian diffusion, Fickian diffusion and non-Fickian diffusion. While  $n$  value equals to 0.5, water diffusion is rate limiting [32]. In case of  $n < 0.5$ , less Fickian diffusion takes place which means that water diffusion rate is lower than relaxation rate of the polymer chains [33]. Non-Fickian diffusion is observed when  $0.5 < n < 1.0$  that is indication of dominance of water diffusion rate or comparable relaxation and diffusion rate [34]. In this study,  $n$  values were lower than 0.5 which is evidence of less Fickian diffusion.

#### 4. CONCLUSIONS

This work was related to reswelling properties and water diffusion mechanism of the hydrogel composites. Hydrogel composites were prepared by using sepiolite and alkyl ammonium salt modified sepiolite by free radical polymerization technique. Amorphous structure of the hydrogel composites was observed by XRD analyses. Characteristic peaks in the FTIR spectrum of the hydrogel composites were indication of successful preparation of the samples. Dispersion of the filler in the polymer chains was investigated by SEM analyses. Uniform dispersion of the modified sepiolite in the hydrogel network was specified in the SEM image in contrast to sepiolite.

Ability of the hydrogel composites to swell in the water over several cycles was examined. The swelling percentage of the hydrogel composites was higher than that of their original swelling percentage, after the repeated swelling tests without crack or degradation. Based on the EWC of the samples, the lowest swelling percentage belonged to NVP+SP hydrogel. However, NVP+MSP hydrogel composite exhibited higher swelling percentage by the help of regular layered structure. The highest EWC of the NVP+MSP hydrogel composite was determined at pH 9 due to the ionization of  $-\text{COOH}$  groups.  $n$  values lower than 0.5 obtained from  $\ln F$  vs.  $\ln t$  curves revealed that water diffusion mechanism of the hydrogel composites can be explained with lower water diffusion rate than relaxation rate of the polymer chains.

The results showed that hydrogel composite especially including the modified sepiolite can be used in various applications required the reswelling ability and high EWC value.

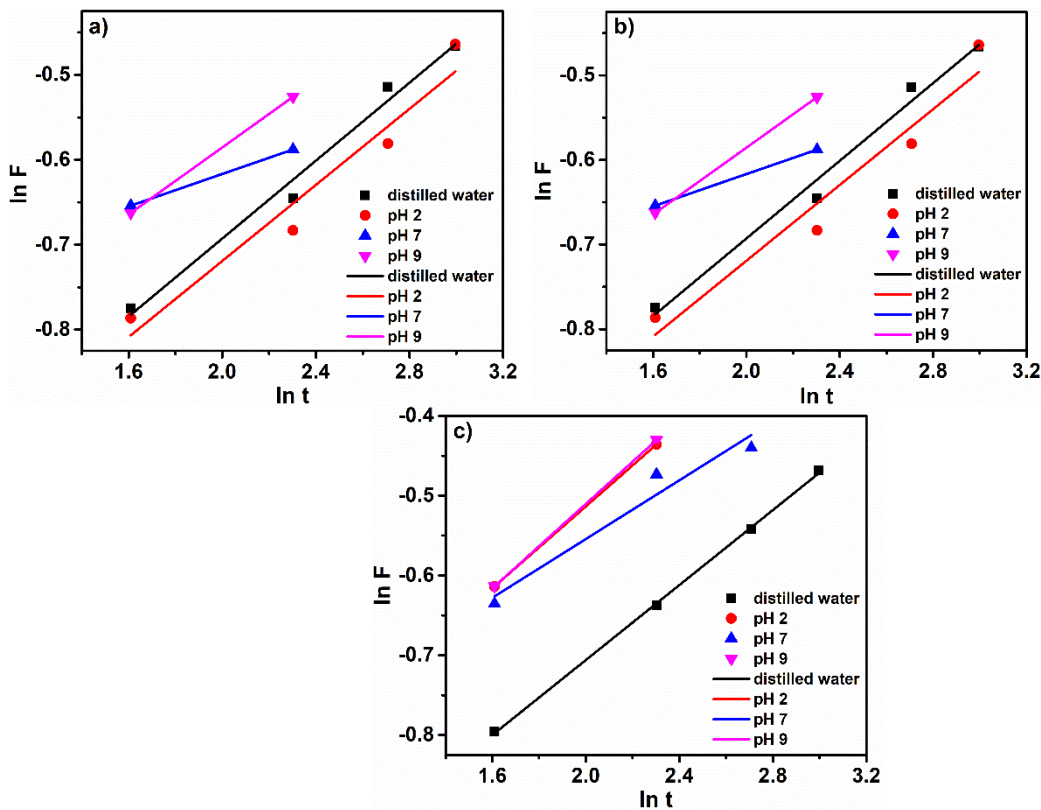


Figure 5.  $\ln F$  vs.  $\ln t$  curve of a) NVP hydrogel, b) NVP+SP hydrogel composite and c) NVP+MSP hydrogel composite

### Declaration of Competing Interest

The authors declare that they have no known competing financial interests or personal relationships that could have appeared to influence the work reported in this paper.

### Funding / Acknowledgements

The authors thank to the Konya Technical University Coordinatorship of Scientific Research Projects (Grant number: 211016001).

### REFERENCES

- [1] A. Maleki, J. He, S. Bochani, V. Nosrati, M.-A. Shahbazi, and B. Guo, "Multifunctional Photoactive Hydrogels for Wound Healing Acceleration," *ACS Nano*, vol. 15, no. 12, pp. 18895-18930, 2021.
- [2] S. Huang *et al.*, "Nanocomposite hydrogels for biomedical applications," *Bioengineering & Translational Medicine*, vol. 7, no. 3, p. e10315, 2022.
- [3] F. Ullah, M. B. Othman, F. Javed, Z. Ahmad, and H. Md Akil, "Classification, processing and application of hydrogels: A review," *Materials Science and Engineering C: Materials for Biological Applications*, vol. 57, pp. 414-33, 2015.
- [4] G. Stojkov, Z. Niyazov, F. Picchioni, and R. K. Bose, "Relationship between structure and rheology of hydrogels for various applications," *Gels*, vol. 7, no. 4, p. 255, 2021.
- [5] E. Caló and V. V. Khutoryanskiy, "Biomedical applications of hydrogels: A review of patents and commercial products," *European Polymer Journal*, vol. 65, pp. 252-267, 2015.

- [6] P. Sikdar *et al.*, "Recent advances in the synthesis of smart hydrogels," *Materials Advances*, vol. 2, no. 14, pp. 4532-4573, 2021.
- [7] W. E. Hennink and C. F. van Nostrum, "Novel crosslinking methods to design hydrogels," *Advanced Drug Delivery Reviews*, vol. 64, pp. 223-236, 2012.
- [8] W. Hu, Z. Wang, Y. Xiao, S. Zhang, and J. Wang, "Advances in crosslinking strategies of biomedical hydrogels," *Biomaterials Science*, vol. 7, no. 3, pp. 843-855, 2019.
- [9] S. Bashir *et al.*, "Fundamental concepts of hydrogels: Synthesis, properties, and their applications," *Polymers (Basel)*, vol. 12, no. 11, 2020.
- [10] A. H. Karoyo and L. D. Wilson, "A review on the design and hydration properties of natural polymer-based hydrogels," *Materials*, vol. 14, no. 5, p. 1095, 2021.
- [11] A. Pourjavadi, S. Barzegar, and G. R. Mahdavinia, "MBA-crosslinked Na-Alg/CMC as a smart full-polysaccharide superabsorbent hydrogels," *Carbohydrate Polymers*, vol. 66, no. 3, pp. 386-395, 2006.
- [12] U. S. K. Madduma-Bandarage and S. V. Madihally, "Synthetic hydrogels: Synthesis, novel trends, and applications," *Journal of Applied Polymer Science*, vol. 138, no. 19, p. 50376, 2020.
- [13] W. A. Laftah, S. Hashim, and A. N. Ibrahim, "Polymer hydrogels: A review," *Polymer-Plastics Technology and Engineering*, vol. 50, no. 14, pp. 1475-1486, 2011.
- [14] P. Thoniyot, M. J. Tan, A. A. Karim, D. J. Young, and X. J. Loh, "Nanoparticle-hydrogel composites: Concept, design, and applications of these promising, multi-functional materials," *Advanced Science*, vol. 2, no. 1-2, p. 1400010, 2015.
- [15] K. Kabiri, H. Omidian, M. J. Zohuriaan-Mehr, and S. Doroudiani, "Superabsorbent hydrogel composites and nanocomposites: A review," *Polymer Composites*, vol. 32, no. 2, pp. 277-289, 2011.
- [16] S. A. Khan and T. A. Khan, "Clay-hydrogel nanocomposites for adsorptive amputation of environmental contaminants from aqueous phase: A review," *Journal of Environmental Chemical Engineering*, vol. 9, no. 4, p. 105575, 2021.
- [17] G. I. Nakas and C. Kaynak, "Use of different alkylammonium salts in clay surface modification for epoxy-based nanocomposites," *Polymer Composites*, vol. 30, no. 3, pp. 357-363, 2009.
- [18] E. Yilmaz, G. Guzel Kaya, and H. Deveci, "Preparation and characterization of pH-sensitive semi-interpenetrating network hybrid hydrogels with sodium humate and kaolin," *Applied Clay Science*, vol. 162, pp. 311-316, 2018.
- [19] S. Bian *et al.*, "An injectable rapid-adhesion and anti-swelling adhesive hydrogel for hemostasis and wound sealing," *Advanced Functional Materials*, vol. 32, no. 46, p. 2207741, 2022.
- [20] H. Jiang, N. Bao, J. Tang, and H. Li, "Anomalous mechanical strengthening of nanocomposite hydrogels upon swelling," *Chemical Engineering Journal*, vol. 455, p. 140573, 2023.
- [21] Y. Ding, R. Tang, Y. Feng, M. Yuan, H. Li, and M. Yuan, "Synthesis and characterisation of high resilience collagen-polyacrylamide semi-interpenetrating network hydrogel," *Materials Today Communications*, vol. 32, p. 103955, 2022.
- [22] Z. E. Ibraeva, A. A. Zhumaly, E. Blagih, and S. E. Kudaibergenov, "Preparation and characterization of organic-inorganic composite materials based on poly(acrylamide) hydrogels and clay minerals," *Macromolecular Symposia*, vol. 351, no. 1, pp. 97-111, 2015.
- [23] N. Sarkar, G. Sahoo, and S. K. Swain, "Nanoclay sandwiched reduced graphene oxide filled macroporous polyacrylamide-agar hybrid hydrogel as an adsorbent for dye decontamination," *Nano-Structures & Nano-Objects*, vol. 23, p. 100507, 2020.
- [24] V. D. Mane, N. J. Wahane, and W. B. Gurnule, "Copolymer resin. VII. 8-hydroxyquinoline-5-sulfonic acid-thiourea-formaldehyde copolymer resins and their ion-exchange properties," *Journal of Applied Polymer Science*, vol. 111, no. 6, pp. 3039-3049, 2009.
- [25] E. Erizal, T. Tjahyono, P. P. Dian, and D. Darmawan, "Synthesis of polyvinyl pyrrolidone (PVP)/k-carrageenan hydrogel prepared by gamma radiation processing as a function of dose and PVP concentration," *Indonesian Journal of Chemistry*, vol. 13, no. 1, pp. 41-46, 2013.

- [26] A. Olad, H. Zebhi, D. Salari, A. Mirmohseni, and A. Reyhani Tabar, "Water retention and slow release studies of a salep-based hydrogel nanocomposite reinforced with montmorillonite clay," *New Journal of Chemistry*, vol. 42, no. 4, pp. 2758-2766, 2018.
- [27] Y. Tan *et al.*, "Electric field-induced gradient strength in nanocomposite hydrogel through gradient crosslinking of clay," *Journal of Materials Chemistry B*, vol. 3, no. 21, pp. 4426-4430, 2015.
- [28] C. Teng, D. Xie, J. Wang, Y. Zhu, and L. Jiang, "A strong, underwater superoleophobic PNIPAM-clay nanocomposite hydrogel," *Journal of Materials Chemistry A*, vol. 4, no. 33, pp. 12884-12888, 2016.
- [29] D. Shi, X. Zhang, W. Dong, and M. Chen, "Synthesis and biocompatibility of phosphoryl polymer and relationship between biocompatibility and water structure," *Polymer Science Series B*, vol. 54, no. 5, pp. 335-341, 2012.
- [30] T. Çaykara and İ. Ayçiçek, "pH-responsive ionic poly(N,N-diethylaminoethyl methacrylate-co-N-vinyl-2-pyrrolidone) hydrogels: Synthesis and swelling properties," *Journal of Polymer Science Part B: Polymer Physics*, vol. 43, no. 19, pp. 2819-2828, 2005.
- [31] C. Özyürek, T. Çaykara, Ö. Kantoğlu, and O. Güven, "Characterization of network structure of poly(N-vinyl 2-pyrrolidone/acrylic acid) polyelectrolyte hydrogels by swelling measurements," *Journal of Polymer Science Part B: Polymer Physics*, vol. 38, no. 24, pp. 3309-3317, 2000.
- [32] Y. Li *et al.*, "A rapid, non-invasive and non-destructive method for studying swelling behavior and microstructure variations of hydrogels," *Carbohydrate Polymers*, vol. 151, pp. 1251-1260, 2016.
- [33] B. Singh, G. S. Chauhan, D. K. Sharma, A. Kant, I. Gupta, and N. Chauhan, "The release dynamics of model drugs from the psyllium and N-hydroxymethylacrylamide based hydrogels," *International Journal of Pharmaceutics*, vol. 325, no. 1, pp. 15-25, 2006.
- [34] J. Wang, W. Wu, and Z. Lin, "Kinetics and thermodynamics of the water sorption of 2-hydroxyethyl methacrylate/styrene copolymer hydrogels," *Journal of Applied Polymer Science*, vol. 109, no. 5, pp. 3018-3023, 2008.



## MODELLING APPROACH FOR ENERGY DEMAND AND CONSUMPTION USING GENERALIZED LINEAR MODELS

\*Fuad ALHAJ OMAR 

*Zonguldak Bülent Ecevit University, Electric and Energy Department, Zonguldak, TÜRKİYE*  
[fuad.a@beun.edu.tr](mailto:fuad.a@beun.edu.tr)

### *Highlights*

- Statistical analysis of energy consumption data using R-Studio.
- Energy consumption model for households in Syria.
- The most cost-effective energy sources in Syria.

### *Graphical Abstract*





## MODELLING APPROACH FOR ENERGY DEMAND AND CONSUMPTION USING GENERALIZED LINEAR MODELS

\*Fuad ALHAJ OMAR 

Zonguldak Bülent Ecevit University, Electric and Energy Department, Zonguldak, TÜRKİYE  
[fuad.a@beun.edu.tr](mailto:fuad.a@beun.edu.tr)

(Geliş/Received: 09.12.2022; Kabul/Accepted in Revised Form: 25.05.2023)

**ABSTRACT:** Energy management is an important process for maintaining available energy resources and meeting basic household energy needs. Many studies seek to optimize the household energy consumption patterns to manage the load demand and minimize energy costs. Adopting such optimizations in conflict-affected countries is more beneficial due to limited energy sources. This study identifies the optimal energy consumption model for households in northern Syria. The objective is to identify the most cost-efficient energy sources while considering the prices, average monthly household income, the main source of electricity, battery storage capacity, and energy demands for space heating, water heating and cooking. One hundred and thirty-six (136) standardized surveys of residential households are collected and used as a test case. Statistical analysis of the data was carried out using the R-Studio software, where Poisson regression and negative binomial regression were employed. Findings revealed that the Negative Binomial (NB) model used has high explanatory power. In addition, the energy sources used for space heating and water heating have a direct impact on monthly expenditures. The produced model showed that the most cost-effective energy sources are coal for space heating and natural gas and kerosene for water heating.

**Keywords:** Energy Efficient, Energy Management, Optimizing Energy, Poisson Regression, Negative Binomial Regression

### 1. INTRODUCTION

Most of the electricity infrastructures during the Syrian civil war have been destroyed [1-3]. This has been having a devastating effect on more than 90% of Syrians. As the main source of power supplies dropped off, Syrians had to be creative in finding alternative sources for light and power. Across Syria, people survive with little or no energy. Energy poverty has a knock-on effect on other basic services like water supplies and health services [4, 5]. We have seen first-hand the damaging effects of power shortages in Syria. We witnessed the devastating effect of the energy shortage on millions of Syrians. Aleppo city was Syria's powerhouse and home to over four million people. It became a battleground and remained so for more than four years. Syrians were undergoing enormous suffering because of cuts to energy supplies, used by each of the opposing parties to pressure the other. Energy shortage became a matter of life or death. Our recent pilot research (submitted for publication) showed that energy shortages have a direct impact on displacement and immigration, create barriers to education, and reduce social and psychological well-being. Therefore, the most cost-effective energy sources must be urgently identified to help people secure their main energy needs at the lowest costs. Thus, improving the energy use efficiency according to the household's monthly income. This research focuses on creating societal and ecosystem changes and develops a novel solution to the energy efficiency problem in north Syria that is more effective, efficient, sustainable and is beneficial primarily to society as a whole rather than private individuals. The results will have an impact on improving the households' living conditions where perceived self-efficacy with energy-saving behaviors and knowledge about behaviors all relate to achieving sustainability.

\*Corresponding Author: Fuad ALHAJ OMAR, [fuad.a@beun.edu.tr](mailto:fuad.a@beun.edu.tr)

Existing literature has highlighted the management and optimization of energy consumption. The challenge is that Syria has been ranked as one of the fragile states globally in the past decade [6]. In fact, the conflicts between two parties, which are the prevailing form in most countries in the Middle East, do not result in positive social change or military victory for any party [7, 8]. Moreover, the prolonged period of conflicts in the Middle East may generate successive waves of conflicts [9]. Armed conflict may be exacerbated by natural and environmental threats such as climate change and urbanization. As well, the rapid change in advanced technology, communication systems, and the media may produce new and unfamiliar forms of wars [10]. Wherefore, any conventional development plans may be condemned to failure [11], and hence energy planning models are also susceptible to failure [12]. Therefore, there is a need to understand the complex structure of conflicts in order to develop flexible and long-term plans and strategies to address the energy problem [13, 14].

Some studies have considered the context when seeking to solve energy problems facing fragile societies by attempting to achieve the best available options [15-18]. For instance, the cost of capital for investing in solar energy has been changed according to different political situations [19]. Pettersson and Wallenstein [20] examined how the energy and water infrastructure can be made more resilient in the face of armed conflicts between two parties.

Zerriffi et al. [21] explained how the system attributes that are useful under conflict might undervalue if the reliability assessment takes into account only normal operating situations. Brazilian et al. [22] explained that typical values of parameters in a fragile country are unrealistic, which makes the resulting recommendations also irrelevant. Instead of that, they considered the fragility when developing the least expensive planning models through lower available capital, higher interest rates, extended construction time, and damages over the entire planning period.

Patankar et al. [23] believed that the generating assets could be damaged as a result of the conflict in South Sudan, so they decided to use stochastic programming to test power system plans that are not affected by risks.

In any case, all the proposed models and strategies were simulating the context in the studied area, whose conditions differ from one country to another. In other words, the strategies and models proposed in a particular context cannot be fully adopted in another context because the conditions and the nature of the conflict are different.

After the 2011 Arab spring, the Middle East was affected by socioeconomic factors. That pushed states deeper into a vicious cycle of poverty and deterioration [24]. Socio-economic factors are associated with high unemployment, poverty, social inequality, and frustration, all of which lead to the loss of human capital that is exacerbated after adding the high cost of living and unemployment [25]. The depletion of available resources, inflation, dependence on imports and price fluctuations exacerbate the social-economic problems [26, 27]. All of these factors combined can lead to internal and international displacement, and these displacement movements can be exacerbated as a result of protracted armed conflicts [28]. The displacement movements and the concentration of population in a limited area can lead to the collapse of infrastructure and insufficient resources available to meet the growing need [13, 29, 30].

As a result of the ongoing conflict in Syria, there has been a significant exodus towards northern Syria. Our recent research showed that there are about four million people living in North and Northwest Syria. As a result of this population density, there is a huge gap between available energy and household requirements. The energy burden for limited-income households has increased due to fluctuating prices of fossil fuels, outdated appliances, and energy inefficient homes [4]. Accordingly, there is an urgent need to build an energy consumption model to identify the most cost-effective energy sources to help people in northern Syria optimize their energy use.

In this paper, we have developed a feasible and actionable model that identifies the most cost-effective energy sources according to the household's monthly income. Two models were built based on Poisson

regression and negative binomial regression, and according to the regression model evaluation criteria, the optimal model was determined. Note that this model only fits the context in northern Syria. However, the modelling and analysis method can be applied to propose a model compatible with any context elsewhere.

## 2. METHODOLOGY

In the framework of this study, the methodology was based on the collection of statistical information by using structured questionnaires. These served to explore deeply the reality of energy in northern Syria. We focused on families (head of household) for determining the daily need and consumption of energy in the target region. The questionnaire was coded to be used by the program “KoBo Toolbox”; this is a free open-source tool to collect data using mobile devices without a network connection. Before starting the questionnaire, the team consisting of 22 specialized data collectors (12 males and 10 females) was well trained on the questionnaire, and several experimental questionnaires were conducted to ensure the quality of the method used, also to ensure that the questions are clear, understandable, and appropriate to the context of the target region.

Also, considering the Syrian context, we were keen to form teams for data collectors, each team consisting of a male and a female, and therefore we did not face any challenges related to conducting the interviews with the female adults when the head of household is not available at home, so the sample was representative of females as well. The sample size was 136 samples of both genders and of different ages. The collected samples were randomly selected from 35 communities located in northern Syria as shown in Fig. 1. After reviewing the collected data, the analysis and modelling process was performed. Parameters of the Negative Binomial and Poisson regression models are estimated using the maximum likelihood (ML) method with “Newton Raphson (NR)” and “Fisher-Scoring (FS)” iterative algorithms in R software. Figure 2 shows the flow chart of the methodology stages.

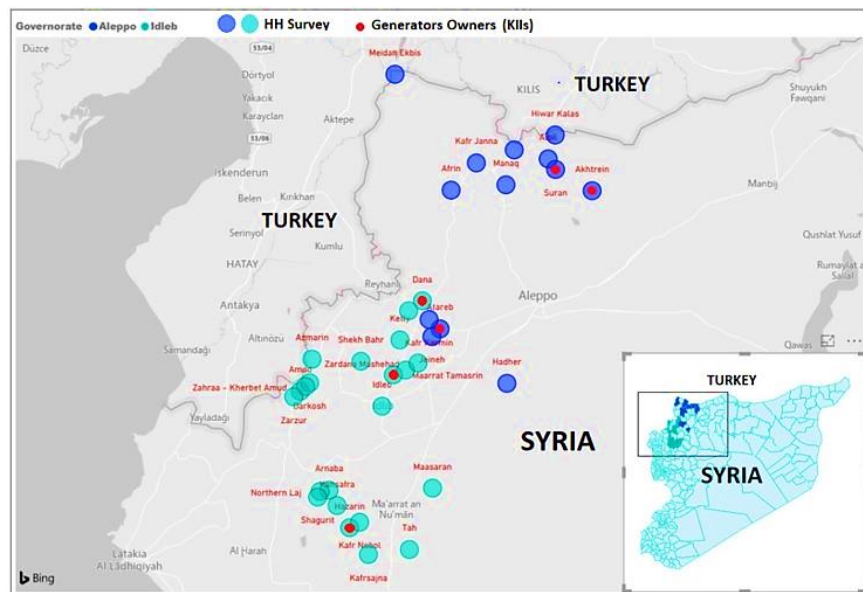
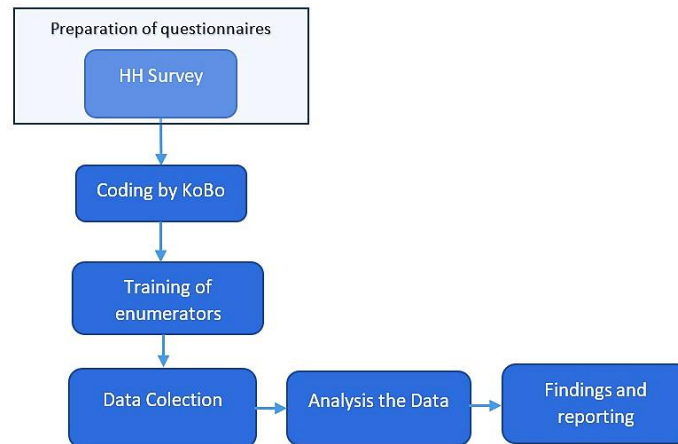


Figure 1. Mapping of targeted communities studied by household survey



**Figure 2.** Flow chart of the methodology

### 3. REGRESSION MODELS

Regression analysis is one of the methods of inferential statistics that is concerned with estimating the relationships between a dependent variable (often called the 'outcome' or 'response' variable) and one or more independent variables [31-33].

The concept of regression dates to the 18th century when it was used to solve astronomical navigation problems. In 1805 Legendre developed the method of least squares to determine the averages of a regression model [34]. Then Gauss showed that this method is really the best solution when the distribution of random errors is normal [35]. This methodology was later used in the physical sciences until the 19th century. Galton was one of the first to use the term "meaning regression," and then regression, in his study of the height of fathers and their children in the late nineteenth century [36, 37].

If the regression model contains one independent variable, it is called a simple regression model, and if it contains more than one independent variable, it is a multiple regression model, and the regression model can be linear or non-linear [33]. The mentioned models are based on quantitative variables, but if the dependent variable is categorical (it has a finite number of categories and therefore has a non-normal distribution), then another model should be used, such as a logistic regression model. Which studies the relationship between a response variable of two classes and the independent variable which can be continuous (quantitative) or discontinuous [38]. When the dependent variable follows a distribution from the exponential family, such as the Poisson distribution, the gamma distribution, and the negative binomial distribution, then in this case generalized linear models are used [39].

#### 3.1. Poisson Regression model

The Poisson regression model is also called the log-linear model and is often used to model count data. In addition, it allows the frequencies of events to depend on one or more variables, provided that the events are independent given these variables [40, 41]. If  $Y$  is the number of occurrences, its probability distribution can be written as [42, 43]:

$$P(y) = \frac{e^{-\mu} \mu^y}{y!}; \quad y = 0, 1, 2, \dots \quad (1)$$

where  $\mu$  is the average number of occurrences and it requires careful definition. Often it needs to be described as a rate.

Let  $Y_1, \dots, Y_N$  be independent random variables with  $Y_i$  denoting the number of events observed from

exposure  $n_i$  for the  $i$ th covariate pattern. The expected value of  $Y_i$  can be written as :

$$E(Y_i) = \mu_i = n_i \cdot \theta_i \quad (2)$$

The dependence of  $\theta_i$  on the explanatory variables is usually modelled by [39]:

$$\theta_i = e^{x_i^T \beta} \quad (3)$$

Therefore, the generalized linear model is:

$$E(Y_i) = \mu_i = n_i e^{x_i^T \beta} ; \quad Var(Y_i) = \mu_i \quad (4)$$

According to the generalized linear model concept, three components are required to form a Poisson model. The first of these is the Poisson distribution, the second one is a linear predictor that describes the relationship between the independent variables and coefficients as follows:

$$\eta_i = \beta_0 + \beta_1 y_{i1} + \beta_2 y_{i2} + \dots + \beta_p y_{i(p)} \quad (5)$$

The third component is a link function to obtain a functional relationship between the expectation of the response variable to linear predictors. There are many link functions for the studied model and the most significant link function is the log link function, which is given as follows:[38, 44, 45];

$$\log \mu_i = \log n_i + x_i^T \beta \quad (6)$$

Equation (6) differs from the usual specification of the linear component due to the inclusion of the term  $\log n_i$ . This term is called the offset. It is a known constant which is readily incorporated into the estimation procedure. As usual, the terms  $x_i$  and  $\beta$  describe the covariate pattern and parameters, respectively.

### 3.2. Negative Binomial (NB) Regression

The negative binomial regression model is derived from Poisson-gamma distribution [46]. The classic derivation of the negative binomial distribution is as the number of failures in Bernoulli trials until  $r$  successes. If  $\pi$  is the probability of success on each Bernoulli trial, then the number of failures  $y$  has the probability function [42]:

$$f(y) = \pi \times \binom{r+y-1}{r-1} \pi^{r-1} (1-\pi)^y \quad (7)$$

$$f(y) = \binom{r+y-1}{r-1} \pi^r (1-\pi)^y, \quad y = 0, 1, 2, \dots \quad (8)$$

which depends on  $\pi$  and  $r$ .

The above formulation supposes  $r$  is a positive integer. However, the negative binomial distribution can be defined for any positive values of  $r$ , by using the gamma function in place of factorials:

$$f(y) = \frac{\Gamma(y+r)}{y! \Gamma(r)} \pi^r (1-\pi)^y, \quad y = 0, 1, 2, \dots \quad (9)$$

In generalized linear modeling the following parametrization is convenient:

$$\mu = \frac{r(1-\pi)}{\pi}, \quad \kappa = \frac{1}{r} \quad (10)$$

Using this notation, the probability function of  $y$  is:

$$f(y) = \frac{\Gamma(y + \frac{1}{\kappa})}{y! \Gamma(\frac{1}{\kappa})} \left( \frac{1}{1 + \kappa \mu} \right)^{\frac{1}{\kappa}} \left( \frac{\kappa \mu}{1 + \kappa \mu} \right)^y, \quad y = 0, 1, 2, \dots \quad (11)$$

The mean and variance of response variable of NB distribution are given as follows:

$$E(y) = \mu, \quad Var(y) = \mu(1 + \kappa \mu) \quad (12)$$

The parameter  $\kappa$  is called the "overdispersion" or "shape" parameter.

The log link function is used for Negative Binomial Regression Model as link function and given as follows:

$$\log(\mu_i) = X' \beta \quad (13)$$

Where:

$X_{i1}, \dots, X_{iq}$  are the independent variables.

$\pi$  is the probability of a claim,

$\mu$  is the mean claim size (the average number of occurrences).

### 3.3. Poisson and NB regression models assumptions

There are some assumptions related to both the Poisson regression and the Negative Binomial regression:

1. Assumption: the conditional probability function of the response variable follows the Poisson distribution with  $\mu$  (the average number of occurrences) [47, 48].

2. Assumption: the Poisson distribution parameter  $\mu$  for the  $i_{th}$  subject equals the exponential form of the linear predictor [39, 45]:

3. Assumption: there is independence between the explanatory and the response variables. By applying the properties of the Poisson distribution to the Poisson regression, the expected value and the variance of the response variable can be written as follows: [41];

$$E(Y_i/X) = Var(Y_i/X) = \mu_i = n_i e^{x_i^T \beta} \quad (15)$$

The conditions of negative binomial models are similar to those of the Poisson model, except that the conditional means do not equal the conditional variance. This variance is calculated by estimating the dispersion coefficient [46].

### 3.4. Overdispersion

The Poisson distribution is often suggested for count data but found to be inadequate because the data displays far greater variance than that predicted by the Poisson. This is termed overdispersion or extra-Poisson variation. Overdispersion occurs when  $Var(Y_i)$  is greater than  $E(Y_i)$ , although  $Var(Y_i) = E(Y_i)$  for the Poisson distribution. Solving the overdispersion problem in the Poisson model is by using an alternative model as the Negative Binomial model where the variance is greater than the mean [45]. The negative binomial distribution provides an alternative model with  $Var(Y_i) = \varphi E(Y_i)$ , where  $\varphi > 1$  is a parameter that can be estimated [42, 43].

### 3.5. Goodness of fit of Statistical regression models

Information criteria (IC) are used as the method of choosing the best generalized linear models such as Akaike information criteria (AIC) and Bayesian information criteria (BIC) [45].

The two criteria require the sum of two main parts, the natural logarithm of a maximum likelihood and the number of parameters of the model as follows: [45];

$$AIC = -2(\log likelihood) + 2S \quad (16)$$

$$BIC = -2(\log likelihood) + S \cdot \log(N) \quad (17)$$

Where:

N: The sample size studied.

S: Estimated number of parameters in the model.

Loglikelihood: The maximum likelihood function of the model.

The decision to choose the best generalized linear model by using the AIC and BIC depends on getting the lowest value for these two criteria.

## 4. RESULT

Statistical analysis of the data for 136 households in northern Syria was carried out using the R-Studio software. The descriptive statistical analysis was conducted for the dependent variable and the percentage and frequency of the independent variables were calculated. The data was modeled using Poisson and negative binomial regression models, and a comparison was made between the two models according to the

regression model evaluation criteria.

The response and the independent variables used in this study are as follows:

**Y:** Average monthly household income in US dollars.

**X<sub>1</sub>:** The type of energy used for cooking (X<sub>10</sub>: firewood, X<sub>11</sub>: natural gas, X<sub>12</sub>: kerosene oil).

**X<sub>2</sub>:** The type of energy used for heating (X<sub>20</sub>: firewood, X<sub>21</sub>: coal, X<sub>22</sub>: Diesel, X<sub>23</sub>:no energy is used, X<sub>24</sub>: kerosene oil, X<sub>25</sub>: natural gas).

**X<sub>3</sub>:** The capacity of the batteries used to store energy (X<sub>30</sub>: not found, X<sub>31</sub>: small, X<sub>32</sub>: medium, X<sub>33</sub>: big).

**X<sub>4</sub>:** The type of energy used to heat water (X<sub>40</sub>: firewood, X<sub>41</sub>: coal, X<sub>42</sub>: Diesel, X<sub>43</sub>: kerosene oil, X<sub>44</sub>: natural gas, X<sub>45</sub>: solar system, X<sub>46</sub>: Burning household waste).

**X<sub>5</sub>:** Electricity source (X<sub>50</sub>: No electricity at home, X<sub>51</sub>: Subscribe amperes, X<sub>52</sub>: Diesel generator, X<sub>53</sub>: Gasoline generator, X<sub>54</sub>: solar energy).

According to the data collected from the target area, the descriptive statistics of the response and independent parameters are summarized in Tables 1, 2, 3, 4, 5 and 6.

**Table 1:** Descriptive statistics for the average monthly household income in US dollars for 136 households.

Descriptive Statistics		
income		
N	Valid	136
	Missing	0
Mean		128.75
Median		100.00
Std. Deviation		93.178
Range		480
Minimum		20
Maximum		500

**Table 2:** The type of energy used for cooking: out of 136 households, 88.2% of them use natural gas, 11% use firewood and 0.7% use kerosene oil.

	Frequency	Percent	Valid Percent
Valid	firewood	15	11.0
	natural gas	120	88.2
	kerosen	1	0.7
	Total	136	100.0

**Table 3:** The type of energy used for space heating: Out of 136 households, 40.04% use firewood, 6.6% use coal, 33.1% use diesel, 2.9% have no energy source, 16.2% use kerosene oil, and 0.7% use natural gas.

	Frequency	Percent	Valid Percent
Valid	firewood	55	40.4
	coal	9	6.6
	Diesel	45	33.1
	No energy source	4	2.9
	kerosene oil	22	16.2
	natural gas	1	0.7
	Total	136	100.0



**Table 4:** The capacity of the batteries used to store energy: 66.2% of 136 households do not use batteries, 0.7% use small capacity batteries, 10.3% use medium capacity batteries and 22.8 use big capacity batteries.

		Frequency	Percent	Valid Percent
	no batteries	90	66.2	66.2
	small	1	0.7	0.7
Valid	medium	14	10.3	10.3
	big	31	22.8	22.8
	Total	136	100.0	100.0

**Table 5:** The type of energy used to heat water: Out of 136 households, 44.9% of them use firewood, 5.9% use coal, 5.1% use kerosene oil, 21.3% use natural gas, 19.1% use solar energy and 3.7% burn household waste.

		Frequency	Percent	Valid Percent
	firewood	61	44.9	44.9
	coal	8	5.9	5.9
	kerosene	7	5.1	5.1
Valid	natural gas	29	21.3	21.3
	solar system	26	19.1	19.1
	Burning household waste	5	3.7	3.7
	Total	136	100.0	100.0

**Table 6:** Electricity source: 2.9% of households have no electricity, 66.9% depend on ampere subscriptions, 21.3% use small diesel generators, 0.7% use small gasoline generators, and 8.1% use solar energy systems.

		Frequency	Percent	Valid Percent
	No electricity at home	4	2.9	2.9
	Subscribe amperes	91	66.9	66.9
Valid	Diesel generator	29	21.3	21.3
	Gasoline generator	1	0.7	0.7
	solar energy	11	8.1	8.1
	Total	136	100.0	100.0

The data were analyzed according to the Poisson model and the Negative Binomial model. The results are presented in Table 7.

Table 7: Results of Poisson and NB regression models

Type of Model	cod	Poisson regression model			NB regression model		
Explanatory variables		Estimate	Std. Error	Pr(Z> z )	Estimate	Std. Error	Pr(Z> z )
Intercept	-	4.372	0.056	2e-16***	4.440	0.298	2e-16***
Energy used for cooking	X <sub>10</sub>	-	-	-	-	-	-
	X <sub>11</sub>	0.127	0.033	0.000	0.196	0.207	0.342
	X <sub>12</sub>	-0.829	0.136	1.13e-09***	-0.702	0.621	0.258
Energy used for space heating	X <sub>20</sub>	-	-	-	-	-	-
	X <sub>21</sub>	0.273	0.035	1.83e-16***	0.217	0.232	0.350
	X <sub>22</sub>	0.263	0.020	2e-16***	0.272	0.128	0.033*
	X <sub>23</sub>	0.143	0.056	0.010*	0.094	0.312	0.763
	X <sub>24</sub>	0.169	0.052	0.001**	0.114	0.330	0.730
	X <sub>25</sub>	1.309	0.063	2e-16***	1.323	0.565	0.0192*
Capacity of the batteries	X <sub>30</sub>	-	-	-	-	-	-
	X <sub>31</sub>	0.290	0.083	0.000***	0.254	0.595	0.668
	X <sub>32</sub>	-0.049	0.028	0.078	-0.040	0.175	0.815
	X <sub>33</sub>	0.224	0.023	2e-16***	0.218	0.152	0.151
Energy used to heat water	X <sub>40</sub>	-	-	-	-	-	-
	X <sub>41</sub>	-0.176	0.035	4.36e-07***	-0.239	0.226	0.291
	X <sub>42</sub>	-0.138	0.039	0.000***	-0.110	0.250	0.658
	X <sub>43</sub>	-0.500	0.033	2e-16***	-0.483	0.193	0.012*
	X <sub>44</sub>	-0.382	0.025	2e-16***	-0.396	0.155	0.010*
	X <sub>45</sub>	-0.265	0.045	4.18e-09***	-0.267	0.294	0.363
	X <sub>46</sub>	-0.435	0.101	1.97e-05***	-0.443	0.566	0.433
Electricity source	X <sub>50</sub>	-	-	-	-	-	-
	X <sub>51</sub>	0.277	0.063	1.13e-05***	0.138	0.345	0.687
	X <sub>52</sub>	0.655	0.067	2e-16***	0.560	0.388	0.149
	X <sub>53</sub>	-0.460	0.152	0.002**	-0.528	0.634	0.404
	X <sub>54</sub>	0.426	0.069	7.42e-10***	0.365	0.398	0.359

Signif. codes: 0 '\*\*\*' 0.001 '\*\*' 0.01 '\*' 0.05 '.' 0.1 ' ' 1

P=0.05

As a starting point in modelling the count data, the data was modelled using the Poisson model. After estimating the regression parameters, we calculated the dispersion in the Poisson model by dividing the ratio of deviance by the degrees of freedom [49]. The result was  $(5889.2 / 115) = 51.21$ , which indicates an overdispersion of our data and that the Poisson regression model is inappropriate while the negative binomial model is more suitable for such a large rate of overdispersion.

From Table 7, there are differences between the coefficients as follows: The coefficients  $X_{12}, X_{21}, X_{23}, X_{24}, X_{31}, X_{33}, X_{41}, X_{42}, X_{45}, X_{46}, X_{51}, X_{52}, X_{53}$  and  $X_{54}$  are highly statistically significant at the  $\alpha = 0.05$  level in the Poisson model. While in the Negative Binomial model the coefficients  $X_{12}, X_{21}, X_{23}, X_{24}, X_{31}, X_{33}, X_{41}, X_{42}, X_{45}, X_{46}, X_{51}, X_{52}, X_{53}$  and  $X_{54}$  aren't statistically significant at the  $\alpha = 0.05$  level. The coefficients  $X_{11}$  and  $X_{32}$  aren't statistically significant at the  $\alpha = 0.05$  level in both regression models where the coefficients  $X_{10}, X_{20}, X_{30}, X_{40}$ , and  $X_{50}$  are reference variables.

The reason for the significant difference between the results of the two models is due to the overdispersion in the data by 51.21, which causes some variables to appear statistically significant when in fact they are completely opposite.

Goodness-of-fit test according to the evaluation criteria (AIC, BIC, and log-likelihood) of the two regression models is shown in Table 8, where it is known that the smaller the evaluation criteria, the better the model. Accordingly, the negative binomial model fitted the data better than the Poisson model. It can be explained by taking into account the “overdispersion” problem when the variance of the response variable is greater than its mean. On the other hand, Poisson regression model is based on the “equidispersion” assumption, meaning that the variance of the response variable is equal to its mean.

**Table 8:** The evaluation criteria of Poisson and NB regression models

Type of model	AIC	BIC	Log -likelihood value
Poisson model	6815.56	6876.72	-3386.78
NB model	1549.03	1613.10	-752.51

To test the ability of the negative binomial model in fitting the data as shown in Fig. 3, the relationship between residuals and fitted values is a linear relationship because the sediment is spread randomly. This is a good indication of the commitment of the negative binomial model to the linearity condition, that is, there is no non-linearity relationship between the independent and dependent variables that the model could not explain.

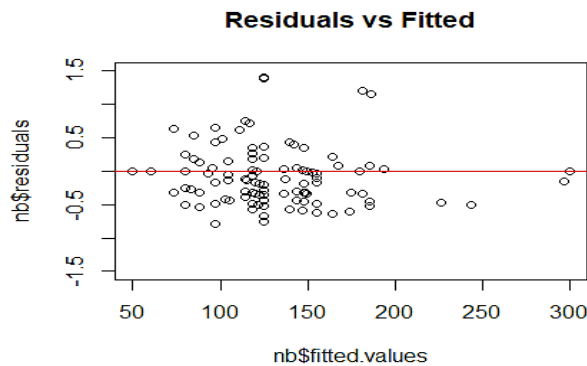


**Figure 3.** The relationship between Fitted values and residuals for NB regression model.

Before interpreting the coefficients in terms of incidence rate ratios (IRR), it is necessary to clarify how to move from interpreting the regression coefficients and the incidence rate ratios.

The outputs in Table (9) refer that the incidence rate ratio for cooking = 1 is 1.21 times compared with the incident rate for the reference group (cooking=0). Similarly, the incident rate ratio for cooking=2 is 0.49 times comparing the incident rate for the reference group holding the other variables constant. In a similar way, the results can be interpreted for the rest of the variables.

**Table 9:** Incidence rate ratios (IRR) for coefficients of the NB model.

Explanatory variables	cod	Estimate	2.5%	97.5%
Intercept	-	84.83	50.38	155.08
Energy used for cooking	X <sub>10</sub>	-	-	-
	X <sub>11</sub>	1.21	0.78	1.84
	X <sub>12</sub>	0.49	0.16	2.01
Energy used for space heating	X <sub>20</sub>	-	-	-
	X <sub>21</sub>	1.24	0.79	2.01
	X <sub>22</sub>	1.31	1.02	1.68
	X <sub>23</sub>	1.09	0.30	2.13
	X <sub>24</sub>	1.12	0.56	2.17
	X <sub>25</sub>	3.75	1.42	14.06
Capacity of the batteries	X <sub>30</sub>	-	-	-
	X <sub>31</sub>	1.29	0.44	5.04
	X <sub>32</sub>	0.96	0.68	1.36
	X <sub>33</sub>	1.24	0.92	1.69
Energy used for water heating	X <sub>40</sub>	-	-	-
	X <sub>41</sub>	0.78	0.50	1.27
	X <sub>42</sub>	0.89	0.54	1.53
	X <sub>43</sub>	0.61	0.042	0.91
	X <sub>44</sub>	0.67	0.50	0.90
	X <sub>45</sub>	0.76	0.44	1.42
	X <sub>46</sub>	0.64	0.24	2.39
Electricity source	X <sub>50</sub>	-	-	-
	X <sub>51</sub>	1.14	0.56	2.21
	X <sub>52</sub>	1.75	0.81	3.63
	X <sub>53</sub>	0.58	0.18	2.40
	X <sub>54</sub>	1.44	0.64	3.13

By using the statistically significant parameter estimates of the NB regression model given in Table (7), and using the IRLS parameter estimates of the NB regression model belonging “an average monthly household income in US dollars” data, the expected value (mean) of the NB regression model is given as follows;

$$\log(\hat{\lambda}) = 4.40 + 0.272X_{22} + 1.323X_{25} - 0.483X_{43} - 0.396X_{44} \quad (13)$$

Where  $\hat{\lambda}$  indicates the estimation of average monthly household income in US dollars.

The equation can be written as:

$$\hat{\lambda} = e^{4.40 + 0.272X_{22} + 1.323X_{25} - 0.483X_{43} - 0.396X_{44}} \quad (14)$$

From the obtained model, the result can be summarized as follows:

- The fuel used for space heating and water heating has a direct impact on households' monthly income.
- The expected value of the monthly expenditure as a result of using diesel for heating will be 1.32% higher than the expected value of the monthly expenditure when using coal.
- The expected value of the monthly expenditure as a result of using natural gas for heating will be 3.754 % higher than the expected value of monthly expenditure when using coal.
- The expected value of the monthly expenditure from using natural gas to heat water will be 1.620 % less than the expected value of the monthly expenditure when using coal

- The expected value of the monthly expenditure from using kerosene to heat water will be 1.485 % less than the expected value of the monthly expenditure when using coal.

Based on these results, coal is the least expensive energy source for space heating compared to other energy sources, meanwhile, natural gas and kerosene are the least expensive energy sources for heating water.

## 5. CONCLUSION

Efficient use of energy sources is understood differently depending on the context and the country of reference. It may be challenging to provide a universal definition for energy efficiency but based on the results of the various studies conducted it is evident that there are still many people worldwide who use energy sources inefficiently. The environment targeted in this study is a crisis-affected region where fuel and energy are subject to restrictions and high prices. Thus, relieving the energy burden of low-income families requires a joint effort to ensure tangible benefits for these families. However, there is no published work on optimizing energy use or identifying cost-effective energy sources at local levels in Syria.

In this study, a mathematical model identifying the most cost-efficient energy sources for households in northern Syria is proposed. The proposed model considers average household monthly income, the main available energy sources, and prices. Poisson regression and Negative Binomial (NB) regression were used to apply the statistical analysis of the data and produce the required model. According to the evaluation criteria, evidence indicates that the NB model has a better fit than the Poisson regression model for a large rate of overdispersion. According to statistically significant parameters of the NB regression model given, only the fuel used for space heating and water heating has a direct impact on the monthly income. The model showed that the most cost-effective fuel for space heating is coal, and the most cost-effective fuel for water heating is natural gas and kerosene. The model can be used as a rapid indicative approach to reducing energy expenditure as it has functional flexibility integrating cost reduction, mitigation of energy problems and helping families to obtain energy services at affordable prices commensurate with their monthly income.

A future study will focus on whether energy issues can be addressed through investment in solar energy systems. In light of this, it will be concluded whether solar energy systems can protect families, especially those with low incomes, from energy poverty and price fluctuations in the energy market. Moreover, increasing citizens' investment in renewable energy can contribute to the desired transition to a low-carbon energy system, climate protection, and advancing sustainable development by encouraging individuals and policymakers to solve the energy problem, relying on sustainable and environmentally friendly energy sources.

### **Declaration of Ethical Standards**

The author declares that the study complies with all applicable laws and regulations and meets ethical standards.

### **Credit Authorship Contribution Statement**

The author contributed to the data collection and modelling, the results analysis and the manuscript writing.

### Declaration of Competing Interest

The author declares that he has no known competing financial interests or personal relationships that could have appeared to influence the work reported in this paper.

### Funding / Acknowledgements

The author declares that there is no financial support.

### Data Availability

Data will be available upon reasonable request.

### REFERENCES

- [1] S. Ri, A. H. Blair, C. J. Kim, and R. J. Haar, "Attacks on healthcare facilities as an indicator of violence against civilians in Syria: an exploratory analysis of open-source data," *PLoS One*, vol. 14, no. 6, p. e0217905, 2019.
- [2] L. Tichý, "Energy infrastructure as a target of terrorist attacks from the Islamic state in Iraq and Syria," *International Journal of Critical Infrastructure Protection*, vol. 25, pp. 1-13, 2019.
- [3] S. Jabbour *et al.*, "10 years of the Syrian conflict: a time to act and not merely to remember," *The Lancet*, vol. 397, no. 10281, pp. 1245-1248, 2021.
- [4] F. A. Omar, I. Mahmoud, A. Hussian, L. Mohr, H. O. Abdullah, and A. Farzat, "The effect of the Syrian crisis on electricity supply and the household life in North-West Syria: a university-based study," *Education and Conflict Review*, vol. 3, pp. 77-86, 2020.
- [5] F. Alhaj Omar, I. Mahmoud, and K. G. Cedano, "Energy poverty in the face of armed conflict: The challenge of appropriate assessment in wartime Syria," *Energy Research & Social Science*, vol. 95, p. 102910, 2023/01/01/ 2023, doi: <https://doi.org/10.1016/j.erss.2022.102910>.
- [6] J. Messner, "Fragile States Index 2017: Factionalization and Group Grievance Fuel Rise in Instability. The Fund for Peace," ed, 2017.
- [7] C. International Committee of the Red, *Urban services during protracted armed conflict: a call for a better approach to assisting affected people*. International Committee of the Red Cross, 2015.
- [8] S. Gates, H. Hegre, H. M. Nygard, and H. Strand, "Consequences of armed conflict in the Middle East and north Africa region," mimeo, 2010.
- [9] I. P. Conflict and H. Action, "some recent ICRC experiences," *Geneva: ICRC*, 2016.
- [10] C. Bennett, M. Foley, and S. Pantuliano, "Time to let go: Remaking humanitarian action for the modern era," *ODI, London*, 2016.
- [11] P. Collier, "Fragile States and International Support," *Development*, vol. 175, 2016.
- [12] E. Spyrou, B. F. Hobbs, M. D. Bazilian, and D. Chattopadhyay, "Planning power systems in fragile and conflict-affected states," *Nature energy*, vol. 4, no. 4, pp. 300-310, 2019.
- [13] P. B. Anand, *Getting infrastructure priorities right in post-conflict reconstruction*. WIDER Research Paper, 2005.
- [14] J. Goodhand, "Violent conflict, poverty and chronic poverty," *Chronic Poverty Research Centre Working Paper*, no. 6, 2001.
- [15] K. Lyra, S. Mirasgedis, and C. Tourkolias, "From measuring fuel poverty to identification of fuel poor households: a case study in Greece," *Energy Efficiency*, vol. 15, no. 1, p. 6, 2022/01/07 2022, doi: 10.1007/s12053-021-10017-6.

- [16] A. Acakpovi, G. Botwe-Ohenewaa, and D. M. Sackey, "Impact of energy efficiency and conservation programs on the national grid in some selected households in Ghana," *Energy Efficiency*, vol. 15, no. 1, p. 5, 2022/01/06 2022, doi: 10.1007/s12053-021-09998-1.
- [17] S. Oguah and D. Chattopadhyay, "Planning in fragile and conflict states:: Case study for West Bank and Gaza," in *2018 IEEE Power & Energy Society General Meeting (PESGM)*, 2018: IEEE, pp. 1-5.
- [18] E. L. Roach and M. Al-Saidi, "Rethinking infrastructure rehabilitation: Conflict resilience of urban water and energy supply in the Middle East and South Sudan," *Energy Research & Social Science*, vol. 76, p. 102052, 2021.
- [19] M. Labordena, A. Patt, M. Bazilian, M. Howells, and J. Lilliestam, "Impact of political and economic barriers for concentrating solar power in Sub-Saharan Africa," *Energy Policy*, vol. 102, pp. 52-72, 2017.
- [20] T. Pettersson and P. Wallensteen, "Armed conflicts, 1946–2014," *Journal of peace research*, vol. 52, no. 4, pp. 536-550, 2015.
- [21] H. Zerriffi, H. Dowlatabadi, and N. Strachan, "Electricity and conflict: Advantages of a distributed system," *The Electricity Journal*, vol. 15, no. 1, pp. 55-65, 2002.
- [22] M. Bazilian and D. Chattopadhyay, "Considering power system planning in fragile and conflict states," *Energy for Sustainable Development*, vol. 32, pp. 110-120, 2016.
- [23] N. Patankar, A. R. de Queiroz, J. F. DeCarolis, M. D. Bazilian, and D. Chattopadhyay, "Building conflict uncertainty into electricity planning: A South Sudan case study," *Energy for Sustainable Development*, vol. 49, pp. 53-64, 2019.
- [24] J. L. Sowers, E. Weinthal, and N. Zawahri, "Targeting environmental infrastructures, international law, and civilians in the new Middle Eastern wars," *Security Dialogue*, vol. 48, no. 5, pp. 410-430, 2017.
- [25] P. Justino, "Violent conflict and human capital accumulation," *IDS Working Papers*, vol. 2011, no. 379, pp. 1-17, 2011.
- [26] H. Sun, S. Lu, and S. Solaymani, "Impacts of oil price uncertainty on energy efficiency, economy, and environment of Malaysia: stochastic approach and CGE model," *Energy Efficiency*, vol. 14, no. 2, p. 21, 2021/02/04 2021, doi: 10.1007/s12053-020-09924-x.
- [27] A. O'Sullivan, M.-E. Rey, and J. G. Mendez, "Opportunities and Challenges in the MENA Region," *Arab world competitiveness report*, vol. 2012, pp. 42-67, 2011.
- [28] N. R. C. Idmc, "Global Report on Internal Displacement 2019," ed, 2019.
- [29] T. A. A. People, "URBAN SERVICES DURING PROTRACTED ARMED CONFLICT," 2015.
- [30] C. International Committee of the Red, "Bled Dry: How War in the Middle East is Bringing the Region's Water Supplies to Breaking Point," 2015: ICRC Geneva.
- [31] N. R. Draper and H. Smith, *Applied regression analysis*. John Wiley & Sons, 1998.
- [32] A. O. Sykes, "An introduction to regression analysis," 1993.
- [33] D. C. Montgomery, E. A. Peck, and G. G. Vining, *Introduction to linear regression analysis*. John Wiley & Sons, 2021.
- [34] A. M. Legendre, *Nouvelles méthodes pour la détermination des orbites des comètes; par AM Legendre*. chez Firmin Didot, libraire pour lew mathematiques, la marine, l ..., 1806.
- [35] C. F. Gauss, *Theoria combinationis observationum erroribus minimis obnoxiae*. H. Dieterich, 1823.
- [36] F. Galton, "Regression towards mediocrity in hereditary stature," *The Journal of the Anthropological Institute of Great Britain and Ireland*, vol. 15, pp. 246-263, 1886.
- [37] S. Weisberg, *Applied linear regression*. John Wiley & Sons, 2005.
- [38] U. Olsson, "Generalized linear models," *An applied approach. Studentlitteratur, Lund*, vol. 18, 2002.
- [39] J. Fox, *Applied regression analysis and generalized linear models*. Sage Publications, 2015.
- [40] Ö. Deniz, "Poisson regresyon analizi," *İstanbul Ticaret Üniversitesi Fen Bilimleri Dergisi*, vol. 4, no. 7,

- pp. 59-72, 2005.
- [41] R. Winkelmann, *Econometric analysis of count data*. Springer Science & Business Media, 2008.
  - [42] P. De Jong and G. Z. Heller, "Generalized linear models for insurance data," *Cambridge Books*, 2008.
  - [43] A. J. Dobson and A. G. Barnett, *An introduction to generalized linear models*. CRC press, 2018.
  - [44] A. Agresti, *Analysis of ordinal categorical data*. John Wiley & Sons, 2010.
  - [45] J. M. Hilbe, *Negative binomial regression*. Cambridge University Press, 2011.
  - [46] A. C. Cameron and P. K. Trivedi, *Regression analysis of count data*. Cambridge university press, 2013.
  - [47] C. Walck, "Hand-book on statistical distributions for experimentalists," *University of Stockholm*, vol. 10, pp. 96-01, 2007.
  - [48] K. J. Hastings, *Probability and statistics*. Addison-Wesley Reading, MA, 1997.
  - [49] E. H. Payne, J. W. Hardin, L. E. Egede, V. Ramakrishnan, A. Selassie, and M. Gebregziabher, "Approaches for dealing with various sources of overdispersion in modeling count data: Scale adjustment versus modeling," *Statistical methods in medical research*, vol. 26, no. 4, pp. 1802-1823, 2017.





## MODEL REFERANS UYARLAMALI PID DENETLEYİCİ TASARIMI VE DENETLEYİCİ PARAMETRELERİNİN SİSTEM DAVRANIŞINA ETKİ ANALİZİ: DC MOTOR KONUM KONTROLÜ

<sup>1</sup>Akif YAVUZSOY , <sup>2</sup>Hüseyin SARGIN , <sup>3</sup>Tuğçe YAREN , <sup>4</sup>Selçuk KIZIR 

Kocaeli Üniversitesi, Mühendislik Fakültesi, Mekatronik Mühendisliği Bölümü, Kocaeli, TÜRKİYE  
<sup>1</sup>yavuzsoyakif@gmail.com, <sup>2</sup>hseyin.sargin@gmail.com, <sup>3</sup>tugce.yaren@kocaeli.edu.tr,  
<sup>4</sup>selcuk.kizir@kocaeli.edu.tr

### Önemli Katkılar (Highlights)

- Uyarlamalı kontrolcü tasarımı detaylı şekilde sunulmuştur.
- Tasarlanan kontrol algoritmasının pratiğe dökülmesi ile teorinin uygulanabilirliği ve geçerliliğinin ispatı gerçekleştirilmiştir.
- Denetleyici parametrelerinin değişimlerinin sistem davranışına etkileri analiz edilmiştir.
- Düşük maliyetli STM32F4 kiti ve Waijung blok seti ile hızlı ve kolay bir şekilde uygulama geliştirilebileceği ve geliştirilen uygulamaların kontrol eğitiminde kolaylıkla kullanılabilceği vurgulanmıştır.



## MODEL REFERANS UYARLAMALI PID DENETLEYİCİ TASARIMI VE DENETLEYİCİ PARAMETRELERİNİN SİSTEM DAVRANIŞINA ETKİ ANALİZİ: DC MOTOR KONUM KONTROLÜ

<sup>1</sup>Akif YAVUZSOY , <sup>2</sup>Hüseyin SARGIN , <sup>3,\*</sup>Tuğçe YAREN , <sup>4</sup>Selçuk KIZIR 

Kocaeli Üniversitesi, Mühendislik Fakültesi, Mekatronik Mühendisliği Bölümü, Kocaeli, TÜRKİYE

<sup>1</sup>yavuzsoyakif@gmail.com, <sup>2</sup>hseyin.sargin@gmail.com, <sup>3</sup>tugce.yaren@kocaeli.edu.tr,

<sup>4</sup>selcuk.kizir@kocaeli.edu.tr

(Geliş/Received: 13.12.2022; Kabul/Accepted in Revised Form: 30.05.2023)

**ÖZ:** Oransal-integral-türev (PID) kontrol yöntemi, basit mimarisi, kolay tasarım ve otomatik kazanç ayarlama gibi çekici özellikleri nedeniyle endüstride yaygın olarak uygulanmaktadır. Bununla birlikte, PID denetleyicisiyle başarılı bir endüstriyel uygulama yapabilmek için genellikle denetleyicinin önceden manuel olarak yeniden ayarlanması gerekmektedir. Bu sorunu çözmek için çalışma kapsamında, düşük maliyetli STM32F4 uygulama geliştirme kiti ve Waijung blok seti kullanılarak uyarlamalı kontrol yöntemlerinden biri olan Model Referans Uyarlamalı PID Denetleyici (MRUPIDD) tasarımı gerçekleştirilmiştir. Uyarlanabilir PID denetleyicisi, sistem parametreleri zamanla değişse bile istenen kontrol performansını sağlamak için parametre ayarlama mekanizmasına sahiptir. Parametre ayarlama mekanizması ve denetleyici tasarımı için Massachusetts Teknoloji Enstitüsü (Massachusetts Institute of Technology-MIT) kuralı kullanılmıştır. Çalışma kapsamında tasarlanan denetleyicinin DC motor üzerinde konum kontrol uygulaması gerçekleştirilmiş ve PID denetleyicisi ile karşılaştırılarak hata maliyetleri hesaplanmıştır. Uyarlama kazanç parametrelerinin sistem davranışına etkisinin incelenmesi için ise farklı gama kazanç değerleri sisteme uygulanmış ve kararlılığı bozan durumlar incelenmiştir.

**Anahtar Kelimeler:** Uyarlamalı PID, Model Referans Uyarlamalı PID Denetleyici, STM32F4, Waijung Blok Seti, DC Motor

### Model Reference Adaptive PID Controller Design and Analysis of the Impact of Controller Parameters on System Behavior: DC Motor Position Control

**ABSTRACT:** The proportional-integral-derivative (PID) control method is widely applied in the industry due to its attractive features such as simple architecture, easy design, and automatic gain adjustment. However, in order to have a successful industrial application with the PID controller, the controller has to be manually reconfigured. In order to solve this problem, the Model Reference Adaptive PID Controller (MRUPIDD), which is one of the adaptive control methods, was designed by using a low-cost STM32F4 application development kit and Waijung block set. The adaptive PID controller has a parameter adjustment mechanism to provide the desired control performance even if the system parameters change over time. Massachusetts Institute of Technology (MIT) rule is used for the parameter setting mechanism and controller design. Position control application of the controller designed within the scope of the study was carried out on the DC motor and error costs were calculated by comparing it with the PID controller. In order to examine the effects of the adaptive gain parameters on the system behavior, different gamma gain values were applied to the system and the unstable conditions were examined.

**Keywords:** Adaptive PID, Model Reference Adaptive Controller, STM32F4, Waijung Block Set, DC Motor

\*Corresponding Author: Tuğçe YAREN, [tugce.yaren@kocaeli.edu.tr](mailto:tugce.yaren@kocaeli.edu.tr)

## 1. GİRİŞ (INTRODUCTION)

Yüksek performanslı elektrikli tahrik sistemleri, çelik haddehaneleri, elektrikli otomobiller, robotik ve elektrikli çekiş gibi birçok endüstriyel uygulama için önemlidir [1]. Yüksek güvenilirlik, esneklik ve başarılı performansları nedeniyle, DC motorlar endüstriyel uygulamalarda yoğun olarak yer almaktadır [2].

Oransal-integral-türev (PID) kontrolü hem geçici hem de kararlı durum yanıtlarını işleyebilen üç terimli işlevselliği ile birçok gerçek dünya sorununa basit ve en etkili yöntemi sunmaktadır [3]. Bu nedenle, PID denetleyicileri geleneksel hız ve konum kontrol döngülerinde çok yaygın olarak kullanılmaktadır [4]. Çalışma koşullarında motor parametrelerinin değişken davranışı ve sistemdeki gürültünün varlığı, motor kontrolündeki iki temel problemdir. Bu nedenle, geleneksel yöntemleri kullanarak karmaşık, doğrusal olmayan ve zamana göre değişen sistemlerin motor kontrolü zorlu bir görev haline gelmektedir [2]. Uyarlamalı kontrol, parametreleri değişen veya başlangıçta belli olmayan sistemleri kontrol etmek için kullanılan bir kontrol yöntemidir. Örneğin, bir hava aracı uçtukça yakıt tüketimine bağlı olarak kütlesi yavaşça azalacaktır. Bu durumda, bu tür değişen durumlara karşı adapte olabilecek bir kontrol yöntemi gerekmektedir [5].

Uyarlamalı kontrol, daha iyi performans ve doğruluk için gelişmiş kontrol sistemleri tasarlamak için yaygın olarak kullanılan kontrol stratejilerinden biridir [6]. Model Referans Uyarlamalı Kontrol (MRUK) ise kontrol edilen süreç parametrelerinin az bilindiği veya normal çalışma sırasında değiştiği durumlarda kontrol problemlerini çözmek için kullanılan tekniklerden biridir. Bu kontrol tekniğinde bulunan elemanlardan biri referans modelidir. İstenilen çıkış referans modeli olarak adlandırılan transfer fonksiyonu tarafından üretilir. Kontrolün sağlanması için gerekli olan kontrol parametreleri ayarlama mekanizmasında oluşturulur [7].

Çakar ve arkadaşları [8] DC motorun konum kontrolü için Massachusetts Teknoloji Enstitüsü (Massachusetts Institute of Technology-MIT) kuralı kullanarak Model Referans Uyarlamalı PID Denetleyici tasarlamışlardır. Tasarladıkları denetleyiciyi gerçek zamanlı olarak test etmişler, ayrıca PID ve bulanık mantık kontrol yöntemleri ile karşılaştırmışlardır. Model referans uyarlamalı denetleyicinin diğer yöntemlere kıyasla ölçüm gürültüsünden daha az etkilendiği sonucuna varmışlardır. Emiroğlu ve arkadaşları [9], DC motorun hız kontrolü için bilinmeyen sistem parametreleri varlığında, kendinden ayarlamalı denetleyici algoritması geliştirmişler ve geliştirdikleri algoritmayı deney seti üzerinde test ederek başarılı sonuçlar almışlardır. Parametre kestirimi ve denetleyici tasarımı için özyinelemeli en küçük kareler yöntemi ve kutup atama yöntemini kullanmışlardır. Mahmud ve arkadaşları [10] adaptif PID yöntemi kullanarak, sabit mıknatıslı fırçasız bir DC motorun (BLDC) hız kontrolünü gerçekleştirmişlerdir. BLDC' nin daha yüksek çıkış verimliliğinde hız kontrolü zor bir kontrol problemidir. Bu nedenle daha iyi verimlilik sağlamak için adaptif PID denetleyicisini tercih etmişlerdir. Gerçek zamanlı deneyler sonucunda adaptif PID denetleyicisinin diğer denetleyicilere göre çok daha başarılı performans gösterdiği sonucuna varmışlardır. Ali ve arkadaşları [11] yapmış oldukları çalışmada model referanslı uyarlanabilir PID denetleyicisini incelemişlerdir. Kontrol edilen DC motor, parametre farklılıkları gibi belirsizliklere maruz kaldığı için geleneksel model referans uyarlamalı kontrol yönteminin eksikliklerini en aza indirmeyi hedeflemişlerdir. Model referans uyarlamalı kontrol yöntemi için daha başarılı bir çözüm bulmayı ve DC motorun daha iyi performanslı kontrolünü sağlamayı amaçlamışlardır. Bu amaç doğrultusunda ise model referans uyarlamalı kontrol yöntemi ile PID kontrolünü birleştirmişler ve elde ettikleri denetleyicinin performansını test edebilmek için MATLAB/Simulink simülasyon ortamını kullanmışlardır. Gueye ve arkadaşları [12] sabit mıknatıslı bir DC motorun uyarlanabilir referans modeline dayalı, sensörsüz (Kalman filtresi ile hız tahmini gerçekleştirerek) hız kontrolünü gerçekleştirmişlerdir. MIT kuralı ile tasarlanan model referans uyarlamalı PID sonucunda ise %0,15'lik düşük bir hata oranı ile başarılı bir performans elde edilmiştir. Jain ve Nigam [13] top ve kiriş sisteminin gerçek zamanlı kontrolü için MIT kuralının kullanıldığı bir model referans uyarlamalı kontrol sistemi tasarlamışlar ve başarılı performans elde etmişlerdir.

Bu çalışmada, sabit mıknatıslı fırçalı bir DC motorun konum kontrolüne yönelik MRUK tabanlı PID denetleyicisi tasarlanmış ve STM32F4 uygulama geliştirme kiti kullanılarak gerçek zamanlı kontrolü

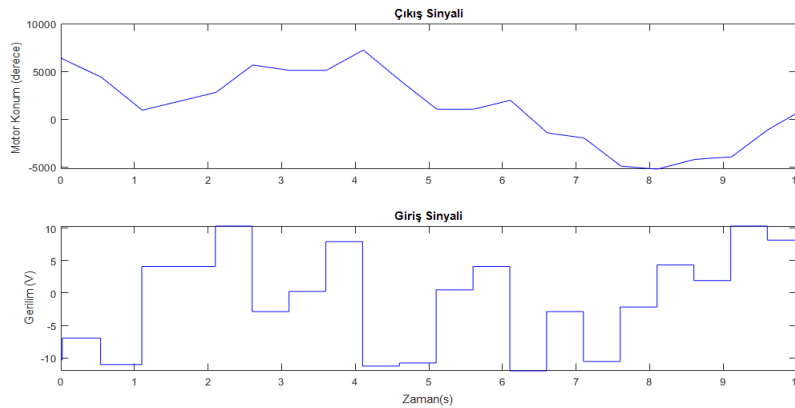
sağlanmıştır. PID denetleyici tasarımı ayrıntılı ele alınmış, kök yer eğrisi analizi gerçekleştirilmiştir. Tasarlanan klasik PID ve uyarlamalı PID denetleyicileri gerçek zamanlı deney setinde test edilmiş ve sonuçlar gözlenmiştir. Başarılı kontrolcü performansları elde edilmiş böylece tasarlanan denetleyicilerin performansı gerçek zamanlı olarak doğrulanmıştır. Ayrıca uyarlamalı kontrol yapısında önemli bir yere sahip denetleyici parametrelerinin değişimlerinin sistem davranışına etkileri incelenmiş ve tasarım sürecinin iyileştirilmesi hedef alınmıştır.

Çalışma kapsamında sırasıyla Bölüm 2'de DC motor modeli sunulmuş, Bölüm 3'te kontrol metotları ayrıntılı olarak verilmiş ve kontrolcü tasarımı gerçekleştirilmiş, gerçek zamanlı sonuçlar Bölüm 4'te sunulmuş ve son olarak sonuçlar tartışılmıştır. Gerçekleştirilen çalışma i) uyarlamalı kontrolcü tasarımı, ii) tasarlanan kontrol algoritmasının pratiğe dökülmesi ile teorinin uygulanabilirliği ve geçerliliğinin ispatı, iii) denetleyici parametrelerinin değişimlerinin sistem davranışına etkilerinin incelenmesi, iv) düşük maliyetli STM32F4 kiti ve Waijung blok seti ile hızlı ve kolay bir şekilde uygulama geliştirilebileceği ve geliştirilen uygulamaların kontrol eğitiminde kolaylıkla kullanılabilirliğini gösterme açısından ön plana çıkmaktadır.

## 2. DC MOTOR MODELİ (DC MOTOR MODEL)

Bu çalışma kapsamında kullanılan DC motorun modeli, sistem tanımlama yöntemlerinden biri olan kara kutu yaklaşımıyla deneysel verilerden hesaplanarak elde edilmiştir. Sistem tanımlaması, sistemin giriş ve çıkış sinyallerinin ölçümlerini kullanarak dinamik sistemlerin matematiksel modellerini oluşturmak için kullanılan bir metodolojidir [14,15]. Sistem tanımlama, ölçülen verilerden dinamik sistemlerin matematiksel modellerini oluşturmak için istatistiksel yöntemler kullanır [16]. Kara kutu modeli yaklaşımında, sistemin matematiksel modelini türetmek için sadece deneysel veriler kullanılır. Bu yaklaşımda, içeriği hakkında hiçbir bilgisi olmayan sisteme çeşitli giriş sinyallerinin uygulanması sonucunda çıkış sinyalleri izlenerek bir model oluşturulur. Çalışma kapsamında model tabanlı bir denetleyici tasarlanacağı için elde edilecek modelin gerçek sistemi temsil etmesi hedeflenmektedir.

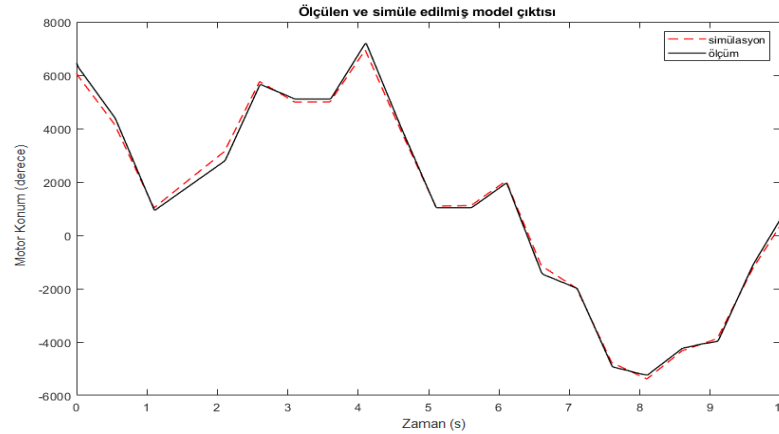
Sürekli ve ayrık zamanlı transfer fonksiyonlarını, süreç modellerini ve durum uzayı modelini tanımlamak için zaman ve frekans alanında girdi ve çıktı verilerini elde etmeye ihtiyaç vardır [17]. Bu nedenle, giriş verileri proses tanımlaması için gereklidir. Bu çalışmada, giriş sinyali Şekil 1'de görüldüğü gibi kullanıcı tanımlı fonksiyon olarak seçilmiştir. DC motorun bu giriş sinyaline karşılık gelen konumu olan çıkış sinyali de aynı şekilde gösterilmiştir.



**Şekil 1.** Deneysel sistem giriş ve çıkış verisi

*Figure 1. Experimental system input and output data*

MATLAB Sistem Tanımlama Araç Kutusu ile sistem tanımlama işleminden sonra 2 kutuplu ve 1 sıfırlı olarak elde edilen sistemin transfer fonksiyonu Denklem 1'de görülmektedir.



**Şekil 2.** Motor konum verisi (ölçüm ve simülasyon sonucu)

*Figure 2.* Motor position data (measurement and simulation result)

$$\frac{\theta(s)}{V(s)} = \frac{7.523 s + 71070}{s^2 + 132.2 s + 0.0000134} \quad (1)$$

Denklem 1’de verilen transfer fonksiyonu kullanılarak elde edilen sonuç grafiğinin gerçek motor verisi ile karşılaştırılması Şekil 2’de verilmiştir. Şekil 2’den görüleceği üzere kara kutu yaklaşımı kullanılarak %94 doğruluk oranına sahip DC motor transfer fonksiyonu elde edilmiştir. Elde edilen transfer fonksiyonunda, klasik yöntemler kullanılarak elde edilemeyecek olan motor sürücü entegresinin etkileri, sıcaklık, titreşim, sürtünme kuvvetleri gibi ölçülemeyen fiziksel parametrelerin etkileri bulunmaktadır. Elde edilen benzerlik yüzdesi yüksek bir oran olduğundan gerçek zamanlı kontrol uygulamaları için DC motor konum matematiksel modeli olarak kabul edilebilir [14].

### 3. KONTROL METODLARI (CONTROL METHODS)

DC motor konum kontrolü uygulanacak model için farklı kontrol metotları kullanılmıştır. Bu metotlar ise PID denetleyicisi, Model Referans Uyarlamalı PID denetleyicisi olarak seçilmiştir. PID denetleyicisi tasarımı ve kök yer eğrisi analizi gerçekleştirilmiştir. Aynı zamanda Model Referans Uyarlamalı PID denetleyicisi için MIT kuralından yararlanılmıştır.

#### 3.1. PID Denetleyici (PID Controller)

PID denetleyici, basitliği, net işlevselliği, uygulanabilirliği ve kullanım kolaylığı ile geri beslemeli kontrol sistemleri arasında en yaygın kullanılan kontrol sistemidir. PID kontrol, orantısal, integral ve türev etkisi ile referans değerinden geri besleme sinyalinin çıkarılmasıyla elde edilen hatayı paralel olarak işleyerek sistemin istenilen referans değerine ulaşmasını sağlayan bir yöntemdir. PID kontrol sistemindeki P, I ve D işlemleri farklı formlarda birleştirilebilir ve P, PI, PD gibi kontrol yöntemleri haline gelebilir. PID kontrol yapısının matematiksel modeli Denklem 2’de, hata sinyali ise Denklem 3’de verilmiştir.

$$u(t) = K_p e(t) + K_i \int e(t) + K_d \frac{d}{dt} e(t) \quad (2)$$

$$e(t) = r(t) - y(t) \quad (3)$$

Burada  $u(t)$  kontrol sinyalini,  $y(t)$  çıkış sinyalini,  $r(t)$  referans sinyalini ve  $e(t)$  hata sinyalini gösterir. Denklemdeki  $K_p$ ,  $K_i$  ve  $K_d$  katsayıları sırasıyla orantısal, integral ve türev kazanç sabitleridir. Uygulanan referans sinyalinin çıkış sinyalini takip etmesi isteniyorsa bu parametrelerin doğru seçilmesi gerekmektedir. PID katsayılarının ayarlanmasında, kapalı çevrim Ziegler-Nichols yöntemi veya röle geri besleme yöntemi kullanılabilir. Ayrıca PID denetleyicisi, denetleyici parametreleri değiştirilerek kabul

edilebilir bir performans elde edilmesi için kök-yer eğrisi kullanılarak tasarlanabilir. Bu çalışmada klasik PID denetleyici tasarımı, kök-yer eğrisi kullanılarak gerçekleştirilmiştir.

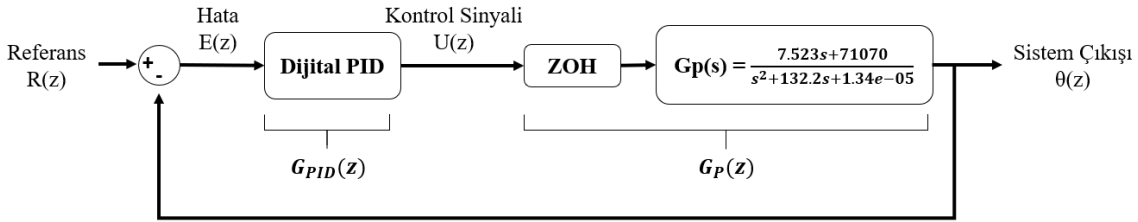
### 3.2. PID Denetleyici Tasarımı (PID Controller Design)

DC motorun PID denetleyici ile konum kontrolü için dijital kapalı çevrim kontrol yapısı Şekil 3'de gösterilmiştir. Kontrol yapısında  $T=0.01s$  ile elde edilen sıfırncı dereceden tutucunun (ZOH) sürekli zaman transfer fonksiyonunu Denklem 4 sağlamaktadır. Sıfır dereceli tutucu ile sistem transfer fonksiyonu ileri yolda yer aldığından Denklem 5'deki transfer fonksiyonu elde edilmiştir. Denklem 5'e z-dönüşüm uygulandıktan sonra, ayrık zamanlı transfer fonksiyonu ise Denklem 6'da görüldüğü gibi elde edilmektedir.

$$G_{ZOH}(s) = \frac{1 - e^{-Ts}}{s} = \frac{1 - e^{-0.01s}}{s} \quad (4)$$

$$G(s) = G_{ZOH}(s) \cdot G_p(s) = \frac{1 - e^{-0.01s}}{s} \frac{7.523s + 71070}{s^2 + 132.2s + 0.0000134} = A \quad (5)$$

$$G_p(z) = Z\{A\} = \frac{2.435z + 1.507}{z^2 - 1.267z + 0.266} \quad (6)$$



Şekil 3. Kapalı çevrim dijital PID kontrol yapısı [14]

Figure 3. Closed loop digital PID control structure [14]

PID parametrelerinin ( $K_p$ ,  $K_i$ ,  $K_d$ ) kök yer eğrisi yardımı ile teorik olarak bulunması için dijital PID transfer fonksiyonu Denklem 7'de verilmiştir.

$$G_{PID}(z) = \frac{(K_p T + K_d) z^2 + (K_i T^2 - K_p T - 2K_d) z + K_d}{Tz(z - 1)} \quad (7)$$

İkinci dereceden ideal transfer kullanılarak kutup atama işlemi için tasarım kriterleri olarak %5 aşım ve 0,5 saniye oturma zamanı tasarım kriteri olarak belirlenmiştir. İkinci dereceden sistemin kökleri Denklem (8-12) kullanılarak Denklem 13'teki gibi elde edilir. Denklem 8'de yer alan  $\zeta$  sönümleme oranını,  $\omega_n$  doğal frekansı, Denklem 10'da yer alan %OS ifadesi ise istenilen aşım yüzdesini ifade etmektedir.

$$G(s) = \frac{\omega_n^2}{s^2 + 2\zeta\omega_n s + \omega_n^2} \quad (8)$$

$$s_{1,2} = -\zeta\omega_n \pm j\omega_n\sqrt{1 - \zeta^2} \quad (9)$$

$$\zeta = \frac{-\ln(\%OS/100)}{\sqrt{\pi^2 + (\ln(\%OS/100))^2}} \quad (10)$$

%5 aşım için;

$$\zeta = \frac{-\ln\left(\frac{5}{100}\right)}{\sqrt{\pi^2 + \left(\ln\left(\frac{5}{100}\right)\right)^2}} \rightarrow \zeta = 0.69$$

0.5s oturma zamanı için ( $T_s = 0.5$ );

$$\omega_n \cong \frac{4}{T_s \zeta} \rightarrow \omega_n = 11.59$$

$$s_{1,2} \cong -8 \pm j8.4$$

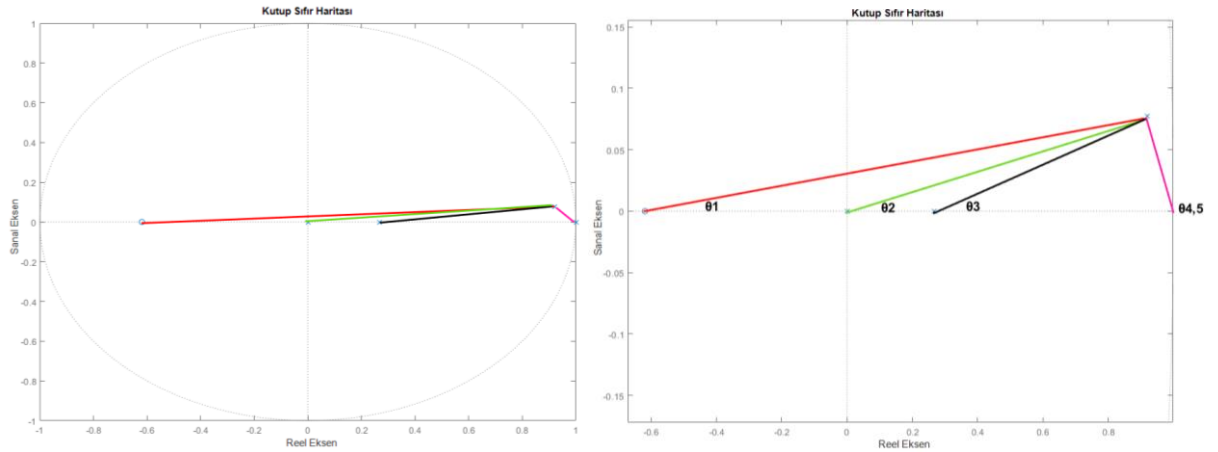
Denetleyici ayrık zamanda tasarlanacağından, bulunan sürekli zaman köklerinin z-düzlemine dönüştürülmesi gerekir. Sisteme ayrık zamanda atanacak kutbu belirlemek için Denklem 14'de gösterildiği gibi 0,01s örnekleme zamanı ile dönüştürme işlemi yapılmıştır.

$$z_{1,2} = \exp(T(-8 \pm j8.4))$$

$$z_{1,2} \cong 0.92 \pm j0.077$$

### 3.3. Kök Yer Eğrisi Analizi (Root Locus Analysis)

DC motorun ayrık zamanlı transfer fonksiyonu iki kutup ve bir sifıra sahiptir. PID denetleyicisinin iki sıfırı ve iki kutbu olmak üzere açık çevrim transfer fonksiyonunun toplamda dört kutup, üç sıfırı bulunmaktadır. PID' nin bilinmeyen iki sıfırı, atanan kutbun bilinen kutup ve sıfırlara göre açıları hesaplanarak denetleyici tasarımı gerçekleştirilir. Şekil 4'deki tüm açılar hesaplanmış ve PID denetleyicisinin sıfırlarının alması gereken açılar Denklem 15-16'daki gibi belirlenmiştir.



Şekil 4. Sıfır kutbundaki atama kutbuna göre PID denetleyicisinin sıfırlarının belirlenme haritası  
Figure 4. Determination map of the zeros of the PID controller relative to the assignment pole at the zero pole

$$\theta_1 = \tan^{-1}\left(\frac{0.077}{|-0.81 - 0.92|}\right) = 2.55^\circ$$

$$\theta_2 = \tan^{-1}\left(\frac{0.077}{|0 - 0.92|}\right) = 4.78^\circ$$

$$\theta_3 = \tan^{-1}\left(\frac{0.077}{|0.266 - 0.92|}\right) = 6.71^\circ$$

$$\theta_{4,5} = 90 + \tan^{-1}\left(\frac{1 - 0.92}{|0.077|}\right) = 136.09^\circ$$

$$\pm 180(2k + 1) = \emptyset + 2.55 - 4.78 - 6.71 - 136.09 - 136.09$$

$$k = 0 \rightarrow -180^\circ = \emptyset - 281.12 \rightarrow \emptyset = 101^\circ$$

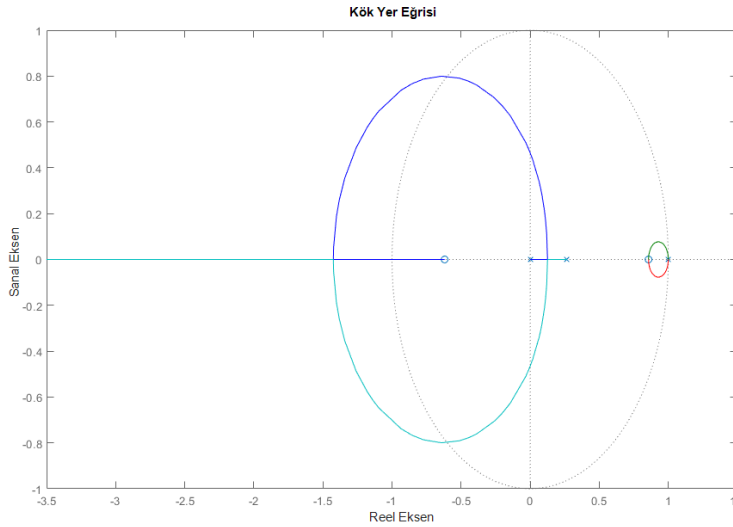
Kök yer eğrisinin atanan noktadan geçebilmesi için PID denetleyicisinin sıfırları sistem üzerinde toplam  $101^\circ$  etkiye sahip olmalıdır. İki sıfır aynı yerde ise, gerekli açı değeri  $50,5^\circ$ 'dir ve hedeflenen açı değerlerini sağlayan sıfır yerleri Denklem 17'de gösterildiği gibi elde edilir.

$$\tan^{-1} \frac{0.077}{0.92 - z_{pid}} = 50.5^\circ \rightarrow \frac{0.077}{0.92 - z_{pid}} = \tan(50.5^\circ) \rightarrow z_{pid} = 0.8567 \quad (17)$$

PID sıfırları bulunduğundan sonra, Denklem 14'teki PID transfer fonksiyonu Denklem 18'e dönüşür. İleri beslemeli transfer fonksiyonu (Denklem 19) kullanılarak Şekil 5'deki kök yer eğrisi elde edilir. Şekil 5'de sistem kutuplarının artan kazançla nasıl hareket ettiği görülmektedir. Sistem davranışında birim çembere yakın baskın kutuplar etkili olduğu için Şekil 6'daki "+1" noktası etrafındaki kök yörüngesi dikkate alınır. Ancak bu kök yer eğrisinden kazanç değeri belirlenirken +1 noktasından uzakta oluşan kök yer eğrisinin kararlılık limiti dikkate alınmalıdır. +1 noktası etrafında oluşan kök yer eğrisinde seçilen kazanç değeri, diğer kök yer eğrisinin kritik kazanç değerini geçmemelidir. Kritik kazanç değeri aşılmadan Şekil 6'da gösterildiği gibi  $K = 0.554$  seçilir.

$$G_{PID}(z) = \frac{(z - 0.8567)^2}{z(z - 1)} = \frac{z^2 - 1.713z + 0.7339}{z^2 - z} \quad (18)$$

$$KG_{PID}(z)G_P(z) = K \frac{z^2 - 1.713z + 0.7339}{z^2 - z} \frac{2.435z + 1.507}{z^2 - 1.267z + 0.2666} \quad (19)$$



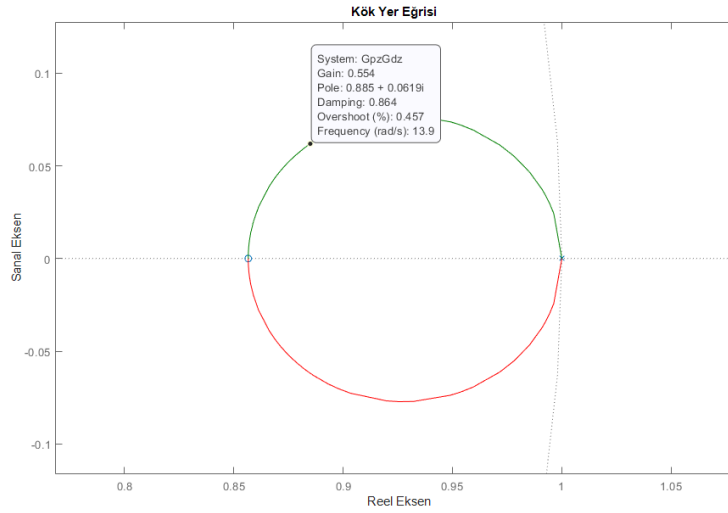
Şekil 5. Sistem kök yer eğrisi  
Figure 5. The root locus diagram of the system

PID denetleyici parametreleri Denklem 20-21'de gösterildiği gibi kök yer eğrisinde seçilen kazanç değeri ( $K=0.554$ ) kullanılarak hesaplanır.

$$G_{PID}(z) = K \frac{z^2 - 1.713z + 0.7339}{z^2 - z} = \frac{(K_p T + K_d) z^2 + (K_i T^2 - K_p T - 2K_d) z + K_d}{Tz(z - 1)} \quad (20)$$

$$\begin{aligned} \frac{K_d}{T} &= (K)(0.7339) \rightarrow K_d = (0.554)(0.7339)(0.01) = \mathbf{0.00406} \\ K_p + \frac{K_d}{T} &= K \rightarrow K_p = (0.554) - \frac{0.00406}{0.01} = \mathbf{0.148} \\ K_i T - K_p - 2 \frac{K_d}{T} &= (K)(-1.713) \rightarrow K_i = \mathbf{0.1097} \end{aligned} \quad (21)$$



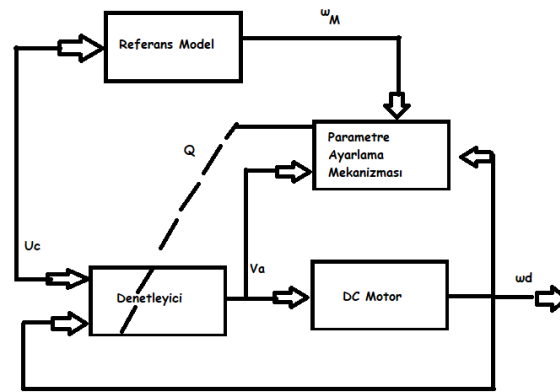


Şekil 6. +1 noktası etrafında oluşan kök yer eğrisi

Figure 6. The root locus diagram of the system around point +1

### 3.4. Model Referans Uyarlamalı Kontrol (Model Reference Adaptive Control)

Model Referans Uyarlamalı Kontrol (MRUK), Whitaker tarafından 1958'de önerilmiştir [18]. Motor konum kontrolü için istenilen çıkış, referans modele uygulanan giriş sinyali ile üretilir. Ayarlama mekanizması, sistemi istenilen çıkışa uyacak şekilde ve parametre değişikliği veya rahatsız edici etkilerde değişiklik olması durumunda bile istenilen çıkışı koruyacak şekilde tasarlanmıştır. Şekil 7'de MRUK'un blok diyagramı verilmiştir. Şekilden görüldüğü üzere MRUK çalışma yapısında, sistem çalışmaya başladığında referans modele göre denetleyici parametreleri ayarlanır ve sonrasında sistemin zamana bağlı parametrelerine göre "Parametre Ayarlama Mekanizması", denetleyici parametrelerini güncelleyerek motorun istenilen konumda kalmasını sağlar. Sistemin zamana bağlı etkenlerine göre hatayı sıfır yapabilmek ve kararlı bir sistem elde etmek için ayar mekanizmasının belirlenmesi, MRUK sistemi ile ilgili önemli bir sorundur. Bu makalede Parametre Ayarlama Mekanizması MIT kuralına göre tasarlanmış olup, kural Denklem 22'de verilmiştir.



Şekil 7. MRUK blok diyagramı

Figure 7. MRUK block diagram

$$\frac{d\theta}{dt} = -\gamma \frac{\partial J}{\partial \theta} = -\gamma \frac{\partial J}{\partial e} \frac{\partial e}{\partial \theta} = -\gamma e \frac{\partial e}{\partial \theta} \quad (22)$$

$$e = y_{system} - y_{model} \quad (23)$$

### 3.5. Massachusetts Teknoloji Enstitüsü (MIT) Kuralı (MIT Rule)

MIT Kuralı ilk olarak Massachusetts Teknoloji Enstitüsü (MIT)'nün araştırmacıları tarafından 1960 yılında geliştirilmiş olup hava araçlarında oto pilot sistemi tasarlamak için kullanılmıştır. Maliyet fonksiyonunun düşürülmesi, takip etme hatasının ( $e$ ) azalmasına ve sistem çıktısının istenen çıktıya yaklaşması anlamına gelmektedir ve maliyet fonksiyonuna Denklem 24'de yer verilmiştir. Maliyet fonksiyonunun azaltılması, takip etme hatasının ( $e$ ) azalması ve sistem çıkışının istenilen referansa yaklaşmasını sağlar. Bu nedenle maliyet fonksiyon değerini en aza indirecek bir denkleme ihtiyaç vardır. Bu denklem, Denklem 22'de verilmiştir. Denklemdaki  $\gamma$  sabiti uyarılama kazancı olarak bilinir.

$$J(\theta) = \frac{1}{2} e^2(\theta) \quad (24)$$

Motorun konuma bağlı transfer fonksiyonu Denklem 25'te verilmiştir ve  $a_0$ ,  $a_1$ ,  $a_2$  ve  $b_0$  denklemdaki sabitlerdir.

$$G(s) = \frac{y_s(s)}{u(s)} = \frac{b_0}{a_2 s^2 + a_2 s + a_0} \quad (25)$$

Frekans uzayında PID Transfer Fonksiyonu Denklem 26'da yer almaktadır.  $e_p$  değeri ise sisteme verilen girdi ile sistemden yani enkoderden alınan konum bilgisi arasındaki farkı verir ve bu ifadeye Denklem 27'de yer verilmiştir.

$$\frac{u(s)}{e_p(s)} = \frac{K_d s^2 + K_p s + K_i}{s} \quad (26)$$

$$e_p = u_{input} - y_{system} \quad (27)$$

Kapalı çevrim transfer fonksiyonu, motorun konumuna bağlı transfer fonksiyonundan ve PID transfer fonksiyonundan elde edilmiş olup Denklem 28'de verilmiştir.

$$\frac{y_s(s)}{u_g(s)} = \frac{b_0(K_d s^2 + K_p s + K_i)}{a_2 s^3 + (a_1 + b_0 K_d) s^2 + (a_0 + b_0 K_p) s + K_i} \quad (28)$$

MIT kuralının son hali Denklem 29'da görülmektedir.

$$\frac{d\theta}{dt} = -\gamma e \frac{\partial e}{\partial y_s} * \frac{\partial y_s}{\partial \theta} = -\gamma e \frac{\partial y_s}{\partial \theta} \quad (29)$$

$K_p$ ,  $K_i$  ve  $K_d$  değerleri Denklem 30'da ki  $\theta$  değişkeni yardımıyla elde edilecektir.

$$\theta = \left(-\frac{\gamma}{s}\right) e \frac{\partial y_s}{\partial \theta} \quad (30)$$

Denklem 30'da bulunan  $\frac{\partial y_s}{\partial \theta}$  işlemini gerçekleştirebilmek için  $\theta$  yerine sırasıyla  $K_p$ ,  $K_i$  ve  $K_d$  değerleri koyulmuştur.  $\frac{\partial y_s}{K_p}$ ,  $\frac{\partial y_s}{K_i}$  ve  $\frac{\partial y_s}{K_d}$  değerlerini bulabilmek için Denklem 28'de içler dışlar çarpımı yapılarak Denklem 31 elde edilmiştir. Denklem 31'in  $K_p$ ,  $K_i$  ve  $K_d$  değişkenlerine göre kısmi türevleri alınarak sırasıyla  $\frac{\partial y_s}{K_p}$ ,  $\frac{\partial y_s}{K_i}$  ve  $\frac{\partial y_s}{K_d}$  değerleri elde edilmiş ve sırasıyla Denklem (32-34)'de yer verilmiştir.

$$y_s(s)[a_2 s^3 + (a_1 + b_0 K_d) s^2 + (a_0 + b_0 K_p) s + K_i] = u_g(s)[b_0(K_d s^2 + K_p s + K_i)] \quad (31)$$

$$\frac{\partial y_s}{K_p} = \frac{b_0 s (u_g - y_s)}{s^3 + \left(\frac{a_1 + b_0 K_d}{a_2}\right) s^2 + \left(\frac{a_0 + b_0 K_p}{a_2}\right) s + \frac{K_i}{a_2}} \quad (32)$$

$$\frac{\partial y_s}{K_i} = \frac{b_0 (u_g - y_s)}{s^3 + \left(\frac{a_1 + b_0 K_d}{a_2}\right) s^2 + \left(\frac{a_0 + b_0 K_p}{a_2}\right) s + \frac{K_i}{a_2}} \quad (33)$$

$$\frac{\partial y_s}{K_d} = \frac{b_0 s^2 (u_g - y_s)}{s^3 + \left(\frac{a_1 + b_0 K_d}{a_2}\right) s^2 + \left(\frac{a_0 + b_0 K_p}{a_2}\right) s + \frac{K_i}{a_2}} \quad (34)$$

Denklem (32-34) yeniden düzenlenerek Denklem (35-37) elde edilmiştir.

$$K_p = \left(-\frac{\gamma_p}{s}\right) e^{-\frac{b_0 s (u_g - y_s)}{s^3 + \left(\frac{a_1 + b_0 K_d}{a_2}\right) s^2 + \left(\frac{a_0 + b_0 K_p}{a_2}\right) s + \frac{K_i}{a_2}}} \quad (35)$$

$$K_i = \left(-\frac{\gamma_i}{s}\right) e^{-\frac{b_0 (u_g - y_s)}{s^3 + \left(\frac{a_1 + b_0 K_d}{a_2}\right) s^2 + \left(\frac{a_0 + b_0 K_p}{a_2}\right) s + \frac{K_i}{a_2}}} \quad (36)$$

$$K_d = \left(-\frac{\gamma_d}{s}\right) e^{-\frac{b_0 s (u_g - y_s)}{s^3 + \left(\frac{a_1 + b_0 K_d}{a_2}\right) s^2 + \left(\frac{a_0 + b_0 K_p}{a_2}\right) s + \frac{K_i}{a_2}}} \quad (37)$$

Denklem (32-34)'de yer alan  $\gamma_p$ ,  $\gamma_i$  ve  $\gamma_d$  değerleri, PID katsayılarının bulunmasında kullanılan yöntemlerden birisi olan manuel ayarlama yöntemi ile bulunmuştur. Manuel ayarlama yönteminde  $K_p$ ,  $K_i$  ve  $K_d$  değişkenleri yerine sırasıyla  $\gamma_p$ ,  $\gamma_i$  ve  $\gamma_d$  değişkenleri kullanılmıştır.

Manuel ayarlama, ilk önce  $K_i$  ve  $K_d$  değerleri sıfıra ayarlanır. Döngünün çıkışı salınım yapana kadar  $K_p$  değeri artırılmalı, ardından  $K_p$ , çeyrek genlikli azalma tipi yanıtı için bu değer yaklaşık yarısına ayarlanmalıdır. Ardından, işlem için yeterli sürede kararlı durum hatası azalana kadar  $K_i$  değeri artırılmalıdır. Ancak, çok yüksek  $K_i$  kazancı problem oluşturacaktır. Son olarak, gerekirse, döngü bir yük bozulmasından sonra kabul edilebilir bir sürede referansa ulaşmak için  $K_d$  değeri artırılmalıdır. Ancak, yüksek  $K_d$  kazancı aşırı tepkiye ve salınımlara neden olacaktır. Hızlı bir PID döngü ayarı, ayar noktasına daha hızlı ulaşmak için genellikle biraz aşar; ancak, bazı sistemler aşmayı kabul edemez, bu durumda aşırı sönümlü bir kapalı döngü sistemi gerekir, bu da salınımlara neden olan  $K_p$  ayarının yarısından daha düşük bir  $K_p$  ayarı gerektirir [8].

Sistemin transfer fonksiyonunun kutupları, sistem yanıtının davranışını etkilediği için karakteristik denklemin kökleri önemlidir. Kutupların yer değiştirmesi, sistemin yerleşme süresi, yükselme süresi ve aşma gibi özelliklerini belirler. İstenen karakteristiğe sahip ikinci dereceden bir sistemin transfer fonksiyonu  $\zeta$  (sönümleme oranı) ve  $w_n$  (doğal frekans) ile oluşturulabilir. Bu özellik kullanılarak referans modelin transfer fonksiyonu Denklem 38'de verilen ikinci mertebe olarak seçilir. Yüzde aşım ve salınım istenmediğinden  $\zeta$  ve  $w_n$  değerleri sırasıyla 1 ve 5 rad/s olarak seçilmiştir.

$$G_m = \frac{w_n^2}{s^2 + 2\zeta w_n s + w_n^2} \quad (38)$$

$$s^3 + \left(\frac{a_1 + b_0 K_d}{a_2}\right) s^2 + \left(\frac{a_0 + b_0 K_p}{a_2}\right) s + \frac{K_i}{a_2} \equiv (s + \sigma) * (s^2 + 2\zeta w_n s + w_n^2) \quad (39)$$

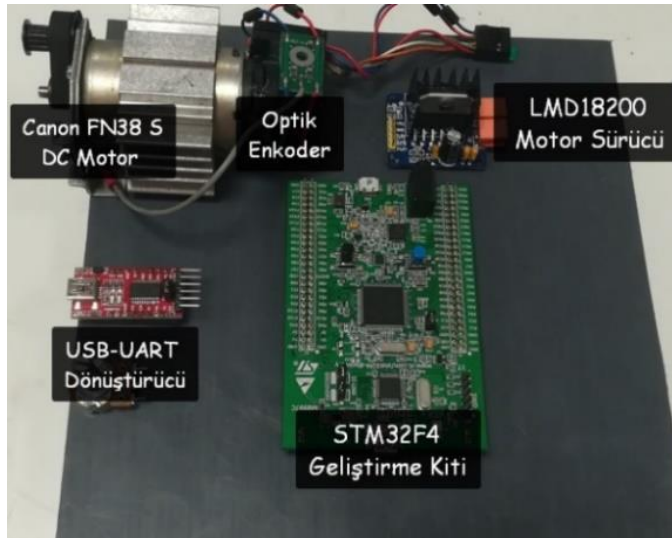
Denklem 28'deki transfer fonksiyonu, Denklem 38'deki referans model transfer fonksiyonundan daha yüksek bir dereceye sahip olduğundan, kararlı kutbun ( $-\sigma$ ) yeri sistem performansını büyük ölçüde etkilediği için orijine yakın uzaklıkta olan 0.001 noktası seçilmiştir. Denklem 39'daki denklik kullanılarak Denklem 38 yeniden düzenlendiğinde Denklem 40 elde edilir ve bu denklem Şekil 10'da görüleceği üzere parametre ayarlama mekanizması için kullanılmıştır.

$$G_i(s) = \frac{b_0}{s^3 + (2\zeta\omega_n + \sigma)s^2 + (\omega_n^2 + 2\zeta\omega_n\sigma)s + \sigma\omega_n^2} \quad (40)$$

#### 4. GERÇEK ZAMANLI KONTROL (REAL TIME CONTROL)

Şekil 8'de denetleyicinin test edildiği deney düzeneği görülmektedir. Deney düzeneğinde 24V beslemeli, sabit mıknatıslı Canon FN38-S fırçalı DC motor yer almaktadır. Motora ek olarak, çözünürlüğü 168 CPR (Counts Per Revolution) olan iki kanallı enkoder bulunmaktadır. Aynı zamanda deney düzeneğinde STM32F4 uygulama geliştirme kartı, H köprü yapısına sahip LMD 18200 motor sürücüsü ve seri haberleşme için USB-UART dönüştürücü bulunmaktadır.

Bu bölümde gerçek zamanlı kontrol sonuçları sunulmaktadır. Klasik PID ve model referans uyarlamalı PID denetleyicileri aşım (*overshoot*), oturma zamanı (*settling time*), yükselme zamanı (*rise time*) ve kalıcı durum hatası (*steady state error*) performans kriterleri bakımından değerlendirilmiştir. Sisteme giriş olarak 1 saniye gecikmeli, 200 genlikli birim basamak işareti verildikten sonra iki farklı kontrol sisteminin verdiği sonuçlar gözlemlenmiş ve gerçek zamanlı sonuçlar karşılaştırılmıştır.



Şekil 8. Deney düzeneği  
Figure 8. Experimental setup

##### 4.1. PID Kontrol Uygulaması (PID Control Experiment)

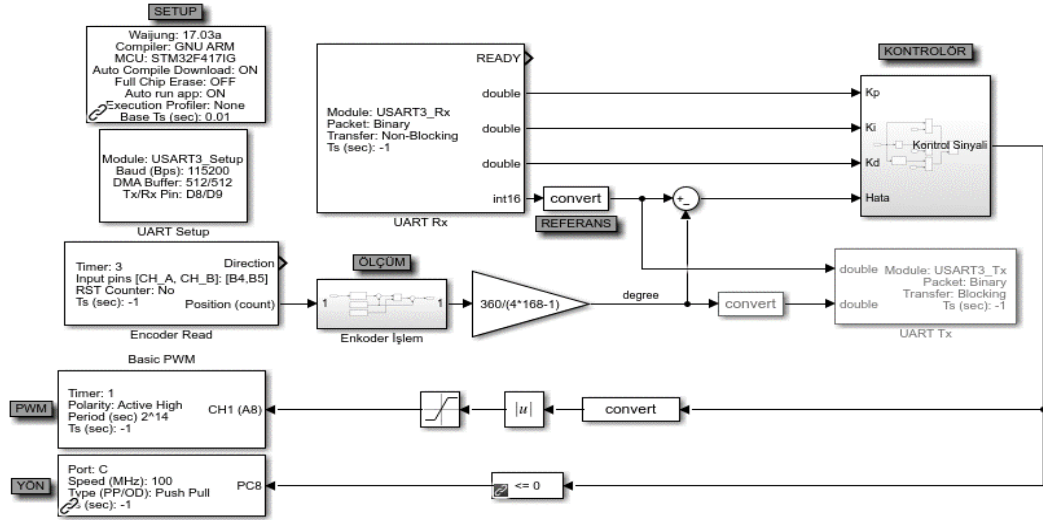
Şekil 9, gerçek zamanlı Simulink denetleyici modelini, Şekil 10 ise bilgisayardan referans sinyali ve PID kontrolörün parametrelerini ( $K_p$ ,  $K_i$  ve  $K_d$ ) göndermek için UART iletişim protokolü kullanılarak tasarlanan PC (host) modeli göstermektedir. Kök yer eğrisi yöntemi kullanılarak elde edilen PID parametreleri host model üzerinden gerçek sistem üzerine aktarılarak DC motorun referans konuma göre kontrolü sağlanır.

PID kontrol sonucu sistemin verdiği basamak yanıtı Şekil 11'de verilmiştir. Basamak yanıtında PID kontrolcüsü istenen referans değerine ulaşmakta, yükselme süresi uygun ve salınım miktarı yok denecek kadar azdır. Ancak klasik PID denetleyicisi sonucunda aşım meydana gelmiştir. Klasik PID kullanan sistemin performans sonuçları Çizelge 1'de verilmiştir.

**Çizelge 1.** Sistemin klasik PID kontrol basamak yanıtı

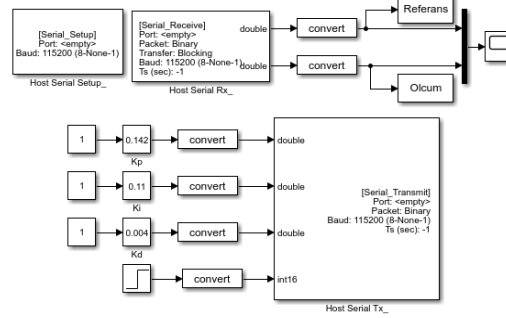
*Table 1. Classical PID control step response of the system*

	Yüzde Aşım	Yerleşme Zamanı	Yükselme Zamanı	Kalıcı Durum Hatası
<b>Klasik PID</b>	2.14 %	3.51 s	0.06 s	0°



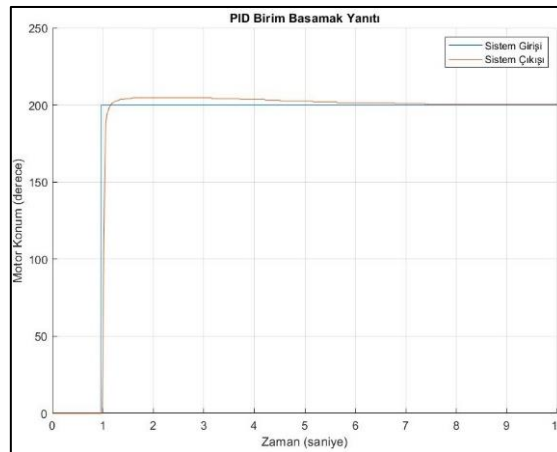
**Şekil 9.** Gerçek zamanlı DC motor PID kontrol Simulink modeli

*Figure 9. Real-time DC motor PID control Simulink model*



**Şekil 10.** Host modeli (Klasik PID kontrol)

*Figure 10. Host model (classic PID control)*



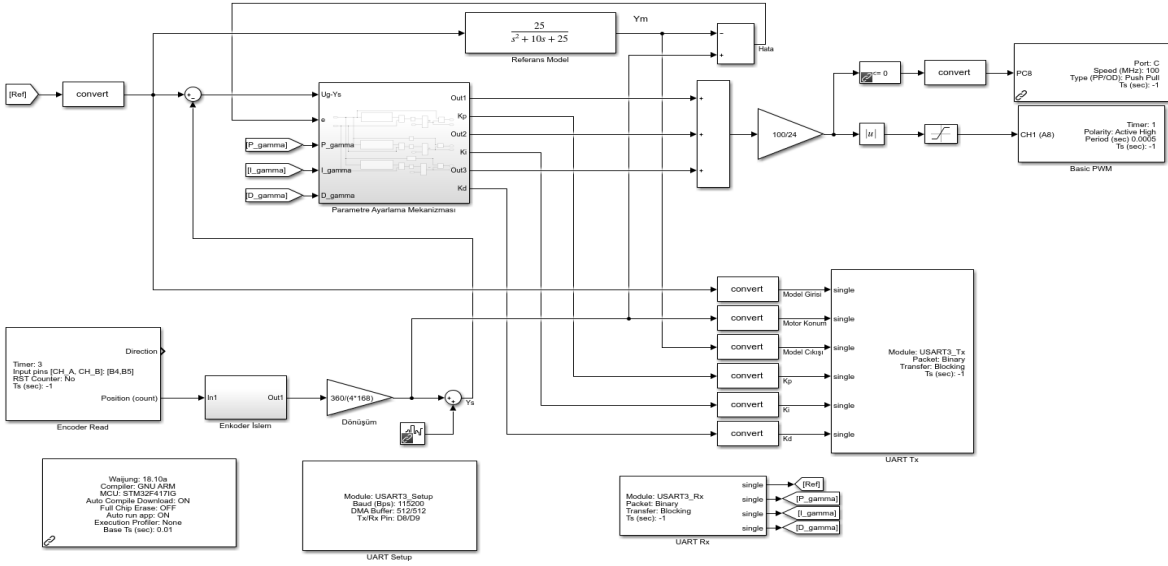
**Şekil 11.** PID kontrol basamak yanıtı

*Figure 11. PID control step response*

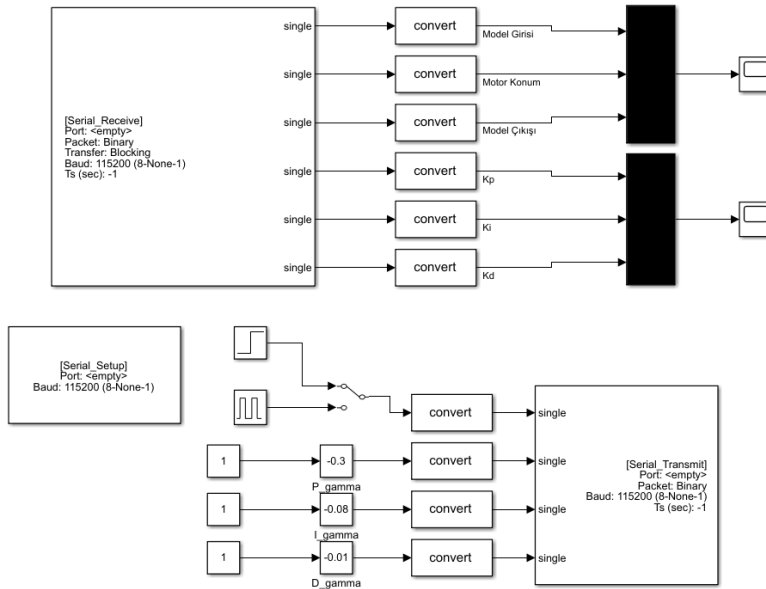
4.2. Referans Uyarlamalı PID Kontrol Uygulaması (Reference Adaptive PID Control Experiment)

Uyarlamalı PID denetleyicisinin STM32F4 geliştirme kartı için tasarlanan modeli Şekil 12’de görülmektedir. Sonuçları gözlemleyebilmek ve motora istenilen konuma yönlendirme yapabilmek için PC (host) uygulama modeli Şekil 13’de verilmiştir.

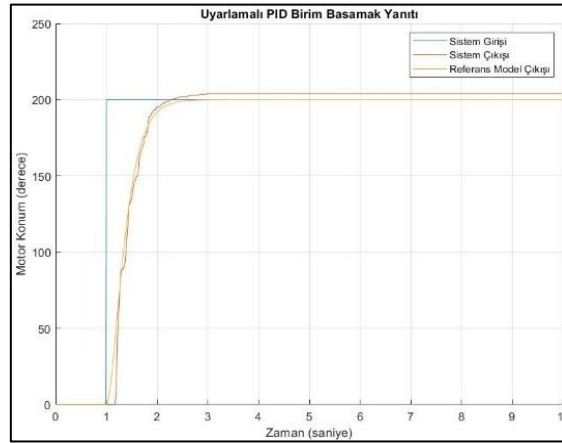
Şekil 14, model referans uyarlamalı PID denetleyicisinin yanıtını göstermektedir. Uyarlamalı PID kontrolörde, salınım miktarının oldukça az olduğu, oturma zamanının az olduğu, yükselme zamanının diğer kontrolörlere göre daha yüksek olduğu ve kalıcı durum hatasının az olduğu gözlemlenmiştir.



Şekil 12. Gerçek zamanlı DC motor uyarlamalı PID kontrol Simulink modeli  
 Figure 12. Real-time DC motor adaptive PID control Simulink model



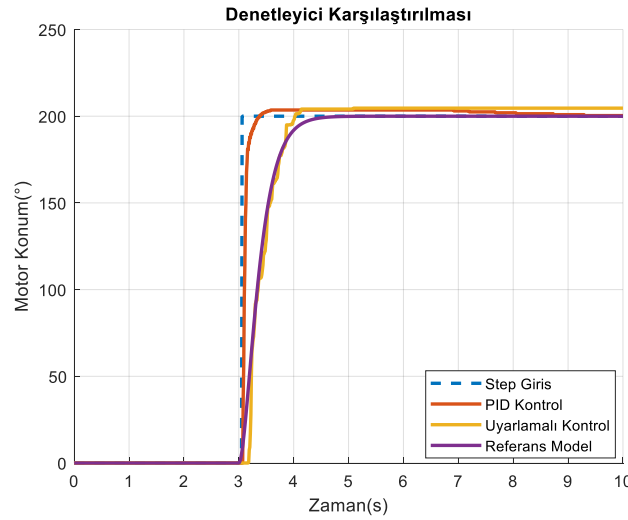
Şekil 13. Host model (uyarlamalı kontrol)  
 Figure 13. Host model (adaptive control)



Şekil 14. Uyarlamalı PID kontrol basamak yanıtı  
Figure 14. Adaptive PID control step response

#### 4.2. Karşılaştırma (Comparison)

PID ve uyarlamalı kontrol sistemlerinin daha net karşılaştırılabilmesi için sonuçlar üst üste Şekil 15’de çizdirilmiş ve her iki denetleyicinin hata sinyalleri karşılaştırılmıştır. Uyarlamalı PID kullanan sistemin denetleyici parametreleri Denklem 38’de oluşturulan referans modele göre elde edilmiştir. Klasik PID kontrol parametreleri ise kök yer eğrisi analizi sonucu elde edilmiştir.



Şekil 15. PID ve uyarlamalı PID kontrol basamak yanıtları  
Figure 15. PID and adaptive PID control step responses

Denetleyici performansları hata maliyeti açısından karşılaştırılmış ve maliyet fonksiyonu olarak Denklem 41’de tanımları verilen ortalama karesel hata karekökü (Root Mean Square Error-RMSE), ortalama karesel hata (Mean Squared Error-MSE), karesel hatanın integral (Integral Square Error-ISE) ölçütü kullanılmıştır.

$$\text{RMSE} = \sqrt{\frac{1}{N} \sum_{i=1}^N (e(t))^2}, \text{MSE} = \frac{1}{N} \sum_{i=1}^N (e(t))^2, \text{ISE} = \int (e(t))^2 dt \quad (41)$$

Çizelge 2, sisteme denetleyici uygulanması sonucunda elde edilen DC motor konum sinyallerinin (PID ve uyarlamalı PID) referanslarına göre hatalarının RMSE ve MSE değerlerini göstermektedir. Çizelgeden görülebileceği üzere PID sonucu elde edilen konum sinyalinin hata maliyeti, uyarlamalı PID

sonucu elde edilen konum sinyalinin hata maliyetine göre yüksektir. Karşılaştırmaya göre uyarlamalı PID kontrol uygulamasında referansa daha yakın, hata maliyeti daha düşük çıkış sinyali elde edildiği sonucuna varılmaktadır.

Yanıtların her ikisi de basamak girişine göre incelendiğinde uyarlamalı PID yanıtının daha yavaş olduğu (yükselme zamanı daha fazla) görülmektedir. Uyarlamalı PID yapısı referans modele göre çalıştığı için yükselme zamanı seçilen referans modele göre değişiklik gösterecektir. Performans kriterlerine göre tasarımcının farklı referans modelleri seçmesi ve farklı denetleyici performansı elde etmesi mümkündür.

**Çizelge 2.** PID ve uyarlamalı PID kontrol hata maliyeti karşılaştırılması

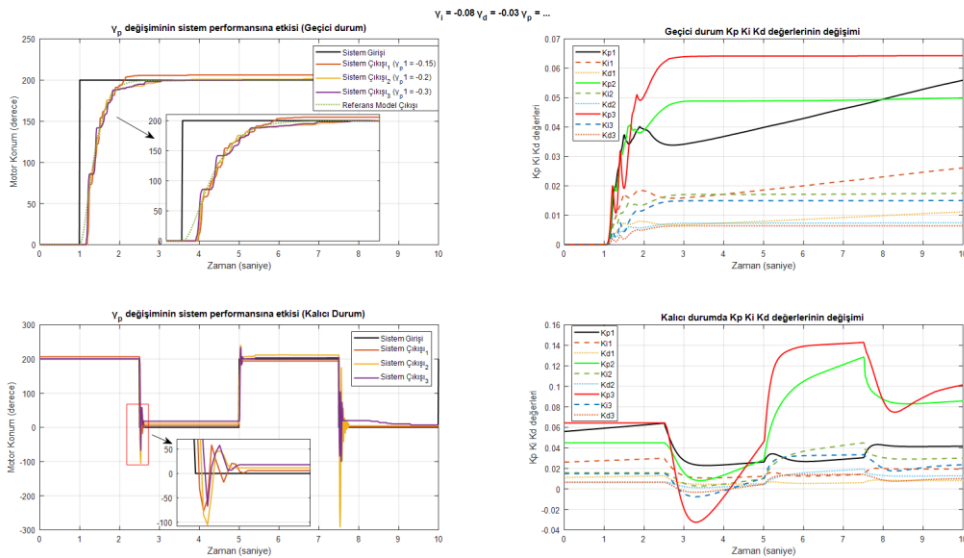
Table 2. Comparison of PID and adaptive PID control error cost			
	RMSE	MSE	ISE
PID	0.3995	159.7790	1523
Uyarlamalı PID	0.1852	34.3209	350.5

### 4.3. Gama Kazanç Değerlerinin Sistem Davranışına Etkisi (Effect of Gamma Gain Values on System Behavior)

Tasarlanan model referans uyarlamalı kontrol sisteminin değişen  $\gamma_p$ ,  $\gamma_i$  ve  $\gamma_d$  değerlerinin sistem davranışına etkisi incelenecektir. Kontrolör tasarımında optimum sonuç için bulunan  $\gamma_p = -0.015$ ,  $\gamma_i = -0.08$  ve  $\gamma_d = -0.03$  değişkenleri baz alınarak sisteme etkisi incelenecek değişken dışındaki parametreler sabit tutulup, değişken parametrenin sisteme etkisi incelenip bu inceleme sonuçları ayrıntılı olarak Şekil (16–18) arasında çizdirilmiş ve gerekli karşılaştırmalar yapılmıştır.

İlk olarak  $\gamma_i = -0.08$  ve  $\gamma_d = -0.03$  değerleri sabit tutulup  $\gamma_p$  parametresinin değişim etkisi  $\gamma_p = -0.015$ ,  $\gamma_p = -0.02$  ve  $\gamma_p = -0.03$  değerleri ele alınarak incelenmiştir. Sisteme geçici rejim durumu için 200 genlikli basamak fonksiyonu giriş olarak uygulanmış ve sistemin buna karşı cevabı Şekil 16'da gösterilmiştir.

Şekil 16 geçici durum yanıtından görüleceği üzere,  $\gamma_p$  parametresi düşürüldüğünde sistemin kalıcı durum hatası azalmıştır fakat yerleşme zamanı artmıştır. Geçici durum cevabının incelenmesinden sonra sisteme kare darbe fonksiyonu giriş olarak uygulanmış ve  $\gamma_p$  parametresinin kalıcı duruma etkisi incelenmiştir. Kalıcı durumda  $\gamma_p$  parametresi düşürüldüğünde maksimum aşım ve osilasyonlar artmış ve diğer kazançlar için performansın kabul edilebilir olmadığı gözlemlenmiştir.



**Şekil 16.**  $\gamma_p$  parametre değişiminin sistem davranışına etkisi

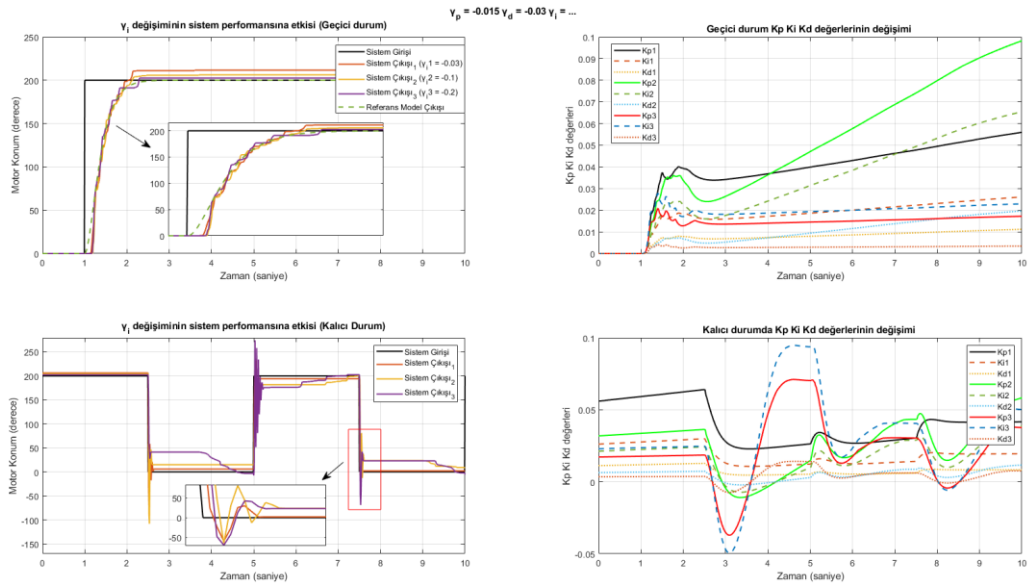
*Figure 16. Effect of  $\gamma_p$  parameter change on system behavior*

İkinci olarak sistemin  $\gamma_p = -0.015$  ve  $\gamma_d = -0.03$  değerleri sabit tutulup  $\gamma_i$  parametresinin değişim etkisi  $\gamma_i = -0.03$ ,  $\gamma_i = -0.1$  ve  $\gamma_i = -0.2$  değerleri ele alınarak incelenmiştir. Sisteme geçici rejim durumu için 200

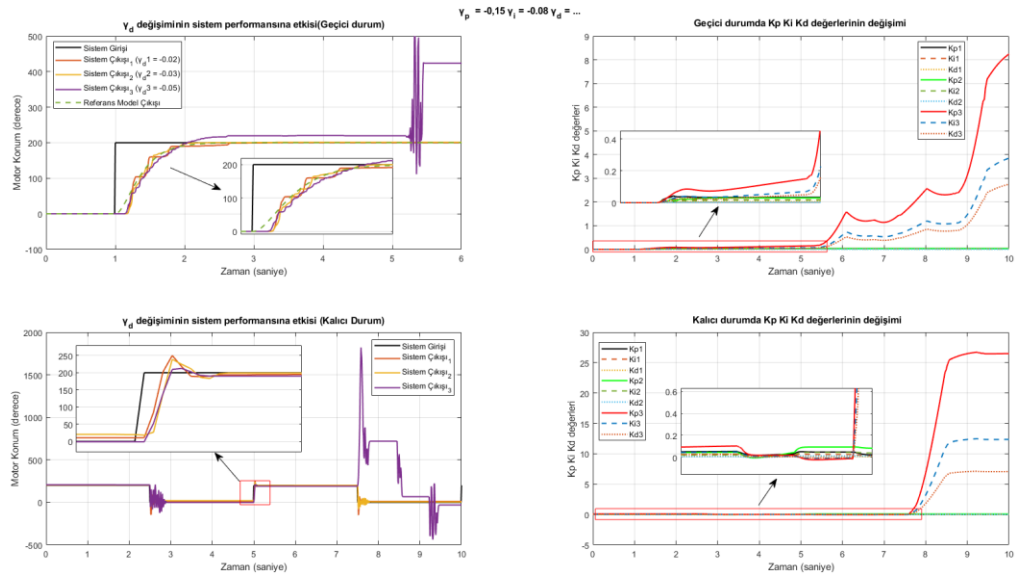


genlikli basamak fonksiyonu giriş olarak uygulanmış ve sistemin buna karşı cevabı Şekil 17’de gösterilmiştir.

Şekil 17 geçici durum yanıtından görüleceği üzere,  $\gamma_i$  parametresinin artışında sistemin kalıcı durum hatası ile maksimum aşım oranı artmış fakat yerleşme zamanı azalmıştır.  $\gamma_i$  parametresinin düşürülmesinde ise tam tersi durum gözlenmiştir. Tüm  $\gamma_i$  değerleri için sistemin referans modeli takip ettiği gözlemlenmiştir. Geçici durum cevabının incelenmesinden sonra sisteme kare darbe fonksiyonu giriş olarak uygulanmış ve değişen  $\gamma_i$  parametresinin kalıcı duruma etkisi incelenmiştir. Kalıcı durumda  $\gamma_p$  parametresi düşürüldüğünde maksimum aşımı, oturma zamanını ve osilasyonları arttırdığı ancak kontrol performansının kabul edilebilir olmadığı sonucuna varılmıştır.



Şekil 17.  $\gamma_i$  parametre değişiminin sistem davranışına etkisi  
Figure 17. Effect of  $\gamma_i$  parameter change on system behavior



Şekil 18.  $\gamma_d$  parametre değişiminin sistem davranışına etkisi  
Figure 18. Effect of  $\gamma_d$  parameter change on system behavior

Son durum olarak sistemin  $\gamma_p = -0.015$  ve  $\gamma_i = -0.08$  değerleri sabit tutulup  $\gamma_d$  parametresinin değişim etkisi  $\gamma_d = -0.02$ ,  $\gamma_d = -0.03$  ve  $\gamma_d = -0.05$  değerleri ele alınarak incelenmiştir. Sisteme geçici rejim durumu

için 200°lik basamak fonksiyonu giriş olarak uygulanmış ve sistemin buna karşı cevabı Şekil 18'de gösterilmiştir.

Şekil 18 geçici durum yanıtından görüleceği üzere,  $\gamma_d$  parametresi düşürüldüğünde kalıcı durum hatasının arttığı gözlemlenmiştir. Sistem kritik olan  $\gamma_d = -0.05$  değerini aldıktan sonra geçici durumda belirli bir süre sonrasında sistemin kontrolden çıktığı gözlemlenmiştir. Geçici durum cevabının incelenmesinden sonra sisteme kare darbe fonksiyonu giriş olarak uygulanmış ve değişen  $\gamma_d$  parametresinin kalıcı duruma etkisi incelenmiştir. Kalıcı durumda  $\gamma_d$  parametresi düşürüldüğünde sistemin kararsızlığa gittiği sonucuna varılmıştır.

## 5. SONUÇ ve TARTIŞMALAR (RESULTS and DISCUSSIONS)

Yapılan bu çalışmada STM32F4 uygulama geliştirme kiti ve Waijung blok seti kullanılarak uyarlamalı kontrol yöntemlerinden biri olan Model Referans Uyarlamalı PID Denetleyici (MRUPIDD) tasarımı gerçekleştirilmiştir. Parametre ayarlama mekanizması ve denetleyici tasarımı için MIT kuralı kullanılmıştır. Çalışma kapsamında tasarlanan denetleyicinin DC motor üzerinde gerçek zamanlı konum kontrol uygulaması gerçekleştirilmiş ve PID denetleyicisi ile karşılaştırılarak hata maliyetleri hesaplanmış ve uyarlamalı PID performansı, klasik PID denetleyicisine göre %53,7 daha başarılı elde edilmiştir.

Uyarlama kazanç parametrelerinin sistem davranışına etkisinin incelenmesi için ise farklı gama kazanç değerleri sisteme uygulanmış ve kararlılığı bozan durumlar incelenmiştir. Optimum sonuç olan  $\gamma_p = -0.015$ ,  $\gamma_i = -0.08$  ve  $\gamma_d = -0.03$  parametreleri baz alınarak sırasıyla ( $\gamma_i = -0.08$  ve  $\gamma_d = -0.03$  sabit;  $\gamma_{p1} = -0.015$ ,  $\gamma_{p2} = -0.02$ ,  $\gamma_{p3} = -0.03$ ), ( $\gamma_p = -0.015$  ve  $\gamma_d = -0.03$  sabit;  $\gamma_{i1} = -0.03$ ,  $\gamma_{i2} = -0.1$ ,  $\gamma_{i3} = -0.2$ ), ( $\gamma_p = -0.015$  ve  $\gamma_i = -0.08$  sabit;  $\gamma_{d1} = -0.02$ ,  $\gamma_{d2} = -0.03$ ,  $\gamma_{d3} = -0.05$ ) senaryoları esas alınmıştır. Bu senaryolar ile birlikte kontrolcü parametrelerinin etkileri detaylı bir şekilde ele alınarak yorumlanmış, kontrol algoritması tasarım süreci iyileştirilmiş ve birçok endüstriyel sistemin kontrol çalışmaları için teorik altyapı oluşturulmuştur.

Kontrol eğitiminde öğrencilerin yaparak ve yaşayarak öğrenme düzeyini arttırmaya yönelik düşük maliyetli, hızlı ve kolayca programlanabilen STM32F4 uygulama geliştirme kitinin kontrol uygulamalarında kullanımına dair temel bir çerçeve sunulmuştur. Lisans ve lisansüstü seviyelerinde veri toplama, analiz, sistem tanımlama ve denetleyici tasarımı hakkındaki teorik bilgilerin pratiğe dökülmesinde kolaylıkla uygulanabilir bir deney süreci vurgulanmıştır.

### Etik Standartlar Bildirimi (Declaration of Ethical Standards)

Bu çalışmada kullanılan materyal ve yöntemler etik kurul izni ve/veya yasal-özel bir izin gerektirmemektedir.

### Yazar Katkı Beyannamesi (Credit Authorship Contribution Statement)

Akif YAVUZSOY: Tasarım, deneyler, sonuç analizi; Hüseyin SARGIN: Tasarım, deneyler, sonuç analizi; Tuğçe YAREN: Yazım, düzenleme, denetleme; Selçuk KIZIR: Tasarım, düzenleme, denetleme.

### Çıkar Çatışması Beyannamesi (Declaration of Competing Interest)

Yazarların herhangi bir çıkar çatışması yoktur.

### Destek / Teşekkür (Funding / Acknowledgements)

Bu çalışmanın yürütülmesi esnasında herhangi bir kurum veya kuruluştan maddi bir destek alınmamıştır.

### Veri Kullanılabilirliği (Data Availability)

Bu çalışmadan elde edilen veriler diğer araştırmacılar tarafından kullanılabilir.

### KAYNAKLAR (REFERENCES)

- [1] M. A. Shamseldin, A. A. E. El-Samahy, "Speed Control of BLDC Motor by Using PID Control and Self-tuning Fuzzy PID Controller", in *15th International Workshop on Research and Education in Mechatronics (REM)*, 2014, pp. 1-9: IEEE.
- [2] W. Gubara, M. Elnaim, S. F. Babiker, "Comparative Study on the Speed of DC Motor Using PID and FLC", in *Conference of Basic Sciences and Engineering Studies (SGCAC)*, 2016, pp. 24-29: IEEE.
- [3] A. K. Heong, G. Chong, L. Yun, "PID Control System Analysis, Design, and Technology", *IEEE Transactions on Control Systems Technology*, vol. 13, pp. 559-576, 2005.
- [4] R. Kandiban, R. Arulmozhiyal, "Speed Control of BLDC Motor Using Adaptive Fuzzy PID Controller", *Procedia Engineering*, vol. 38, pp. 306-313, 2012.
- [5] S. Sastry, M. Bodson, *Adaptive Control: Stability, Convergence, and Robustness*. New York: Prentice-Hall, 1994.
- [6] D. Zhang, B. Wei, "A Review on Model Reference Adaptive Control of Robotic Manipulators", *Annual Reviews in Control*, vol. 43, pp. 188-198, 2017.
- [7] M. Kushwah, A. Patra, "Tuning PID Controller for Speed Control of DC Motor Using Soft Computing Techniques-A Review", *Advance in Electronic and Electric Engineering*, vol 4, pp. 141-148, 2014.
- [8] Y. Çakar, Y. Orman, S. Kizir, "Design of a Model Reference Adaptive PID Controller for DC Motor Position Control: COMPARED WITH PID AND FUZZY CONTROLLERS", *Mugla Journal of Science and Technology*, vol. 6, no. 0, pp. 25-35, 2020.
- [9] A. Emiroğlu, T. Yaren, S. Kizir, "Kendinden Ayarlamalı Denetleyici ile DA Motor Hız Kontrolü", *Politeknik Dergisi*, vol. 25, no. 2, pp. 757-765, 2022.
- [10] M. Mahmud, S. M. A. Motakabber, "Adaptive PID Controller Using for Speed Control of the BLDC Motor", in *International Conference on Semiconductor Electronics (ICSE)*, 2020, pp. 168-171: IEEE.
- [11] A. T. Ali, E. B. M. Tayeb, O. B. Mohd, "Adaptive PID Controller for DC Motor Speed Control" *International Journal of Engineering Inventions*, vol. 1, no. 5, pp. 26-30, 2012.
- [12] S. Gueye, L. Thiaw, M. F. Ndiaye, I. Ngom, M. Diop, E. H. M. Ndiaye, "A Sensorless Speed Control of DC Motor Based on an Adaptive Reference Model", in *4th Biennial International Conference on Nascent Technologies in Engineering (ICNTE)*, 2021, pp. 1-5: IEEE.
- [13] P. Jain, M. J. Nigam, "Real Time Control of Ball and Beam System with Model Reference Adaptive Control Strategy Using MIT Rule", in *International Conference on Computational Intelligence and Computing Research*, 2013, pp. 1-4: IEEE.
- [14] S. Kizir, T. Yaren, E. Kelekçi, *Matlab Simulink Destekli Gerçek Zamanlı Kontrol: Teori ve Mühendislik Uygulamaları*. Ankara: Seçkin Yayıncılık, 2019.
- [15] K. Worden, C. X. Wong, U. Parlitz, A. Hornstein, D. Engster, T. Tjahjowidodo, F. Al-Bender, D. D. Rzos, S. D. Fassois, "Identification of Pre-Sliding and Sliding Friction Dynamics: Grey Box and Black-Box Models", *Mechanical Systems and Signal Processing*, vol. 21, pp. 514-534, 2007.
- [16] T. Söderström, P. Stoica, *System Identification*. New York: Prentice-Hall, 1989.
- [17] Y. Naung, A. Sachagin, O. H. Lin, Y. K. Zaw, Z. Khaing, "Implementation of Data Driven Control System of DC Motor by Using System Identification Process", in *Conference of Russian Young Researchers in Electrical and Electronic Engineering (EIConRus)*, 2018, pp. 1801-1804: IEEE.
- [18] A. Nikranjbar, "Model Reference Adaptive PID Control of Servo Speed DC Motor", *Majlesi Journal of Mechatronic Systems*, vol. 2, pp. 7-13, 2013.

## PHENYLETHYLAMINE DERIVATIVE OF CALIX[4]ARENE SCHIFF BASE FOR FLUOROMETRIC DETECTION OF ZINC ION

<sup>1</sup>Egemen OZCELIK , <sup>2</sup>Clever NG'ANDU , <sup>3</sup>Begum TABAKCI , <sup>4\*</sup>Mustafa TABAKCI 

<sup>1,4</sup>Konya Technical University, Engineering and Natural Sciences Faculty, Chemical Engineering Department, Konya, TÜRKİYE

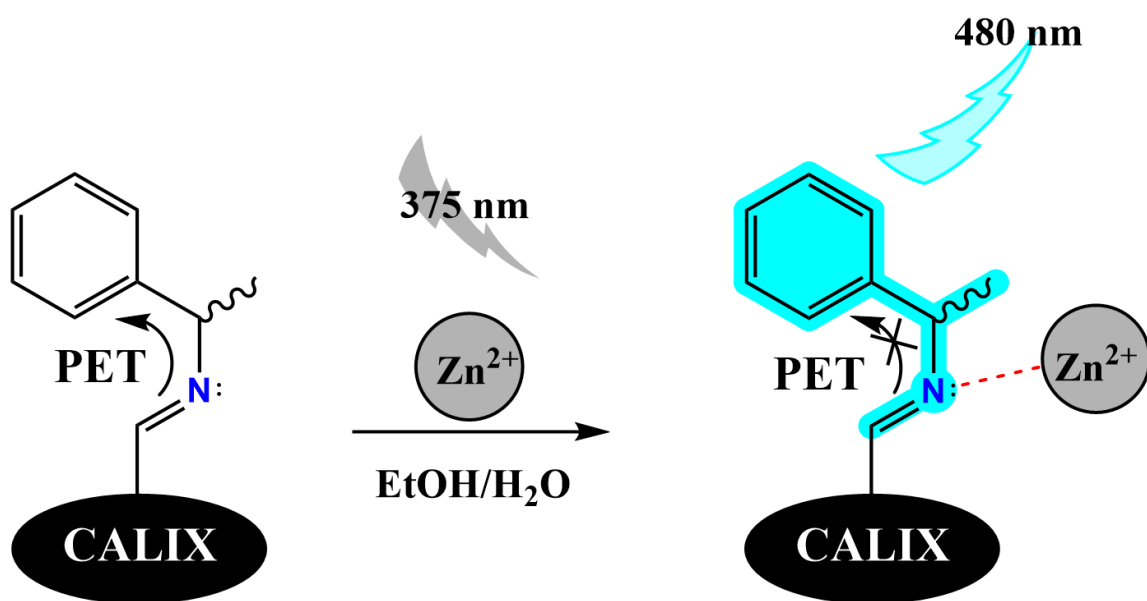
<sup>2,3</sup>Selcuk University, Science Faculty, Chemistry Department, Konya, TÜRKİYE

<sup>1</sup>egemen.ozcelik@gmail.com, <sup>2</sup>mweembela@gmail.com, <sup>3</sup>btabakci@selcuk.edu.tr, <sup>4</sup>mtabakci@ktun.edu.tr

### Highlights

- It was synthesized a new type of calixarene Schiff-base ligand (L) as the fluorophore and the receptor.
- Fluorescent L demonstrated high selectivity and sensitivity towards Zn<sup>2+</sup> compared to other metal ions.
- Limit of detection (LOD) reached 4.8 x 10<sup>-7</sup> M.
- It was determined that probe L can be utilized for the detection and monitoring of Zn<sup>2+</sup> in the environment.

### Graphical Abstract



Possible interaction presentation of calixarene-based probe (L) and Zn<sup>2+</sup> ion.



## PHENYLETHYLAMINE DERIVATIVE OF CALIX[4]ARENE SCHIFF BASE FOR FLUOROMETRIC DETECTION OF ZINC ION

<sup>1</sup>Egemen OZCELIK , <sup>2</sup>Clever NG'ANDU , <sup>3</sup>Begum TABAKCI , <sup>4,\*</sup>Mustafa TABAKCI

<sup>1,4</sup>Konya Technical University, Engineering and Natural Sciences Faculty, Chemical Engineering Department, Konya, TÜRKİYE

<sup>2,3</sup>Selcuk University, Science Faculty, Chemistry Department, Konya, TÜRKİYE

<sup>1</sup>egemen.ozcelik@gmail.com, <sup>2</sup>mweembela@gmail.com, <sup>3</sup>btabakci@selcuk.edu.tr, <sup>4</sup>mtabakci@ktun.edu.tr

(Received: 18.05.2023; Accepted in Revised Form: 02.06.2023)

**ABSTRACT:** As a Zn<sup>2+</sup> fluorescent probe, we have designed and synthesized a new type of calixarene Schiff-base ligand (L) possessing a 1-phenylethylamine group as the fluorophore and the receptor. As only Zn<sup>2+</sup> caused a significant increase in fluorescence emission intensity at 480 nm and the limit of detection (LOD) reached 4.8 × 10<sup>-7</sup> M, the synthesized fluorescent probe L demonstrated high selectivity and sensitivity towards Zn<sup>2+</sup> compared to other metal ions. In addition, the formation of a 1:1 complex between probe L and Zn<sup>2+</sup> was determined. As a consequence, it was determined that probe L can be utilized for the detection and monitoring of Zn<sup>2+</sup> in the environment.

**Keywords:** Calixarene, Schiff Base, Fluorometric Detection, Zinc, Sensor

### 1. INTRODUCTION

The exponential advancement in the application of heavy metals in pharmaceuticals, waste-water treatment and manufacturing industry has consequently elevated their levels in the environment and atmosphere [1, 2]. Heavy metal pollution has the potential to cause adverse impact on the ecosystem and therefore, the detection of these elements at trace concentrations is of paramount importance [3]. Zinc is one of the most abundant transitional metal elements in the earth's crust and it is the second most prevalent trace element in the human body after aluminium. It is extensively involved in diverse and significant biological processes such as gene expression, neurotransmission, apoptosis, as well as catalysis by functioning as a cofactor in more than 300 metalloenzymes [4-9]. Nonetheless, excessive accumulation of zinc in the body may disrupt the nervous and immune system thereby causing detrimental neurological effects such as Alzheimer's disease, cerebral ischemia, epilepsy and prostate cancer. In addition, toxic levels of zinc in the soil may inhibit the growth and development of plants due to nutrient imbalance and reduced photosynthetic rate [10, 11]. Therefore, many heavy metals such as Zn<sup>2+</sup> ion need to be detected in a sensitive and selective way. In recent years, many different molecules have been studied in the literature for the optical detection of Zn<sup>2+</sup> ion by using benzothiazole [12, 13], anthracene [14], benzidine [15], triphenylamine [16, 17], cyanobiphenyl [18], benzotriazole [19], tetrahydroquinazole [20], dinitrophenyl [21], thiophene [22], rhodanine [23], benzoimidazole [24], phenanthroline [25], naphthalene [26], 1,10-phenanthroline [27], BINOL [28] and sulphonamide [29]. Among these molecules, calixarenes play an important role. Heterocyclic structures formed as a result of the condensation reaction of p-terbutylphenol with formaldehyde in basic medium may have different functional groups in their structure and may have different uses. In the literature about calixarene derivatives, pyrene [30, 31], 4-biphenylcarbonitrile [32], bis(iminomethyl)phenyl [33], bis-terpyridinyl [34], 2,2'-bipyridine [35], imidazobenzimidazole [36], salicylidene imine [37] and triazole [38] structures are used for the optical detection of Zn<sup>2+</sup> ion. In these studies, especially the efficiency of Schiff base (-C=N-) functional groups for the detection of Zn<sup>2+</sup> ion is remarkable. During complexation, fluorescence properties emerge with the electron transfer disrupted as a result of the interaction of the nitrogen group in the Schiff base with ions [39]. In this study, a calix[4]arene-based ligand functionalized with a simple 1-phenylethylamine structure

\*Corresponding Author: Mustafa TABAKCI, [mtabakci@ktun.edu.tr](mailto:mtabakci@ktun.edu.tr)

was synthesized and its optical properties against different cations in solution were investigated by fluorescence spectroscopy.

## 2. MATERIAL AND METHODS

### 2.1. Chemicals and Equipment

In this study, the characterization of the synthesized calix[4]arene derivatives were performed with Varian brand 400 MHz NMR spectroscopy. The PerkinElmer brand Spectrum 100 FT-IR spectrometer model was used for the FTIR spectrum analysis. During synthesis, the progress of the reactions were monitored using thin layer chromatography Merck brand Kieselgel 60 F254. Fluorescence studies were performed using PerkinElmer brand LS55 spectrometer. While UV-Vis studies were carried out with PG Instrument brand T80+ UV/Vis spectrophotometer model. All chemicals and reagents used during the study were of analytical quality acquired from Merck, Sigma Aldrich, Alfa Aesar, Acros Organics, ISOLAB.

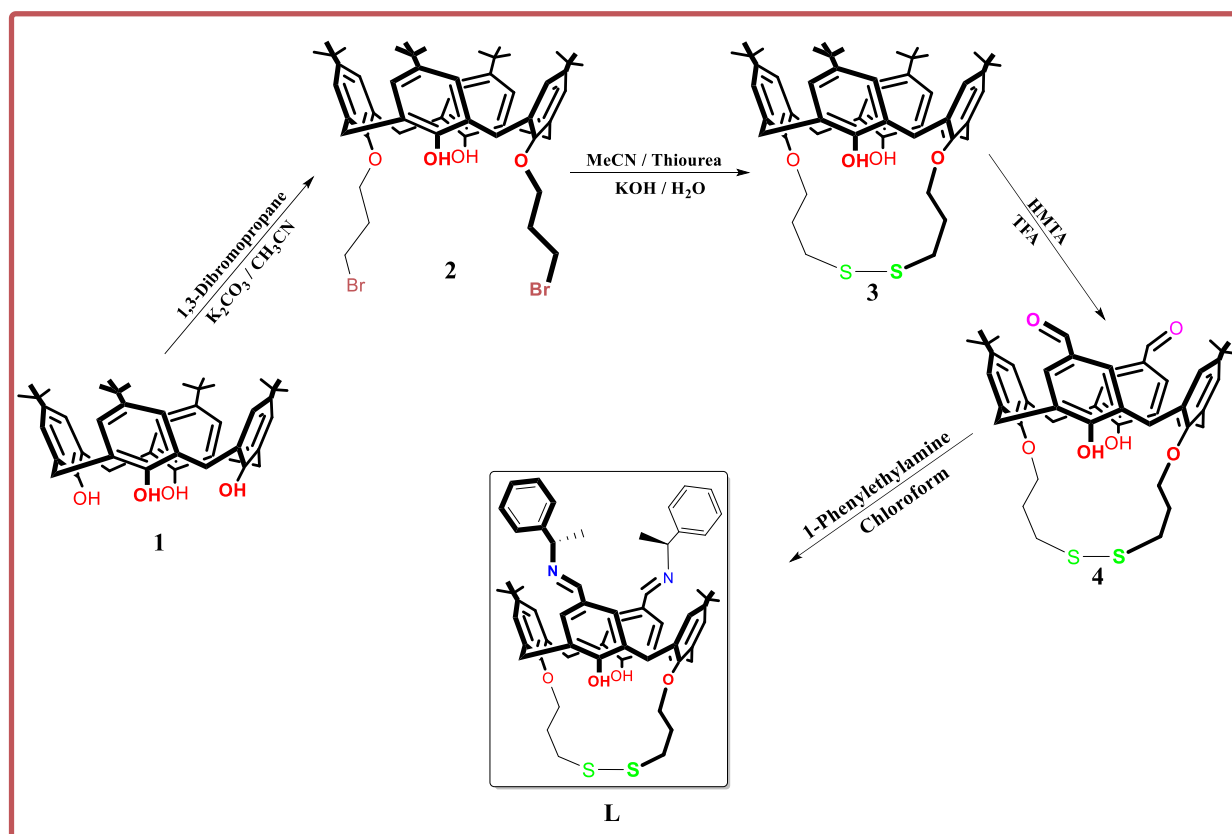


**Figure 1.** Presentation of synthesis scheme of calixarene based ligand (L).

### 2.2. Synthesis of Calixarene Based Ligand and Investigation of Sensing Properties

The final calix[4]arene derivative (L) using as a ligand in the study given in Figure 1 was synthesized according to the method in literature [40] and its structural characterization was performed.

For the spectroscopic measurements, the stock solutions ( $10^{-2}$  M) of various metal ions ( $\text{Li}^+$ ,  $\text{Na}^+$ ,  $\text{Cs}^+$ ,  $\text{Ag}^+$ ,  $\text{Ca}^{2+}$ ,  $\text{Mg}^{2+}$ ,  $\text{Sr}^{2+}$ ,  $\text{Ba}^{2+}$ ,  $\text{Hg}^{2+}$ ,  $\text{Zn}^{2+}$ ,  $\text{Ni}^{2+}$ ,  $\text{Cu}^{2+}$ ,  $\text{Cd}^{2+}$ ,  $\text{Co}^{2+}$ ,  $\text{Mn}^{2+}$ ,  $\text{Fe}^{2+}$ ,  $\text{Fe}^{3+}$ ,  $\text{Cr}^{3+}$ , and  $\text{Al}^{3+}$ ) were separately prepared in deionized water using their perchlorate salt. On the other hand, the solution of L ( $3 \times 10^{-6}$  M) was prepared in 3 mL of ethanol and water (99:1, v/v) at room temperature.

The fluorescence titration study was conducted for **L** in 3 mL ethanol-water (99/1, V/V) system at a concentration of  $3 \times 10^{-6}$  M. Fluorescence spectrums of the solutions were taken by adding different cation solutions in certain volumes to realize the fluorescence titration on the solution. Excitation wavelength of the probe was 375 nm, the maximum emission wavelength was 480 nm and the slit width is 8/8 nm. In the UV-vis titration experiments, the solution of **L** was firstly added, followed by metal ions with different concentrations in a 3 mL of sample cuvette, the UV-vis spectral intensity of the mixture was tested after the reaction was complete, with scanning wavelength 200–800 nm.

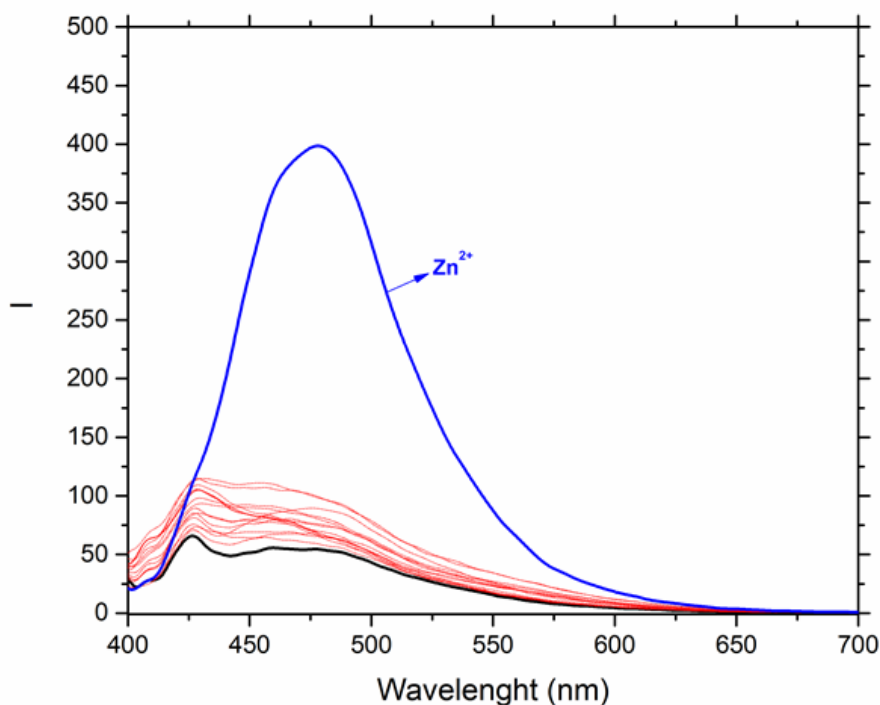


**Figure 2.** Fluorescence spectra of **L** towards various ion in ethanol-water media ( $[L] = 3 \times 10^{-6}$  M,  $[M] = 3 \times 10^{-6}$  M, ( $\lambda_{ex} = 375$  nm)).

### 3. RESULTS AND DISCUSSIONS

#### 3.1. Synthesis of Calixarene Based Ligand (**L**)

The amount of pollution caused by different cationic compounds in an aqueous environment should be measured accurately and efficiently. Thanks to the optical sensors developed for this purpose, compounds can be detected by selective, sensitive and reliable fluorimetric or colorimetric means. Among the fluorescence sensors, perception of different cations can be carried out by structures that contain different fluorophore groups. In this study, a 1-phenylethylamine functionalized Schiff base calix[4]arene (**L**) was prepared and its optical properties against various cations ( $\text{Li}^+$ ,  $\text{Na}^+$ ,  $\text{Cs}^+$ ,  $\text{Ag}^+$ ,  $\text{Ca}^{2+}$ ,  $\text{Mg}^{2+}$ ,  $\text{Sr}^{2+}$ ,  $\text{Ba}^{2+}$ ,  $\text{Hg}^{2+}$ ,  $\text{Zn}^{2+}$ ,  $\text{Ni}^{2+}$ ,  $\text{Cu}^{2+}$ ,  $\text{Cd}^{2+}$ ,  $\text{Co}^{2+}$ ,  $\text{Mn}^{2+}$ ,  $\text{Fe}^{2+}$ ,  $\text{Fe}^{3+}$ ,  $\text{Cr}^{3+}$ , and  $\text{Al}^{3+}$ ) were examined. Following the synthesis scheme given in Figure 1, calix[4]arene derivatives were synthesized according to literature [40]. Firstly, the basic calix[4]arene **1** was synthesized according to literature, then the calix[4]arene derivative **2** consisting of the 3-bromopropoxyl group was synthesized in acetonitrile and 1,3-dibromopropane by the Williamson ether synthesis. As a result of the oxidation reaction of the obtained halide-containing calix[4]arene derivative with thiourea, the disulfide-linked calix[4]arene derivative **3** was synthesized and characterized. Then, calix[4]arene derivative **4** containing aldehyde groups was synthesized by the Duff

reaction with hexamethylenetetramine in trifluoroacetic acid medium. And finally, as a result of the condensation reaction of the calix[4]arene derivative containing aldehyde groups 4 and 1-phenylethylamine, L was synthesized and its characterization was carried out according to literature [40].

### 3.2. Investigation of Sensing Properties of Calixarene Based Ligand (L) Towards Various Ions

Examination of the optical properties of the prepared calix[4]arene-based ligand (L) against different cations ( $\text{Li}^+$ ,  $\text{Na}^+$ ,  $\text{Cs}^+$ ,  $\text{Ag}^+$ ,  $\text{Ca}^{2+}$ ,  $\text{Mg}^{2+}$ ,  $\text{Sr}^{2+}$ ,  $\text{Ba}^{2+}$ ,  $\text{Hg}^{2+}$ ,  $\text{Zn}^{2+}$ ,  $\text{Ni}^{2+}$ ,  $\text{Cu}^{2+}$ ,  $\text{Cd}^{2+}$ ,  $\text{Co}^{2+}$ ,  $\text{Mn}^{2+}$ ,  $\text{Fe}^{2+}$ ,  $\text{Fe}^{3+}$ ,  $\text{Cr}^{3+}$ , and  $\text{Al}^{3+}$ ) was conducted at a concentration value of  $3 \times 10^{-6}$  M in an ethanol-water medium (99/1, v/v). The plot of the change in the fluorescence spectrum obtained is given in Figure 2. When the fluorescence spectrum of L is examined, it is observed that it emits weakly at 430 nm and 470 nm as a result of inhibition of photoinduced electron-transfer (PET) and C=N isomerization by excitation at 375 nm.

PET occurs towards the aromatic ring *via* the unshared electron pair on the nitrogen donor in the C=N group in the structure of L. Emission occurs when this PET mechanism breaks down after the addition of  $\text{Zn}^{2+}$  ion. According to literature, Zhu et al. (2017), Li et al. (2023) and Mu et al. (2021), in their study, determined that there is a PET mechanism towards the aromatic ring through the imine group in the ligands they have prepared, and this is deteriorated with the addition of  $\text{Zn}^{2+}$  to the medium [26, 41, 42]. In addition, due to the selective feature of the C=N structure, which is the chelating group, against transition metals [32], this PET mechanism is interrupted as a result of the interaction of the unshared electron pair on the nitrogen donor and the  $\text{Zn}^{2+}$  ion, which occurs as a result of the interaction of the  $\text{Zn}^{2+}$  ion after stimulation and the interaction of the  $\text{Zn}^{2+}$  ion. As a result of its interaction with the nitrogen donor, an emission peak occurred at 480 nm. The resulting interaction mechanism is given in Figure 3.

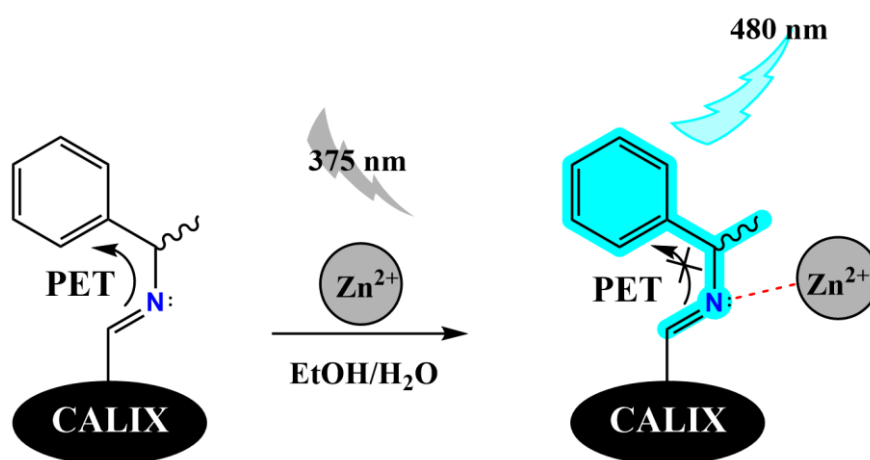


**Figure 3.** Possible interaction presentation of calixarene-based fluorescent probe (L) and  $\text{Zn}^{2+}$  ion.

In order to better examine the interactions between L and  $\text{Zn}^{2+}$  ion, both fluorescence and UV titration studies were performed by the addition of different amounts of  $\text{Zn}^{2+}$  ion. The changes in the fluorescence spectrum were recorded by adding 0-8 equivalents  $\text{Zn}^{2+}$  ion upon the solution of L at  $3 \times 10^{-6}$  M concentration in ethanol-water (99/1, v/v). It is observed that the fluorescence intensity increases at 480 nm in the spectrum however, this increase rate decreases, after the addition of 0.6 eq.  $\text{Zn}^{2+}$ . In case of UV titration, it is seen that the absorbance value increases at 340 nm in the spectrum, but this increase rate decreases, after the addition of 0.6 eq.  $\text{Zn}^{2+}$ .



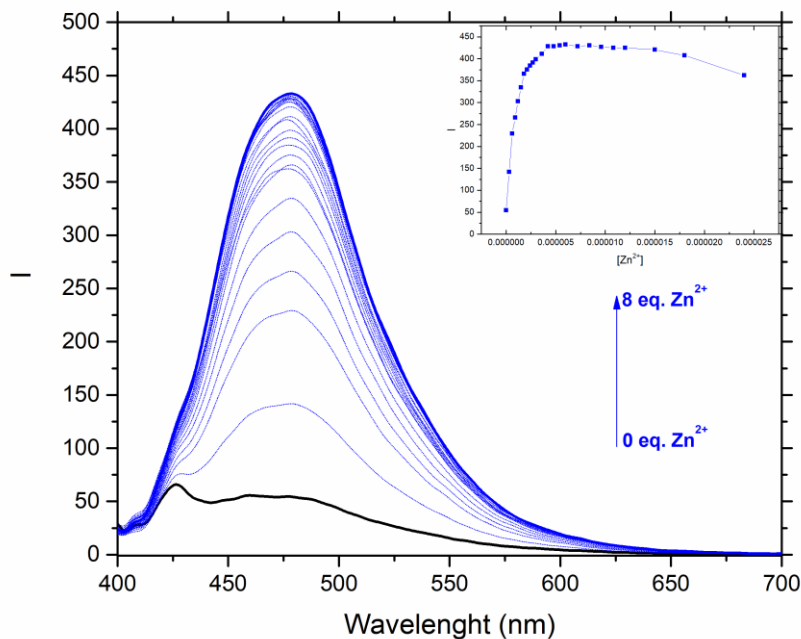


**Figure 4.** Fluorescence spectra of L solution (EtOH/H<sub>2</sub>O, 99:1, v/v) upon addition of different amounts of Zn<sup>2+</sup> ion (0-8 equivalents) ( $\lambda_{ex} = 375$  nm).

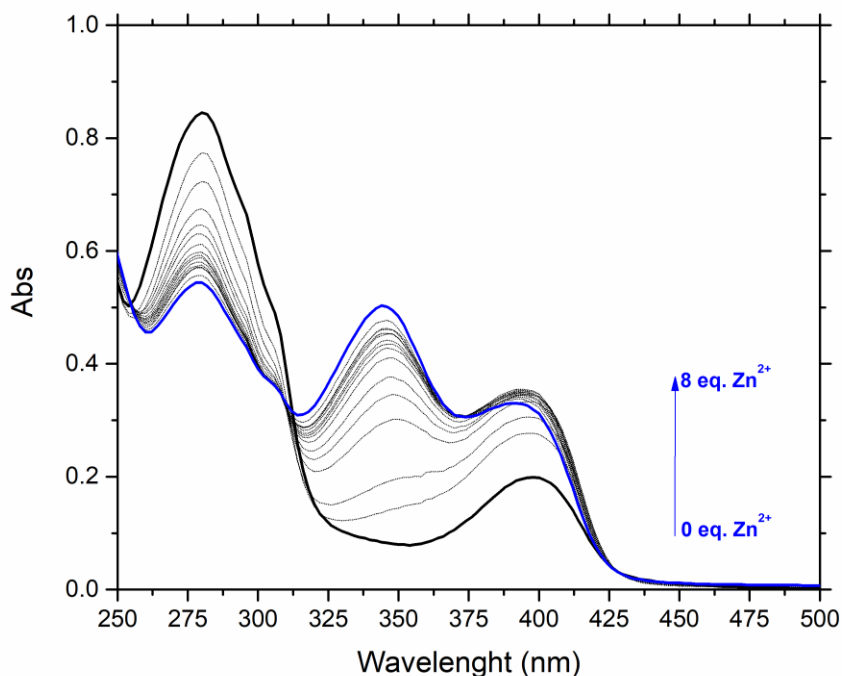


**Figure 5.** UV spectra of L solution (EtOH/H<sub>2</sub>O, 99:1, v/v) upon addition of different amounts of Zn<sup>2+</sup> ion (0-8 equivalents).

In order to determine the stoichiometry of the complex formed between the L and the Zn<sup>2+</sup> ion, the Job plot was drawn using the titration data and is given in Figure 6. When the obtained data was examined,

the fact that the peak of the mole fraction was close to the value of 0.66 suggested that the complexation occurred at a ratio of 2:1, that is, the two ligand L molecules complexed with a  $Zn^{2+}$  ion. On the other hand, in the fluorescence studies, as a result of the interaction with the unshared electron pairs on the nitrogen donor L possesses, it is seen that emission occurs with the inhibition of the PET mechanism. More, since L has two functional groups in its structure, the binding phenomena at the same conditions were examined using the Benesi-Hildebrand equation to better determine the complexation stoichiometry. Thus, the binding coefficient ( $K$ ) was calculated by the Benesi-Hildebrand equation using titration data to calculate the binding coefficient.

$$\frac{1}{I - I_0} = \frac{1}{\left\{ K (I_{\max} - I) [Zn^{2+}]^n \right\}} + \frac{1}{(I_{\max} - I)}$$

Here,  $I_0$  is the initial fluorescence intensity,  $I$  is the fluorescence intensity after cation addition,  $I_{\max}$  is the maximum absorbance value obtained and  $K$  is the binding constant ( $1/M$ ). In order to confirm the complexation between  $Zn^{2+}$  ion and L, Benesi-Hildebrand plots were plotted for assuming both 1:1 complexation and 2:1 complexation and given in Figure 6A and Figure 6B, respectively. According to the results obtained, it is seen that the slope of the graph obtained for 1:1 complexation has a higher linearity ( $R^2 = 0.9847$ ). When the results obtained with Job's graph are analyzed together, it is thought that a weak complex is formed between L and  $Zn^{2+}$  ion. The value of the binding constant ( $K = 1.8 \text{ M}^{-1}$ ) calculated from the slope of the  $1/[Zn^{2+}]$  versus  $1/(I - I_0)$  graph seems to confirm this.

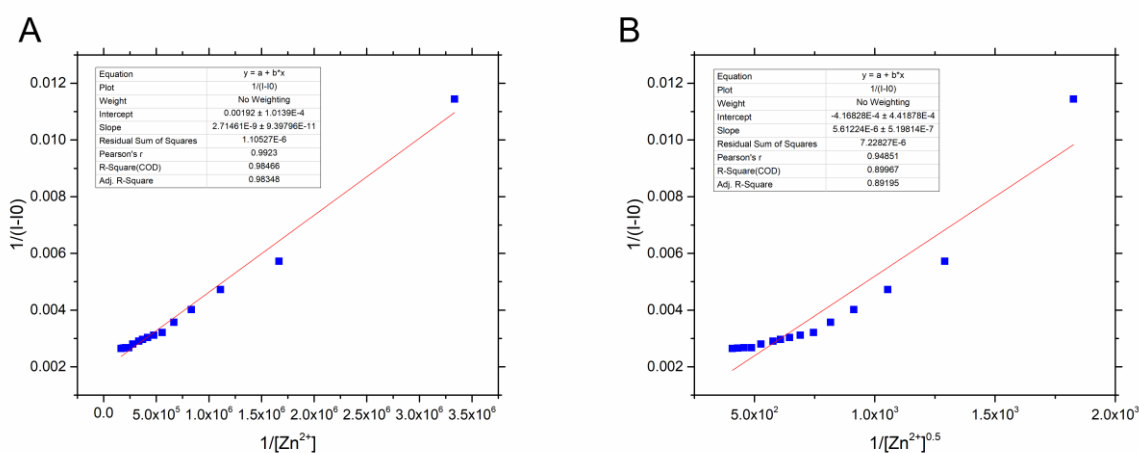


**Figure 6.** Benesi-Hildebrand plots for assuming (A) 1:1 complexation and (B) 2:1 complexation.

Using the data obtained as a result of the titration study, a graph of fluorescence intensity versus  $Zn^{2+}$  concentration was drawn as given in Figure 7. Using the data in the linear part of this graph, the limit detection (LOD) value was calculated as  $4.8 \times 10^{-7} \text{ M}$  using the formula  $LOD = 3\sigma/m$ , where  $\sigma$  denotes the standard deviation of the 10 blank samples, and  $m$  denotes the slope of the linear regression (Figure 7). This limit is discovered to be substantially lower than the WHO recommended limit for  $Zn^{2+}$  in drinking water ( $7.65 \times 10^{-5} \text{ M}$ ). As a result, with an increase in fluorescence, the probe would have extremely low detection limits and be suitable for usage in real-world scenarios.

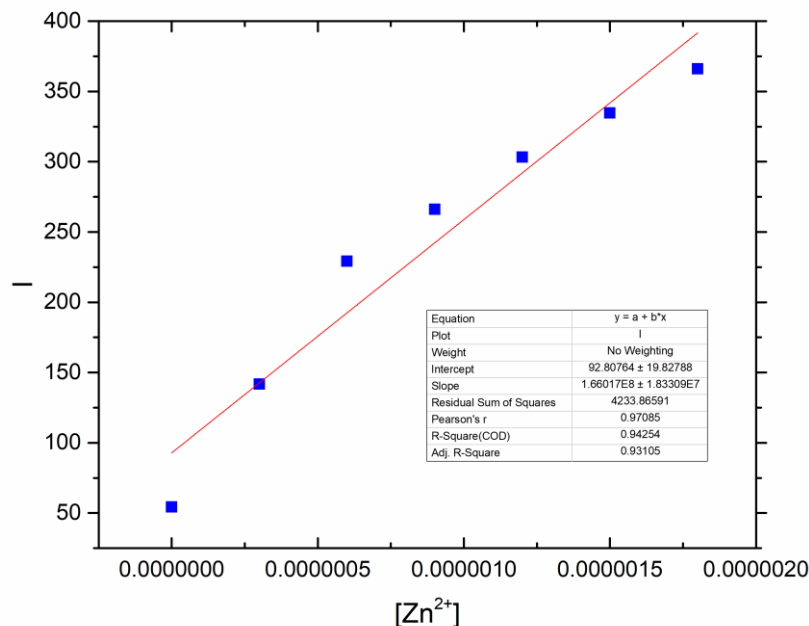


**Figure 7.** The graph of change in fluorescence intensity towards  $Zn^{2+}$  ion in different concentrations.

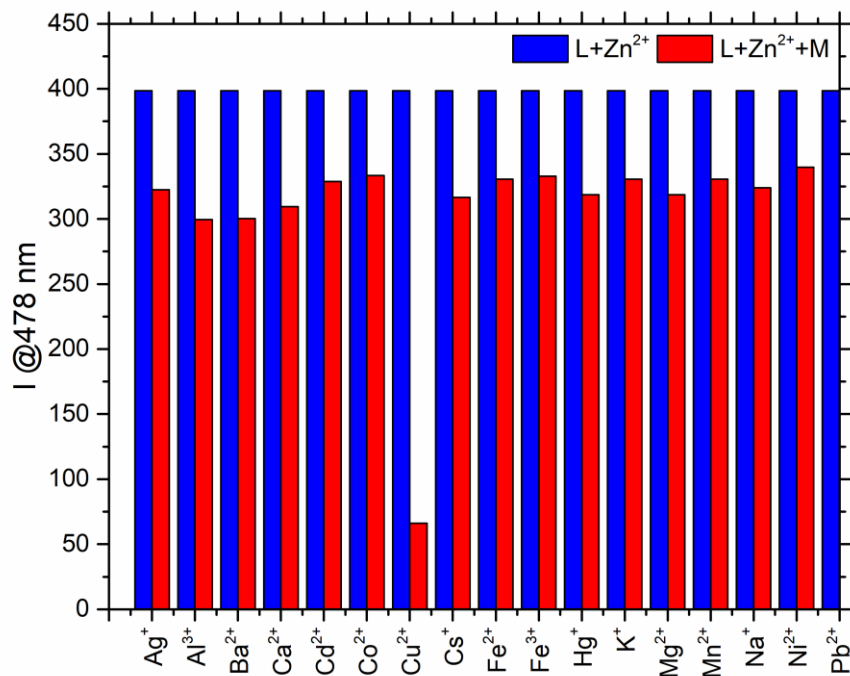


**Figure 8.** Fluorescence intensities of L ( $3 \times 10^{-6}$  M) upon addition of various metal ions ( $6 \times 10^{-6}$  M) ( $Zn^{2+}$ ,  $Al^{3+}$ ,  $Ag^+$ ,  $Cd^{2+}$ ,  $Co^{2+}$ ,  $Mn^{2+}$ ,  $Na^+$ ,  $Pb^{2+}$ ,  $K^+$ ,  $Ca^{2+}$ ,  $Mg^{2+}$ ,  $Ba^{2+}$ ,  $Cu^{2+}$ ,  $Fe^{2+}$ ,  $Hg^{2+}$ , and  $Ni^{2+}$ ) and that of the respective solution added  $Zn^{2+}$  ( $3 \times 10^{-6}$  M). EtOH/ $H_2O$  solution (99:1, v/v),  $\lambda_{ex} = 375$  nm.

Upon the determination that L is selective against  $Zn^{2+}$  ion among different cations, the effect of other

cations on the L - Zn<sup>2+</sup> complex was investigated and the changes obtained are given in Figure 8. When the changes in fluorescence intensity obtained as a result of the addition of different cations as 2 equivalents on the L - Zn<sup>2+</sup> complex are examined, it is seen that the fluorescence intensity is seriously quenched with the addition of Cu<sup>2+</sup> ion. The results demonstrate that, with the exception of Cu<sup>2+</sup> ion, other interferences on Zn<sup>2+</sup> detection can be disregarded. In order to as far as feasible, the probe can be used in the environment to detect zinc ions without Cu<sup>2+</sup> ions.

#### 4. CONCLUSIONS

In this study, a 1-phenylethylamine-functionalized calix[4]arene-based ligand (L) was prepared and its optical properties against different cations were investigated. In the case of Zn<sup>2+</sup>, L exhibited an intense fluorescence at 480 nm when excited at 375 nm in an ethanol-water medium, which indicated that it is a selective sensor for the Zn<sup>2+</sup> ion among cations. This is due to the inhibition of the PET mechanism on the L probe as a result of its interaction with the Zn<sup>2+</sup> ion and the interaction mechanism with the C=N isomerization *via* its imine group. It was found that the composition of the complex formed by the coordination of L with Zn<sup>2+</sup> is 1:1. On the basis of fluorescence titration studies, the complex binding constant and the detection limit of the L probe were calculated to be 4.8x10<sup>-7</sup> M and 1.8 M<sup>-1</sup>, respectively. Consequently, this study presents that the 1-phenylethylamine-functionalized calix[4]arene-based ligand (L) prepared in this study can be an efficient and effective fluorescence sensor for Zn<sup>2+</sup> ions.

#### Declaration of Ethical Standards

The authors declare that all ethical guidelines including authorship, citation, data reporting, and publishing original research are followed.

#### Declaration of Competing Interest

The authors declare that there is no conflict of interest.

#### Data Availability

The data that support the findings of this study are available from the corresponding author upon reasonable request.

#### REFERENCES

- [1] A. Kim, J. H. Kang, H. J. Jang, and C. Kim, "Fluorescent detection of Zn (II) and In (III) and colorimetric detection of Cu (II) and Co (II) by a versatile chemosensor," *Journal of industrial and engineering chemistry*, vol. 65, pp. 290-299, 2018.
- [2] S. Sakunkaewkasem *et al.*, "Dual-analyte fluorescent sensor based on [5] helicene derivative with super large stokes shift for the selective determinations of Cu<sup>2+</sup> or Zn<sup>2+</sup> in buffer solutions and its application in a living cell," *ACS sensors*, vol. 3, no. 5, pp. 1016-1023, 2018.
- [3] J. Briffa, E. Sinagra, and R. Blundell, "Heavy metal pollution in the environment and their toxicological effects on humans. Heliyon," ed: Elsevier Ltd, 2020.
- [4] C. Andreini, L. Banci, I. Bertini, and A. Rosato, "Zinc through the three domains of life," *Journal of proteome research*, vol. 5, no. 11, pp. 3173-3178, 2006.
- [5] M. P. Cuajungco, M. S. Ramirez, and M. E. Tolmasky, "Zinc: multidimensional effects on living organisms," *Biomedicines*, vol. 9, no. 2, p. 208, 2021.
- [6] A. M. Hessels and M. Merckx, "Genetically-encoded FRET-based sensors for monitoring Zn<sup>2+</sup> in living cells," *Metallomics*, vol. 7, no. 2, pp. 258-266, 2015.
- [7] L. Maxfield, S. Shukla, and J. S. Crane, "Zinc deficiency," in *StatPearls [Internet]*: StatPearls Publishing, 2021.

- [8] T. S. Singh, P. C. Paul, and H. A. Pramanik, "Fluorescent chemosensor based on sensitive Schiff base for selective detection of Zn<sup>2+</sup>," *Spectrochimica Acta Part A: Molecular and Biomolecular Spectroscopy*, vol. 121, pp. 520-526, 2014.
- [9] B. L. Vallee and K. H. Falchuk, "The biochemical basis of zinc physiology," *Physiological reviews*, vol. 73, no. 1, pp. 79-118, 1993.
- [10] H. Kaur and N. Garg, "Zinc toxicity in plants: a review," *Planta*, vol. 253, no. 6, p. 129, 2021.
- [11] L. M. Plum, L. Rink, and H. Haase, "The essential toxin: impact of zinc on human health," *International journal of environmental research and public health*, vol. 7, no. 4, pp. 1342-1365, 2010.
- [12] L. Chen *et al.*, "A Schiff-based AIE fluorescent probe for Zn(2+) detection and its application as "fluorescence paper-based indicator"," *Spectrochim Acta A Mol Biomol Spectrosc*, vol. 268, p. 120704, Mar 5 2022.
- [13] D. Musib, M. K. Raza, S. S. Devi, and M. Roy, "A reversible, benzothiazole-based "Turn-on" fluorescence sensor for selective detection of Zn<sup>2+</sup> ions in vitro," *Journal of Chemical Sciences*, vol. 132, no. 1, 2020.
- [14] X. Wei, L. Bu, W. Tang, S. Zhao, and Y. Xie, "Selective and sensitive fluorescence "turn-on" Zn<sup>2+</sup> probes based on combination of anthracene, diphenylamine and dipyrin," *Science China Chemistry*, vol. 60, no. 9, pp. 1212-1218, 2017.
- [15] M. Kumar, A. Kumar, M. K. Singh, S. K. Sahu, and R. P. John, "A novel benzidine based Schiff base "turn-on" fluorescent chemosensor for selective recognition of Zn<sup>2+</sup>," *Sensors and Actuators B: Chemical*, vol. 241, pp. 1218-1223, 2017.
- [16] P. S. Hariharan and S. P. Anthony, "Selective turn-on fluorescence for Zn(2+) and Zn(2+)+Cd(2+) metal ions by single Schiff base chemosensor," *Anal Chim Acta*, vol. 848, pp. 74-79, Oct 27 2014.
- [17] G. Xu, S. J. Ma, H. H. Zhang, J. Jing, X. H. Chen, and X. P. Zhang, "A Fluorescent Probe Based on the Hydrazone Schiff Base for the Detection of Zn(2+) and its Application on Test Strips," *J Fluoresc*, Jan 9 2023.
- [18] F. Bie *et al.*, "A cyanobiphenyl-based ratiometric fluorescent sensor for highly selective and sensitive detection of Zn<sup>2+</sup>," *Inorganica Chimica Acta*, vol. 508, 2020.
- [19] J. Liu *et al.*, "Two Schiff-base fluorescence probes based on triazole and benzotriazole for selective detection of Zn<sup>2+</sup>," *Sensors and Actuators B: Chemical*, vol. 227, pp. 296-303, 2016.
- [20] J. Yang *et al.*, "A novel tetrahydroquinazolin-2-amine-based high selective fluorescent sensor for Zn<sup>2+</sup> from nopinone," *Tetrahedron*, vol. 72, no. 30, pp. 4503-4509, 2016.
- [21] R. Behura *et al.*, "A Schiff base luminescent chemosensor for selective detection of Zn<sup>2+</sup> in aqueous medium," *Journal of Molecular Structure*, vol. 1264, 2022.
- [22] M. Mary Mathew and A. Srekanth, "Zn<sup>2+</sup>ion responsive fluorescent chemosensor probe of Thiophene-diocarbonylhydrazide derivatives," *Inorganica Chimica Acta*, vol. 516, 2021.
- [23] H. Kim, D. Gil, and C. Kim, "Selective fluorescent detection of Zn<sup>2+</sup> by a rhodanine-based chemosensor," *Journal of the Chinese Chemical Society*, vol. 69, no. 5, pp. 856-863, 2022.
- [24] X. Wang, Z. Liu, F. Qian, and W. He, "A bezimidazole-based highly selective and low-background fluorescent sensor for Zn<sup>2+</sup>," *Inorganic Chemistry Communications*, vol. 15, pp. 176-179, 2012.
- [25] C. Quan, J. Liu, W. Sun, and X. Cheng, "Highly sensitive and selective fluorescence chemosensors containing phenanthroline moieties for detection of Zn<sup>2+</sup> and Cd<sup>2+</sup> ions," *Chemical Papers*, vol. 74, no. 2, pp. 485-497, 2019.
- [26] Y. Li, R. Song, J. Zhao, Y. Liu, and J. Zhao, "Synthesis, structure, and properties of a novel naphthalene-derived fluorescent probe for the detection of Zn<sup>2+</sup>," *Polyhedron*, vol. 234, 2023.
- [27] G. Tian, Y.-Z. Han, and Q. Yang, "1, 10-phenanthroline derivative as colorimetric and ratiometric fluorescence probe for Zn<sup>2+</sup> and Cd<sup>2+</sup>," *Results in Chemistry*, vol. 5, 2023.
- [28] K. Lu *et al.*, "Synthesis of a BINOL-Based C(3) Symmetric Schiff Base and Its Fluorescence Response to Zn(2)," *Chempluschem*, vol. 88, no. 3, p. e202300036, Mar 2023.

- [29] C. Amoah, C. Obuah, M. K. Ainooson, L. Hamenu, A. Oppong, and A. Muller, "A new sulfonamide-based chemosensor for potential fluorescent detection of Cu<sup>2+</sup> and Zn<sup>2+</sup> ions," *Tetrahedron*, vol. 133, 2023.
- [30] S. Y. Park *et al.*, "A Pyrenyl-Appended Triazole-Based Calix[4]arene as a Fluorescent Sensor for Cd<sup>2+</sup> and Zn<sup>2+</sup>," *The Journal of Organic Chemistry*, vol. 73, no. 21, pp. 8212-8218, 2008/11/07 2008.
- [31] P. G. Sutariya, H. Soni, S. A. Gandhi, and A. Pandya, "Luminescent behavior of pyrene-allied calix[4]arene for the highly pH-selective recognition and determination of Zn<sup>2+</sup>, Hg<sup>2+</sup> and I<sup>-</sup> via the CHEF-PET mechanism: computational experiment and paper-based device," *New Journal of Chemistry*, 10.1039/C9NJ01388A vol. 43, no. 25, pp. 9855-9864, 2019.
- [32] S. Erdemir and B. Tabakci, "Highly sensitive fluorometric detection of Zn<sup>2+</sup> ion by calix [4] arene derivative appended 4-biphenylcarbonitrile," *Dyes and Pigments*, vol. 151, pp. 116-122, 2018.
- [33] S. Ullmann *et al.*, "Zn<sup>2+</sup>-Ion Sensing by Fluorescent Schiff Base Calix[4]arene Macrocycles," *Chemistry – A European Journal*, vol. 23, no. 16, pp. 3824-3827, 2017.
- [34] L. Li, L.-t. Du, J. Sun, and C.-g. Yan, "Synthesis, crystal structure of bis-terpyridinyl-calix[4]arene derivatives and fluorescent sensor for Zn<sup>2+</sup>," *Chemical Research in Chinese Universities*, vol. 29, no. 5, pp. 874-878, 2013/10/01 2013.
- [35] J. F. Zhang, S. Bhuniya, Y. H. Lee, C. Bae, J. H. Lee, and J. S. Kim, "Novel 2,2'-bipyridine-modified calix[4]arenes: ratiometric fluorescent chemosensors for Zn<sup>2+</sup> ion," *Tetrahedron Letters*, vol. 51, no. 29, pp. 3719-3723, 2010/07/21/ 2010.
- [36] Y.-T. Huang, M. Xue, and Y. Yang, "Imidazobenzimidazole fused azacalix [4]arenes: Synthesis, structure, and Zn<sup>2+</sup>-selective colorimetric-fluorometric sensor," *Chinese Chemical Letters*, p. 108294, 2023/03/05/ 2023.
- [37] R. Joseph, J. P. Chinta, and C. P. Rao, "Lower Rim 1,3-Derivative of Calix[4]arene-Appended Salicylidene Imine (H<sub>2</sub>L): Experimental and Computational Studies of the Selective Recognition of H<sub>2</sub>L toward Zn<sup>2+</sup> and Sensing Phosphate and Amino Acid by [ZnL]," *The Journal of Organic Chemistry*, vol. 75, no. 10, pp. 3387-3395, 2010/05/21 2010.
- [38] R. K. Pathak, A. G. Dikundwar, T. N. G. Row, and C. P. Rao, "A lower rim triazole linked calix[4]arene conjugate as a fluorescence switch on sensor for Zn<sup>2+</sup> in blood serum milieu," *Chemical Communications*, 10.1039/C0CC00219D vol. 46, no. 24, pp. 4345-4347, 2010.
- [39] B. Tabakci, H. M. A. Ahmed, and S. Erdemir, "Fast and Reversible "Turn on" Fluorescent Sensors Based on Bisphenol-a for Zn<sup>2+</sup> in Aqueous Solution," *Journal of Fluorescence*, vol. 29, no. 5, pp. 1079-1087, 2019/09/01 2019.
- [40] E. Ozcelik, F. Temel, S. Erdemir, B. Tabakci, and M. Tabakci, "QCM sensors coated with calix [4] arenes bearing sensitive chiral moieties for chiral discrimination of 1-phenylethylamine enantiomers," *Journal of Inclusion Phenomena and Macrocyclic Chemistry*, vol. 95, pp. 35-48, 2019.
- [41] X. Mu, L. Shi, L. Yan, and N. Tang, "A 2-Hydroxy-1-naphthaldehyde Schiff Base for Turn-on Fluorescence Detection of Zn(2+) Based on PET Mechanism," *J Fluoresc*, vol. 31, no. 4, pp. 971-979, Jul 2021.
- [42] J. Zhu *et al.*, "A Schiff base fluorescence probe for highly selective turn-on recognition of Zn<sup>2+</sup>," *Tetrahedron Letters*, vol. 58, no. 4, pp. 365-370, 2017.



## IMPROVEMENT OF HEAT AFFECTED ZONE OF GTAWed 5754 ALUMINUM ALLOY WITH FSP

<sup>1</sup>\*Fatih KAHRAMAN , <sup>2</sup>Gökçe Mehmet GENÇER , <sup>3</sup>Coşkun YOLCU 

<sup>1</sup>Dokuz Eylül University, Mechanical Engineering Department, İzmir, TÜRKİYE

<sup>1</sup>[fatih.kahraman@deu.edu.tr](mailto:fatih.kahraman@deu.edu.tr), <sup>2</sup>[mehmet.gencer@deu.edu.tr](mailto:mehmet.gencer@deu.edu.tr), <sup>3</sup>[coskun.yolcu@deu.edu.tr](mailto:coskun.yolcu@deu.edu.tr)

### *Highlights*

- Defect-free weld seam with low heat input value
- Fine-grained micro structure in the heat-affected zone
- Eliminated welding brittleness and uniform hardness distribution
- Enhanced elongation for approximate ultimate tensile stress values
- Breaking in the base material instead of the weld seam



## IMPROVEMENT OF HEAT AFFECTED ZONE OF GTAWed 5754 ALUMINUM ALLOY WITH FSP

<sup>1</sup>\*Fatih KAHRAMAN<sup>ID</sup>, <sup>2</sup>Gökçe Mehmet GENÇER<sup>ID</sup>, <sup>3</sup>Coşkun YOLCU<sup>ID</sup>

*Dokuz Eylül University, Mechanical Engineering Department, Izmir, TÜRKİYE*

<sup>1</sup>[fatih.kahraman@deu.edu.tr](mailto:fatih.kahraman@deu.edu.tr), <sup>2</sup>[mehmet.gencer@deu.edu.tr](mailto:mehmet.gencer@deu.edu.tr), <sup>3</sup>[coskun.yolcu@deu.edu.tr](mailto:coskun.yolcu@deu.edu.tr)

(Received: 23.02.2023; Accepted in Revised Form: 13.06.2023)

**ABSTRACT:** In this study, post-weld friction stir processing (FSP) was applied to eliminate the grain coarsening disadvantages encountered in the heat-affected zone when joining AA5754 aluminum alloy with Gas Tungsten Arc Welding (GTAW). As a result of welding in two passes and with the low heat input by selecting the appropriate welding parameters, all welding seams were produced without macro defects. Despite all these precautions, grain coarsening has occurred in the Heat Affected Zone (HAZ), as expected. Significant amounts of grain refinement were detected as a result of the FSP applied to the regions with grain coarsening. Consequently, the grain refinement in the HAZ, the tensile strength increased slightly, in contrast with ductility has significantly increased (around from 6% to 19%). In the tensile tests, the rupture occurred in the HAZ in the GTAWed specimens, while the rupture occurred in the base material close to the HAZ in all FSPed specimens. In addition, the high hardness values of HAZ of the GTAWed samples were reduced to the base material hardness values in all FSPed samples, resulting in a more homogeneous hardness distribution.

**Keywords:** AA5754, Gas Tungsten Arc Welding, Friction Stir Processing, Mechanical Properties, Microstructure

### 1. INTRODUCTION

Energy consumption and air pollution are important problems to be overcome for today's automotive industry. The studies carried out for this purpose in literature especially focus on the development of vehicles that operate more efficiently [1-4]. Applications for the reduction in fuel consumption are generally aimed to reduce vehicle weight. This situation has led to the increasing use of aluminum alloys in the automotive industry in recent years, due to their high strength compared to their low density. However, there are very important problems in joining aluminum alloys with fusion welding methods. The fusion welding behavior of aluminum alloys differs significantly from conventional materials such as steel [5-6]. The properties that affect the weldability of aluminum alloys are high thermal conductivity, high solidification shrinkage, oxide formation on the surface, high coefficient of thermal expansion, the high solubility of hydrogen in the molten state, and relatively wide solidification-temperature ranges [7-9].

As it is well known, friction stir welding (FSW), which is one of the solid-state welding methods, is recommended by many researchers for welding these materials due to the limited weldability of aluminum alloys by arc welding methods [10-13]. However, this welding method requires special equipment depending on the base material being welded, and the shape and geometry of the part. In addition, the welding process becomes more difficult, especially as the materials having high thickness values. For this reason, the use of solid state welding methods such as FSW in industrial production applications is still very inadequate [14-16].

Due to these factors, traditional welding methods such as Gas Tungsten Arc Welding (GTAW) and Gas Metal Arc Welding (GMAW) are generally used for aluminum and its alloys, which have high power density and use inert gas as shielding gas atmosphere. In general, it has been reported by many researchers that coarse-grained microstructures occur in the fusion zone (FZ) and the heat-affected zone (HAZ) after the welding process is performed with arc welding methods [17-19]. Grain coarsening after welding is an important issue, especially for non-heat treatable aluminum alloys. For this reason, methods having higher



energy density such as laser welding have been used to prevent coarse grain formation in the welding process of these alloys. However, even though this method that has a higher energy density is used, a dendritic grain structure is formed in the fusion zone increasing the risk of hot crack formation, although a finer grain structure can be obtained [20-22].

One of the most common methods used to prevent hot crack formation is preheating in the welding of aluminum and there are many studies in the literature. As given in these studies, preheating increases the risk of coarse grain formation. The coarse-grained structure formed in the weld zone adversely affects the strength of the weld joint as given above [23-25].

As it is well known, grain refinement significantly increases both the strength of the material (this is especially important at low temperatures) and its ductility. Therefore, in recent years, there have been many important commercial attempts at the development of fine-grained materials for various applications. In particular, controlling the grain refinement by processing is preferred instead of alloying due to being cheaper, simpler, and recycling advantages [26-27].

Welding wire manufacturers produce welding wire with a suitable chemical composition, taking into account the defects such as hot cracks, grain coarsening, etc. that may be encountered in the weld filler. However, only the use of welding wire is generally insufficient to prevent the formation of hot cracks [28-30]. Therefore, in aluminum fusion welding, it is preferred the pre-annealing treatment before the welding. The pre-annealing process used supports grain coarsening especially in the heat-affected zone (HAZ), making the grain coarsening problem in this region even more critical. Unfortunately, grain refiners in the welding wire have no effect on this grain coarsening in HAZ. Therefore, ensuring grain refinement in HAZ has critical importance in the fusion welding of aluminum alloys [31].

In this study, friction stir processing (FSP) application after welding is proposed to solve the grain coarsening in the HAZ that is encountered in joining aluminum alloys with arc welding. AA5754 aluminum alloy which is one of the most widely used alloys in the automotive industry was chosen for experimental studies. This alloy was joined with ER5356 welding wire without preheating by GTAW and then FSP was applied in the weld area for beneficial grain refinement.

## 2. EXPERIMENTAL DETAILS

### 2.1. Gas Tungsten Arc Welding

In the experimental studies, AA 5754 alloy, whose chemical composition is shown in Table 1 and mechanical properties are shown in Table 2, with a thickness of 5 mm was used. After the V-shaped welding groove was formed on the edge of the plates with dimensions of 200x100 mm, according to EN ISO 9692-3:2016 standard, the surfaces were degreased and welding processes were carried out using GTAW process. The used GTAW process parameters were given in Table 3. ER 5356 with a diameter of 1.2 mm, the chemical composition of which is presented in Table 1, was used as filler wire, and pure argon gas was also used as a shielding gas in the welding process, which was carried out in a total of two passes, on both surfaces.

**Table 1.** The chemical compositions of the base material and filler wire

	Si	Mg	Mn	Fe	Cr	Cu	Zn	Ti	Al
AA 5754	0.124	2.789	0.355	0.397	0.068	0.059	0.037	0.017	Balance
ER 5356	<0.25	5	0.3	<0.4	-	-	-	-	Balance

**Table 2.** The mechanical properties of the AA5754 alloy

	$\sigma_{YS}$ (MPa)	$\sigma_{UTS}$ (MPa)	Strain (%)
AA5754	112.2	208.8	15.8

**Table 3.** GTAW and FSP parameters

Parameter	
Welding current (A)	235
Welding speed (mm/min)	130
Shielding gas flow rate (L/min)	18
FSP tool rotation speed (rpm)	900
FSP tool travel speed (mm/min)	20
Tilt angle	2°

## 2.2. Friction stir processing

After the welding processes were completed, FSP was performed with predetermined process parameters (Table 3) on a plate while another plate was directly used as-welded for the testing. From now on, the sample names are referred to as GTAWed and GTAWed+FSPed for arc welded and friction stir processed following arc welding, respectively. FSP was carried out using hot work tool steel with AISI H13 (X40CrMoV5-1) material. Having a hardness of 55 HRC, the tool also has a cylindrical shoulder and a conical pin. The pin, which has a diameter of 5 mm at the bottom and 6 mm at the top, has also a 3 mm length. The FSP, having 0.33 overlapping ratio [32] is given in the Figure 1.

$$\text{Overlap Ratio} = 1 - \left[ \frac{l}{d_{pin}} \right] \quad (1)$$

Where  $l$  designates the distance between pin axes in passes and  $d$  is the top diameter of the pin. In FSP, the tool was plunged 0.4 mm to welded sample and initial preheating was achieved by keeping the penetration speed constant at 1 mm/min.

**Figure 1.** Friction stir processing of GTAWed AA5754

## 2.3 Microstructural Characterization and Mechanical Testing

Tucker etchant (25 ml of water, 15 ml HF, 25 ml HCl, 15 ml HNO<sub>3</sub>) was used for macro examinations and Keller etchant (50 ml of water, 10 ml HF, 15 ml HCl and 25 ml of HNO<sub>3</sub>) was also used for micro examinations of the fabricated samples. In order to determine the hardness distribution of the samples,

Vickers test examinations were carried out on the line with a depth of 2 mm from the surface. The tests carried out with a load of 200 grams were also repeated on the same line at 0.5 mm intervals. Tensile tests of the samples were also carried out at a testing speed of 1 mm/min.

### 3. RESULTS AND DISCUSSION

AA5754 aluminum alloy was first joined with ER5356 welding wire by GTAW without preheating. As a result of the macro examination carried out after the welding process, no macro defect was detected in the structure (Figure 2). The macrograph of the GTAWed+FSPed sample also shows the proper processing was performed via FSP. Any defects, such as wormhole and porosity which are particular with FSW/FSP were not observed.

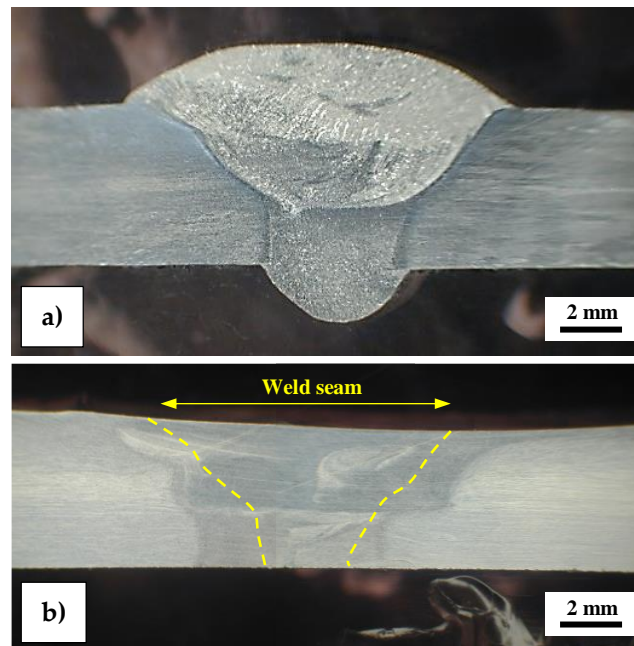


**Figure 2.** Cross-sectional macrographs of the samples; a) GTAWed sample, b) GTAWed+FSPed sample

It can be also seen that the HAZ is not relatively wide compared to the base material with high thermal conductivity. Keeping the HAZ narrow is ensured by the selected welding parameters (higher welding speed in addition to higher current and voltage values). A high increase in the heat input was prevented by selecting the current and voltage higher values, and by keeping the welding speed also higher. Thus, the 5mm thick plate was welded in two passes, trying to prevent the expansion of the HAZ. This welding process with a lower amount of heat input is also preferred to prevent grain coarsening in the FZ [33, 34].

Welding with low heat input, chosen to prevent grain coarsening, causes the formation of pores in the welding of aluminum alloys having high thermal conductivity. For this reason, the using heat input should be low enough not to cause grain coarsening, it should also has a value that will not cause porosities in the weld due to rapid solidification [35]. As can be seen from Figure 2, there was no porosity in the seam after the fusion welding process.

The metallographic examination of the weld seams was obtained after the welding process as can be seen in Figure 3. Although partial grain growth occurred in HAZ, this area could be kept narrower as much as possible. This is another important point that shows that the selected welding parameters are suitable for the process.

After the welding process, FSP was applied in order to obtain grain refinement in the weld zone. As can be seen in Figure 4, grain refinement has occurred in the coarse-grained weld seam and oriented-grained HAZ resulting from the FSP.

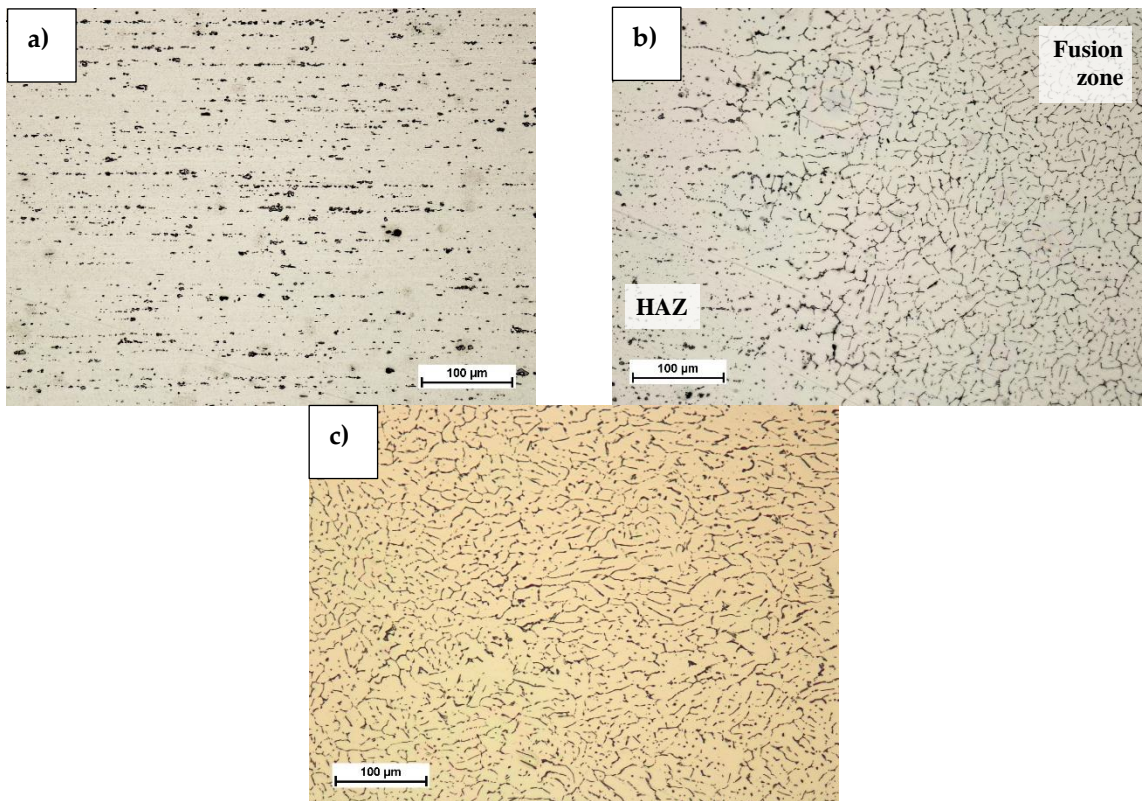


**Figure 3.** The microstructural zones of the GTAWed sample; a) Base material, b) Transition zone ( weld metal-HAZ), c) Fusion zone

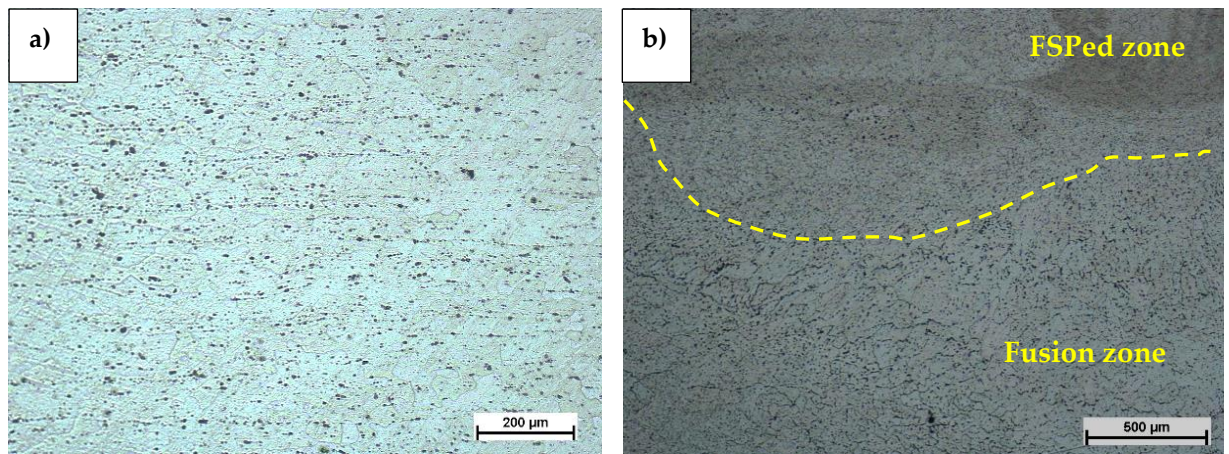


**Figure 4.** Grain refinement after FSP treatment applied to the heat affected area of the welded sample. a) Base material b) Transition zone between the FSPed area and weld metal

The onion ring microstructure and thus the material flow form can be clearly seen in the areas where the FSP has been applied (Figure 5). It was also determined that any porosity and cracks did not occur in the areas where FSP was applied. The onion ring forms occurring in the microstructure also clearly show adequate bond strength resulting from the grain refinement and dynamic recrystallization [36-38].

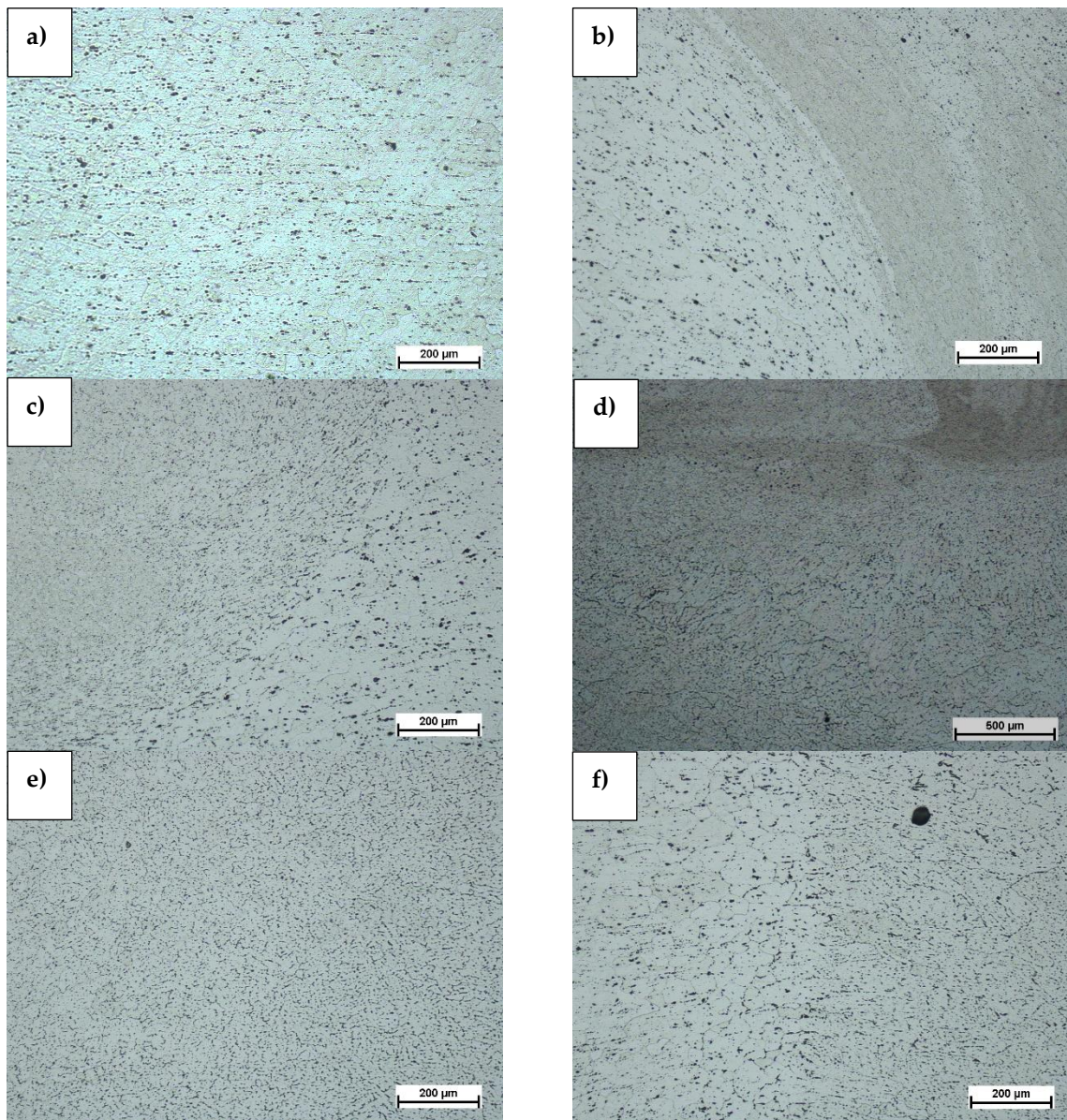


**Figure 5.** Onion ring microstructure and material flow in the FSP-ed areas a) base material b) TMAZ advancing side c) transition zone between the FSPed area base material d) transition zone between FSPed area and weld metal, e) Weld metal, f) transition zone between the weld metal and base material

When the tensile test results were examined (Figure 6), it was determined that the mechanical strength of the GTAW specimen was compatible with the values in the literature. However, it is also seen that higher elongation values are obtained compared to the low ductility values expected in fusion welding methods. This situation is attributed to the formation of a fine-grained structure in the weld metal due to the fact that the FSP was made with two passes and the low heat input is used in the passes [39, 40]. As well-known, fine-grain structure increases the strength and ductility of metallic materials. Following the FSP, it was determined that the average grain size in HAZ was measured between 60-90  $\mu\text{m}$ .

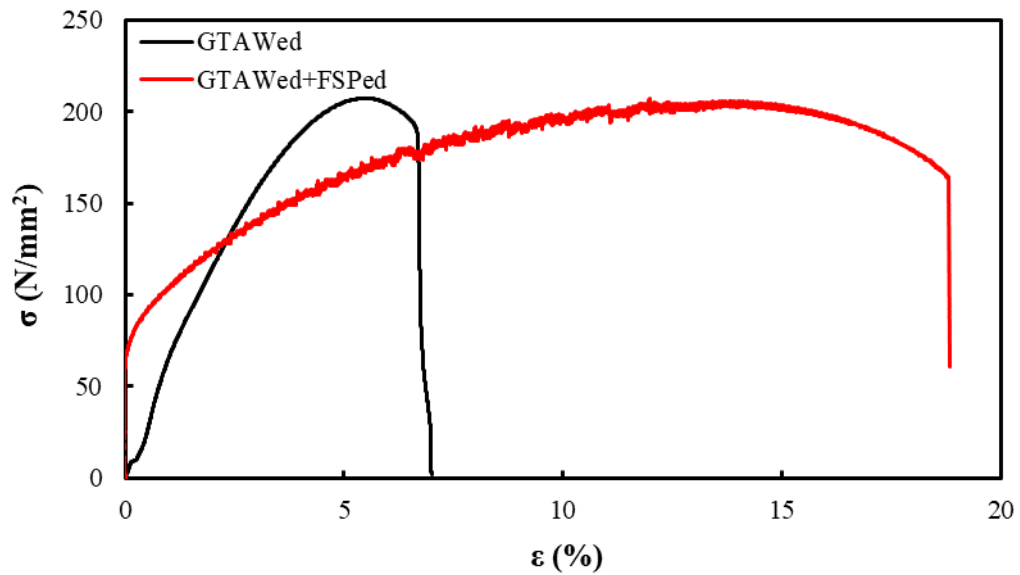


**Figure 6.** Representative tensile test results of the samples

When Figure 6 is examined, it is seen that the tensile strengths are slightly higher than the base material (Table 2). According to the tensile test results of welded joints without FSP, it has been observed that the welding parameters selected for GTAW welding provide acceptable weldability and strength values. This result also shows that it is possible to obtain sufficient tensile strengths for welded joints of 5xxx series (Al-Mg) aluminum alloys by the GTAW method. The FSP process applied after the welding process did not significantly change the strength values of the joints. However, the ductility of welded joints has increased remarkably. This situation can effectively contribute to the elimination of the brittleness/low toughness problem, which is a major disadvantage, especially for welded joints [41-43]. With the increase in ductility, the elongation values of the base material were regained for the welded structure.

During the tensile tests, none of the specimens broke from the weld fill and each specimen ruptured in base materials regions close to the HAZ (Figure 7). When the elongation results of the FSPed samples are examined, a significant increase in ductility was achieved compared to the as-welded sample. FSPed samples' elongation have a slight decrease (almost the same) in elongation values can be obtained compared to the base material. As it is known, it is an expected result that the ductility of welded joints will decrease significantly due to the negative effects of the thermal effect that given during the welding process [44]. This is a very important gain, especially for aluminum alloys joined by fusion welding, where the ductility is expected to decrease further as a result of the thermal effect.



Figure 7. Failure zones of the GTAWed samples after tensile testing

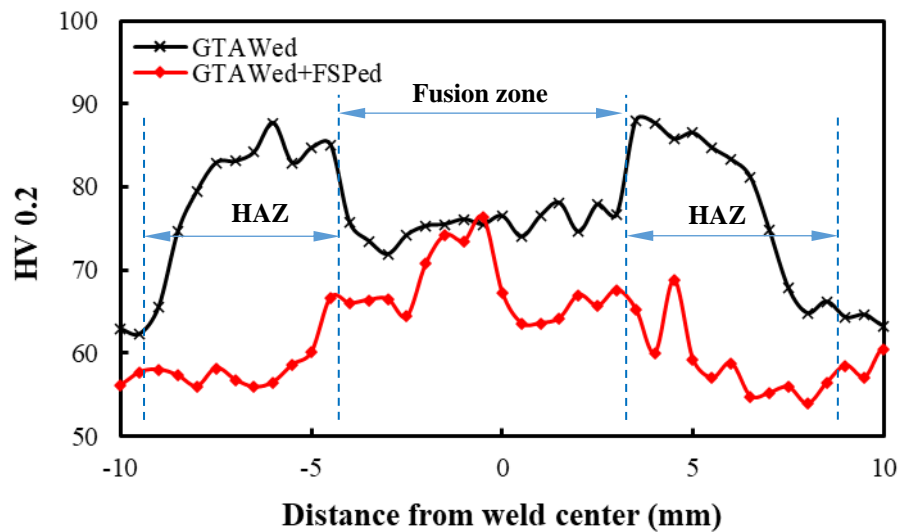


Figure 8. Cross-sectional microhardness profiles of the samples

When the hardness distribution is examined, it is clearly seen that the hardness distribution of the GTAWed sample has characteristically high hardness values from the sides of the weld seam to the base material throughout the HAZ (Figure 8). The highest hardness values were measured as 88 HV including this region in HAZ. It can be given the main reasons for high hardness in HAZ as grain coarsening (Figure 3b), and residual stresses due to rapid cooling after welding resulting from thermal shrinkage caused by the heating-cooling cycle. Because of the high residual stresses, these areas are the weakest region of the welded joint. For this reason, the FSP was applied to these areas of GTAWed parts as given in the experimental studies section of this study. The applied FSP resulted in a stress relief effect as well as grain refinement. With the FSP, both thermal stress and mechanical stress relief occurred and the hardness values decreased in the HAZ. The stress-relieving effect of the FSP is adequately efficient in that the high hardness values formed in HAZ can be reduced to the hardness values of the base material. As given before, another effect of the FSP is the increase in ductility as given in the tensile test. This is an important desired result in welded samples [45].

#### 4. CONCLUSION

In this study, AA5754 alloy was joined with GTAW and then FSP was used in order to modify the coarse grain structure formed in the HAZ. The results obtained after the FPS performed in two passes for enhancing the HAZ grain structure on both sides of the weld seam are as follows;

- The microstructure, which did not have any welding defects after GTAW, had a fine-grained structure with dynamic recrystallization after the applied FSP.
- The low ductility that occurred after the GTAW was eliminated thanks to the fine-grained microstructure created in the microstructure. While approximate ultimate tensile strength values were obtained after the GTAW and FSP, a remarkable improvement was achieved in the elongation values after the FSP.
- All FSPed specimens ruptured in base materials regions close to the HAZ due to the significant increase in ductility. FSPed samples' elongation is almost the same as the elongation values of the base material.
- The hardness tests demonstrated that the grain coarsening and the harmful effects that occurred after the thermal cycle during the GTAW were eliminated efficiently. Characteristic high hardness values in the HAZ were reduced to base material hardness values because of the FSP's stress relief effect. After the FSP, approximately uniform hardness distribution was obtained clearly.

#### Declaration of Ethical Standards

Authors declare to comply with all ethical guidelines, including authorship, citation, data reporting and original research publication.

#### Credit Authorship Contribution Statement

**Fatih Kahraman:** Methodology, writing, reviewing, supervision

**Gökçe Mehmet Gençer:** Methodology, experiments, writing, editing

**Coşkun Yolcu:** Experiments, writing

#### Declaration of Competing Interest

The authors declared that they have no conflict of interest.

#### Funding / Acknowledgements

The authors are grateful to Mustafa SAYAR and Türev Mechatronics employees for their valuable support.

#### Data Availability

The datasets collected during the current study are not publicly available but are available from the corresponding author on reasonable request.

#### REFERENCES

- [1] M. R. Islam, M. Ishak, L. H. Shah, S. R. A. Idris, C. Meriç, "Dissimilar welding of A7075-T651 and AZ31B alloys by gas metal arc plug welding method," *The International Journal of Advanced Manufacturing Technology*, vol. 88, June, pp. 2773-2783, 2017.
- [2] H. Okuyucu, A. Kurt, E. Arcaklioglu, "Artificial neural network application to the friction stir welding of aluminum plates," *Materials & Design*, vol. 28, no. 1, Aug., pp. 78-84, 2007.





- [3] P. Bamberg, G. Gintrowski, Z. Liang, A. Schiebahn, U. Reisgen, N. Precoma, C. Geffers, "Development of a new approach to resistance spot weld AW-7075 aluminum alloys for structural applications: an experimental study–Part 1," *Journal of Materials Research and Technology*, vol. 15, Nov. Dec., pp. 5569-5581, 2021.
- [4] N. Karunakaran, V. Balasubramanian, "Effect of pulsed current on temperature distribution, weld bead profiles and characteristics of gas tungsten arc welded aluminum alloy joints," *Transactions of Nonferrous Metals Society of China*, vol. 21, no. 2, Feb., pp. 278-286, 2011.
- [5] P. Praveen, P. K. D. V. Yarlalagadda, "Meeting challenges in welding of aluminum alloys through pulse gas metal arc welding," *Journal of Materials Processing Technology*, vol. 164-165, May, pp. 1106-1112, 2005.
- [6] P. Kah, R. Rajan, J. Martikainen, R. Suoranta, "Investigation of weld defects in friction-stir welding and fusion welding of aluminium alloys," *International Journal of Mechanical and Materials Engineering*, vol. 10, no. 1, Dec., pp. 1-10, 2015
- [7] C. Zhao, Z. Luo, Y. Li, M. Feng, W. Xuan, "Inverse heat conduction model for the resistance spot welding of aluminum alloy," *Numerical Heat Transfer, Part A: Applications*, vol. 70, no. 12, Nov., pp. 1330-1344, 2016.
- [8] R. Xiao, X. Zhang, "Problems and issues in laser beam welding of aluminum–lithium alloys," *Journal of Manufacturing Processes*, vol. 16, no. 2, April, pp. 166-175, 2014.
- [9] R. Xiao, J. Yang, C. Tan, Z. Shen, Z. Yu, "Fabrication of high strength and lightweight dissimilar material joints by laser: a review," *Advanced Laser Processing and Manufacturing III*, vol. 11183, Nov., pp. 32-37, 2019.
- [10] A. Yazdipour, K. Dehghani, "Modeling the microstructural evolution and effect of cooling rate on the nanograins formed during the friction stir processing of Al5083," *Materials Science and Engineering: A*, vol. 527, no. 1-2, Dec., pp. 192-197, 2009.
- [11] A. K. Bodukuri, K. Eswaraiyah, K. Rajendar, "Comparison of Aluminum Alloy 5083 properties on TIGW and FSW Processes," *Materials Today: Proceedings*, vol. 4, no. 9, Oct., pp. 10197-10201, 2017.
- [12] S. B. Aziz, M. W. Dewan, D. J. Huggett, M. A. Wahab, A. M. Okeil, T. Warren Liao, "Impact of Friction Stir Welding (FSW) process parameters on thermal modeling and heat generation of aluminum alloy joints," *Acta Metallurgica Sinica (English Letters)*, vol. 29, July, pp. 869-883, 2016.
- [13] T. Hirata, T. Oguri, H. Hagino, T. Tanaka, S. W. Chung, Y. Takigawa, K. Higashi, "Influence of friction stir welding parameters on grain size and formability in 5083 aluminum alloy," *Materials Science and Engineering: A*, vol. 456, no. 1-2, May, pp. 344-349, 2007.
- [14] A. Ghiasvand, M. Kazemi, M. Mahdipour Jalilian, H. Ahmadi Rashid, "Effects of tool offset, pin offset, and alloys position on maximum temperature in dissimilar FSW of AA6061 and AA5086," *International Journal of Mechanical and Materials Engineering*, vol. 15, May, pp. 1-14, 2020.
- [15] P. Upadhyay, A. Reynolds, "Effect of backing plate thermal property on friction stir welding of 25-mm-thick AA6061," *Metallurgical and Materials Transactions A*, vol. 45, Nov., pp. 2091-2100, 2014.
- [16] C. T. Canaday, M. A. Moore, W. Tang, A. P. Reynolds, "Through thickness property variations in a thick plate AA7050 friction stir welded joint," *Materials Science and Engineering: A*, vol. 559, Jan., pp. 678-682, 2013.
- [17] A. K. Lakshminarayanan, V. Balasubramanian, K. Elangovan, "Effect of welding processes on tensile properties of AA6061 aluminium alloy joints," *The International Journal of Advanced Manufacturing Technology*, vol. 40, Jan., pp. 286-296, 2009.
- [18] K. Vasu, H. Chelladurai, A. Ramaswamy, S. Malarvizhi, V. Balasubramanian, "Effect of fusion welding processes on tensile properties of armor grade, high thickness, non-heat treatable aluminium alloy joints," *Defence Technology*, vol. 15, no. 3, June, pp. 353-362, 2019.
- [19] A. Kumar, S. Sundarajan, "Optimization of pulsed TIG welding process parameters on mechanical properties of AA 5456 Aluminum alloy weldments," *Materials & Design*, vol. 30, no. 4, April, pp. 1288-1297, 2009.

- [20] L. Wang, M. Gao, C. Zhang, X. Zeng, "Effect of beam oscillating pattern on weld characterization of laser welding of AA6061-T6 aluminum alloy," *Materials & Design*, vol. 108, Oct., pp. 707-717, 2016.
- [21] Z. Tang, F. Vollertsen, "Influence of grain refinement on hot cracking in laser welding of aluminum," *Welding in the World*, vol. 58, March, pp. 355-366, 2014.
- [22] M. Sheikhi, F. M. Ghaini, H. Assadi, "Prediction of solidification cracking in pulsed laser welding of 2024 aluminum alloy," *Acta Materialia*, vol. 82, Jan., pp. 491-502, 2015.
- [23] M. Chludzinski, R. E. dos Santos, C. Churiaque, M. Ortega-Iguña, J. M. Sánchez-Amaya, "Pulsed laser welding applied to metallic materials—A material approach," *Metals*, vol. 11, no. 4, April, pp. 640, 2021.
- [24] H. Hekmatjou, H. Naffakh-Moosavy, "Hot cracking in pulsed Nd: YAG laser welding of AA5456," *Optics & Laser Technology*, vol. 103, July, pp. 22-32, 2018.
- [25] H. Ebrahimzadeh, H. Farhangi, S. A. A. A. Mousavi, "Hot cracking in autogenous welding of 6061-T6 aluminum alloy by rectangular pulsed Nd: YAG laser beam," *Welding in the World*, vol. 64, April, pp. 1077-1088, 2020.
- [26] S. Mironov, Y. S. Sato, H. Kokawa, "Microstructural evolution during friction stir-processing of pure iron," *Acta Materialia*, vol. 56, no. 11, June, pp. 2602-2614, 2008.
- [27] C. Vidal, V. Infante, "Fatigue behavior of friction stir-welded joints repaired by grinding," *Journal of Materials Engineering and Performance*, vol. 23, Jan., pp. 1340-1349, 2014.
- [28] P. Schempp, C. Schwenk, M. Rethmeier, C. Edward, "Weld metal grain refinement of aluminium alloy 5083 through controlled additions of Ti and B," *Materials Testing*, vol. 53, no. 10, May, pp. 604-609, 2011.
- [29] N. Murali, M. Sokoluk, X. Li, "Study on aluminum alloy joints welded with nano-treated Al-Mg-Mn filler wire," *Materials Letters*, vol. 283, Jan., pp. 128739, 2021.
- [30] N. K. Babu, M. K. Talari, D. Pan, Z. Sun, J. Wei, K. Sivaprasad, "Microstructural characterization and grain refinement of AA6082 gas tungsten arc welds by scandium modified fillers," *Materials Chemistry and Physics*, vol. 137, no. 2, Dec., pp. 543-551, 2012.
- [31] V. Patel, W. Li, A. Vairis, V. Badheka, "Recent development in friction stir processing as a solid-state grain refinement technique: microstructural evolution and property enhancement," *Critical Reviews in Solid State and Materials Sciences*, vol. 44, no. 5, July, pp. 378-426, 2019.
- [32] J. Gandra, R. M. Miranda, P. Vilaça, "Effect of overlapping direction in multipass friction stir processing," *Materials Science and Engineering: A*, vol. 528, no. 16-17, June, p. 5592-5599, 2011.
- [33] M. Samiuddin, J. L. Li, M. Taimoor, M. N. Siddiqui, S. U. Siddiqui, J. T. Xiong, "Investigation on the process parameters of TIG-welded aluminum alloy through mechanical and microstructural characterization," *Defence Technology*, vol. 17, no. 4, Aug., pp. 1234-1248, 2021.
- [34] Y. Zhao, F. Chen, C. Cao, C. Chen, R. Xie, "Effect of CMT welding heat input on microstructure and properties of 2A14 aluminum alloy joint," *Metals*, vol. 12, no. 12, Dec., pp. 2100, 2022.
- [35] G. Çam, G. İpekoğlu, "Recent developments in joining of aluminum alloys," *The International Journal of Advanced Manufacturing Technology*, vol. 91, Dec., pp. 1851-1866, 2017.
- [36] V. V. Bulatov, W. Cai, R. Baran, K. Kang, "Geometric aspects of the ideal shear resistance in simple crystal lattices," *Philosophical Magazine*, vol. 86, no. 25-26, Nov., pp. 3847-3859, 2006.
- [37] M. Grujicic, S. Ramaswami, J. S. Snipes, V. Avuthu, R. Galgalikar, Z. Zhang, "Prediction of the grain-microstructure evolution within a Friction Stir Welding (FSW) joint via the use of the Monte Carlo simulation method," *Journal of Materials Engineering and Performance*, vol. 24, Aug., pp. 3471-3486, 2015.
- [38] Y. Hu, Y. Niu, Y. Zhao, W. Yang, X. Ma, J. Li, "Friction stir welding of CoCrNi medium-entropy alloy: recrystallization behaviour and strengthening mechanism," *Materials Science and Engineering: A*, vol. 848, July, pp. 143361, 2022.

- [39] S. Kumar, A. S. Shahi, "Effect of heat input on the microstructure and mechanical properties of gas tungsten arc welded AISI 304 stainless steel joints," *Materials & Design*, vol. 32, no. 6, June, pp. 3617-3623, 2011.
- [40] P. C. Adamczuk, I. G. Machado, J. A. E. Mazzaferro, "Methodology for predicting the angular distortion in multi-pass butt-joint welding," *Journal of Materials Processing Technology*, vol. 240, Feb., pp. 305-313, 2017.
- [41] A. G. Rao, V. P. Deshmukh, N. Prabhu, B. P. Kashyap, "Ductilizing of a brittle as-cast hypereutectic Al-Si alloy by friction stir processing," *Materials Letters*, vol. 159, Nov., pp. 417-419, 2015.
- [42] S. Tutunchilar, M. B. Givi, M. Haghpanahi, P. Asadi, "Eutectic Al-Si piston alloy surface transformed to modified hypereutectic alloy via FSP," *Materials Science and Engineering: A*, vol. 534, Feb., pp. 557-567, 2012.
- [43] Y. Yang, P. Hua, X. Li, K. Chen, W. Zhou, "Effect of multipass on microstructure and impact toughness of as-cast Al-20Si alloy via friction stir processing," *Physics of Metals and Metallography*, vol. 120, Dec., pp. 1126-1132, 2019.
- [44] S. Malarvizhi, V. Balasubramanian, "Effect of welding processes on AA2219 aluminium alloy joint properties," *Transactions of Nonferrous Metals Society of China*, vol. 21, no. 5, May, pp. 962-973, 2011.
- [45] H. Mehdi, R. S. Mishra, "Study of the influence of friction stir processing on tungsten inert gas welding of different aluminum alloy," *SN Applied Sciences*, vol. 1, June, pp. 1-11, 2019.



## ENHANCED OSTEOGENIC DIFFERENTIATION OF HUMAN MESENCHYMAL STEM CELLS BY FLEXIBLE $\beta$ -TCP/PLA BONE GRAFTS WITH SILICATE ADDITIVE

<sup>1\*</sup>Günnur ONAK PULAT , <sup>2</sup>Gülşah SUNAL , <sup>3</sup>Ozan KARAMAN 

<sup>1,3</sup>İzmir Katip Çelebi University, Biomedical Engineering, Department, Tissue Engineering and Regenerative Medicine Laboratory, İzmir, TÜRKİYE


<sup>2</sup>Bonegraft Biomaterials Co., Ege University Technopolis, İzmir, TÜRKİYE

<sup>1</sup>[gunnur.onak@ikcu.edu.tr](mailto:gunnur.onak@ikcu.edu.tr), <sup>2</sup>[gulsah17@outlook.com](mailto:gulsah17@outlook.com), <sup>3</sup>[ozan.karaman@ikcu.edu.tr](mailto:ozan.karaman@ikcu.edu.tr)

### Highlights

- $\beta$ -tricalcium phosphate ( $\beta$ -TCP)-poly (lactic acid) (PLA) composite scaffolds containing two different concentrations (0.8% and 1%) of silicate additives were designed.
- The characterization results demonstrated that  $\beta$ -TCP-PLA-based scaffolds had porous and flexible structures.
- The designed synthetic flexible bone grafts with 0.8% and 1% silicate-additive significantly encouraged the proliferation and osteogenic differentiation of human bone marrow-derived mesenchymal stem cells (hMSCs). Moreover, 0.8% silicate-additive  $\beta$ -TCP-PLA grafts showed increased alkaline phosphatase (ALP) activity.

## ENHANCED OSTEOGENIC DIFFERENTIATION OF HUMAN MESENCHYMAL STEM CELLS BY FLEXIBLE $\beta$ -TCP/PLA BONE GRAFTS WITH SILICATE ADDITIVE

<sup>1,\*</sup>Günnur ONAK PULAT , <sup>2</sup>Gülşah SUNAL , <sup>3</sup>Ozan KARAMAN 

<sup>1,3</sup>*İzmir Katip Çelebi University, Biomedical Engineering, Department, Tissue Engineering and Regenerative Medicine Laboratory, İzmir, TÜRKİYE*

<sup>2</sup>*Bonegraft Biomaterials Co., Ege University Technopolis, İzmir, TÜRKİYE*

<sup>1</sup>[gunnur.onak@ikcu.edu.tr](mailto:gunnur.onak@ikcu.edu.tr), <sup>2</sup>[gulsah17@outlook.com](mailto:gulsah17@outlook.com), <sup>3</sup>[ozan.karaman@ikcu.edu.tr](mailto:ozan.karaman@ikcu.edu.tr)

**ABSTRACT:** In recent years, ceramics, polymers, and composites have been used to develop biologically and mechanically suitable bone scaffolds.  $\beta$ -tricalcium phosphate ( $\beta$ -TCP) is a widely used bioceramic in bone tissue engineering. It shows excellent osteoconductivity, osteoinductivity, and good biocompatibility properties, as its chemical composition is similar to the original chemical structure of bone. Herein, we designed  $\beta$ -TCP-PLA composite scaffolds containing two different concentrations of silicate additives. We aimed to investigate the effect of silicate-additive with varying concentrations (0.8% and 1%) on osteogenic differentiation of human bone marrow-derived mesenchymal stem cells (hMSCs) seeded flexible bone grafts. The morphological structure of  $\beta$ -TCP-PLA-based bone grafts was assessed by scanning electron microscopy (SEM) and the tensile strength of grafts was evaluated. The results showed that scaffolds had porous and flexible structures. hMSCs osteogenic differentiation was evaluated with the alkaline phosphatase (ALP) activity and DNA content measurements. Compared with  $\beta$ -TCP-PLA grafts, these designed synthetic flexible bone grafts with 0.8% and 1% silicate-additive significantly promoted hMSCs proliferation and osteogenic differentiation. Moreover, 0.8% silicate-additive  $\beta$ -TCP-PLA grafts showed increased ALP activity. The outcomes of the present study suggest that synthetic flexible bone grafts with silicate-additive might be useful for encouraging the regeneration of bone.

**Keywords:** Bone Tissue Engineering,  $\beta$ -TCP/PLA Bone Grafts, Silicate, Osteogenesis

### 1. INTRODUCTION

Bone diseases which correspond to half of the chronic diseases among people over 50 years old, continue to exist as a crucial problem in the clinic [1, 2]. Due to the enhanced life expectancy and aging population, there is a fast increment in musculoskeletal cases and disorders including fractures, osteoporosis, and bone metastases. Thus, bone-associated medical treatments and costs are increasing gradually [3]. Although bone has an exceptional capability for regenerating and healing itself, large bone defects and complex bone breakages lead to important difficulties in medicine [3]. To repair bone defects, the autologous bone grafting technique is accepted as the “gold standard”. However, it possesses drawbacks such as secondary damages, donor site morbidity, limitation of a specific form, inadequacy of autologous bone tissue, and long surgery times [3, 4]. These shortcomings limit the use of autografts in clinical settings. Therefore, bone tissue engineering strategies as novel alternative treatment approaches aim to repair or regenerate the damaged bone tissue after a bone loss, defect, or injury by replacing three-dimensional (3D) scaffolds to build a supportive environment for the growth of bone [5]. Bone scaffolds should ideally be osteoinductive to encourage the differentiation of progenitor cells down an osteoblastic lineage, be osteoconductive to help the growth of bone tissue and promote ingrowth of surrounding bone tissue, and also have the capability for osseointegration to integrate scaffold into surrounding bone tissue [6]. Also, a bone scaffold should have proper mechanical features such as having high porosity to allow vascularization and migration of the cells and have the ability to fill irregular shapes to avoid insufficient micro-cavities around the bone defect area, and lastly have the possibility for commercialization [7, 8].

In recent years, ceramics, polymers, and composites have been used by researchers to produce biologically and mechanically suitable bone scaffolds [6]. Ceramic materials possess a huge compressive

\*Corresponding Author: Günnur ONAK PULAT, [gunnur.onak@ikcu.edu.tr](mailto:gunnur.onak@ikcu.edu.tr)

strength and low ductility and show good resistance to deformation [9].  $\beta$ -tricalcium phosphate ( $\beta$ -TCP), commonly utilized ceramic in bone tissue engineering, demonstrates excellent osteoconductivity, osteoinductivity, and good biocompatibility features since the chemical composition of  $\beta$ -TCP ceramics is resembling the chemical composition of native bone [10-13]. A main drawback of  $\beta$ -TCP is that it has a sintered solid and hard form resulting in difficulties for the surgeon to ensure the needed form of the graft in the surgical field and insufficient micro-cavities in the bone defect area. Giving shape to the graft substance in the surgical field during the surgery extends the surgical period and enhances the infection risk [14, 15]. Therefore, during a surgical operation, to allow the surgeon for giving the needed form to the scaffold in the surgical field, flexibility is very important in clinical applications. Collagen fibers and polymeric biomaterials like poly (lactic acid) (PLA) have been used to provide flexibility to ceramic materials [16]. PLA-based materials are advantageous since they possess perfect mechanical features, processability, biological compatibility, and suitable degradation rates, and don't cause an important inflammatory reaction. Nevertheless, their main disadvantage of them is the absence of bioactivity for bone regeneration [16].

Silicate-based bioceramics show perfect bioactivity that could encourage the reproduction of osteoblasts, increase the creation of bone and trigger the osteogenic differentiation of stem cells [17]. Although calcium phosphate ceramics such as  $\beta$ -TCP and their composites with PLA have great biocompatibility, they do not have an evident stimulatory impact on osteoblasts proliferation and differentiation [17]. Since a certain concentration of silicate additive increases bone regeneration capacity and osteogenesis, silicate-substituted calcium phosphate materials have been used as novel and commercialized porous ceramic graft substitutes for bone tissue, and their crystal construction is doped by silicate ions [18-20]. Silicate contribution resulted in better *in vitro* and *in vivo* osteogenic differentiation and controllable biodegradability compared to  $\beta$ -TCP [21, 22]. For instance, Coathup *et al.* aimed to assess the impact of silicate substitution on calcium phosphate's osteoinductive ability without exogenously given growth factors and reported that silicate substitution remarkably enhanced the quantity of bone created and the quantity of bone tissue that is bonded to the surface of the implant [23]. Furthermore, researchers investigated whether hydroxyapatite (HA) or silicate-substituted HA can encourage mesenchymal stem cells (MSCs) osteogenic differentiation without soluble factors, and reported that silicate-substituted calcium phosphate assisted the adhesion and proliferation of MSCs and also triggered the osteogenesis to a larger degree than HA [24]. Moreover, Chan *et al.* studied the silicate substituted calcium phosphate substances having different strut porosities in *in vivo* ectopic ovine model for comparing its osteoinductivity, and reported that bone graft substitutes having higher strut porosity are more osteoinductive [25].

Importantly, a bone scaffold must have an interconnected porous structure, and for needed nutrients and oxygen diffusion, the size of pores would be at least 100  $\mu\text{m}$  in diameter [26]. The pores facilitate the homogeneous distribution of cells in the scaffold, the connection of newly created tissue with neighboring tissues, and the carriage of nutrients and oxygen to cells so that new tissue formation and vascularization can occur more quickly [27]. Particulate-leaching is an easy method to produce 3D porous tissue engineering scaffolds using polymer solution mixed uniformly with salt or porogen particles of a certain diameter. Then the solvent is evaporated, and it leaves at the back a polymer matrix in which salt or porogen particles are embedded. Lastly, whenever composite material is submerged in water, embedded particles start to reach out to create a porous structure [28, 29]. By changing the size of the particle, this method can simply control the pore size and thickness of the septum of the 3D porous scaffold construct [28]. Scaffolds produced by solvent casting and particle-leaching techniques possess a porosity between 50% and 90%. It is a relatively simple and low-cost methodology, and also the developed scaffolds possess high porosity and the ability for tuning the pore size [30]. In the current study, by adding porogen particles to the bone scaffolds, it was aimed to gain the scaffolds a highly porous structure.

It is reported that the newer generation of ceramics has been formulated at 0.8 wt% Si and supported significantly more bone formation (Hing, Revell *et al.* 2006, Nagineni, James *et al.* 2012). Herein, we decided to alter the silicate amount to observe the effect of silicate amount in the scaffold. To the best of

our knowledge, the present study investigated for the first time the followings: (i) combining  $\beta$ -TCP-PLA with silicate-additive to fabricate a composite scaffold; (ii) characterization of the morphological structure, and mechanical features of these three different composite scaffolds; and (iii) observing the effect of  $\beta$ -TCP-PLA composite scaffolds with two different ratios of silicate-additive (0.8% and 1%) on osteogenic differentiation of human bone marrow-derived mesenchymal stem cells (hMSCs). In this study, we aimed to produce porous  $\beta$ -TCP-PLA composite scaffolds with silicate additive to increase osteogenic differentiation by mimicking the extracellular matrix (ECM) with its polymeric structure and by mimicking the bone tissue with its ceramic structure with osteoconductive and osteoinductive properties. Furthermore, flexibility and porosity were gained from the designed scaffolds to provide convenience to the surgeon during surgery to give the intended shape, and to allow vascularization and migration of the cells, respectively. First,  $\beta$ -TCP was mixed with PLA for imitating bone ECM and for providing flexibility to osteoconductive and osteoinductive  $\beta$ -TCP. Then, porogen was added and removed via the particulate leaching method to make the scaffold porous.  $\beta$ -TCP-PLA flexible grafts were used as the control group, while 1% and 0.8% silicate-additive flexible grafts are experimental groups to investigate the effect of silicate-additive with ranging concentrations on osteogenic differentiation by seeding hMSCs on bone grafts and incubating in an osteogenic medium for 21 days. hMSCs osteogenic differentiation on synthetic bone grafts were evaluated concerning the ALP activity and DNA content measurements. We demonstrated that designed synthetic flexible bone grafts encouraged the proliferation and osteogenic differentiation of hMSCs. The incorporation of silicate in synthetic  $\beta$ -TCP bone grafts significantly promotes the expression of ALP which is an early osteogenic marker by seeded hMSCs. Our results suggest that these synthetic flexible bone grafts may be useful for promoting the repair and regeneration of bone tissue.

## 2. MATERIALS and METHOD

### 2.1 Fabrication of Synthetic Flexible Bone Grafts

Bone grafts were fabricated in Bonegraft Biyolojik Malzemeler San. ve Tic. A. Ş. During the fabrication of the synthetic flexible bone graft, firstly  $\beta$ -TCP and silicate in determined ratios (0.8% and 1%) were mixed and added into %10 Poly (D, L-lactide-co-caprolactone) polymer solution. Then, porogen with the size of 1/1 ratio 100-250  $\mu$ m and 250-500  $\mu$ m were incorporated into the mixture in determined quantity for giving it a porous structure. The material was thoroughly mixed in the beaker, and after that, it was poured into Teflon-coated mold structures. The flexible bone graft was held in distilled water in a shaker water bath for removing the porogen and to acquire a porous structure of the material. For the analyzes to be performed in a sterile environment, the grafts were used after being exposed to ultraviolet (UV) for 1 hour, and stored for the following characterizations.

### 2.2 Characterization of Synthetic Flexible Bone Grafts

To image synthetic bone grafts, a Scanning Electron Microscope (SEM; Carl Zeiss Microscopy, Germany) at 3 kV accelerating voltage upon coating with gold (QUORUM; Q150 RES; East Sussex; United Kingdom) was used at 20 mA for 60 seconds. The scale bars found in the pictures were obtained with SEM software.

A universal testing machine with a 5 kN load cell (Shimadzu AGS-X Model, Japan) was used to perform Tensile Test. The tensile test of bone grafts was carried out according to the ASTM D638 standard, and the speed was 50 mm/min. For checking the repeatability of experiments, the tensile test was repeated at least three times.

### 2.3 Cell Culture and Cell Seeding

hMSCs (HMSC-AD-500, CLS cell lines Service, Lot #102, Eppelheim, Germany) were cultured within

the basal media (DMEM including 10% FBS, 250 ng/mL fungizone, 100 units/mL penicillin, 50 µg/mL gentamicin, 100 µg/mL streptomycin) in flasks. L929 cells (kindly donated from Ege University Research Group of Animal Cell Culture and Tissue Engineering Laboratory) were cultured within the basal media (DMEM including 10% FBS, 100 units/mL penicillin, 100 µg/mL streptomycin) in flasks. When the cells achieve 80-90% confluency, they were passaged by utilizing a 0.25% trypsin/EDTA solution and taken to a novel flask containing fresh medium. For obtaining enough stocks in the related passage number, cells were frozen in the freezing medium at every passage and stored at -196 °C in a liquid nitrogen tank (ThermoScientific, Bio-cane 47). Before cell seeding, synthetic bone grafts were sterilized by UV radiation and washed with 70 % ethanol for 30 minutes, and then rinsed with sterile phosphate-buffered saline (PBS) three times. Following this step, synthetic flexible grafts were conditioned within the basal medium for 1 hour, and then cell suspension ( $10^6$  cells / cm<sup>3</sup>) was seeded on each sample in the basal medium. The cell-seeded grafts were incubated for the adhesion of cells for 24 hours. For cell viability and osteogenic differentiation experiments, L929 cells and hMSCs were seeded on scaffolds, respectively. For cell viability, the L929 cells were cultivated for 7 days in basal media. For osteogenic differentiation, the media on hMSCs seeded scaffolds was changed with osteogenic medium (basal medium supplemented with 10 mM β-glycerophosphate, 50 µg/mL ascorbic acid, and 100 nM dexamethasone) and cells were cultivated for 21 days.

#### 2.4 Cell Viability Analysis of L929 Cells on Synthetic Bone Grafts

3- (4, 5-dimethylthiazol-2-yl)- 2, 5-diphenyltetrazolium bromide (MTT) (Vybrant® MTT Cell Proliferation Assay Kit, Invitrogen, Waltham, MA, USA) test was used based on the manufacturer's instructions at 1., 4. and 7. days of the cell culture. For evaluating cell viability and proliferation, L929 (Mouse fibroblast cell line) cells were used for MTT assay. First, the culture medium was removed from cell-seeded grafts found in the well plate. 10% MTT dye in a culture medium was added to the cell-seeded grafts. Bone grafts were incubated in the incubator for 4 hours at 37°C and 5% CO<sub>2</sub>. Next, the medium was removed from grafts again, and then 500 µL dimethyl sulfoxide (DMSO, Sigma-Aldrich, Steinheim, Germany) was given on cell-seeded grafts to dissolve the formed formazan crystals. After incubation for 15 minutes, a microplate reader (Biotek Synergy HTX, Winooski, VT, USA) was used to measure the absorbance values of each well at 570 nm.

#### 2.5 Osteogenic Differentiation of hMSCs on Synthetic Bone Grafts

For stem cell differentiation studies, pure β-TCP-PLA without silicate-additive was utilized as the control group, and β-TCP-PLA with 0.8% silicate-additive and β-TCP-PLA with 1% silicate-additive were utilized as experimental groups. As additional information, the biological replicate number of the stem cell differentiation experiment was 3 meaning experiments were carried out with 3 replications from each group.

At each time point (7, 14, and 21 days), first, the cell-seeded grafts were washed with PBS, and then they were lysed with 10-mM Tris supplemented with 0.2% Triton in PBS. The lysed samples were used for the measurement of DNA content and ALP activity. To observe primary cellular concentration on bone grafts, the DNA content at day 0 was measured. Double-stranded DNA content and ALP activity of the samples were measured with DNA Quantification Kit (Sigma Aldrich, St. Louis, MO, USA) and QuantiChrom ALP assay (Bioassay Systems, Hayward, CA, USA), respectively, based on the manufacturer's directives [31]. In brief, the bisBenzimide H 33258 Solution was prepared and added to lysed samples found in 96-well plates. Then, fluorescence intensity (excited at a wavelength of 360 nm) was measured using a spectrophotometer (BioTek, Winooski, VT, USA) at an emission wavelength of 460 nm, and at ambient temperature. By using the ALP kit, ALP activity was evaluated by p-nitrophenylphosphate (pNPP) at 405 nm in an alkaline solution. Firstly, 50 µL of lysed sample to 200 µL total reaction volume were utilized for starting the reaction by the addition of assay buffer, 5 mM magnesium acetate, and 10 mM pNPP in a 96-well plate. We measured the optical density (OD) at 405 nm



for the first time ( $t=0$ ) and after 4 minutes ( $t=4$  min) with a multi-plate reader (BioTek, Winooski, VT, USA). Lastly, obtained ALP activities were normalized to cell numbers by dividing to DNA contents at every time point.

## 2.6 Statistical Analysis

All the obtained information was statistically analyzed via one-way ANOVA (SPSS 12.0, SPSS GmbH, Germany) and the Student-Newman-Keuls method as a post hoc test. Significant differences among groups were defined using p-values lower than 0.05. (\* $p < 0.05$ , \*\* $p < 0.01$ , \*\*\* $p < 0.001$ ).

## 3. RESULTS

### 3.1 Characterization of Synthetic Flexible Bone Grafts

SEM imaging was used to assess the morphology of flexible synthetic bone grafts. SEM images of three bone grafts were demonstrated in Figure 1. In SEM analysis, it was observed that these synthetic bone grafts have a porous structure as seen in Figure 1A-C. Although silicate particles were observed in 0.8% and 1% of silicate-additive  $\beta$ -TCP-PLA groups, the density of silicate was higher in the 1% silicate-additive  $\beta$ -TCP-PLA group as expected. SEM images show that the pore size and porosity of  $\beta$ -TCP-PLA composite scaffolds were decreased with the increased silicate ratio. The porosity of the scaffolds was measured by using Image J. The porosity of the control, 0.8% silicate-additive  $\beta$ -TCP-PLA, and 1% silicate-additive  $\beta$ -TCP-PLA scaffolds were found as 67.98%, 38.65%, and 42.14%, respectively.

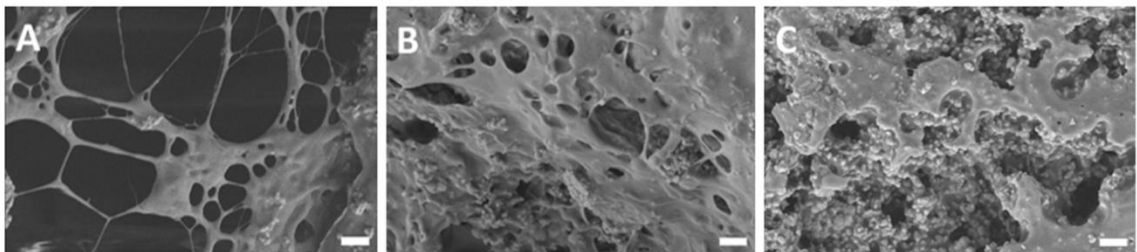


**Figure 1.** Scanning electron microscopy images of  $\beta$ -TCP-PLA (A),  $\beta$ -TCP-PLA with 0.8% silicate-additive (B), and  $\beta$ -TCP-PLA with 1% silicate-additive (C) grafts (Scale bar represents 2  $\mu\text{m}$ ).

Tensile strength analysis was fulfilled to observe the mechanical properties of the synthetic scaffolds (Figure 2). The tensile strength of control, 0.8% silicate, and 1% silicate groups were measured as  $451,8 \pm 35,06$  kPa,  $390,63 \pm 7,21498672$  kPa, and  $343,02 \pm 20,9923835$  kPa, respectively. As demonstrated in Figure 2, tensile strength was decreased with the increase of silicate additive.

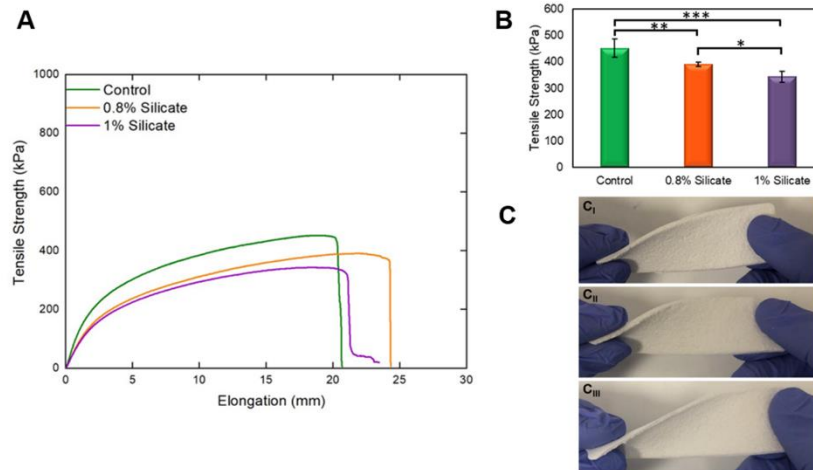


**Figure 2.** Tensile strength of  $\beta$ -TCP-PLA-based scaffolds (A-B) ( $*p < 0.05$ ,  $**p < 0.01$ ,  $***p < 0.001$ ). Images of control (C<sub>I</sub>), 0.8% silicate (C<sub>II</sub>), and 1% silicate (C<sub>III</sub>) group flexible grafts.

### 3.2 Cell Viability Analysis of Cells on Synthetic Flexible Bone Grafts

In this study, the effect of  $\beta$ -TCP-PLA-based bone scaffolds on cell viability and proliferation was assessed by MTT analysis. For this assay, L929 cells were seeded on bone grafts and incubated for 7 days. MTT analysis was carried out at 1, 4, and 7 days of the cell culture. As demonstrated in Fig.3, cell numbers of all three groups increased from Day 1 to Day 4, and then decreased from Day 4 to Day 7. At all time points during 7 days of cell cultivation, the cell numbers for 0.8% silicate-additive and 1% silicate-additive  $\beta$ -TCP-PLA bone grafts were higher than the cell numbers for the control group. This result shows the positive effect of silicate-additive bone grafts on cellular viability. Moreover, the cell numbers for 1% silicate-additive  $\beta$ -TCP-PLA bone grafts were the greatest at all time points.

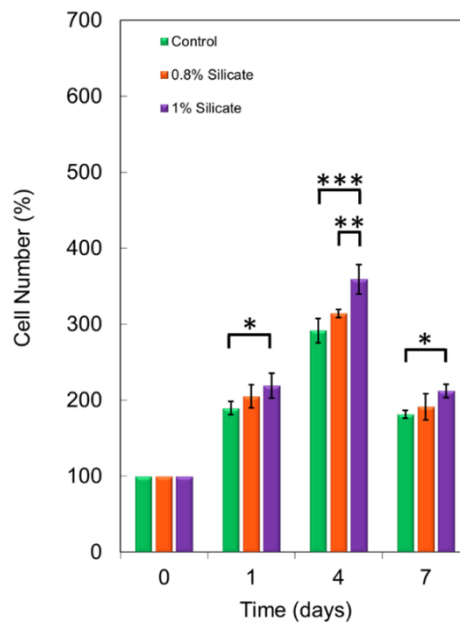


**Figure 3.** Cell proliferation analysis of L929 cells seeded in control, 0.8% silicate, and 1% silicate grafts. Error bars indicate mean  $\pm$  SE (n = 3) [significant differences were defined by one-way ANOVA [Newman-Keuls multiple comparison tests, ( $*p < 0.05$ ,  $**p < 0.01$ ,  $***p < 0.001$ )].

### 3.3 Osteogenic Differentiation of hMSCs on Synthetic Flexible Bone Grafts

Osteogenic differentiation capability of hMSCs seeded on the control group, 0.8% silicate-additive and 1% silicate-additive bone grafts were evaluated for 7, 14, and 21 days. DNA content and ALP activity of the scaffolds were quantified for 21 days. The measured ALP activities were normalized to cell numbers by dividing DNA contents at each time point.

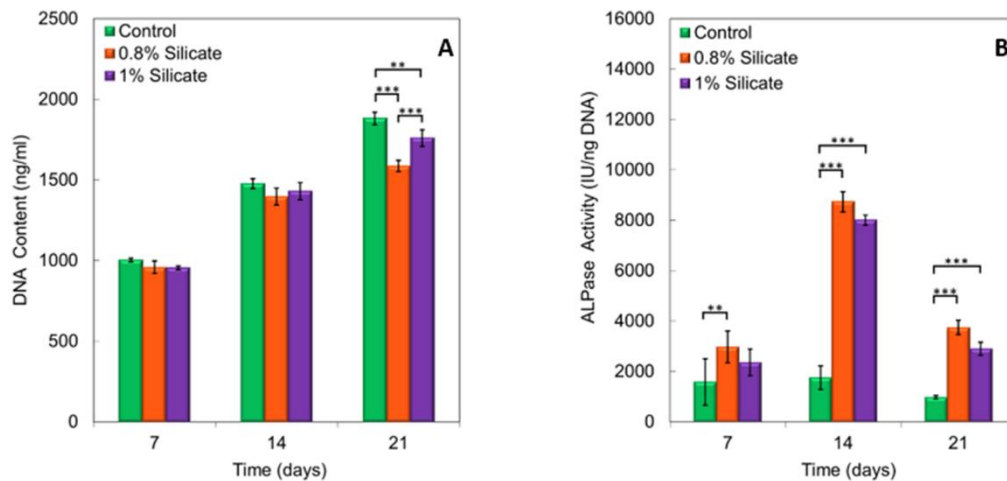


Figure 4: DNA content (A), ALPase activity (B), of hMSCs seeded in control, 0.8% and 1% silicate-additive grafts, and incubated in the osteogenic medium for 21 days. Error bars indicate mean  $\pm$  SE (n = 3) [significant differences were defined by one-way ANOVA [Newman–Keuls multiple comparison tests, (\*p < 0.05, \*\*p < 0.01, \*\*\*p < 0.001)].

hMSCs were seeded and incubated on control, 0.8% silicate, and 1% silicate graft groups. While the control group always had the highest DNA content depending on time, the DNA content of the groups containing 0.8% silicate and 1% silicate increased with time, but this increase was less than the control group. As shown in Fig.4, on Day 21, DNA contents of control, 0.8% silicate, and 1% silicate graft groups were measured as  $1881,359333 \pm 38,86$  ng/ml,  $1586,487333 \pm 34,67$  ng/ml, and  $1759,564667 \pm 50,88$  ng/ml, respectively. As shown in Figure 4, the ALP activity of three graft groups peaked on Day 14 and began to decrease from Day 14 to Day 21, which was consistent with previous findings [32]. It was seen that hMSCs ALP activity increased significantly with silicate addition to grafts. For instance, peak ALP activity of the groups containing 0.8% silicate, and 1% silicate increased to  $8737,517667 \pm 400,8848672$  IU/ng DNA, and  $8005,144667 \pm 201,9006029$  IU/ng DNA, respectively whereas that of the control group was  $1748,337333 \pm 464,6124603$  IU/ng DNA (\*\*p < .001). Moreover, the ALP activity of the group containing 0.8% silicate was the highest at all times.

## 4. DISCUSSIONS

Herein, our objective was to develop porous  $\beta$ -TCP-PLA composite scaffolds with silicate additive to enhance osteogenic differentiation of hMSCs, and to assess the effect of silicate additive with ranging concentrations on osteogenic differentiation. For this purpose, we have designed three different graft groups which were  $\beta$ -TCP-PLA,  $\beta$ -TCP-PLA with 0.8% silicate-additive, and  $\beta$ -TCP-PLA with 1% silicate-additive. Briefly, SEM imaging and the tensile test were performed, and then hMSCs osteogenic differentiation was evaluated concerning the ALP activity and DNA content analysis. The major findings of this study include; all graft types have a porous structure confirmed by SEM imaging, the tensile strength was decreased with silicate-additive, and silicate addition resulted in enhanced ALPase activity and osteogenesis.

Vascularization of bone tissue scaffolds is of great importance for mimicking complex natural tissues, enhancing bone ingrowth and osseointegration, and especially for clinical applications. At this point, it is necessary to highlight the significance of porosity for the vascularization of bone tissue constructs. Adequate porosity with proper size and interconnections among pores ensures an environment for encouraging infiltration and migrating of cells, vascularization, transfer of nutrients and oxygen, and elimination of wastes, as well as being capable of withstanding the external stresses [33, 34]. Scaffolds porosity and pore size take a significant role in bone creation both *in vitro* and *in vivo* [35]. For bone formation, pores are needed since they let migration and reproduction of osteoblasts and mesenchymal cells, as also vascularization [35, 36]. Within the scope of this study, for fabricating synthetic bone grafts, the particulate-leaching method was used and porogen particles were added to the scaffolds. By incorporation of porogen particles, it was aimed to make the scaffold porous, and our SEM images showed that fabricated synthetic bone grafts have a highly porous structure. In the SEM images, pores can be observed, and these pores allow the synthetic bone tissue scaffolds to be vascularized better.

The production of composite scaffolds is a favorable approach since the combination of benefits of two or more materials may ensure better mechanical and physiological necessities for the host bone [21]. In addition, the formability of polymer materials in participation with a controlled-volume fraction of bioactive ceramic might result in the mechanical reinforcement of produced scaffold constructs and also increase the low bioactivity of most polymers [37]. In the current study, it was observed that the tensile strength of  $\beta$ -TCP grafts was decreased with increasing concentration of silicate-additive. Dalgic *et al.* used graphene oxide (GO)-incorporated silicate-doped nano HA composite materials with different ratios and examined the potential usage for bone tissue engineering via producing and reinforcing electrospun poly( $\epsilon$ -caprolactone) (PCL) scaffold construct. It was reported that PCL tensile feature did not enhance by the addition of HA to the fiber. Young's modulus also declined upon the addition of HA and silicate-doped hydroxyapatite (SiHA) to PCL. Similar to our results, tensile strength values have further declined via the incorporation of SiHA. It was also reported that silicate substitution may alter the surface properties of HA. When compared with HA, SiHA could have further moved off from PCL using structural resemblances and there might be a lower number of interfacial bonding ending up with decreased tensile strength [38]. To stabilize metallic implants, suitable flexible scaffolds should be placed on the surgical site just before surgical site closure. Higher elasticity is suitable for bone defects in the pelvis and lower extremities [39]. However, both flexibility and osseointegration are critical around the implant site. The composition of the scaffold used in this study allows osseointegration with the silicate additive by providing osteoinductivity. Therefore, the group with a high elastic modulus among silicate-containing groups which is 0.8% silicate might be considered optimal, although the silicate additive-free group has a higher elastic modulus than the silicate-containing groups of 0.8% and 1%, respectively.

The silicate-substitution stimulates the negative surface charge of material and importantly increases bone formation performance in comparison to present materials by the influence of it on the activity of bone-forming and resorbing cells [40-44]. This permits the vascularization of silicate-substituted calcium phosphate (Si-CaP) matrix, assisting differentiation of cells, making easy the rapid bone ingrowth, a larger volume of bone growth, and encouraging nutrition transfer to host bone tissue, with following graft remodeling to mature bone [45]. Herein, the effect of  $\beta$ -TCP-PLA-based scaffolds on the viability and proliferation of L929 cells was determined based on MTT analysis. Cell numbers for 0.8% silicate-additive and 1% silicate-additive bone grafts were higher than that of control grafts at all time points. This finding suggests that the functionalization of  $\beta$ -TCP-PLA grafts by silicate-additive induces cell proliferation, and silicate-additive bone grafts facilitated the proliferation of L929 cells compared with the control group. However, the cell numbers of the three scaffold groups increased from Day 1 to Day 4 and then decreased from Day 4 to Day 7. Figure 3 demonstrates that the cell number decreased significantly after Day 4. At the end of Day 7, it was observed that the excessive cell multiplication within the composite scaffolds led to the death of seeded cells due to the restricted area, It can be explained by the excessive cells which could not adhere to the scaffold surface. Since these excessive cells affected proliferation negatively, the cell number on Day 7 decreased in the cell number. Moreover, cell numbers on 0.8% silicate-additive and 1%

silicate-additive bone grafts suggested that silicate-additive graft groups did not have a toxic effect on cells. Furthermore, cell numbers for 1% silicate-additive grafts were the highest at all time points. Similarly, DNA content measurement results revealed that 1% silicate-additive bone grafts showed more amount of DNA content when compared to 0.8% silicate-additive bone grafts. This result suggests that the DNA content was correlated with the cell number.

hMSCs differentiation into osteoblastic lineage is a complicated procedure, containing the attachment, reproduction, maturation, differentiation, and mineralization of them [46]. The most important parameters which can be used for assessing osteogenic differentiation are known as adequate cellular growth, ALP activity, calcium deposition, and also osteogenic markers expression [31]. hMSCs osteogenic differentiation capability on bone grafts was quantified by measuring DNA content and ALP activity over 21 days. At that step, cells were seeded and then incubated on  $\beta$ -TCP/PLA-based grafts for 7, 14, and 21 days, and at the termination of every culture time point, we measured the hMSCs DNA content. Our results demonstrate that the control group showed greater DNA content than other groups, suggesting that hMSCs on the control group grafts proliferated more. On the other hand, 0.8% silicate and 1% silicate groups showed less increase in DNA content than the control group. However, the DNA content of silicate-additive groups enhanced with time during 21 days of incubation, indicating that cells showed enhanced proliferation at each time point. ALP activity measurement was evaluated utilizing the time-dependent *p*NPP creation in an alkaline solution. In correlation with prior findings, ALP activity of whole groups seemed to increase from Day 7 to Day 14 and began to decline with a longer period of incubation with mineralization [18]. The ALP activity of 0.8% silicate and 1% silicate groups was importantly greater than the ALP activity of the control group at all time points during 21 days of incubation. Functionalization with silicate promoted the ALP activity of hMSCs on  $\beta$ -TCP/PLA grafts. Similarly, in literature, silicate addition ended up with better *in vitro* and *in vivo* osteogenic differentiation of cells, and also guidable biodegradability properties when compared with  $\beta$ -TCP [21, 22]. Moreover, the ALP activity was the greatest in the 0.8% silicate group at all time points when compared with other groups proposing that hMSCs did not take as much osteogenic induction in control and 1% silicate grafts, and this indicates the positive effect of 0.8% silicate concentration on osteogenic differentiation. Cameron *et al.* used silicate-substituted calcium phosphate (Si-CaP) and nonmodified HA for testing if they can encourage MSCs osteogenic differentiation in the nonexistence of soluble factors or not, and reported that Si-CaP assisted the MSCs' attachment and reproduction and also triggered the osteogenesis to a larger degree than HA, as proofed by osteoblast-related genes upregulation [24]. Nagineni *et al.* aimed to evaluate the clinical and radiographical findings in spinal fusion processes by using Si-CaP material and reported that Si-CaP can be an alternative to autogenous bone material for spinal arthrodesis processes, and for a 12-month follow-up period, they observed high grades of bony fusion by utilizing Si-CaP in integration with several surgical spinal methods. In another study, researchers evaluated the osteoinductivity of silicate-substituted calcium phosphate and stoichiometric calcium phosphate using ectopic implantation. Silicate substitution importantly enhanced the quantity of bone created and the quantity of bone that is bonded to the surface of the implant, and it was reported that utilizing silicate-substituted calcium phosphate in place of stoichiometric calcium phosphate for orthopedic surgeries might significantly increase bone tissue repair and regeneration [23].

In summary, our results revealed that 0.8% silicate additive is the best concentration of silicate addition. Also, in this study, a mechanically targeted issue was to provide convenience to the surgeon during the application by adding the PLA polymer to the graft and to provide flexibility to give the desired shape. Herein, the flexible structure of these synthetic bone grafts will provide an important advantage by facilitating the surgeon for giving the intended form of the graft substance in the surgical area throughout the surgical process. Moreover, for a tissue scaffold, having a highly porous structure is very crucial, and these synthetic flexible bone grafts will have a positive effect on the pre-vascularization of scaffolds and differentiation of hMSCs due to their porous structure and interconnected pores.

## 5. CONCLUSIONS

In summary,  $\beta$ -TCP-PLA composite scaffolds were produced with two different concentrations of silicate-additive. Characterization tests showed that designed scaffolds had flexibility and porosity. We found that 1% and 0.8% silicate-additive flexible grafts improved the osteoinductive capacity of the  $\beta$ -TCP-PLA composite scaffolds, and encouraged the proliferation and osteogenic differentiation of hMSCs. Moreover, 0.8% silicate-additive flexible grafts showed sharply increased ALP activity when compared with 1% silicate-additive flexible grafts and  $\beta$ -TCP-PLA grafts. Our findings revealed that  $\beta$ -TCP-PLA composite scaffolds functionalized with 0.8% silicate-additive possessed more potential for inducing osteogenesis. It is believed that our results will assist scientists in enhancing and further optimization of the activity of composite scaffolds for more effective and better bone tissue repair and regeneration.

### Declaration of Ethical Standards

The authors declare that all ethical guidelines including authorship, citation, data reporting, and publishing original research are followed.

### Credit Authorship Contribution Statement

**Günnur Onak Pulat:** Performing experiments, Writing-reviewing-editing the manuscript. **Gülşah Sunal:** Performing experiments, Writing-reviewing-editing the manuscript. **Ozan Karaman:** Designing experiments, Writing-reviewing-editing the manuscript.

### Declaration of Competing Interest

Authors have declared that there is no conflict of interest.

### Funding / Acknowledgements

The authors acknowledge raw material support from Bonegraft Biyolojik Malzemeler San. ve Tic. A. Ş. to perform experiments. Also the authors thank to Oğuzhan GÖKMEN, İlker GÜRGİT and Aybike KOCATÜRKMEN for their help.

### Data Availability

Data will be made available on request.

## REFERENCES

- [1] M. R. Brinker and D. P. O'Connor, "The incidence of fractures and dislocations referred for orthopaedic services in a capitated population," *J Bone Joint Surg Am*, vol. 86, no. 2, pp. 290-7, 2004.
- [2] B. Baroli, "From natural bone grafts to tissue engineering therapeutics: brainstorming on pharmaceutical formulative requirements and challenges," *Journal of Pharmaceutical Sciences*, vol. 98, no. 4, pp. 1317-1375, 2009.
- [3] R. Agarwal and A. J. García, "Biomaterial strategies for engineering implants for enhanced osseointegration and bone repair," *Advanced Drug Delivery Reviews*, vol. 94, pp. 53-62, 2015.
- [4] H. Qu, H. Fu, Z. Han, and Y. Sun, "Biomaterials for bone tissue engineering scaffolds: a review," *RSC Adv*, vol. 9, no. 45, pp. 26252-26262, 2019.
- [5] A. Wubneh, E. K. Tsekoura, C. Ayranci, and H. Uludağ, "Current state of fabrication technologies and materials for bone tissue engineering," *Acta Biomaterialia*, vol. 80, pp. 1-30, 2018.

- [6] M. M. Stevens, "Biomaterials for bone tissue engineering," *Materials Today*, vol. 11, no. 5, pp. 18-25, 2008.
- [7] P. Chocholata, V. Kulda, and V. Babuska, "Fabrication of scaffolds for bone-tissue regeneration," *Materials*, vol. 12, no. 4, p. 568, 2019.
- [8] Q. Z. Chen, I. D. Thompson, and A. R. Boccaccini, "45S5 Bioglass®-derived glass–ceramic scaffolds for bone tissue engineering," *Biomaterials*, vol. 27, no. 11, pp. 2414-2425, 2006.
- [9] F. Matassi, L. Nistri, D. C. Paez, and M. Innocenti, "New biomaterials for bone regeneration," *Clinical Cases in Mineral and Bone Metabolism*, vol. 8, no. 1, p. 21, 2011.
- [10] T. Matsuno et al., "Development of  $\beta$ -tricalcium phosphate/collagen sponge composite for bone regeneration," *Dental Materials - Journals*, vol. 25, no. 1, pp. 138-144, 2006.
- [11] R. W. Nicholas and T. A. Lange, "Granular tricalcium phosphate grafting of cavitary lesions in human bone," *Clinical Orthopaedics and Related Research*, no. 306, pp. 197-203, 1994.
- [12] M. P. McAndrew, P. W. Gorman, and T. A. Lange, "Tricalcium phosphate as a bone graft substitute in trauma: preliminary report," *Journal of Orthopaedic Trauma*, vol. 2, no. 4, pp. 333-339, 1988.
- [13] M. Bohner, B. L. G. Santoni, and N. Döbelin, " $\beta$ -tricalcium phosphate for bone substitution: Synthesis and properties," *Acta Biomaterialia*, vol. 113, pp. 23-41, 2020.
- [14] G. Lewis, "Injectable bone cements for use in vertebroplasty and kyphoplasty: state-of-the-art review," (in eng), *Journal of Biomedical Materials Research Part B: Applied Biomaterials*, vol. 76, no. 2, pp. 456-68, Feb 2006, doi: 10.1002/jbm.b.30398.
- [15] G. Daculsi, "Biphasic calcium phosphate concept applied to artificial bone, implant coating and injectable bone substitute," *Biomaterials*, vol. 19, no. 16, pp. 1473-1478, 1998/08/01/ 1998, doi: [https://doi.org/10.1016/S0142-9612\(98\)00061-1](https://doi.org/10.1016/S0142-9612(98)00061-1).
- [16] G. Narayanan, V. N. Vernekar, E. L. Kuyinu, and C. T. Laurencin, "Poly (lactic acid)-based biomaterials for orthopaedic regenerative engineering," *Advanced Drug Delivery Reviews*, vol. 107, pp. 247-276, 2016.
- [17] C. Ning, "Biomaterials for Bone Tissue Engineering," in *Biomechanics and Biomaterials in Orthopedics*: Springer, 2016, pp. 35-57.
- [18] S. Xu et al., "Reconstruction of calvarial defect of rabbits using porous calcium silicate bioactive ceramics," (in eng), *Biomaterials*, vol. 29, no. 17, pp. 2588-96, Jun 2008, doi: 10.1016/j.biomaterials.2008.03.013.
- [19] K. A. Hing, L. F. Wilson, and T. Buckland, "Comparative performance of three ceramic bone graft substitutes," (in eng), *The Spine Journal*, vol. 7, no. 4, pp. 475-90, Jul-Aug 2007, doi: 10.1016/j.spinee.2006.07.017.
- [20] V. V. Nagineni et al., "Silicate-substituted calcium phosphate ceramic bone graft replacement for spinal fusion procedures," (in eng), *Spine (Phila Pa 1976)*, vol. 37, no. 20, pp. E1264-72, Sep 15 2012, doi: 10.1097/BRS.0b013e318265e22e.
- [21] M. Ahmadipour et al., "A review: silicate ceramic-polymer composite scaffold for bone tissue engineering," *International Journal of Polymeric Materials and Polymeric Biomaterials*, vol. 71, no. 3, pp. 180-195, 2022.
- [22] C. Wu and J. Chang, "A review of bioactive silicate ceramics," *Biomedical Materials*, vol. 8, no. 3, p. 032001, 2013.
- [23] M. J. Coathup, S. Samizadeh, Y. S. Fang, T. Buckland, K. A. Hing, and G. W. Blunn, "The osteoinductivity of silicate-substituted calcium phosphate," *Journal of Bone and Joint Surgery*, vol. 93, no. 23, pp. 2219-2226, 2011.
- [24] K. Cameron, P. Travers, C. Chander, T. Buckland, C. Champion, and B. Noble, "Directed osteogenic differentiation of human mesenchymal stem/precursor cells on silicate substituted calcium phosphate," *Journal of Biomedical Materials Research Part A*, vol. 101, no. 1, pp. 13-22, 2013.
- [25] O. Chan et al., "The effects of microporosity on osteoinduction of calcium phosphate bone graft substitute biomaterials," *Acta Biomaterialia*, vol. 8, no. 7, pp. 2788-2794, 2012.

- [26] S. Bose, M. Roy, and A. Bandyopadhyay, "Recent advances in bone tissue engineering scaffolds," *Trends in Biotechnology*, vol. 30, no. 10, pp. 546-554, 2012.
- [27] M. Büyüköz and S. A. Aktınkaya, "Jelatin Doku İskelesinin Mekanik Özellikleri Üzerine Gözenek Oluşturucu Ajanın Boyutu ve Bağlantı Süresinin Etkileri-The Effects of Porogen Agent Size and Interconnection Time on the Mechanical Properties of Gelatin Scaffold," *Celal Bayar University Journal of Science*, vol. 11, no. 2, 2015.
- [28] H. J. Park et al., "Fabrication of 3D porous silk scaffolds by particulate (salt/sucrose) leaching for bone tissue reconstruction," *International Journal of Biological Macromolecules*, vol. 78, pp. 215-223, 2015.
- [29] A. G. Mikos et al., "Preparation and characterization of poly (L-lactic acid) foams," *Polymer*, vol. 35, no. 5, pp. 1068-1077, 1994.
- [30] A. Eltom, G. Zhong, and A. Muhammad, "Scaffold techniques and designs in tissue engineering functions and purposes: a review," *Advances in Materials Science and Engineering*, vol. 2019, 2019.
- [31] O. Karaman, A. Kumar, S. Moeinzadeh, X. He, T. Cui, and E. Jabbari, "Effect of surface modification of nanofibres with glutamic acid peptide on calcium phosphate nucleation and osteogenic differentiation of marrow stromal cells," *Journal of Tissue Engineering and Regenerative Medicine*, vol. 10, no. 2, pp. E132-E146, 2016.
- [32] G. Onak et al., "Aspartic and glutamic acid templated peptides conjugation on plasma modified nanofibers for osteogenic differentiation of human mesenchymal stem cells: a comparative study," *Scientific Reports*, vol. 8, no. 1, pp. 1-15, 2018.
- [33] N. Abbasi, S. Hamlet, R. M. Love, and N.-T. Nguyen, "Porous scaffolds for bone regeneration," *Journal of Science: Advanced Materials and Devices*, vol. 5, no. 1, pp. 1-9, 2020.
- [34] S. Limmahakhun, A. Oloyede, K. Sitthiseripratip, Y. Xiao, and C. Yan, "3D-printed cellular structures for bone biomimetic implants," *Additive Manufacturing*, vol. 15, pp. 93-101, 2017.
- [35] V. Karageorgiou and D. Kaplan, "Porosity of 3D biomaterial scaffolds and osteogenesis," *Biomaterials*, vol. 26, no. 27, pp. 5474-5491, 2005.
- [36] Y. Kuboki et al., "BMP-induced osteogenesis on the surface of hydroxyapatite with geometrically feasible and nonfeasible structures: topology of osteogenesis," *Journal of Biomedical Materials Research: An Official Journal of The Society for Biomaterials, The Japanese Society for Biomaterials, and the Australian Society for Biomaterials*, vol. 39, no. 2, pp. 190-199, 1998.
- [37] A. R. Boccaccini and V. Maquet, "Bioresorbable and bioactive polymer/Bioglass® composites with tailored pore structure for tissue engineering applications," *Composites Science and Technology*, vol. 63, no. 16, pp. 2417-2429, 2003.
- [38] A. D. Dalgic, A. Z. Alshemary, A. Tezcaner, D. Keskin, and Z. Evis, "Silicate-doped nano-hydroxyapatite/graphene oxide composite reinforced fibrous scaffolds for bone tissue engineering," *Journal of Biomaterials Applications*, vol. 32, no. 10, pp. 1392-1405, 2018.
- [39] M. G. Axelsen, S. Overgaard, S. M. Jespersen, and M. Ding, "Comparison of synthetic bone graft ABM/P-15 and allograft on uninstrumented posterior lumbar spine fusion in sheep," *Journal of Orthopaedic Surgery and Research*, vol. 14, no. 1, p. 2, 2019/01/03 2019. [Online]. Available: <https://doi.org/10.1186/s13018-018-1042-4>.
- [40] N. Patel et al., "A comparative study on the in vivo behavior of hydroxyapatite and silicon substituted hydroxyapatite granules," *Journal of Materials Science: Materials in Medicine*, vol. 13, no. 12, p. 1199, 2002.
- [41] K. A. Hing, P. A. Revell, N. Smith, and T. Buckland, "Effect of silicon level on rate, quality and progression of bone healing within silicate-substituted porous hydroxyapatite scaffolds," *Biomaterials*, vol. 27, no. 29, pp. 5014-5026, 2006.
- [42] A. E. Porter, T. Buckland, K. Hing, S. M. Best, and W. Bonfield, "The structure of the bond between bone and porous silicon-substituted hydroxyapatite bioceramic implants," *Journal of Biomedical Materials Research Part A: An Official Journal of The Society for Biomaterials, The Japanese*



- Society for Biomaterials, and The Australian Society for Biomaterials and the Korean Society for Biomaterials, vol. 78, no. 1, pp. 25-33, 2006.
- [43] K. A. Hing, L. F. Wilson, and T. Buckland, "Comparative performance of three ceramic bone graft substitutes," *The Spine Journal*, vol. 7, no. 4, pp. 475-490, 2007.
- [44] D. L. Wheeler, L. G. Jenis, M. E. Kovach, J. Marini, and A. S. Turner, "Efficacy of silicated calcium phosphate graft in posterolateral lumbar fusion in sheep," *The Spine Journal*, vol. 7, no. 3, pp. 308-317, 2007.
- [45] T. Lerner and U. Liljenqvist, "Silicate-substituted calcium phosphate as a bone graft substitute in surgery for adolescent idiopathic scoliosis," *European Spine Journal*, vol. 22, pp. 185-194, 2013.
- [46] P. J. Marie and O. Fromigué, "Osteogenic differentiation of human marrow-derived mesenchymal stem cells," *Regenerative Medicine*, vol. 1, no. 4, pp. 539-48, 2006.



## DETERMINING THE MOST POWERFUL FEATURES IN THE DESIGN OF AN AUTOMATIC SLEEP STAGING SYSTEM

<sup>1,\*</sup>Seral ÖZŞEN , <sup>2</sup>Yasin KOCA , <sup>3</sup>Gülay TEZEL , <sup>4</sup>Sena ÇEPER ,  
<sup>5</sup>Serkan KÜÇÜKTÜRK , <sup>6</sup>Hülya VATANSEV 

<sup>1,2</sup>Konya Technical University, Electrical and Electronics Engineering Department, Konya, TÜRKİYE

<sup>3,4</sup>Konya Technical University, Computer Engineering Department, Konya, TÜRKİYE

<sup>5,6</sup>Necmettin Erbakan University, Medicine Faculty, Sleep Laboratory, Konya, TÜRKİYE

<sup>1</sup>[sozsen@ktun.edu.tr](mailto:sozsen@ktun.edu.tr), <sup>2</sup>[kocayasiin@gmail.com](mailto:kocayasiin@gmail.com), <sup>3</sup>[gtezel@ktun.edu.tr](mailto:gtezel@ktun.edu.tr), <sup>4</sup>[sceper@ktun.edu.tr](mailto:sceper@ktun.edu.tr),

<sup>5</sup>[skuccukturk@kmu.edu.tr](mailto:skuccukturk@kmu.edu.tr), <sup>6</sup>[hulyavatansev@hotmail.com](mailto:hulyavatansev@hotmail.com)

### Highlights

- The accuracies of automatic sleep staging systems using real sleep data are generally under 85% and studying with real datasets is very hard because extracting useful features from a noisy environment is more complex. This study used real sleep dataset to reach high accuracy.
- The automatic sleep stage classifiers used in literature are generally designed for known state-of-art datasets and they are taken from healthy persons. A real dataset including healthy and Obstructive Sleep Apnea patients is used in this dataset.
- The main contribution of this study is feature engineering in that we scrutinized which features are more useful in a sleep staging system which uses real dataset with healthy and OSA patients.



## DETERMINING THE MOST POWERFUL FEATURES IN THE DESIGN OF AN AUTOMATIC SLEEP STAGING SYSTEM

<sup>1,\*</sup>Seral ÖZŞEN , <sup>2</sup>Yasin KOCA , <sup>3</sup>Gülay TEZEL , <sup>4</sup>Sena ÇEPER ,  
<sup>5</sup>Serkan KÜÇÜKTÜRK , <sup>6</sup>Hülya VATANSEV 

<sup>1,2</sup>Konya Technical University, Electrical and Electronics Engineering Department, Konya, TÜRKİYE

<sup>3,4</sup>Konya Technical University, Computer Engineering Department, Konya, TÜRKİYE

<sup>5,6</sup>Necmettin Erbakan University, Medicine Faculty, Sleep Laboratory, Konya, TÜRKİYE

<sup>1</sup>sozsen@ktun.edu.tr, <sup>2</sup>kocayasiin@gmail.com, <sup>3</sup>gtezel@ktun.edu.tr, <sup>4</sup>sceper@ktun.edu.tr,

<sup>5</sup>skuccukturk@kmu.edu.tr, <sup>6</sup>hulyavatansev@hotmail.com

(Received: 15.02.2023; Accepted in Revised Form: 21.06.2023)

**ABSTRACT:** Spending too much time on manual sleep staging is tiring and challenging for sleep specialists. In addition, experience in sleep staging also creates different decisions for sleep experts. The search for finding an effective automatic sleep staging system has been accelerated in the last few years. There are many studies dealing with this problem but very few of them were conducted with real sleep data. Studies have been carried out on mostly processed and cleaned-ready data sets. In addition, there are few studies in which the data distribution in sleep stages is balanced (equal numbers of epochs from each stage are used), and it is seen that the performance of these studies is quite low compared to other studies. When the literature studies are examined, there is a wide range of studies in which many features are extracted, many feature selection methods are used, many classifiers are applied and various combinations of these are available. For this reason, to determine the best-performing features and the most powerful features, 168 features were extracted from the real EEG, EOG, and EMG signals of 124 patients. These features were selected with 7 different feature selection methods, and classification was carried out with 4 classifiers. In general, the ReliefF feature selection method has performed best, and the Bagged Tree classifier has reached the highest classification accuracy of 67.92% with the use of nonlinear features.

**Keywords:** Automatic Sleep Staging, Frequency Analysis of EEG Signals, Sleep Signal Detection

### 1. INTRODUCTION

Sleep staging is a process that is done for many reasons such as to detect sleep-related disorders, determine sleep quality,...etc. According to AASM standards, [27] sleep can be categorized into Wake, REM, and Non-REM stages. The Non-REM stages are further divided into Non-REM1, Non-REM2, and Non-REM3 stages. The staging is done by examining sleep-related signals which are named Polysomnography Signals (PSG) by a sleep expert. The most used ones in PSG signals are electroencephalogram (EEG), electrooculogram (EOG), and electromyogram (EMG) signals. These signals are divided into 30 sec-long epochs and then the expert decides which stages should be selected as a label of the related epoch. In doing this, the experts use rules [27] and their experience. Whereas this seems to be a very straightforward process, making the correct decision would be cumbersome in many cases. First of all, the signals are mainly noisy, and recognizing some signal patterns which are used in making decisions is sometimes very hard in this noisy environment. Also, there isn't a clear distinction in some epochs between the stages. For example, an EEG signal belonging to a Wake stage can be very similar to one of the Non-REM1 stages. In such cases, the experience of the sleep expert can result in different staging labels. The manual staging process is also time-consuming and tiring because the expert should examine many signals in 30-second epochs in detail (the duration of the overall signals is 6-8 hours) and interpret

the rules according to the overall sleep to make the decision. So, based on these reasons in place, the research for automatic sleep-staging systems has begun many years ago.

It can be found in a huge literature in the search for automatic sleep staging studies. In the study of Lee et. al. [33], a Detrended Fluctuation Analysis (DFA) was used for the classification of sleep data which is taken from the MIT/BIH sleep database [33]. Liu and Sun [36] conducted a three-class staging study on MIT/BIH database by using multifractal DFA [36]. In another study using DFA, Farag et. al. [17] reached an overall classification accuracy of 85.18% on their real recorded dataset with 22 patients [17]. Hassan et. al. [22] used a tunable Q-factor wavelet transform to classify sleep stages of Physionet and Dream datasets and obtained a classification accuracy of 91.50% [22]. Other methods were also applied to this dataset in similar studies [23, 24, 25] and performances between 90-94% were reached. Chlon et. al. [13] proposed a different method for the classification of sleep stages. They combined Hierarchical Dirichlet Process-Hidden Markov Model (HMM) with Wide-sense-stationary time series analysis and conducted the tests of the proposed method on simulated sleep data [13]. In the study of Jiang et. al. [29], a new method based on Empirical Mode Decomposition (EMD) was proposed and they reached a 92% classification accuracy on Physionet data [29]. They also applied a new rule-free refinement based on HMM to optimize classification results. In their study, Acharya et. al. extracted features by using nonlinear dynamic analysis, Higher Order Spectra (HOS), and Recurrence Quantification Analysis (RQA) [2]. They analyzed the effectiveness of these features by ANOVA. Chaozen et. al. used Hilbert Huang Transform (HHT) to obtain spectral features [10]. By adding a sample entropy feature to their feature set, they obtain 89.9% classification accuracy on the MIT database. In another study, Peker used Complex valued Neural Network to classify the Sleep-EDF database by extracting complex-valued nonlinear features and he obtain a classification accuracy of 91.57% [41]. Tian et. al. [44] used the aid of Multiscale entropy features of the Sleep-EDF database and they classified them by proportion-based SVM with a classification accuracy of 91.4% [44]. In their study, Liua et. al. [37] conducted a comprehensive feature selection application for automatic sleep staging [37]. They extracted 50 features from the EEG signals of the MIT/BIH database by using Multifractal DFA, visibility graph algorithm (VGA), frequency analysis, and nonlinear analysis. They utilized genetic algorithm (GA) as feature selector and used Least Squares SVM to compare the performances. In a study conducted with real data, Zhang et. al. [49] used frequency, time-domain, and nonlinear features and reached an average accuracy of 82.18% in three subjects [49]. Zhang et. al. [50] applied band-pass filtering, spectral feature extraction, gaussian parameters, and statistic-based feature selection [50]. They reached a classification accuracy of 85.5% in their dataset consisting of 39 subjects. In their study, Henri Korkalainen et. al. used overlapping different-size epochs (Korkalainen et. al., 2021). They reached 81.9% accuracy but their dataset includes many NonREM3 and REM epochs and they used deep learning. Ghimatgar et. al. [20] used HMM for staging with single-channel EEG [20]. They used four public EEG datasets and comparatively low accuracies for such public datasets (between 77.6%-97.4%). In their study, Arslan et. al used machine learning methods for sleep stage classification for data taken from 50 patients with sleep-related diseases (not from the OSA patients) [3]. They obtained comparatively high accuracies but 19 channels were used in that study.

Some literature reviews can be found in [1, 7, 18, 19, 26].

The vast majority of these studies use standard datasets such as the Sleep-EDF dataset, and MIT/BIH database. The accuracy ratios in these studies are generally over 85%. But when the studies using real data are analyzed, the accuracy values decrease under 85%. Dealing with real datasets is very hard because extracting useful features from a noisy environment is more complex. Besides, if the used dataset is taken from patients rather than healthy persons, the problem becomes more complicated. Besides this, when the studies obtaining high accuracy rates were searched, it can be seen that they used deep learning methods. In deep learning methods, it is not possible to see which feature gave the best result. Thus our study differs from theirs in that we also tried to see which features are more useful in the staging process. In our study, we used a dataset consisting of PSG signals of 124 persons (93 of them have Obstructive sleep apnea (OSA) and 31 of them are healthy). By utilizing time-domain analysis, frequency analysis, nonlinear analysis, and MDFA, 168 features were extracted from the EEG, EOG, and EMG signals. To detect best performing

features, 7 feature selection methods were used in 5 applications. In performance comparison, classification was carried out with k-nearest neighbor (kNN), decision tree (DT), SVM, and Bagged Tree methods.

## 2. MATERIALS and METHOD

### 2.1. Used Data

During the study, PSG data were obtained from a total of 124 people, 31 of whom were healthy, and 93 patients, who were hospitalized in the sleep laboratory of the Meram Medical Faculty hospital. Whereas many signals are recorded in PSG, EEG, EOG, and EMG signals are the most commonly used ones in manual and automatic sleep staging studies. Patients with an AHI value above 5 were accepted. Using the EEG, EOG, and EMG signals from the obtained PSG data, these signals were divided into 30-sec epochs. PSG signals were sampled at 200 Hz. The signals obtained for each patient were normalized to avoid inter-patient amplitude differences. The EEG signals used were 0.3Hz-35Hz, EMG signals 1Hz-45Hz, and EOG signals were filtered between 0.3Hz-30Hz with a 6th-order Butterworth bandpass filter. The stage of these epochs was determined by the sleep specialist. The total number of epochs was noted as 67443. The distribution of these epochs according to the sleep stages is given in Table 1.

*Table 1. Distributions of epochs after electrode disconnection deleting process*

	Patient	Healthy	Total
Wake	13600	3712	17312
NonREM-1	6031	1496	7527
NonREM-2	23066	7858	30924
NonREM-3	4765	1269	6034
REM	3625	2021	5646

As seen, there is a very high imbalance between the stages. This results in inappropriately trained classifiers because the classifiers arrange their parameters according to the most seen classes. To avoid this situation, almost equal numbers of epochs from each stage were selected and included in the study. 5000 epochs were selected from each stage and a data set consisting of 25000 epochs in total was prepared. When selecting 5000 epochs, a balanced distribution was taken into account between the sick and healthy individuals. In summary, the generated dataset consists of a total of Nx25000 epochs, 5000 epochs per stage, with N being the number of features. In this dataset, 1000 epochs from each stage are reserved for feature selection, 3000 epochs are reserved for training testing with 5-fold cross-validation, and 1000 epochs are reserved for validation. As a result, three sub-datasets were obtained: the dataset to be used for feature selection (Nx5000 size), the dataset to be used in cross-validation (Nx15000) and the dataset to be used in validation (Nx5000). Random epoch selection was carried out in these selections.

### 2.2. Feature Extraction

From the EEG, EOG (left eye and differential EOG), and EMG signals, time, frequency, nonlinear, and MDFA features were obtained.

#### Time Domain Features:

The time domain features used in the study were determined by examining the literature studies as Mean value, Standard deviation, Skewness, Kurtosis, Signal energy, Zero crossing rate, and maximum-minimum distance (MMD) [1]. These 7 features were extracted from the EEG, left-eye EOG, difference EOG (difference EOG signal is obtained by subtracting left eye EOG signal from the right-eye EOG signal), and EMG signal. Thus, 28 features were obtained as time features.

Frequency Domain Features:

The frequency content of the signals used for feature extraction in the frequency domain was obtained by the Welch method [40]. Many methods have been used to obtain the frequency content in sleep staging applications. In a recent study, many frequency analysis methods were compared in an application and it was concluded that the Welch method was more successful because it was less sensitive to noise than other methods [7]. In other similar studies, it has been seen that the Welch method has achieved successful results, so the Welch method has been preferred as a frequency analysis method. The frequency resolution was chosen as 0.05 Hz. The following frequency features were extracted from the

EEG signals after obtaining their Power Spectral Distributions (PSD) by the Welch method:

1. Relative power ratio of the alpha frequency band (8-12 Hz)
2. Relative power ratio of the Beta frequency band (12-16 Hz)
3. Relative power ratio of Theta frequency band (4-8 Hz)
4. Relative power ratio of Delta frequency band (0-4 Hz)
5. Difference of Alpha power between the current epoch and precious epoch
6. Difference of Beta power between current epoch and precious epoch
7. Difference of Theta power between the current epoch and precious epoch
8. Difference of Delta power between the current epoch and precious epoch
9. Relative power ratio of 12-14 Hz band (for sleep spindles)
10. Difference of 12-14Hz power between current epoch and precious epoch
11. Mean value of power spectra
12. Standard deviation of power spectra
13. Skewness of power spectra
14. Kurtosis of power spectra

Besides these 14 frequency features obtained from the EEG signal, 12 frequency features were taken from the EOG signals (6 features from the left-eye EOG, 6 features from the difference EOG). These are the Relative power of the 0.5 Hz-2 Hz frequency band, the Difference of 0.5-2Hz power between the current epoch and precious epoch, the Mean value of power spectra, the Standard deviation of power spectra, the Skewness of power spectra and Kurtosis of power spectra. Two more features were added to these frequency features which were extracted from the EMG signals: The total energy of EMG power spectra and the Difference of total power spectral energy between the current epoch and the previous epoch. Thus, 28 frequency features were obtained in total (14 from EEG, 12 from EOG, and 2 from EMG).

Nonlinear Features:

While there are many nonlinear features used in the literature, the most commonly used ones were identified and included in the study. Accordingly, the nonlinear features extracted from EEG, EOG, and EMG signals are [2]: Approximate Entropy, Sample Entropy, Fuzzy Entropy, Renyi's Entropy, Permutation Entropy, Hurst Exponent, Lyapunov Exponent, Correlation Dimension, Kolmogorov Complexity, Lempel-Ziv Complexity, Higuchi Fractal Dimension, Hjorth mobility, Hjorth complexity. As a result, a total of 52 nonlinear features were obtained, 13 from EEG, 13 from left-eye-EOG, 13 from difference-EOG, and 13 from EMG.

MDFA features:

Peng et al. [42] proposed the Detrended Fluctuation Analysis (DFA) method to analyze the similarity and correlation in DNA sequences. Since then, this method has been frequently used to identify mono-fractal scaling features in non-stationary time series in many fields such as financial market analysis [14], analysis of biomedical time series, and detection of abnormal conditions [6,47], natural and social events [11]. is used. However, many time series, including biomedical signals, may not exhibit a mono-fractal

structure [30]. In particular, biomedical signals may exhibit transient variations and erratic fluctuations. These variations and fluctuations cannot be explained by a single scale provided by the DFA method and are suitable for multiple fractal structures. Therefore, Kantelhardt et al. [30] removed the limitations of CFA by introducing the Multifractal Detrended Fluctuation Analysis (MDFA) method, which is the advanced version of the DFA method [8, 16, 38].

In the study, the following features were extracted from the time series obtained by the analysis of EEG, EOG, and EMG signals with MDFA [21]: maximum hurst exponent, minimum hurst exponent, generalized hurst exponent, maximum singularity exponent, minimum singularity exponent, Mean singularity exponent, Singularity exponent corresponding to the peak of the multifractal spectrum, Asymmetric index, Multifractal spectrum corrs. to max sing exp [8], multifractal spectrum corrs. to min sing exp [8], Vertical distance between  $f(\text{amin})$ -  $f(\text{amax})$  [8], Skewness of Multifractal spectrum, Kurtosis of Multifractal spectrum, the width of Multifractal spectrum, the height of Multifractal spectrum. Accordingly, a total of 60 MDFA features were obtained, 15 from the EEG signal, 15 from the left-eye-EOG signal, 15 from the differential EOG signal, and 15 from the EMG signal.

In summary, during the feature extraction process, features were extracted in 4 groups: time, frequency, nonlinear, and MDFA. 28 time, 28 frequency, 52 nonlinear, and 60 MDFA features were extracted from EEG, EOG, and EMG signals (See Table 2).

*Table 2. Summary of the extracted features*

	EEG	Left-eye-EOG	Differential EOG	EMG	Total
Time Features	7	7	7	7	28
Frequency Features	14	6	6	2	28
Nonlinear Features	13	13	13	13	52
MDFA Features	15	15	15	15	60

### 2.3. Feature Selection

As in other fields, the feature selection stage is as valuable as the feature extraction stage in biomedical classification problems. Studies using feature selection methods among sleep staging studies were examined in detail and it was concluded that these feature selection methods would be appropriate to use and compare in the study: Canonical Correlation Analysis (CCA) [35], 2016), Sequential Feature Selection (SFS) [43]. Feature selection with Fisher Score (FS) [34], Feature selection with chi-square test, ReliefF [45], Feature selection with Information Gain (IG) method [4], Feature selection with fast correlation-based filter method (FCBF) [31].

5 feature selection applications were conducted in the study. 4 of them were conducted to determine the best features in each feature sub-set (time-, frequency-, nonlinear- and MDFA-subsets) and the last one was done to determine the best-performing features among the whole feature set with 168 features. For each application, combinations of all the above-mentioned feature selection methods and all classification methods were run within the application. For example, in the 1st application done with the time-domain features, the number of features selected by the CCA feature selection method was made 2,3,4,5, ... 27,28. Afterward, the same process was carried out by choosing SFS as the feature selection method. In this way, with each feature selection method, features are selected in all possible number of features and all classifiers are run for these feature combinations. Other applications (applications 2-4) with frequency properties, nonlinear properties, and MDFA properties were carried out in the same way. In application-2 made with frequency features, the number of features was from 2 to 28; In application-3 with nonlinear features, the number of features was from 2 to 52; In application-4 made with MDFA features, the number of features was changed from 2 to 60.

## 2.4. Classification

To compare the performances of the selected features, 4 different classification method was utilized. They are:

- K-nearest neighbor method-kNN [15]
- Support vector machines- SVM [46]
- Decision trees-DT [39]
- Bagged tree classifier-BT [9]

They have commonly used classifiers in automatic sleep staging literature. The following criteria were used while evaluating the classification performances [28]:

$$Accuracy = \frac{TP+TN}{TP+TN+FP+FN} \quad (1)$$

$$Sensitivity = \frac{TP}{TP+FN} \quad (2)$$

$$Specificity = \frac{TN}{TN+FP} \quad (3)$$

$$Precision = \frac{TP}{TP+FP} \quad (4)$$

$$F1 - score = \frac{2TP}{2TP+FP+FN} \quad (5)$$

Where TP: true positive, TN: true negative, FP: false positive, FN: false negative.

These criteria were calculated separately for each stage using the complexity matrix obtained as a result of the classification, as well as the average values of all stages were calculated.

## 3. RESULTS

### 3.1. Results of Application-1 for Time Domain Features

In the feature selection application conducted with time features, the number of features was changed from 2 to 28 for each of the 7 feature selection methods, and classification was made with 4 different classifiers. In Figure 1, for the CCA feature selection method, the test classification accuracies of the classification methods concerning the number of features are seen. As can be seen, the highest classification accuracy was obtained with the Bagged tree classifier at 64.9% for 13 features.



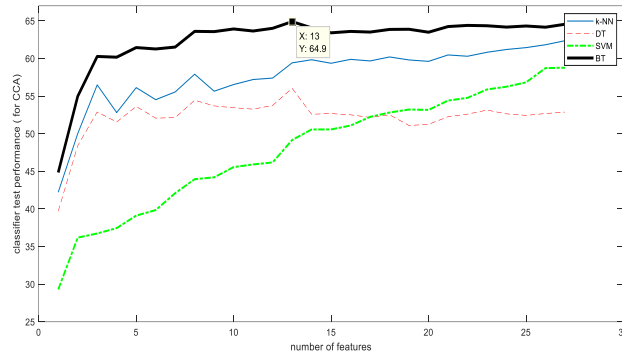


Figure 1. Comparison of classifiers’ test performances concerning the number of features for the CCA feature selection method (for frequency domain features).

When the same procedure was conducted for other feature selection methods, the best performances were obtained as given in Table 3.

Table 3. Comparison of feature selection methods for time domain features

Applied feature selection method	Best performed classifier	The optimum number of features	Highest test classification accuracy (%)
CCA	BT classifier	13	64.90
Chi-square	BT classifier	22	65.07
FS	BT classifier	24	64.89
FCBF	BT classifier	19	65.91
IG	BT classifier	18	65.57
<b>ReliefF</b>	BT classifier	<b>20</b>	<b>65.96</b>
SFS	BT classifier	25	65.02

When the results of Table 3 is analyzed, it was observed that the highest classification accuracy was obtained with ReliefF, although there was no significant difference between the feature selection methods. On the other hand, in all feature selection methods except the Canonical Correlation Method, the highest performances were obtained for the cases where the number of features was in the range of 18-25. Considering that only time features are used in practice, this can be interpreted as an expected result because the system needs as much information as possible to make an accurate classification.

When the performances of the classifiers are compared, kNN and BT classifiers have similar performance, while DT and SVM have relatively lower classification accuracies. When ranking in terms of performance in the classifications, it is striking that the classifiers are ranked from best to worst as BT, kNN, SVM, and DT, respectively. In addition, it was observed that while the DT performed better than SVM at low feature counts, SVM performance was better than the DT when the number of features increased.

### 3.2. Results of Application-2 for Frequency domain features

In this application, where only frequency features are used as in-time features, the number of features for each of the 7 feature selection methods is changed from 2 to 28 (because there are 28 frequency features), and classification with 4 different classifiers for each feature set. The change in test classification accuracy according to the feature number was recorded for each feature selection method and classifier.

This change is seen in Figure 2 for the ReliefF feature selection method. Again, as for the time domain features, the highest test classification accuracy was reached by the BT classifier as 61.99% with 11 features.

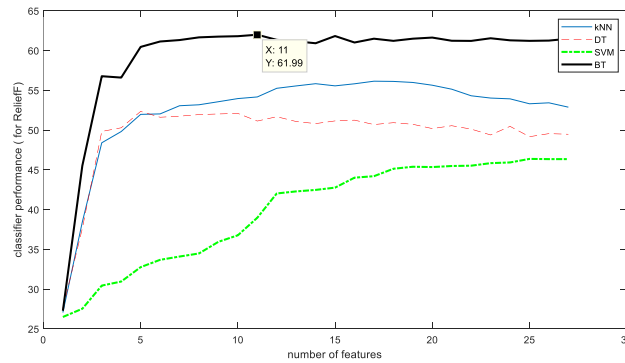


Figure 2. Comparison of classifiers’ test performances with regard to the number of features for the ReliefF feature selection method (for frequency domain features).

The highest accuracy values obtained by the feature selection methods are summarized in Table 4.

Table 4. Comparison of feature selection methods for frequency domain features

Applied feature selection method	Best performed classifier	The optimum number of features	Highest test classification accuracy (%)
CCA	BT classifier	27	61.06
Chi-square	BT classifier	27	61.53
FS	BT classifier	27	61.11
FCBF	BT classifier	25	61.38
IG	BT classifier	24	61.55
<b>ReliefF</b>	BT classifier	<b>11</b>	<b>61.99</b>
SFS	BT classifier	15	61.94

When the results given in Table 4 are examined, the highest accuracy was reached with the ReliefF method, as in the time properties. The highest performances have been obtained when almost all features are used in feature selection methods except ReliefF and SFS methods. The fact that the features extracted during the study were determined to be those that are thought to give the best results based on the literature has a great effect on this. When the classifier performances were compared, it was observed that the BT method obtained the best performance, as in the time properties, followed by the kNN, DT, and SVM methods, respectively.

### 3.3. Results of Application-3 for Nonlinear Features

In this application, as stated before, a total of 52 features, 13 from each signal, were obtained and classification processes were carried out with feature selection methods. Thus, the feature number was changed from 1 to 52 in the feature selection applications. The same procedure was performed and the best feature number, best feature selection method, and best classifier were tried to be found. The change in test classification accuracy for the Chi-square method with regard to the feature number is given in Figure 3.

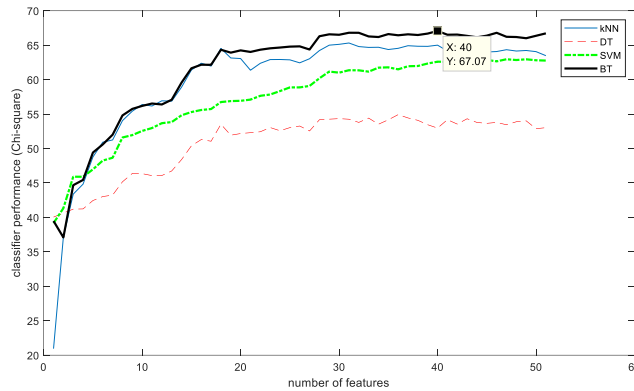


Figure 3. Comparison of classifiers’ test performances with regard to the number of features for the Chi-square feature selection method (for nonlinear features).

The highest accuracy values obtained by the feature selection methods are summarized in Table 5.

Table 5. Comparison of feature selection methods for nonlinear features

Applied feature selection method	Best performed classifier	The optimum number of features	Highest test classification accuracy (%)
CCA	BT classifier	36	66.88
Chi-square	BT classifier	40	67.07
FS	BT classifier	49	66.97
FCBF	BT classifier	50	66.49
IG	BT classifier	50	66.25
<b>ReliefF</b>	BT classifier	<b>24</b>	<b>67.92</b>
SFS	BT classifier	17	67.26

When the results in Table 5 are examined, the highest classification accuracy was again obtained with ReliefF as a feature selection method. As a classifier, the BT method showed a more successful performance than in the previous applications. 24 features were selected in the ReliefF method, where the highest accuracy was obtained, and 17 features were selected in the sequential feature selection method. The performance is the best when almost all of the features are used in the other feature selection methods.

### 3.4. Results of Application-4 for MDFA features

As a result of MDFA applied to EEG, EOG, and EMG signals, a total of 60 features, 15 from each signal, were obtained as stated before, and classification processes were carried out with feature selection methods. Again, as with the other applications the feature number was changed, and the performances of feature selection methods were compared with the use of four classifiers. The results obtained for FCBF are shown in Figure 4.

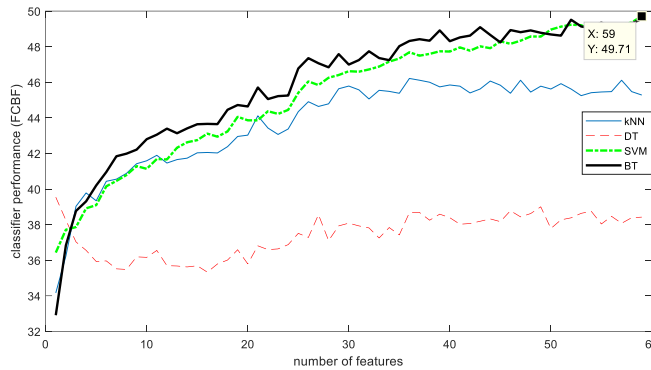


Figure 4. Comparison of classifiers’ test performances with regard to the number of features for the FCBF feature selection method (for MDFA features).

Here, as seen from the figure, the performance of BT and SVM classifiers is close to each other. This was the case for other feature selection methods, too. Meanwhile, the performance of DT was very poor for all feature selection methods. The best accuracies reached for each feature selection method can be seen in Table 6.

Table 6. Comparison of feature selection methods for MDFA features

Applied feature selection method	Best performed classifier	The optimum number of features	Highest test classification accuracy (%)
CCA	BT classifier	46	49.51
Chi-square	BT classifier	57	49.79
FS	SVM	54	49.77
FCBF	SVM	59	49.71
IG	BT classifier	59	49.52
<b>ReliefF</b>	BT classifier	<b>50</b>	<b>49.95</b>
SFS	BT classifier	58	49.59

When the results in Table 6 are examined, it is seen that MDFA features are not successful enough in this classification problem. It has been determined that the feature selection methods have obtained very close results (49. xx) and these results have been achieved with a very large number of features. On the other hand, what stands out for this feature set is the better performance of the SVM, unlike the situation with other feature sets.

### 3.5. Comparison of Results

In the above 4 applications, 5-fold cross-validation and validation processes were carried out for each number of features by applying 7 different feature selection methods and 4 different classifiers. The highest cross-validation results obtained for each application are summarized in Table 7.

*Table 7. Comparison of application results*

	Feature set	Best feature selector	Best classifier	Total number of features	Number of selected features	Highest accuracy (%) - test in CV	Highest accuracy (%) - validation
Application-1	Time	RelieFF	BT	28	20	65.96	64.94
Application-2	Frequency	RelieFF	BT	28	11	61.99	62.36
Application-3	Nonlinear	RelieFF	BT	52	24	<b>67.92</b>	<b>66.66</b>
Application-4	MDFA	RelieFF	BT	60	50	49.95	50.14

When Table 7 is examined, it has been observed that the best feature selection method in all applications is RelieFF, although there are no high differences between the feature selection methods. On the other hand, it has been determined that the best classification method is the BT classifier. When the number of selected features is evaluated, it is observed that most of the extracted features are used in applications where time and MDFA features are used. In time features, this can be attributed to the use of necessary features in the study based on literature and past studies. Considering the low accuracies obtained for MDFA, it can be concluded that MDFA features alone are insufficient in classification. On the other hand, a remarkable feature reduction was made in frequency and nonlinear features. 11 of 28 frequency features were selected in frequency domain analysis and 24 of 52 nonlinear features were selected in application-3 in which nonlinear features were used. This gives the impression that some (nearly half) of the frequency and nonlinear features used are unnecessary. If an evaluation is made between the feature sets, the highest accuracy was achieved with nonlinear features (67.92%), followed by time (65.96%), frequency (61.99%), and MDFA (49.95%), respectively.

When the obtained results were examined, it was observed that there were no high differences between the cross-validation results and the validation results. For example, Table 8 shows the cross-validation and validation results obtained with the Bagged tree method for the case where the RelieFF method is used in Application-3 (nonlinear properties). In Figure 5, the variation of cross-validation and validation accuracies according to the number of features is visualized for the situation in question. This situation was seen similarly for all other application results.

In Table 9, the complexity matrix obtained in cross-validation is given for the case where the highest classification accuracy is obtained. Almost similar results were obtained in other applications. Accordingly, while high accuracy was achieved in the classification of Non-REM 3 and REM stages, lower success was observed in the classification of Wake, Non-REM 1, and Non-REM 2 stages. When the previous studies are examined, the classification performances of the Wake and Non-REM 1 stages are generally poor. However, performances in the Non-REM 2 stage are generally higher. The reason for the low performance of the Non-REM 2 stage in this study can be interpreted as the low number of data used to create a balanced data set compared to other studies. In future studies, solutions will be explored at this point.

Table 8. CV and Validation results of Application-3 (nonlinear features) for ReliefF feature selector and BT classifier.

Number of features	CV results					Validation results				
	Accuracy	Sensitivity	Specificity	Precision	F1-score	Accuracy	Sensitivity	Specificity	Precision	F1-score
2	0.5159	0.5159	0.8790	0.5113	0.5133	0.5106	0.5106	0.8777	0.5060	0.5080
3	0.5567	0.5567	0.8892	0.5505	0.5529	0.5410	0.5410	0.8853	0.5344	0.5369
4	0.6140	0.6140	0.9035	0.6087	0.6107	0.5932	0.5932	0.8983	0.5884	0.5899
5	0.6299	0.6299	0.9075	0.6247	0.6267	0.6218	0.6218	0.9055	0.6176	0.6192
6	0.6267	0.6267	0.9067	0.6207	0.6229	0.6262	0.6262	0.9066	0.6231	0.6233
7	0.6399	0.6399	0.9100	0.6341	0.6363	0.6312	0.6312	0.9078	0.6251	0.6269
8	0.6580	0.6580	0.9145	0.6522	0.6545	0.6518	0.6518	0.9130	0.6471	0.6487
9	0.6529	0.6529	0.9132	0.6476	0.6497	0.6514	0.6514	0.9129	0.6460	0.6479
10	0.6550	0.6550	0.9138	0.6500	0.6520	0.6546	0.6546	0.9137	0.6512	0.6523
11	0.6619	0.6619	0.9155	0.6582	0.6597	0.6516	0.6516	0.9129	0.6492	0.6502
12	0.6568	0.6568	0.9142	0.6523	0.6541	0.6502	0.6502	0.9126	0.6465	0.6479
13	0.6588	0.6588	0.9147	0.6544	0.6561	0.6552	0.6552	0.9138	0.6503	0.6523
14	0.6581	0.6581	0.9145	0.6532	0.6551	0.6524	0.6524	0.9131	0.6494	0.6506
15	0.6627	0.6627	0.9157	0.6575	0.6595	0.6564	0.6564	0.9141	0.6543	0.6550
16	0.6755	0.6755	0.9189	0.6696	0.6717	0.6678	0.6678	0.9170	0.6631	0.6648
17	0.6685	0.6685	0.9171	0.6628	0.6649	0.6658	0.6658	0.9165	0.6598	0.6621
18	0.6703	0.6703	0.9176	0.6649	0.6670	0.6658	0.6658	0.9165	0.6606	0.6625
19	0.6733	0.6733	0.9183	0.6681	0.6702	0.6606	0.6606	0.9152	0.6563	0.6580
20	0.6713	0.6713	0.9178	0.6649	0.6675	0.6694	0.6694	0.9174	0.6631	0.6654
21	0.6765	0.6765	0.9191	0.6710	0.6732	0.6746	0.6746	0.9187	0.6704	0.6721
22	0.6759	0.6759	0.9190	0.6704	0.6726	0.6676	0.6676	0.9169	0.6636	0.6651
23	0.6704	0.6704	0.9176	0.6647	0.6670	0.6740	0.6740	0.9185	0.6701	0.6717
24	0.6717	0.6717	0.9179	0.6650	0.6676	0.6646	0.6646	0.9162	0.6581	0.6604
25	0.6792	0.6792	0.9198	0.6731	0.6754	0.6666	0.6666	0.9167	0.6608	0.6630
26	0.6716	0.6716	0.9179	0.6658	0.6681	0.6750	0.6750	0.9188	0.6703	0.6721
27	0.6751	0.6751	0.9188	0.6689	0.6713	0.6688	0.6688	0.9172	0.6632	0.6651
28	0.6715	0.6715	0.9179	0.6647	0.6672	0.6688	0.6688	0.9172	0.6641	0.6659
29	0.6737	0.6737	0.9184	0.6676	0.6700	0.6682	0.6682	0.9171	0.6631	0.6649
30	0.6771	0.6771	0.9193	0.6706	0.6730	0.6714	0.6714	0.9179	0.6654	0.6677
31	0.6681	0.6681	0.9170	0.6616	0.6641	0.6678	0.6678	0.9170	0.6616	0.6640
32	0.6709	0.6709	0.9177	0.6655	0.6676	0.6726	0.6726	0.9182	0.6678	0.6696
33	0.6766	0.6766	0.9192	0.6707	0.6730	0.6630	0.6630	0.9158	0.6566	0.6587
34	0.6780	0.6780	0.9195	0.6715	0.6740	0.6652	0.6652	0.9163	0.6607	0.6621
35	0.6701	0.6701	0.9175	0.6637	0.6662	0.6704	0.6704	0.9176	0.6665	0.6679
36	0.6687	0.6687	0.9172	0.6622	0.6647	0.6716	0.6716	0.9179	0.6661	0.6683
37	0.6760	0.6760	0.9190	0.6696	0.6722	0.6678	0.6678	0.9170	0.6630	0.6648
38	0.6727	0.6727	0.9182	0.6660	0.6686	0.6674	0.6674	0.9169	0.6614	0.6637
39	0.6739	0.6739	0.9185	0.6680	0.6703	0.6606	0.6606	0.9152	0.6566	0.6580
40	0.6729	0.6729	0.9182	0.6671	0.6694	0.6638	0.6638	0.9160	0.6584	0.6605
41	0.6723	0.6723	0.9181	0.6660	0.6685	0.6670	0.6670	0.9168	0.6620	0.6638
42	0.6748	0.6748	0.9187	0.6684	0.6709	0.6656	0.6656	0.9164	0.6594	0.6619
43	0.6769	0.6769	0.9192	0.6701	0.6726	0.6718	0.6718	0.9180	0.6666	0.6686
44	0.6696	0.6696	0.9174	0.6633	0.6657	0.6640	0.6640	0.9160	0.6586	0.6607
45	0.6717	0.6717	0.9179	0.6653	0.6677	0.6628	0.6628	0.9157	0.6564	0.6588
46	0.6666	0.6666	0.9167	0.6598	0.6624	0.6648	0.6648	0.9162	0.6597	0.6618
47	0.6718	0.6718	0.9180	0.6649	0.6674	0.6658	0.6658	0.9165	0.6596	0.6620
48	0.6715	0.6715	0.9179	0.6649	0.6674	0.6668	0.6668	0.9167	0.6606	0.6628
49	0.6727	0.6727	0.9182	0.6655	0.6681	0.6694	0.6694	0.9174	0.6629	0.6653
50	0.6738	0.6738	0.9185	0.6671	0.6696	0.6626	0.6626	0.9157	0.6574	0.6596
51	0.6673	0.6673	0.9168	0.6601	0.6629	0.6662	0.6662	0.9166	0.6597	0.6622
52	0.6673	0.6673	0.9168	0.6602	0.6629	0.6678	0.6678	0.9170	0.6627	0.6646

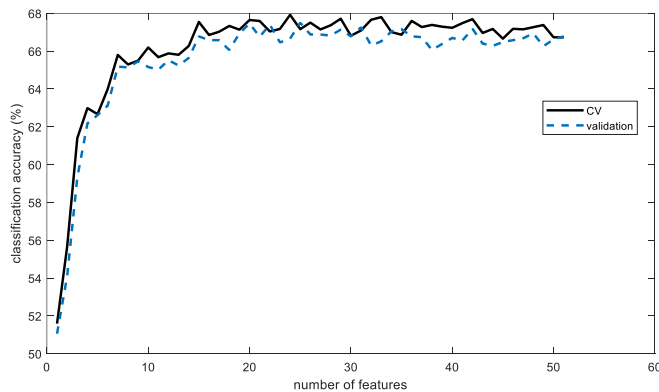


Figure 5. The variation of cross-validation and validation accuracies according to the number of features.

**Table 9.** Complexity matrix of CV results where the highest accuracy was reached (67.92%)

Predicted class \ Real class	Wake	Non- REM 1	Non- REM 2	Non- REM 3	REM	Total	accuracy
	Wake	1872	625	303	76	124	3000
Non- REM 1	641	1565	430	98	266	3000	0.5216
Non- REM 2	324	472	1552	317	335	3000	0.5173
Non- REM 3	49	61	218	2630	42	3000	0.8766
REM	101	190	209	45	2455	3000	0.8183

### 3.6. Results of Application-5 for the Whole Features

In the applications made with the feature sets described above, the performance of the individual feature sets was observed and compared. In this application, in which all features are used, only the ReliefF method (because ReliefF gives the highest result in all applications) was changed from 2 to 168 and the classification results were obtained with the Bag Tree method (bag tree method shows the best performance). Accordingly, while the highest accuracy in cross-validation was 66.21% for 157 features, 66.44% classification accuracy was achieved for 84 features in validation. On the other hand, when the number of features is increased up to approximately 40, classification accuracy increases significantly, while increasing the number of features after 40 does not cause a significant increase in classification performance. Therefore, it can be interpreted that the first 40 features provide sufficient information for the classification process. These features are listed as follows (by selection order):

1. Kolmogorov complexity of EOG-diff signal (nonlinear)
2. Higuchi fractal dimension of EOG-left signal (nonlinear)
3. Fuzzy Entropy of EEG signal (nonlinear)
4. Kolmogorov complexity of EEG signal (nonlinear)
5. Lampel-Ziv complexity of EEG signal (nonlinear)
6. Hjorth mobility of EOG-diff signal (nonlinear)
7. Correlation dimension of EEG signal (nonlinear)
8. MMD-Maximum Minimum Distance of EEG signal (time)
9. Lyapunov exponent of EEG signal (nonlinear)
10. Sample entropy of EOG-diff signal (nonlinear)
11. Total energy of EEG signal (time)
12. Approximate entropy of EEG signal (nonlinear)
13. Hurst Exponent of EEG signal (nonlinear)
14. Asymmetric index of EEG signal (MDFA)
15. Renys' entropy of EOG-left signal (nonlinear)
16. Asymmetric index of EOG-diff signal (MDFA)
17. ZCR of EMG signal (time)
18. Sample entropy of EEG signal (nonlinear)
19. Total energy of EOG-left signal (time)
20. Lampel-Ziv complexity of EOG-left signal (nonlinear)
21. Higuchi Fractal Dimension of EOG-left signal (nonlinear)
22. Asymmetric index of EOG-left signal (MDFA)

23. Hjorth complexity of EMG signal (nonlinear)
24. Correlation dimension of EOG-diff signal (nonlinear)
25. Mean value of time domain EEG signal (time)
26. The difference of 0.5-2 Hz between the current and previous epoch in the EOG-diff signal (frequency)
27. Hjorth mobility of EMG signal (nonlinear)
28. Permutation entropy of EMG signal (nonlinear)
29. Fuzzy entropy of EOG-left signal (nonlinear)
30. Permutation entropy of EEG signal (nonlinear)
31. Mean value of time domain EOG-left signal (time)
32. Kolmogorov complexity of EOG-left signal (nonlinear)
33. Mean value of time domain EOG-diff signal (time)
34. Renys' entropy of EEG signal (nonlinear)
35. MMD-Maximum Minimum Distance of EOG-left signal (time)
36. Multifractal spectrum corr. to max sing exp [16] of EEG signal (MDFA)
37. MMD-Maximum Minimum Distance of EOG-diff signal (time)
38. Hjorth mobility of EEG signal (nonlinear)
39. Approximate entropy of EOG-diff signal (nonlinear)
40. Renys' entropy of EOG-diff signal (nonlinear)

As can be seen, the majority of these features are nonlinear features (26 nonlinear features). Then time (9 features), MDFA (4 features), and frequency (1 feature) features are seen. As can be understood from this, it has been observed that the effect of nonlinear features on the classification performance is quite high. On the other hand, when evaluated based on the signals used, it is seen that 16 features are used for EEG, 20 features are from EOG (12 for difference EOG and 8 for left-eye EOG), and 4 features for EMG. Again, it can be interpreted that EOG and EEG signals are more decisive.

When the obtained results were examined, it should be noted that the obtained accuracies are not high enough. The use of real noisy data is the major reason for this. Besides we recorded the data mostly from the patients. Also, we used balanced data in classifications to increase the accuracy of all stages and when the studies in literature conducted with balanced data are examined, it can be seen that the accuracies are not very high as the unbalanced ones. In the study [5], done with real data, the authors have reached a classification accuracy of 76.30% in their 19-subject data.

#### 4. CONCLUSIONS

For the search for an effective automatic sleep staging system that can be used in real data, we conducted a comparative sleep staging study in which feature types, feature selection methods, and classifiers were compared. PSG data (EEG, EOG, and EMG signals) were obtained from a total of 124 people, 31 of whom were healthy and 93 patients. By using the epochs obtained from this dataset, 28 time-domain, 28 frequency-domain, 52 nonlinear, and 60 MDFA features were extracted. For selecting appropriate features; CCA, SFS, Fisher Score, Chi-square, ReliefF, IG, and FCBF feature selection methods were used. 5 feature selection applications were conducted in the study. 4 of them were conducted to determine the best features in each feature sub-set (time-, frequency-, nonlinear- and MDFA-subsets) and the last one was done to determine the best-performing features among the whole feature set with 168 features. Also, k-NN, SVM, DT, and BT classifiers were used for the classification of stages. For each application, combinations of all the above-mentioned feature selection methods and classification methods were run within the application. ReliefF feature selection method and BT classifier have given the best performance in all applications. In the first application in which Time domain features were used, 20 features reached the highest accuracy as 67.92%. When frequency features were used, the maximum



accuracy was obtained as 61.99% with 11 features. In the case of nonlinear features, 24 features were selected over 52 features giving the highest accuracy of 67.92%. Lastly, MDFA features resulted in a poor accuracy level of 49.95% with the best 50 features. As seen from these results, nonlinear features give the best performance. This situation was seen in Application-5, too. In application-5 in which all of the 168 features were selected by ReliefF feature selector, 40 features were selected to give better performance. There are 26, 9, 4, and 1 feature from the nonlinear, time, MDFA, and frequency set respectively. The highest accuracy was reached as 66.21% in this application. The obtained performance is yet not sufficient to use practically in real life but after some further improvements, it will hopefully be possible to use automatic sleep scoring systems. Also maybe the other PSG recordings would be used by the other signals.

### Acknowledgement

This study is supported by the Scientific and Technological Research Council of Turkey (TUBITAK) with project number: 119E127.

### REFERENCES

- [1] Aboalayon, K.A.I., Faezipour, M., Almuhammadi, W.S. & Moslehpour, S., (2016), Sleep Stage Classification Using EEG Signal Analysis: A Comprehensive Survey and New Investigation, *Entropy*, 18, 272; doi:10.3390/e18090272.
- [2] Acharya, U.R., Bhat, S., Faust, O., Adeli, H., Chua, E.C., Lim, W.J., & Koh, J.E. (2015). Nonlinear Dynamics Measures for Automated EEG-Based Sleep Stage Detection. *European Neurology*, 74, 268 - 287.
- [3] Arslan, R. S., Ulutaş, H., Köksal, A.S., Bakır, M., Çiftçi, B. (2022), "Automated sleep scoring system using multi-channel data and machine learning", *Computers in Biology and Medicine* 146, 105653.
- [4] Azhagusundari, B., & Thanamani, A.S. (2013). Feature Selection based on Information Gain. *International Journal of Innovative Technology and Exploring Engineering (IJITEE)* ISSN: 2278-3075.
- [5] Balci, M., Tasdemir, S., Ozmen, G., Golcuk A., (2022), Machine Learning-Based Detection of Sleep-Disordered Breathing Type Using Time and Time-Frequency Features, *Biomedical Signal Processing and Control*, 73, 103402.
- [6] Barbi, M., Chillemi, S., Garbo, A. D., Balocchi, R., Carpeggiani, C., Emdin, M., Michelassi, C. & Santarcangelo, E., (1998), Predictability and nonlinearity of the heart rhythm, *Chaos, Solitons & Fractals*, 9 (3), 507-515.
- [7] Boostani, R., Karimzadeh, F., & Nami, M. (2017). A comparative review on sleep stage classification methods in patients and healthy individuals. *Computer methods and programs in biomedicine*, 140, 77-91.
- [8] Bose, R., Pratiher, S., & Chatterjee, S. (2019). Detection of epileptic seizure employing a novel set of features extracted from multifractal spectrum of electroencephalogram signals. *IET Signal Process.*, 13, 157-164.
- [9] Breiman, L. (2004). Bagging predictors. *Machine Learning*, 24, 123-140.
- [10] Chaozhen, G., Siyang, L., Fulan, L. & Weichao, X., (2015), Sleep EEG staging based on Hilbert-Huang transform and sample entropy, 2015 International Conference on Computational Intelligence and Communication Networks
- [11] Chattopadhyay, G. & Chattopadhyay, S., (2014), Study on statistical aspects of monthly sunspot number time series and its long-range correlation through detrended fluctuation analysis, *Indian Journal of Physics*, 88 (11), 1135-1140.
- [12] Chi-Square. Available online: <https://towardsdatascience.com/chi-square-test-for-feature-selection-in-machine-learning-206b1f0b8223>

- [13] Chlon, L., Song, A.H., Subramanian, S., Soulat, H., Tauber, C., Ba, D. & Prerau, M., Multitaper Spectral Estimation HDP-HMMs for EEG Sleep Inference, arXiv:1805.07300v1 [stat.ML] 18 May 2018, (last visited on 7 October 2021)
- [14] Di Matteo, T., Aste, T. & Dacorogna, M. M., (2003), Scaling behaviors in differently developed markets, *Physica A: Statistical Mechanics and its Applications*, 324 (1-2), 183-188.
- [15] Fix, E. & Hodges, J.L., (1951), An Important Contribution to Nonparametric Discriminant Analysis and Density Estimation, *International Statistical Review / Revue Internationale de Statistique* Vol. 57, No. 3 (Dec. 1989), pp. 233-238
- [16] Erdoğan, N. K., (2017), BİST100 Endeksinin Çokfraktallı Eğimden Arındırılmış Dalgalanma Analizi, *Journal of Current Researches on Business and Economics*, 7 (2), 555-564.
- [17] Farag, A.F., El-Metwally, S.M., & Morsy, A.A. (2014). A Sleep Scoring System Using EEG Combined Spectral and Detrended Fluctuation Analysis Features. *Journal of Biomedical Science and Engineering*, 07, 584-592.
- [18] Faust, O., Razaghi, H., Barika, R., Ciaccio, E. J., & Acharya, U. R. (2019). A review of automated sleep stage scoring based on physiological signals for the new millennia. *Computer methods and programs in biomedicine*, 176, 81–91. <https://doi.org/10.1016/j.cmpb.2019.04.032>
- [19] Fiorillo, L., Puiatti, A., Papandrea, M., Ratti, P. L., Favaro, P., Roth, C., Bargiotas, P., Bassetti, C. L., & Faraci, F. D. (2019). Automated sleep scoring: A review of the latest approaches. *Sleep medicine reviews*, 48, 101204. <https://doi.org/10.1016/j.smr.2019.07.007>
- [20] Ghimatgar H., Kazemi K., Helfroush M. S., Aarabi A. (2019) "An automatic single-channel EEG-based sleep stage scoring method based on hidden Markov Model", *Journal of Neuroscience Methods*, 324, 1082320
- [21] Göğüş, F. Z., 2020, Osas Hastaları için CPAP Cihazlarındaki Optimum Basıncın Yapay Zeka ile Tahmini, PhD thesis, Konya-Türkiye
- [22] Hassan, A. R., & Bhuiyan, M.I.H., (2016a). A decision support system for automatic sleep staging from EEG signals using tunable Q-factor wavelet transform and spectral features. *Journal of neuroscience methods*, 271, 107–118. <https://doi.org/10.1016/j.jneumeth.2016.07.012>
- [23] Hassan, A.R., & Bhuiyan, M.I.H., (2016b), Automatic sleep scoring using statistical features in the EMD domain and ensemble methods, *Biocybernetics and Biomedical Engineering* 36, 248-255
- [24] Hassan, A.R., & Subasi, A. (2016). Automatic identification of epileptic seizures from EEG signals using linear programming boosting. *Computer methods and programs in biomedicine*, 136, 65-77.
- [25] Hassan, A.R., & Bhuiyan, M.I.H., (2017), An automated method for sleep staging from EEG signals using normal inverse Gaussian parameters and adaptive boosting, *Neurocomputing* 219, 76–87
- [26] Huang, W., Guo, B., Shen, Y., Tang, X., Zhang, T., Li, D., & Jiang, Z. (2020). Sleep staging algorithm based on multichannel data adding and multifeature screening. *Computer methods and programs in biomedicine*, 187, 105253.
- [27] Iber, C., Ancoli-Israel, S., Chesson, A. L., Quan, S. L., (2007), *The AASM Manual for the Scoring of Sleep and Associated Events: Rules, Terminology and Technical Specifications*, American Academy of Sleep Medicine, Westchester.
- [28] Japkowicz, N., Shah, M., (2014), *Evaluating Learning Algorithms: A Classification Perspective*, Cambridge University Press.
- [29] Jiang, D., LU, Y., Ma, Y. & Wang, Y., (2019), Robust sleep stage classification with single-channel EEG signals using multimodal decomposition and HMM-based refinement, *Expert Systems With Applications* 121, 188–203
- [30] Kantelhardt, J. W., Zschiegner, S. A., Koscielny-Bunde, E., Havlin, S., Bunde, A. & Stanley, H. E., (2002), Multifractal detrended fluctuation analysis of nonstationary time series, *Physica A: Statistical Mechanics and its Applications*, 316, 87-114.

- [31] Khourdifi, Y., & Bahaj, M. (2018). Feature Selection with Fast Correlation-Based Filter for Breast Cancer Prediction and Classification Using Machine Learning Algorithms. 2018 International Symposium on Advanced Electrical and Communication Technologies (ISAECT), 1-6.
- [32] Korkailen, H., Leppanen, T., Duce, B., Kainulainen, S., et. al. (2021), "Detailed Assessment of Sleep Architecture With Deep Learning and Shorter Epoch-to-Epoch Duration Reveals Sleep Fragmentation of Patients With Obstructive Sleep Apnea", *IEEE Journals of Niomedical and Health Informatics*, 25(7)
- [33] Lee, J. M., Kim, D. J., Kim, I. Y., Suk Park, K., & Kim, S. I. (2004). Nonlinear analysis of human sleep EEG using detrended fluctuation analysis. *Medical Engineering & Physics*, 26(9), 773-776. <https://doi.org/10.1016/j.medengphy.2004.07.002>
- [34] Li, C., & Xu, J. (2019). Feature selection with the Fisher score followed by the Maximal Clique Centrality algorithm can accurately identify the hub genes of hepatocellular carcinoma. *Scientific reports*, 9(1), 17283. <https://doi.org/10.1038/s41598-019-53471-0>
- [35] Liu, L., Wang, Q., Adeli, E., Zhang, L., Zhang, H., & Shen, D. (2016). Feature Selection Based on Iterative Canonical Correlation Analysis for Automatic Diagnosis of Parkinson's Disease. *Medical image computing and computer-assisted intervention: MICCAI ... International Conference on Medical Image Computing and Computer-Assisted Intervention*, 9901, 1-8. [https://doi.org/10.1007/978-3-319-46723-8\\_1](https://doi.org/10.1007/978-3-319-46723-8_1)
- [36] Liu, Z., & Sun, J. (2015). Sleep Staging from the EEG Signal Using Multifractal Detrended Fluctuation Analysis. 2015 Fifth International Conference on Instrumentation and Measurement, Computer, Communication and Control (IMCCC), 63-68.
- [37] Liua, Z., Suna, J., Zhanga, Y. & Rolfea, P., (2016), Sleep staging from the EEG signal using multi-domain feature extraction, *Biomedical Signal Processing and Control* 30, 86-97
- [38] Márton, L. F., Brassai, S. T., Bakó, L. & Losoncz, L., (2014), Detrended Fluctuation Analysis of EEG Signals, *Procedia Technology*, 12, 125-132.
- [39] Myles, A.J., Feudale, R.N., Liu, Y., Woody, N., & Brown, S.D. (2004). An introduction to decision tree modeling. *Journal of Chemometrics*, 18.
- [40] Otis M. Solomon, Jr, PSD Computations Using Welch's Method, SANDIA REPORT, S A N D 91-1533 • U C -7 0 6, Unlimited Release, Printed December 1991, USA
- [41] Peker, M. (2016). An efficient sleep scoring system based on EEG signal using complex-valued machine learning algorithms. *Neurocomputing*, 207, 165-177.
- [42] Peng, C., Havlin, S., Stanley, H.E., & Goldberger, A.L. (1995). Quantification of scaling exponents and crossover phenomena in nonstationary heartbeat time series. *Chaos*, 5 1, 82-7.
- [43] Rückstieß, Thomas., Osendorfer, Christian., & van der Smagt, Patrick. (2011). Sequential Feature Selection for Classification. 10.1007/978-3-642-25832-9\_14.
- [44] Tian, P., Hua, J., Qi, J., Ye, X., Che, D., Ding, Y. & Peng, Y., (2017), A hierarchical classification method for automatic sleep scoring using multiscale entropy features and proportion information of sleep architecture, *Biocybernetics and Biomedical Engineering* 37, 263-271
- [45] Urbanowicz, R.J., Meeker, M., Cava, W.L., Olson, R.S., & Moore, J. (2018). Relief-Based Feature Selection: Introduction and Review. *Journal of biomedical informatics*, 85, 189-203.
- [46] Vapnik, V. N., (2000), *The Nature of Statistical Learning Theory.*, New York: Springer
- [47] Vaquerizo-Villar, F., Alvarez, D., Kheirandish-Goza, L., Gutiérrez-Tobal, G. C., Barroso-García, V., Crespo, A., Campo, F. d., Gozal, D. & Hornero, R., (2018), Detrended fluctuation analysis of the oximetry signal to assist in pediatric sleep apnoea-hypopnoea syndrome diagnosis, *Physiological Measurement*, 39 (11).
- [48] Zero Crossing Rate[online], <https://www.sciencedirect.com/topics/engineering/zero-crossing-rate>
- [49] Zhang, Y., Wang, B., Jing, J., Zhang, J., Zou, J., & Nakamura, M. (2017). A Comparison Study on Multidomain EEG Features for Sleep Stage Classification. *Computational Intelligence and Neuroscience*, 2017.

- [50] Zhang, Z. & Guan, C., (2017), An Accurate Sleep Staging System with Novel Feature Generation and Auto-Mapping, IEEE International Conference on Orange Technologies (ICOT)



## OPTIMAL LOCATION OF ACTION POTENTIAL GENERATION BASED ON ACTIVATION FUNCTION USING COMPUTATIONAL MODELLING

<sup>1,2,\*</sup>Enver SALKIM 

<sup>1</sup>Mus Alparslan University, Department of Electronics and Automation, Mus, TÜRKİYE

<sup>2</sup>University College London (UCL), Department of Electronics and Electrical Engineering, London, UK

<sup>1</sup>[e.salkim@alparslan.edu.tr](mailto:e.salkim@alparslan.edu.tr), <sup>2</sup>[e.salkim@ucl.ac.uk](mailto:e.salkim@ucl.ac.uk)

### *Highlights*

- Transcutaneous electrical nerve stimulation (TENS)
- Activation function (AF)
- Finite element simulation (FEM)
- Bio-computational modeling simulation
- Nerve action potential generation
- Extracellular electrical potential



## OPTIMAL LOCATION OF ACTION POTENTIAL GENERATION BASED ON ACTIVATION FUNCTION USING COMPUTATIONAL MODELLING

<sup>1,2,\*</sup>Enver SALKIM 

<sup>1</sup>Mus Alparslan University, Department of Electronics and Automation, Mus, TÜRKİYE

<sup>2</sup>University College London (UCL), Department of Electronics and Electrical Engineering, London, UK

<sup>1</sup>e.salkim@alparslan.edu.tr, <sup>2</sup>e.salkim@ucl.ac.uk

(Received: 20.01.2023; Accepted in Revised Form: 05.07.2023)

**ABSTRACT:** Transcutaneous electrical nerve stimulation is used to elevate health-related disorders. This technology is now an important therapeutic system for medical science. In this system, the electrical current pulse is applied over the skin through the inner layers via electrodes to activate excitable tissue layers. Activating other excitable tissue layers may cause discomfort. Thus, it is vital to design electrode configuration arrangements to activate the target anatomical layers without affecting the neighboring ones. A device for primary headaches showed mixed results. This may be related to the electrode position that requires higher stimulus current levels to activate target nerve fibers. This may stimulate neighboring nerve fibers which resulted in the discomfort of patients. A feasible solution is to identify the optimal electrode configuration based on the activation function which is the second derivative of the electric potential along an axon. This may guide to estimate of the possibility of action potential generation on the neural tissue layer using a specified electrode arrangement. In this study, the multilayered human head was developed based on MRI data set using pre and post-processing. Then multi-electrode arrangements were developed to examine the possible nerve activation location. Results showed that the nerve fibers were activated at the same location of the trajectory for the anodal and cathodal stimulation. This may be proof that the activation function can be used to define the optimal location of nerve activation. This may lead to lower thresholds for similar therapeutic benefits in transcutaneous electrical nerve stimulation with decreased power consumption.

**Keywords:** Action Potential, Activation Function, Extracellular Potential, Finite Element Simulation

### 1. INTRODUCTION

Transcutaneous electrical nerve stimulation (TENS) is a non-invasive therapy method. This alternative procedure is widely preferred for its non-invasiveness, ease of use, reusability, and reconfigurability [1]–[3]. By using the TENS method, the action potential is achieved by applying stimulus current levels to the excitable neural tissue layers over the skin using electrode arrangements [4], [5]. It is desired to activate target excitable tissue without activating other neural tissue in the vicinity. However, it may not be possible to achieve optimal stimulation as always. There are many factors that may affect the outcome. i) it may not be possible to control the transcutaneous delivery of charges which may lead to activating the excitable tissue nearby apart from the target neural tissue, ii) the relatively higher current levels may activate the neighboring excitable tissue which results in discomfort, iii) it has been shown that sensory nerve fibers may require lower current levels than motor nerve fibers. This may activate superficial pain nerve fibers which are not desired [1], [6], [7]. Consequently, it is required to apply a higher stimulus current when targeting deeper excitable tissue layers. This will, in turn, result in a large volume of the electrical potential distributions within the volume conductor. Also, using higher current levels may result in higher current density which may cause inflammations and skin burns [8], [9]. A neuromodulator for primary headaches showed mixed results. It has been shown that most users complain about discomfort, pain, and inflammation [10], [11]. This may be related to the higher stimulus current levels that are applied through the electrodes which may be caused to activate the pain sensory nerve fibers of neighboring neural elements. A feasible solution to reduce the required current levels by re-defining the location of the

\*Corresponding Author: Enver SALKIM, [e.salkim@ucl.ac.uk](mailto:e.salkim@ucl.ac.uk), [e.salkim@alparslan.edu.tr](mailto:e.salkim@alparslan.edu.tr)

stimulation electrodes for optimal stimulation strategy. It has been shown that the activation function (AF) can be used to determine the possible place of the neural action potential generating based on given neuromodulator settings. This may lead to lower thresholds for similar therapeutic benefits in transcutaneous electrical nerve stimulation with decreased power consumption using appropriate simulation settings. It is not possible to analyze the location of the action potential generation using experimental methods due to possible risks. Computational modeling methods can be an appropriate alternative, and it has been used for many designing and optimization neuromodulators to analyze the impact of electrical stimulation on neural elements [4], [12], [13]. In this alternative method, the neural response to electrical stimulation is calculated using a finite element model (FEM). These computational FEM models are constructed based on a volume conductor model representing various anatomical structures and the electrodes by their respective electrical parameters (conductivity, dielectric permittivity) and appropriate boundary conditions. It has been shown that the possible location of the action potential generation can be predicted using AF for different neuroanatomical targets using such computational methods [14], [15]. Also, studies have shown that AF can be used for different simulation methods (e.g., magnetic simulation) [16] and invasive neuromodulation techniques including deep brain stimulation [17]. In this procedure, the electrical potential distributions were calculated then the response of the neural elements was calculated based on the second derivative of electrical potential using electrode settings.

In this study, the human head volume conductor based on various tissue layers was generated using FEM and TENS-based strategy to investigate the possible nerve activation location on the forehead. The human head's fundamental anatomical layers including skin, muscle, skull, and brain were constructed based on an adult magnetic resonance image (MRI) data set. The pre-process was applied to the MRI data set to identify tissue layers' grayscale and their boundary in MATLAB v.R2019 (MathWorks, Inc., Natick, MA, USA) as shown in Fig. 1 and 3. Then, each tissue layer was imported to COMSOL Multiphysics (COMSOL, Ltd, Cambridge, UK) to generate the complete human head model. The anatomical variation of the nerve was obtained from [18], [19] and the nerve model was generated based on Supraorbital (SON) and Supratrochlear (STN) nerve branches of the frontal nerve. The models were merged with the human head in COMSOL accordingly. The electrode configuration was generated in COMSOL and merged with the head model volume conductor to calculate AF using appropriate current settings as shown in Fig. 3. The electrical potential was simulated for a given electrode configuration with incremental steps on the forehead. The AF was calculated for both anodic and cathodic stimulation to define the optimal nerve fiber activation on the forehead.

## 2. MATERIAL AND METHODS

### 2.1 MRI Data Processing

The pre-process was applied to the MRI data set to generate a computational efficiency human head model. The multi-tissue layers and their relative coordinate points were derived from the MRI data set of the human head. This data set was obtained from [20] which is called MIDA. The MIDA model is a multimodal imaging-based detailed anatomical computer model of the human head and neck. The overall model includes 350 sagittal, 480 coronal, and 480 transverse planes of MRI slices. It is available in different voxel data formats (.nii, .mat, .raw) and the model spatial resolution (0.5 mm isotropic). The transverse MRI data and (.nii) voxel data format was performed in this study. To visualize and process the data, *NIFTI* (Neuroimaging Informatics Technology Initiative) and *ANALYZE* image tools were applied according to the required setting. It was noted that *load\_nii* and *view\_nii* functions were applied based on their library settings to visualize the MRI data set in three-dimensional (3D) in MATLAB. These functions were activated individually for each visualization and processing step. Different transverse human head slices were visualized in MATLAB as shown in Fig. 1. It was shown that the data constructed many slices and different ranges of gray-scale values. Thus, it is required to do image pre-processing to generate a computationally efficient model.

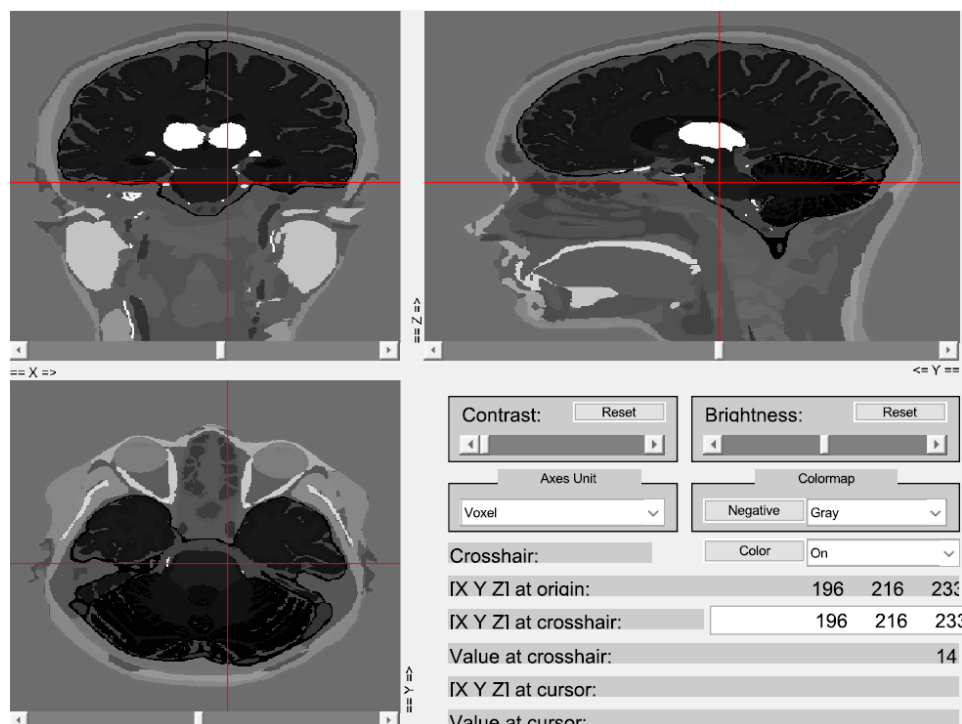


**Figure 1.** Visualization of the 3D MRI data set using required functions in MATLAB. It is shown that the data includes many slices and a large scale of the gray scale.

## 2.2 Volume Conductor Development

The pre-processing was applied to the MRI data set to generate an efficient and accurate human-head computational model. The 3D human head model was constructed from 30 transverse two-dimensional (2D) MRI image slices with minimum spacing, which was 5 mm, whilst maximum spacing was 12.5 mm. Each tissue layer's coordinate points were manually selected on the same MRI image to define contours. Then, the arc-length vector of the contours was defined with different amounts of denser points for each tissue layer in MATLAB. These denser points were interpolated with *Piecewise Cubic Hermite Interpolating Polynomial* (PCHIP) function to have more smooth contours in MATLAB.

The work plane (z coordinate) was defined for each smooth contour slice, according to image slice spacing in COMSOL Multiphysics. The related contour denser points were imported into COMSOL Multiphysics as an interpolation solid curve. To generate volume from two different work planes, the *loft function* in Design Module in COMSOL software was applied. To have a better meshed solid object, columns face partitioning was adjusted to apply *loft function* properly to the overall of the 30 transverse slices. The lofted profiles should be adjusted as a union after generating an individual tissue in 3D volume because the union function provides the user to control tissue (which could have intersections with each other) and add this tissue's electrical features manually to obtain simulation results. These steps are summarized in Fig. 2.



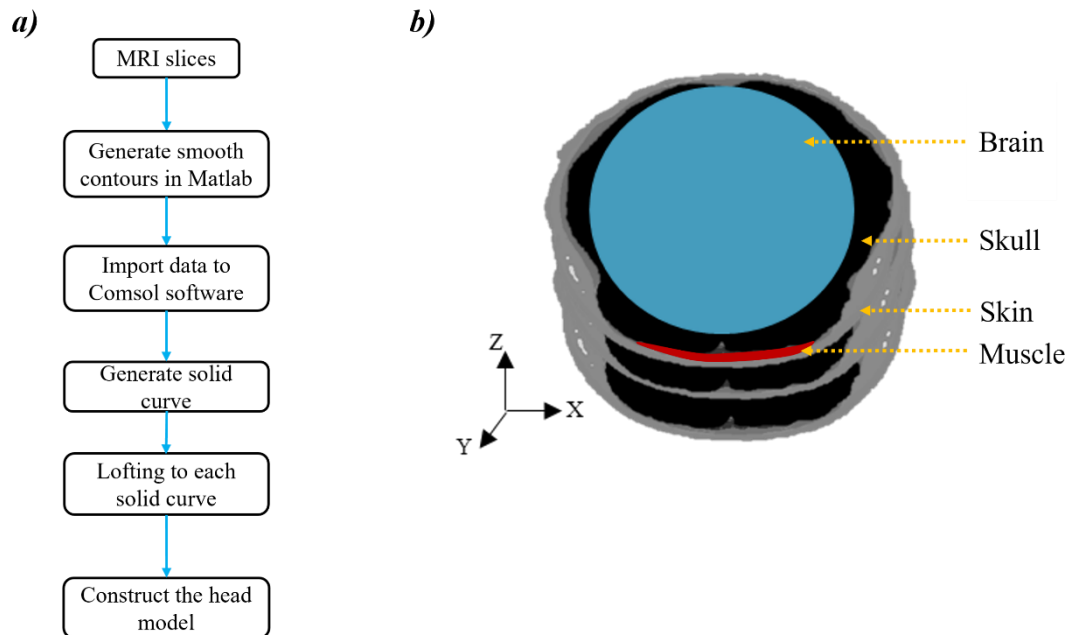


**Figure 2.** (a) Shows the process steps of generating the 3D CAD human head model. The smooth contours were generated using image processing filters then these were exported to COMSOL to generate 3D models. (b) shows the visualization of the smooth MRI data set. The image data was processed to generate the fundamental tissue layers including the brain, skull, muscle, and skin.

The current study volume model was composed of six tissue layers. These are, in turn, electrode patches, skin, nerve, muscle, skull, and the rest of the volume was assumed as a brain. These layers are represented in Fig. 2. The skin layer is built from 30 MRI slices, muscle volume was generated based on 10 slices, the skull was constructed from 27 slices, and the brain was assumed to be an ellipsoid shape due to simplicity. The supraorbital and supratrochlear nerves' trajectory cannot be distinguished from the MRI images because of having small diameters (which foramen of mentioned nerves are smaller than 1 mm, hence is assumed to be 1 mm in this study). Thus, these nerve volume models were extracted from the University College London library database which is called *ANATOMY.TV* (powered by primal pictures) and based on available anatomical data [18], [21].

### 2.3 Electrode Model

A gel patch was designed to cover the forehead due to the lower conductivity of the skin. The height of the gel patch was designed to be 35 mm and the length is 50 mm whilst the thickness was 1 mm (half of the patch thickness is pushed in the forehead skin layer to encourage appropriate simulation). An electrode matrix (8 × 4) was generated based on the forehead as shown in Fig. 3. The electrodes were spaced 10 mm vertically and 7 mm horizontally as shown in Fig. 3(c). It is not possible to decide which electrode arrangement results in better performance. Thus, all possible electrode configuration results were investigated by following the procedure. On the vertical axis for the first row, the first electrode was used as an *anode*, then the second one was used *cathode*. Then, the *anode* recording simulation position was kept constant, which is electrode 1 (E1) and the *cathode* electrode position was shifted at the horizontal axis until the E8 as detailed in matrix A and Fig. 3(c). The same procedure was applied to all rows. Then, E1 was defined *anode* and E9 was defined *cathode* then the *cathode* was shifted on the vertical axis. The same method was applied to all columns in the matrix A and Fig. 3(c). This resulted in 67 different electrode simulation configurations.

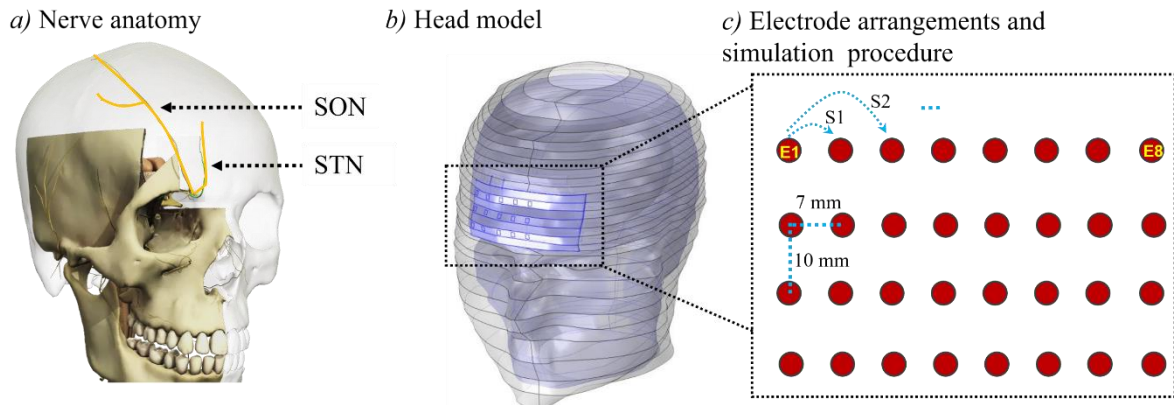


**Figure 3.** (a) Shows the anatomy of target nerve branches which are STN and SON, (b) Shows the 3D volume conductor of the human head that was generated in COMSOL. (c) Shows a schematic representation of electrode arrangements over the forehead of the human. The model was discretized and simulated to calculate electrical potential distribution within each domain. S1 represents simulation 1.

$$A = \begin{bmatrix} E1 & \dots & E8 \\ \vdots & \ddots & \vdots \\ E17 & \dots & E24 \end{bmatrix}$$

The electrodes are defined as equipotential surfaces where the electric current was conducted to the volume conductor of the human head model. In the current study, rectangular series of electrodes were placed on the patch. Each of the electrodes was designed to be in contact with the skin layer. In the COMSOL, *Terminal 1* was adjusted as an anode, and the current level of 1 mA was assigned in all cases. While *Terminal 2* was adjusted as cathode and -1 mA current level was applied. The air domain is set to ground (these cases are applied in all bipolar electrode configurations). The voltage simulation results are recorded for both STN and SON nerve fibers. This process was applied for 67 different bipolar electrode configurations for each nerve trajectory to estimate the optimal nerve activation location.

## 2.4 Finite Element Simulation

After generating a realistic volume of the human head model, the FEM process was performed to compute electric potential distributions along the neural tissue layer and the layers in the vicinity as shown in Fig.3. This electrical voltage distribution was generated by injecting current through electrode configuration. A sphere with a large diameter was defined around the model and the *Dirichlet boundary condition* ( $V = 0$ ) was applied to the external boundaries of the sphere to obtain an accurate solution. This approximates ground condition at infinity. Additionally, external current density and the current source were set to zero everywhere in the model and the domains were discretized with *tetrahedral finite elements* to divide the model into small geometrical shapes. Whilst skin, muscle, electrode patch, and nerves finely meshed; brain, skull, and air layers were coarser meshed. This resulted in approximately 6.2 million elements (about 7.7 million degrees of freedom). After adjusting the optimum sphere radius and optimum meshing quality, the simulation results were obtained by means of quasi-static approximation of Maxwell Equations in COMSOL that can be expressed through Laplace formulation, as shown in (1).

$$\nabla \cdot ([\sigma] \nabla V) = 0 \quad (1)$$

where  $\sigma$  is the conductivity of each of the tissue layers;  $V$  is the electrical potential in representing geometry. The electrical potential distributions within the volume conductor were calculated by applying the dielectric parameter of the associated layers. These tissues' dielectric properties are depicted in Table 1. To highlight, the sphere (air) domain conductivity was set to  $(1e-10)$  S/m, whilst gel conductivity, gel

relative permittivity, and air relative permittivity are all set to 1 to obtain a unique solution in COMSOL. It is noted that the tissue dielectric parameters were suited based on low frequency (10 Hz).

**Table 1.** Tissue conductivity.

Tissue layers	Conductivity [S/m]	Reference
Skin	2.00e-4	[25]
Nerve	1.71e-2	[26]
Muscle	2.02e-1	[27]
Skull	2.00e-2	[28]
Brain	4.75e-2	[25]
Gel	1	
Air	1e-10	

After adjusting the conductivity of different domains in the model, the radius of the external sphere was changed from 40 cm to 300 cm in steps and the resulting simulation of the electric potential along the trajectory of the nerve was recorded. These results were simulated and indicated only a shift in the electrical potential along the nerve fiber. There was less than a 3 % variation in voltage results across the nerve for an external sphere radius between 60 cm to 300 cm. Thus, the external sphere radius was set at 60 cm for the rest of the study due to low computational time.

## 2.5 Nerve Model

Myelinated fiber diameter was obtained from [22] as 12  $\mu\text{m}$  with a standard deviation of 2  $\mu\text{m}$  in MATLAB to generate fiber diameter distribution. The node of Ranvier was randomly placed between 0 and  $\Delta x$  (node-to-node distance for the mentioned nerve diameter) along the arc length of the said nerve. The geometric parameters of passive compartments were generated by linear interpolation based on fiber diameter. These passive compartments were placed in sequence along the arc length of nerve and fiber completed by a node. These processes were iterated 100 times for approximately 3.6 cm nerve trajectory. The electrical potential along the nerve was calculated in COMSOL for each electrode configuration. This step was repeated for each nerve potential distribution.

## 2.6 Activation Function (AF)

The AF is a powerful tool used to obtain a view along the given nerve with possible positions of depolarization and hyperpolarization. More precisely, Rattay et al. [23] have introduced the AF as a second spatial derivative of the extracellular voltage which is shown in (2). This simplistic calculation provides to predict action potential generation. The voltage which was generated in COMSOL referred to as extracellular voltage was applied in MATLAB to generate the AF.

$$AF = \frac{\Delta^2 V_e}{\Delta l^2} = \frac{V_e(n-1) - 2V_e(n) + V_e(n+1)}{\Delta x^2} \quad (2)$$

$V_{e(n)}$  = extracellular potential on the nth node of the myelinated fiber

$l$  = arc-length of the nerve

$\Delta x$  = node to node distance

AF distributions were generated in MATLAB for 100 axons randomly placed along both STN and SON nerve trajectories with the normal distribution of fibre diameter for all the possible bipolar electrode configurations. The extracellular voltage that was generated in FEM is multiplied by -1 to get AF distribution for reverse electrode configuration. The same process was repeated for all nerve trajectories.

### 3. RESULTS

#### 3.1 Electrical Potential Variation

The electrical potential distributions across the different nerve fibers of STN and SON based on different electrode arrangements for different polarities of the current are shown in Fig. 4, and Fig. 5, respectively. Since the AF is the main finding of this study, the electrical potential distribution across the nerve fiber for the electrode configuration is shown for two samples.

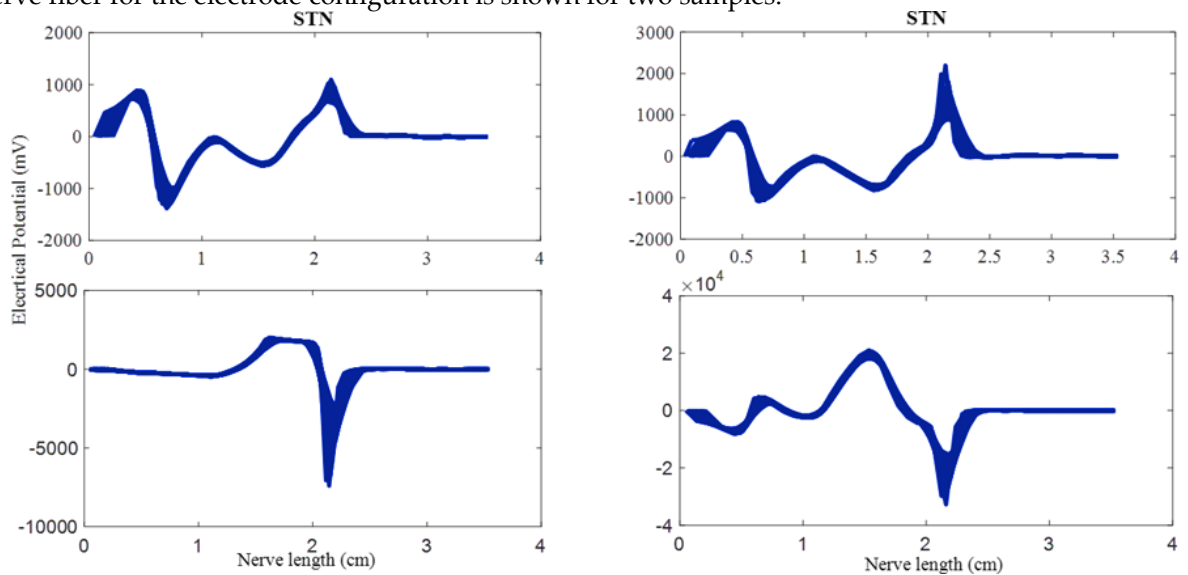


**Figure 4.** Electrical potential distributions across the STN nerve fibers for different electrode arrangements using both positive and negative values of the same current levels.

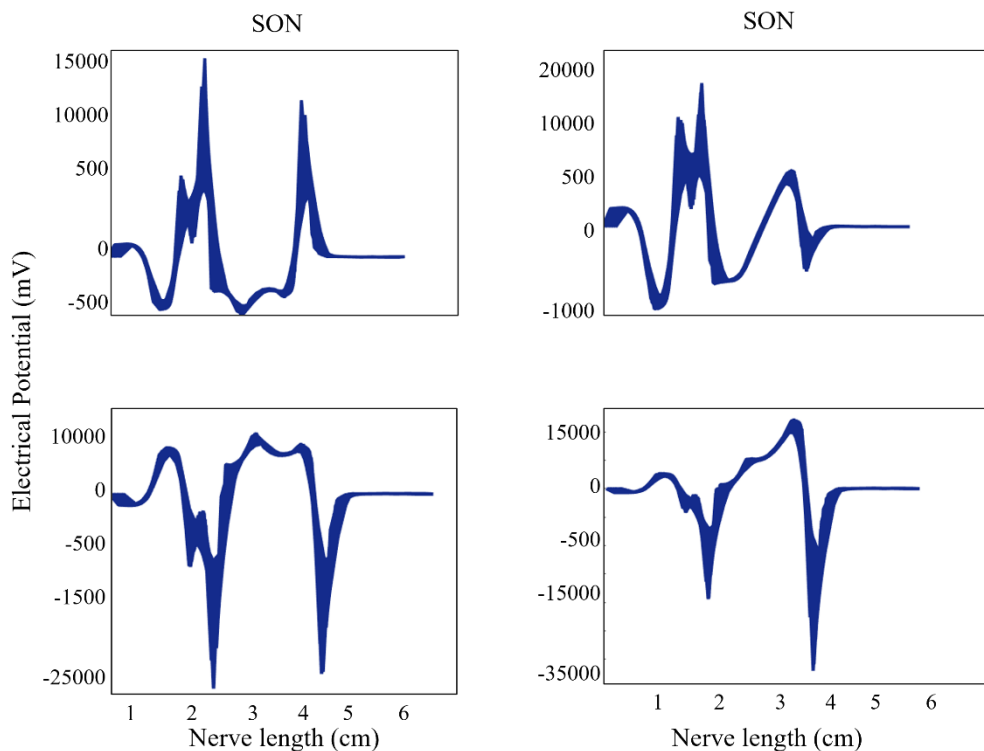


**Figure 5.** Electrical potential distributions across the SON nerve fibers for different electrode arrangements using both positive and negative values of the same current levels.

It is clearly shown that the extracellular potential distributions along the nerve fibers are various for the given electrode settings. The anodic and cathodic stimulation shows different electrical potential variations based on given neuromodulator settings. The recorded electrical potential range for the anodic stimulation is about -2 V to 3 V. This range is about -40 V to 40 V for cathodic stimulation. It is noted that the sharp variation in the electric potential variations is recorded approximately at the same location of the nerve fibers for the STN and SON nerves based on both anodic and cathodic stimulations. Although the electrical potential variation for the nerve fibers varies, this is not a significant variation ( $\approx 1$  mV) to affect the outcome of the action potential generation position as all nerve fibers show the same electrical potential trend versus the arc length is similar.

### 3.2. Action Potential Based on AF

The AF variation versus the nerve length for both STN and SON nerve branches is shown in Fig. 5. The AF variation for both cathodic and anodic stimulation of SON and STN nerve fibers are shown in Fig. 6(a), and (b), respectively. The AP results for different nerve fibers are highlighted.

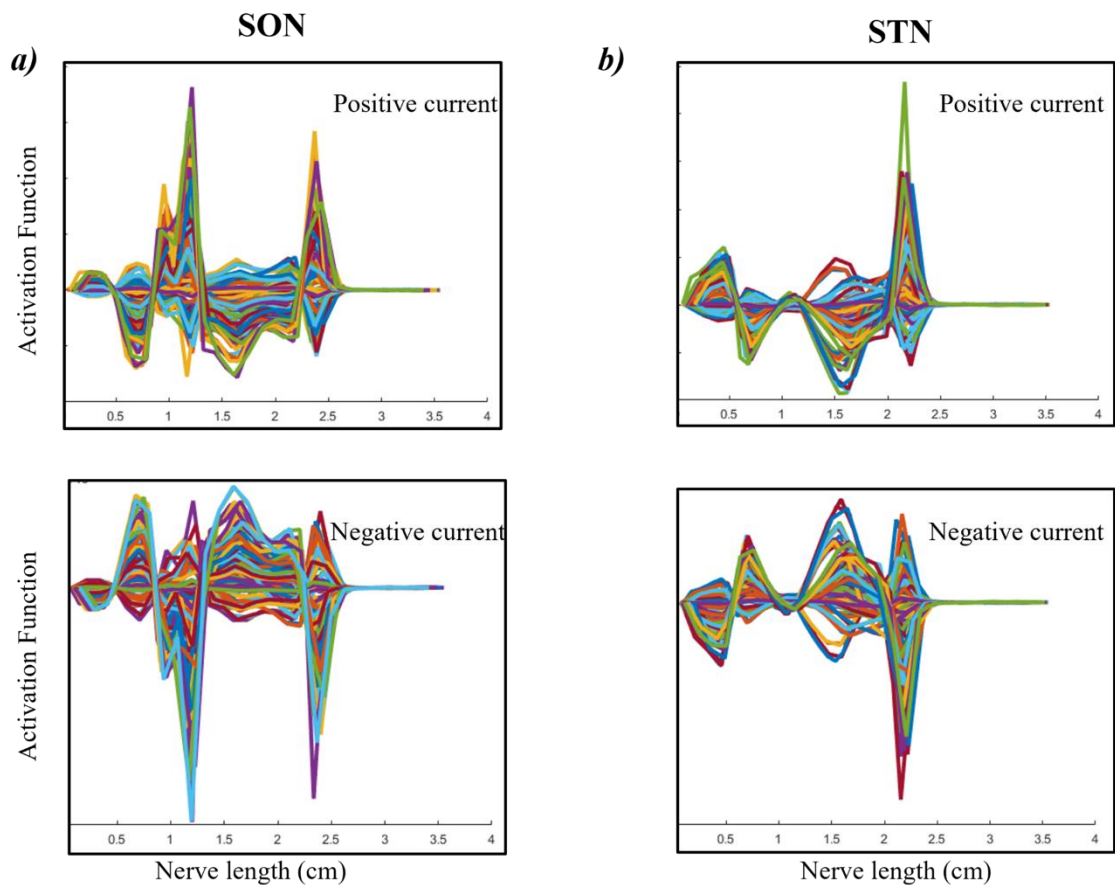


**Figure 6.** (a) Shows AF versus nerve length for SON nerve fibers based on different current polarities. (b) Shows AF versus nerve length for STN nerve fibers based on different current polarities.

It is shown that the maximum positive and maximum negative values of the AF are nearly observed at the same place of the nerve length for both SON and STN nerves. The SON may be activated at the places along the nerve trajectory as there are two sudden changes in the AF. For STN, the nerve fibres can be activated only in a region of the nerve trajectory. When the AF is positive, that means the nerve can be activated. As can be seen from Fig. 4, Fig. 5, and Fig. 6, the AF varies for STN and SON nerves. The possibility of generating AP along the STN nerve is around 2.3 cm. Whilst, the depolarization possibility of the SON nerve can occur at two different places along the nerve (about 1.2 cm and 2.5 cm). It is noted

that although the electrical potential variation across the nerve fibers showed various patterns, the possible place of the action potential generation is the same for both SON and STN nerves.

#### 4. DISCUSSION

TENS neuromodulation has a wide variety of applications in basic research, medical treatments, and the design of neuronal prostheses. The research of neural responses to electrical stimuli is focused on both invasive and non-invasive experiments. It may not be possible to investigate the exact location of the neural tissue activation due to the complexity of the experiments. Thus, the computational methods are used as an alternative which has a significant role in the interpretation of the experimental results, the prediction of the outcome of adapted experiments, and the translation of the experimental findings into possible technical strategies for treatments. The neural response to the electrical potential can be calculated using a multi-compartment model composed of the fundamental tissue layers by stimulating electrode arrangements [4], [5], [16], [17], [24]. In this study, an accurate multi-layered human head was developed based on MRI data to define the optimal location of the nerve fiber activation based on AF using such models. The volume conductor was simulated, and the results were recorded.

The electrical potential for STN based on different current and electrode arrangements was shown in Fig. 4. It was shown that although the electrical potential was significantly varied, the peak location of the electrical potential was about the same. This was valid for both anodic and cathodic stimulations. This may show the vicinity of functioning neurons. Thus, the generating action potentials can be triggered in the proximity of that region [16]. It was noted that the anodic stimulation showed at least two peak variations in the electrical potential for both electrode arrangement samples. This variation was only observed for a sample of cathodic stimulation. This can be associated with nerve fibers with cell bodies in proximity. These nerve fibers can be activated on lower thresholds using anodic stimulation [16].

The results in Fig. 6 suggested that the nerve fibers can be activated at the different locations of the nerve arc length for some samples. However, it was clear that AF was observed at a certain arc length of the nerve fibers ( $\approx 2.3$  cm) for all samples. Thus, the results of this study suggested that the nerve fibers can be activated at this location of nerve fibers-based AF.

Also, it was suggested that it may not be possible to generate action potential along the nerve fibers, although the electrical potential variation was relatively higher. The magnitude of the electrical potential variation was higher for the second sample of the anodic stimulation as shown in Fig. 4. The nerve fibers were activated at two locations along the nerve fibers as shown in Fig. 6.

Although an accurate and multi-layered human head model was developed and appropriate boundary conditions were applied to generate possible activation locations, the study was constructed based on low frequency. Since the dielectric properties of the anatomical tissue vary, this may influence the outcome.

#### 5. CONCLUSIONS

FEM modeling is commonly applied in many branches of biomedical engineering and basic research in neurosciences for both invasive and non-invasive applications. Thus, a multi-layered human head was generated based on accurate FEM-based computational models to investigate the possible and feasible location of the nerve fibers activation based on electrode configuration using dielectric properties of the anatomical tissue layers. The AF was used to predict the possible location of the action potential generation of the nerve fibers using such computational methods. The results showed that action potential can be generated at the location of the nerve trajectory that showed a sudden change in the extracellular electrical potential. Also, it was suggested that the electrode proximity to the neural tissue may influence the outcome. It was noted that the magnitude of the extracellular electrical potential was not always proportional to AF.

## REFERENCES

- [1] N. Ravichandran, M. Y. Teo, K. Aw, and A. McDaid, "Design of Transcutaneous Stimulation Electrodes for Wearable Neuroprostheses," *IEEE Transactions on Neural Systems and Rehabilitation Engineering*, vol. 28, no. 7, pp. 1651–1660, Jul. 2020, doi: 10.1109/TNSRE.2020.2994900.
- [2] B. A. Karamian *et al.*, "The role of electrical stimulation for rehabilitation and regeneration after spinal cord injury," *Journal of Orthopaedics and Traumatology*, vol. 23, no. 1. Springer Science and Business Media Deutschland GmbH, Dec. 01, 2022. doi: 10.1186/s10195-021-00623-6.
- [3] A. Gupta, N. Vardalakis, and F. B. Wagner, "Neuroprosthetics: from sensorimotor to cognitive disorders," *Communications biology*, vol. 6, no. 1. NLM (Medline), p. 14, Dec. 01, 2023. doi: 10.1038/s42003-022-04390-w.
- [4] E. Salkim, A. Shiraz, and A. Demosthenous, "Impact of neuroanatomical variations and electrode orientation on stimulus current in a device for migraine: A computational study," *J Neural Eng*, vol. 17, no. 1, 2020, doi: 10.1088/1741-2552/ab3d94.
- [5] E. Salkim, A. Shiraz, and A. Demosthenous, "Influence of cellular structures of skin on fiber activation thresholds and computation cost In fl uence of cellular structures of skin on fi ber activation thresholds and computation cost," *Biomed Phys Eng Express*, vol. 5, no. 1, p. 015015, 2018.
- [6] S. Joucla, A. Glière, and B. Yvert, "Current approaches to model extracellular electrical neural microstimulation," *Front Comput Neurosci*, vol. 8, no. February, pp. 1–12, 2014, doi: 10.3389/fncom.2014.00013.
- [7] S. F. Cogan, "Neural Stimulation and Recording Electrodes," *Annu Rev Biomed Eng*, vol. 10, no. 1, pp. 275–309, 2008, doi: 10.1146/annurev.bioeng.10.061807.160518.
- [8] A. Kuhn, T. Keller, M. Lawrence, and M. Morari, "The influence of electrode size on selectivity and comfort in transcutaneous electrical stimulation of the forearm," *IEEE Transactions on Neural Systems and Rehabilitation Engineering*, vol. 18, no. 3, pp. 255–262, Jun. 2010, doi: 10.1109/TNSRE.2009.2039807.
- [9] A. Patriciu, K. Yoshida, J. J. Struijk, T. P. DeMonte, M. L. G. Joy, and H. Stødkilde-Jørgensen, "Current density imaging and electrically induced skin burns under surface electrodes," *IEEE Trans Biomed Eng*, vol. 52, no. 12, pp. 2024–2031, Dec. 2005, doi: 10.1109/TBME.2005.857677.
- [10] D. Magis, S. Sava, T. S. d'Elia, R. Baschi, and J. Schoenen, "Safety and patients' satisfaction of transcutaneous supraorbital neurostimulation (tSNS) with the Cefaly® device in headache treatment: a survey of 2,313 headache sufferers in the general population.," *J Headache Pain*, vol. 14, p. 95, 2013, doi: 10.1186/1129-2377-14-95.
- [11] J. Schoenen *et al.*, "Migraine prevention with a supraorbital transcutaneous stimulator: A randomized controlled trial," *Neurology*, vol. 80, no. 8, pp. 697–704, 2013, doi: 10.1212/WNL.0b013e3182825055.
- [12] E. Salkim, "Electrode Array Position Guiding in Cochlea Based on Impedance Variation : Computational Study," *Muş Alparslan Üniversitesi Mühendislik Mimarlık Fakültesi Dergisi*, vol. 1, no. 1, pp. 64–71, 2020.
- [13] A. Fellner, A. Heshmat, P. Werginz, and F. Rattay, "A finite element method framework to model extracellular neural stimulation," *J Neural Eng*, vol. 19, no. 2, Apr. 2022, doi: 10.1088/1741-2552/ac6060.
- [14] F. Rattay, S. M. Danner, U. S. Hofstoetter, and K. Minassian, "Finite Element Modeling for Extracellular Stimulation," in *Encyclopedia of Computational Neuroscience*, Springer New York, 2014, pp. 1–12. doi: 10.1007/978-1-4614-7320-6\_593-5.
- [15] S. Joucla and B. Yvert, "Modeling extracellular electrical neural stimulation: From basic understanding to MEA-based applications," *Journal of Physiology-Paris*, vol. 106, no. 3–4, pp. 146–158, 2012, doi: 10.1016/j.jphysparis.2011.10.003.

- [16] H. Ye, "Finding the Location of Axonal Activation by a Miniature Magnetic Coil," *Front Comput Neurosci*, vol. 16, Jun. 2022, doi: 10.3389/fncom.2022.932615.
- [17] D. N. Anderson, G. Duffley, J. Vorwerk, A. D. Dorval, and C. R. Butson, "Anodic stimulation misunderstood: Preferential activation of fiber orientations with anodic waveforms in deep brain stimulation," *J Neural Eng*, vol. 16, no. 1, Feb. 2019, doi: 10.1088/1741-2552/aae590.
- [18] K. N. Christensen, N. Lachman, W. Pawlina, and C. L. Baum, "Cutaneous Depth of the Supraorbital Nerve," *Dermatologic Surgery*, vol. 40, no. 12, pp. 1342–1348, 2014, doi: 10.1097/DSS.000000000000174.
- [19] Y.-C. Gil, K.-J. Shin, S.-H. Lee, W.-C. Song, K.-S. Koh, and H. J. Shin, "Topography of the supraorbital nerve with reference to the lacrimal caruncle: danger zone for direct browplasty," *British Journal of Ophthalmology*, vol. 101, no. 7, pp. 940–945, 2017, doi: 10.1136/bjophthalmol-2016-309332.
- [20] "OVERVIEW » IT'IS Foundation." <https://itis.swiss/virtual-population/regional-human-models/overview/> (accessed Jan. 20, 2023).
- [21] A. K. D. Harold Ellis, Bari M Logan, *Human Sectional Anatomy*, Third Edit. London: Hodder Arnold, 2009.
- [22] M. Z. Siemionow, "The Face as a Sensory Organ," in *The Know-How of Face Transplantation*, M. Siemionow, Ed., Springer, 2011, pp. 207–212. doi: 10.1007/978-0-85729-253-7.
- [23] F. Rattay, "Analysis of models for extracellular fiber stimulation.pdf," *IEEE Trans. Biomed. Eng.*, vol. 36, no. 7, pp. 676–682, 1989.
- [24] A. Fellner, A. Heshmat, P. Werginz, and F. Rattay, "A finite element method framework to model extracellular neural stimulation," *J Neural Eng*, vol. 19, no. 2, Apr. 2022, doi: 10.1088/1741-2552/ac6060.
- [25] "Low Frequency (Conductivity) » IT'IS Foundation." <https://itis.swiss/virtual-population/tissue-properties/database/low-frequency-conductivity/> (accessed May 20, 2019).
- [26] E. Salkim, "Optimisation of a Wearable Neuromodulator for Migraine Using Computational Methods."
- [27] E. Salkim, "Analysis of tissue electrical properties on bio-impedance variation of upper limbs", doi: 10.3906/elk-1300-0632.3908.
- [28] T. F. Oostendorp, J. Delbeke, and D. F. Stegeman, "The conductivity of the human skull: Results of in vivo and in vitro measurements," *IEEE Trans Biomed Eng*, vol. 47, no. 11, pp. 1487–1492, Nov. 2000, doi: 10.1109/TBME.2000.880100.





## BELEDİYE OTOBÜSLERİNİN YHT İSTASYONU İÇİN İLÇE GÜZERGÂHLARININ ÇKKV İLE BELİRLENMESİ: KIRIKKALE İLİ ÖRNEĞİ

<sup>1</sup>Buse BAYRAM , <sup>2</sup>Mert KARA , <sup>3</sup>Rabia YUMUŞAK ,  
<sup>4</sup>Ahmet CÜREBAL , <sup>5,\*</sup>Tamer EREN 

<sup>1,5</sup>Kırıkkale Üniversitesi, Mühendislik-Mimarlık Fakültesi, Endüstri Mühendisliği Bölümü, Kırıkkale,  
TÜRKİYE

<sup>2</sup>İzmir Ekonomi Üniversitesi, Lisansüstü Eğitim Enstitüsü, Endüstri Mühendisliği Bölümü, İzmir, TÜRKİYE

<sup>3</sup>Kapadokya Üniversitesi, Kapadokya Meslek Yüksekokulu, Bilişim Güvenliği Teknolojisi Bölümü, Nevşehir,  
TÜRKİYE

<sup>4</sup>University of Hamburg, Institute of Information Systems, Hamburg, GERMANY

<sup>1</sup>busebayram9@gmail.com, <sup>2</sup>mert.k@std.izmir ekonomi.edu.tr, <sup>3</sup>rabia.yumusak@kapadokya.edu.tr,

<sup>4</sup>ahmet.curebal@uni-hamburg.de, <sup>5</sup>tamereren@gmail.com

### Önemli Katkılar (Highlights)

- Kırıkkale ilindeki tüm ilçe ve üniversite bağlantısının sağlanmasında ilk kapsamlı araştırma niteliği taşımaktadır.
- AHP, TOPSIS ve PROMETHEE yöntemleri kullanılarak model önerisi sunulmuştur.
- Sunulan model benzer güzergâh belirleme problemlerinden farklı olarak, problemin kapsadığı geniş alan ve değerlendirmeye aldığı veri miktarının büyüklüğü açısından literatüre önemli katkı sağlamaktadır.



## BELEDİYE OTOBÜSLERİNİN YHT İSTASYONU İÇİN İLÇE GÜZERGÂHLARININ ÇKKV İLE BELİRLENMESİ: KIRIKKALE İLİ ÖRNEĞİ

<sup>1</sup>Buse BAYRAM , <sup>2</sup>Mert KARA , <sup>3</sup>Rabia YUMUŞAK ,  
<sup>4</sup>Ahmet CÜREBAL , <sup>5,\*</sup>Tamer EREN 

<sup>1,5</sup>Kırıkkale Üniversitesi, Mühendislik-Mimarlık Fakültesi, Endüstri Mühendisliği Bölümü, Kırıkkale, TÜRKİYE

<sup>2</sup>İzmir Ekonomi Üniversitesi, Lisansüstü Eğitim Enstitüsü, Endüstri Mühendisliği Bölümü, İzmir, TÜRKİYE

<sup>3</sup>Kapadokya Üniversitesi, Kapadokya Meslek Yüksekokulu, Bilişim Güvenliği Teknolojisi Bölümü, Nevşehir, TÜRKİYE

<sup>4</sup>University of Hamburg, Institute of Information Systems, Hamburg, GERMANY

<sup>1</sup>buseebayram9@gmail.com, <sup>2</sup>mert.k@std.izmirekonomi.edu.tr, <sup>3</sup>rabia.yumusak@kapadokya.edu.tr,

<sup>4</sup>ahmet.curebal@uni-hamburg.de, <sup>5</sup>tamereren@gmail.com

(Geliş/Received: 15.06.2022; Kabul/Accepted in Revised Form: 13.07.2023)

**ÖZ:** Günümüzde artan nüfusla birlikte bireysel araç sayısı ve dolayısıyla trafik yoğunluğu da her geçen gün artmaktadır. Hem şehir içi hem de şehirlerarası trafik yoğunluğunu azaltmaya yönelik olarak çalışmalar yapılmakta olup, şehirleri daha hızlı ve ekonomik bir şekilde birbirlerine bağlayan yüksek hızlı tren (YHT) projesi bunlardan biridir. Kırıkkale ilinde YHT istasyonunun kurulacak olması, efektif ilçe bağlantıları yapılarak daha fazla insanın kolay bir şekilde YHT hizmetini kullanması trafik yoğunluğu sorununa büyük etki edecektir. Bu bağlamda belediye otobüslerinin YHT istasyonu için ilçe bağlantılarının sağlanmasında Çok Kriterli Karar Verme (ÇKKV) yöntemlerinden AHP (Analytic Hierarchy Process), TOPSIS (Technique for Order Preference by Similarity to An Ideal Solution) ve PROMETHEE (The Preference Ranking Organization Method for Enrichment Evaluation) entegre şekilde kullanılmıştır. Yöntem sonuçları karşılaştırıldığında Kırıkkale Üniversitesi – Osmangazi hattı için 2. güzergâhın seçildiği görülmekte olup, diğer ilçeler için de alternatif güzergâhların sıralamaları elde edilmiştir. Çalışma, Kırıkkale’de açılacak YHT durağı ile ilçelerin ve binlerce öğrencisi bulunan üniversitenin bağlantısını sağlamakta olduğundan, il bazında yapılmış en kapsamlı çalışma özelliğini taşımasının yanı sıra YHT için güzergâh belirleme çalışması olarak da literatüre önemli bir katkı sağlamaktadır.

**Anahtar Kelimeler:** Güzergâh Belirleme, ÇKKV, AHP, TOPSIS, PROMETHEE

### Determination of District Routes of Municipal Buses for YHT Station with MCDM: The Case of Kırıkkale Province

**ABSTRACT:** Today, with the increasing population, the number of individual vehicles and therefore traffic density is increasing day by day. Efforts are being made to reduce both urban and intercity traffic density, and the high-speed train (HSR) project, which connects cities faster and more economically, is one of them. The fact that the HSR station will be established in Kırıkkale province, and more people will easily use the HSR service by making effective district connections will have a great impact on the problem of traffic density. In this context, AHP (Analytic Hierarchy Process), TOPSIS (Technique for Order Preference by Similarity to An Ideal Solution) and PROMETHEE (The Preference Ranking Organization Method for Enrichment Evaluation), which are Multi-Criteria Decision-Making (MCDM) methods, were used in an integrated manner. Based on the findings, it is observed that the second route is the preferred choice for the Kırıkkale University-Osmangazi line, with the optimal routes for the other lines also being determined. Since the HSR station to be opened in Kırıkkale will connect the districts and the university

\*Corresponding Author: Tamer EREN, [tamereren@gmail.com](mailto:tamereren@gmail.com)

with thousands of students, the study is the most comprehensive study conducted on a provincial basis and makes an important contribution to the literature as a route determination study for HSR.

**Keywords:** *Route Selection, Multi Criteria Decision Making (MCDM), AHP, TOPSIS, PROMETHEE*

## 1. GİRİŞ (INTRODUCTION)

Nüfusun artışına bağlı olarak şehir merkezlerinde trafik yoğunluğu günden güne artmaktadır. Toplu taşıma sisteminin çeşitli iyileştirmeler ile birlikte teşvik edilmesi trafik sorunu çözümüne büyük katkı sağlayacaktır. Sorunun çözüme ulaştırılması, talebe cevap verilebilmesi aşamasında yapılacak yatırımlar büyük önem arz etmektedir. Türkiye’de şehirler arası ulaşımda seyahat süresinin azaltılması, hızlı, konforlu ve güvenli bir ulaşım imkânı oluşturulması ve aynı zamanda ulaşımdaki demiryolu payının artırılması amacı ile hızlı tren projeleri hayata geçirilmiştir [1]. İlk seferine 2009 yılında başlayan YHT, Ankara-İstanbul, Ankara-Eskişehir, Ankara-Konya ve Konya-İstanbul hatlarında hizmet vermeye devam etmektedir.

Yolculuk planının hızlı şekilde internet aracılığıyla yapılabilmesi, yolculara yapılan servis hizmetleri, güvenli ve hızlı ulaşım sunması gibi avantajlar YHT hizmetinin devamlılığında ve talebin artmasında büyük rol oynamaktadır. Artan bu talebe en etkili şekilde cevap verebilmek, memnuniyeti maksimum seviyede tutmak, toplu taşımanın teşvik edilmesi ve kullanımının sürdürülebilirliği açısından oldukça önemli olduğundan dolayı bu durum güzergâh belirleme problemini ortaya çıkarmaktadır. Güzergâh belirleme problemi şehir içi ve şehirler arası ulaşım açısından büyük önem arz etmektedir. Konforlu ve hızlı ulaşım yolcu memnuniyetinin sağlanması açısından önemli etmenlerdir. Talepler doğrultusunda darboğaz alanlar öncelikli olarak değerlendirilerek, en iyi güzergâhın belirlenmesi önem arz etmektedir [2]. Bu çalışmada Kırıkkale’de açılacak YHT istasyonuna lokal ulaşımın efektif bir şekilde sağlanması üzerine çalışılmıştır. Çalışmanın yapılacağı şehrin Ankara’ya yakın konumlu olması, Ankara’ya seyahat edebilecek öğrenci nüfusunun da göz önünde bulundurulmasını gerektirmektedir. Bu bağlamda bahsi geçen ilde belediye otobüslerinin faaliyete geçmesi durumunda, YHT-ilçeler, YHT-üniversite bağlantısının yapılması üzerine çalışılmıştır.

Ele alınan problemde, üniversite ile ilçelerin dahil olduğu 10 adet hattın alternatif güzergâhları kendi içerisinde değerlendirilmiş, değerlendirme sırasında CO<sub>2</sub> salınımı, hizmet süresi, nüfus yoğunluğu, önemli merkezlere yakınlık, yakıt maliyeti ve yolculuk süresi olmak üzere altı adet kriter dikkate alınmıştır. Güzergâhın belirlenmesi aşamasında birden çok kriter bulunduğu için, en sık kullanılan ÇKKV yöntemlerinden AHP, TOPSIS ve PROMETHEE’nin entegre bir şekilde kullanımından yararlanılmıştır.

Bu çalışmada Kırıkkale ilindeki Yahşihan, Bahşili, Balışeyh, Çelebi, Delice, Karakeçili, Keskin, Merkez, Sulakyurt olmak üzere 9 ilçe ve üniversite bölgesinin YHT istasyonu ile bağlantılarının yapılabilmesi için hatlardaki alternatif güzergâhlar belirlenip, 6 adet kriter göz önünde bulundurularak, ÇKKV yöntemlerinin kullanıldığı bir optimum güzergâh seçimi ele alınmıştır. Seçim probleminin tüm ili kapsadığı geniş alan ve değerlendirmeye aldığı veri miktarının büyüklüğü ile son derece kapsamlı bir çalışma olarak ilk defa yapılmış olup, yapılan diğer benzer güzergâh seçimi problemlerinden ayrılarak, bu özelliği ile literatüre katkı sağlamaktadır.

Çalışmanın ikinci bölümünde güzergâh belirleme problemine ve literatür taramasına yer verilmiştir. Üçüncü bölümde çözüm aşamasında kullanılan AHP, TOPSIS ve PROMETHEE yöntemleri açıklanmıştır. Dördüncü bölümde ele alınan kriterler ve alternatiflerin ÇKKV yöntemleriyle çözümü ve yorumu yer almaktadır. Çözüm önerisi sunulan problemin özeti ve önerileri beşinci bölümde sunulmuş olup, altıncı bölümde kaynakçaya yer verilmiştir.

## 2. GÜZERGÂH BELİRLEME PROBLEMİ VE LİTERATÜR TARAMASI (ROUTE SELECTION PROBLEM AND LITERATURE REVIEW)

Şehirleri ve önemli merkezleri birbirine bağlaması, ulaşım altyapısının kurulabilmesi için güzergâh belirleme önemli bir karar aşamasıdır. Yolcu memnuniyetini ve talebini karşılayarak, ulaşım süresini ve yakıt maliyetini en küçükleyecek bir planlama yapmak gerekir. Ulaşım planlamasında önemli bir adımı teşkil eden güzergâhın belirlenmesi süreci doğru bir şekilde ele alınırsa yapılan yatırım veya kurulan yeni sistem trafikte iyileşmeyi sağlayacak ve akabinde olabilecek yatırım ve düzenlemeler için başlangıç oluşturmaktadır [3].

Güzergâh belirleme üzerine literatürde birçok çalışma bulunmaktadır. Özellikle yol, otobüs, raylı sistem, tramvay, hızlı tren ve tren güzergâhları için çalışmalar mevcuttur [4].

Farkas [5] çalışmasında birden fazla kriter altında metro-ray ağı rota ve yer seçimi üzerinde durmuştur. CBS, Uzman Sistemler ve ÇKKV yöntemlerinden yararlanmıştır. Chang ve Hsieh [6] Tayvan'daki bisiklet yollarının ilgi görmesine karşılık, devletin isteği üzerine bisiklet rotalarını değerlendirmişlerdir. Çalışmada Bulanık Delfi Metodu, ANP, 0-1 Hedef Programlama yöntemlerini kullanmışlardır. Kim vd. [7] Teksas Kent Üçgeninde sürdürülebilir ulaşımı sağlamaya çalışmışlardır. CBS ve Mekânsal Karar Destek Sistemlerini kullanmışlardır. Kırangoçoğlu ve Ekinci [8] çalışmada ilk olarak raylı sistem güzergâh tasarımı için geleneksel yöntemleri analiz etmiş, nasıl geliştirebileceği hakkında araştırmalar yapmıştır. ÇKKV ve CBS'den yararlanarak İstanbul için güzergâh tasarımı yapmıştır. Hamurcu ve Eren [4] Ankara'da nüfusun ve kentleşmenin giderek artmasına bağlı olarak trafik yoğunluğunun artmasına dikkat çekmişlerdir. Büyükşehir Belediye'nin de planları arasında olan Monoray ulaşım sistemine AHP yöntemiyle güzergâh seçmişlerdir. Alkawaaz ve Asmael [9] çalışmada Bağdat şehrindeki trafik yoğunluğuna değinmiş ve çözüm önerisi olarak kentsel raylı ulaşımı sunmuşlardır. Değerlendirmelerini CBS, AHP ve TOPSIS yöntemleriyle yapmışlardır. Tezcan vd. [10] üç aşamadan oluşan çalışmada alternatif ilçeler ve 16 adet kriter değerlendirilip araç rotalama problemine odaklanılmıştır. AHP, BAHP, TOPSIS, PROMETHEE ve VIKOR yöntemlerini kullanarak afet sonrası geçici depo yeri seçimi ve araç rotalama sorununu Kırıkkale ili için çözmüşlerdir.

Çok kriterli karar verme yöntemlerinin bu problemde yoğun olarak kullanıldığı görülmektedir. Bu çalışmalardan bazıları aşağıda verilmiştir.

Arslan ve Yavuzylmaz [11] çalışmasında müşteri istekleri doğrultusunda, Düzce ilindeki seyahat işletmesi için, Gri İlişkisel Analiz ve MOORA yöntemlerini kullanarak optimum güzergâh önerisinde bulunmuşlardır. Eren vd. [1] çalışmasında bazı kriterleri göz önünde bulundurarak AHP yöntemiyle istasyon yeri belirlemiştir. Güvez vd. [12] Tam Sayılı Programlama Modeli kullanarak Kırıkkale'de atık sektöründeki bir işletmenin tıbbi atık toplama işlemi için en uygun rotayı belirleyerek, rotanın maliyetinin en küçüklenmesini amaçlamıştır. Hamurcu [3] yüksek lisans tezinde Ankara'da tek ray üzerinde hızlı ve güvenli ulaşım sağlayan monoray için AHS, ANP ve TOPSIS yöntemleri en iyi güzergâh seçimi yapılmaya çalışılmıştır. Hamurcu ve Eren [13] yaptıkları literatür araştırmasında kentsel toplu ulaşımında güzergâh belirlemek için kullanılan kriterleri incelemişlerdir. Hamurcu ve Eren [14] çalışmasında kent içi ulaşım probleminin çözümü olan toplu ulaşım için AHP ve ANP yöntemlerini kullanarak alternatifler arasından seçim yaparak öneride bulunmuşlardır. Hamurcu ve Eren [15] İstanbul için planlanan monoray projelerinin seçiminde AHP ve Hedef Programlama yöntemlerini kullanmışlardır. Özçelik ve Eren [16] dolmuş hattındaki çalışma dengesizliğini giderme amaçlı, AHP ve TOPSIS yöntemlerini kullanarak Kütahya-Tavşanlı hattına en uygun atamayı yapmıştır. Dinç vd. [17] çalışmasında Ankara-Sivas YHT hattında istasyon yerlerini AHP ve Hedef Programlama ile belirlemiştir. Dinç vd. 18 Kırıkkale'nin en uzun dolmuş hattı olan kampüs hattının değerlendirilmesinde AHP yöntemini kullanarak iyileştirme önerileri sunmuştur. Sarımehter vd. [2] Kırıkkale'de YHT istasyonunun açılacak olması sebebiyle YHT-Şehir merkezi ve üniversite bağlantısını sağlamak amaçlı AHP ve TOPSIS yöntemleriyle en uygun güzergâhları belirlemiştir. Eren vd. [18] AHS yöntemini kullanarak Ankara-Sivas YHT güzergâhını değerlendirmiştir. Toraman [19] yüksek lisans tezinde ulaşım ağına yeni güzergâh ekleme konusu üzerinde çalışmış, CBS ve ÇÖKA yöntemlerinden yararlanmıştır. Yıldırım ve Bediroğlu [20] çalışmalarında Trabzon limanı için optimum güzergâhları CBS ve AHP yöntemleriyle oluşturmuşlardır. Baran [21] çalışmasında günümüz

rekabet ortamına uyum sağlayabilmek ve doğru yönlendirmeler ile sevkiyatın yapılabilmesi adına güzergahlar belirlemiştir. Yıldırım ve Yomralıoğlu [22] CBS ve AHP yöntemleriyle boru hattı projeleri için maliyet ve inşaat süresinin minimizasyonun sağlanması adına doğru güzergahların belirlenmesi üzerine çalışmışlardır. Silman vd. [23] şehir içi otobüsler için planlama yapmışlardır. Wang ve Ziatonava [24] ilk müdahale ekipleri için güvenli ve hızlı rotaların belirlenmesi üzerine çalışmışlardır. Navratil [25] makalesinde motosiklet sürücüleri ve kamyon sürücülerinin özel gereksinimlerini göz önünde bulundurup bir model ortaya koymuştur. Almasi vd. [26] deprem ardından yardım sağlayabilmek için vaka çalışması yapmışlardır. Hariharan vd. [27] insanların trafikte beklemesini engellemek amacıyla DESBOR ve GPS teknolojilerini incelemişlerdir. Kang ve Kim [28] en hızlı rotayı bulabilecek trafik tahmin stratejileri ortaya koymuşlardır.

Literatür taraması sonucunda çalışmaların uygulama alanı ve yöntemlerine göre Çizelge 1’de özeti verilmiştir.

Çizelge 1’de görüldüğü üzere güzergâh belirleme problemi kapsamında ağırlıklı olarak ÇKKV yöntemlerinden faydalanılmıştır. Bu yöntemlerden en çok AHP yöntemi kullanıldığı görülmektedir. Güzergâhların belirlenmesi ve araç rotalama problemlerinde araştırmacılar birden çok kriter altında optimum sonuca ulaşmaya çalışmışlardır. Bu kriterlerden başlıcaları; önemli merkezlere yakınlık ve müşteri memnuniyetidir. Çalışmanın literatüre katkıları şu şekilde listelenmektedir:

- Kırıkkale ilindeki tüm ilçelerin ve üniversitenin bağlantısını sağlayan kapsamlı bir araştırma olduğundan bir ilk niteliği taşımaktadır.
- Literatürde YHT ile ilgili çalışmalara ÇKKV yöntemlerinden AHP, TOPSIS ve PROMETHEE kullanılmasıyla model önerisi sunulmuştur.
- Literatürde YHT istasyonu için fazla sayıda bağlantı sağlanması ve güzergâh belirlenmesi ile kapsamlı bir çalışması olarak ilk niteliği taşımaktadır.

### 3. MATERYAL ve YÖNTEM (MATERIAL and METHOD)

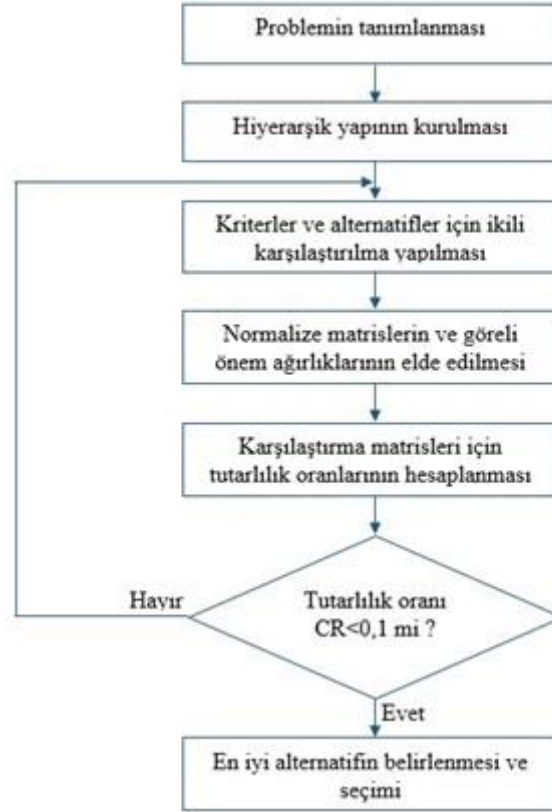
Belirli bir amaca yönelik olarak birden fazla kriterin bulunduğu karar verme problemlerinin çözümlenmesinde özellikle son zamanlarda literatürde sıklıkla ÇKKV yöntemlerinin kullanıldığını görülmektedir. Yöntemin verdiği etkin sonuçlardan ötürü karar vericiler tarafında kullanılan bir yöntemdir. ÇKKV yöntemleri ile pek çok kriteri bir arada değerlendirerek en iyi çözümü veren alternatifleri üretmek mümkündür [29]. Bu uygulamada ÇKKV yöntemlerinden AHP, TOPSIS ve PROMETHEE kullanılmıştır.

#### 3.1. Analitik Hiyerarşi Prosesi (Analytic Hierarchy Process)

Saaty tarafından geliştirilen AHP, çok kriterli karar verme durumları içeren problemlerde kullanılmak üzere başvurulan bir yöntemdir [30]. AHP tekniğinde en üst düzeyde bir amaç ve bu amacın altında sırasıyla kriterler, alt-kriterler ve seçeneklerden oluşan hiyerarşik bir model kullanılmaktadır. Bu yöntem sayesinde kriterlerin amaca katkısı belirlenir, kriter ağırlıkları oluşturulur ve uygun alternatif belirlenir [31]. Çalışmada, kişisel önyarguların azaltılarak [32], doğrusal programlama gibi [33], analitik yöntemlerle entegrasyon esnekliğine sahip olması [10] ve etkin sonuçlar vermesi nedeni ile AHP yönteminden yararlanılmış ve yöntemin sırası ile uygulanan aşamaları Şekil 1’de gösterilmiştir.

**Çizelge 1.** Güzergâh belirleme literatür özeti*Table 1. Route designation literature summary*

<b>Yazarlar</b>	<b>Uygulama Alanı</b>	<b>Kullanılan Yöntemler</b>
Alkawaaz ve Asmael [9]	Kentsel raylı ulaşım	CBS, AHP ve TOPSIS
Almasi vd. [26]	Afet yönetimi güzergâh belirleme	Sistem Analizi
Arslan ve Yavuzylmaz [11]	Optimum güzergahın belirlenmesi	Gri İlişkisel Analiz ve MOORA
Baran [21]	Sevkiyat alanında güzergâh belirleme	KTA Algoritması ve Van Breedam Metodu
Chang ve Hsieh (2013)	Bisiklet rotalarını değerlendirilmesi	Bulanık Delfi Metodu, ANP, 0-1 Hedef Programlama
Dinç vd. [17]	YHT hattında istasyon yerlerinin seçimi	AHP ve Hedef Programlama
Dinç vd. (2018)	Dolmuş hattı etkinliğinin değerlendirilmesi	AHP
Eren vd. (2017)	Yüksek hızlı tren istasyon yerinin seçimi	AHP
Eren vd. [18]	YHT hat güzergahının değerlendirilmesi	AHP
Farkas (2009)	Metro-ray ağı rota ve yer seçimi	CBS, Uzman Sistemler ve ÇKKV
Güvez vd. [12]	Araç rotalama problemi ile tıbbi atıkların toplanması	Tam Sayılı Programlama Modeli
Hamurcu ve Eren (2015)	Monoray güzergâh seçimi	AHP
Hamurcu [3]	Monoray güzergahı belirleme	AHP, ANP, TOPSIS
Hamurcu ve Eren [13]	Kentsel ulaşımda güzergâh belirleme için kullanılan kriterler	Sistem Analizi
Hamurcu ve Eren [14]	Toplu taşıma türünün seçimi	AHP ve ANP
Hamurcu ve Eren [15]	Ulaşım planlaması	AHP ve Hedef Programlama
Hariharan vd. [27]	Ulaşım planlaması	DESBOR ve GPS
Kang ve Kim [28]	Ulaşım planlaması	Doğrusal Olmayan Entegratör Geri Adım Teorisi
Kırlançoğlu ve Ekinci (2014)	Raylı sistem güzergâh tasarımı	CBS
Kim vd. (2013)	Sürdürülebilir ulaşım	CBS ve Mekânsal Karar Destek Sistemleri
Navratil [25]	Ulaşımında özel gereksinimler göz önünde bulundurularak model sunma	Modelleme ve Simülasyon
Özçelik ve Eren [16]	Dolmuş hattının değerlendirilmesi	AHP ve TOPSIS
Sarimehmet vd. [2]	YHT istasyonu ve şehir bağlantısının sağlanması	AHP ve TOPSIS
Silman vd. [23]	Şehir içi otobüsler için güzergâh belirleme	Doğrusal Hedef Programlama
Tezcan vd. (2021)	Depo yeri seçimi ve çok araçlı araç rotalaması	AHP, Bulanık AHP, TOPSIS, PROMETHEE ve VIKOR
Toraman [19]	Ulaştırma için güzergâh seçenekleri	CBS, ÇÖKA
Wang ve Ziatonava [24]	İlk müdahale ekipleri için güzergâh belirleme	Dijkstra Algoritması
Yıldırım ve Bediroğlu [20]	Güzergâh belirleme	CBS ve AHP
Yıldırım ve Yomralıoğlu [22]	Boru hattı projeleri için güzergâh belirleme	CBS ve AHP
Yomralıoğlu (2011)		

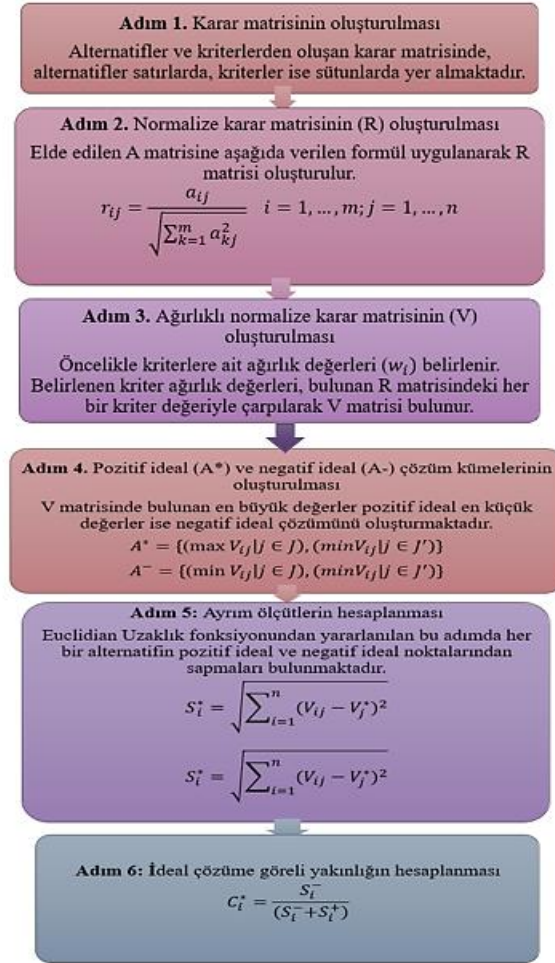


Şekil 1. AHP yöntemi akış şeması [34]

Figure 1. AHP method flow chart

### 3.2. TOPSIS Yöntemi (TOPSIS Method)

Hwang ve Yoon tarafından 1981 yılında geliştirilmiş ve birçok alanda kullanılmış bir ÇKKV yöntemidir [35]. Yöntem karar noktalarının ideal çözüme yakınlığı ana prensibine dayanarak, tercih sıralaması yapmak için geliştirilmiştir [36]. Çalışmada, alternatiflerin kolay ve etkin bir şekilde sıralandırılması [37], literatürde geniş kapsama sahip problemlerde sıralama yapmak için sıklıkla kullanılması [33][38] nedeniyle TOPSIS yöntemi tercih edilerek, kullanılmasına karar verilmiştir. Literatürde geniş kapsamlı sıralama problemleri için sıkça kullanılmakta olan TOPSIS yönteminin adımları özetlenerek Şekil 2'de verilmiştir.



Şekil 2. TOPSIS yöntemi akış şeması [35]

Figure 2. TOPSIS method flow chart

### 3.3. PROMETHEE Yöntemi (PROMETHEE Method)

Brans [39] tarafınca geliştirilen PROMETHEE yöntemi, tercih fonksiyonları dikkate alınarak alternatiflerin seçilen kriterler altında ikili karşılaştırılması yapıp, değerlendirilmesine dayanan bir yöntemdir. PROMETHEE yöntemi ile sonlu sayıda alternatifler üzerinde hem kısmi sıralama (PROMETHEE I) hem de tam sıralama (PROMETHEE II) yapmak mümkündür, alternatifler ( $a_1, a_2, \dots, a_n$ ) ve kriterler ( $q_1, q_2, \dots, q_k$ ) tarafından oluşan karar matrisi ile karar verme sürecine başlanır. Yöntem karar vericiye karar matrisi oluşturulduktan sonra 5 adımın izlenmesi sonucunda PROMETHEE tam ve kısmi sıralama sonuçlarını sunmaktadır [40]. PROMETHEE yönteminin aşamaları özetlenerek Şekil 3'te verilmiştir.



**Adım 1:** Alternatif, kriter ve ağırlıklarının belirlenmesi

**Adım 2:** Kriterler için tercih fonksiyonlarının belirlenmesi

**Adım 3:** Ortak tercih fonksiyonlarının belirlenmesi

**Adım 4:** Tercih indekslerinin belirlenmesi

**Adım 5:** Pozitif ve negatif üstünlüklerin belirlenmesi

**Adım 6:** Kısmi önceliklerin belirlenmesi (PROMETHEE-1)

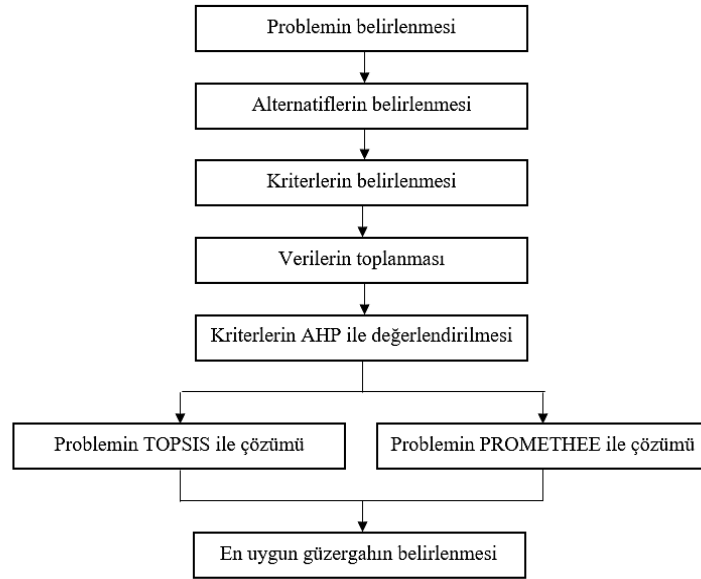
**Adım 7:** Net önceliklerin belirlenmesi (PROMETHEE-2)

**Şekil 3.** PROMETHEE yöntemi akış şeması [39]

*Figure 3. PROMETHEE method flow chart*

#### 4. UYGULAMA (CASE STUDY)

Bu çalışmada Kırıkkale ilinde kurulacak olan YHT istasyonunun belediye otobüsleri ile 9 ilçe ve 1 üniversite bağlantısı için ÇKKV yöntemlerinden AHP, TOPSIS ve PROMETHEE' den yararlanarak optimum güzergâhlar ile bağlanması üzerine çalışılmıştır. Çalışmada problemin belirlenmesi aşamasından sonra alternatifler belirlenmiş, çeşitli araştırmalar ve uzman görüşü sonucunda da kriterlerin belirlenmesi aşaması tamamlanmıştır. Daha sonra sırasıyla AHP, TOPSIS ve PROMETHEE yöntemleri uygulanmıştır. Uygulamanın akış süreci Şekil 4'te gösterilmiştir.



**Şekil 4.** Problem akış şeması

*Figure 4. Problem flow chart*

##### 4.1. Problemin Tanımlanması (Problem Defination)

Kırıkkale'nin Ankara'ya yakın olması, bu iki şehir arasında trafik yoğunluğunun artmasına sebebiyet vermiştir. YHT istasyonunun açılacak olması Kırıkkale-Ankara arası ulaşımda bir alternatif oluşturmuştur. Fakat YHT durağının konumu incelendiğinde önemli merkezlere uzak olduğu ve durağa ulaşımın etkili bir şekilde sağlanması gerektiği görülmüştür. İlçe ve üniversite bağlantısının belediye otobüsleriyle optimum güzergâhların oluşturulması şartıyla sağlanması gerektiği tespit edilmiştir.

#### 4.2. Alternatiflerin Belirlenmesi (Determination of Alternatives)

Problemin tanımlanmasının ardından YHT istasyonu ile Kırıkkale ilinin 9 ilçesinin ve üniversitesinin bağlantısını kurabilmek için alternatif güzergâhlar belirlenmiştir. Balışeyh, Bahşili, Çelebi, Delice, Karakeçili, Keskin, Merkez, Sulakyurt, Yahşihan ve Kırıkkale Üniversitesi olmak üzere tüm alternatifler için belirlenen güzergâh alternatiflerinin her biri için hat uzunluğu ve zaman verisi Google Maps' ten yararlanarak bulunmuştur. Bahsi geçen 9 ilçe ve üniversitenin her biri için kendi güzergâh alternatifleri arasından optimum olanların belirlenmesi hedeflenmiştir. Oluşturulacak hatlardaki alternatif güzergâhlar Tablo 3'te gösterilmiştir. Kırıkkale Üniversitesi: (K), Osmangazi: (O), Yahşihan: (Y), Karakeçili: (KA), Merkez: (M), Bahşili: (B), Balışeyh: (BA), Çelebi: (C), Delice: (D), Keskin: (KE), Sulakyurt: (S) olacak şekilde kısaltmalar kullanılmıştır.

#### 4.3. Kriterlerin Belirlenmesi (Determination of Criteria)

Alternatifleri belirlenen çalışmanın kriterlerini belirleme safhasında daha önce benzer konular üzerine yapılmış çalışmalar incelenmiştir. Problemin çözümünde maliyet, zaman, çevre gibi faktörler üzerinde durularak, birbirleri arasında sonuçları olumsuz etkileyecek şekilde korelasyon bağı bulunan kriterlerin belirlenmesinden kaçınılmıştır. Kriterler; yakıt maliyeti, hizmet süresi, yolculuk süresi, önemli merkezlere yakınlık, CO<sub>2</sub> salınımı, nüfus yoğunluğu olarak belirlenmiştir.

Yakıt maliyeti; aracın km başına yaktığı miktarı (4.39₺/km) temsil etmektedir. Hat seçiminde en kısa olan hattın seçilmesi ile problem çözümüne en fazla faydayı sağlamaktadır. Hizmet süresi; toplu taşıma aracı fazla km yol yapar ise metal yorgunluğuna bağlı olarak çabuk bir şekilde hurdaya ayrılacağı için problemde ne kadar az km'lik hat tercih edilir ise o kadar değerlidir. Yolculuk süresi müşteri memnuniyeti bakımından önemlidir. Bundan kaynaklı olarak yolculuk süresi ne kadar kısa olur ise o kadar değerlidir. Önemli merkezlere yakınlık hem müşteri memnuniyeti hem de kazanç açısından güzergâh ne kadar çok önemli merkeze yakın olursa o kadar faydalıdır. CO<sub>2</sub> salınımının çevreye zararı bakımından ne kadar az olur ise o kadar değerlidir. CO<sub>2</sub> salınımı, gidilen km ile doğru orantılı olduğu için km bakımından kısa olan güzergâhlar öncelikli tercihimizdir. Nüfus yoğunluğu, kazanç açısından ele alınmıştır. Güzergâh üzerindeki nüfus yoğunluğu ne kadar fazla olur ise ulaşımda taşınacak yolcu sayısının fazla olacağından kazanılacak miktarda da doğru orantılı artış olacaktır. Bu yüzden güzergâh üzerindeki nüfus yoğunluğunun fazla olması problem çözümünde değerlidir.

Kriterler; Yakıt maliyeti [41][42], hizmet süresi [2], yolculuk süresi [2][16][43][44], önemli merkezlere yakınlık [2][3][18][19][44], CO<sub>2</sub> salınımı [3][14][19][41][43][44] ve nüfus yoğunluğu [19][43] olarak belirlenmiştir.

#### 4.4. Verilerin Toplanması (Data Collection)

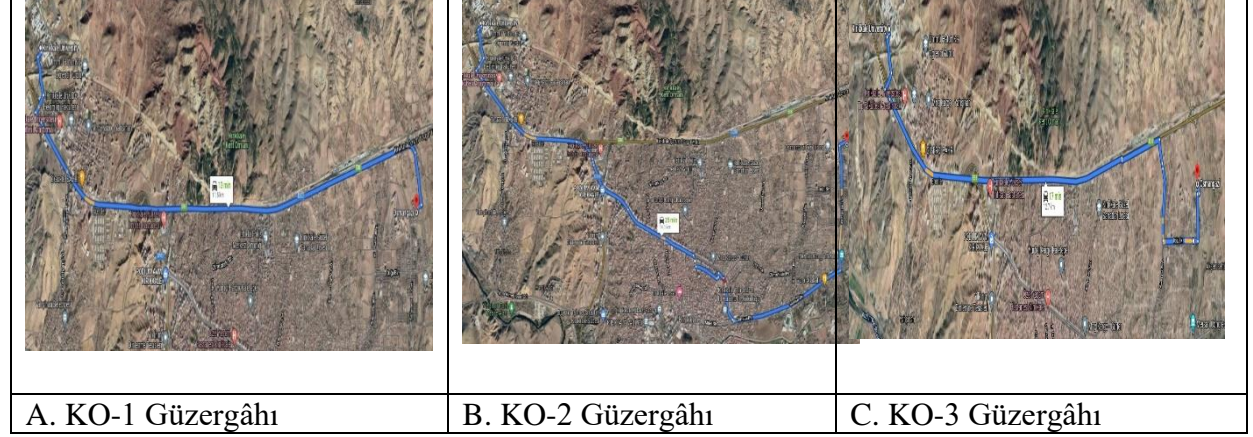
- Yakıt maliyeti: Projenin yapıldığı dönemin güncel mazot fiyatlarından elde edilmiştir.
- Yolculuk süresi ve önemli merkezlere yakınlık: Yolculuk sürelerinin zaman verileri ve önemli merkezlere yakınlık sayılarının belirlenmesinde Google Maps'ten yararlanılmıştır.
- Hizmet süresi: Metal yorgunluğu üzerine internette yapılan araştırmalar sonucunda yazarlar tarafından ortalama bir değer belirlenmiştir.
- CO<sub>2</sub> salınımı: Diler vd. [45] yaptığı çalışmadan belediye otobüslerinin CO<sub>2</sub> salınım değerleri belirlenmiştir.
- Nüfus yoğunluğu: İlçe nüfuslarının artması, güzergâhlar üzerindeki yolcu sayılarının artması ile doğru orantılı olacağından problem çözümünde nüfus yoğunluğu sayıları ele alınmıştır. İlçe nüfus değerleri elde edilirken TÜİK'ten yararlanılmıştır.
- Çalışmanın alternatifleri ve kriterleri belirlenmesi sonucunda Çizelge 2 ortaya çıkmıştır.

**Çizelge 2.** Oluşturulacak hatlardaki alternatif güzergâhlar*Table 2. Alternative routes on the lines to be created*

Hat İsmi	Güzergâh Alternatifi	Güzergâh	Hat Uzunluğu	Zaman Verisi	Yakıt Verisi (4.39€/km)	Emisyon Değeri (1.15CO <sub>2</sub> /km)
KKU-OSM	Kırıkkale-Çorum-Yozgat Yolu	KO-1	11,5 km	13 dk.	50.49	13.22
	Samsun Bul.	KO-2	14,1 km	25 dk.	61.90	16.21
	Samsun Bul. ve Doğu Bul.	KO-3	12,7 km	17 dk.	55.75	14.6
Yahşihan-OSM	Cumhuriyet Cad. ve Kırıkkale-Çorum-Yozgat Yolu	YO-1	11,7 km	13 dk.	51.36	13.45
	Hoca Ahmet Yesevi Cad. ve Kırıkkale-Çorum-Yozgat Yolu	YO-2	13,1 km	15 dk.	57.51	15.06
	Hoca Ahmet Yesevi Cad., Millet Bul., Samsun Bul. ve Şirinevler Cad.	YO-3	13,9 km	24 dk.	61.02	15.98
Merkez-OSM	Millet Bul., Samsun Bul. ve Şirinevler Cad.	MO-1	6,1 km	10 dk.	26.78	7.01
	Millet Bul., Samsun Bul., Kanuni Bul. ve Doğu Bul.	MO-2	6,3 km	13 dk.	27.66	7.24
	Millet Bul., Karacalı Cad. ve Kırıkkale-Çorum-Yozgat Yolu	MO-3	8,1 km	12 dk.	35.56	9.31
Bahşili-OSM	Atatürk Bul., Kırıkkale-Kırşehir Yolu ve Kırıkkale-Çorum-Yozgat Yolu	BO-1	14,3 km	16 dk.	62.78	16.44
	Atatürk Bul., Millet Bul., Samsun Bul. ve Kırıkkale-Çorum-Yozgat Yolu	BO-2	13,7 km	24 dk.	60.14	15.75
	Atatürk Bul., Millet Bul., Samsun Bul. ve Şirinevler Cad.	BO-3	11,7 km	23 dk.	51.36	13.45
Balıseyh-OSM	Kırıkkale-Çorum-Yozgat Yolu	BAO-1	17,3 km	13 dk.	75.95	19.89
	Kırıkkale-Çorum-Yozgat Yolu ve Samsun Bul.	BAO-2	18 km	16 dk.	79.02	20.7
Çelebi-OSM	Çelebi Yolu, Kırıkkale-Karakeçili Yolu, Kırıkkale-Kırşehir Yolu ve Kırıkkale-Çorum-Yozgat Yolu	CO-1	61,9 km	48 dk.	271.74	71.18
	Keskin Yolu, Kırıkkale-Kırşehir Yolu ve Kırıkkale-Çorum-Yozgat Yolu	CO-2	61,5 km	51 dk.	269.99	70.72
	Çelebi Yolu, Karakeçili-Kaman Yolu, Cemal Gürsel Cad., Samsun Bul. ve Şirinevler Cad.	CO-3	59,2 km	52 dk.	259.89	68.08
Delice-OSM	Kırıkkale-Çorum Yolu ve Kırıkkale-Çorum-Yozgat Yolu	DO-1	46,9 km	33 dk.	205.89	53.93
	Kırıkkale-Çorum Yolu, Kırıkkale-Çorum-Yozgat Yolu ve Samsun Bul.	DO-2	47,6 km	35 dk.	208.96	54.74
Keskin-OSM	Ankara Cad., Kırıkkale-Kırşehir Yolu, Millet Bul., Samsun Bul. ve Şirinevler Cad.	KEO-1	33,1 km	37 dk.	145.31	38.06
	Ankara Cad., Kırıkkale-Kırşehir Yolu ve Kırıkkale-Çorum-Yozgat Yolu	KEO-2	35,6 km	30 dk.	156.28	40.94
Karakeçili-OSM	Şehit İsmail Taşdelen Sok., Karakeçili-Kaman Yolu, Kırıkkale-Kırşehir Yolu ve Cemal Gürsel Cad.	KAO-1	43,3 km	45 dk.	190.09	49.79
	Şehit İsmail Taşdelen Sok., Karakeçili-Kaman Yolu, Kırıkkale-Kırşehir Yolu ve Kırıkkale-Çorum-Yozgat Yolu	KAO-2	44,9 km	38 dk.	197.11	51.635
Sulakyurt-OSM	Balıseyh-Sulakyurt Yolu ve Kırıkkale-Çorum-Yozgat Yolu	SO-1	48,6 km	40 dk.	213.35	55.89
	Balıseyh-Sulakyurt Yolu, Balıseyh Yolu ve Kırıkkale-Çorum-Yozgat Yolu	SO-2	55,1 km	53 dk.	241.89	63.36
	Yükselen Cad. Ve Fatih Cad.	SO-3	46,3 km	59 dk.	203.26	53.24

\*Hat uzunluğu verileri, belirlenen alternatif güzergahların yolculuk süresi ile birlikte yalnızca uzunluklarının gösterilmesi amacı ile verilmiş olup, hiçbir hesaplama dahil edilmemiştir.

Çizelge 2'deki verilen hatlara bir örnek olarak Kırıkkale Üniversitesi-Osmangazi hattının üç alternatifi Şekil 5'teki haritalarda gösterilmiştir.



Şekil 5. Kırıkkale Üniversitesi – Osmangazi hattının alternatif güzergâhları

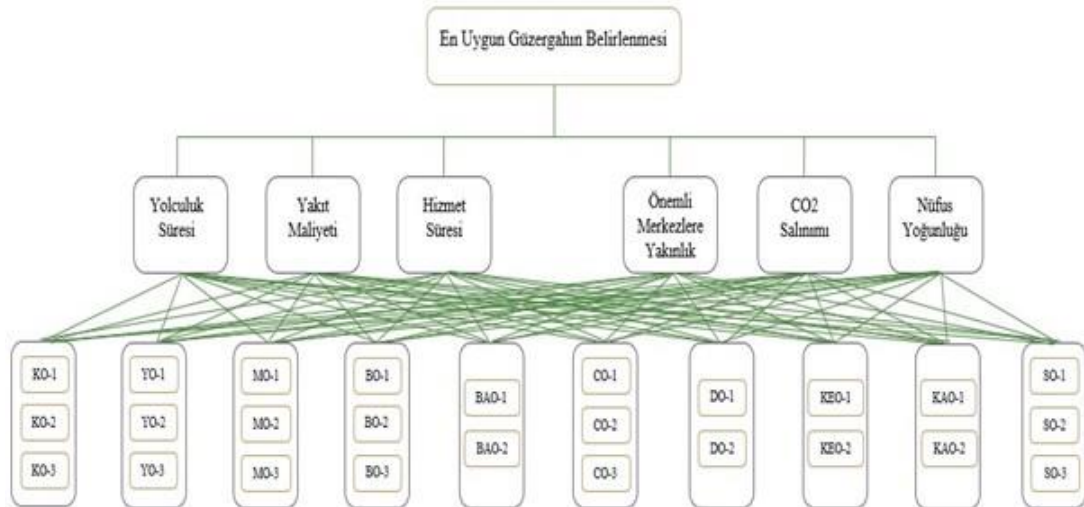
Figure 5. Alternative routes of Kırıkkale University – Osmangazi line

#### 4.5. Problemin Çözümü (Solution of the Problem)

Probleme ilgili veriler toplanmış, optimum güzergâha ulaşabilmek amacıyla sırasıyla AHP, TOPSIS ve PROMETHEE ile çözüme hazır hale getirilmiştir.

##### 4.5.1. Kriterlerin AHP yöntemi ile değerlendirilmesi (Evaluation of criteria with the AHP method)

Kriter ağırlıkları, uzmanların kıyaslaması sonucunda değer almıştır. AHP yönteminden elde edilen kriter ağırlıkları, TOPSIS ve PROMETHEE yönteminde kullanılmıştır. İlgili yöntemlerde alternatiflerin kendi değerleri kullanılarak değerler elde edilmiştir. İlk olarak hiyerarşik yapı oluşturulmuştur. AHP yönteminde güzergâhların belirlenmesinde oluşturulan kriterlerin ve alternatiflerin hiyerarşik yapısı Şekil 6'da gösterilmiş, ardından problemde ele alınan kriterler AHP yöntemi ile değerlendirilmiştir.



Şekil 6. AHP karar hiyerarşisi

Figure 6. AHP decision hierarchy

Kriterlerin ikili karşılaştırılması yapılırken, ÇKKV yöntemlerinin kullanıldığı, güzergâh belirleme problemlerinin de içinde bulunduğu çeşitli amaçlara yönelik olarak gerçekleştirilen akademik çalışmalarda bulunan alanında uzman yazarlar, ele alınan problemin amacını göz önünde bulundurup, amaca yönelik olarak belirlenen kriterlerin birbirlerine kıyasla önemlerine karar vermiş, bunun sonucunda elde edilen kriter ağırlıkları alternatiflerin güzergâh alternatiflerini sonuçlandırmada kullanılmıştır. Her alternatif, her kritere göre kendi güzergâhları arasında ikili karşılaştırma yapılarak, sonuca varılmıştır. Kriterlerin ikili karşılaştırması Çizelge 3'te verilmiştir.

**Çizelge 3.** Kriterler arası ikili karşılaştırma matrisinin oluşturulması

*Table 3. Establishment of pairwise comparison matrix between criteria*

Kriterler	Yolculuk Süresi	Yakıt Maliyeti	Hizmet Süresi	Önemli Merkezlere Yakınlık	CO2 Salınımı	Nüfus Yoğunluğu
Yolculuk Süresi	1	3	4	0.25	5	2
Yakıt Maliyeti	0.33	1	4	0.33	3	0.5
Hizmet Süresi	0.25	0.25	1	0.2	2	0.2
Önemli Merkezlere Yakınlık	4	3.03	5	1	6	1
CO2 Salınımı	0.2	0.33	0.5	0.17	1	0.17
Nüfus Yoğunluğu	0.5	2	5	1	6	1

İkili karşılaştırılması oluşturulan kriterlerin, normalize matrisi Çizelge 4'te verilmiştir.

**Çizelge 4.** Kriterler için normalize karar matrisi

*Table 4. Normalized decision matrix for criteria*

Kriterler	Yolculuk Süresi	Yakıt Maliyeti	Hizmet Süresi	Önemli Merkezlere Yakınlık	CO2 Salınımı	Nüfus Yoğunluğu
Yolculuk Süresi	0.16	0.31	0.21	0.08	0.22	0.41
Yakıt Maliyeti	0.05	0.10	0.21	0.11	0.13	0.10
Hizmet Süresi	0.04	0.03	0.05	0.07	0.09	0.04
Önemli Merkezlere Yakınlık	0.64	0.32	0.26	0.34	0.26	0.21
CO2 Salınımı	0.03	0.03	0.03	0.06	0.04	0.03
Nüfus Yoğunluğu	0.08	0.21	0.26	0.34	0.26	0.21

Normalize matrisi de belirlenen kriterler için AHP adımları uygulanmaya devam ettiğinde sonuca ulaşılmıştır. Sonuç Çizelge 5'te verilmiştir.

**Çizelge 5.** Kriterlerin yüzde önemleri ve tutarlılık oranı*Table 5. Percent significance and consistency of criteria*

Kriterler	Yüzde Önemi	CI	CR
Yolculuk Süresi	0.23	0.09	
Yakıt Maliyeti	0.12		
Hizmet Süresi	0.05	Lamda ( $\lambda$ )	0.073
Önemli Merkezlere Yakınlık	0.34		
CO2 Salınımı	0.04		
Nüfus Yoğunluğu	0.22	6.45	

#### 4.5.2. Problemin TOPSIS yöntemi ile çözümü (Solving the problem with the TOPSIS method)

AHP ile çözümü yapılarak kriter ağırlıkları bulunan problemin TOPSIS yöntemi ile çözümü yapılırken kriter ağırlıkları kullanılmış, hatlardaki alternatifler için en uygun sonuca ulaşılmıştır. KO için karşılaştırma matrisi Çizelge 6'da verilmiştir.

**Çizelge 6.** KO'nun TOPSIS karar matrisi*Table 6. KO's TOPSIS comparison matrix*

	Yolculuk Süresi	Yakıt Maliyeti	Hizmet Süresi	Önemli Merkezlere Yakınlık	CO2 Salınımı	Nüfus Yoğunluğu
KO-1 Güzergâhı	90	90	100	60	95	70
KO-2 Güzergâhı	75	70	75	100	85	95
KO-3 Güzergâhı	85	80	85	80	90	80

KO'da örnek gösterildiği gibi tüm alternatifler sırası ile tüm kriterler için puanlandırılmış, verilen puanlara göre pozitif ve negatif ideal çözümlerine ulaşılmış ve Çizelge 7'de gösterilmiştir. Ulaşılan ideal çözümlere göre ideal çözüme görece yakınlıkları bulunmuştur. Çizelge 8'de bulunan ideal çözüme görece yakınlıkları büyükten küçüğe numaralandırılarak alternatifler arasından optimum güzergâh bulunmuştur.

**Çizelge 7.** KO'nun Pozitif İdeal ve Negatif İdeal çözümlerin oluşturulması*Table 7. Creation of KO's Positive Ideal and Negative Ideal solutions*

<b>Pozitif İdeal Çözüm</b>	14.30	7.75	3.31	24.04	4	14.65
<b>Negatif İdeal Çözüm</b>	11.92	6.03	2.48	14.42	2.43	10.8

**Çizelge 8.** S1+, S1- ve Ci\* değerleri*Table 8. S1+, S1- ve Ci\* values*

Alternatif	S1+	S1-	Ci*
KO-1 Güzergâhı	10.479	3.055	0.226
KO-2 Güzergâhı	2.420	10.487	0.813
KO-3 Güzergâhı	5.929	5.367	0.475

#### 4.5.3. Problemin PROMETHEE yöntemi ile çözümü (Solving the problem with the PROMETHEE method)

AHP ile çözümü yapılarak kriter ağırlıkları bulunan problemde örnek olarak Sulakyurt-Osmangazi (SO) alternatifi için PROMETHEE yöntemi ile çözüm yapılırken kriter ağırlıkları kullanılmış ve tercih fonksiyonu seçilerek, kriterlere göre alternatiflerin değerleri girilmiştir. Bahsedilen tüm değerler Şekil 7’de gösterilmiştir.

Scenario1	Yolculuk Suresi	Yakit Maliyeti	Hizmet Suresi	Onemli Merk...	CO2 Salinimi	Nufus Yogun...	
Unit	unit	unit	unit	unit	unit	unit	
Cluster/Group	◆	◆	◆	◆	◆	◆	
<b>Preferences</b>							
Min/Max	min	min	max	max	min	max	
Weight	1,00	1,00	1,00	1,00	1,00	1,00	
Preference Fn.	Linear	Linear	Linear	Linear	Linear	Linear	
Thresholds	absolute	absolute	absolute	absolute	absolute	absolute	
- Q: Indifference	1,00	1,00	1,00	1,00	1,00	1,00	
- P: Preference	n/a	n/a	n/a	n/a	n/a	n/a	
- S: Gaussian	n/a	n/a	n/a	n/a	n/a	n/a	
<b>Statistics</b>							
Minimum	40,00	203,26	17,00	1,00	53,25	1700,00	
Maximum	59,00	241,89	19,00	2,00	63,27	3000,00	
Average	50,67	219,50	18,00	1,67	57,47	2171,00	
Standard Dev.	7,93	16,36	0,82	0,47	4,24	588,00	
<b>Evaluations</b>							
<input checked="" type="checkbox"/>	SO-1	40,00	213,35	18,00	2,00	55,89	1813,00
<input checked="" type="checkbox"/>	SO-2	53,00	241,89	17,00	2,00	63,27	3000,00
<input checked="" type="checkbox"/>	SO-3	59,00	203,26	19,00	1,00	53,25	1700,00

Şekil 7. SO'nun PROMETHEE ağırlıklı matrisi tablosu

Figure 7. SO'S PROMETHEE weighted matrix table

Şekil 7’deki gerekli hücrelerin doldurulmasının ardından program içerisinde bulunan “PROMETHEE Table” butonuna basarak Şekil 8’deki PROMETHEE sonuç tablosu elde edilmiştir. Buna göre Sulakyurt-Osmangazi (SO) için en uygun güzergâh, SO-1 güzergahı olarak seçilmiştir.

Rank	action	Phi	Phi+	Phi-
1	SO-1	0,2158	0,4167	0,2008
2	SO-3	-0,0283	0,3050	0,3333
3	SO-2	-0,1875	0,2500	0,4375

Şekil 8. SO'nun PROMETHEE sonuç tablosu

Figure 8. SO's PROMETHEE result table

#### 4.5.4. Güzergahın Belirlenmesi (Determining the Route)

AHP yöntemi ile elde edilen kriter ağırlıkları, TOPSIS ve PROMETHEE yöntemlerinde kullanılması sonucunda her iki çözüm yöntemine göre de KO-2, YO-3, MO-3 ve BO-2 güzergahları birinci sırada yer almış, geriye kalan alternatiflerdeki ilk, ara ve son sırada yer alan güzergahlar ise çözüm yöntemlerine göre farklılıklar göstermiştir. Sonuçların daha detaylı ve karşılaştırılmalı hali Çizelge 9’da sunulmuştur.

Çizelge 9. Genel sonuç tablosu

Table 9. General result table

Hat	Güzergâh	AHP-TOPSIS Çözümü		AHP-PROMETHEE Çözümü	
		Ci Değeri	Sıra	Net Flow	Sıra
Kırıkkale Üniversitesi – Osmangazi	KO-1	0.226	3	-0.661	3
	KO-2	0.813	1	0.839	1
	KO-3	0.475	2	-0.177	2
Yahşihan-Osmangazi	YO-1	0.334	3	-0.478	3
	YO-2	0.546	2	-0.262	2
	YO-3	0.666	1	0.739	1
Merkez - Osmangazi	MO-1	0.422	2	-0.636	3
	MO-2	0.106	3	0.045	2
	MO-3	0.869	1	0.591	1
Bahşili-Osmangazi	BO-1	0.382	3	-0.324	2
	BO-2	0.587	1	0.668	1
	BO-3	0.495	2	-0.344	3
Balışeyh-Osmangazi	BAO-1	1	1	-0.447	2
	BAO-2	0	2	0.447	1
Çelebi-Osmangazi	CO-1	0.547	1	-0.429	3
	CO-2	0.489	2	-0.174	2
	CO-3	0.404	3	0.603	1
Delice – Osmangazi	DO-1	0.923	1	-0.896	2
	DO-2	0.077	2	0.896	1
Keskin-Osmangazi	KEO-1	0.262	2	0.017	1
	KEO-2	0.738	1	-0.017	2
Karakeçili-Osmangazi	KAO-1	0.233	2	0.688	1
	KAO-2	0.767	1	-0.688	2
Sulakyurt-Osmangazi	SO-1	0.492	2	0.2158	1
	SO-2	0.372	3	-0.1875	3
	SO-3	0.522	1	-0.0283	2

Çözüm yöntemlerinin sonuçları karşılaştırıldığında iki yöntemde de ortak sonuca ulaşılan güzergâhlar şu şekildedir; Kırıkkale Üniversitesi – Osmangazi hattı için 2. güzergâh, Yahşihan – Osmangazi için 3. güzergâh, Merkez – Osmangazi için 3. güzergâh, Bahşili – Osmangazi için 2. güzergâh birinci sırada yer alarak en uygun güzergâh olarak belirlenmişlerdir. Bahsi geçen güzergâhlar dışındaki ilçeler için alternatif güzergâhların sıralamaları çözüm yöntemlerine göre farklılık göstermektedir.

## 5. SONUÇLAR (CONCLUSIONS)

Artan nüfusun sonucu olarak gün geçtikçe şahsi araç sayısı ve trafik yoğunluğunda artış gözlenmektedir. Gözlenen bu yoğunluktan dolayı ulaşımın aksamasını engellemek ve ulaşım yollarını geliştirmek amacıyla yeni yatırımlar yapılmaktadır. Ulaşım için bahsi geçen yeni yatırımlardan birisi de YHT projesidir. Kırıkkale ilinde YHT istasyonunun kurulacak olması ile ilçe bağlantılarının sağlanması amacıyla güzergâh belirleme problemi ortaya çıkmaktadır. Yolcu memnuniyetini en üst seviyede tutacak, işletmenin ise minimum maliyetlerle operasyon yapmasını sağlayacak en iyi güzergâh planlarının yapılması gerekmektedir. Bu çalışmada ise CO<sub>2</sub> salınımı, hizmet süresi, nüfus yoğunluğu, önemli merkezlere yakınlık, yakıt maliyeti ve yolculuk süresi olmak üzere altı adet kriter göz önünde bulundurularak, optimum güzergâh belirlenmesi üzerine çalışılmıştır. Problemin çözümünde birden



fazla kriter bulunduğundan dolayı çok kriterli karar verme (ÇKKV) yöntemlerinin kullanımının uygun olduğuna karar verilmiş, kriterlerin değerlendirilmesi aşamasında AHP yönteminden yararlanılmış, çözüm aşamasında ise alternatiflerin sıralandırılması için AHP metodundan elde edilen kriter ağırlıkları kullanılarak, TOPSIS ve PROMETHEE yöntemlerinden yararlanılmıştır.

Bahsi geçen çözüm yöntemlerinin sonuçları karşılaştırıldığında her iki yöntem için de Kırıkkale Üniversitesi – Osmangazi hattı için 2. güzergâhın, Yahşihan – Osmangazi için 3. güzergâhın, Merkez – Osmangazi için 3. güzergâhın, Bahşili – Osmangazi için 2. güzergâhın birinci sırada yer aldığı tespit edilmiştir. İlgili güzergâhlar dışında yer alan diğer ilçeler için alternatif güzergâhların sıralamaları çözüm yöntemlerine farklılık göstermektedir.

Çalışma Kırıkkale ilindeki tüm ilçelerin YHT bağlantısının sağlanmasının yanında üniversite bağlantısını da içermektedir. Problemin kapsadığı geniş alan ve değerlendirmeye aldığı veri miktarının büyüklüğü ile son derece kapsamlı bir çalışma olarak ilk defa yapılmış olup, yapılan diğer benzer güzergâh belirleme problemlerinden ayrılarak, bu özelliği ile literatüre katkı sağlamaktadır. Problemin amacına yönelik olarak belirlenen kriterler AHP yöntemi ile değerlendirilmiş, değerlendirme sonucunda elde edilen kriter ağırlıkları TOPSIS ve PROMETHEE yöntemlerinde kullanılarak, çözümler gerçekleştirilmiş, çözümlerden sağlanan sonuçların karşılaştırılması ile de literatüre katkı sağlamaktadır.

İleride yapılabilecek projelerde bu çalışmanın sonuçları kullanılarak durak yeri belirleme problemi için farklı ÇKKV yöntemleri kullanılarak, çözülebilir. Aynı zamanda çözüm önerisi sunulan problemin matematiksel modeli kurularak, farklı çözüm yöntemleri ile çözülmesi sonucunda mevcut sonuçlar sıranabilir.

#### **Etik Standartlar Bildirimi (Declaration of Ethical Standards)**

Çalışma etik standartlara uygun olarak gerçekleştirilmiştir.

#### **Yazar Katkı Beyannamesi (Credit Authorship Contribution Statement)**

Buse BAYRAM: Çalışmada ele alınan probleme ilişkin verilerin toplanması, çözüm yöntemlerinin uygulanması ve sonuçların raporlanması.

Mert KARA: Çalışmada ele alınan probleme ilişkin verilerin toplanması, çözüm yöntemlerinin uygulanması ve sonuçların raporlanması.

Ahmet CÜREBAL: Problemin tanımlanması, literatürün taranması ve sonuçların yorumlanması.

Rabia YUMUŞAK: Çalışmada kullanılan yöntemlerin belirlenmesi ve sonuçların yorumlanması.

Tamer EREN: Çalışmada kullanılan yöntemlerin belirlenmesi ve sonuçların doğrulanması.

#### **Çıkar Çatışması Beyannamesi (Declaration of Competing Interest)**

Yazarların arasında herhangi bir çıkar çatışması bulunmamaktadır.

#### **Veri Kullanılabilirliği (Data Availability)**

Makalede kullanılan veriler paylaşımına açıktır.

#### **KAYNAKLAR (REFERENCES)**

- [1] T. Eren, M. Hamurcu and H. M. Alağaç, "Çok Kriterli Karar Verme yöntemleri ile Kırıkkale yüksek hızlı tren istasyon yerinin seçimi", *In 5th International Symposium on Innovative Technologies*


- in Engineering and Science (ISITES2017)*, Baku-Azerbaijan, pp. 29-30, September 2017.
- [2] B. Sarımehtem, M. Hamurcu and T. Eren, "Çok Kriterli Karar Verme: Kırıkkale YHT istasyonu-şehir bağlantısının sağlanması", *Demiryolu Mühendisliği*, Vol. 11, pp. 26-40, 2020.
- [3] M. Hamurcu, "Ankara'da Çok Ölçütlü Karar Verme yöntemleriyle monoray güzergâhu belirleme", Yüksek Lisans Tezi, Kırıkkale Üniversitesi, Fen Bilimleri Enstitüsü, Kırıkkale, 2016.
- [4] M. Hamurcu and T. Eren, "Ankara Büyükşehir Belediyesi'nde Çok Ölçütlü Karar Verme Yöntemi ile monoray güzergâh seçimi", *Transist 8. Uluslararası Ulaşım Teknolojileri Sempozyumu ve Fuarı*, İstanbul, Türkiye, pp 410-419, 2015.
- [5] A. Farkas, "Route/site selection of urban transportation facilities: An integrated GIS/MCDM Approach", *In 7th International Conference On Management, Enterprise and Benchmarking*, June, pp. 5-6, 2009.
- [6] H. W. Chang and H. N. Hsieh, "Recreational cycling routes investment selection-hsinchu technopolis case by Applying ZOGP", *Journal Of The Eastern Asia Society For Transportation Studies*, Vol. 10, No. 0, pp. 1227-1242, 2013.
- [7] H. Y. Kim, D. F. Wunneburger and M. Neuman, "High-Speed rail route and regional mobility with A Raster-Based Decision Support System: The Texas Urban Triangle Case", *Journal Of Geographic Information System*, Vol. 5, No. 6, pp. 559, 2013.
- [8] C. Kurlangoğlu, "Coğrafi Bilgi Sistemleri Tabanlı Raylı Sistem Güzergâh Tasarımı: İstanbul Örneği", Doktora Tezi, İstanbul Üniversitesi, Sosyal Bilimler Enstitüsü, İstanbul, 2014.
- [9] N. G. A. Alkawaaz and N. M. Asmael, "A GİS-Assisted optimal BAGHDAD Metro Route Selection based On Multi Criteria Decision Making", *Journal Of Engineering and Development*, Vol. 19, No. 6, pp. 44-58, 2015.
- [10] B. Tezcan, H. M. Alakaş, E. Özcan and T. Eren, "Afet sonrası geçici depo yeri seçimi ve çok araçlı araç rotalama uygulaması: Kırıkkale ilinde bir uygulama", *Politeknik Dergisi*, 2021.
- [11] H. M. Arslan and E. Yavuzylmaz, "Seyahat işletmelerinde Çok Kriterli Karar Verme yöntemleri ile optimum güzergâhın belirlenmesi", *Dicle Üniversitesi Sosyal Bilimler Enstitüsü Dergisi*, Vol. 26, pp. 171-185, 2021.
- [12] H. Güvez, M. Dege and T. Eren, "Kırıkkale'de araç rotalama problemi ile tıbbi atıkların toplanması", *International Journal of Engineering Research and Development*, Vol. 4, No. 1, pp. 41-45, 2012.
- [13] M. Hamurcu and T. Eren, "Kentsel ulaşımında güzergâh belirleme için kullanılan kriterler: literatür araştırması" *Transist 9. Uluslararası Ulaşım Teknolojileri Sempozyumu ve Fuarı*, İstanbul, pp. 280-286, 2016.
- [14] M. Hamurcu and T. Eren, 2017 "Toplu taşıma türünün seçiminde Çok Kriterli Karar Verme uygulaması", *In International Conference on Advanced Engineering Technologies (ICADET)*, Cilt 3, ss. 1-13.
- [15] M. Hamurcu and T. Eren, "Transportation planning with Analytic Hierarchy Process and Goal Programming", *International Advanced Researches and Engineering Journal*, Vol. 2, No. 2, pp. 92-97, 2018.
- [16] İ. C. Özçelik and T. Eren, "Kütahya-Tavşanlı dolmuş hattının Çok Ölçütlü Karar Verme Yöntemleri ile Değerlendirilmesi", *Harran Üniversitesi Mühendislik Dergisi*, Vol. 4, No. 3, pp. 97-111, 2019.
- [17] S. Dinç, M. Hamurcu and T. Eren, "Ankara-Sivas yüksek hızlı tren hattında istasyon yerlerinin seçiminde Çok Kriterli Karar Verme destekli 0-1 Hedef Programlama Modeli", *Demiryolu Mühendisliği*, Vol. 9, pp. 1-16, 2019.
- [18] T. Eren, M. Hamurcu and N. İ. Süt, "Analitik Hiyerarşi Süreci kullanılarak Ankara-Sivas yüksek hızlı tren hat güzergâhının değerlendirilmesi", *Harran Üniversitesi Mühendislik Dergisi*, Vol. 3, No. 3, pp. 22-30, 2018.
- [19] D. Toraman, "Mekansal Çok Ölçütlü Karar Analizi: Ulaştırma İçin Güzergâh Seçenekleri", Yüksek Lisans Tezi, İstanbul Teknik Üniversitesi, Fen Bilimleri Enstitüsü, İstanbul,

- 2009.
- [20] V. Yildirim and S. Bediroglu, "A geographic information system-based model for economical and eco-friendly high-speed railway route determination using analytic hierarchy process and least-cost-path analysis", *Expert Systems*, Vol. 36, No. 3, pp. e12376, 2019.
- [21] Baran E., "Route determination for capacitated vehicle routing problem with two different hybrid heuristic algorithm", *International Journal of Engineering Science and Application*, Vol. 2, No. 2, pp. 41-46, 2018.
- [22] V. Yıldırım, T. Yomralıoğlu, "Nabucco pipeline route selection through Turkey comparison of a GIS-Based Approach to a traditional route selection approach", *Oil Gas European Magazine*, Vol. 37, No. 1, pp. 20-24, 2011.
- [23] L. A. Silman, Z. Barzily and U. Passy, "Planning the route system for urban buses", *Computers & operations research*, Vol. 1, No. 2, pp. 201-211, 1974.
- [24] Z. Wang and S. Zlatanova, "Safe route determination for first responders in the presence of moving obstacles", *Ieee Transactions On Intelligent Transportation Systems*, Vol. 21, No. 3, pp. 1044-1053, 2019.
- [25] G. Navratil, "Curviness as a Parameter for Route Determination", *GI\_Forum*, pp.355-364, 2012.
- [26] S. A. Almasi, M. M. Khabiri, M. F. Tafti and M. Akbarzadeh, "Optimal route determination to provide relief following an earthquake using the traffic density ratio (case study: Isfahan's fire stations)", *Communications-scientific letters of the University of Zilina*, Vol. 23, No. 1, pp. F20-F32, 2021.
- [27] N. Hariharan, S. P. Sankar, V. Vishnu and A. Meignanavel, "Route determining technology using DESBOR and GPS", *In 2010 IEEE International Conference on Computational Intelligence and Computing Research*, pp. 1-6, 2010.
- [28] Y. B. Kang, S. S. Kim, "A new route determination approach using future traffic prediction", *WSEAS Transactions on Systems*, Vol. 4, No. 6, pp. 804-811, 2005.
- [29] Ö. Özkan, "Personel seçiminde karar verme yöntemlerinin incelenmesi: AHP, ELECTRE ve TOPSIS örneği", Yayınlanmamış Yüksek Lisans Tezi, İzmir Dokuz Eylül Üniversitesi Sosyal Bilimler Enstitüsü, 2007.
- [30] T. L. Saaty, "The Analytic Hierarchy Process", McGraw-Hill, USA, 1980.
- [31] Ö. Aydın, "Bulanik AHP ile Ankara için hastane yer seçimi. Dokuz Eylül Üniversitesi İktisadi İdari Bilimler Fakültesi Dergisi, Vol. 24, No. 2, pp. 87-104, 2009.
- [32] T. Eren, T. Danişan, A. Deringöz and G. Aksüt, "Comparison and selection of patient follow-up systems for covid-19 pandemic patients", *Fashion and Textiles*, Vol. 9, No. 1, pp. 1-13, 2022.
- [33] R. Yumuşak, E. C. Özcan, T. Danişan and T. Eren, "AHP – TOPSIS - Tam Sayılı Programlama entegrasyonu ile hidroelektrik santrallarda bakım strateji optimizasyonu", *Uluslararası GAP Yenilenebilir Enerji ve Enerji Verimliliği Kongresi*, pp. 80-84, Şanlıurfa, 10-12 Mayıs, 2018.
- [34] Z. N. Turgut, T. Danişan and T. Eren, "Spor yapanlar için en uygun akıllı saatin AHP ve PROMETHEE yöntemleri ile seçimi", *Uluslararası Beden Eğitimi Spor ve Teknolojileri Dergisi*, Vol. 1, No. 2, pp. 1-11, 2020.
- [35] C. L. Hwang and K. Yoon, "Multiple attribute decision making: Methods and applications", Berlin: Springer, 1981.
- [36] M. Akçay and M. Atak, "Optimal site selection for a solar power plant in Turkey using a hybrid AHP-TOPSIS method", *Celal Bayar University Journal of Science*, Vol. 14, No. 4, pp. 413-420, 2018.
- [37] E. C. Özcan, T. Danişan, R. Yumuşak and T. Eren, "An artificial neural network model supported with multi criteria decision making approaches for maintenance planning in hydroelectric power plants", *Eksploatacja I Niezawodność- Maintenance and Reliability*, Vol. 21, No. 3, pp. 400-418, 2020.
- [38] E. C. Özcan, R. Yumuşak and T. Eren, "Risk Based Maintenance in the Hydroelectric Power Plants", *Energies*, Vol. 12, pp. 1502-1523, 2019.
- [39] J. P. Brans, "L'ingenierie de la decision: Elaboration d'instruments d'aide a la decision. La Methode

- PROMETHEE", Universite Laval, Colloque d'aide a la Decision, Quebec, Canada, pp. 183- 213, 1982.
- [40] S. E. Dinçer, E. Ekin and K. S. Karakaş, "Promethee yöntemiyle uçak komponentlerinin önceliklendirilmesi problemlerine çözüm yaklaşımı", *Sosyal Bilimler Araştırma Dergisi*, Vol. 6, No. 3, pp. 106-125, 2017.
- [41] M. Taş, Ş. N. Özlemiş, M. Hamurcu and T. Eren, "Ankara'da AHP ve PROMETHEE yaklaşımıyla monoray hat tipinin belirlenmesi", *Ekonomi İşletme Siyaset ve Uluslararası İlişkiler Dergisi*, Vol. 3, No. 1, pp. 65-8, 2017.
- [42] E. Yazıcı, H. M. Alakaş, S. Cebeci, E. E. Yılmaz and Eren T., "Toplu ulaşım sistemlerinde araç tipi seçimi: Kırıkkale kampüs hattı örneği", *Kırıkkale Üniversitesi Sosyal Bilimler Dergisi*, Vol. 11, No. 1, pp. 269-287, 2021.
- [43] S. Dinç, M. Hamurcu and Eren T., "Kırıkkale kampüs dolmuş hattı etkinliğinin Çok Kriterli Karar Verme ile değerlendirilmesi", *Mehmet Akif Ersoy Üniversitesi Fen Bilimleri Enstitüsü Dergisi*, Vol. 9, No. 1, pp. 238-247, 2018.
- [44] K. Üke, "AHP yöntemi ile Çorum şehrinde avm kuruluş yeri seçimi", Yüksek Lisans Tezi, Hitit Üniversitesi, Sosyal Bilimler Enstitüsü, Çorum, 2016.
- [45] A. Diler, M. Tektanlı, C. Soruşbay and M. Ergeneman, "Doğalgaz yakıtlı otobüslerin sera gazı emisyonlarına etkisi", Hava Kirliliği ve Kontrolü Ulusal Sempozyumu-2008, Hatay, pp. 244-255, 22-25 Ekim 2008.



## NEW METRIC FOR THE CALCULATION OF SENSITIVITY ANALYSIS INDEX OF FLEXIBLE PAVEMENT USING MECHANISTIC-EMPIRICAL APPROACH, TURKEY-CASE STUDY

<sup>1,2,\*</sup>Saadoon Obaid EYADA , <sup>3</sup>Osman Nuri ÇELİK , <sup>4</sup>Nibras Y. ABDULLA 

<sup>1</sup>Konya Technical University, Civil Engineering Department, Konya, TÜRKİYE

<sup>2</sup>Anbar Health Directorate, Iraqi Ministry of Health, Ramadi, Anbar, IRAQ

<sup>3</sup>Konya Technical University, Civil Engineering Department, Konya, TÜRKİYE

<sup>4</sup>Anbar University, Biology Department, College of Science, Ramadi, Anbar, IRAQ

<sup>1,2</sup>saadooneyada@gmail.com, <sup>3</sup>oncelik@ktun.edu.tr, <sup>4</sup>nib19s3017@uoanbar.edu.iq

(Received: 07.06.2023; Accepted in Revised Form: 18.07.2023)

**ABSTRACT:** The application of new Mechanistic-Empirical Pavement Design Method (M-EDM) in Turkey needs a huge data about the materials properties under specific climate and traffic conditions. Sensitivity Analysis (SA) can reduce time, effort and cost required for the determination and collection of this data. One-At-a-Time (OAT) SA was conducted using different Quantitative and Qualitative methods. Graphical, Normalized Sensitivity Index NSI and Distance Sensitivity Index DSI were used to determine the most sensitive factors (property). DSI was used for the first time in this study to conduct SA for both continuous and categorical parameters using one equation. Two climate regions, three traffic categories and different types of asphalt were used. MnPave software was used to conduct Mechanistic-Empirical analysis. The results were important and many conclusions and recommendations were reported.

**Keywords:** Mechanistic-Empirical Design Method, Sensitivity Analysis, Normalized Sensitivity Index, Premature deterioration, MnPave, Distance Sensitivity Index, Turkey

### 1. INTRODUCTION

The application of new Mechanistic-Empirical Pavement Design Method (M-EDM) in Turkey needs a huge data about the materials properties under specific climate and traffic conditions. The collection of such a data is costly and time consuming. The Sensitivity Analysis (SA) can reduce time, effort and cost required for the determination and collection of this data by focusing on the most important (very sensitive and sensitive) properties that have a significant effect on pavement life and performance. So, one of the main objectives of this research is to conduct a SA of Typical Pavement Sections (TTS) in Turkey as a part of the implementation of M-EDM in Turkey.

The M-EDM analysis cannot be made by hand, so the MnPave design software developed by Minnesota Department of Transportation MDOT in the USA is used. The analysis is conducted using the Base and Base (+/-20%) of the property using One At a Time OAT analysis by changing one factor at a time which is called Local Sensitivity Analysis.

#### 1.1. Objectives

One of the main objectives of this study are:

Starting the first steps towards the application of M-EDM in Turkey.

Determinations of Material, Traffic and Climate properties (Factors) that have a significant effect on pavement performance (pavement life). This can reduce the time and effort required for collection of data about less important.

## 1.2. Sensitivity Metrics

One-At-a-Time (OAT) sensitivity analysis is the commonly used method to conduct SA. In OAT, each potentially sensitive design input is varied individually for a given base case or reference condition in order to assess qualitatively and quantitatively the local sensitivity of the predicted output (pavement life). There are two types of OAT:

### 1.1.1. Qualitative Sensitivity Analysis (Graphical Assessment Method)

In this method, the assessment of the importance of each factor is based on its range or span in the scheme. The higher span can be considered very sensitive and so on. The assessment of this method is highly dependent on human assessment so it's expected that its results would be less accurate.

### 1.1.2. Quantitative Sensitivity Analysis

This method is depends on mathematical evaluation, so it's expected that the results will be more accurate. Two methods are used:

#### 1.1.1.1. Normalized Sensitivity Index NSI

The NSI always uses the design limit as the normalizing factor for the predicted design life as shown in Equation 1 for most design inputs. However, in some cases the design input can be categorical rather than continuous (e.g., binder grade). For these design inputs, a modified non-normalized NSI Equation 2 is used:

$$NSI = \frac{\Delta y}{\Delta x} \times \frac{X_{base}}{DL} \quad (1)$$

$$NSI = \frac{\Delta y}{DL} \quad (2)$$

In which ( $\Delta y$ ) is the change in pavement life ( Fatigue or rutting life) caused by the change in property magnitude from the base ( $\Delta x$ ) ( e.g. changing base layer thickness +20% from base), ( $X_{base}$ ) is the base of the property and (DL) is the design life (assumed 20 years).

#### 1.1.1.2. Distance Sensitivity Index DSI

It can be seen that NSI method needs two different equations to calculate NSI. It is prefer to find new method to solve this problem so that the results can be compared. Distance Sensitivity Index method is one of the results of this study and it can be used to conduct SA for both continuous and categorical parameters using one equation. The method is depends on the distance between the resulted Fatigue Life (FL) or Rutting Life (RL) at (Base+/- 20%) case and that at Base case. Figure 1. shows the scheme of this method.

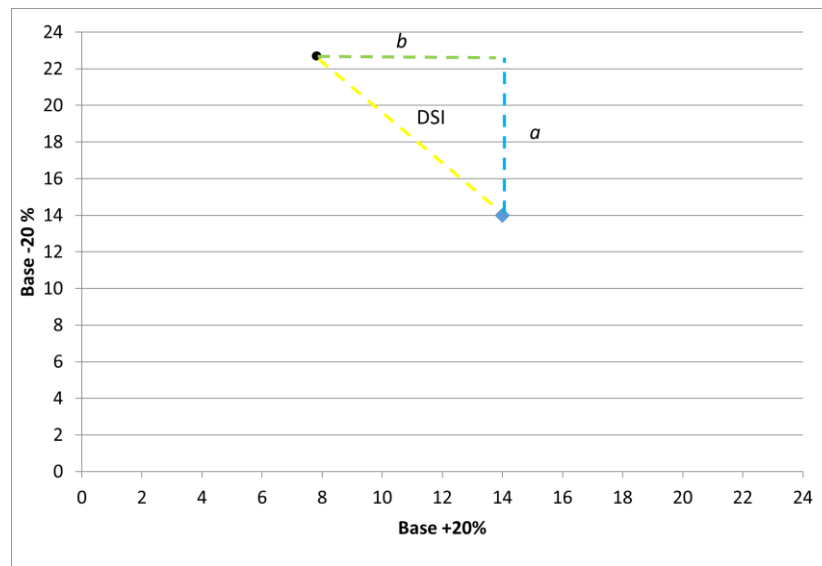


Figure 1. Scheme of DSI method

Equations 3 through 5 can be used for the calculation of DSI. These equations can be used for both categorical and continuous values.

$$DSI = \sqrt{a^2 + b^2} \tag{3}$$

$$a=(y_1-z_0) \tag{4}$$

$$b=(x_1-z_0) \tag{5}$$

where:

y<sub>1</sub>: the RL or FL (or distress) at (Base-20%)

x<sub>1</sub>: the RL or FL (or distress) at (Base+20%)

z<sub>0</sub>: the RL or FL (or distress) at Base.

An example of the method can be shown Table 1 for FL.

Table 1. Example of the parameters used in the calculations of DSI.

Parameter	FL at Base (z <sub>0</sub> )	FL at Base+20% (x <sub>1</sub> )	FL at Base-20% (y <sub>1</sub> )	DSI
Value	14	8	23	
Equation used for calculation	-	a=(x <sub>1</sub> -z <sub>0</sub> )=-6	a=(y <sub>1</sub> -z <sub>0</sub> )=9	$DSI = \sqrt{a^2 + b^2}$
				11.18

## 2. LITERATURE REVIEW

Traffic, material and climate data collection is one of the most Time and Effort-Consuming stage in the Implementation of M-EDM. Not all data at the same level of importance and have the same effect on the results of design, so it is important that the SA be conducted to shadow the light on the properties and factors that have a significant effect on the results of pavement performance [1-5].

Researchers and transportation authorities started the implementation plan of M-EDM by conducting SA to reduce the time and effort required for collection of data of less significance.

NCHRP Report 1-47 was the unique among the SA studies which reviewed recently SA researches and identified several main problems common to existing literature. Within the scope of

this report Schwartz et al. undertook a detailed two-part SA involving an initial OAT analysis followed by a Global Sensitivity Analysis (GSA) [6].

Compared to OAT, the GSA allowed inputs to be varied simultaneously across their entire problem domain. This allows to look for interactions between design inputs. GSA is much more computationally intensive than a traditional OAT. Sensitivity results in NCHRP 1-47 were reported in terms of NSI.

The results of GSA revealed that [7]:

- HMA E\* Alpha Parameter,
- HMA E\* Delta Parameter and
- HMA Thickness.

were Hypersensitive, while :

- Base Resilient Modulus,
- HMA Poisson's Ratio,
- Subgrade Resilient Modulus,
- Base Thickness and
- Operational Speed. were Very sensitive.

In Florida state, SA were performed on material property inputs at different hierarchical levels using OAT. The flexible pavement consisted of four layer structure. An AADTT of 70,000, 20 year design period, and Orlando climatic input were used in the analyses. The M-EDM software was used for conducting SA by adjusting each input within an acceptable range. Variables with high sensitivity based on predicted performance were found to be:

- AC dynamic modulus,
- Layer thickness,
- Base modulus,
- Subgrade modulus,

It was found that the pavement with a higher AC modulus were perform better. The results provided information on how to proceed with establishing the input database [8].

The OAT SA of the M-EDM performance predictions to input parameters was studied in Maryland. Typical sections were selected. The studied parameters include: base and asphalt layer thickness, traffic loadings, design criteria, material properties, performance model parameters, and climate. The results showed that :

- Base thickness,
- Class 9 percentage trucks as the vehicle class,
- Temperature and precipitation,
- Binder grade and
- Asphalt concrete material properties.

were the most sensitive parameters [9].

Minnesota Department of Transportation MnDoT conducted SA for flexible pavements at 20 year design life and two different traffic levels, 10 and 1 million ESAL. SA was made by changing specific inputs within a reasonable range from the base values. For the 10 million ESAL analyses, longitudinal cracking was shown to be highly sensitive to:

- Asphalt concrete layer thickness and
- Soil type.

For transverse cracking the most sensitive parameters were found to be climate, asphalt concrete layer thickness, and asphalt concrete binder grade. While asphalt concrete layer thickness was found to be the only highly sensitive input for rutting and alligator cracking [10].

Focusing on traffic inputs, SA was performed using data from five LTPP sites in New Jersey. OAT



analysis was conducted using M-EDM default values as a base values. It has been found that [11] :

- Rutting was highly sensitive to the monthly adjustment factor and number of axles per truck.
- Alligator cracking was found to be sensitive to the hourly distribution of truck traffic and number of axles per truck.
- Longitudinal cracking was also sensitive to hourly distribution of truck traffic and the monthly adjustment truck factor.

North Carolina utilized data from 27 LTPP sections to conduct SA. The pavement structures were divided by pavement type and climatic area. The SA was associated with materials and traffic inputs. The results of the study found that [12]:

- Alligator cracking was sensitive to air voids and dynamic modulus.
- Longitudinal cracking was sensitive to air voids, dynamic modulus, and surface shortwave absorptivity.
- Rutting was sensitive to the asphalt mixture dynamic modulus.

Table 2 below summarizes significant M-EDM inputs in some states in the USA according to SA [13].

**Table 2.** Results of SA in different states in the USA.

State	Inputs (Properties)
Florida	HMA Dynamic Modulus
	HMA Layer Thickness
	Base Modulus
	Subgrade Modulus
	Coefficient of Thermal Expansion
	Joint Spacing
	Dowel Bar Diameter
Maryland	PCC Compressive Strength
	HMA Layer Thickness
	Vehicle Class Distribution
	Climatic Location
	HMA Binder Content
	HMA Air Voids
Minnesota	Subgrade Modulus
	Soil Type
	Climatic Location
	HMA Binder Grade
	Traffic Volume
	Slab Thickness
New Jersey	Base Thickness
	Coefficient of Thermal Expansion
	Monthly Adjustment Factor
	Number of Axles Per Truck
North Carolina	Hourly Distribution of Traffic
	HMA Air Voids
	HMA Dynamic Modulus
	Surface Shortwave Absorptivity
	Coefficient of Thermal Expansion
	Thermal Conductivity
	Joint Spacing
Dowel Bar Diameter	

### 3. METHODOLOGY

As mentioned previously, the SA is conducted using OAT approach. NSI and DSI metrics were used. It is claimed that DSI is used in this work for the first time. Figure 2 shows the implementation plan used to conduct SA.

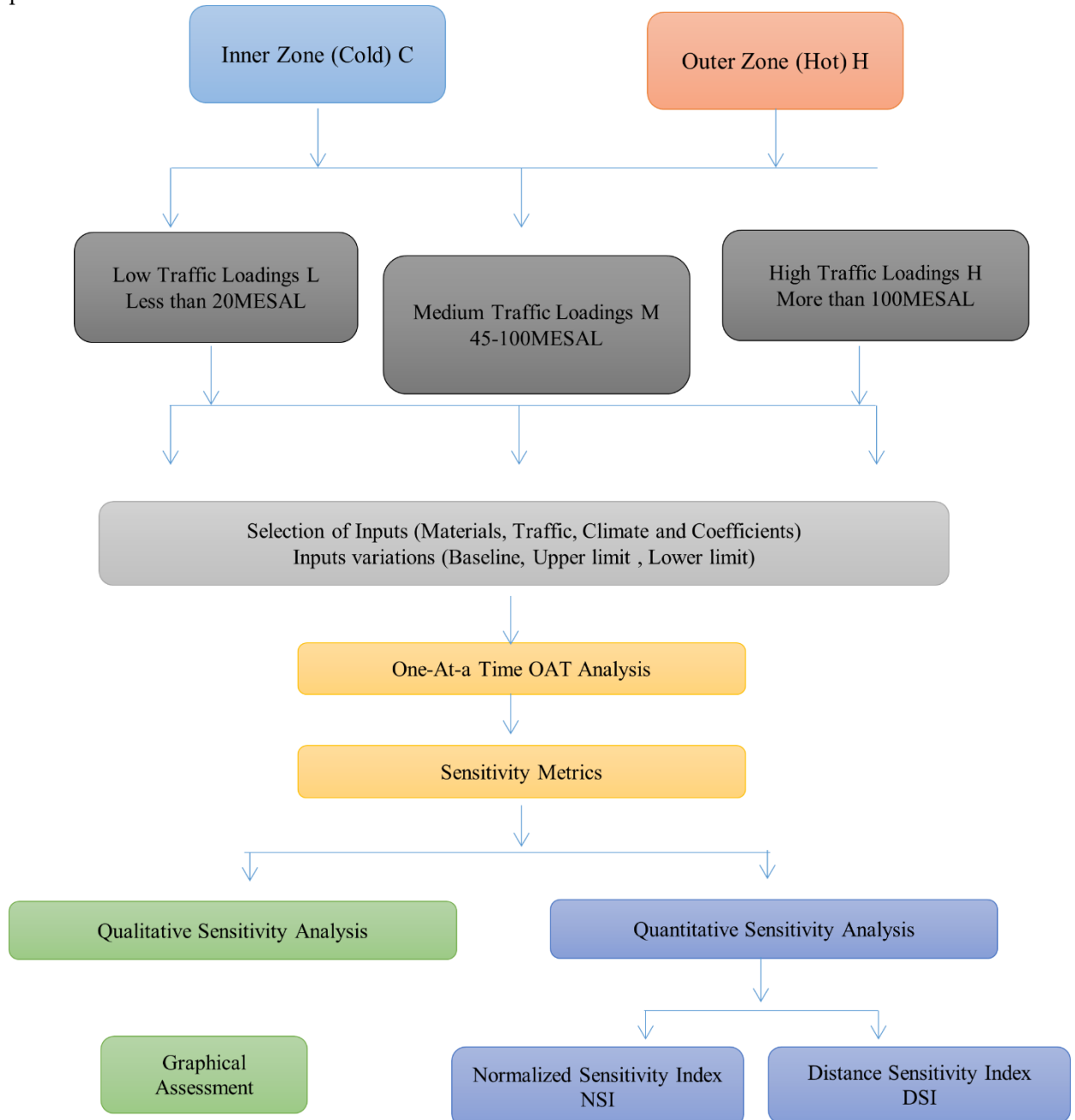


**Figure 2.** Methodology plan of SA

#### 3.1. Inputs

The Inputs (variables) used in SA are collected from available resources (e.g. Turkish standards, specifications, manuals and literature). Inputs associated with climate, materials and traffic typical values of Turkey are used for SA. The value of each input is varied from the Base case by  $\pm 20\%$ .

### 3.1.1. General Inputs

The general inputs are those still constant during conducting SA. Table 3 tabulates these inputs and their values.

**Table 3.** General inputs in SA

Input	Value	Unit
Design life	20	year
Confidence level	70	%

#### 3.1.1.1. Climate Inputs

To show the effect of climate on SA of different variables, two climatic zones are selected:

1- The Inner Region (Cold). This region is denoted as Co. Afyon city in Turkey is selected to represents the Cold region.

2- The Outer Region (Hot). This region is denoted as Ho. Antalya city in Turkey is selected to represents the Cold region.

The climate inputs used in the SA under each climate and traffic condition are shown in Table 4.

**Table 4.** Climate Inputs and Ranges for M-EDM Sensitivity Analysis.

Inputs	Abbreviations	Values		
		-20%	Base	+20%
Depth (z) in Pavement Temperature Equation, (Ratio of (z))	ZD	1/5	1/3	1/2

#### 3.1.1.2. Traffic Inputs

The traffic loadings of each climatic zone can be divided into the groups shown in Table 5. Traffic is represented by Million Equivalent Single Axle Loads (MESAL). Traffic loading is sub grouped into three different groups to represent High, Medium and Low traffic condition. This can identify the effect of traffic loading variation on SA results.

**Table 5.** Traffic Inputs and ranges for M-EDM Sensitivity Analysis for Cold and Hot regions.

Inputs	Abb.	Traffic Category								
		Low (L) 3-20 MESAL			Medium (M) 45-100 MESAL			High (H) 150-200 MESAL		
		-20%	Base	+20%	-20%	Base	+20%	-20%	Base	+20%
Traffic Loadings, MESAL	TRL	9.2	11.5	13.8	58	72.5	87	140	175	210
Speed, Km/h	SP	48	60	72	48	60	72	48	60	72
Tire Pressure, kpa	TP	442	552	662	442	552	662	442	552	662
Axle Weight, kN	AW	64	80	96	64	80	96	64	80	96
Growth Rate (Simple), %	GR	2.4	3	3.6	2.4	3	3.6	2.4	3	3.6

### 3.1.1.3. Materials Inputs

Materials inputs can be discussed in the following subsections.

#### 3.1.1.3.1. Asphaltic Layers Inputs

The TTS consists of three asphaltic layers:

- Surface layer.
- Binder layer.
- Base layer.

Each layer is a HMA layer. The inputs of each layer under each climate region and traffic category are shown in Tables 6 through 9.

According to Flexible Pavement Design Catalogue of Turkey, asphalt types are the same for all traffic conditions. Therefore and for the Base cases, asphalt types used in SA are assumed to be fixed for all traffic conditions. At the same time the Performance Grade PG of each Base case is shifted one degree upward and downward from the Base case according to the catalogue.

**Table 6.** Inputs of Asphaltic layers and ranges for SA for H and C regions under All Traffic Categories.

Layer type	Inputs	Abbr.	Inputs values		
			-20%	Base	+20%
Surface layer	Percentage of binder, %	Pb	4.4	5.5	6.6
	Percentage passing sieve 3/4, %	P3/4-S	66.7	83.3	100
	Percentage passing sieve 3/8, %	P3/8-S	64.8	81	97.2
	Percentage passing sieve 1/2, %	P1/2-S	37.6	47	56.4
	Percentage passing sieve No.200, %	P200-S	4.4	5.5	6.6
Binder layer	Percentage of binder, %	Pb-B	4	5	6
	Percentage passing sieve 3/4, %	P3/4-B	66.7	83.3	100
	Percentage passing sieve 3/8, %	P3/8-B	47.2	59	70.8
	Percentage passing sieve 1/2, %	P1/2-B	32.8	41	49.2
	Percentage passing sieve No.200, %	P200-B	3.6	4.5	5.4
Base layer	Percentage of binder, %	Pb-Ba	2.8	3.5	4.2
	Percentage passing sieve 3/4, %	P3/4-Ba	66.7	83.3	100
	Percentage passing sieve 3/8, %	P3/8-Ba	60	75	90
	Percentage passing sieve 1/2, %	P1/2-Ba	45.2	56.5	67.8
	Percentage passing sieve No.200, %	P200-Ba	3.6	4.5	5.4
All layers	Asphalt type, PG <sup>a</sup> (for Hot Region)	PGH	PG 64-10	PG 70-10	PG 76-10
	Asphalt type, PG <sup>a</sup> (for Cold Region)	PGC	PG 58-28	PG 64-28	PG 70-28
	Air voids at bottom of HMA layer, %	AV	4.8	6	7.2
	Poisson ratio	PR	0.38	0.41	0.44
	Bulk specific gravity of aggregate.	Gbs	2.12	2.65	3.18

<sup>a</sup> Asphalt types are the same for all asphaltic layers (Surface, Binder and Base).

**Table 7.** Thicknesses of asphaltic layers and ranges for SA for Ho and Co regions under Low traffic category.

Layer type	Inputs	Abbr.	L (3-20) MESAL		
			Inputs values		
			-20%	Base	+20%
Surface layer	Layer thickness, cm	ASTH.	4	5	6
Binder layer	Layer thickness, cm	ABiTH.	5.6	7	8.4
Base layer	Layer thickness, cm	ABaTH.	6.4	8	9.6

**Table 8.** Asphaltic layers thicknesses and ranges for M-EDM SA for Ho and Co regions under Medium Traffic Category.

Layer type	Inputs	Abbreviations	M (45-100) MESAL		
			-20%	Base	+20%
Surface layer	Layer thickness, cm	ASTH.	4	5	6
Binder layer	Layer thickness, cm	ABiTH.	8	10	12
Base layer	Layer thickness, cm	ABaTH.	8.8	11	13.2

**Table 9.** Asphaltic Layers Thicknesses and ranges for M-EDM SA for Ho and Co regions under High traffic category.

Layer type	Inputs	Abbreviations	H (150-200) MESAL		
			-20%	Base	+20%
Surface layer	Layer thickness, cm	ASTH.	4	5	6
Binder layer	Layer thickness, cm	ABiTH.	9.6	12	14.4
Base layer	Layer thickness, cm	ABaTH.	11.2	14	16.8

**3.1.1.3.2. Plant Mix Base PMB layer.**

The properties of PMB layer used in the SA for all climate zones (Ho and Co) and under different traffic categories (H, M and L) are shown in Table 10.

**Table 10.** Plant Mix Base PMB layer properties and ranges for SA of Ho and Co regions under all traffic categories.

Layer type	Inputs	Abbreviations	All Traffic categories		
			-20%	Base	+20%
Plant Mix Base PMB layer	Layer thickness, cm	PMBTH.	16	20	24
	MR, Mpa	PMBMR	176.8	221	265.2
	Poisons ratio.	PMBPR.	0.29	0.36	0.43

**3.1.1.3.3. Sub Base SB Layer**

The properties of SB layer used in the SA for all climate zones (Ho and Co) and under different traffic categories (H, M and L) are shown in Table 11.

**Table 11.** Sub Base SB Layer Properties and ranges for M-EDM SA for Ho and Co regions for All Traffic Categories.

Layer type	Inputs	Abbreviations	All traffic categories		
			-20%	Base	+20%
Sub Base SB Layer	Layer thickness, cm	SBTH.	16	20	24
	MR, Mpa	SBMR	99.6	124.5	149.4
	Poisons ratio.	SBPR.	0.29	0.36	0.43

**3.1.1.3.4. Sub Grade SG Layer**

The properties of SG layer used in the SA for all climate zones (Ho and Co) and under different

traffic categories (H, M and L) are shown in Table 12.

**Table 12.** Subgrade layer properties and ranges for M-EDM SA for Ho and Co regions for All Traffic Categories.

Layer type	Inputs	Abbreviations	All traffic categories		
			Inputs values		
			-20%	Base	+20%
Sub Base SB Layer	MR, Mpa	SGMR	48.8	61	73.2
	Poissons ratio.	SGPR.	0.26	0.32	0.38

## 4. RESULTS AND DISCUSSION

The results are discussed under each climate condition as in the following subsections.

### 4.1. Results of Cold Climate Condition

Afyon city was selected to represent cold climate condition in Turkey. MnPave design software was used for conducting the M-E analysis. The screenshot of the software is shown in Figure 3. MnPave software is used by the MDoT for the M-E design of flexible pavement. The M-EDM analysis is conducted using MnPave software for the determination of FL and RL of TTS under different traffic categories (L, M and H) for Base and Base +/-20% cases. Different methods are used to conduct SA as in the following subsections.

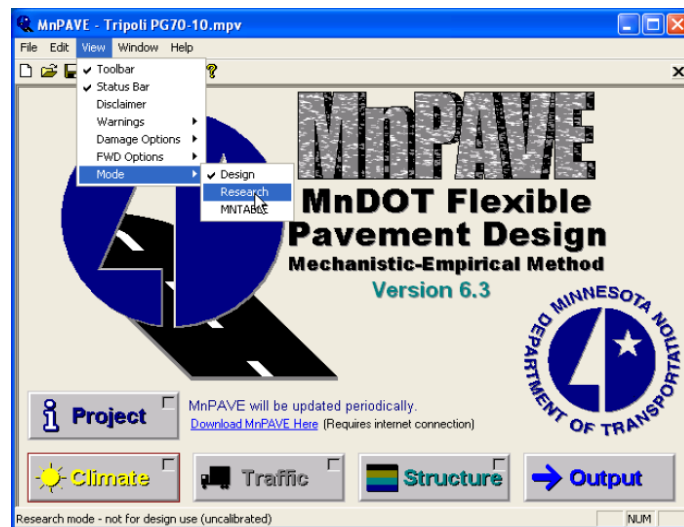


**Figure 3.** Screenshot of MnPave software.

#### 4.1.1. Qualitative Sensitivity Analysis (Graphical Assessment Method)

The results of SA using graphical method under Light, Medium and High traffic conditions are shown in Figure 4 through 9.

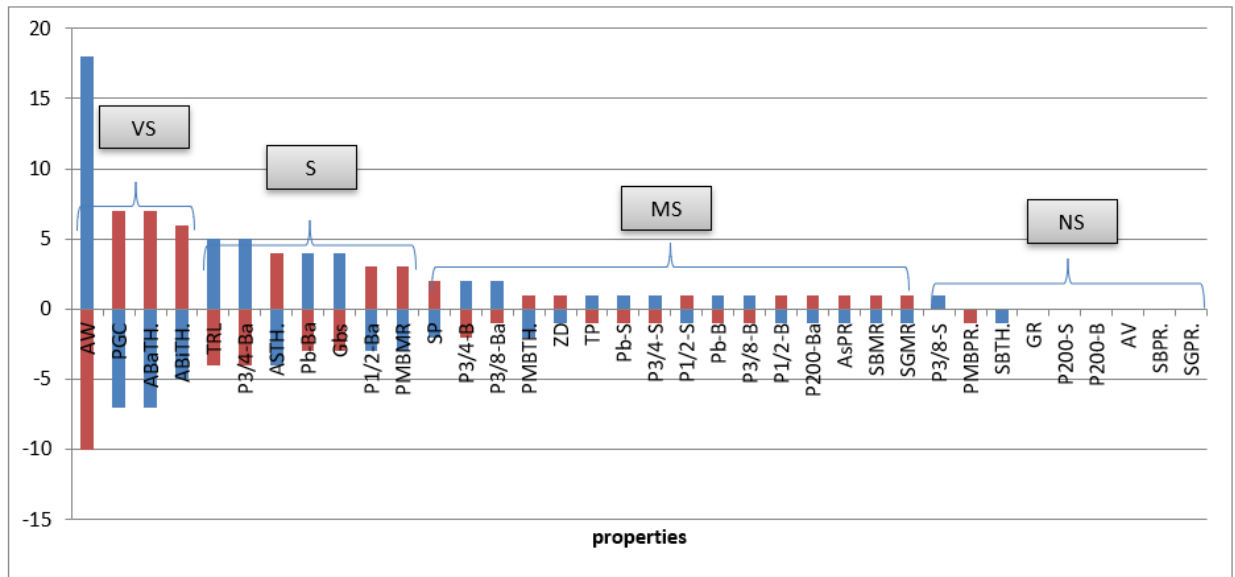


Figure 4. SA results under Light Traffic condition and Cold Climate for FL.

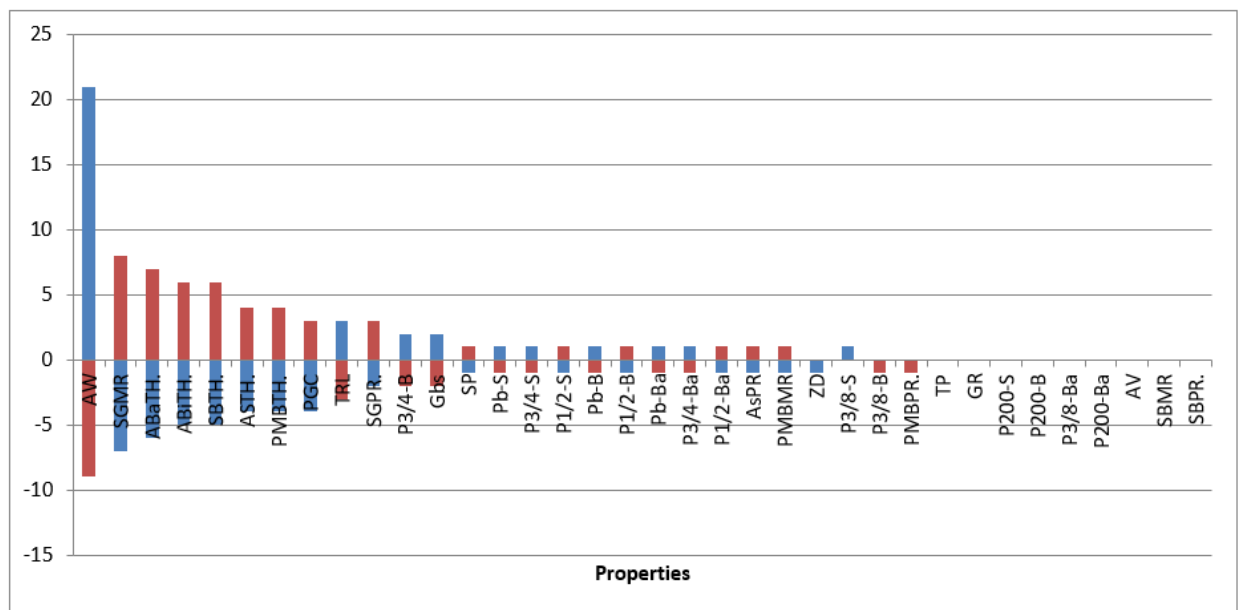


Figure 5. SA results under Light Traffic condition and Cold Climate for RL.

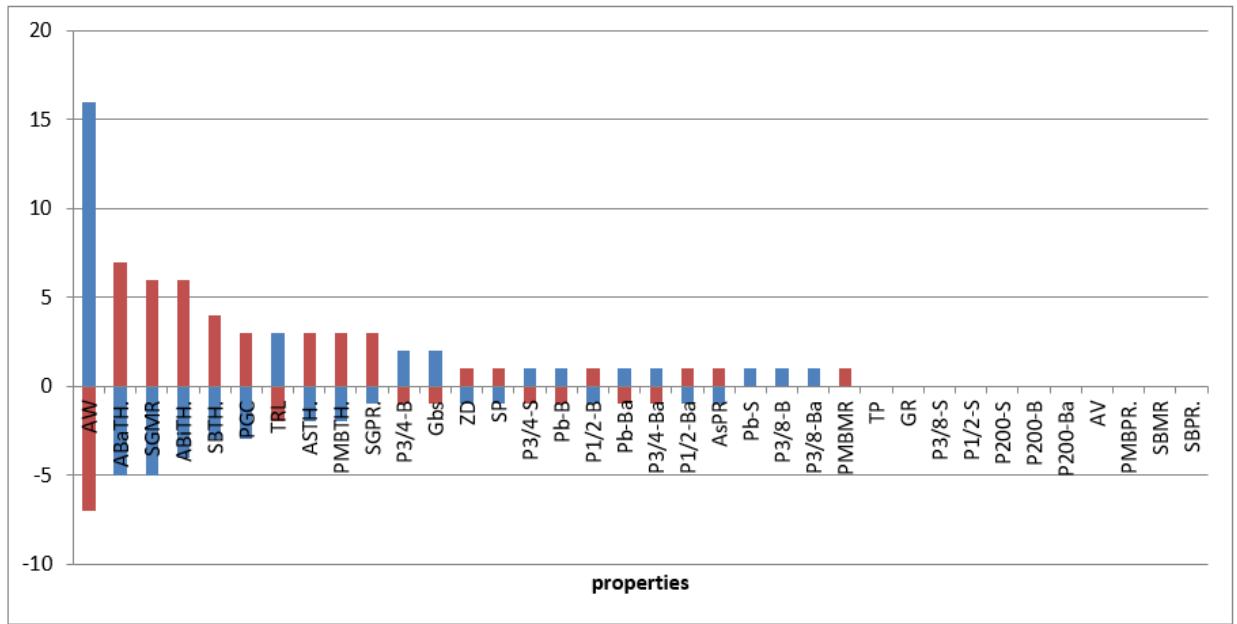


Figure 6. SA results under Medium Traffic condition and Cold Climate for RL.

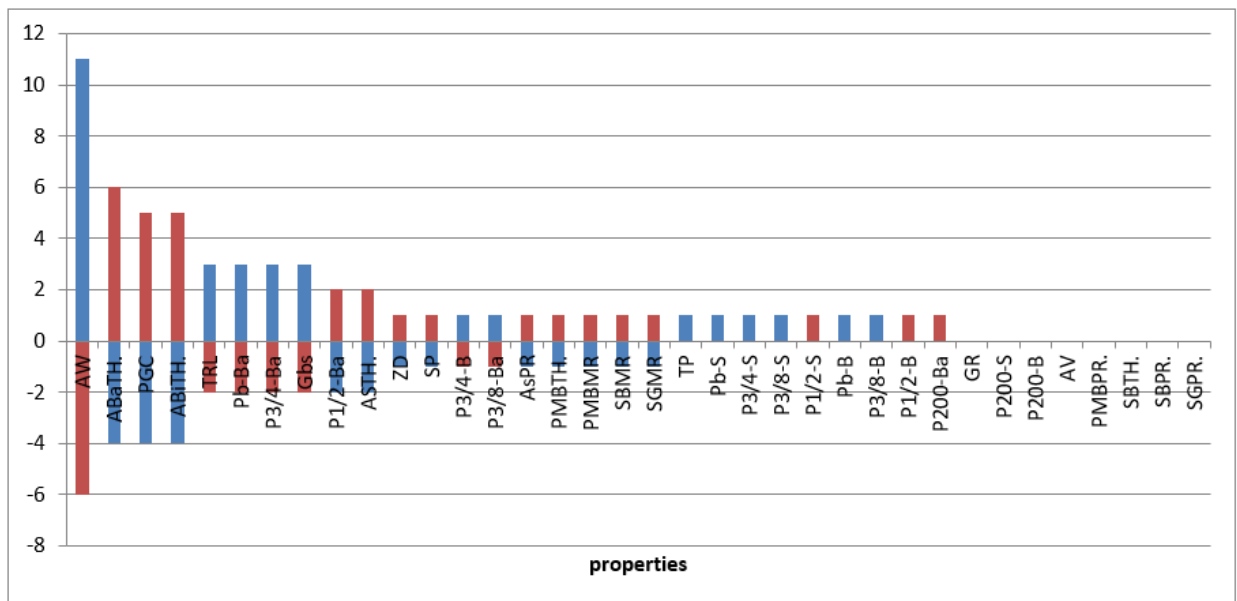


Figure 7. SA results under Medium Traffic condition and Cold Climate for FL.



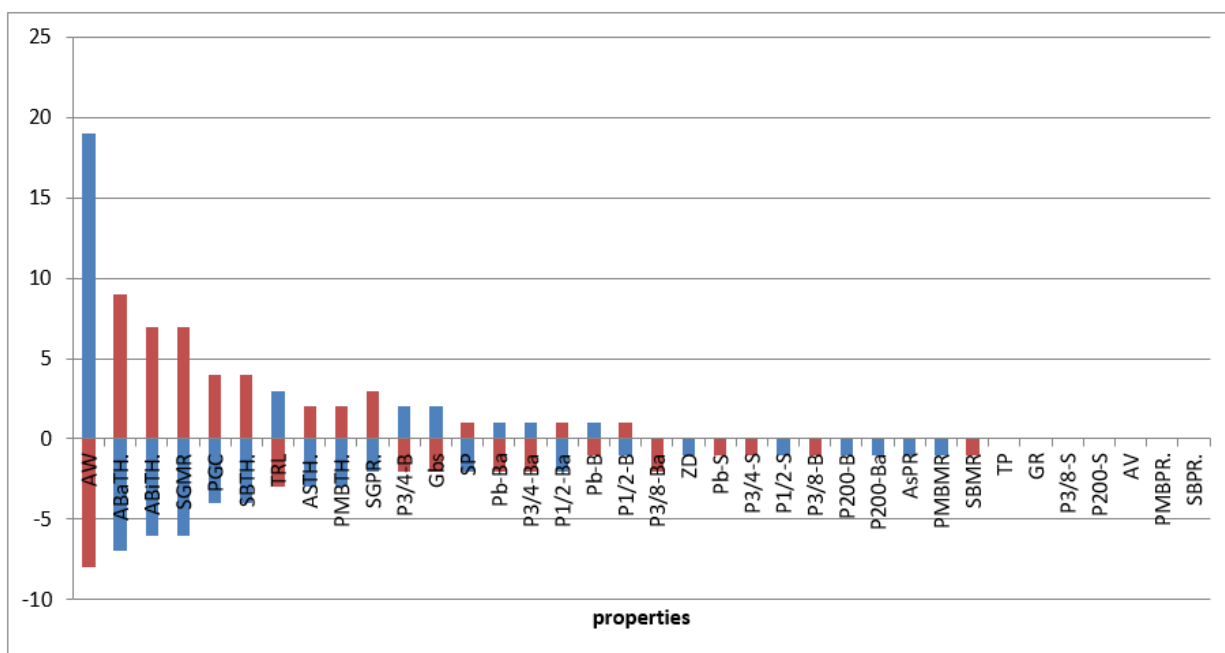


Figure 8. SA results under High Traffic condition and Cold Climate for RL.

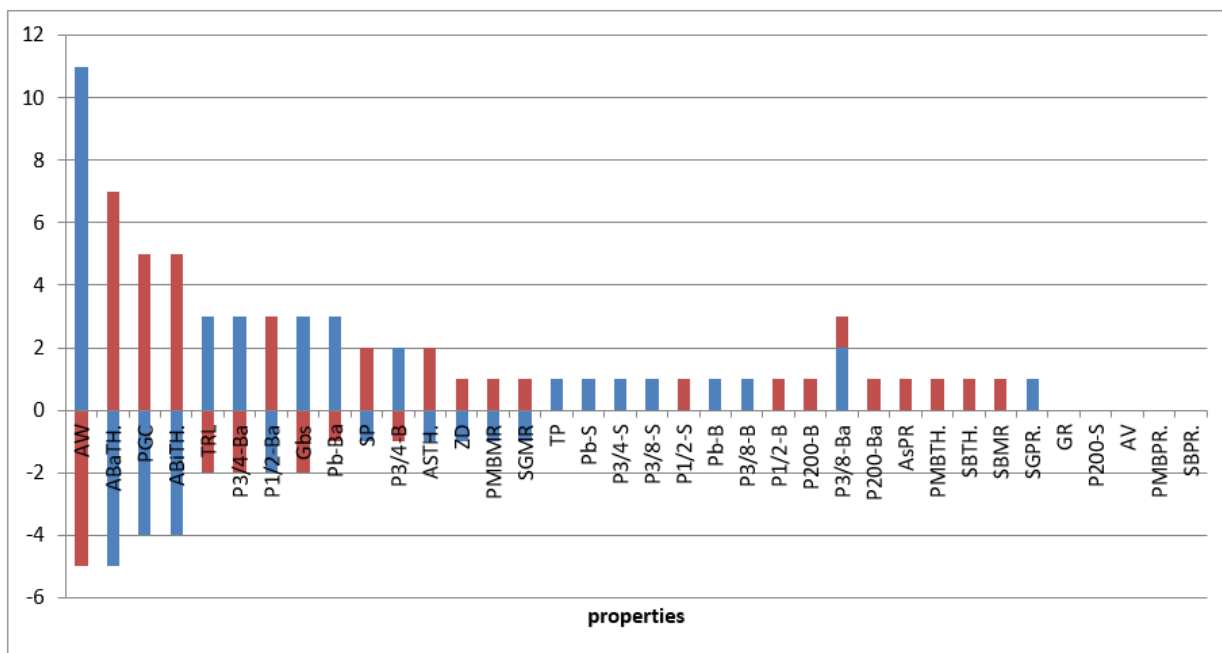


Figure 9. SA results under High Traffic condition and Cold Climate for FL.

The results of graphical method are classified graphically into, Very Sensitive (VS), Sensitive (S), Medium Sensitive (MS) and Non Sensitive (NS) as shown in Figure 4. To make a comparison between graphical method and other metrics of SA, the results are classified as shown in Tables 13 through 15.

**Table 13.** SA metrics of graphical method under Light traffic and Cold climate conditions for RL and FL

Property	Sensitivity index		Property	Sensitivity index	
	RL			FL	
AW	VS		AW	VS	
SGMR	VS		PGC	VS	
ABaTH.	VS		ABaTH.	VS	
ABiTH.	VS		ABiTH.	VS	
SBTH.	VS		TRL	S	
ASTH.	S		P3/4-Ba	S	
PMBTH.	S		ASTH.	S	
PGC	S		Pb-Ba	S	
TRL	S		Gbs	S	
SGPR.	S		P1/2-Ba	S	
P3/4-B	S		PMBMR	S	
Gbs	S		SP	MS	
SP	MS		P3/4-B	MS	
Pb-S	MS		P3/8-Ba	MS	
P3/4-S	MS		PMBTH.	MS	
P1/2-S	MS		ZD	MS	
Pb-B	MS		TP	MS	
P1/2-B	MS		Pb-S	MS	
Pb-Ba	MS		P3/4-S	MS	
P3/4-Ba	MS		P1/2-S	MS	
P1/2-Ba	MS		Pb-B	MS	
AsPR	MS		P3/8-B	MS	
PMBMR	MS		P1/2-B	MS	
ZD	NS		P200-Ba	MS	
P3/8-S	NS		AsPR	MS	
P3/8-B	NS		SBMR	MS	
PMBPR.	NS		SGMR	MS	
TP	NS		P3/8-S	NS	
GR	NS		PMBPR.	NS	
P200-S	NS		SBTH.	NS	
P200-B	NS		GR	NS	
P3/8-Ba	NS		P200-S	NS	
P200-Ba	NS		P200-B	NS	
AV	NS		AV	NS	
SBMR	NS		SBPR.	NS	
SBPR.	NS		SGPR.	NS	

**Table 14.** SA metrics of graphical method under Medium traffic and Cold climate conditions for RL and FL.

Property	Sensitivity index		Property	Sensitivity index	
	RL			FL	
AW	VS		AW	VS	
ABaTH.	VS		ABaTH.	VS	
SGMR	VS		PGC	VS	
ABiTH.	VS		ABiTH.	VS	
SBTH.	VS		TRL	S	
PGC	S		Pb-Ba	S	
TRL	S		P3/4-Ba	S	
ASTH.	S		Gbs	S	
PMBTH.	S		P1/2-Ba	S	
SGPR.	S		ASTH.	S	
P3/4-B	S		ZD	MS	
Gbs	S		SP	MS	
ZD	MS		P3/4-B	MS	
SP	MS		P3/8-Ba	MS	
P3/4-S	MS		AsPR	MS	
Pb-B	MS		PMBTH.	MS	
P1/2-B	MS		PMBMR	MS	
Pb-Ba	MS		SBMR	MS	
P3/4-Ba	MS		SGMR	MS	
P1/2-Ba	MS		TP	MS	
AsPR	MS		Pb-S	MS	
Pb-S	MS		P3/4-S	MS	
P3/8-B	MS		P3/8-S	MS	
P3/8-Ba	MS		P1/2-S	MS	
PMBMR	MS		Pb-B	MS	
TP	NS		P3/8-B	MS	
GR	NS		P1/2-B	MS	
P3/8-S	NS		P200-Ba	MS	
P1/2-S	NS		GR	NS	
P200-S	NS		P200-S	NS	
P200-B	NS		P200-B	NS	
P200-Ba	NS		AV	NS	
AV	NS		PMBPR.	NS	
PMBPR.	NS		SBTH.	NS	
SBMR	NS		SBPR.	NS	
SBPR.	NS		SGPR.	NS	

**Table 15.** SA metrics of graphical method under High traffic and Cold climate conditions for RL and FL.

Property	Sensitivity index		Property	Sensitivity index	
	RL			FL	
AW	VS		AW	VS	
ABaTH.	VS		ABaTH.	VS	
ABiTH.	VS		PGC	VS	
SGMR	VS		ABiTH.	VS	
PGC	S		TRL	S	
SBTH.	S		P3/4-Ba	S	
TRL	S		P1/2-Ba	S	
ASTH.	S		Gbs	S	
PMBTH.	S		Pb-Ba	S	
SGPR.	S		SP	S	
P3/4-B	S		P3/4-B	S	
Gbs	S		ASTH.	S	
SP	S		ZD	MS	
Pb-Ba	S		PMBMR	MS	
P3/4-Ba	S		SGMR	MS	
P1/2-Ba	S		TP	MS	
Pb-B	S		Pb-S	MS	
P1/2-B	S		P3/4-S	MS	
P3/8-Ba	S		P3/8-S	MS	
ZD	MS		P1/2-S	MS	
Pb-S	MS		Pb-B	MS	
P3/4-S	MS		P3/8-B	MS	
P1/2-S	MS		P1/2-B	MS	
P3/8-B	MS		P200-B	MS	
P200-B	MS		P3/8-Ba	MS	
P200-Ba	NS		P200-Ba	MS	
AsPR	NS		AsPR	MS	
PMBMR	NS		PMBTH.	MS	
SBMR	NS		SBTH.	MS	
TP	NS		SBMR	MS	
GR	NS		SGPR.	MS	
P3/8-S	NS		GR	NS	
P200-S	NS		P200-S	NS	
AV	NS		AV	NS	
PMBPR.	NS		PMBPR.	NS	
SBPR.	NS		SBPR.	NS	

Under Low, Medium and High traffic conditions and according to the results of RL, SA metrics obtained from graphical method show that each of AW, ABaTH, ABiTH, SBTH and SGMR are VS and each one of them can alter the RL of pavement significantly. On the other hand, for the same traffic condition and for FL, results show that each of AW, ABaTH, ABiTH and PGC are VS and can change the FL of pavement dramatically.

The VS factors mentioned previously need to be considered carefully. Axle Weight AW can be controlled by reducing the number of overloaded axles passing the highway, while suitable selection of the thicknesses of Asphalt Base layer ABaTH, Asphaltic Binder layer ABiTH and Subbase layer SBTH is recommended when designing of pavement section. Subgrade Resilient Modulus SGMR is very

important, so that it is recommended that laboratory tests should be conducted for determination of SGMR. The results show that asphalt grade PG is VS, so that asphalt type should be selected carefully using SuperPave tests.

Other properties such as TRL, ASTH, PMBTH, SGPR, Gbs and SP as well as the volumetric properties of asphaltic Base layer ( e.g. P3/4-Ba and P1/2-Ba) can be considered S.

It is prefer to ensure that suitable method is used to conduct Traffic Survey for the determination of traffic loadings TRL. Subgrade Poisson Ratio SGPR is also S and it is recommended to be tested using triaxial test. The effect of vehicle speed SP is associated with high traffic loadings only and caused a considerable effect on RL and FL.

#### **4.1.2. Quantitative Sensitivity Analysis**

This method consists of two methods, NSI and DSI. The results of NSI and DSI are discussed in the following subsections.

##### **4.1.2.1. Normalized Sensitivity Index NSI Results.**

The results of SA using this method is based on mathematical solution rather than qualitative assessment, therefore it is expected that the results are more reasonable and comparable.

The results of SA using NSI metric and under Light, Medium and High traffic conditions are shown in Tables 16 through 18.

**Table 16.** Results of SA using NSI metric under Low traffic and Cold climate conditions for RL and FL.

Property	Sensitivity index		Property	Sensitivity index	
	RL			FL	
AW	VS		AW	VS	
SGMR	VS		ABaTH.	VS	
ABaTH.	VS		ABiTH.	VS	
SBTH.	VS		P3/4-Ba	VS	
ABiTH.	VS		TRL	VS	
ASTH.	S		ASTH.	S	
PMBTH.	S		Gbs	S	
TRL	S		Pb-Ba	S	
AsPR	S		PMBMR	S	
SGPR.	S		P1/2-Ba	S	
P3/4-B	S		PGC	S	
Gbs	S		AsPR	S	
PGC	MS		P3/4-B	S	
P3/4-S	MS		SP	S	
P3/4-Ba	MS		P3/8-Ba	MS	
Pb-S	MS		PMBTH.	MS	
P1/2-Ba	MS		TP	MS	
PMBMR	MS		P3/4-S	MS	
P1/2-S	MS		Pb-S	MS	
SP	MS		P3/8-B	MS	
Pb-B	MS		P1/2-S	MS	
Pb-Ba	MS		Pb-B	MS	
P1/2-B	MS		P200-Ba	MS	
P3/8-S	MS		SBMR	MS	
PMBPR.	MS		SGMR	MS	
P3/8-B	MS		P1/2-B	MS	
ZD	NS		P3/8-S	MS	
TP	NS		PMBPR.	MS	
GR	NS		SBTH.	MS	
P200-S	NS		ZD	MS	
P200-B	NS		GR	NS	
P3/8-Ba	NS		P200-S	NS	
P200-Ba	NS		P200-B	NS	
AV	NS		AV	NS	
SBMR	NS		SBPR.	NS	
SBPR.	NS		SGPR.	NS	

**Table 17.** Results of SA using NSI metric under Medium traffic and Cold climate conditions for RL and FL.

Property	Sensitivity index		Property	Sensitivity index	
	RL			FL	
AW	VS		AW	VS	
ABaTH.	VS		ABaTH.	VS	
SGMR	VS		ABiTH.	VS	
ABiTH.	VS		AsPR	S	
SBTH.	S		P3/4-Ba	S	
AsPR	S		TRL	S	
TRL	S		Gbs	S	
ASTH.	S		Pb-Ba	S	
PMBTH.	S		P1/2-Ba	S	
SGPR.	S		ASTH.	S	
P3/4-B	MS		PGC	MS	
Gbs	MS		P3/8-Ba	MS	
PGC	MS		P3/4-B	MS	
P3/4-S	MS		PMBMR	MS	
P3/4-Ba	MS		SP	MS	
P1/2-Ba	MS		PMBTH.	MS	
SP	MS		SBMR	MS	
Pb-B	MS		SGMR	MS	
Pb-Ba	MS		P3/8-S	MS	
P1/2-B	MS		TP	MS	
P3/8-Ba	MS		P3/4-S	MS	
Pb-S	MS		Pb-S	MS	
P3/8-B	MS		P3/8-B	MS	
PMBMR	MS		P1/2-S	MS	
ZD	MS		Pb-B	MS	
TP	NS		P200-Ba	MS	
GR	NS		P1/2-B	MS	
P3/8-S	NS		ZD	MS	
P1/2-S	NS		GR	NS	
P200-S	NS		P200-S	NS	
P200-B	NS		P200-B	NS	
P200-Ba	NS		AV	NS	
AV	NS		PMBPR.	NS	
PMBPR.	NS		SBTH.	NS	
SBMR	NS		SBPR.	NS	
SBPR.	NS		SGPR.	NS	

**Table 18.** Results of SA using NSI metric under High traffic and Cold climate conditions for RL and FL.

Property	Sensitivity index		Property	Sensitivity index	
	RL			FL	
AW	VS		AW	VS	
ABaTH.	VS		ABaTH.	VS	
ABiTH.	VS		ABiTH.	VS	
SGMR	VS		P3/4-Ba	S	
SBTH.	S		P1/2-Ba	S	
TRL	S		TRL	S	
SGPR.	S		Gbs	S	
ASTH.	S		Pb-Ba	S	
PMBTH.	S		PGC	MS	
P3/4-B	S		P3/4-B	MS	
Gbs	S		SP	MS	
PGC	MS		ASTH.	MS	
P3/4-Ba	MS		AsPR	MS	
P1/2-Ba	MS		PMBMR	MS	
SP	MS		SGMR	MS	
Pb-Ba	MS		P3/8-S	MS	
AsPR	MS		P3/8-Ba	MS	
P3/8-Ba	MS		SGPR.	MS	
Pb-B	MS		TP	MS	
P1/2-B	MS		P3/4-S	MS	
P3/4-S	MS		Pb-S	MS	
Pb-S	MS		P3/8-B	MS	
P3/8-B	MS		P1/2-S	MS	
PMBMR	MS		Pb-B	MS	
P1/2-S	MS		PMBTH.	MS	
P200-B	MS		SBTH.	MS	
P200-Ba	MS		P200-B	MS	
SBMR	MS		P200-Ba	MS	
ZD	NS		SBMR	MS	
TP	NS		P1/2-B	MS	
GR	NS		ZD	MS	
P3/8-S	NS		GR	NS	
P200-S	NS		P200-S	NS	
AV	NS		AV	NS	
PMBPR.	NS		PMBPR.	NS	
SBPR.	NS		SBPR.	NS	

The results of NSI revealed that the RL is VS to ABaTH, ABiTH, SGMR and AW, while S to SBTH, TRL, SGPR, PMBTH, ASTH, PMBTH and some volumetric properties of Binder layer. FL was VS to ABaTH, ABiTH and AW especially at high traffic loading but it was S to SBTH, TRL, SGPR, PMBTH a some volumetric properties of Base layer. It was surprisingly that FL eas S to AsPR.

#### 4.1.2.2. Distance Sensitivity Index DSI Results.

As in NSI metric, the results of SA using DSI metric are based on mathematical solution rather than qualitative assessment as explained previously. It is expected that the results are similar to NSI metric.

The results of SA using DSI metric under Light, Medium and High traffic conditions are shown in Tables 19 through 21.



**Table 19.** Results of SA using DSI metric under Low traffic and Cold climate conditions for RL and FL.

Property	Sensitivity index		Property	Sensitivity index	
	RL			FL	
AW	VS		AW	VS	
SGMR	VS		PGC	VS	
ABaTH.	VS		ABaTH.	VS	
ABiTH.	VS		ABiTH.	VS	
SBTH.	VS		TRL	VS	
ASTH.	VS		P3/4-Ba	VS	
PMBTH.	VS		ASTH.	VS	
PGC	S		Pb-Ba	S	
TRL	S		Gbs	S	
SGPR.	S		P1/2-Ba	S	
P3/4-B	S		PMBMR	S	
Gbs	S		SP	S	
SP	MS		P3/4-B	S	
Pb-S	MS		P3/8-Ba	S	
P3/4-S	MS		PMBTH.	S	
P1/2-S	MS		ZD	MS	
Pb-B	MS		TP	MS	
P1/2-B	MS		Pb-S	MS	
Pb-Ba	MS		P3/4-S	MS	
P3/4-Ba	MS		P1/2-S	MS	
P1/2-Ba	MS		Pb-B	MS	
AsPR	MS		P3/8-B	MS	
PMBMR	MS		P1/2-B	MS	
ZD	MS		P200-Ba	MS	
P3/8-S	MS		AsPR	MS	
P3/8-B	MS		SBMR	MS	
PMBPR.	MS		SGMR	MS	
TP	NS		P3/8-S	MS	
GR	NS		PMBPR.	MS	
P200-S	NS		SBTH.	MS	
P200-B	NS		GR	NS	
P3/8-Ba	NS		P200-S	NS	
P200-Ba	NS		P200-B	NS	
AV	NS		AV	NS	
SBMR	NS		SBPR.	NS	
SBPR.	NS		SGPR.	NS	

**Table 20.** Results of SA using DSI metric under Medium traffic and Cold climate conditions for RL and FL.

Property	FL.		Property	FL.	
	Sensitivity index			Sensitivity index	
	RL		FL		
AW	VS	AW	VS		
ABaTH.	VS	ABaTH.	VS		
SGMR	VS	PGC	VS		
ABiTH.	VS	ABiTH.	VS		
SBTH.	S	TRL	S		
PGC	S	Pb-Ba	S		
TRL	S	P3/4-Ba	S		
ASTH.	S	Gbs	S		
PMBTH.	S	P1/2-Ba	S		
SGPR.	S	ASTH.	S		
P3/4-B	S	ZD	MS		
Gbs	S	SP	MS		
ZD	MS	P3/4-B	MS		
SP	MS	P3/8-Ba	MS		
P3/4-S	MS	AsPR	MS		
Pb-B	MS	PMBTH.	MS		
P1/2-B	MS	PMBMR	MS		
Pb-Ba	MS	SBMR	MS		
P3/4-Ba	MS	SGMR	MS		
P1/2-Ba	MS	TP	MS		
AsPR	MS	Pb-S	MS		
Pb	MS	P3/4-S	MS		
P3/8-B	MS	P3/8-S	MS		
P3/8-Ba	MS	P1/2-S	MS		
PMBMR	MS	Pb-B	MS		
TP	NS	P3/8-B	MS		
GR	NS	P1/2-B	MS		
P3/8-S	NS	P200-Ba	MS		
P1/2-S	NS	GR	NS		
P200-S	NS	P200-S	NS		
P200-B	NS	P200-B	NS		
P200-Ba	NS	AV	NS		
AV	NS	PMBPR.	NS		
PMBPR.	NS	SBTH.	NS		
SBMR	NS	SBPR.	NS		
SBPR.	NS	SGPR.	NS		

**Table 21.** Results of SA using DSI metric under High traffic and Cold climate conditions for RL and FL.

Property	Sensitivity index		Property	Sensitivity index	
	RL			FL	
AW	VS		AW	VS	
ABaTH.	VS		ABaTH.	VS	
ABiTH.	VS		PGC	VS	
SGMR	VS		ABiTH.	VS	
PGC	VS		TRL	S	
SBTH.	VS		P3/4-Ba	S	
TRL	S		P1/2-Ba	S	
ASTH.	S		Gbs	S	
PMBTH.	S		Pb-Ba	S	
SGPR.	S		SP	S	
P3/4-B	S		P3/4-B	S	
Gbs	S		P3/8-Ba	S	
SP	S		ASTH.	S	
Pb-Ba	S		ZD	MS	
P3/4-Ba	S		PMBMR	MS	
P1/2-Ba	S		SGMR	MS	
P3/8-Ba	MS		TP	MS	
Pb-B	MS		Pb-S	MS	
P1/2-B	MS		P3/4-S	MS	
ZD	MS		P3/8-S	MS	
Pb-S	MS		P1/2-S	MS	
P3/4-S	MS		Pb-B	MS	
P1/2-S	MS		P3/8-B	MS	
P3/8-B	MS		P1/2-B	MS	
P200-B	MS		P200-B	MS	
P200-Ba	MS		P200-Ba	MS	
AsPR	MS		AsPR	MS	
PMBMR	MS		PMBTH.	MS	
SBMR	MS		SBTH.	MS	
TP	NS		SBMR	MS	
GR	NS		SGPR.	MS	
P3/8-S	NS		GR	NS	
P200-S	NS		P200-S	NS	
AV	NS		AV	NS	
PMBPR.	NS		PMBPR.	NS	
SBPR.	NS		SBPR.	NS	

It can be noted that, DSI metric has the ability to differentiate between the effect of different traffic loading conditions on the results of SA. Under Low traffic loading and based on the results of RL, all layers thicknesses, AW and SGMR were VS. Asphalt grade PG and TRL were also VS according to FL results. When traffic loading is Medium, RL was VS to ABaTH, ABiTH, AW and SGMR, while it was S to PG, TRL, PMBTH, SBTH, SP and some volumetric properties of Binder layer. The results show that FL was VS to ABaTH, ABiTH, AW and PG.

On the other hand, FL was S to TRL and some volumetric properties of Base layer. Under High traffic condition and for RL, the result were similar to that of Medium traffic condition. Layers thicknesses, AW and SGMR were VS which is the same as in the case of Low traffic condition, while it

was S to some of volumetric properties of Binder layer, PMBTH, TRL and ASTH. The results show that FL was VS to ABaTH, ABiTH, AW and PG while it was S to some of volumetric properties of Base layer, SP, TRL and ASTH.

Summary of the results:

The results of SA under cold climate condition and according to the results of RL can be summarized in the followings:

1- Under L and M traffic conditions:

- a) It can be seen that AW and Layers thicknesses (e.g. ABaTH and ABiTH) were S and VS. High AW and low thicknesses of layers due to poor design decreased the RL of pavement. There is a need for the improvement of flexible pavement design method and enhance the monitoring system of axel weight in highways.
- b) It is also found that RL is S to PG of asphalt. Higher PG can increase the RL significantly. A special consideration must be paid when selecting type of asphalt.
- c) RL is also S to TRL. Higher traffic loadings can increase the deterioration of pavement structure in the form of rutting.
- d) It was surprising that RL is S to Poisson Ratio PR of asphalt and Subgrade. This agreed with the findings of different researches in the literature. It could be associated with high flexibility of pavements layers thus low RL.

2- Under H traffic conditions:

The result was similar to the results of L and M traffic loadings. It is also discovered that pavement RL is S to the properties of Base layer (e.g. P3/4-Ba and Pb-Ba). High traffic loadings can increase the vertical stresses on Base layer. That can increase the vertical stresses on the subgrade layer and can increase rutting potential.

3- It is found that the number of S and VS parameters using Graphical method is higher than that using NSI and DSI metrics. This can be due to the difficulty associated with graphical differentiation between the sensitivity of parameters.

4- The results revealed that the result using DSI metric was similar to NSI metric under L and M traffic conditions, while it was similar to the Graphical method under H traffic condition. It can be assumed that DSI metric can be considered the solution for the differences between graphical and NSI methods.

The results of SA under cold climate condition and according to FL can be summarized in the followings

1- Under H, M and L traffic conditions:

- a) It can be seen that AW and Layers thicknesses (e.g. ABaTH and ABiTH) were VS and S. High AW and low thicknesses of layers due to poor design decreased the RL of pavement. There is a need for the improvement of flexible pavement design method and enhance the monitoring system of axel weight in highways.
- b) It is also found that the pavement is S to the PG of asphalt. Higher PG can increase the FL significantly. A special consideration must be paid when selecting the appropriate type of asphalt that can decrease the tensile strain at the bottom of asphalt layer.
- c) Pavement was also S to TRL and the speed SP of vehicles. Higher traffic loadings with low traffic speed induce higher tensile strains at the bottom of asphalt layers. This can increase the deterioration of pavement structure in the form of fatigue cracking.
- d) The FL is also S to the properties of asphaltic Base layer (e.g. P3/4-Ba and Pb-Ba) where the tensile strains accrue.
- e) It was found that the FL is S to  $M_R$  of PMB. The PMB layer is the base of asphaltic layers where the tensile strains take place. The strength of this layer can increase the FL of pavement.

- f) As expected, the FL of pavement was S to the thickness of asphalt layer ASTH. Sufficient thickness of asphaltic layer can increase the FL significantly. The selection of appropriate thickness is related to the design method that need to be enhanced.
- 2- It is found that the number of S and VS parameters found using different methods (i.e. Graphical, NSI and DSI methods) are different under different traffic conditions.

**4.2. Results of Hot Climate Condition**

Antalya city was selected to represent hot climate condition in Turkey. M-EDM analysis was conducted using MnPave software for the determination of FL and RL of TTS under different traffic categories (L, M and H) for Base and Base+/-20% cases. Different methods were used to conduct SA as in the following subsections.

**4.2.1. Results of Qualitative (Graphical Assessment Method)**

The results of SA using graphical method under Light, Medium and High traffic conditions are shown in Figures 10 through 15.

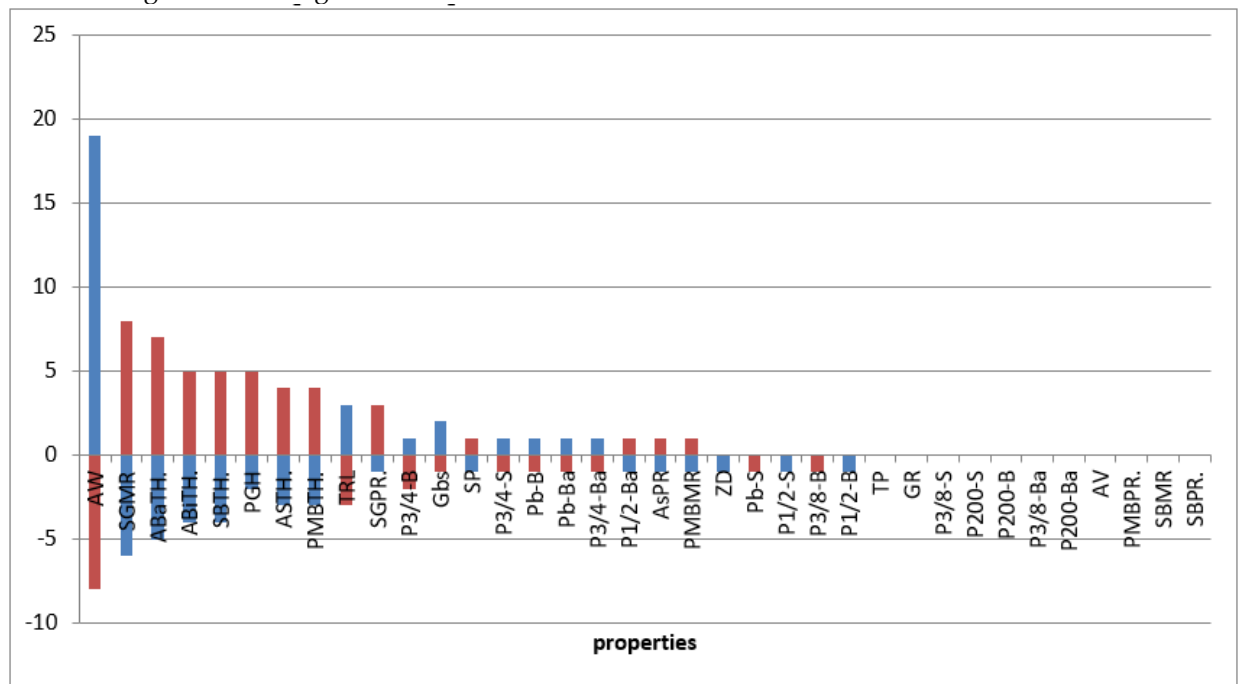


**Figure 10.** Results of SA under Low Traffic condition and Hot Climate using RL.

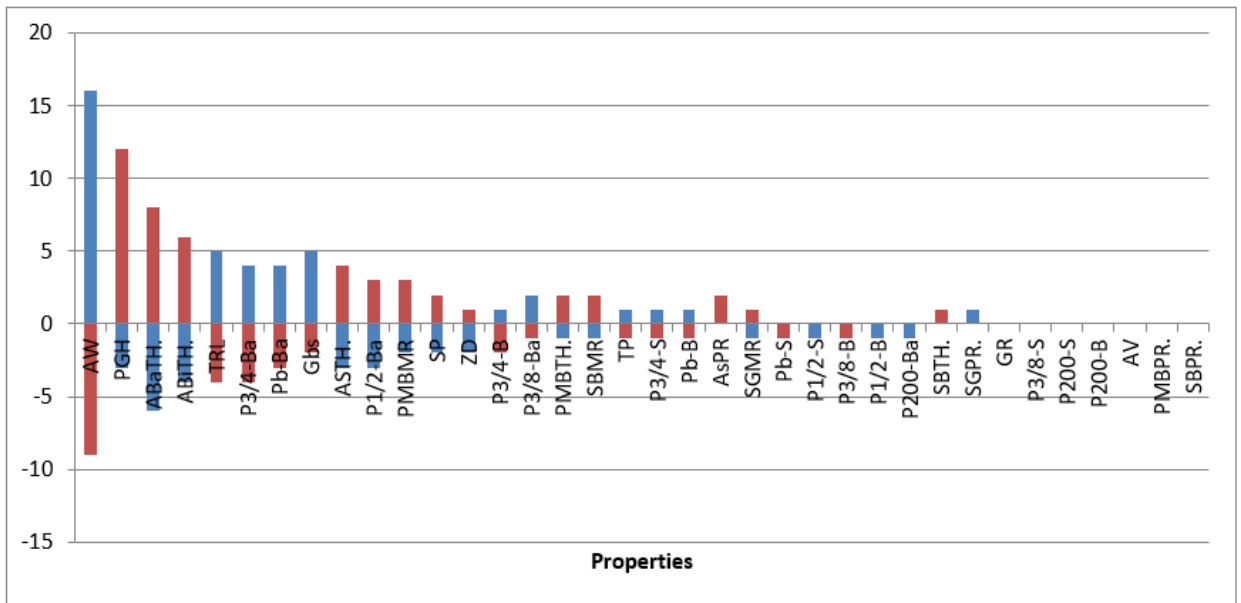


Figure 11. Results of SA under Low Traffic condition and Hot Climate using FL.

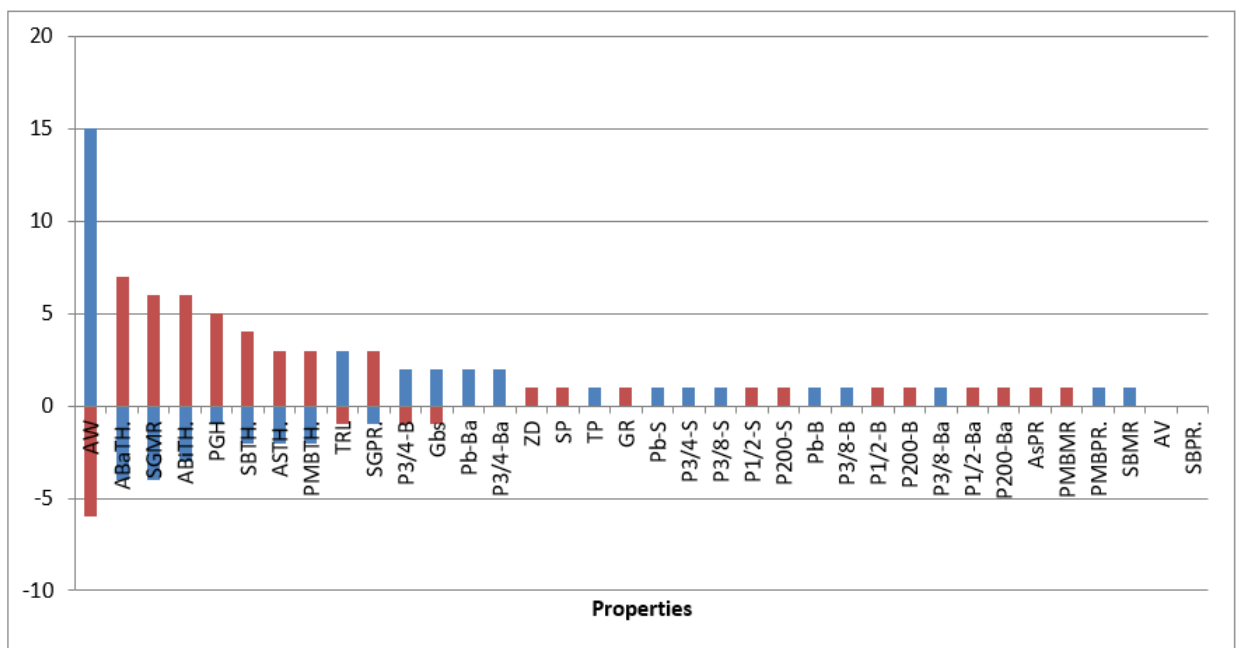


Figure 12. Results of SA under Medium Traffic condition and Hot Climate using RL.

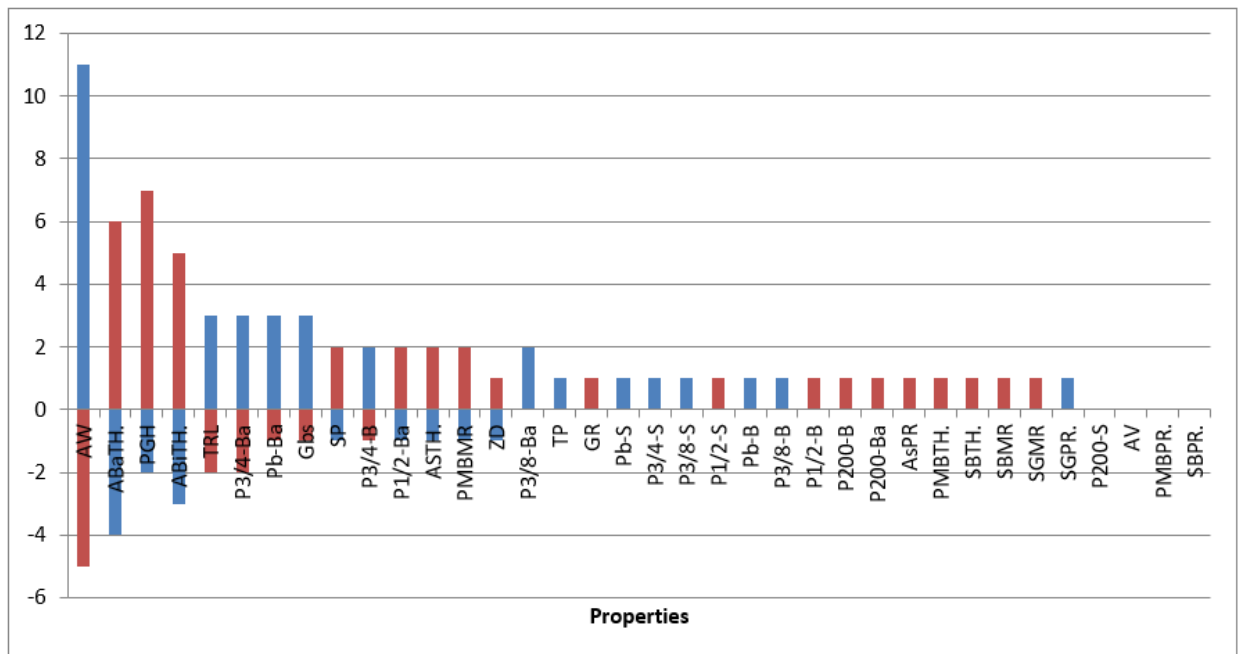


Figure 13. Results of SA under Medium Traffic condition and Hot Climate using FL.

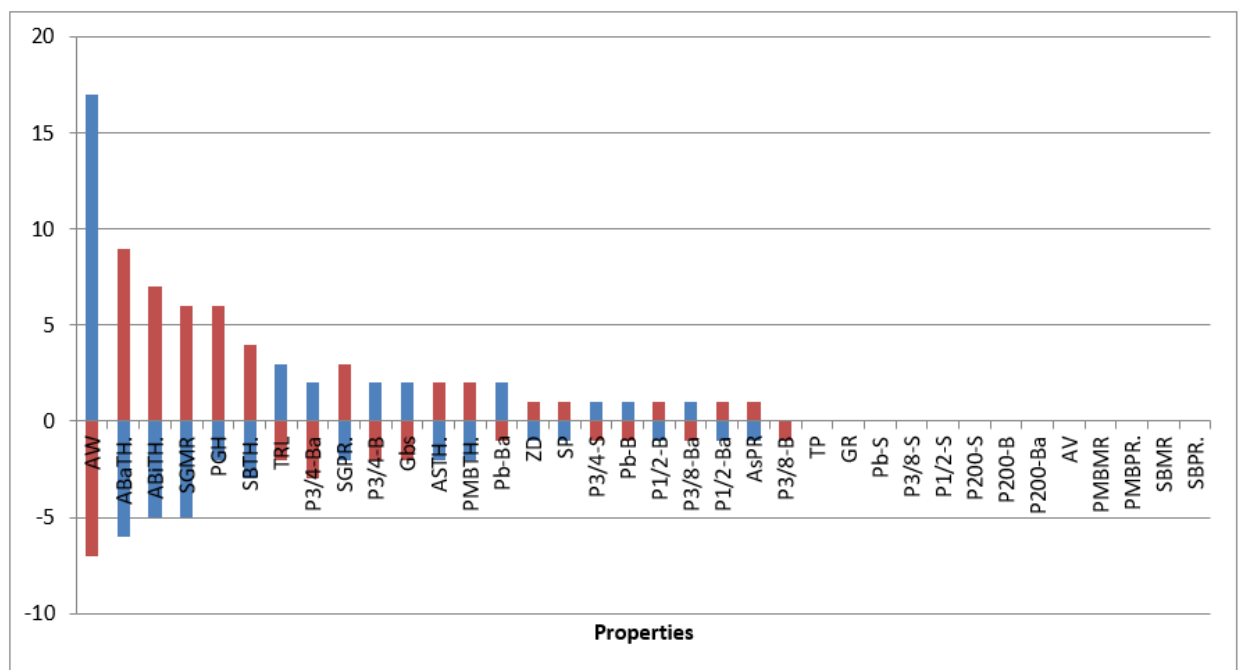


Figure 14. Results of SA under High Traffic condition and Hot Climate using RL.

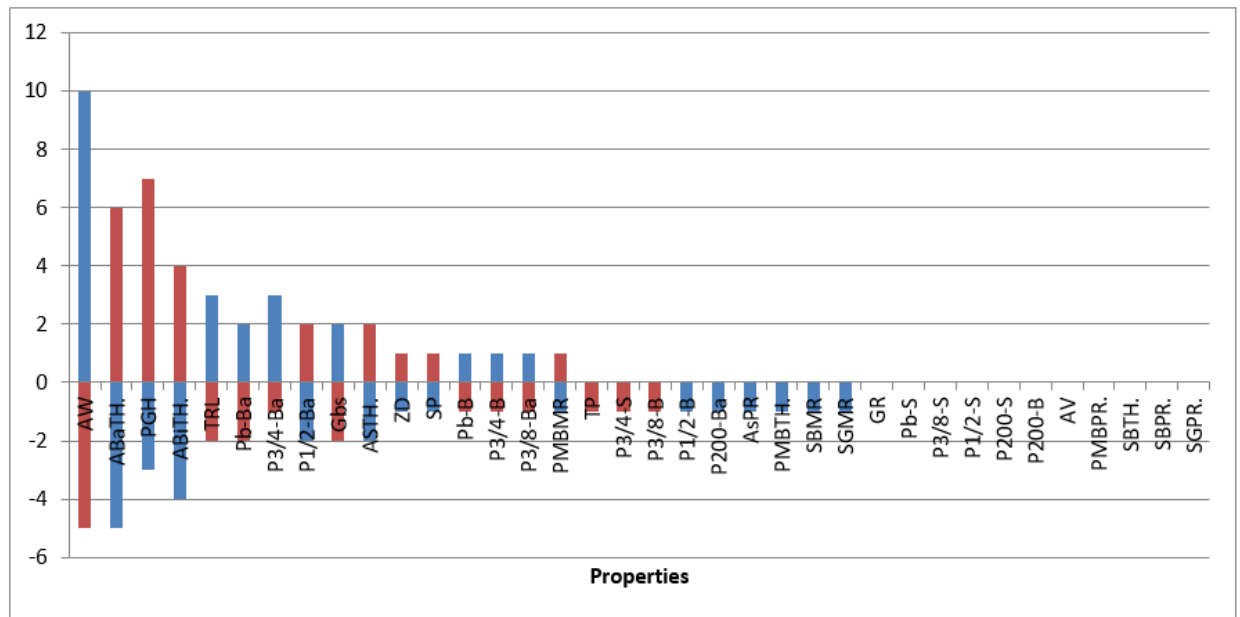


Figure 15. Results of SA under High Traffic condition and Hot Climate using FL.

To make a comparison between Graphical method and other NSI and DSI metrics, SA results of graphical method are classified under (VS, S, MS and NS) categories. The results are shown in Tables 22 through 24.



**Table 22.** SA results of graphical method under Light traffic and Hot climate conditions using RL and FL.

Property	Sensitivity index		Property	Sensitivity index	
	RL			FL	
AW	VS		AW	VS	
SGMR	VS		PGH	VS	
ABaTH.	VS		ABaTH.	VS	
ABiTH.	S		ABiTH.	VS	
SBTH.	S		TRL	S	
ASTH.	S		P3/4-Ba	S	
PMBTH.	S		ASTH.	S	
PGH	S		Pb-Ba	S	
TRL	S		Gbs	S	
SGPR.	MS		P1/2-Ba	S	
P3/4-B	MS		PMBMR	S	
Gbs	MS		SP	MS	
SP	MS		P3/4-B	MS	
Pb-S	MS		P3/8-Ba	MS	
P3/4-S	MS		PMBTH.	MS	
P1/2-S	MS		ZD	MS	
Pb-B	MS		TP	MS	
P1/2-B	MS		Pb-S	MS	
Pb-Ba	MS		P3/4-S	NS	
P3/4-Ba	MS		P1/2-S	NS	
P1/2-Ba	MS		Pb-B	NS	
AsPR	MS		P3/8-B	NS	
PMBMR	MS		P1/2-B	NS	
ZD	NS		P200-Ba	NS	
P3/8-S	NS		AsPR	NS	
P3/8-B	NS		SBMR	NS	
PMBPR.	NS		SGMR	NS	
TP	NS		P3/8-S	NS	
GR	NS		PMBPR.	NS	
P200-S	NS		SBTH.	NS	
P200-B	NS		GR	NS	
P3/8-Ba	NS		P200-S	NS	
P200-Ba	NS		P200-B	NS	
AV	NS		AV	NS	
SBMR	NS		SBPR.	NS	
SBPR.	NS		SGPR.	NS	

**Table 23.** SA results of graphical method under Medium traffic and Hot climate conditions using RL and FL.

Property	Sensitivity index		Property	Sensitivity index	
	RL	FL		RL	FL
AW	VS	VS	AW	VS	VS
ABaTH.	VS	VS	ABaTH.	VS	VS
SGMR	VS	VS	PGH	VS	VS
ABiTH.	VS	VS	ABiTH.	VS	VS
PGH	S	S	TRL	S	S
SBTH.	S	S	P3/4-Ba	S	S
ASTH.	S	S	Pb-Ba	S	S
PMBTH.	S	S	Gbs	S	S
TRL	MS	MS	SP	MS	MS
SGPR.	MS	MS	P3/4-B	MS	MS
P3/4-B	MS	MS	P1/2-Ba	MS	MS
Gbs	MS	MS	ASTH.	MS	MS
Pb-Ba	MS	MS	PMBMR	MS	MS
P3/4-Ba	MS	MS	ZD	MS	MS
ZD	MS	MS	P3/8-Ba	MS	MS
SP	NS	NS	TP	NS	NS
TP	NS	NS	GR	NS	NS
GR	NS	NS	Pb-S	NS	NS
Pb-S	NS	NS	P3/4-S	NS	NS
P3/4-S	NS	NS	P3/8-S	NS	NS
P3/8-S	NS	NS	P1/2-S	NS	NS
P1/2-S	NS	NS	Pb-B	NS	NS
P200-S	NS	NS	P3/8-B	NS	NS
Pb-B	NS	NS	P1/2-B	NS	NS
P3/8-B	NS	NS	P200-B	NS	NS
P1/2-B	NS	NS	P200-Ba	NS	NS
P200-B	NS	NS	AsPR	NS	NS
P3/8-Ba	NS	NS	PMBTH.	NS	NS
P1/2-Ba	NS	NS	SBTH.	NS	NS
P200-Ba	NS	NS	SBMR	NS	NS
AsPR	NS	NS	SGMR	NS	NS
PMBMR	NS	NS	SGPR.	NS	NS
PMBPR.	NS	NS	P200-S	NS	NS
SBMR	NS	NS	AV	NS	NS
AV	NS	NS	PMBPR.	NS	NS
SBPR.	NS	NS	SBPR.	NS	NS

**Table 24.** SA results of graphical method under High traffic and Hot climate conditions using RL and FL.

Property	Sensitivity index		Property	Sensitivity index	
	RL			FL	
AW	VS		AW	VS	
ABaTH.	VS		ABaTH.	VS	
ABiTH.	VS		PGH	VS	
SGMR	VS		ABiTH.	VS	
PGH	VS		TRL	S	
SBTH.	VS		Pb-Ba	S	
TRL	S		P3/4-Ba	S	
P3/4-Ba	S		P1/2-Ba	S	
SGPR.	S		Gbs	S	
P3/4-B	S		ASTH.	S	
Gbs	S		ZD	MS	
ASTH.	S		SP	MS	
PMBTH.	S		Pb-B	MS	
Pb-Ba	MS		P3/4-B	MS	
ZD	MS		P3/8-Ba	MS	
SP	MS		PMBMR	MS	
P3/4-S	MS		TP	NS	
Pb-B	MS		P3/4-S	NS	
P1/2-B	MS		P3/8-B	NS	
P3/8-Ba	MS		P1/2-B	NS	
P1/2-Ba	MS		P200-Ba	NS	
AsPR	MS		AsPR	NS	
P3/8-B	NS		PMBTH.	NS	
TP	NS		SBMR	NS	
GR	NS		SGMR	NS	
Pb-S	NS		GR	NS	
P3/8-S	NS		Pb-S	NS	
P1/2-S	NS		P3/8-S	NS	
P200-S	NS		P1/2-S	NS	
P200-B	NS		P200-S	NS	
P200-Ba	NS		P200-B	NS	
AV	NS		AV	NS	
PMBMR	NS		PMBPR.	NS	
PMBPR.	NS		SBTH.	NS	
SBMR	NS		SBPR.	NS	
SBPR.	NS		SGPR.	NS	

Under Low traffic conditions and according to the results of RL, SA metrics obtained from graphical method show that RL was VS to AW, ABaTH, ABiTH and SGMR. While it was S to ASTH, ABiTH, TRL, PMBTH and PGH. On the other hand, for the same traffic condition, FL was VS to AW, ABaTH, ABiTH and PGH. FL was S to ASTH, TRL, PMBMR and some volumetric properties of Base layer.

Under Medium traffic conditions, it can be noted that RL was VS to AW, ABaTH, ABiTH and SGMR. While it was S to ASTH, TRL, PMBTH and PGH. On the other hand, FL was VS to AW, ABaTH, ABiTH and PG. FL was S to TRL and some volumetric properties of Base layer.

Under High traffic conditions, RL was VS to AW, ABaTH, ABiTH, ASTH, PG and SGMR. While it was S to ASTH, SGPR, TRL, PMBTH and some volumetric properties of Base and Binder layers. On the

other hand, for the same traffic condition, FL was VS to AW, ABaTH, ABiTH and PG. FL was S to ASTH and some volumetric properties of Base layer.

#### 4.2.2. Quantitative Sensitivity Analysis

There are two metrics. NSI and DSI. The results are discussed in the following subsections.

##### 4.2.2.1. Normalized Sensitivity Index NSI Results.

The results of SA using NSI metric and under Light, Medium and High traffic conditions are shown in Tables 25 through 27.

**Table 25.** Results of NSI under Low traffic and Hot climate conditions for RL and FL.

Property	Sensitivity index		Property	Sensitivity index	
	RL			FL	
AW	VS		AW	VS	
SGMR	VS		ABaTH.	VS	
ABaTH.	VS		ABiTH.	VS	
SBTH.	VS		TRL	VS	
ABiTH.	VS		P3/4-Ba	VS	
ASTH.	S		ASTH.	S	
PMBTH.	S		Gbs	S	
TRL	S		Pb-Ba	S	
AsPR	S		P1/2-Ba	S	
SGPR.	S		PGH	S	
PGH	MS		AsPR	S	
P3/4-B	MS		PMBMR	S	
Gbs	MS		SP	S	
P3/4-Ba	MS		P3/8-Ba	MS	
P3/4-Ba	MS		P3/4-B	MS	
P1/2-S	MS		PMBTH.	MS	
PMBMR	MS		SBMR	MS	
SP-B	MS		TP	MS	
Pb-Ba	MS		P3/4-S	MS	
Pb-S	MS		Pb-B	MS	
Pb-B	MS		SGMR	MS	
P3/8-S	MS		ZD	MS	
P1/2-B	MS		SGPR.	MS	
P1/2-Ba	NS		P3/8-B	MS	
ZD	NS		Pb-S	MS	
TP	NS		P1/2-S	MS	
GR	NS		SBTH.	MS	
P3/8-S	NS		P200-Ba	MS	
P200-S	NS		P1/2-B	MS	
P200-B	NS		PMBPR.	NS	
P3/8-Ba	NS		SBPR.	NS	
P200-Ba	NS		P200-S	NS	
AV	NS		P200-B	NS	
PMBPR.	NS		P3/8-S	NS	
SBMR	NS		GR	NS	
SBPR.	NS		AV	NS	

**Table 26.** Results of NSI under Medium traffic and Hot climate conditions for RL and FL.

Property	Sensitivity index		Property	Sensitivity index	
	RL			FL	
AW	VS		AW	VS	
ABaTH.	VS		ABaTH.	VS	
SGMR	VS		ABiTH.	VS	
ABiTH.	VS		P3/4-Ba	S	
SBTH.	S		TRL	S	
ASTH.	S		Gbs	S	
PMBTH.	S		Pb-Ba	S	
SGPR.	S		PGH	MS	
TRL	S		P3/4-B	MS	
P3/4-B	MS		PMBMR	MS	
Gbs	MS		P1/2-Ba	MS	
AsPR	MS		SP	MS	
PGH	MS		ASTH.	MS	
P3/4-Ba	MS		AsPR	MS	
Pb-Ba	MS		P3/8-Ba	MS	
P3/8-S	MS		P3/8-S	MS	
P3/8-Ba	MS		SGPR.	MS	
PMBPR.	MS		TP	MS	
TP	MS		P3/4-S	MS	
P3/4-S	MS		Pb-S	MS	
Pb-S	MS		P3/8-B	MS	
P200-S	MS		P1/2-S	MS	
P3/8-B	MS		Pb-B	MS	
P1/2-Ba	MS		PMBTH.	MS	
PMBMR	MS		SBTH.	MS	
P1/2-S	MS		GR	MS	
SP	MS		P200-B	MS	
Pb-B	MS		P200-Ba	MS	
GR	MS		SBMR	MS	
P200-B	MS		SGMR	MS	
P200-Ba	MS		P1/2-B	MS	
SBMR	MS		ZD	MS	
P1/2-B	MS		P200-S	NS	
ZD	NS		AV	NS	
AV	NS		PMBPR.	NS	
SBPR.	NS		SBPR.	NS	

**Table 27.** Results of NSI under High traffic and Hot climate conditions for RL and FL.

Property	Sensitivity index		Property	Sensitivity index	
	RL			FL	
AW	VS		AW	VS	
ABaTH.	VS		ABaTH.	VS	
ABiTH.	VS		ABiTH.	VS	
SGMR	VS		TRL	S	
SBTH.	S		P3/4-Ba	S	
AsPR	S		P1/2-Ba	S	
SGPR.	S		PGH	S	
P3/4-Ba	S		Gbs	S	
TRL	S		ASTH.	S	
P3/4-B	S		Pb-Ba	S	
Gbs	S		AsPR	MS	
ASTH.	S		P3/8-Ba	MS	
PMBTH.	S		P3/4-B	MS	
PGH	MS		PMBMR	MS	
Pb-Ba	MS		SP	MS	
P3/8-Ba	MS		Pb-B	MS	
P3/4-S	MS		TP	MS	
P1/2-Ba	MS		P3/4-S	MS	
SP	MS		P3/8-B	MS	
Pb-B	MS		PMBTH.	MS	
P1/2-B	MS		P200-Ba	MS	
P3/8-B	MS		SBMR	MS	
ZD	MS		SGMR	MS	
TP	NS		P1/2-B	MS	
GR	NS		ZD	MS	
Pb-S	NS		GR	NS	
P3/8-S	NS		Pb-S	NS	
P1/2-S	NS		P3/8-S	NS	
P200-S	NS		P1/2-S	NS	
P200-B	NS		P200-S	NS	
P200-Ba	NS		P200-B	NS	
AV	NS		AV	NS	
PMBMR	NS		PMBPR.	NS	
PMBPR.	NS		SBTH.	NS	
SBMR	NS		SBPR.	NS	
SBPR.	NS		SGPR.	NS	

Under Low and Medium traffic conditions, RL was VS to AW, ABaTH, ABiTH, SBTH and SGMR. While it was S to ASTH, SGPR, TRL, PMBTH and AsPR. On the other hand, for the same traffic condition, FL was VS to AW, ABaTH, ABiTH and TRL. FL was S to ASTH, SP, AsPR, PGH, PMBMR and some volumetric properties of Base layer. It can be noted that the results Under Medium traffic conditions were very similar to the results of Graphical method.

Under High traffic conditions, the results were also resembled to the results of Graphical method. Moreover, RL was S to AsPR and SGPR.

4.2.2.2. Results of Distance Sensitivity Index DSI.

The results of SA using DSI metric under Light, Medium and High traffic conditions are shown in Tables 28 through 30.

**Table 28.** Results of DSI under Low traffic and Hot climate conditions for RL and FL.

Property	Sensitivity index		Property	Sensitivity index	
	RL			FL	
AW	VS		AW	VS	
SGMR	VS		PGH	VS	
ABaTH.	VS		ABaTH.	VS	
ABiTH.	VS		ABiTH.	VS	
SBTH.	VS		TRL	VS	
PGH	VS		P3/4-Ba	VS	
ASTH.	S		Gbs	VS	
PMBTH.	S		Pb-Ba	S	
TRL	S		ASTH.	S	
SGPR.	S		P1/2-Ba	S	
P3/4-B	S		PMBMR	S	
Gbs	S		SP	S	
SP	MS		ZD	S	
P3/4-S	MS		P3/4-B	S	
Pb-B	MS		P3/8-Ba	S	
Pb-Ba	MS		PMBTH.	S	
P3/4-Ba	MS		SBMR	S	
P1/2-Ba	MS		AsPR	MS	
AsPR	MS		TP	MS	
PMBMR	MS		P3/4-S	MS	
ZD	MS		Pb-B	MS	
Pb-S	MS		SGMR	MS	
P1/2-S	MS		Pb-S	MS	
P3/8-B	MS		P1/2-S	MS	
P1/2-B	MS		P3/8-B	MS	
TP	NS		P1/2-B	MS	
GR	NS		P200-Ba	MS	
P3/8-S	NS		SBTH.	MS	
P200-S	NS		SGPR.	MS	
P200-B	NS		GR	NS	
P3/8-Ba	NS		P3/8-S	NS	
P200-Ba	NS		P200-S	NS	
AV	NS		P200-B	NS	
PMBPR.	NS		AV	NS	
SBMR	NS		PMBPR.	NS	
SBPR.	NS		SBPR.	NS	

**Table 29.** Results of DSI under Medium traffic and Hot climate conditions for RL and FL.

Property	Sensitivity index		Property	Sensitivity index	
	RL			FL	
AW	VS		AW	VS	
ABaTH.	VS		PGH	VS	
SGMR	VS		ABaTH.	VS	
ABiTH.	VS		ABiTH.	VS	
PGH	VS		TRL	S	
SBTH.	S		P3/4-Ba	S	
ASTH.	S		Pb-Ba	S	
PMBTH.	S		Gbs	S	
TRL	S		SP	S	
SGPR.	S		P3/4-B	S	
P3/4-B	S		P1/2-Ba	S	
Gbs	S		ASTH.	S	
Pb-Ba	MS		PMBMR	S	
P3/4-Ba	MS		P3/8-Ba	MS	
ZD	MS		ZD	MS	
SP	MS		TP	MS	
TP	MS		GR	MS	
GR	MS		Pb-S	MS	
Pb-S	MS		P3/4-S	MS	
P3/4-S	MS		P3/8-S	MS	
P3/8-S	MS		P1/2-S	MS	
P1/2-S	MS		Pb-B	MS	
P200-S	MS		P3/8-B	MS	
Pb-B	MS		P1/2-B	MS	
P3/8-B	MS		P200-B	MS	
P1/2-B	MS		P200-Ba	MS	
P200-B	MS		AsPR	MS	
P3/8-Ba	MS		PMBTH.	MS	
P1/2-Ba	MS		SBTH.	MS	
P200-Ba	MS		SBMR	MS	
AsPR	MS		SGMR	MS	
PMBMR	MS		SGPR.	MS	
PMBPR.	MS		P200-S	NS	
SBMR	MS		AV	NS	
AV	NS		PMBPR.	NS	
SBPR.	NS		SBPR.	NS	



**Table 30.** Results of DSI under High traffic and Hot climate conditions for RL and FL.

Property	Sensitivity index		Property	Sensitivity index	
	RL			FL	
AW	VS		AW	VS	
ABaTH.	VS		ABaTH.	VS	
ABiTH.	VS		PGH	VS	
SGMR	VS		ABiTH.	VS	
PGH	VS		TRL	S	
SBTH.	S		P3/4-Ba	S	
TRL	S		Pb-Ba	S	
P3/4-Ba	S		P1/2-Ba	S	
SGPR.	S		Gbs	S	
P3/4-B	S		ASTH.	S	
Gbs	S		ZD	MS	
ASTH.	S		SP	MS	
PMBTH.	S		Pb-B	MS	
Pb-Ba	S		P3/4-B	MS	
ZD	MS		P3/8	MS	
SP	MS		PMBMR	MS	
P3/4-S	MS		TP	MS	
Pb-B	MS		P3/4-S	MS	
P1/2-B	MS		P3/8-B	MS	
P3/8-Ba	MS		P1/2-B	MS	
P1/2-Ba	MS		P200-Ba	MS	
AsPR	MS		AsPR	MS	
P3/8-B	MS		PMBTH.	MS	
TP	NS		SBMR	MS	
GR	NS		SGMR	MS	
Pb-S	NS		GR	NS	
P3/8-S	NS		Pb-S	NS	
P1/2-S	NS		P3/8-S	NS	
P200-S	NS		P1/2-S	NS	
P200-B	NS		P200-S	NS	
P200-Ba	NS		P200-B	NS	
AV	NS		AV	NS	
PMBMR	NS		PMBPR.	NS	
PMBPR.	NS		SBTH.	NS	
SBMR	NS		SBPR.	NS	
SBPR.	NS		SGPR.	NS	

Under Low traffic conditions, the results of DSI metric were similar to that of NSI metric. Moreover, FL was S to SBMR and PMBMR.

Under Medium traffic conditions it can be noted that RL was VS to AW, ABaTH, ABiTH, PG and SGMR. While it was S to ASTH, ABiTH, TRL, PMBTH and PG. On the other hand, FL was VS to AW, ABaTH, ABiTH and PGH. While it was S to TRL, SP, ASTH, PMBMR and some volumetric properties of Base layer.

Under High traffic conditions , RL was VS to AW, ABaTH, ABiTH, PG and SGMR. While it was S to ASTH, TRL, PMBTH, SBTH, SGPR and some volumetric properties of Base layer. While, FL was VS to AW, ABaTH, ABiTH and PG. Where FL was S to ASTH, TRL, PMBMR and some volumetric properties of Base layer.

#### Summary of the results:

The results of SA under hot climate condition and according to the results of RL can be summarized in the followings:

##### 1- Under L and M traffic conditions:

- a) It can be seen that AW and Layers thicknesses (e.g. ABath and ABith) were S and VS. High AW accompanied with insufficient design with low thicknesses of layers can decrease the RL of pavement. There is a need for the improvement of flexible pavement design method and enhance the monitoring system of axel weight in highways.
- b) It is found that RL is S to the PG of asphalt. Asphalt of high PG can increase the RL significantly. A special consideration must be paid when selection the appropriate type of asphalt.
- c) Pavement is also S to TRL. Higher traffic loadings can increase the deterioration of pavement structure in the form of rutting.
- d) It is discovered that the RL of pavement is S to the specification of SG (Poisson ratio and  $M_R$ ). This agreed with the findings of different researches in the literature. High Poisson ratio is associated with high flexibility of pavements layers thus low RL. At the meantime, higher  $M_R$  of SG can significantly increase the RL.

##### 2- Under H traffic conditions:

The results are similar to the results of L and M traffic loadings. But it was found that RL is S to the properties of Base layer (e.g. P3/4-Ba and Pb-Ba). High traffic loadings can increase the vertical stresses on Base layer. This can increase the vertical stresses on the subgrade layer and increasing rutting potential.

##### 3- It is discovered that the number of S and VS parameters found using DSI metric is higher than that using NSI and Graphical methods.

The results of SA under hot climate condition and according to FL can be summarized in the followings

##### 1- Under H, M and L traffic conditions:

- a) It can be concluded that FL was VS and S to AW and Layers thicknesses. High AW accompanied with insufficient thicknesses of pavements layers due to poor design reduced the FL of pavement. There is a need for the improvement of flexible pavement design method and enhance the monitoring system of axel weight in highways.
- b) It is found that the FL was S to the PG of asphalt. Higher PG can increase the FL significantly. A special consideration must be paid when selection the appropriate type of asphalt that can decrease the tensile strain at the bottom of asphalt layer.
- c) FL was S to TRL and the speed of vehicles SP. Higher traffic loadings with low traffic speed induce higher tensile strains at the bottom of asphalt layers. This can increase the deterioration of pavement structure in the form of fatigue cracking.
- d) The FL is also S to the properties of asphaltic Base layer (e.g. P3/4-Ba and Pb-Ba) where the tensile strains accrue.
- e) It was found that the FL is S to  $M_R$  of PMB. The PMB layer is the base of asphaltic layers where the tensile strains take place. The strength of this layer can increase the FL of pavement significantly.
- f) As expected, the FL of pavement is S to the thickness of asphalt layer ASTH. Sufficient thickness of asphaltic layer can increase the FL significantly. The selection of appropriate thickness is related to the design method that need to be enhanced.
- g) It was surprising that the FL of pavement is S to Bulk specific gravity Gbs of aggregate. More investigation about the effect of this factor need to be conducted.

##### 2- It is found that the number of S and VS parameters found using different metrics (i.e. Graphical, NSI and DSI) are different under different traffic conditions, but it was higher when using DSI.

## 5. CONCLUSIONS AND RECOMMENDATIONS

According to the results of M-EDM and SA of TTS for hot and cold regions in Turkey under H,M and L traffic conditions discussed previously, it can be concluded that:

- 1- It can be seen that AW and layers thicknesses were S and VS. High AW accompanied with insufficient design with low thicknesses of layers can decrease the RL of pavement. There is a need for the improvement of flexible pavement design method and enhance the monitoring system of axel weight in highways.
- 2- It is also found that the pavement is S to the PG of asphalt. Higher PG can increase the RL and FL significantly. A special consideration must be paid when selection the appropriate type of asphalt.
- 3- Pavement is also S to TRL. Higher traffic loadings can increase the deterioration of pavement structure in the form of rutting and fatigue cracks.
- 4- It is discovered that the RL of pavement is S to the specification of SG (Poisson ratio and  $M_R$ ). This agreed with the findings of different researches in the literature. High Poisson ratio is associated with high flexibility of pavements layers thus low RL. At the meantime, higher  $M_R$  of SG can significantly increase the RL.
- 5- It is also discovered that pavement is S to the properties of Base layer (e.g. P3/4-Ba and Pb-Ba). High traffic loadings can increase the vertical stresses on Base layer. That can increase the vertical stresses on the subgrade layer causing rutting.
- 6- It was found that the pavement is S to  $M_R$  of PMB. The PMB layer is the base of asphaltic layers where the tensile strains take place. The strength of this layer can increase the FL of pavement.
- 7- As expected, the FL of pavement is S to the thickness of asphalt layer ASTH. Sufficient thickness of asphaltic layer can increase the FL significantly. The selection of appropriate thickness is related to the design method that need to be enhanced.
- 8- The new proposed DSI method for SA which based on mathematical approach can be considered better than graphical method and can be used to overcome the shortcoming of inability of NSI method for conducting SA on categorical parameters.

### Declaration of Ethical Standards

Authors followed all ethical guidelines including authorship, citation, data reporting, and publishing original research.

### Credit Authorship Contribution Statement

Saadoon Obaid Eyada developed the theoretical formalism, performed the analytic calculations and performed the numerical simulations. Both Osman Nuri ÇELİK and Nibras Y. Abdulla authors contributed to the final version of the manuscript. Osman Nuri ÇELİK supervised the project.

### Declaration of Competing Interest

The authors declare that they have no known competing financial interests or personal relationships that could have appeared to influence the work reported.

### Acknowledgements

We are also grateful to the Department of civil Engineering at Konya Technical University and Selçuk University for providing us with the resources and support we needed to complete this project.

### Data Availability




The authors confirm that the data supporting the findings of this study are available within the article.

### REFERENCES

- [1] MnDOT, "MnDOT PAVEMENT DESIGN MANUAL," ed: Minnesota Department of Transportation 2014.
- [2] O. S. a. H. V. Quintus, "TRAFFIC LOAD SPECTRA FOR IMPLEMENTING AND USING THE MECHANISTIC-EMPIRICAL PAVEMENT DESIGN GUIDE IN GEORGIA," Department of Transportation State of Georgia 10-09, PI # 0010110, 2014.
- [3] G. Kollaros, A. Athanasopoulou, and A. Kokkalis, "Perpetual flexible pavement design life," *CD-ROM Proceedings of BCRRA*, pp. 537-542, 2017.
- [4] I. Yut, J. Mahoney, and D. A. Larsen, "Preparation of the implementation plan of AASHTO Mechanistic-Empirical Pavement Design Guide (M-EPDG) in Connecticut: Phase II: expanded sensitivity analysis and validation with pavement management data," University of Connecticut 2017.
- [5] L. S. P. Gopiseti, H. Ceylan, B. Cetin, S. Kim, and O. Kaya, "Sensitivity Analysis of New Reflective Cracking Model in Pavement Mechanistic-Empirical Design," in *Geo-Congress 2020: Geotechnical Earthquake Engineering and Special Topics*, 2020, pp. 508-516.
- [6] C. W. Schwartz, R. Li, S. Kim, H. Ceylan, and K. Gopalakrishnan, "Sensitivity evaluation of MEPDG performance prediction," 2011.
- [7] H. Ceylan, S. Kim, K. Gopalakrishnan, C. W. Schwartz, and R. Li, "Sensitivity analysis frameworks for mechanistic-empirical pavement design of continuously reinforced concrete pavements," *Construction and Building Materials*, vol. 73, pp. 498-508, 2014.
- [8] E. G. Fernando, J. Oh, and D. Ryu, "Phase I of ME PDG Program Implementation in Florida," 2007.
- [9] C. Schwartz, "Implementation of the NCHRP 1-37A Design Guide, Report No," SP0077B41, Maryland State Highway Administration, Lutherville, MD, 2007.
- [10] R. Velasquez, K. Hoegh, I. Yut, N. Funk, G. Cochran, M. Marasteanu, et al., "Implementation of the MEPDG for new and rehabilitated pavement structures for design of concrete and asphalt pavements in Minnesota," 2009.
- [11] S. Esfandiarpour, M. A. Ahammed, A. Shalaby, T. Liske, and S. Kass, "Sensitivity of pavement ME design predicted distresses to asphalt materials inputs," in *Proceedings of the 2013 Conference and Exhibition of the Transportation Association of Canada-Transportation: Better-Faster-Safer (TAC/ATC'13)*, 2013.
- [12] Y. R. Kim, Implementation plan for the new mechanistic-empirical pavement design guide: NC Department of Transportation Research and Analysis Group, 2007.
- [13] R. Baus and N. Stires, "Mechanistic-empirical pavement design guide implementation," 2010.



## NEW METRIC FOR THE CALCULATION OF SENSITIVITY ANALYSIS INDEX OF FLEXIBLE PAVEMENT USING MECHANISTIC-EMPIRICAL APPROACH, TURKEY-CASE STUDY

<sup>1,2,\*</sup>Saadoon Obaid EYADA , <sup>3</sup>Osman Nuri ÇELİK , <sup>4</sup>Nibras Y. ABDULLA 

<sup>1</sup>Konya Technical University, Civil Engineering Department, Konya, TÜRKİYE

<sup>2</sup>Anbar Health Directorate, Iraqi Ministry of Health, Ramadi, Anbar, IRAQ

<sup>3</sup>Konya Technical University, Civil Engineering Department, Konya, TÜRKİYE

<sup>4</sup>Anbar University, Biology Department, College of Science, Ramadi, Anbar, IRAQ

<sup>1,2</sup>saadooneyada@gmail.com , <sup>3</sup>oncelik@ktun.edu.tr, <sup>4</sup>nib19s3017@uoanbar.edu.iq

### Highlights

- New metric for the conducting Sensitivity Analysis
- Turkiye- Case study
- MECHANISTIC-EMPIRICAL design parameters



## THE EMPIRICAL STABILITY EVALUATION OF THE KÖRÜKINI CAVE, DEREBUCAK, KONYA

<sup>1\*</sup>Ali Ferat BAYRAM , <sup>2</sup>Naji Saleh AL-QUBALI 

<sup>1</sup>*Konya Technical University, Engineering and Natural Sciences Faculty, Geological Engineering Department, Konya, TÜRKİYE*

<sup>2</sup>*Konya Technical University, Graduate Education Institute, Konya, TÜRKİYE*



<sup>1</sup>[afbayram@ktun.edu.tr](mailto:afbayram@ktun.edu.tr), <sup>2</sup>[najiqubaly@gmail.com](mailto:najiqubaly@gmail.com)

### *Highlights*

- The Körükini cave is one of the most important caves of the Derebucak area (Konya, Türkiye).
- The empirical method was applied to the cave for evaluation its stability.
- Collapses may occur in the Körükini Cave and support is recommended.



## THE EMPIRICAL STABILITY EVALUATION OF THE KÖRÜKİNİ CAVE, DEREBUCAK, KONYA

<sup>1\*</sup>Ali Ferat BAYRAM , <sup>2</sup>Naji Saleh AL-QUBALI 

<sup>1</sup>Konya Technical University, Engineering and Natural Sciences Faculty, Geological Engineering Department,  
Konya, TÜRKİYE

<sup>2</sup>Konya Technical University, Graduate Education Institute, Konya, TÜRKİYE

<sup>1</sup>[afbayram@ktun.edu.tr](mailto:afbayram@ktun.edu.tr), <sup>2</sup>[najiqubaly@gmail.com](mailto:najiqubaly@gmail.com)

(Received: 13.07.2023; Accepted in Revised Form: 21.07.2023)

**ABSTRACT:** Located 145 km away from Konya, the Körükini cave is one of the most important caves of the Derebucak area. In this study, it is aimed to evaluate the stability of the Körükini cave. For this purpose, we conducted geological field trips, took block samples and made in-situ field tests. Following these steps, we applied laboratory tests to determine physico-mechanical properties on rock samples taken from the cave.

Based on the RMR, GSI, Q, R<sub>Mi</sub> classification, rock mass values were determined for the Körükini Cave. Thus, average RMR is 60, average Q is 8.2, average GSI is 75 and average R<sub>Mi</sub> 11.64. the obtained data show that the Körükini Cave is unstable in all locations according to empirical stability evaluation. Thus, support (e.g. systematic bolting, fibre reinforced shotcrete and bolting, and fibre reinforced shotcrete and bolting) is needed for the Körükini Cave.

**Keywords:** Karstic Derebucak Caves, Stability, Empirical, Rock Mass Classification.

### 1. INTRODUCTION

Located 145 km away from Konya, the Körükini cave is one of the most important caves of the Derebucak area (Figure 1). The entry of the Körükini cave is 1340 m height above sea level (Figure 2). The height of the entry is 30 m. There are eroded rock fragments with equal size in the passage and a deep lake 130 m ahead. There are also exits from the cave with more than 12x12 m size and a lot of stalactite and stalagmite. The cave has increasingly attracted visitors in the last years.

About 30% of Turkey is covered with carbonate rocks. Taurus Karst Belt, Southeast Anatolian Karst Belt, Northwest Anatolian Karst Belt and Konya Closed Basin Karst Belt are the most common [1]. The extensive limestone outcrops and thicknesses in Turkey facilitated the formation of caves.

Caves are classified in different ways according to their formation, development, physico-chemical structures and cover thickness. In general, underground cavities can be artificial or natural according to their formation, caves are among the natural formations. There are many artificial caves in our country, especially in the Taurus belt. Artificial caves are mostly created for shelter, storage, burial and mining purposes [2-3]. Natural caves, on the other hand, are formed as a result of the erosion of soluble rocks by natural processes. In natural caves, cave formation may occur during the formation of the main rock (such as travertine cavities, lava and glacial caves). In addition, secondary (karstic) caves can be formed by the effect of water from rocks such as soluble limestone, gypsum, etc. [4]. There are approximately 35,000 to 40,000 karst caves in Turkey, most of which are located in the Taurus Mountain Belt [5-6].

In this study, it is aimed to evaluate the stability of the Körükini cave, based on the empirical method that is mainly for the man-made engineering structures (e.g. tunnel, slope etc.). For this purpose, we conducted geological field trips, took block samples and made in-situ field tests. Following these steps, we applied laboratory tests to determine physico-mechanical properties on rock samples taken from the cave.

## 2. GENERAL GEOLOGY

The study area is located on the Anatolide-Tauride block, which formed as an extensive carbonate platform during the Mesozoic and was intensely deformed and partly metamorphosed during Alpidic orogeny [7].

The oldest unit in the study area is Early to Middle Cambrian autochthon carbonates which are mostly recrystallized and dolomitized. The Cretaceous Peridotite and ophiolitic melange are observed above the carbonates. The Jurassic to Cretaceous allochthon units composed of neritic carbonates exist in the South of the study area. They have thickness with more than 10 m, which is suitable for cave formation and karst structure such as karren, doline etc. Plio-Quaternary units unconformably overlie all the older units in the study area (Figure 1).

## 3. MATERIAL AND METHODS

Field observations and many measurements were done on layerings and joints to determine strike and dip both in and outside the Körükini cave. A Schmidt hammer was used in the field to indirectly determine uniaxial compressive strength. Block samples were taken from both inside and outside of the cave, and mechanical tests were done on these samples in the rock mechanics laboratory in the Konya Technical University. Core samples were taken from the rock blocks using NX-type core barrel, and they were cut and polished according to the ISRM [8-9].

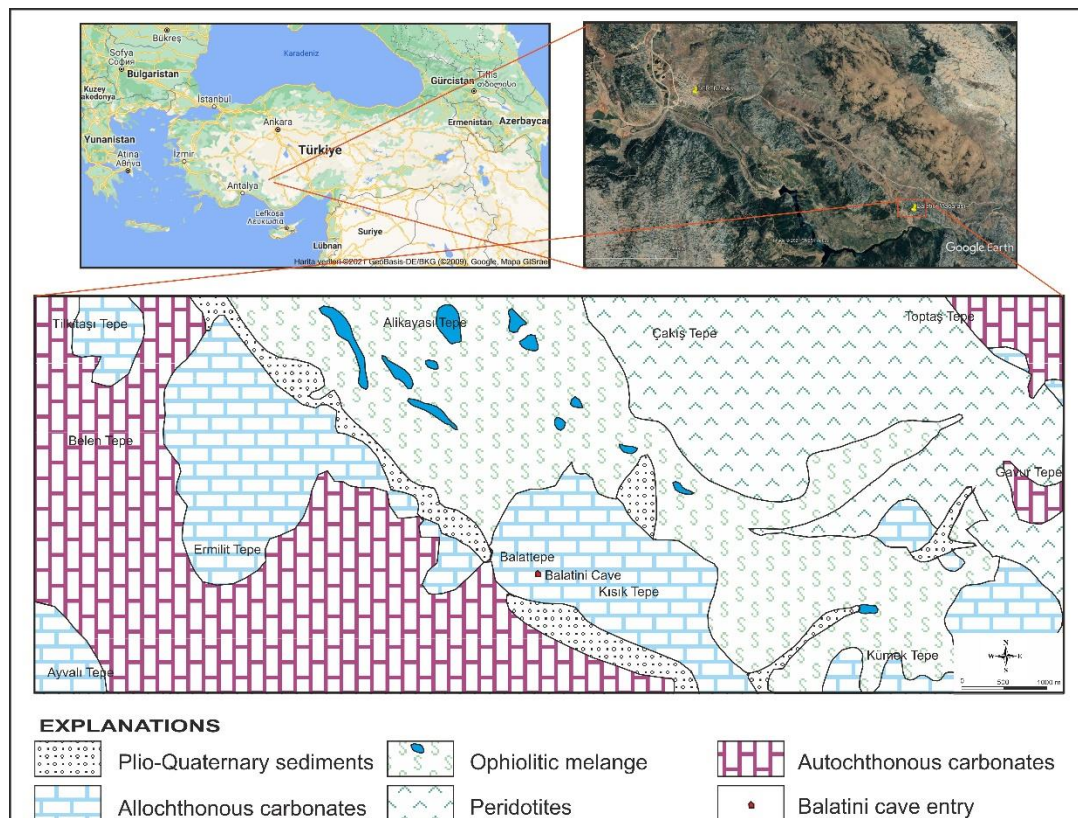


Figure 1. Simplified geological map of the Körükini cave and its surroundings [10]



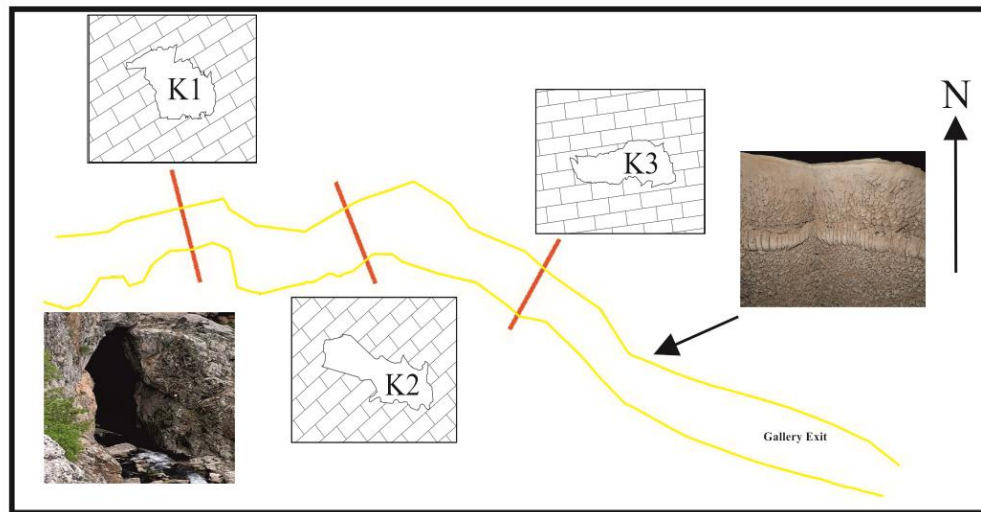


Figure 2. Plan and sections of Körükini cave

### 3.1. Status of Discontinuities around the Körükini Cave

Measurements of strike and dip from discontinuities were evaluated according to the method by Allmendinger [11] and constructed contour and rose diagrams (Figure 3). Thus, two joint sets were determined. Fractures strike NW-SE and dip to SW with  $10^{\circ}$  to  $40^{\circ}$  (average  $30^{\circ}$ ). Contour diagrams in Figure 3 clearly show two joint sets. Dominant orientations of the fractures are N24W/60 SW and N53W/72SW. Rose diagram given in Figure 4 shows that their direction is NW-SE.

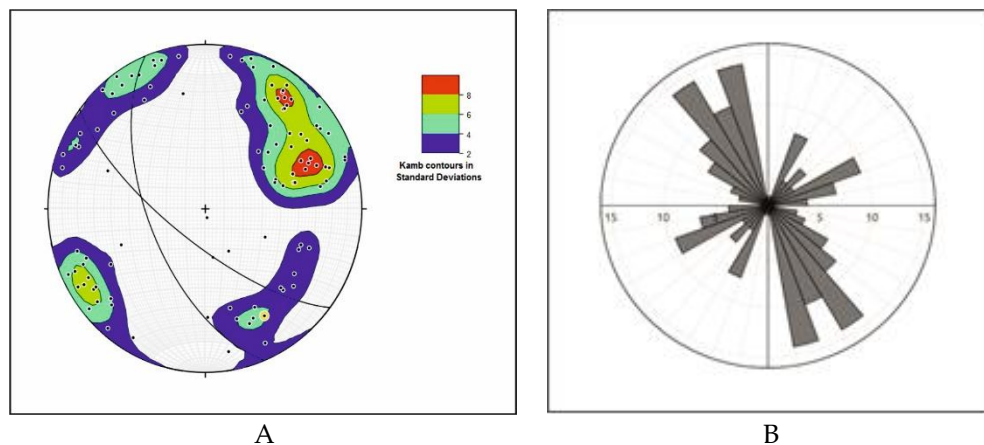


Figure 3. Contour and rose diagram of joint measurements around the Körükini Cave.

### 3.2. Schmidt Hammer Test in the Field

According to filling status of the caves, average uniaxial compressive strength of the joint surface are given in Table 1. Thus, this value is  $\sigma_c$  (MPa): 76

### 3.3. Determination of JCS and JRC

JCS (Joint Wall Compressive Strength) is accepted as 63.5 MPa using the Barton- Bandis [12] sliding

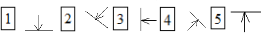
criteria for filled or infilled surface of discontinuities in limestone's in the study area (Table 1).

In the field, roughness ranges from 2 to 30, corresponding to JRC (Joint Roughness Coefficient) of 4 to 10 according to the profilometer for the Körükini cave.

**Table 1.** Schmidt Hardness Test in Field

Name	Fill State	Tilt Angle	Position of the hammer*	Rebound Numbers	** $\sigma_c$ (MPa)	* $\sigma_c$ (MPa)
Körükini	Infilled	71°	3	46	77	76
	Filled	65°	4	48	75	

\*Average, \*\* Uniaxial Compressive Strength (from the chart given in the Schmidt Fig.)

\*\*\* Position of the hammer, 

### 3.4. Estimation of RQD

RQD (Rock Quality Designation) is estimated from following equation [13] in the absence of drilling in the field.

$$RQD = 115 - (3.3 \times J_v) \quad (1)$$

Based on two joint sets measured from outside the cave, the first and second joint numbers are 47 and 40, respectively and measurement length is 10 m and 9 m., respectively. Thus,

$$RQD \text{ value } J_v = (47/10) + (40/9) = 9.14 \text{ joint/m}^2 \text{ and } RQD = 115 - (3.3 \times J_v) = 115 - (3.3 \times 9.14) = 85\%.$$

### 3.5. Uniaxial Compressive Strength Test

This test was made on total 65 core samples according to ISRM [9].  $\sigma_c$  was calculated 48.17 MPa for the Körükini cave, pointing to medium strength according to ISRM [8] (Tablo 2).

**Tablo 2.** Uniaxial compressive strength values of limestone rock samples in the Körükini Cave

	N. No	Diameter D-mm	Length L-mm	Cross- Sectional Area A-m <sup>2</sup>	Failure Load P- kN	$\sigma_c$ -MPa	UCS $\sigma_c$ (50)
							-MPa
Körükini	1	53.73	137,51	0,0022672	119,30	52,62	53,31
	2	53.62	137,51	0,0022577	121,80	53,95	54,63
	3	53.70	137,55	0,0022651	98,50	43,49	44,05
	4	53.65	137,36	0,0022606	91,70	40,56	41,08
	5	53.80	137,91	0,0022735	201,40	88,59	89,76
	6	53.63	137,29	0,0022587	146,00	64,64	65,46
	7	53.66	137,67	0,0022615	110,20	48,73	49,35
	8	53.62	137,41	0,0022577	110,70	49,03	49,65
	9	53.70	137,41	0,0022644	71,60	31,62	32,03
	10	53.72	137,81	0,0022665	116,30	51,31	51,98
	11	53.55	137,59	0,0022522	53,80	23,89	24,18
	12	53.51	137,67	0,0022486	101,70	45,23	45,78
	13	53.73	138,39	0,0022672	92,70	40,89	41,42
	14	53.64	137,51	0,0022594	66,90	29,61	29,99
	15	53.73	138,32	0,0022672	112,10	49,45	50,09
	16	53.75	137,68	0,0022691	108,30	47,73	48,35
	17	53.62	137,29	0,0022579	58,40	25,86	26,19
	18	53.70	137,82	0,0022646	114,50	50,56	51,21
	19	53.73	137,81	0,0022674	124,50	54,91	55,63
	20	53.66	137,71	0,0022615	62,80	27,77	28,12
	21	53.79	137,56	0,0022722	91,70	40,36	40,89
	22	53.75	138,25	0,0022691	182,30	80,34	81,39
	23	53.74	137,09	0,0022680	119,50	52,69	53,38
<b>Average</b>						<b>47.56</b>	<b>48.17</b>
<b>Standard Deviation</b>							<b>15.87</b>

## 4. ROCK MASS CHARACTERISTICS

### 4.1. RMR

Parameters and values to determine RMR (Rock Mass Rating) for the Körükini Cave are given Table 3. Thus, RMR point ranges from 53 to 71.

### 4.2. Q System

Q (or Norwegian Geotechnical Institute) value of the Körükini cave is calculated according to the parameters in Table 4. Thus, “the best value” is (RQD for 90);  $Q = (90/4) (1.5/1) (1/2.5) = 13.5$  and “the worst value” is (RQD for 75);  $Q = (75/4) (1/2) (0.3/3) = 0.93$ .

### 4.3. GSI

For Late Cretaceous limestone from the Körükini cave, GSI (Geological Strength Index) was calculated as 75. Rock mass of the limestone has two joint sets with undisturbed.

### 4.4. R<sub>Mi</sub>

Joint Length (jL) was taken 2 because joint width is from 0.1 to 1 m [14]. Block volume was found from Figure 6 and R<sub>Mi0</sub> value is 22 and 25 for jC 1.75. According to equation “Rock Mass Index (R<sub>Mi</sub> = R<sub>Mi0</sub>\* $\sigma_c/100$ )”,  $R_{Mi_{min}} = 22*41.85/100 = 9.20$  and  $R_{Mi_{max}} = 25*70.41/100 = 17.60$ .

**Table 3.** Input parameters to RMR system in Körükini Cave

A. Parameter			
	<b>Strength of intact rock material (<math>\sigma_c</math>)</b>	50-100 MPa (76MPa)	
<b>1.</b>	Rating	7	
	<b>Drill core quality, RQD</b>	75- 90% (85%)	
<b>2.</b>	Rating	17	
	<b>Spacing of discontinuities</b>	200- 600 mm	
<b>3.</b>	Rating	10	
	<b>Ground water</b>	WET	DRY
<b>4.</b>	Puan	7	15
B. Condition of discontinuities			
	<b>Length, persistence</b>	1- 3 m	<1 m
	Rating	4	6
	<b>Separation</b>	>5mm	1-5 mm
	Rating	0	1
	<b>Roughness</b>	slightly rough	rough
	Rating	3	5
	<b>Infilling (gouge)</b>	Soft filling <5 mm	Hard filling <5 mm
	Rating	2	4
	<b>Weathering</b>	moderately w	unweathered
	Rating	3	6
	<b>RMR (min.):</b>	53	
	<b>RMR (max):</b>	71	
	<b>RMR (avg):</b>	62	

**Tablo 4.** Input parameters to Q system in Körükini Cave

Parameter	Rating
<b>1. Rock quality designation (RQD)</b>	<b>RQD</b>
Good	75%-90% (85%)
<b>2. Joint set number (Jn)</b>	<b>Jn</b>
Two joint sets	4
Two joint sets plus random	6
<b>3. Joint roughness number</b>	<b>Jr</b>
Smooth, planar	1.0
Rough or irregular, planar	1.5
<b>4. Joint alteration number</b>	<b>Ja</b>
No coating or filling, except from staining (rust)	1.0
Non-softening mineral coatings, clay-free particles, etc.	2.0
<b>5. Joint water reduction factor</b>	<b>Jw</b>
Dry excavations or minor inflow, i.e. < 5 l/min locally	1.0
Medium inflow or pressure, occasional outwash of joint fillings	0.66
Large inflow or high pressure in competent rock with unfilled joints	0.5
Large inflow or high pressure, considerable outwash of joint fillings	0.33
<b>6. Stress reduction factor</b>	<b>SRF</b>
Low stress, near surface, open joints.	2.5

## 5. EVALUATION OF EMPIRICAL STABILITY

The minimum width of the Körükini Cave is 6.4 m. According to the RMR classification, maximum unsupported span and stand up time values were given in Figure 4.

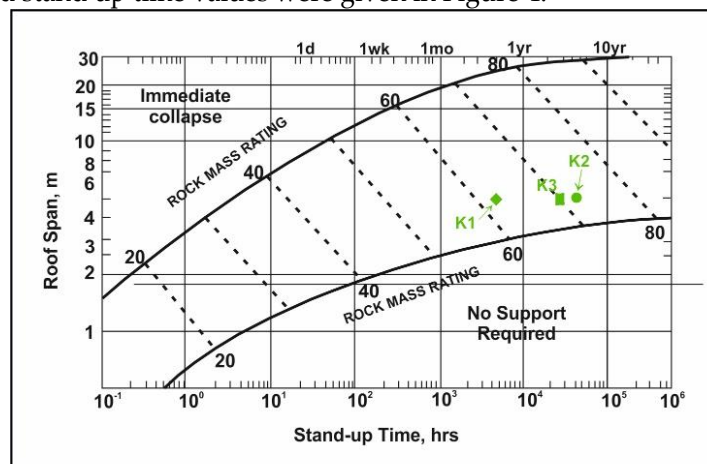


**Figure 4.** Classification and support recommendations based on RMR-values

RMR points of the Körükini Cave range from 53 to 71, the minimum opening was accepted as 5.4 m. According to Figure 5, sudden collapse may be where opening is more than 15 m. Based on the criteria by Bieniawski [15], stand up time is from 4 to 7 month. According to Figure 5, support system for the Körükini cave are (1) systematic bolting (and unreinforced shotcrete, 4-10 cm), (2) fibre reinforced shotcrete and bolting 5-9 and (3) fibre reinforced shotcrete and bolting 9-12 cm.

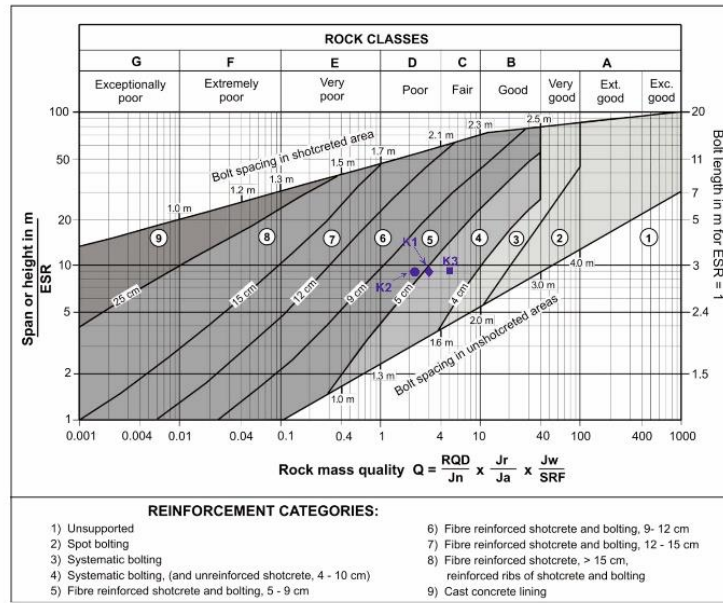


Figure 5. Classification and support recommendations based on Q-values

According to Palmström [14], support type for the Körükini Cave is “shotcrete and rock bolt” with concrete thickness between 40 and 80 mm. when the size ratio (Sr) linearly reduce, rock bolt spacing ranges from 1.7 to 3 m (Figure 6). Based on the evaluation of Empirical stability, support is needed for the Körükini Cave.

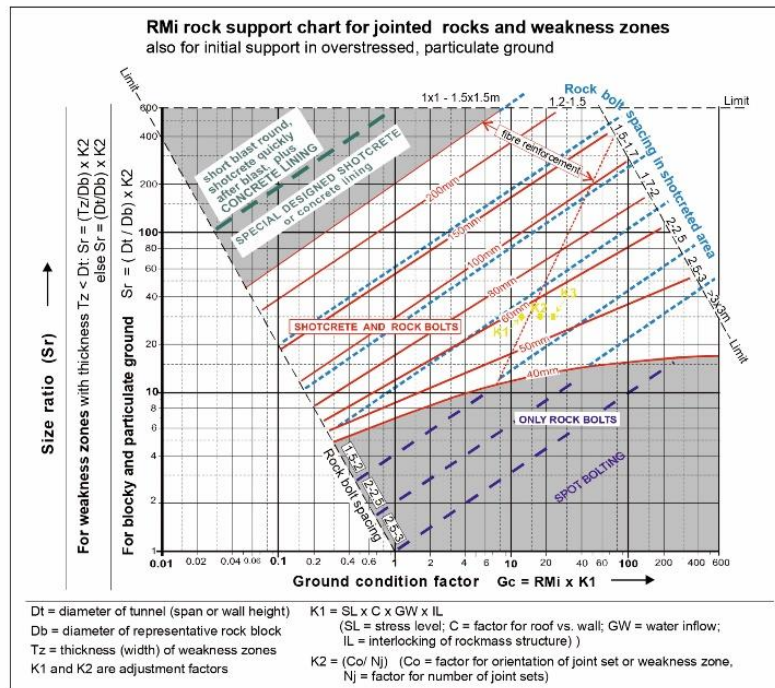


Figure 6. The Rmi charts for estimates of rock support in Körükini Cave

## 6. CONCLUSIONS

In this study, evaluation of Empirical stability was made for the Körükini Cave. Based on the RMR, GSI, Q and Rmi systems applied to the Körükini Cave, following conclusions may be reached.

1. Block fall/sliding and collapse are potential risk in the Körükini cave

2. Movement in the hole is higher than those of the entry in the Cave.
3. Support is needed for the Körükini Cave.
4. Blasting should not be allowed around the Körükini Cave.
5. Dynamic condition should be considered in the future studies, because stability evaluation is made under static condition in this study.

### Credit Authorship Contribution Statement

Material preparation, data collection and analysis were performed by Ali Ferat BAYRAM and Naji Saleh AL-QUBALI.

### Declaration of Competing Interest

The authors declare they have no competing interests

### Acknowledgements

We thank to Republic of Türkiye Ministry of Agriculture and Forestry, 8<sup>th</sup> Regional Directorate. We also thank to three anonymous reviewers, and Prof. Dr. Mustafa TABAKÇI and Prof. Dr. Niyazi BİLİM for editorial contributions.

### REFERENCES

- [1] Nazik, L. and Poyraz, M. "A region that characterise the general karst geomorphology of Turkey: Central Anatolia Plateau karst zone" *Turkish Ceographical Review*(68), 43-56., 2017. (in Turkish)
- [2] Nazik, A. "Planktonic foraminiferal biostratigraphy of the Neogene sequence in the Adana Basin, Turkey, and its correlation with standard biozones" *Geological Magazine*, 141 (3), 379-387., 2004. (in Turkish)
- [3] Dönmez, A. "Protection of Caves in Turkish Law" MSc Dissertation, University of Akdeniz, Institute of Social Sciences, Antalya, 98 p., 2006 (in Turkish)
- [4] Ozansoy, C. and Mengi, H. "Speleology and Caving" 1<sup>st</sup> edition, *TUBITAK Popular Science Books Publications, Nurol printing*, Ankara, 337 p., 2006 (in Turkish)
- [5] Nazık, L. "La morphologie des grottes et ses implications géologiques, géomorphologiques et écologiques (fr)" *Geomorphology bulletin* (17), 53-62., 1989. (in Turkish)
- [6] Sür, A. "Karst landforms and examples from Turkey" *Ankara University, Journal of Turkish Geography Research and Application Center*, 3, 1-28, 1994. (in Turkish)
- [7] Okay, A.I. "Geology of Turkey: A Synopsis" *Anschnitt* (21), p 19-42, 2008.
- [8] ISRM "ISRM Suggested Methods: Rock Characterization, Testing and Monitoring" ed. E. T. Brown, *Pergamon Press, London*, 211 p., 1981
- [9] ISRM "The Complete ISRM Suggested Methods for Rock Characterization, Testing and Monitoring: 1974 – 2006" R. Ulusay and J. A. Hudson (eds.), *Suggested Methods Prepared by the Commission on Testing Methods, International Society for Rock Mechanics, Compilation Arranged by the ISRM Turkish National Group, Kozan Ofset, Ankara, Turkey*, 628 p., 2007
- [10] Alqubali, N. " Investigation Of The Stability Of Caves Around Derebucak (Beysehir Konya)" MSc Dissertation, Konya Technical University, Institute of Graduate Studies, 130 p., 2023, (in Turkish)
- [11] Allmendinger, R. W., Cardozo, N., and Fisher, D., "Structural geology algorithms: Vectors and tensors in structural geology" *Cambridge University Press (book to be published in early 2012)*, 2012
- [12] Barton, N. and Bandis, S., "Review of predictive capabilities of JRC-JCS model in engineering practice" *Proc. int. symp. on rock joints, Loen, Norway, Rotterdam: Balkema*, pp., 603-610. 1990
- [13] Palmstrom, A. "The volumetric joint count—a useful and simple measure of the degree of rock mass jointing" *International Association of Engineering Geology. International congress. 4*, 221-228, 1982

- [14] Palmström, A. "Combining the RMR, Q, and RMI classification systems" *Tunnelling Underground Space Technology*, 24 (4), 491., 2009, [http://www.rockmass.net/files/combining\\_RMR-Q-RMI.pdf](http://www.rockmass.net/files/combining_RMR-Q-RMI.pdf)
- [15] Bieniawski, Z.T. "Engineering rock mass classifications: a complete manual for engineers and geologists in mining, civil, and petroleum engineering" *John Wiley & Sons*, 237 p., 1989



## COMPARISON OF INNOVATIVE TREND ANALYSIS METHODS FOR HYDROMETEOROLOGICAL PARAMETERS IN THE KARASU SUB-BASIN

<sup>1</sup>Cihangir KÖYCEĞİZ , <sup>2,\*</sup>Meral BÜYÜKYILDIZ 

*Konya Technical University, Engineering and Natural Sciences Faculty, Civil Engineering Department,  
Konya, TÜRKİYE*

<sup>1</sup>[ckoycegiz@ktun.edu.tr](mailto:ckoycegiz@ktun.edu.tr), <sup>2</sup>[mbuyukyildiz@ktun.edu.tr](mailto:mbuyukyildiz@ktun.edu.tr)



### *Highlights*

- The temporal trend was investigated based on hydrometeorological data of the Karasu Sub-Basin
- The temporal trends were identified using innovative graphical and statistical trend approaches including Şen-ITA, OTT, CWTSD methods.
- Innovative trend methods were compared with the classical MK test.





## COMPARISON OF INNOVATIVE TREND ANALYSIS METHODS FOR HYDROMETEOROLOGICAL PARAMETERS IN THE KARASU SUB-BASIN

<sup>1</sup>Cihangir KÖYCEĞİZ , <sup>2</sup>\*Meral BÜYÜKYILDIZ 

Konya Technical University, Engineering and Natural Sciences Faculty, Civil Engineering Department,  
Konya, TÜRKİYE

<sup>1</sup>ckoycegiz@ktun.edu.tr, <sup>2</sup>mbuyukyildiz@ktun.edu.tr

(Received: 02.05.2023; Accepted in Revised Form: 22.07.2023)

**ABSTRACT:** Türkiye, which has a complex climate structure, is shown among the countries that will be most affected by climate change with the effect of global warming. These effects will differ in different regions due to their topographic structure, location, and orographic characteristics. Trend analyzes are used to determine the direction and magnitude of this variability. In this study, trend analysis was carried out by using hydrometeorological data obtained from streamflow and meteorology stations located in the Karasu Sub-Basin located in the Euphrates-Tigris Basin. Three innovative trend methods, namely the Şen-Innovative Trend Analysis, Onyutha Trend Test, Combination of Wilcoxon Test and Scatter Diagram trend tests, were used together with the classical Mann-Kendall method in the monthly scale analysis of hydrometeorological data of the 1979-2020 period. Both graphical and statistical trend analysis can be done with innovative methods. The results obtained in the study, in which trend analyses were evaluated at the  $\alpha=0.05$  significance level, reveal significant and insignificant decreasing trends in the parameters of mean streamflow, maximum precipitation, total precipitation, mean and minimum relative humidity. Significant and insignificant increasing trends were determined in the maximum, minimum, and mean temperature, maximum relative humidity, and mean wind speed data. The trends obtained in the methods used in general are consistent with each other. The findings of this study could lead to a better knowledge of the region's hydrology and contribute sustainable water management. The trend analysis methods used in the study are thought to be quite helpful in the analysis of hydro-meteorological time series.

**Keywords:** Climate Change, Hydrometeorological, Mann-Kendall, Onyutha, Şen Innovative Trend Analysis, Wilcoxon Test

### 1. INTRODUCTION

Climate change as a result of global warming shows its effect on many hydrometeorological parameters. As a result of the changes in hydrometeorological parameters, there is an increase in events such as the rise of sea level due to the melting of glaciers, the occurrence of hurricanes, floods, and droughts in many parts of the world as a result of sudden temperature changes, and the increase in forest fires [1-2]. These global effects of climate change include regional differences [3-4]. Natural disasters such as floods and droughts in recent years threaten the ecosystem, water resources, and agricultural activities, especially human life [5]. Increases are observed in the incidence, impact, and duration of these natural disasters [6]. Certain regions of the world have difficulties in accessing fresh water or using water in sectors such as agriculture and industry and are faced with drought disasters. Some regions are also exposed to irregular and excessive rainfall and have to struggle with natural disasters such as floods and landslides [7-8].

It is clear that climate change will change water resources in terms of quantity and quality by changing the hydrological cycle and systems and will also directly or indirectly affect socio-economic and environmental goods and services. The significant possible impact of climate change on the water cycle (hydrological cycle) will appear as changes in water resource availability and water quality [9-10]. Examining the temporal changes of many hydrometeorological parameters with trend analysis to

\*Corresponding Author: Meral BÜYÜKYILDIZ, [mbuyukyildiz@ktun.edu.tr](mailto:mbuyukyildiz@ktun.edu.tr)

determine the possible effects of climate change is the focus of many studies [11-15]. For this purpose, statistical and graphical trend analysis methods are used. Mann-Kendall trend analysis is the most widely used statistical trend method [16-18]. The Innovative Şen Trend method, on the other hand, is a method that has been used for about ten years in the analysis of the variability of hydrometeorological parameters and offers the opportunity to evaluate trends both graphically and statistically [18-22]. In recent years, innovative graphical trend methods have been used. Some of these methods are Innovative Polygon Trend Analysis (IPTA), Trend Polygon Star Concept (TPSC), Innovative trend pivot analysis method (ITPAM), Onyutha Trend Test (OTT), Combination of Wilcoxon test and scatter diagram trend (CWTSD).

Since Türkiye is located in the east of the Mediterranean, where the effects of climate change will be felt intensely due to its geographical location, it is considered among the high-risk countries. Especially forest fires, floods, and drought in recent years reveal the effects of climate change in Türkiye. In this study, trend analysis of various hydrometeorological parameters in the Karasu Basin, which is a sub-basin of the transboundary Euphrates-Tigris Basin, one of Türkiye's arid basins, was performed using the classical Mann-Kendall method. In addition, temporal variability was investigated comprehensively and comparatively with the Onyutha Trend Test (OTT), Şen-Innovative Trend Analysis (Şen-ITA), and Combination of Wilcoxon Test and Scatter Diagram (CWTSD), which is a relatively new trend method.

## 2. MATERIAL AND METHOD

### 2.1. Study Area and Data

The Karasu Basin is a sub-basin of the Euphrates-Tigris Basin and takes its name from the Karasu River, which is one of the main tributaries of the Euphrates River (Figure 1).

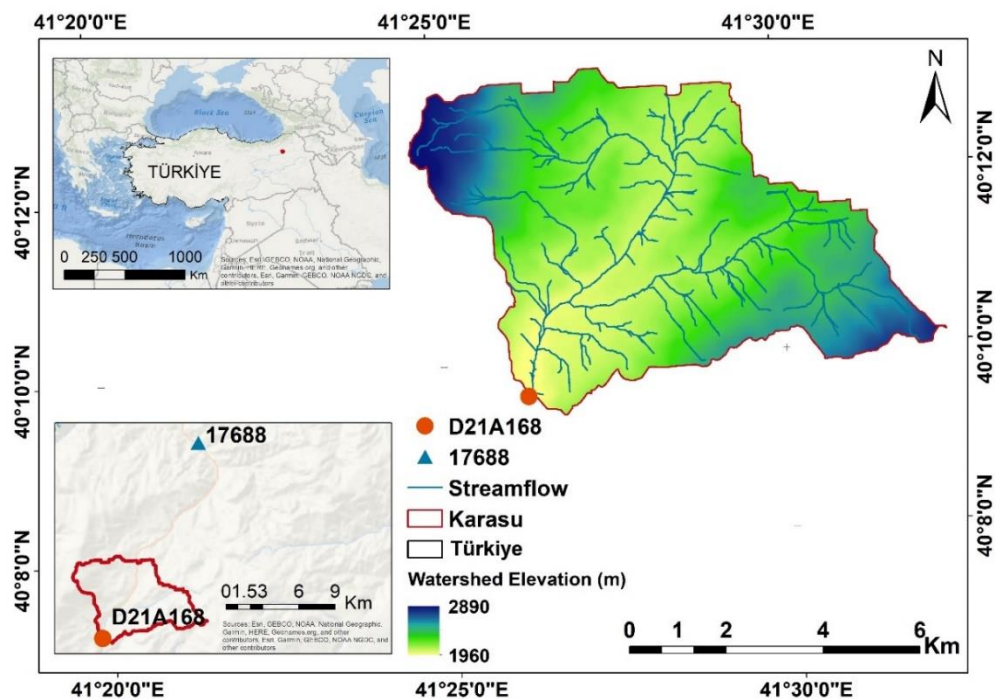


Figure 1. Karasu elevation map and locations of stations used in the study

The Karasu Basin is a high-altitude sub-basin with a continental climate. Most of the precipitation falls on the surface as snowfall. Snow cover remains on the surface for about 150 days a year. Day and night temperature differences are always high throughout the four seasons. The annual average temperature varies between 10°C and -5°C [23]. The altitude in the basin varies between 1960-2890 m. The surface area of the basin is 43.95 km<sup>2</sup> [24]. In low-altitude areas, agriculture is done partially. However,

the surface cover of the majority of the basin consists of shrubs and herbaceous plants. It is a basin with heavy snowfall. It is a rich headwater basin due to its water potential and high altitude. The digital elevation model of the Karasu sub-basin used in the formation of the location map was provided by Amazon Web Services with a resolution between 3 m and 2.5 km. Streamflow data of the sub-basin are measured at D21A168 (Karagöbek-Büyük River) flow observation station. Meteorological parameters were obtained from Tortum meteorological observation station no 17688. It was chosen because it is the closest station to Karasu. In this study, the trend analyses are performed on mean streamflow ( $Q_{\text{mean}}$ ), total precipitation ( $P_{\text{total}}$ ), maximum precipitation ( $P_{\text{max}}$ ), mean, minimum and maximum temperature ( $T_{\text{mean}}$ ,  $T_{\text{min}}$  and  $T_{\text{max}}$ ), mean, minimum and maximum relative humidity ( $RH_{\text{mean}}$ ,  $RH_{\text{min}}$  and  $RH_{\text{max}}$ ), mean wind speed ( $WS_{\text{mean}}$ ). The data have a monthly temporal scale. The basic statistical values of hydrometeorological parameters for the 1979-2020 period are given in Table 1.

**Table 1.** Basic statistical values of hydrometeorological parameters used in the study

Parameter	Min	Mean	Max	Standard Deviation (SD)	Skewness ( $C_s$ )	Kurtosis ( $C_k$ )	Coefficient of Variation (CV)
$Q_{\text{mean}}$ (m <sup>3</sup> /s)	0.02	0.76	4.86	0.81	2.17	5.03	107.58
$P_{\text{total}}$ (mm)	0.0	36.46	170.20	26.42	1.03	1.41	72.46
$P_{\text{max}}$ (mm)	0.0	12.30	43.00	7.79	0.91	0.89	63.30
$T_{\text{mean}}$ (°C)	-10.30	8.48	23.30	8.50	-0.09	-1.24	100.22
$T_{\text{min}}$ (°C)	-26.60	-4.93	11.00	9.69	-0.25	-1.06	-196.68
$T_{\text{max}}$ (°C)	0.0	21.92	38.30	9.58	-0.18	-1.30	43.70
$RH_{\text{mean}}$ (%)	34.0	59.97	76.30	7.30	-0.37	0.11	12.17
$RH_{\text{min}}$ (%)	0.0	18.34	46.00	8.63	0.49	0.23	47.04
$RH_{\text{max}}$ (%)	79.0	96.23	104.00	2.97	-0.89	2.78	3.09
$WS_{\text{mean}}$ (m/s)	0.10	1.26	2.70	0.44	0.06	0.25	34.65

In Table 1, the skewness ( $C_s$ ) values of the investigated hydro-meteorological parameters ranged from -0.89 to 2.17. The  $C_s$  values of  $T_{\text{mean}}$ ,  $T_{\text{min}}$ ,  $T_{\text{max}}$ ,  $WS_{\text{mean}}$ ,  $RH_{\text{mean}}$ , and  $RH_{\text{min}}$  parameters are between  $\pm 0.5$  and there is a very symmetrical distribution. The  $C_s$  values of the  $Q_{\text{mean}}$  and  $P_{\text{total}}$  parameters are 2.17 and 1.03, respectively, which are very skewed ( $>1$ ). Other parameters have moderate skewness. The values of the parameters  $T_{\text{mean}}$ ,  $T_{\text{min}}$ ,  $T_{\text{max}}$ ,  $RH_{\text{mean}}$ , and  $RH_{\text{max}}$  are skewed to the left, while the others are skewed to the right. Kurtosis ( $C_k$ ) values of  $T_{\text{mean}}$ ,  $T_{\text{min}}$ , and  $T_{\text{max}}$  parameters are negative and Platykurtic distribution is present. In the remaining parameters,  $C_k$  values are positive and there is a Leptokurtic distribution. Streamflow ( $Q_{\text{mean}}$ ) data has very thick tails and many outliers with the value  $C_k=5.03$ . Table 1 also gives the coefficient of variation (CV) values representing the degree of variability of hydrometeorological parameters for the 1979-2020 period. In Table 1, coefficient of variation (CV) values for  $Q_{\text{mean}}$ ,  $P_{\text{total}}$ ,  $T_{\text{mean}}$ , and  $T_{\text{min}}$  are  $>70$  and there is extremely high variability. Very high variability with  $CV>40$  for  $P_{\text{max}}$ ,  $T_{\text{max}}$ , and  $RH_{\text{min}}$ , high variability with  $CV>30$  for  $WS_{\text{mean}}$ , and low variability with  $CV<20$  for other parameters.

The correlation matrix is given for ten hydrometeorological parameters used in Table 2. According to Table 2, there is a negative correlation between  $P_{\text{mean}}$  and  $WS_{\text{mean}}$ , as well as between temperature and relative humidity parameters. There is a positive correlation in other parameters. While the  $Q_{\text{mean}}$  shows the highest correlation with  $P_{\text{mean}}$  and  $P_{\text{max}}$ , it has a low correlation with other parameters.  $P_{\text{mean}}$  ( $P_{\text{max}}$ ) parameter has a high correlation with  $Q_{\text{mean}}$  and  $P_{\text{max}}$  ( $Q_{\text{mean}}$  and  $P_{\text{mean}}$ ). Temperature parameters have a high positive correlation with each other and a high negative correlation with  $RH_{\text{mean}}$  and  $RH_{\text{min}}$ . There is also a high positive correlation between  $RH_{\text{mean}}$  and  $RH_{\text{min}}$ .  $RH_{\text{max}}$  shows the highest correlation with  $RH_{\text{mean}}$ .  $WS_{\text{mean}}$  shows the highest correlation with temperature parameters as negative.

**Table 2.** Correlation matrix of hydrometeorological parameters

	$Q_{\text{mean}}$	$P_{\text{mean}}$	$P_{\text{max}}$	$T_{\text{mean}}$	$T_{\text{min}}$	$T_{\text{max}}$	$R_{\text{mean}}$	$R_{\text{min}}$	$R_{\text{max}}$	$WS_{\text{mean}}$
$Q_{\text{mean}}$	1	0.52	0.32	0.06	0.09	0.05	0.05	0.06	0.04	0.11
$P_{\text{mean}}$	0.52	1	0.74	0.08	0.09	0.10	0.32	0.14	0.19	-0.11
$P_{\text{max}}$	0.32	0.74	1	0.08	0.07	0.11	0.24	0.12	0.19	0.01
$T_{\text{mean}}$	0.06	0.08	0.08	1	0.97	0.98	-0.56	-0.57	-0.13	-0.27
$T_{\text{min}}$	0.09	0.09	0.07	0.97	1	0.94	-0.53	-0.54	-0.12	-0.30
$T_{\text{max}}$	0.05	0.10	0.11	0.98	0.94	1	-0.54	-0.58	-0.10	-0.29
$R_{\text{mean}}$	0.05	0.32	0.24	-0.56	-0.53	-0.54	1	0.73	0.31	0.14
$R_{\text{min}}$	0.06	0.14	0.12	-0.57	-0.54	-0.58	0.73	1	0.08	0.19
$R_{\text{max}}$	0.04	0.19	0.19	-0.13	-0.12	-0.10	0.31	0.08	1	0.10
$WS_{\text{mean}}$	0.11	-0.11	0.01	-0.27	-0.30	-0.29	0.14	0.19	0.10	1

## 2.2. Trend Analysis

In this study, three innovative graphical trend methods, namely the Onyutha Trend Test (OTT), Şen-Innovative Trend Analysis (Şen-ITA) and Combination of Wilcoxon Test and Scatter Diagram (CWTSD) were used. These methods also offer the opportunity to make statistical trend interpretations. The statistical test statistics of these three methods were also compared with the results of the classical Mann-Kendall trend method. The methodology for these methods is presented below.

### 2.2.1 Onyutha trend test (OTT)

The OTT, which is applied by converting hydrometeorological time series to non-parametric rescaled time series, is very useful in the analysis of sub-trends [25]. It also provides the opportunity to observe climatic changes between years. Unlike many trend analysis methods in the literature, monotonic and sub-trend analysis can be done visually. Based on the rescaled series obtained,  $a_j$  and  $q_k$  graphs should be drawn to make visual analyzes. These statistics are calculated with the help of the formulas given below.

$$a_j = \sum_{i=1}^j e_{y,i} \text{ for } 1 \leq j \leq n \quad (1)$$

$$q_k = \sum_{i=1}^k a_j \text{ for } 1 \leq k \leq n \quad (2)$$

Here,  $a_j$  is a variance of time, and  $q_k$  is a statistic required for graphical analysis. The Z statistic is calculated to analyze the trend statistically.  $e_{y,i}$  is the rescaled series of the hydrometeorological time series,  $n$  represents the total number of data. Confidence interval limits (CILs) ( $100(1-\alpha)\%$ ) should be determined for analysis according to significance levels. If the  $q_k$  curve falls between CILs, the existence of a significant trend is denied according to the significance level considered. Within the scope of the study, a 95% significance level was considered. CILs and Z are calculated with the help of the following equations.

$$CIL_s = \pm \left| Z_{\alpha/2} \right| x \sqrt{VF(T)} \quad (3)$$

$$Z = \frac{T}{\sqrt{V(T)}} \quad (4)$$

Here, the T value is the standardized version of the Z statistic. VF(T) is expressed as the variance of the T-test statistic. VF(T) is the corrected version of V(T) to save it from permanent effects on the time series [25]. The cumulative sum of difference (CSD)-based variability analyzes tool (CSD-VAT) was used to apply the OTT. To learn more about the OTT, a useful and innovative method, and CSD-VAT refer to

references [25-27].

### 2.2.2 Combination of Wilcoxon test and scatter diagram (CWTSD)

This method was proposed by Saplıoğlu and Güçlü [28] and offers graphical and statistical trend analysis. In the graphical application of the method, first of all, the time series at hand is divided into two equal parts. In the two sub-series obtained, without any order, the first sub-series is represented on the horizontal axis and the second sub-series on the vertical axis, and the data are mutually marked in the Cartesian coordinate system. The triangular area above (below) the 1:1 straight line represents the ascending (descending) trend region. Depending on which triangle region the marked points are located in, the increasing or decreasing trend evaluation is made visually. If the points are equally distributed in both triangle regions, there is no trend, it is interpreted. According to this method, statistical trend evaluation is made to the Wilcoxon test. The calculation procedure of the Wilcoxon test is available in various studies in the literature and is not included here [20, 23]. To the  $Z_{\text{Wilcoxon}}$  value obtained as a result of the application, the trend evaluation is made by comparing the  $Z_{\text{critic}}$  value at the  $\alpha$  significance level obtained from the standard normal distribution table [20, 23].

### 2.2.3 Şen innovative trend analysis (Şen-ITA)

With the non-parametric Şen-ITA method, independent of the distribution suggested by Şen [21], trend interpretation can be made both graphically and statistically. To make a trend analysis visually, the time series is divided into two equal parts as in the CWTSD method. The two sub-series obtained are ordered from smallest to largest (or from largest to smallest). Then, the values in both sub-series are marked mutually, with the first sub-series on the horizontal axis and the second sub-series on the vertical axis. Considering the distribution of the marked points according to the 1:1 straight line, five different trend evaluations can be made monotonic increasing trend, monotonic decreasing trend, non-monotonic increasing trend, non-monotonic decreasing trend, and no trend. See references for details of the method [20-21]. Şen-ITA trend indicator ( $D_{\text{Şen-ITA}}$ ) is calculated by Equation 5.

$$D_{\text{Şen-ITA}} = \frac{1}{n} \sum_{i=1}^n 10 \frac{(y_i - x_i)}{\bar{x}} \quad (5)$$

Here,  $n$ ,  $x_i$ ,  $y_i$ , and  $\bar{x}$  represent the number of data in each subseries, the data value at the time  $i$  in the first ordered subseries, the data value at the time  $i$  in the second ordered subseries, and the mean of the first subseries. The negative (positive) value of  $D_{\text{Şen-ITA}}$  shows a decreasing (increasing) trend [18, 20, 29].

### 2.2.4 Mann-Kendall (MK) trend test

The MK method [30-31], which is a non-parametric and distribution-independent method, is one of the most widely used methods in trend analysis studies. The test statistic of the MK method is calculated by Equation 6.

$$z_{\text{MK}} = \begin{cases} \frac{S-1}{\sqrt{\text{Var}(S)}} & \text{if } S > 0 \\ 0 & \text{if } S = 0 \\ \frac{S+1}{\sqrt{\text{Var}(S)}} & \text{if } S < 0 \end{cases} \quad (6)$$

$S$  value is calculated by Equation 7 and Equation 8 and  $n$  is data length.  $X_i$  and  $X_j$  represent data values at  $i$  and  $j$  times, respectively.  $\text{sgn}$  is the sign function.

$$S = \sum_{i=1}^{n-1} \sum_{j=i+1}^n \text{sgn}(x_j - x_i) \tag{7}$$

$$\text{sgn}(x_j - x_i) = \begin{cases} +1 & \text{if } (x_j - x_i) > 0 \\ 0 & \text{if } (x_j - x_i) = 0 \\ -1 & \text{if } (x_j - x_i) < 0 \end{cases} \tag{8}$$

Var(S) is calculated by equation 9. In Equation 9, k represents the number of connected groups, and  $t_i$  represents the number of data values in the  $i^{\text{th}}$  cluster. If the sign of the MK test statistic ( $Z_{MK}$ ) and S values calculated with Equation 6 and Equation 7 is negative (positive), there is a decreasing (increasing) trend in the time series. The significance of the trends is determined by the selected  $\alpha$  significance level. In this study,  $\alpha=0.05$  significance level ( $Z_{\text{critic}}=1.96$ ) was used. If  $|Z_{MK}| < Z_{1-\alpha/2}$ , the null hypothesis ( $H_0$ ) is accepted and the alternative hypothesis ( $H_1$ ) is rejected. The  $H_1$  hypothesis shows that there is a significant trend at the selected  $\alpha$  significance level in the examined time series [16, 18].

$$\text{Var}(S) = \frac{n(n-1)(2n+5) - \sum_{i=1}^k t_i(t_i-1)(2t_i+5)}{18} \tag{9}$$

Before applying the MK test, it should be checked whether there is a serial correlation in the examined time series. In the serial correlation control, first of all, the autocorrelation value ( $r_1$ ) for lag-1 is calculated with the following equation.

$$r_1 = \frac{\frac{1}{n-1} \sum_{i=1}^{n-1} (x_i - \bar{x})(x_{i+1} - \bar{x})}{\frac{1}{n} \sum_{i=1}^n (x_i - \bar{x})^2} \tag{10}$$

Here,  $n$ ,  $x_i$  and  $\bar{x}$  represent the number of samples, the serial value at the time  $i$ , and the sample mean, respectively. If the calculated  $r_1$  value is between the limit values given by Equation 11 (for  $\alpha=0.05$ ), there is no serial correlation in the time series, otherwise, there is a serial correlation.

$$\frac{-1-1.96\sqrt{(n-2)}}{n-1} \leq r_1 \leq \frac{-1+1.96\sqrt{(n-2)}}{n-1} \tag{11}$$

In this study, in the case of serial correlation, the pre-whitening procedure suggested by Von Storch and Navarra [32] was applied to the time series (Equation 12).

$$y_i = x_{i+1} - r_1 x_i \tag{12}$$

The MK method should be applied to the pre-whitened time series obtained by Equation 12.

#### 4. TREND ANALYSIS RESULTS

##### 4.1. OTT Results

The time series of the different parameters of the Karasu sub-basin within the borders of the Euphrates-Tigris basin and the  $a_j$  and  $q_k$  series obtained by applying the OTT is given in Figure 2.

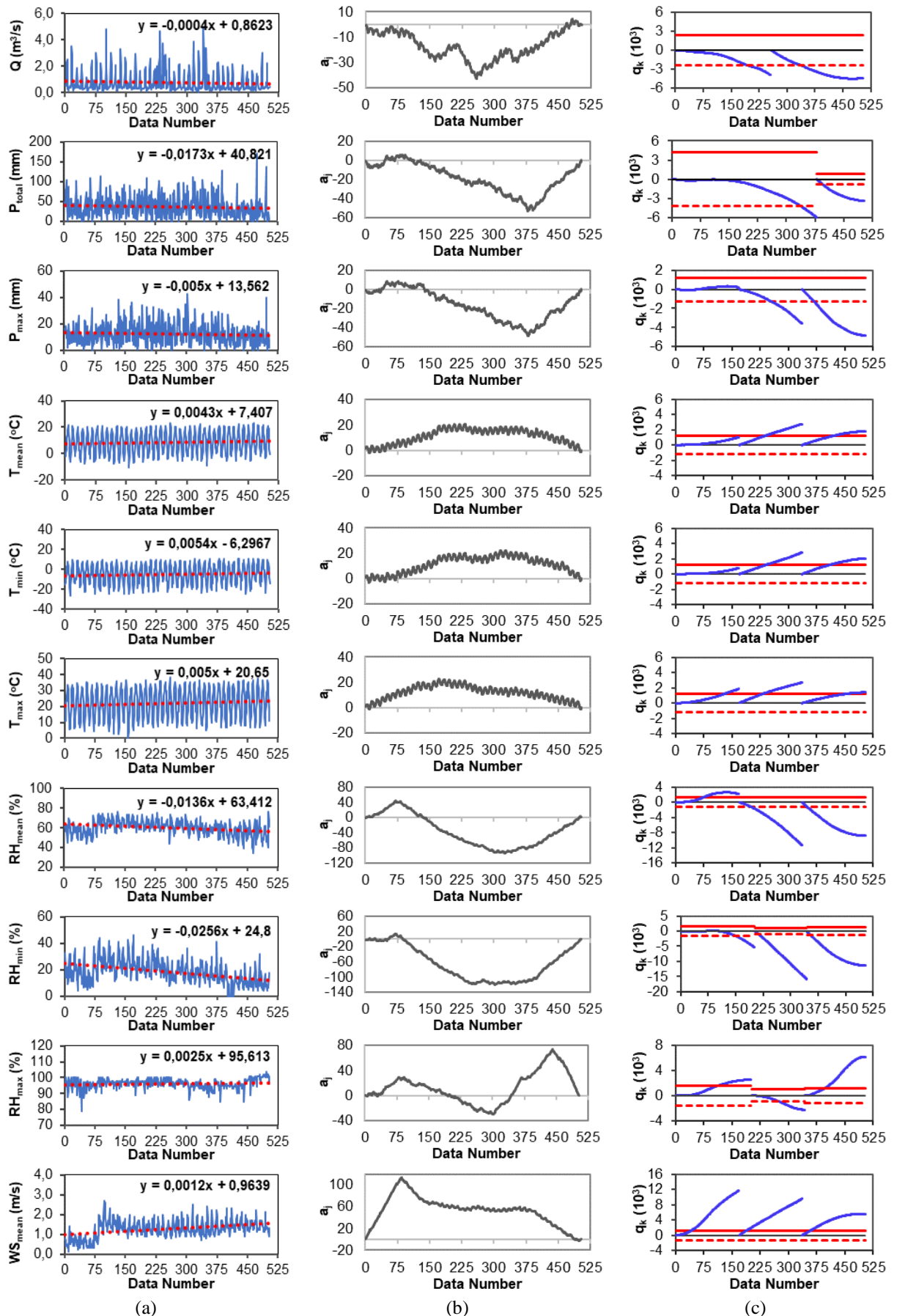


Figure 2. a) Time series, b)  $a_j$  series, and c)  $q_k$  series for the hydrometeorological parameters

Changes that cannot be detected from time series can be observed with the help of  $a_j$  series, which is a variance of time. The sub-periods determined from the  $a_j$  series are examined in the  $q_k$  time series to their significance levels. According to Figure 2, the temperature parameters ( $T_{\min}$ ,  $T_{\max}$ , and  $T_{\text{mean}}$ ) increase throughout the study period. However, it is noteworthy that the trend magnitude of these parameters differs in the sub-periods. Especially in the middle of the study period, they have a strong increasing trend. When the streamflow time series is examined, it is determined from the linear slope that the general behavior is in the decreasing direction. The  $a_j$  series of the flow indicates a break in the middle of the study period (about 1999). There is a significant decreasing trend for the two determined sub-periods. Although a slightly increasing trend, which was not significant until 1990, was observed in two parameters of precipitation ( $P_{\text{total}}$  and  $P_{\max}$ ), the strong decreasing trend dominated the ongoing process. When three different parameters of relative humidity ( $RH_{\text{mean}}$ ,  $RH_{\max}$ , and  $RH_{\min}$ ) are examined, there is a decrease for  $RH_{\min}$  in the first sub-period and an increase for other parameters. Significant decreasing trend behavior was observed for all three parameters in the second sub-period, which coincided with the middle of the study period. In the last sub-period,  $RH_{\max}$  has a significant increase, while other parameters have a significantly decreasing trend. There is a strong increasing trend in all three sub-periods determined for mean wind speed ( $WS_{\text{mean}}$ ). There is a very high increasing trend at a 95% significance level. The break at the beginning of the study period is quite remarkable. Breaks were observed in many parameters between 1985-1990. It is thought that there were important hydrometeorological changes between these years.

#### 4.2. CWTSD and Şen-ITA Results

To apply the CWTSD and Şen-ITA method to the monthly scale values of the meteorological parameters belonging to the meteorological observation station no 17688 and runoff data belonging to the flow observation station D21A168 for the period 1979-2020 (42 years), firstly, the data of each parameter was divided into two sub-series. The first sub-series covers the period 1979-1999, and the second sub-series covers the period 2000-2020. CWTSD graphs were obtained by marking the first (second) sub-series on the horizontal (vertical) axis without any ordering in the two sub-series obtained for each parameter (Non-Ordered ITA=NO-ITA). Şen-ITA graphs were drawn with the mutual marking of the data obtained by ordering the data of the two sub-series from the smallest to the largest on the same graph. The obtained NO-ITA and Şen-ITA graphs are presented in Figure 3. As seen in Figure 3, for the parameters  $Q_{\text{mean}}$ ,  $P_{\max}$ ,  $RH_{\text{mean}}$ , and  $RH_{\min}$ , according to both NO-ITA and Şen-ITA methods, most of the points are in the region below the 1:1 line and there is a decreasing trend. For  $T_{\text{mean}}$ ,  $T_{\min}$ ,  $T_{\max}$ , and  $WS$  parameters, according to both methods, most of the points are in the region above the 1:1 line and there is an increasing trend. As a result of visual inspection for  $P_{\text{total}}$  and  $RH_{\max}$ , it is seen that the distribution of points in both triangular regions for the NO-ITA method is approximately equal. This makes it difficult to interpret a decreasing or increasing trend according to NO-ITA. According to the Şen-ITA method, while there is a decreasing trend in the  $P_{\text{total}}$  parameter, it can be said that there is no trend in the  $RH_{\max}$  parameter.

#### 4.3 Statistical Evaluation of MK, OTT, CWTSD and Şen-ITA Trend Analysis Methods

The hydrometeorological parameters, whose temporal variability in the 1979-2020 period was examined graphically using OTT, Şen-ITA, and CWTSD methods, were also statistically evaluated for the same methods and compared with the classical Mann-Kendall (MK) method. Statistical evaluation of the graphics of the CWTSD method was performed with the Wilcoxon test, and statistical trend evaluation for Şen-ITA was performed with the D indicator.

The results obtained are given in Table 3. Before applying the MK method, it was checked whether there is a serial correlation in the time series of hydrometeorological parameters. For this purpose, the correlation coefficients ( $r_1$ ) calculated with Equation 10 for lag-1 of each parameter are given in Table 3. The  $r_1$  values for all parameters are positive. The highest (lowest) serial correlation was obtained for temperature (precipitation) parameters. Since the calculated  $r_1$  values are outside the limit values of -0.089 and 0.085 determined by Equation 11, there is a serial correlation in the time series of each parameter. The



serial correlation was removed from the time series with pre-whitening (Equation 12), and then the MK test was applied.

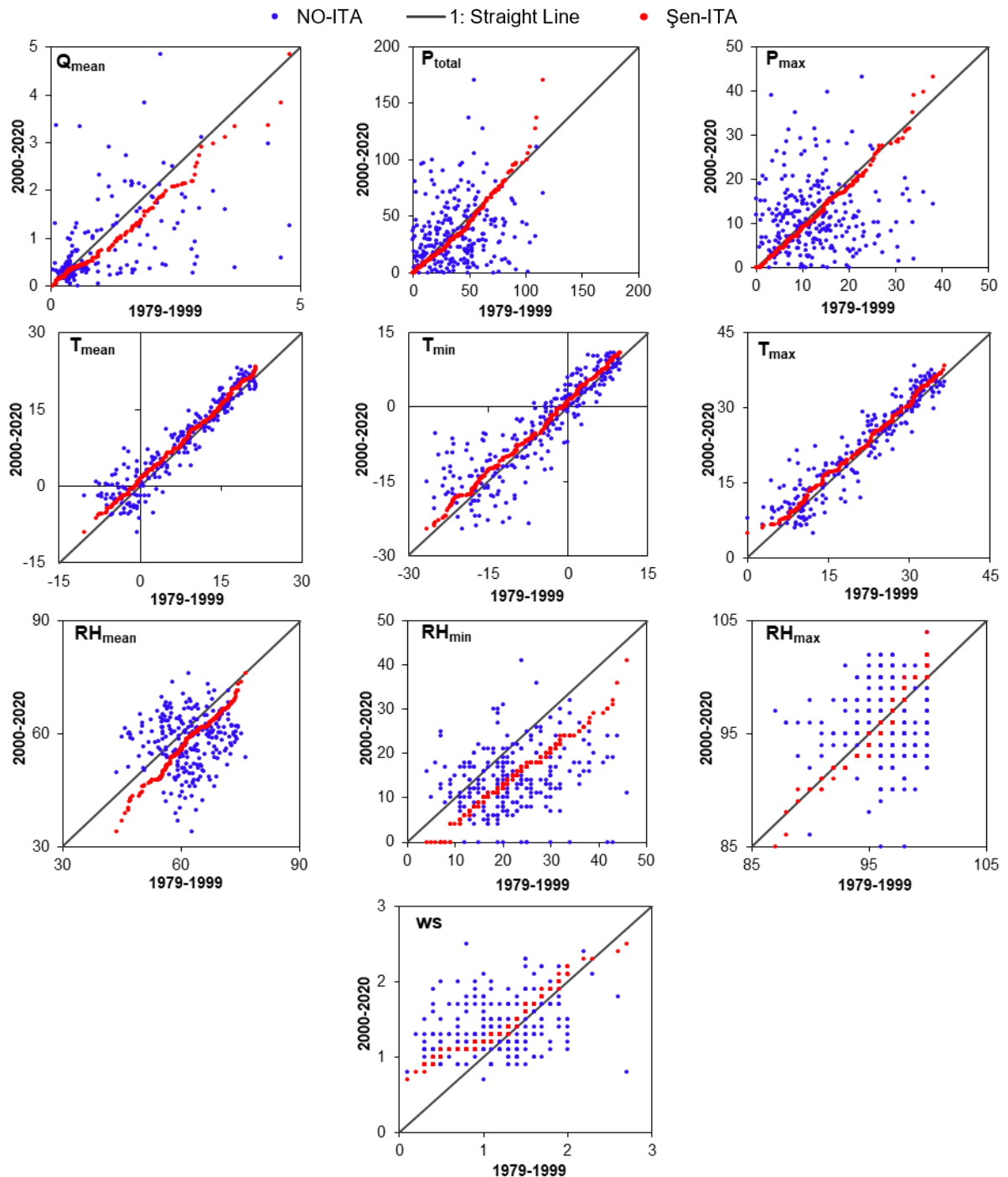


Figure 3. Sen-ITA and NO-ITA graphs

Negative values in Table 3 represent a decreasing trend and positive values represent an increasing trend. Significant trends were determined according to  $\alpha=0.05$  significance level ( $Z_{\text{critical}} = \pm 1.96$ ). According to the results in Table 3, the trend direction for each parameter (except  $RH_{\text{max}}$ ) is generally consistent with each other in all methods. In  $Q_{\text{mean}}$ ,  $P_{\text{total}}$ ,  $P_{\text{max}}$ ,  $RH_{\text{mean}}$ , and  $RH_{\text{min}}$  parameters, there is a decreasing trend in all methods, and in other parameters, there is an increasing trend in all methods. Only a slight decrease trend (insignificant) was determined in Sen-ITA method and an increasing trend (insignificant) was

determined in other methods in the  $RH_{max}$ . In the  $RH_{min}$  and  $WS_{mean}$  parameters, the test statistics values of each method show significant decreasing and significantly increasing trends, respectively. In the  $Q_{mean}$  parameter, MK and OTT test statistics show an insignificant decreasing trend, and Wilcoxon test statistics show a significant decreasing trend. In this parameter, the condition  $|D| > Z_{critical}$  was provided and the decreasing trend was determined according to the Şen-ITA method. In  $P_{total}$ ,  $Z_{MK}$  and  $Z_{OTT}$  values are outside the values of  $\pm 1.96$  and there is a significant decreasing trend due to negative values, while there is an insignificant decreasing trend compared to the other two methods. While there is a decreasing trend for  $P_{max}$  to all methods, there is a significant trend with  $Z_{MK}=-2.14$  value only to the MK method. In the study conducted by Buyukyildiz [20], the trend analysis results for the annual total precipitation in the entire Euphrates-Tigris Basin in the 1965-2020 period also showed a decreasing trend in the precipitation data in the entire basin.

**Table 3.** Statistical trend analysis results

		$Q_{mean}$	$P_{total}$	$P_{max}$	$T_{mean}$	$T_{min}$	$T_{max}$	$RH_{mean}$	$RH_{min}$	$RH_{max}$	$WS_{mean}$
MK	$r_1$	0.487	0.192	0.140	0.835	0.791	0.829	0.613	0.667	0.487	0.700
	$Z_{MK}$	-1.38	<b>-2.40*</b>	<b>-2.14*</b>	0.22	0.61	0.16	<b>-3.47*</b>	<b>-3.99*</b>	0.73	<b>4.46*</b>
OTT	$Z_{OTT}$	-1.84	<b>-2.15*</b>	-1.65	<b>4.40*</b>	<b>3.73*</b>	<b>5.14*</b>	-1.22	<b>-2.24*</b>	0.47	<b>2.77*</b>
CWTSD	$Z_{Wilcoxon}$	<b>-4.30*</b>	-1.77	-1.58	<b>5.60*</b>	<b>4.13*</b>	<b>5.50*</b>	<b>-6.66*</b>	<b>-10.43*</b>	0.99	<b>6.87*</b>
Şen-ITA	$D_{Şen-ITA}$	<b>-1.97</b>	-0.85	-0.82	1.21	<b>2.11</b>	0.51	-0.70	<b>-3.50</b>	-0.02	<b>1.98</b>

\*Significant trend at the  $\alpha=0.05$  confidence level

According to Table 3,  $Z_{OTT}$  and  $Z_{Wilcoxon}$  test statistics in  $T_{mean}$  and  $T_{max}$  parameters are greater than the critical value of 1.96 and there is a significant increase, while in other methods there is an increasing trend, and it is not significant. An increasing trend was determined for  $T_{min}$  in all methods. However, there is an insignificant increase trend with  $Z_{MK}=0.61$ .  $Z_{OTT}$  and  $Z_{Wilcoxon}$  values also show an increasing trend in this parameter with the values of 3.73 and 4.13, respectively. In addition, it is seen that  $D_{Şen-ITA}=2.11 > Z_{critical}$  has occurred. There is a significant decreasing trend in the  $RH_{mean}$  parameter according to the  $Z_{MK}$  and  $Z_{Wilcoxon}$  values, and an insignificant decreasing trend according to the other two methods. In the  $RH_{max}$  parameter, none of the trends determined are significant. The trend evaluations obtained by Şen-ITA and NO-ITA graphs given in Figure 3 and the statistical trend results given for these methods in Table 3 are largely consistent.

## 5. DISCUSSION AND CONCLUSIONS

All methods used in this study are nonparametric methods. Therefore, they do not require criteria such as linearity, normal distribution and independence required in time series for parametric methods to be applied. MK and Şen-ITA methods are frequently used trend analysis methods in the literature. OTT and CWTSD, which are innovative trend analysis methods that are quite new compared to the Şen-ITA method, are increasingly preferred in different fields with their advantages. Both statistical and innovative trend approaches offer holistic trend detection. However, in addition to holistic trend detection, innovative trend methods have the advantages of observing sub-trends, graphically displaying the results, and visually evaluating the trend, unlike statistical methods such as MK. For example, Şen-ITA and CWTSD methods allow more detailed comments on the detection of the trend of "low", "medium" and "high" values of the analyzed climate parameter. In addition to the overall trends in the whole time series, OTT also allows the determination of temporal sub-trends unlike Şen-ITA and CWTSD methods. Sub-trends cannot be detected by traditional trend methods (such as MK, Spearman's Rho, Sen's T). Among the innovative methods, Şen-ITA and CWTSD methods have the additional advantages of being easy to apply and having low computational cost compared to OTT method. The OTT method has a more complex

calculation and visualization procedure. In the visual analysis provided by Şen-ITA, the data set needs to be ordered. This leads to the loss of information about the natural distribution of the data set. This disadvantage is not present in the other two innovative methods.

The results show that there is an increasing trend in temperature (mean, min, max), maximum relative humidity and mean wind speed, and a decreasing trend in other parameters. This indicates that climate change is strongly observed in Karasu basin. In the innovative methods (OTT and CWTSD), it is observed that the direction of trends produces results consistent with the MK. This shows that the strong climatic change detected by the MK is confirmed by innovative methods. However, there are differences in the significance of some parameters compared to the MK. This indicates that the methods may have different sensitivity in trend analysis of different data sets.

MK is a non-parametric method recommended by the World Meteorological Organization, which is often preferred in trend analysis. Since its introduction to the literature, its robustness has been comparatively evaluated in many studies [33]. However, it is still sensitive to serial correlation. Therefore, preprocessing is recommended before applying the MK. The serial correlation control and pre-whitening processes used in this study are examples. In innovative methods, this weakness is eliminated within the method. In addition, visual trend analysis, which is not available in MK, is one of the important differences in innovative methods. The MK test statistic is robust when dealing with non-normally distributed data, censored data, and time series with missing values since it is determined by the rankings and sequences of time series rather than the original values [34]. This is one of the strengths of the MK method.

In this study, the effects of climate change on hydrometeorological parameters in the Karasu Sub-basin, one of the sub-basins of the Euphrates-Tigris Basin in Türkiye, were investigated. Trend analyses of ten hydrometeorological parameters ( $Q_{\text{mean}}$ ,  $P_{\text{total}}$ ,  $P_{\text{max}}$ ,  $T_{\text{mean}}$ ,  $T_{\text{min}}$ ,  $T_{\text{max}}$ ,  $RH_{\text{mean}}$ ,  $RH_{\text{min}}$ ,  $RH_{\text{max}}$ , and  $WS_{\text{mean}}$ ) were carried out with four different methods using monthly scale data for the period 1970-2020. The results obtained by MK, OTT, CWTSD, and Şen-ITA methods were consistent with each other in terms of the direction of the trend. According to the results obtained, a decreasing trend was obtained in  $Q_{\text{mean}}$ ,  $P_{\text{total}}$ ,  $P_{\text{max}}$ ,  $RH_{\text{mean}}$ , and  $RH_{\text{min}}$  parameters compared to all methods, and an increasing trend was obtained in other parameters compared to all methods ( $RH_{\text{max}}$  also decreased compared to Şen-ITA). However, approximately 55% of the trends obtained were significant at the  $\alpha=0.05$  significance level, while the rest gave the result of an insignificant trend. The results show that climate change causes a decrease in precipitation with the increase in temperature in the basin and a decrease in river flow. In a study investigating the sensitivity of streamflow to the effects of climate change in the Euphrates-Tigris basin, a general decrease in precipitation and streamflow data, while an increasing trend in temperature and potential evapotranspiration data was determined [35]. According to projection studies on the relative humidity in Turkey, significant decreases are expected in relative humidity averages, especially in the periods after 2040 [36]. The decrease in relative humidity also has a negative effect on precipitation and causes a decrease in precipitation. This situation also poses a threat to the basin in terms of drought. It is also seen in the trend results obtained. Along with the increase in temperature, the trend of decreasing relative humidity, precipitation, and river flow poses a risk in terms of water resources in the Karasu sub-basin and the transboundary Euphrates-Tigris Basin. Such studies will shed light on decision-makers to eliminate the negative effects of climate change on the management and sustainability of water resources both for Türkiye, which constitutes the upstream part of the basin and for other riparian neighboring countries. Therefore, it is of great importance to carry out such studies on a larger scale.

### Acknowledgements

The authors would like to thank the General Directorate of State Hydraulic Works (Türkiye) for providing the streamflow data, and the State Meteorological Service (Türkiye) for providing the hydrometeorological data.

### Declaration of Ethical Standards

Not applicable.

### Credit Authorship Contribution Statement

The authors contributed equally to the study conception and design.

### Declaration of Competing Interest

The authors declare that they have no known competing interest.

### Funding

The authors declare that they have no fund, or research grant (and their source) received in the course of study, research or assembly of the manuscript.

### Data Availability

Not applicable.

### REFERENCES

- [1] H. J. Marvin, G. A. Kleter, M. Y. Noordam, E. Franz, D. J. Willems, and A. Boxall, "Proactive systems for early warning of potential impacts of natural disasters on food safety: Climate-change-induced extreme events as case in point", *Food Control*, vol. 34, no. 2, pp. 444-456, 2013.
- [2] U. K. Mandal, B. Maji, S. Mullick, D. B. Nayak, K. K. Mahanta, and S. Raut, "Global climate change and human interferences as risk factors, and their impacts on geomorphological features as well as on farming practices in Sundarbans eco-region", *The Sundarbans: A Disaster-Prone Eco-Region: Increasing Livelihood Security*, vol. 30, pp. 405-437, 2019.
- [3] A. Iglesias, L. Garrote, S. Quiroga, and M. Moneo, "A regional comparison of the effects of climate change on agricultural crops in Europe", *Climatic Change*, vol. 112, pp. 29-46, 2012.
- [4] N. W. Arnell, J. A. Lowe, A. J. Challinor, and T. J. Osborn, "Global and regional impacts of climate change at different levels of global temperature increase", *Climatic Change*, vol. 155, pp. 377-391, 2019.
- [5] B. K. Mishra, P. Kumar, C. Saraswat, S. Chakraborty, and A. Gautam, "Water security in a changing environment: Concept, challenges and solutions", *Water*, vol. 13, no. 4, p. 490, 2021.
- [6] M. A. Benevolenza, and L. DeRigne, "The impact of climate change and natural disasters on vulnerable populations: A systematic review of literature", *Journal of Human Behavior in the Social Environment*, vol. 29, no. 2, pp. 266-281, 2019.
- [7] M. Saatsaz, "A historical investigation on water resources management in Iran", *Environment, Development and Sustainability*, vol. 22, pp. 1749-1785, 2020.
- [8] C. Nhemachena, L. Nhamo, G. Matchaya, C. R. Nhemachena, B. Muchara, S. T. Karuaihe, and S. Mpandeli, "Climate change impacts on water and agriculture sectors in Southern Africa: Threats and opportunities for sustainable development", *Water*, vol. 12, no. 10, p. 2673, 2020.
- [9] L. Garrote, "Managing water resources to adapt to climate change: facing uncertainty and scarcity in a changing context", *Water Resources Management*, vol. 31, no. 10, pp. 2951-2963, 2017.
- [10] Y. Pokhrel, F. Felfelani, Y. Satoh, J. Boulange, P. Burek, A. Gädeke, ..., and Y. Wada, "Global terrestrial water storage and drought severity under climate change", *Nature Climate Change*, vol. 11, no.3, pp. 226-233, 2021.
- [11] V. Chandole, G. S. Joshi, and S. C. Rana, "Spatio-temporal trend detection of hydro-meteorological parameters for climate change assessment in Lower Tapi river basin of Gujarat state, India", *J*

- Atmos Solar-Terr Phys*, vol. 195, p.105130, 2019.
- [12] A. I. Ginzburg, A. G. Kostianoy, I. V. Serykh, and S. A. Lebedev, "Climate change in the hydrometeorological parameters of the Black and Azov Seas (1980–2020)", *Oceanology*, vol. 61, no.6, pp. 745-756, 2021.
- [13] M. Zakwan and Z. Ahmad, "Trend analysis of hydrological parameters of Ganga River", *Arab J Geosci* vol. 14, no. 163, pp. 1–15, 2021.
- [14] Z. Sa'adi, S. Shahid, T. Ismail, E. S. Chung, and X. J. Wang, "Trends analysis of rainfall and rainfall extremes in Sarawak, Malaysia using modified Mann-Kendall test", *Meteorol Atmos Phys*, vol. 131, no. 1, pp. 263–277, 2019.
- [15] E. N. Tehrani, H. Sahour, and M. J. Booij, "Trend analysis of hydro-climatic variables in the north of Iran", *Theor Appl Climatol*, vol. 136, no. 1, pp. 85–97, 2019.
- [16] R. Ali, A. Kuriqi, S., Abubaker, and O. Kisi, "Long-term trends and seasonality detection of the observed flow in Yangtze River using Mann-Kendall and Sen's innovative trend method", *Water*, vol. 11, no. 9, p. 1855, 2019.
- [17] M. Collaud Coen, E. Andrews, A. Bigi, G. Martucci, G. Romanens, F. Vogt, and L. Vuilleumier, "Effects of the prewhitening method, the time granularity, and the time segmentation on the Mann–Kendall trend detection and the associated Sen's slope", *Atmospheric measurement techniques*, vol. 13, no. 12, pp. 6945-6964, 2020.
- [18] I. Ahmad, F. Zhang, M. Tayyab, M. N. Anjum, M. Zaman, J. Liu, ..., and Q. Saddique, "Spatiotemporal analysis of precipitation variability in annual, seasonal and extreme values over upper Indus River basin", *Atmospheric Research*, vol. 213, pp. 346-360, 2018.
- [19] T. Caloiero, "Evaluation of rainfall trends in the South Island of New Zealand through the innovative trend analysis (ITA)", *Theoretical and Applied Climatology*, vol. 139, no. (1-2), pp. 493-504, 2020.
- [20] M. Buyukyildiz, "Evaluation of annual total precipitation in the transboundary Euphrates–Tigris River Basin of Türkiye using innovative graphical and statistical trend approaches", *Applied Water Science*, vol. 13, no. 2, p. 38, 2023.
- [21] Z. Şen, "Innovative trend analysis methodology", *J Hydrol Eng*, vol. 17, no. 9, pp.1042–1046, 2012.
- [22] C. Köyceğiz and M. Buyukyildiz, "Temporal trend analysis of extreme precipitation: a case study of Konya Closed Basin", *Pamukkale Üniversitesi Mühendislik Bilimleri Dergisi*, vol. 25, no. 8, pp. 956-961, 2019.
- [23] Z. Eren and F. Kaya, "Fırat-Dicle Havza Koruma Eylem Planı çerçevesinde kentsel atıksu arıtma tesisinin Karasu Nehrinin su kalitesi üzerindeki etkisinin incelenmesi", *Ulusal Çevre Bilimleri Araştırma Dergisi*, vol. 3, no. 2, pp. 95-109, 2020.
- [24] M. C. Ulker and M. Buyukyildiz, "Evaluation of Runoff Simulation Using the Global BROOK90-R Model for Three Sub-Basins in Türkiye", *Sustainability*, vol. 15, no. 6, p. 5103, 2023.
- [25] C. Onyutha, "Graphical-statistical method to explore variability of hydrological time series", *Hydrology Research*, vol. 52, no. 1, pp. 266–283, 2021.
- [26] C. Onyutha, "Identification of sub-trends from hydro-meteorological series", *Stochastic Environmental Research and Risk Assessment*, vol. 30, no. 1, pp. 189–205, 2016a.
- [27] C. Onyutha, "Statistical analyses of potential evapotranspiration changes over the period 1930–2012 in the Nile River riparian countries", *Agricultural and Forest Meteorology*, vol. 226–227, pp. 80–95, 2016b.
- [28] K. Saphioğlu, and Y. S. Güçlü, "Combination of Wilcoxon test and scatter diagram for trend analysis of hydrological data", *Journal of Hydrology*, vol. 612, p. 128132, 2022.
- [29] W. D. S. Nisansala, N. S. Abeysingha, A. Islam, & A.M.K.R. Bandara, "Recent rainfall trend over Sri Lanka (1987–2017)", *Int J Climatol*, vol. 40, no. 7, pp. 3417–3435, 2020
- [30] H. B. Mann, "Nonparametric tests against trend", *Econometrica*, vol. 13, no. 3, pp. 245–259, 1945.
- [31] M. G. Kendall, "Rank correlation methods", 2nd impression. Charles Griffin and Company Ltd. London and High Wycombe, 1975.

- [32] H. Von Storch and A. Navarra (eds), "Analysis of climate variability: applications of statistical techniques", *Proceedings of an Autumn School Organized by the Commission of the European Community on Elba from October 30 to November 6, 1993, vol 2. Springer, 1995.*
- [33] F. Wang, W. Shao, H. Yu, G. Kan, X. He, D. Zhang, M. Ren, and G. Wang, "Re-evaluation of the Power of the Mann-Kendall Test for Detecting Monotonic Trends in Hydrometeorological Time Series", *Front. Earth Sci.*, vol. 8, no. 14, pp. 1-12, 2020.
- [34] R. M. Hirsch and J. R. Slack, "A nonparametric trend test for seasonal data with serial dependence. *Water Resour. Res.*, vol. 20, pp. 727-732, 1984.
- [35] A. Alivi, O. Yıldız, and G. Aktürk, "Fırat-Dicle havzasında yıllık ortalama akımlar üzerinde iklim değişikliği etkilerinin iklim elastikiyeti metodu ile incelenmesi", *Gazi Üniversitesi Mühendislik Mimarlık Fakültesi Dergisi*, vol. 36, no. 3, pp. 1449-1466, 2021.
- [36] O. Eskiöglü, H. Gürkan, H. Arabacı, M. Demircan, S. Şensoy, B. Yazıcı, A. Kocatürk, U.M. Sümer, and M. Coşkun, "İklim Değişikliğinin GFDL-ESM2M Modeline Göre Nispi Nem Üzerine Olası Etkisi", *IV. Türkiye İklim Değişikliği Kongresi, TİKDEK'2017*, 5-7 Temmuz 2017, İstanbul, 2017.